CDRI
Coalition for Disaster Resilient Infrastructure

CDRI Fellowship Programme

Cohort 2022-23

PROJECT REPORTS

CDRI Fellowship Cohort 2022-23 Project Reports

This compendium is a product of the Coalition for Disaster Resilient Infrastructure (CDRI) based on project reports of fellows of the CDRI Fellowship Programme Cohort 2022-23. All Fellowship Programme and project related details are provided at https://cdri.world/fellowship/

9 788196 501174

Disclaimer

The findings, analyses, interpretations and conclusions expressed in this compendium by fellows do not necessarily reflect the views of CDRI, its Executive Committee or the Members of the Coalition.

The boundaries and names shown on the maps and graphs and the designations used in this Report do not imply official endorsement or acceptance by CDRI.

The designations employed and the presentation of material on maps used in this compendium do not imply the expression of any opinion whatsoever on the part of the CDRI Secretariat concerning the legal status of any country, territory, city or area or of its authorities or concerning the delimitation of its frontiers or boundaries.

Nothing herein shall constitute or be considered a limitation upon or waiver of any legal, proprietary rights, privileges and immunities of CDRI, all of which are specifically reserved.

ISBN: 978-81-965011-7-4

Copyright @ 2024 CDRI.

All Right Reserved.

Rights and Permissions

This compendium is available under the Creative Commons Attribution 3.0 IGO license (CC BY 3.0 IGO) http:// creativecommons.org /licenses/by/3.0/igo. Under the Creative Commons Attribution license, you are free to copy, distribute, transmit, and adapt this Work, including for commercial purposes, but only under the following conditions:

Attribution - Every time the 'compendium' is either distributed, transmitted, adapted or in any other manner used, the same has to be cited as follows: "*CDRI (2024). CDRI Fellowship Cohort 2022-23 Project Reports, New Delhi.*"

Translations - If you create a translation of this compendium, the following disclaimer has to be added alongside with the attribution: "This translation was not created by CDRI and should not be considered an official CDRI translation. CDRI shall not be liable for any content or error in this translation."

Adaptations - If you adapt the compendium, the following disclaimer needs to be added along with the attribution: "This is an adaptation of an original compendium by CDRI. Views and opinions expressed in the adaptation are the sole responsibility of the author or authors of the adaptation and are not endorsed by CDRI."

Third-party content - CDRI does not necessarily own each component of the content contained within the compendium. CDRI therefore does not warrant that the use of any third-party-owned individual component or part contained in the compendium will not infringe on the rights of those third parties. The risk of claims resulting from such infringement rests solely with you. If you wish to re-use a component of the compendium, it is your responsibility to determine whether permission is needed for that re-use and to obtain permission from the copyright owner. Examples of components can include, but are not limited to, tables, figures, or images.

Any adaptation, distribution, publication, transmission or any other use of the compendium through this license by you shall not violate any law in force in the territory of use.

All queries with regards to this compendium should be addressed to the CDRI Fellowship Programme Team, Coalition for Disaster Resilient Infrastructure, 4th & 5th Floor, Bharatiya Kala Kendra, 1, Copernicus Marg, New Delhi, 110001, INDIA; e-mail: publications@cdri.world

Edited and Designed by: Rana Divyank Chaudhary, and Dr Saurabh Gupta

COALITION FOR DISASTER RESILIENT INFRASTRUCTURE

Launched by the Honourable Prime Minister of India, Shri Narendra Modi at the UN Climate Action Summit in New York on 23 September 2019, the Coalition for Disaster Resilient Infrastructure (CDRI) is a partnership of national governments, UN agencies and programmes, multilateral development banks and financing mechanisms, the private sector and knowledge institutions that aims to promote the resilience of new and existing infrastructure systems to climate and disaster risks in support of sustainable development.

CDRI FELLOWSHIP PROGRAMME

The CDRI Fellowship Programme was launched in September 2020 with the objective of investing in research and innovation to build back and build forward better as the world navigates through global transitions. The Fellowship Programme is a seed grant, providing financial support, capacity development and peer learning opportunities for individuals designing solutions for real-world problems related to the resilience of infrastructure.

For queries, contact: fellowship@cdri.world

Citation: Coalition for Disaster Resilient Infrastructure (2024) CDRI Fellowship Programme: Cohort 2022-23 - Project Reports.

Disclaimer: The views expressed in this publication reflect the opinions of the authors and not necessarily the official views of CDRI.

Copyright CDRI 2024: The text in this document may be reproduced free of charge provided that it is reproduced accurately, citing appropriately the authors and not used in a misleading context. No use of this publication may be made for resale or for any other commercial purpose whatsoever.

CDRI Fellowship Cohort 2022-23

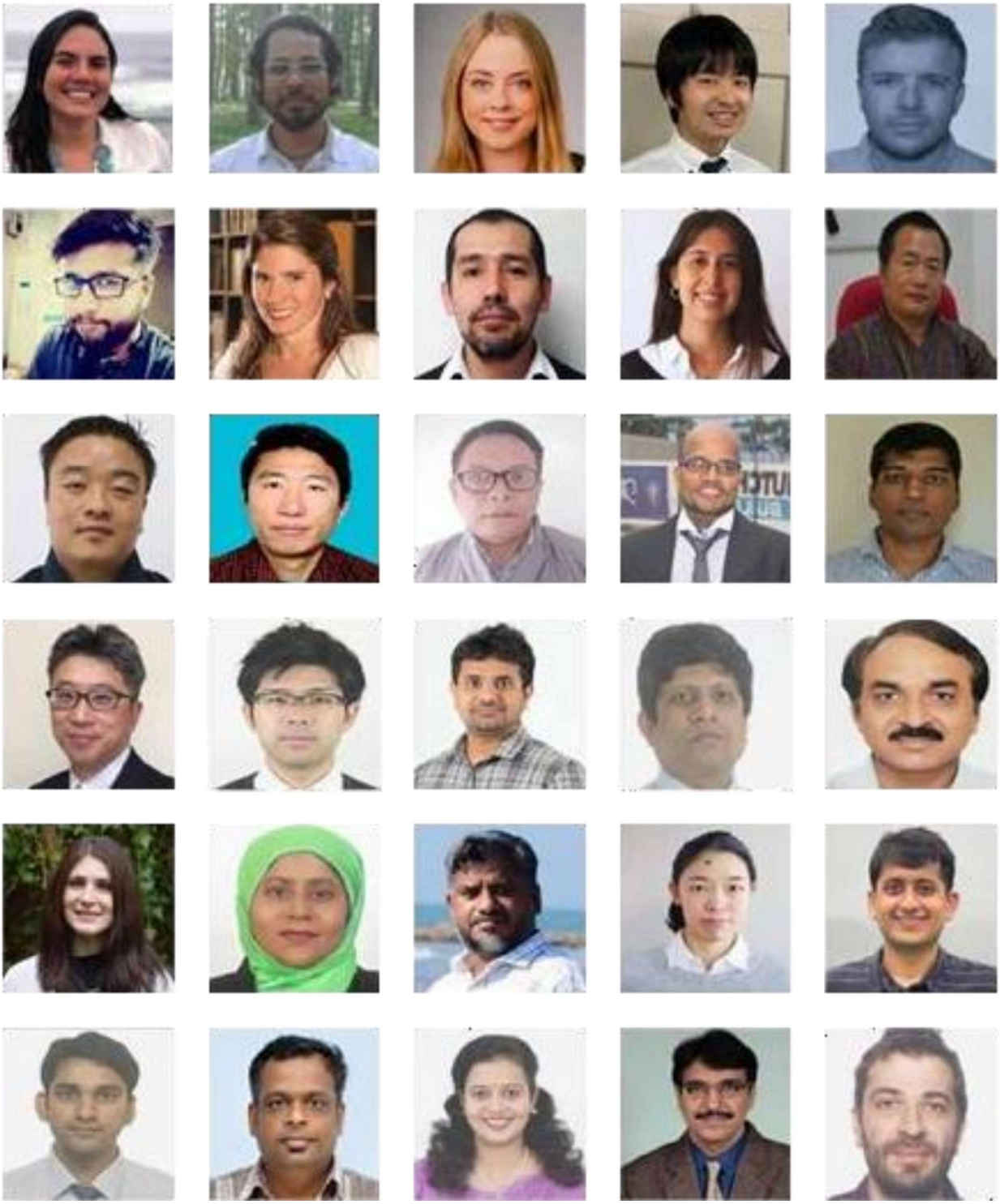

CONTENTS

1. Introduction

2. Managing and Financing Risk for Resilient Rural Road Networks: Standards Recommendations under a Multi-Hazard Approach

3. Water Collection, Storage and Treatment System in Floating Community Space in the Peruvian Amazon

4. Constructed Wetlands for Wastewater Treatment Plant Resilience

5. Risk Assessment and Hazard Mapping of Bhutan's Power System Infrastructure

6. Real-Time Scour Detection and Prediction for Structural Performance and Safety

7. Evaluation of Cyclonic Disaster Resilience of Coastal Healthcare Infrastructure in Bangladesh: A Special Comparison with Japan

8. Development of a Distributed Optical Fibre Sensor Network-Based Condition Monitoring System to Alert Road Collapses

9. Resilience of Power Grid Infrastructure with Renewables to Extreme Events in a Changing Climate

10. Flood Disaster Resilient Hydraulic Design of Bridges Exposed to Climate Change

11. Nature-Based Solutions for Resilient Infrastructure Systems

12. Framework for Evaluating Bridge Network Resilience by Considering Socio-Technical Attributes

13. Robust Approach to Assessing Post-Fire Structural Behaviour of High-Rise Mass Timber Buildings

14. Financial Decision Framework for Infrastructures Based on Disaster Damage Rating Models for Financial Decisions Using Machine Learning Approaches

15. Machine Learning-Based Unified Seismic Vulnerability Prediction Model for Heritage Minarets of India

Introduction

The Coalition for Disaster Resilient Infrastructure (CDRI) recognizes the need to invest in youth as a vital stakeholder group for a better future. The Coalition has designed knowledge initiatives targeting the youth, which foster cutting edge research and innovation towards resilience of infrastructure to climate and disaster risks.

The CDRI Fellowship Programme is one such initiative, launched in September 2020, a 12-month seed grant, providing financial support, peer learning and capacity development opportunities for individuals designing actionable solutions for real-world problems related to infrastructure resilience.

The second Cohort of CDRI Fellows comprises 14 teams from 11 countries engaged in a variety of research projects covering diverse hazard conditions under the following themes: early warning & decision support systems; resilience standards; nature-based solutions; risk finance; and health infrastructure resilience. The teams have successfully completed their Fellowship, demonstrating considerable progress in their research projects.

Innovative solutions that have emerged from this Cohort include guidelines for financing resilient rural road networks; water treatment systems; decision support tools to assess structural safety and health of bridges; framework to identify nature-based solutions for infrastructure resilience; and early warning system for collapses in road infrastructure.

This publication is a compilation of Project Abstracts of Cohort 2022-23 of the CDRI Fellowship Programme. For more details on these projects and the CDRI Fellowship Programme, visit www.cdri.world/fellowship

Managing and Financing Risk for Resilient Rural Road Networks: Standards Recommendations under a Multi-hazard Approach

Dr Alondra Chamorro
Associate Professor
Department of Construction Engineering and Management
School of Engineering, Pontificia, Universidad Católica de Chile

Dr Tomás Echaveguren
Associate Professor
Department of Civil Engineering
University of Concepción, Concepción, Biobío

Ms Natalia Nieto
Research Center for Integrated Disaster Risk Management

Under CDRI Fellowship Programme 2022-23

CDRI
Coalition for Disaster Resilient Infrastructure

Disclaimer: The views expressed in this paper reflect the opinions of the author and not necessarily the official views of CDRI.

Abstract

Damages induced by natural events to transportation systems create significant socioeconomic impacts in vulnerable territories, such as rural areas. Management and funding of rural roads are commonly centred on economic and technical dimensions under normal operational conditions, where the socioeconomic consequences of natural events are rarely accounted for in decision-making and guidelines.

The guidelines proposed in this research are unique and novel, as they suggest a holistic approach where socioeconomic impacts and risk assessment under multi-hazard scenarios are considered for managing and financing risk reduction of rural roads. The methodology is applied to a case study from which guidelines will result.

The research aims to propose holistic resilience guidelines that account for the socioeconomic impacts caused by natural events and financial requirements for resilient rural road networks in vulnerable territories and populations exposed to multiple natural hazards.

A diagnosis of current standards for financing and managing the risk of rural roads was developed. Next, a methodology to assess risk considering socioeconomic impacts was proposed. Subsequently, the method was applied to a rural road network in central Chile. Finally, resilience guidelines and financing recommendations were elaborated.

The proposed methodology was applied to a rural road network in central Chile exposed to seismic and hydro-meteorological hazards. The case study considered geographical, social, and environmental conditions typical of rural settings with limited accessibility. Based on this application and sensitivity analysis, resilience guidelines were proposed.

The analysis considered the simulation of seismic and hydro-meteorological hazards that have historically caused infrastructure damages and socioeconomic consequences in Chile. Economic losses were estimated regarding travel-time increase and agency costs, and social effects were included using social vulnerability of the exposed population in terms of Social Vulnerability Index (SoVI) (Cutter, 2003).

As a result, the document, "Guidelines for Managing Risk of Rural Road Networks", was developed. It consists of practical recommendations for risk management, including on parameters such as scalability, data sources, and Risk Governance, among others.

Acknowledgements

The system of managing risks from natural hazards for road networks called SIGeR-RV was developed as part of Project FONDEF (ANID-Chile) ID14I10309, "Research and Development of Models to Quantify Risk and Mitigation of Natural Events Affecting the National Road Network". This system corresponds to a web platform that considers the fragility of road infrastructures, social vulnerability of the population and critical infrastructure accessibility. It also comprises cost-effective optimization of mitigation strategies, user delay costs, agency costs and increased resilience. It is currently implemented by the Highway Directorate, Ministry of Public Works of Chile, in collaboration with Public-Private Partnerships and the National Office of Emergency of the Interior Ministry (ONEMI).

Funding

This research was supported by the 2022–2023 Fellowship of the Coalition for Disaster Resilient Infrastructure (CDRI), Application ID: 210916566.

1. Introduction

Transportation system damage induced by natural events generates significant socioeconomic impacts in vulnerable territories, such as rural areas. Existent rural road management systems are commonly focused on assets preservation and maintenance under normal operational conditions, mostly neglecting the socioeconomic consequences of extreme natural events (Chamorro et al., 2020).

Transportation systems are highly vulnerable to extreme natural hazards. These include damage to physical assets, operational disruptions in dependent systems, and derived socioeconomic impacts (Argyroudis et al., 2019). Countries with high exposure to natural events assume annual costs that may represent a significant proportion of the Gross Domestic Product (Kellenberg and Mobarak, 2008). These effects increase in highly vulnerable populations and access-dependent territories, such as rural communities in developing countries (Cutter et al., 2013). Rural road networks play a crucial role in societies' economic and social development, linking rural communities to education, health services, and markets.

Regarding financing, several countries have adopted cost-benefit analyses or cost-effectiveness methodologies to justify expenditure on road infrastructure. However, benefits derived from resilience or risk mitigation are rarely found in the literature. The problem is that decision-makers lack toolkits or guidelines for managing risk and financing the resilience of rural road networks.

The guidelines proposed in this research are unique and novel, as they study a scarcely discussed area of knowledge: the inclusion of socioeconomic impacts caused by multiple hazards in the management and finance of resilient rural road networks. The guidelines recommend how to evaluate risk under a multi-hazard approach, how to account for socioeconomic benefits of resilience when comparing mitigation strategies and how to incorporate these findings into the current financing methods. The methodology and proposed guidelines were applied to a case study in central Chile from which various recommendations for resilience were derived. For the application, a risk management system for road networks developed by the research team was used (Chamorro et al., 2023). The system includes a computational platform called SIGeR-RV, which considers the fragility of road infrastructures, social vulnerability of the population and accessibility to critical infrastructure. It also includes cost-effective optimization of mitigation strategies, user delay costs, agency costs, and an increase in resilience.

2. Aim, Objectives and Scope of the Research Study

The proposed research aims to offer holistic resilience standards that account for the socioeconomic impacts caused by natural events and the need to finance resilient rural road networks in vulnerable territories and populations when exposed to multiple natural hazards.

The research considers three objectives, each related to one stage of the methodology and one derived outcome of the study. The first objective is to conduct a complete diagnosis of available standards and methods for risk management and finance of rural road networks exposed to multiple hazards. Based on identified shortcomings in standards and available methodologies, a risk analysis methodology that accounts for socioeconomic impacts in multi-hazard scenarios is to be developed. The second objective is to apply this methodology to a case study. The proposed site for the case study is in a major watershed and mountainous region of Central Chile, with vulnerable communities linked through a rural road network with limited access and redundancy, a common characteristic in developing countries. The idea is to holistically quantify physical risk in terms of travel-time delays caused by simulated multi-hazard scenarios, socioeconomic effects caused by network disruptions and social vulnerability of affected communities due to reduced access. The proposed multi-hazard risk analysis methodology must be integrated into the SIGeR-RV system for application. The analysis outcomes have scientific relevance and will be disseminated in a research article. In addition, the application is expected to be useful for decision-makers and stakeholders in developing countries.

A third and final objective is to develop standard recommendations to manage risk for multi-hazard scenarios from a holistic approach and to account for these recommendations in the available financing methods. These include proposals to integrate the socioeconomic benefits of resilience in the available cost-benefit analysis methods for financing road infrastructures.

The analysis will consider seismic and hydro-meteorological hazards associated with certain damages on rural road networks.

3. Methodology

The research methodology considers the same three stages of the research design (see Figure 1).

The first stage identified the shortcomings in existing guidelines and the key socioeconomic variables to be analyzed. Then, a significant challenge was to develop a multi-hazard model for risk analysis and to address how to assign mitigation strategies under multi-hazard scenarios. The proposed methodology was developed after an extensive review of the state of the art and the state of the practice. Attention was also given to adapting single-hazard risk analysis of road infrastructure to a multi-hazard approach.

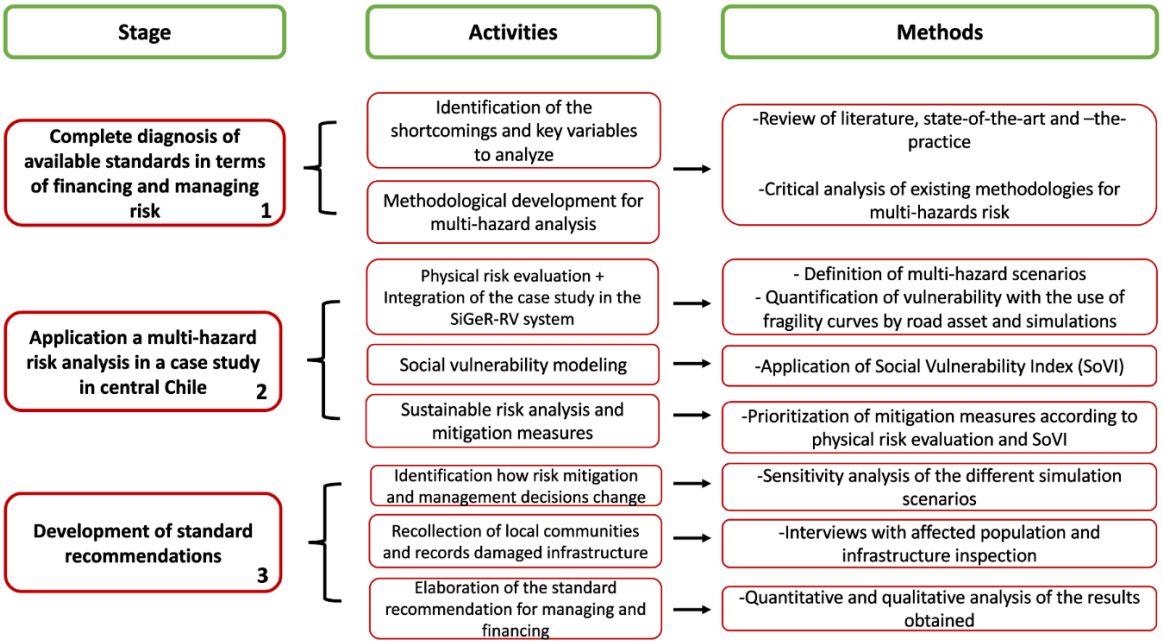

Figure 1 Research Methodology

The second stage proposed to assess physical risk in terms of travel-time delays and expected user and agency costs. The proposed multi-hazard risk analysis model and scenarios were integrated into the SIGeR-RV platform. The vulnerability of exposed infrastructure was obtained using fragility curves developed and calibrated for Chile. Multi-hazard scenarios that would result in travel-time delays, costs and expected socioeconomic impacts and their risk assessment were simulated based on historical data and field surveys. Social vulnerability of the population was modeled using the Social Vulnerability Index (SoVI) of Cutter et al. (2003), adapted to Chile. Finally, an analysis of the effects of mitigation strategies on travel-time delays and socioeconomic impacts was developed using the simulated scenarios. A sensitivity analysis was developed in the final

stage to understand how risk management, socioeconomic impacts, resilience financing and mitigation strategies may change under different simulated scenarios. Outcomes were compared with the state of the practice, including historical data, interviews with local communities and records of damaged infrastructure.

Finally, in the third stage, a document with guidelines for managing and financing resilient rural road networks was proposed. Recommendations included improvements in technical standards for existing and new infrastructure and how to consider resilience.

3.1 Step 1: Literature review

In the first place, according to the proposed methodology, a literature review was carried out to know the current practices in risk management and recommendations applied at the international and national levels. Multi-hazard analysis methods available in the state of the art were also reviewed.

3.1.1 International and national context

The existing guidelines were reviewed, distinguishing between developed and developing countries. At the global level, there are agreements associated with different frameworks, such as the Sendai framework, the Paris Agreement and the Sustainable Development Goals (SDGs), and each country has embraced them through the development of other national disaster risk management plans and policies. The Sendai Framework for Disaster Risk Reduction 2015-2030 was the first main agreement of the post-2015 development agenda defined by the UN, offering member states a series of concrete actions that can be taken to protect the development benefits against disaster risk.

The Sendai Framework goes hand in hand with other agreements of the 2030 Agenda, such as the Paris Agreement on Climate Change and the 17 SDGs. The SDGs are integrated as they recognize that action in one area will affect results in other areas and that development must balance social, economic and environmental sustainability. It was concluded that this project aligns with two of the 17 SDGs, Goals 9 and 11, related to achieving a more sustainable and resilient infrastructure, including the transport system. These two SDGs are given consideration in the multi-hazard risk analysis and the guidelines proposed in this project.

In some developed countries, risk management systems and platforms have been developed to allow decision-makers to achieve the commitments set forth by SDGs. In Chile, in the context of the aforementioned global regulatory frameworks, a National Climate Change Action Plan 2017-2022 was implemented, which establishes as lines of action the need to adapt to climate change by reducing vulnerability and increasing

adaptive capacities, acting transversally on all the elements of the national economy. Likewise, the National Policy for Disaster Risk Reduction 2020-2030 seeks to promote and improve dialogue and cooperation between the scientific and technological community, other relevant actors, and those responsible for formulating policies to facilitate the engagement between science and policies for an effective decision-making process in disaster risk management.

On a technical level, the Chilean Highway Directorate has the Chilean Highways Manual, which through 9 volumes, unifies criteria, procedures, specifications and methodologies involved in the development of road projects during their life cycle (pre-investment, investment, and operation) to grant a minimum technical and service standard on highways and roads. However, the Highways Manual does not include criteria and procedures to evaluate and mitigate natural risks throughout the life cycle of a project. In addition, the Chilean Highway Directorate has the SIGeR-RV platform. However, this is an optional tool since its use is not included in road project design, evaluation and management.

The key finding of the first activity was that developing countries like Chile, lack guidelines that have regulatory frameworks for managing infrastructure risk, drawing upon the quantification of socioeconomic criteria.

3.1.2 Multi-hazard and multi-risk assessment methodologies

From the state of the art and the practice of existing methodologies to assess multi-hazard risk, we identified two approaches. The first focused on multiple hazards aggregated in a multi-hazard index or map and assessing a total territorial vulnerability (i.e. no hazard-dependent vulnerability). Most multi-hazard assessment methodologies consider hazards as independent events, and the potential interactions are analyzed using cause-effect matrices. Other methods perform a qualitative aggregation of hazards and vulnerability using questionnaires or semi-quantitative assessment, assigning scores and weights to the identified classes of risks (Gallina et al., 2016). Another approach is multi-risk assessment wherein risks are analyzed separately and are combined in a multi-risk index. The multi-risk approaches are focused on the quantitative assessment of the multi-risk, allowing a more detailed analysis of hazard and vulnerability correlations (Gallina et al., 2016). Some of these methods consider that the joint occurrence probability of two events is negligible and thus, it is usually not considered, allowing the computation of total risk as the sum of risks due to single hazards (Kameshwar and Padgett, 2014; Martin et al., 2019; Oberndorfer et al., 2020). An advantage of this approach is that single risks within a multi-risk assessment are computed using a common unit of measure, allowing a

direct comparison and aggregation among different kinds of risks.

The key finding in this second activity was that the multi-risk approach is better adjusted to the case study and the available data because it uses quantitative methodologies and allows to combine different kinds of risks expressed in terms of increases in travel-times. The idea of considering a multi-risk index emerged as a result.

Given the various difficulties in the scientific development of a multi-risk approach, a second literature review was carried out. This review made it possible to identify that there is a lack of consensus about the multi-risk (MR) concept, the methodological approaches and the most recommendable tools. MR is often confused with or assimilated into multi-hazard and/or multi-vulnerability assessment. According to Komendantova et al. (2014), decision-making under MR is a nascent field.

As a result of these learnings, it was decided that the development of a multi-hazard methodology exceeds this project's scope. However, recommendations have been made to address the multi-hazard approach from the point of view of some economic impacts as a first approximation.

3.2 Step 2: Development of the conceptual framework

According to the literature review, it was decided to keep the project under the approach proposed by the SIGeR-RV software framework.

Risk management is defined as a set of coordinated activities to control risk (Free et al., 2006). A risk management system (RMS) turns management into a systematic practice where uncertainty is managed to minimize potential damage and losses. It encompasses risk assessment and analysis, and the execution of specific strategies and actions to control, reduce and transfer risk.

The road network risk management system on which the application of this study has been based is presented below. SIGeR-RV is a Web-Geographic Information System (GIS)-based software that aims to estimate the risks for road networks exposed to natural hazards and propose cost-effective actions for risk reduction. The software is based on a conceptual framework organized into three modules: input data, risk models, and outputs. Figure 1 shows the components of the different modules. In addition, the steps in the central part refer to the primary process programmed into the software. The development of the system is presented in detail by Chamorro et al. (2023).

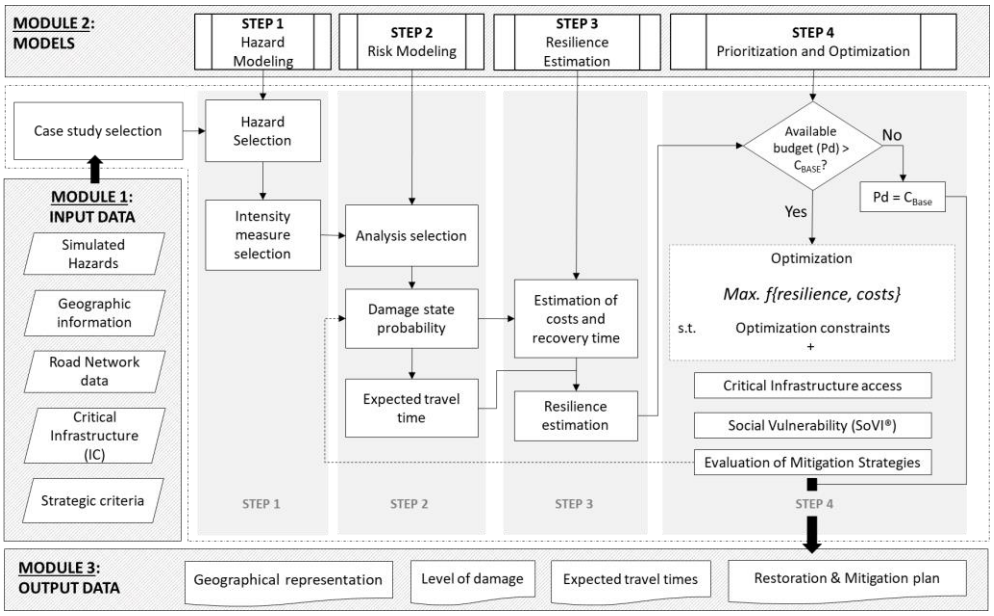

Figure 2. The integrated system risk management framework for road networks exposed to various natural hazards

Module 1: Input data

This module includes all the input data necessary to run the software. Five data sets are included. The first group of data includes the simulation of seismic, hydro-meteorological and volcanic hazards. The second data group includes territorial geographic information of coastal lines, borders and the country's administrative configuration, in a separate GIS interface. The third data group is the Chilean road network and its attributes. The fourth data group includes Critical Infrastructure (CI) data, and the geo location of education, health, power, rural drinking water and all emergency and safety infrastructure.

Module 2: Models

This module includes four steps: hazard modeling, risk modeling, resilience estimation, prioritization and optimization. The first step is hazard modeling and includes natural hazard simulation in the selected study area. Currently, the system has capabilities for modeling only seismic hazards. The hydro-meteorological and volcanic hazards are uploaded as specific hazard maps. The second step of the process is risk modeling, which estimates the consequences of infrastructure damage over the network level of service (LoS) in terms of travel-time increase. The network analysis studies the performance of the whole road network or sub-networks, and users can choose the network to be analyzed. The asset damage states, or failure probabilities are obtained from fragility models preloaded in the software (Chamorro et al., 2023). Damages to road assets are represented as traffic speed reduction, traffic capacity reduction and/or the

interruption of traffic flow. The increase in travel time is estimated using traffic reallocation models based on the user equilibrium principle (Nie t al., 2004). The third step is the resilience estimation which prepares a mitigation plan with a limited budget (Rose & Kraustmann, 2013). The system has a library of recovery actions that includes unitary costs and work duration. The last step is prioritization and optimization of the mitigation strategies in which the software estimates the cost-benefit of each mitigation strategy and its effect on the overall resilience of the road network.

Module 3: Outputs

SIGeR-RV provides the following outputs: (1) a graphic GIS representation of the simulated hazard on the road network; (2) tables with the affected assets in the analyzed road network; (3) a GIS representation of damaged road assets; (4) expected travel time for different scenarios; (5) a set of restoration and mitigation actions; (6) maps with the social vulnerability index of the different geographical units; and (7) a topological network ranking and the most relevant road network links for access to critical infrastructure.

3.3 Step 3: Case study

According to stage 2 of methodology (Figure 1), a case study was developed in central Chile. The SIGeR-RV risk management system was applied to the case study in the Maipo River basin in the Metropolitan Region of Chile.

3.3.1 Description of the case study

The Maipo basin is in the central region of Chile, and the main channel is the Maipo River. The territory considered for the case study occupies the municipalities of Puente Alto, San José del Maipo and Pirque. These last two are predominantly rural.

The Maipo Valley is exposed to seismic, hydro-meteorological and volcanic hazards. This last one was not considered in the case study since there is no detailed study information to simulate lahar flows. Regarding the hydro-meteorological hazard, the summer rainfall has increased recently because the zero level has been lowered. Due to this, the summer rains activate landslides and debris flows.

Regarding the road network, the G-25 road is aside from the main course of the Maipo River, and the road network is not redundant. The population settlements are located around the G-25 road, connected by roads built mostly on embankments that are exposed to floods and have been affected and damaged. These characteristics of the network and the territory entail traffic disruptions and isolation of the communities, with the consequent lack of essential services and restricted access to Santiago City.

3.3.2 Hazard simulation

Finally, for this case study, seismic hazard and debris flow, as a hydro-meteorological hazard, have been considered. Figure 3 shows maps of the respective hazard intensities. The Permanent Ground Displacement (PGD) represents the seismic hazard intensity and the debris flow intensity by water height (in metres). In Figure 3a, warmer colours are associated with greater hazard intensity. Figure 3b represents the return period of 50 years, and the highest water height is represented by darker blue colour.

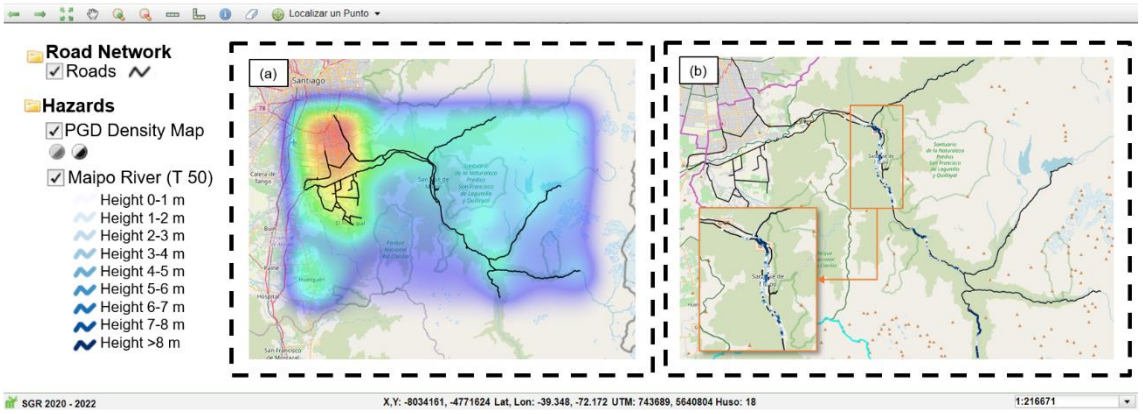

Figure 3. Hazard simulation: (a) Seismic Hazard (b) Debris Flow Hazard

3.3.3 Physical vulnerability

The evaluation of physical vulnerability was performed using fragility curves. It estimates the probability that the infrastructure reaches a damage state when it is affected by a natural hazard of a certain intensity. Damage state is associated with road capacity loss and average traffic speed reduction. Fragility curves are specific for each road asset and hazard. For seismic hazards, we adopt the fragility curve for roads and bridges of Basöz & Mander (1999) and the National Institute of Building Sciences (2004), respectively. The second one was developed for Chilean conditions by Nieto et al. (2021; 2022).

3.3.4 Risk & resilience evaluation

Figure 4 shows the risk maps of the seismic hazard (Figure 4a) and the debris flow hazard (Figure 4b). In Figure 4a, links with a low (green) and very low (blue) probability of damage are predominant. These segments are in the road network's eastern and central parts. Figure 4b shows the road links potentially damaged by debris flows (orange segments). These links are located at the centre of the road network under study.

Comparing both maps, it can be seen that the arcs most exposed to suffering damage are concentrated in the area marked in red since both hazards present critical arcs in that area.

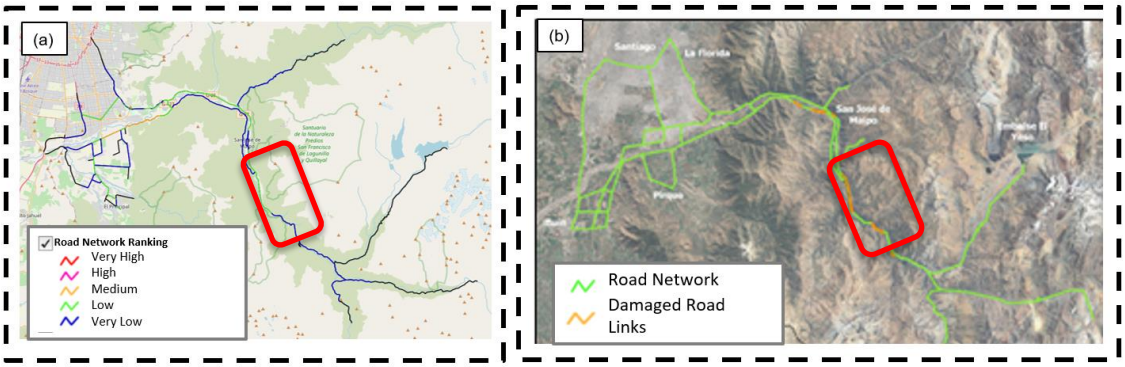

Figure 4. Hazard maps (a) Seismic hazard (b) Debris flow hazard

Finally, the mitigation works prioritization algorithm considers three steps: a) analysis of the road network topology; b) analysis of accessibility to critical infrastructure; and c) social vulnerability index estimation.

Specifically, the social vulnerability analysis is based on SoVI developed by Cutter et al. (2003). This index uses the National Census of 2017 and the National Social and Economic Households Characterization Survey of 2017 as input data. It is explained in more detail by Guerrero et al. (2023).

3.4 Step 4: Comparison with field data

In order to better understand the territory of application, three field visits have been carried out.

3.4.1 Historical events data

A brief review of the data collected both in the analysis and in the field, visits has been presented in the succeeding paragraphs to perform a comparison with the available information.

Below are the historical events compiled by both the road administration and those responsible for emergency management in the municipality of San José de Maipo. Figure 5 shows the historical debris flow events that occurred in the study area up to June 2023. In recent years, events have increased in their frequency; seven of the 14 debris flows studied in the area occurred between 2013 and 2023. According to the information in Figure 8, most of the recent events are concentrated upstream of the municipality of San José de Maipo and downstream of the crossing of the Maipo and Yeso rivers. This area coincides with the most critical area marked on the risk maps in Figure 4. In addition, this area coincides with the extreme event highlighted by the different people interviewed, the January 2021 debris flow in San Alfonso. Consequently, the criticality of the road links of this section of the G-25 becomes evident.

In addition to this critical zone, the risk analysis also highlights critical arcs for both

hazards, downstream of San José de Maipo. Although no historical events have been recorded in this zone to date, according to the analyses carried out, it is important to take this into account in the future management of the road network studied. It is advisable to study the implementation of mitigation measures and monitoring of events in this area.

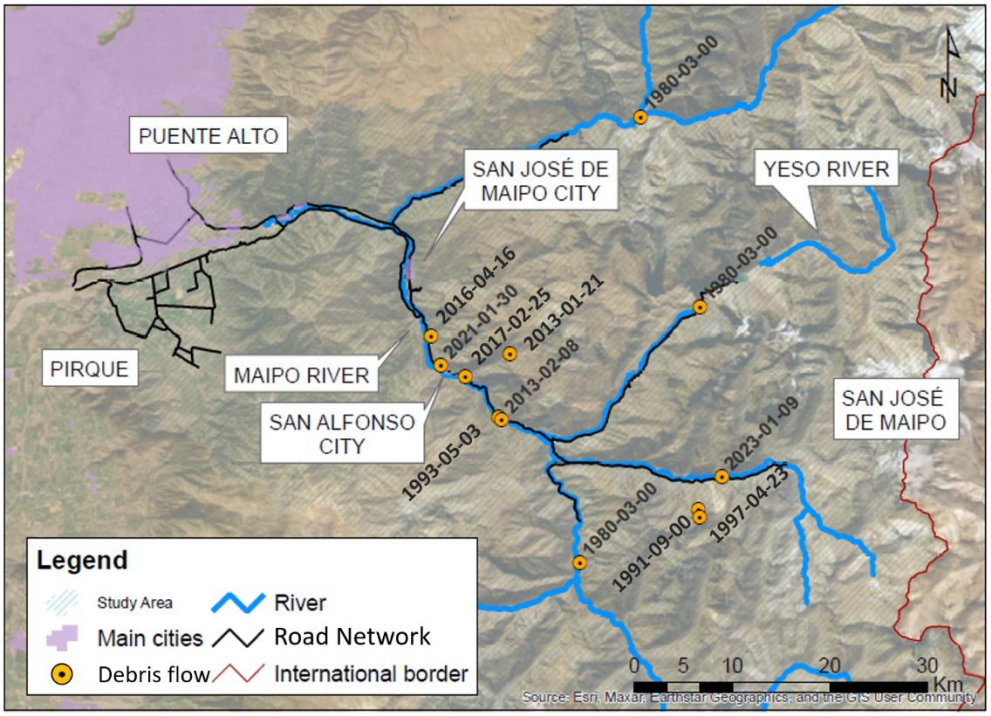

Figure 5. Historical hydro-meteorological event data up to 2017

The embankment protection measures observed in the field are consistent with those collected by the SIGeR-RV System; in both cases, they are aimed at protecting or reinforcing the embankments. In addition, during the field visits, it was possible to observe another very common measure in the area, the rock dams to protect the riverbeds around the bridges. These are not included in the software for the hazard of debris flow.

3.4 Debris flow of June 2023

We want to highlight the last field visit carried out on July 7, 2023, because of the rains that occurred on June 24, 25 and 26. This hydro-meteorological event took place with abnormally high temperatures for that time of the year, causing zero level to be higher than usual. Because of these rains, floods and landslides occurred throughout the country, causing extensive damage to the national road network, especially bridges. Figure 6 shows some of the most relevant affected points.

The first four points are concentrated in the critical zone identified in the risk maps and the record of historical events. Below are some of the most noteworthy aspects found during the field visit. Point 3 is located on the San Alfonso Bridge, affected by past events. Currently, there was a temporary Mecano-type bridge (see Figure 7a), which was

not enabled for traffic of any kind due to settlement in the far north. Figure 7b shows the recovery by filling the access embankments to the bridge. Erosion is observed in the embankment downstream of the bridge, in the western part. The embankment in the eastern part is being filled.

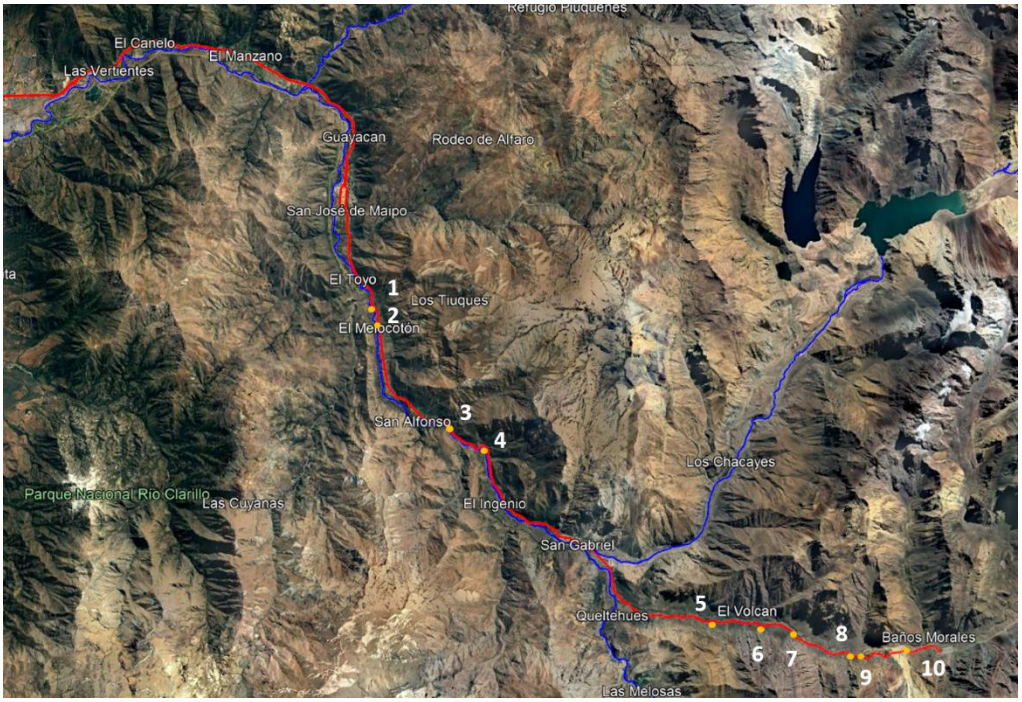

Figure 6. Record of points affected by the hydro-meteorological events of June 2023

Figure 7. (a) San Alfonso bridge, provisional Mecano-type infrastructure (b) Restoration work downstream

At the location of Point 4, longitudinal erosion of the road could be observed due to the increase in speed and flow of the Maipo River. There is only one track enabled for vehicular traffic. In Figure 8, it can be seen how the bank protection carried out previously was not effective enough against the force of the river. Figure 8a shows the situation of the channel during the field visit of November 2022 with respect to Figure 8b, which represents the situation observed after the occurrence of rains in June 2023.

Figure 8. (a) Protection of the Maipo riverbed in November 2022 (b) Longitudinal erosion of the protection of the riverbed

On the other hand, Figure 9 is associated with Point 9 and shows the effectiveness of the slope containment mitigation measure with a vertical wall and breakwater. This measure has prevented the floodwater from dragging the embankment.

Figure 9. (a) Embankment protection in November 2022 (b) Embankment protection in June 2023

With all the damage observed, it can be concluded that the study area is highly exposed to debris flow and floods, which, according to the trend of historical events, have been increasing in recent years. It has been possible to verify that a large part of the measures carried out by the administration have been inefficient given the magnitude of current events. This evidence highlights the need to include the effects of climate change in the simulation of threats and the design of mitigation measures.

3.4.3 Governance analysis.

In-depth interviews were conducted to better understand emergency response and overall disaster risk management and reduction (DRM/DRR) practices in the case study area. Interviews followed a qualitative, semi-structured format (McCracken, 1988), covering the following subjects (see Appendix 2 for a complete interview topic guide): (a) mapping of stakeholder groups involved in emergency response, DRM/DRR and disaster risk governance; (b) identification of emergency response practices to hazard events that disrupt the road network; and (c) identification and assessment of long-term mitigation strategies to implement after such events.

Three interviews were conducted with representatives of different stakeholders involved in the management of the rural road network in the case study. These representatives comprised a local community organization dedicated to natural conservation, environmental education and tourism; the Directorate of Civil Protection, Emergency and Operations of the Municipality of San José de Maipo; and the Metropolitan Region office of the Highway Directorate. The interviews had an average

duration of 91 minutes and were conducted in person (the first two) and remotely (the third). With the consent of the participants, the interviews were recorded to facilitate thematic analysis of the collected qualitative data (Joffe, 2012).

3.5 Step 5: Key findings and validation

The main themes developed from the interview data are presented below.

3.5.1 Theme 1: The hazard profile has changed in the last 10 years: debris flows are the new normal

Overall, the interviewees agree that the hazard profile of the case study area has changed, particularly in the last 10 years. Whereas floods associated with winter rain used to be the main concern, debris flows have intensified both in frequency and magnitude, shifting from exceptional events to the new normal. These events are predominant in the hot and dry season (roughly, October through March) with the continuous rise of the zero-degree isotherm because of climate change. Moreover, environmental degradation of the ravines caused by depletion of native vegetation and people's intervention is increasing the hazard of slope and rock detachment and wildfires. Responding to the challenge, the Ministry of Public Works is updating the design protocols and procedures to incorporate these new hazards into how future infrastructure is delivered.

3.5.2 Theme 2: Disaster risk management is reactive, fragmented and top-down

Interview data confirm that DRM in the study area follows a reactive approach, replicating the weaknesses of the national DRM model (see e.g. Rivera Jofré, 2023; Sehnbruch, 2017). Overall, the interviewees differentiate emergency management from mitigation and preparedness. Whereas the DRM system works well for monitoring, issuing and communicating warnings, and responding to emergencies, it does not work well for long-term DRR and mitigation.

In this context, the increased frequency of hazard events is perceived somehow positively by the interviewees. Disastrous events draw attention to the need for developing knowledge and strengthening local DRM.

The focus on emergency response over long-term mitigation is well-exemplified by the lack of planning regulation as an instrument for DRR.

3.5.3 Theme 3: There are no capacities to anticipate future events and therefore DRR is limited

Interviewees agree that, although there is a solid capacity for responding to repetitive events and emergencies, there is no forecast capacity across stakeholder groups. Therefore, investment always lags behind the reality of the territory, limited to restoration of services (e.g. road connectivity, water drainage, etc.) but not necessarily reducing disaster risk.

Local authorities and agencies lack information to properly guide and implement DRR — including hazard characterization, risk levels and expected impacts of hazard events — which could be incorporated into updated emergency response protocols or evacuation guidelines. Whereas local authorities and third sector organizations engage in occasional collaboration with research centres and universities, interviewees acknowledge the lack of centralization of the knowledge produced in the case study area. This hinders the capacity of local authorities and community-based organisations to incorporate such knowledge into protocols and practice, limiting DRM/DRR.

Partly, interviewees identify a barrier for effective DRR-driven investment in the state's bureaucracy. For example, the Highway Directorate has flexibility and independence for contracting and investing in the maintenance of infrastructure. However, planning and development of new infrastructure requires interaction with the Ministry of Social Development and, specifically, the system of assessment of public investment, which does not incorporate DRR/DRM criteria.

3.6 Step 6: Development of guidelines

As a result of the previous review of the state of the art and the practice, and the application of the Risk Management System to a case study, we have elaborated on the practical recommendations for risk management. These recommendations are contained in the document, "Guidelines for Managing Risk of Rural Road Networks". It includes recommendations about scalability, data sources and Risk Governance, among other topics. For more details about the content, please review the aforementioned document attached to this report.

4. Results and Discussion

This section briefly describes some of the most noteworthy findings and conclusions resulting from the development of this project.

4.1 Findings from planning documents

Extreme events associated with natural hazards have been considered under a reactive approach. Under this approach, the response to emergencies has been taken as the only action against this type of extreme event.

In recent years, in the face of increasingly notable effects of climate change, the most developed countries have begun developing their infrastructure risk management tools, particularly road networks. However, this is still at a nascent stage in developing countries like Chile. To achieve satisfactory risk management, a regulatory and legal framework is required to support the associated activities and allocate resources to mitigation and preventive management.

4.2 Development of the conceptual framework

At this stage, one of the most decisive factors was whether to consider a multi-hazard analysis. As a result of the literature review, it was determined that a multi-hazard or multi-risk analysis has implications that require a research process and resources greater than those covered by this project. It should be noted that in order to carry out this approach, an "overlap" of hazards (multi-hazard) or risks (multi-risk) may be required. For this reason, it is imperative that prior to the development of the models, an equivalent hazard intensity or risk indicator be defined for all the hazards considered. In this way, if necessary, its aggregation can be carried out.

Finally, given hazard simulation, vulnerability assessment and risk models that have already been developed, an approximation can be jointly carried out by assessing the socioeconomic impacts of the different hazards.

4.3 Findings from interviews and validation

The main findings resulting from the application of the interviews are described in detail in section 3.5.1, "Key findings from the interviews".

The application of interviews and field visits has allowed for better case study development. The key finding from the fieldwork was to verify the prevalence of critical points of the network, among them a bridge with notorious scour in its abutments and marks of the passage of a debris flow in the lower part of its deck.

In addition, the application of the interviews made it possible to collect more and better information on the hazards that occurred and their effects on the road network while also learning first-hand about current risk management practices. This information has allowed us to compare them with the results of the analysis. In summary, this comparison has shown that the latest events, in 2016 and 2017, are concentrated in the

most critical area marked on the risk maps in Figure 6. Moreover, the embankment protection measures observed in the field are consistent with those collected by the SIGeR-RV System.

5. Enablers and Barriers

In this section, we want to highlight the most significant challenges in the project.

The literature review of the multi-hazard approach is an emergent topic that is outside the project's scope. It requires further dedication and scientific research that exceeds the time and resources available for this project.

On the other hand, although the application of interviews has been an excellent input for the project's development, its organization and management were slow. Identifying and contacting the key actors has been a laborious and lengthy task. It delays the application of the interviews and, therefore, the analysis of the information they provided.

6. Key Takeaways from CDRI Fellowship Programme

The team is very grateful to the CDRI Fellowship for the opportunity to continue expanding our knowledge on these topics and improving our contributions to infrastructure resilience.

Being part of this project has been a great opportunity to delve into this research topic. It has also been a loudspeaker that has allowed us to spread knowledge about our progress internationally and beyond what could be achieved through scientific journals. Thanks to the CDRI Fellowship, we have contributed to developing and disseminating scientific knowledge associated with managing resilient infrastructure. In this way, we have been able to contribute through our project to the imperatives of the SDGs of expanding universal access to critical services.

In addition, relying on the feedback of technical experts in the field from very diverse realities and backgrounds has enriched the project, allowing us to achieve a more comprehensive approach to risk management and resilience.

7. Conclusion

Finally, the proposed research objective of developing a resilience guide that accounts for the socioeconomic impacts caused by natural events and the need to finance resilient

rural road networks in vulnerable territories and populations exposed to multiple natural hazards was achieved. These recommendations are gathered in the document, "Guidelines for managing risk of rural road networks".

As regards the review of both the current practices in risk management and the standards and recommendations applied at the international and national levels, risk management is a topic of growing interest. Typically, risks associated with natural hazards have been treated under a reactive approach. However, in recent years, the most developed countries have begun developing their infrastructure risk management tools, particularly road networks.

As a result of the literature review of existing methods of multi-hazard analysis, it is determined that a multi-hazard or multi-risk analysis has implications that require a research process and resources greater than those covered by this project.

A case study was developed in central Chile. The SIGeR-RV risk management system has been applied to the case study in the Maipo River basin in the Metropolitan Region of Chile. For this case study, field visits and interviews were carried out. The application of interviews and field visits allowed for better case study development. The key finding from the fieldwork was to verify the prevalence of critical points of the network, among them a bridge with notorious scour in its abutments and marks of the passage of a debris flow in the lower part of its deck. In addition, the application of the interviews made it possible to collect more and better information on the hazards that occurred and their effects on the road network while also learning first-hand about current risk management practices. In turn, this information has allowed us to compare them with the analysis results. In summary, this comparison has shown that the latest events are concentrated in one of the most critical areas on the risk maps. Moreover, the embankment protection measures observed in the field are consistent with those collected by the SIGeR-RV System.

8. Way Forward

According to what has been mentioned throughout this document, the main next step to carry out is the development of a research project that profoundly addresses the multi-hazard risk assessment of road infrastructure. This is a large and complex field of research, where aspects such as the probability of simultaneity of hazards or cascading effects, among others, must be considered.

On the other hand, another major issue to address is focused on the applicability of the proposed methodology. As already mentioned, the applicability of these models to

other realities requires prior calibration and adjustments that allow the risk management process to be adapted to the available data and resources.

References

1. Basöz, N., and J. Mander. Enhancement of the highway transportation lifeline module in HAZUS (Technical report). National Institute of Building Sciences, Washington, D.C., 1999.

2. Chamorro, A., Echaveguren, T., Allen, E., Contreras, M., Dagá, J., de Solminihac, H. & Lara, L.E. (2020). Sustainable Risk Management of Rural Road Networks Exposed to Natural Hazards: Application to Volcanic Lahars in Chile. Sustainability 2020, 12, 6774.

3. Chamorro, A., Echaveguren, T., Pattillo, C., Contreras-Jara, M., Contreras, M., Allen, E., Nieto, N., & de Solminihac, H. (2023). SIGeR-RV: A Web-Geographic Information System-Based System for Risk Management of Road Networks Exposed to Natural Hazards. Transportation Research Record. 2023. 0(0). https://doi.org/10.1177/03611981231169532

4. Cutter, S.L. (1996). Vulnerability to Environmental Hazards. Progress in Human Geography 20(4):529–539.

5. Cutter, S.L., Boruff, B.J. and Shirley, W.L. (2003). Social Vulnerability to Environmental Hazards. Social Science Quarterly, 2003. 84(2), 242–261. https://doi.org/10.1111/1540-6237.8402002

6. Cutter, S.L., Emrich, C.T., Morath, D.P. & Dunning, C.M. (2013). Integrating Social Vulnerability into Federal Flood Risk Management Planning, Journal of Flood Risk Management, 6, 332–344. https://doi.org/10.1111/jfr3.12018.

7. Free, M Anderson, S Milloy, Ch y Mian, J (2006). Geohazard risk management for infrastructure projects. Proceedings of the ICE – Civil Engineering, 159, 28 - 34.

8. FONDEF Project "Research and Development of Models to Quantify and Mitigate the Risk of Natural Hazards in the National Road Network" (grant no. ID14I20309/Fondef/ANID).

9. Guerrero, N., Contreras, M., Chamorro, A. Martinez, C. & Echaveguren, T. (2023) Social vulnerability in Chile: challenges for multi-scale analysis and disaster risk reduction. Nat Hazards. https://doi.org/10.1007/s11069-023-05978-z.

10. Joffe, H., 2012. Thematic Analysis, in: Harper, D., Thompson, A.R. (Eds.), Qualitative Research Methods in Mental Health and Psychotherapy: An Introduction for Students and Practitioners. Wiley-Blackwell, Chichester, pp. 209–223. https://doi.org/10.1002/9781119973249.ch15

11. National Institute of Building Sciences [NIBS]. HAZUS-MH: User's manual and technical manuals (Technical report). National Institute of Building Sciences, Washington, DC. 2004

12. Nie, Y., H.M. Zhang, and D.H. Lee. Models and algorithms for the traffic assignment problem with link capacity constraints. Transportation Research Part B: Methodological, 2004. 38(4), 285–312. https://doi.org/10.1016/S0191-2615(03)00010-9

13. Nieto, N., A. Chamorro, T. Echaveguren, E. Sáez, and A. González. Development of fragility curves for road embankments exposed to perpendicular debris flows. Geomatics, Natural Hazards and Risk, 2021. 12(1), 1560-1583. https://doi.org/10.1080/19475705.2021.1935330

14. Nieto, N., Chamorro, A., Echaveguren, T., & Escauriaza, C. (2022). Fragility curves for road embankments exposed to adjacent debris flow. Progress in Physical Geography: Earth and Environment, 47(1), 105–122. https://doi.org/10.1177/03091333221111444

15. Parker, C., Scott, S., Geddes, A., 2019. Snowball Sampling. SAGE Research Methods Foundations

16. Rose, A., and E. Kraustmann. An economic framework for the development of a resilience index for business recovery. International Journal of Disaster Risk Reduction, 2013. 5, 73-

Water Collection, Storage and Treatment System (CST) in Floating Community Space (FlS) in the Peruvian Amazon

Ms Belen Desmaison
Researcher
Pontificia Universidad Católica del, Perú

Mr Kleber Espinoza
Researcher
Pontificia Universidad Católica del Perú, Peru

Under CDRI Fellowship Programme 2022-23

Disclaimer: The views expressed in this paper reflect the opinions of the author and not necessarily the official views of CDRI.

Abstract

Over 40 percent of the inhabitants of the Amazonian region of Peru do not have access to clean water. It is ironic that, where one of the largest sources of fresh water in the world is found, the population does not have constant access to quality drinking water. We work in Iquitos, the capital of Loreto, which is the largest region in Peru. Loreto covers more than 30 percent of the country and records the highest levels of annual precipitation.

The proposal seeks to provide technological alternatives for access to water that do not depend on a conventional network and are designed for easy installation and maintenance. The proposal also integrates water treatment to reduce pollution after usage. We work closely with the residents in co-production processes, not only in the design and construction of the infrastructure but also in the creation of a management committee for the use of space. The aim is to generate alternative forms of governance for the city and promote more active participation by its inhabitants.

In our previous experiences, we worked on a system in which the rain is captured by the roof and solar panels are used to provide energy for pumping water. Once used, it goes through a phytodepuration system and a grease trap for cleaning. The water is stored in pipes that can be modulated and adapted to different needs. In the present case, we focused on amphibious settlements that are either floating or on stilts and inhabited by 20 percent of the population of Loreto. How to create infrastructures that deliver water, sanitation and collective spaces in this context?

The replicability of the proposal occurs in two dimensions: the first is the technique since the built system is modular and flexible, so it can be adapted to different situations, spaces and capacities. On the other hand, there is the experience of co-production itself, which integrates technical aspects together with social and cultural ones, generating relevant solutions that reinforce and improve relationships between citizens, local government and the academia. Thus, we present the methodology itself as a fundamental aspect to be integrated in the planning and management of the cities of the future.

We understand “infrastructure" more broadly than the concept’s traditional understanding of material objects that cannot be seen but that are vital for the functioning of society. This role of providing “support" to society is also social, as they are the people and human groups that take care of the city. Without them the city would not exist. We aim to build a prototype in amphibious settlements for which we will also develop an implementation and maintenance guide to be available for free and which can be easily

understood by a variety of users. We also aim to work closely with community members so that they can be trained in the construction process, offering them certification as technicians that can replicate the experience elsewhere.

Acknowledgements

We would like to thank our co-researchers without whom this proposal would not have been possible: Emanuele 'Manu' Fabiano and Luis Martin Piccini, for their anthropological insights into working with amphibian communities in Iquitos and Nauta; Jorge Soria and Víctor Ramos, for their knowledge on renewable energy and their support in navigating the protocols and processes within the university; Rosa Souza and Daniel Carrasco, for their explorations on how to treat rainwater to make it drinkable and in a manner that prevents pollution, and also for their support in strengthening the collaborations between PUCP and UNAP; Darwin Auccapuri, for teaching us about telecommunications and developing an adapted proposal for the floating platform; Leonar Ilacctahuaman Hinostroza, Mariano Moscol Proaño and Luis Fernando Concha Figueroa, for their valuable work and mentoring in the design of the platform, making sure it floats!

To our partners from UNAP, the Municipality of Nauta, the Local Health Network, the Radio Kukama and to the communities of 9 de Octubre, San Jorge, San José de Zarapanga and Santa Rita de Florida: thank you for your insights, comments and commitment in making sure this project serves the amphibian communities. We hope this project becomes useful not only for the inhabitants of the Amazon rainforest but also to those living in flood-prone settlements.

Funding

This research was supported by the 2022–2023 Fellowship of the Coalition for Disaster Resilient Infrastructure (CDRI), Application ID: 210917575.

1. Introduction

Human settlements in the Amazon rainforest are dispersed and dynamic. Even in large cities like Iquitos, around 20 percent of the population lives in amphibian settlements, with houses either floating or on stilts. In addition, inhabitants of the Amazonian settlements are constantly moving and traveling by rivers for work and to get access to resources. Thus, the 'division' between rural and urban is blurred. This dynamism also puts into question the permanence and sedentarism of settlements and infrastructure alike, calling for alternative forms of service delivery that can better adapt to the unique social, geographical and territorial characteristics of the Amazon rainforest.

Faced with this situation, we propose a programme of floating platforms that navigate in micro-basins. For this, we will be running a virtual simulation of the floating device prior to its implementation, which will take place after the current funding opportunity.

This floating platform is self-sufficient in that it provides electricity by using solar panels; drinking water by capturing, storing and treating rainwater; a telecommunications system to share data; and will facilitate the treatment of grey and black water. The platform has an open plan that can be adapted to multiple uses, such as laboratory, sleeping facilities, panel exhibition, library, capacity-building workshops or vaccination campaigns, just to name a few.

Thus, this platform could be replicated and used by a variety of public institutions engaged in providing services, including those serving as first responders during natural phenomena like floods, to access settlements that are located near rivers in which large boats are not able to navigate.

2. Aim, Objectives and Scope of the Research Study

The platform's design seeks to propose a base structure that has water supply services through the collection, storage and treatment of rainwater, a grey and black water treatment system, electricity supply through solar panels and batteries, and a telecommunications system that allows data storage. It is also proposed that the platform has an open plan like those of houses and buildings in the Amazon, so that it can be used for various purposes, such as education, health, research, training, etc. Finally, it has a navigation cabin and a rest area for the personnel who will take care of the platform.

In the design of the platform, materials, construction techniques and typical spatialities of the buildings of riverside settlements are considered, for which a field exploration is being carried out in the riverside communities of Kukama descent in the district of Nauta, in Loreto.

3. Methodology

3.1 Step 1: Desk research and literature review

The proposal of a floating platform seeks to generate technologies for Collecting, Storing and Treating (CST) rainwater, thereby generating three modular and flexible technologies that could be replicated individually or as a system that contemplates all three. More than seeking to provide access to water and sanitation to communities through the platform, we envision it as a prototype to demonstrate the technology to communities and to different levels of government, test its efficiency and promote its replicability.

The collaborative design, implementation, monitoring and evaluation of this system with users and local authorities aims for the inclusion of pre-existing knowledge, the promotion of greater ownership of the proposed system and the strengthening of trust between the government, citizens and academia. This allows training and the generation of awareness about the management of water resources and its appropriation allows the replicability of the CST system in similar contexts, promoting its implementation by trained users. We propose a solution that is low-tech and low-cost to facilitate its integration in the on-going development initiatives carried out and financed by the local government. The CDRI Fellowship allowed us to develop Phase I of a longer-term project: the collective design and virtual simulations of the floating platform. Implementation, monitoring and evaluation will occur in the following 18 months with funding that is already secured from the Peruvian Council of Science, Technology and Innovation (CONCYTEC).

We seek to generate a participatory work methodology for the co-construction of appropriate technologies that can be replicated in the development of pertinent projects in other regions of the country or other areas with similar characteristics (amphibian communities). On the other hand, the system will be implemented collectively, within a network of multiple stakeholders from academia and the government to strengthen institutional cooperation and share the costs of maintenance and use of the platform.

The following table summarizes the different stages of the 12-month project:

Timeline in Months	Phase	Details
Months 1, 2 & 3 (July - September 2022)	Diagnosis	Collaborative diagnosis carried out through interviews, direct observation, collecting data on water quality, social programmes occurring in the Amazon rainforest, access to basic services, to health and basic education, and already-existing river boats to build a diagnosis. Objective: gathering data for design phase.
Months 4 & 5 (October - November 2022)	Elaborating preliminary proposals	Various preliminary design proposals that integrate different components (water and sanitation, renewable energy, etc.) to begin collaborative work between architects and naval engineers.
Months 6 (December 2022)	Presentation of proposal to local authorities and universities	Presentation to collectively decide the layout of the platform adjusted to requirements and needs of institutions.
Month 7, 8 & 9 (January - March 2023)	Adjusting proposal + preliminary tests + cost projection	Technical experts (architects and engineers) worked in adjusting the plans following results of participatory workshops and institutional meetings.
Month 10 (April 2023)	Running virtual simulations	Naval engineers ran virtual simulations of the prototype to test its efficiency in floating and easiness in navigating amazonian rivers.
Month 11 (May 2023)	Preparing final plans + revising cost estimates + Presentation to local authorities and academia	Final adjustments were made to the proposal after the virtual simulations were made, which led to the final revision of plans and cost estimates. We presented these results to local authorities and academia.
Month 11 & 12 (May - June 2023)	Preparing final reports and dissemination products + Planning ahead	Writing final reports, preparing final technical plans and dissemination products (video and presentation). Planning next steps (beyond CDRI Fellowship): implementation of prototype (August - October 2023); testing, Monitoring & Evaluating (November 2023 - March 2024); dissemination products of built platform (academic papers, conferences, videos, architectural competitions) (April - August 2024)

As for the CST system, due to its self-sufficiency, it could be used as a solution during post-disaster emergency situations in areas with high rainfall rates where the water supply is cut off or in cases of population resettlement where the implementation of traditional drinking water networks may take time. Although it may not fully satisfy the need for drinking water due to the volumes of water that can be processed (or captured), this technology may partially cover this demand, reducing the costs of providing water by other means (grid-networks, tanker trucks, etc).

The process for the design of the platform was both multidisciplinary and multi-institutional. We worked with anthropologists to gather information on the current living conditions of amphibian communities, their necessities and future aspirations. We also worked with three local naval engineers to make sure that the platform could float and navigate rivers with ease. We worked with telecommunications and mechanical engineers to install a satellite system and electricity on the platform. Lastly, we worked with chemical engineers to explore and propose water treatment to make it drinkable and to reduce pollution by treating grey and black water. All these processes had to be coordinated with each other as the spatial and material form of the platform was under continuous revision to make sure it was compliant with all the requirements.

In addition, work meetings are also held within the academic field for the dissemination and generation of scientific knowledge between the Pontifical Catholic University of Peru (PUCP) and the National University of the Peruvian Amazon (UNAP). One possible use for the itinerant floating platform is for it to become a laboratory or space for exchange workshops between professionals from various disciplines of the university and inhabitants of riverside communities. We also held meetings with local authorities like the municipality and the health centre. They expressed interest in having platforms like these as they currently don’t have boats and must rent them to be able to carry out fieldwork which can be costly.

We consider that these meetings are essential for the sustainability of the project beyond its timeframe, both for the use and maintenance of the prototype to be implemented and for its possible replicability. We understand that we cannot add the economic and labour burden of maintaining the prototype to the communities with difficulties in meeting these expenses and, therefore, we propose to work collaboratively with public institutions. However, working closely with the communities is essential for the proposed prototype to provide relevant solutions adjusted to their ways of living.

3.2 Step 2: Interviews and discussion tables

In Loreto, the region with the highest annual rainfall in Peru and the source of the world's largest river, the Amazon, only 56.3 percent of the population consumes water from the public network. In the district of Nauta, only 16 percent of the population is connected to the network.[1] Regarding sanitation, only 42.8 percent of Loretanos have access to drainage networks. [2] The riverside or amphibious populations and the settlements or communities that live far from urban centres, such as Iquitos and Nauta, are especially affected by the lack of connectivity to water and sanitation networks, and alternatives must be proposed for the provision of water and drainage that work efficiently. These provisions should work autonomously and not require conventional networks, whose implementation and maintenance cost would be very high due to the dynamic and changing territorial conditions themselves. It is these territorial conditions that make Loreto the region with the worst access to drinking water and sanitation in the country.

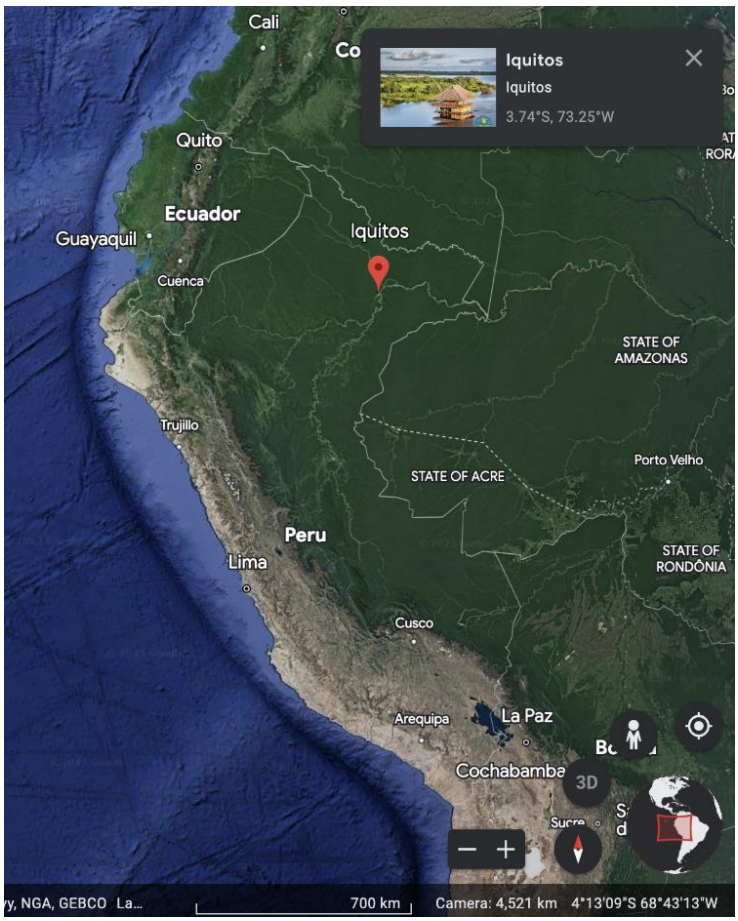

Map of Peru and Iquitos.
Source: Google Earth

[1] Source: https://www.defensoria.gob.pe/wp-content/uploads/2021/02/Informe-002-Bolet%C3%ADn-sobre-la-cobertura-del-agua-en-Loreto.pdf
[2] Source: https://www.inei.gob.pe/media/MenuRecursivo/boletines/boletin_agua_junio2020.pdf

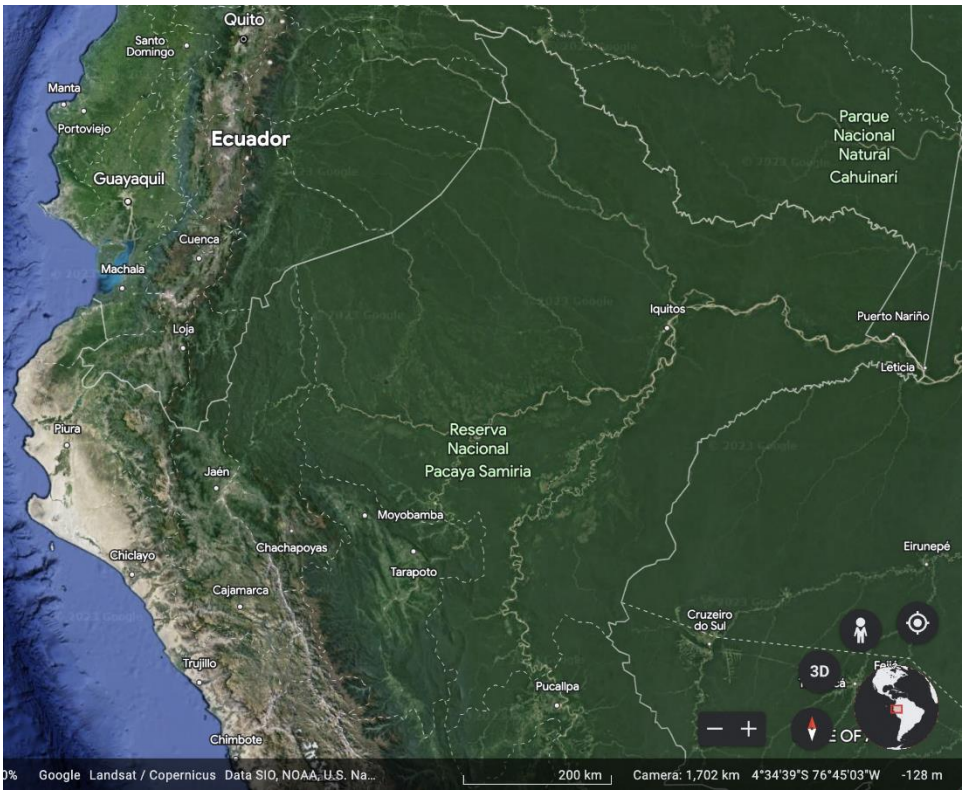

Map of Loreto, Peru.
Source: Google Earth

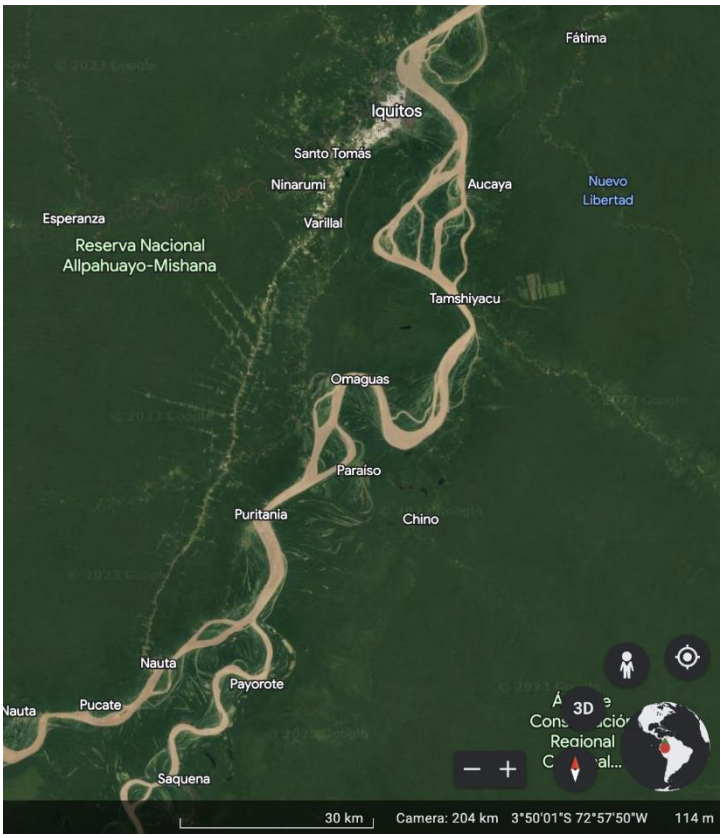

Map of Iquitos and Nauta, Loreto
Source: Google Earth

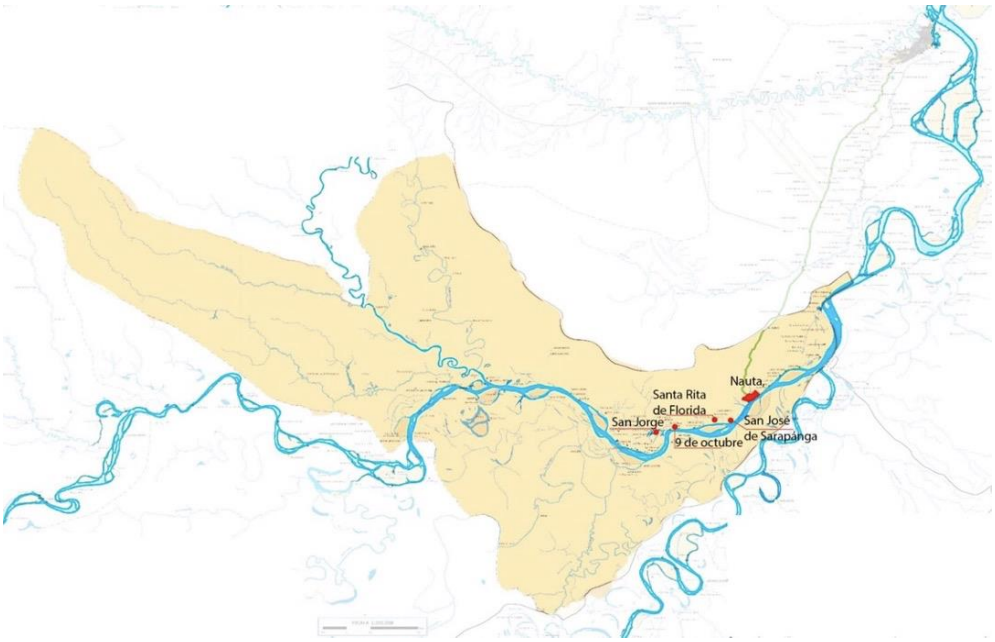

Map of Nauta and the four communities we worked with: San Jose de Sarapanga, Santa Rita de Florida, 9 de Octubre and San Jorge in Loreto, Peru
Source: Urban Development Plan developed by the Municipality of Loreto-Nauta, intervened by the authors to highlight communities involved in the project

Health and education in Loreto, Peru

The dispersed and mobile habitation of Amazonian communities also makes it difficult to access health and education services. In Peru, the lowest rates of school enrolment of the population between 12 and 16 years of age were registered in the departments of Ucayali (67.4%), Loreto (73.0%) and Piura (78.9%). Similarly, the lowest rates of enrolment in higher education for women and men between the ages of 17 and 24 in the period 2011-2021 occurred in the departments of Ucayali (14.4%), Loreto (15.6%) and San Martín (17.8%), all located in the Amazon region of the country.[3]

Amphibian communities in Nauta, Loreto, Peru
Source: Belen Desmaison, 2023

[3] Source: https://www.inei.gob.pe/media/MenuRecursivo/publicaciones_digitales/Est/Lib1871/libro.pdf

This situation is due, in part, to the difficult access to education infrastructure for dispersed populations that live far from urban centres and whose displacement requires hours or days of travel in river boats.

Likewise, access to health services and sexual education is limited. According to the Demographic and Family Health Survey (ENDES) of the National Institute of Statistics and Informatics (INEI),[4] more than half of the children in the region suffer from anaemia.[5] In addition, Loreto has the highest rate of teenage pregnancy in the country.[6] Being in a territory with rich biodiversity, the population is also prone to contracting tropical diseases such as dengue, malaria and chikungunya, among others. This type of situation leads to the need to constantly have training workshops, prevention campaigns and recurring health checkups. For this, having a health service capable of reaching dispersed communities is essential.

A programme with significant success in closing the gaps in access to health and other state services has been the Itinerant Platforms for Social Action (PIAS) programme of the Ministry of Development and Social Inclusion (MIDIS). [7] It brings basic state services closer to the most remote areas of the Amazon and the Altiplano in boats that house or facilitate health services, documentation procedures, banking operations, socioeconomic classification and the supervision and improvement of educational quality, among others. This initiative proposes a relevant alternative to provide state services to dispersed riverside communities. However, the service does not frequently reach the different locations, taking more than two months between visits and, due to the size of the boat, it cannot reach amphibian communities living on the riverside of small tributary rivers.

The Kukamas, native Amazonian inhabitants

The connection that the ancient Amazonian inhabitants had with the rivers of the lowland rainforest, beyond their vital interactions and mobility in daily life, encompasses relationships between humans and non-human surroundings.

In the Kukama cosmic order, there are different categories of people: bird-people, fish-people, spirit-people, plant-people and animal-people (Tello Imagina, 2016). Each possess their own domestic spaces (Piccini, 2023), houses and socio-spatial, interspecific relationships that interweave a network of places within

[4] Source: https://www.inei.gob.pe/media/MenuRecursivo/publicaciones_digitales/Est/Lib1838/
[5] Source: https://inversionenlainfancia.net/?blog/entrada/noticia/3027
[6] Source: https://elcomercio.pe/peru/loreto-tasa-alta-embarazo-adolescente-pais-427675-noticia/
[7] Source: https://www.pais.gob.pe/pias/

affective geographies, (Pile, 2009; Fernandes Moreira and Ramirez, 2019a) which constitute the Amazonian space in a plural, multi-naturalist ontology (Viveros de Castro, 2002) in constant negotiation.

Itinerant Platforms for Social Action (PIAS) by the Ministry of Development and Social Inclusion (MIDIS) of Peru
Source: PIAS[8]

The conception of indigenous territories is not marked by a political limit or exclusively human agreements. There are values of reciprocity with the different categories of people (Tello Imaina, 2016), with the various mothers and owners of the Amazonian geographic components and their interspecific cosmopolitics in a 'time without time' (Tello Imaina, 2018). Water is completely imbricated with the territory and thus, cannot be separated, requiring us to understand it as a complex network of hydro-social relationships (Roca-Servat, 2019).

Co-production and participatory architecture

On the importance of using participatory methods (both with the inhabitants and public representatives), we observed and discussed multiple cases for which the development of technologies that are not accompanied by participatory processes are abandoned or discontinued as viable alternatives due to a lack of knowledge

[8] Source: https://www.pais.gob.pe/pias/

about their management, potentiality and replicability. Additionally, they do not solve particular social, economic or political needs of the population (Ramírez-López et al 2013). For this reason, a participatory process and multi-stakeholder meetings and exchanges are proposed to promote the social and economic sustainability of the project beyond the CDRI Fellowship.

The integration of users in the implementation and maintenance of the platform generates technical knowledge, potentially generating alternative employment. Capacity-building allows the replicability of the system as it is implemented elsewhere by trained users (Pérez-Foguet, 2006; Pérez, 2010). The participatory development of alternative technologies promotes better levels of appropriation by users, by incorporating in the system design local knowledge and materials with which they feel identified. Awareness workshops promote a better understanding of the responsibilities and roles for the system's management and maintenance and its collective use reduces costs per family.

3.3 Step 3: Elaborating preliminary proposals

After a better understanding of potentialities, limitations and needs from both communities and local authorities, researchers, along with a multidisciplinary team, started developing preliminary proposals for the floating platform. It integrated a flexible plan to allow multiple uses and explorations towards possible pathways of integration of the different services, that the platform had to deliver to promote self-sufficiency.

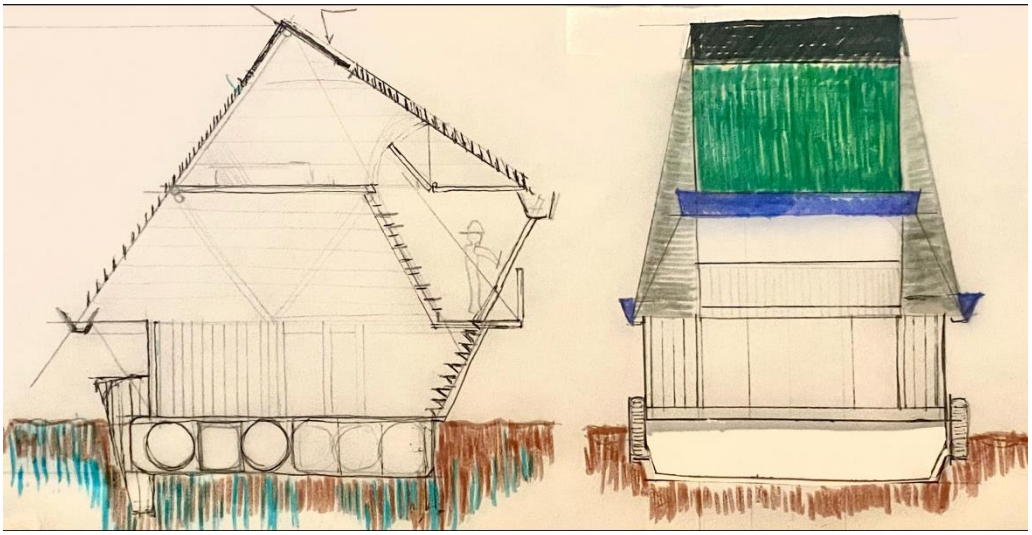

Preliminary drafts of the floating platformSource: Kleber Espinoza, 2022

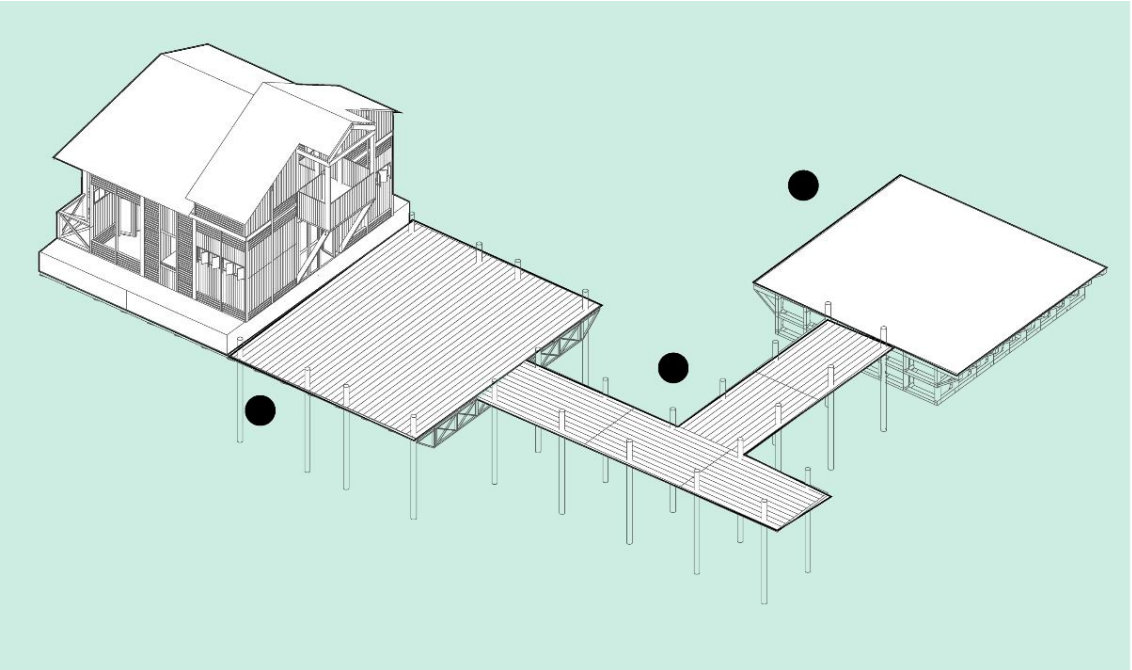

Exploring requirements for the platform to navigate and park easily near amphibian communities
Source: CASA Team, 2022

Architects constantly met with naval engineers to comply with requirements not only in ensuring that the platform could float but also in complying with navigation protocols such as visibility from the crew cabin and protection against collisions.

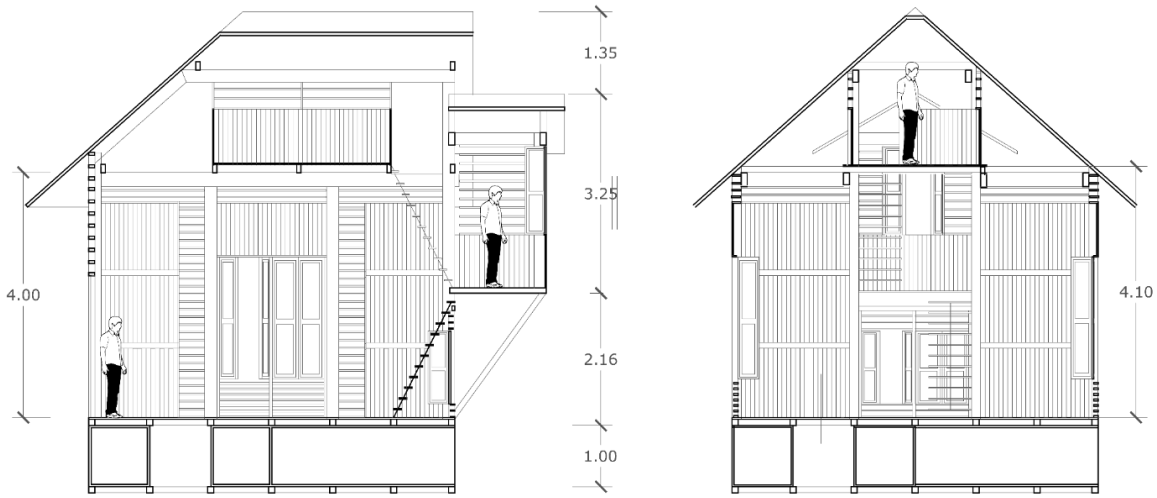

Preliminary drafts of the floating platform after discussions with naval engineers
Source: CASA Team, 2022

We also had discussions with telecommunications engineers to integrate the requirements of installing a satellite system to store and share data collected in the platform (workshops, laboratory samples, personal profiles for patients and/or students, etc).

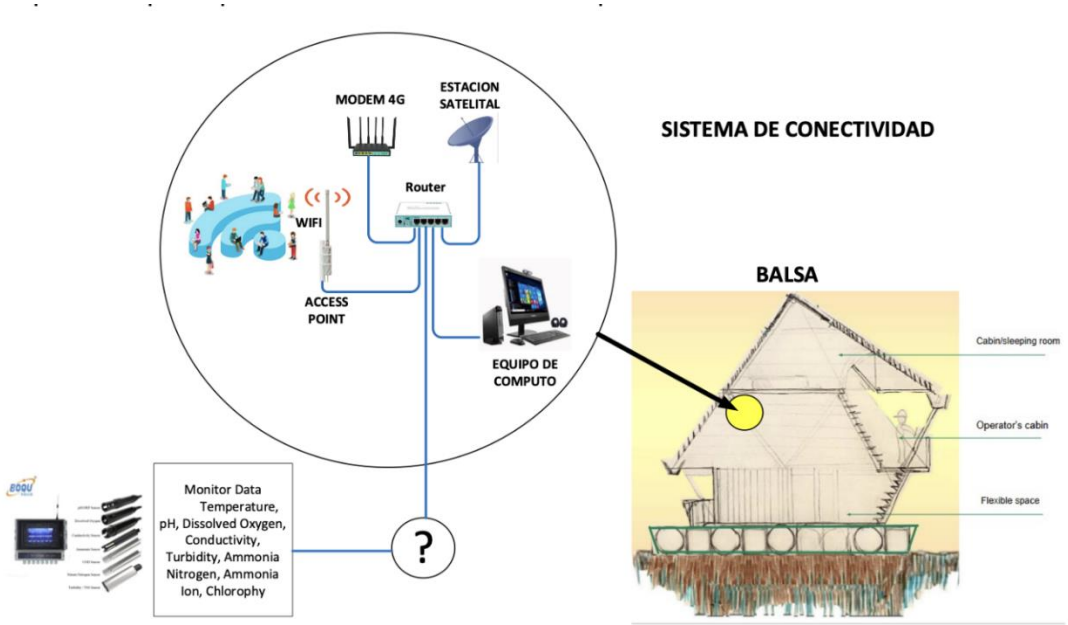

Preliminary proposal of requirements for a telecommunications system
Source: Darwin Auccapuri, 2023

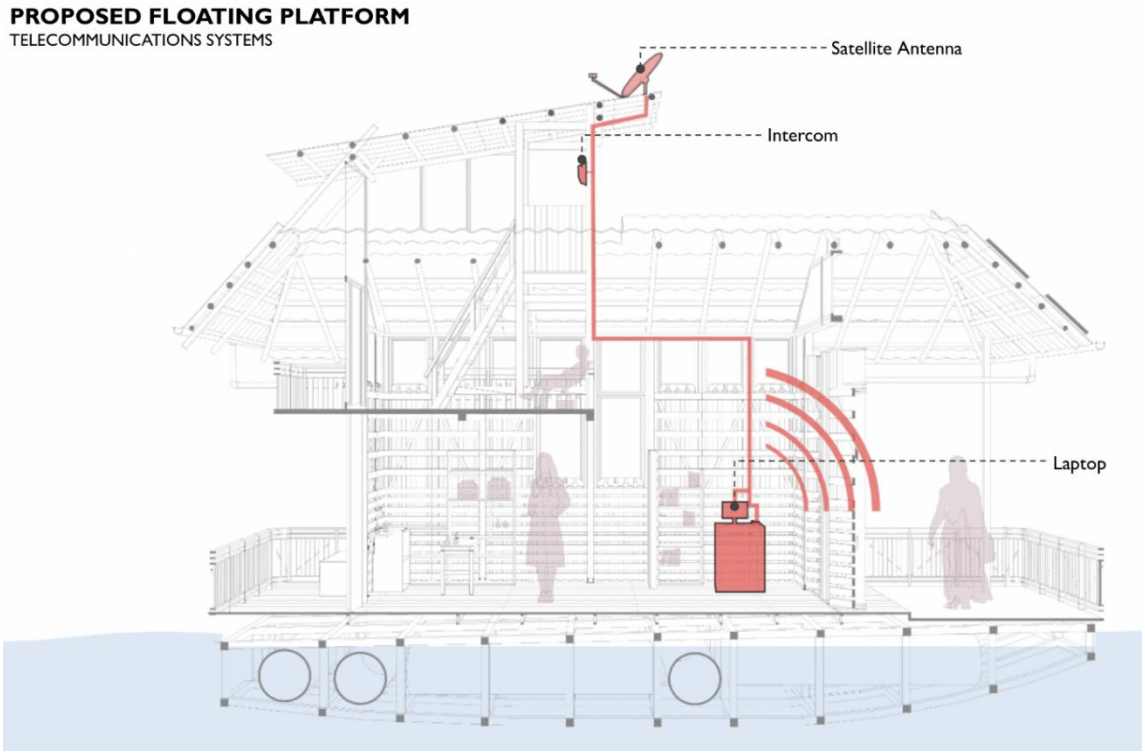

Preliminary proposal of requirements for a telecommunications system integrated to latest version of architectural plans of the floating platform
Source: CASA Team, 2023

The platform will also capture solar energy through solar panels to feed batteries and an electrical system for light fixtures and other laboratory equipment.

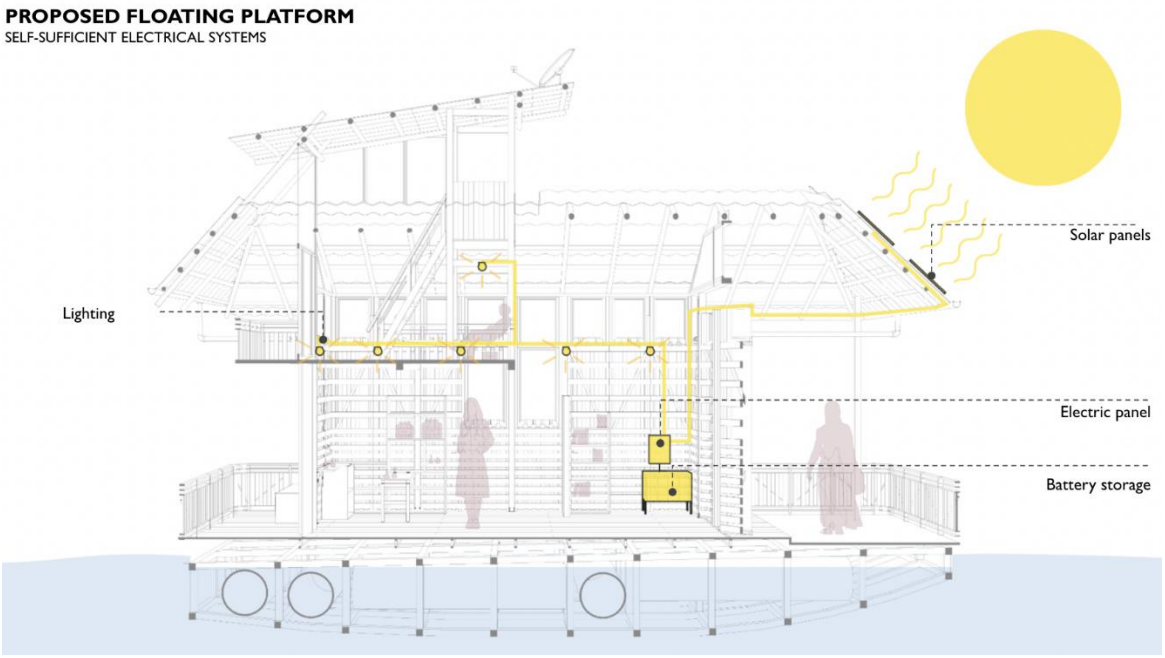

Electrical system proposed for the floating platform
Source: CASA Team, 2023

The researchers also sought to include a previously developed rainwater harvesting system which works autonomously and does not require conventional water and sewage networks. Composed of tubes available at local hardware stores, the system is modular and adaptable to different configurations, becoming architectural components such as walls, columns and railings that, due to their permeability, promote cross ventilation. The incorporation of local resources in its elaboration, as well as the improvement of pre-existing local knowledge of the handling and management of water, seeks to make the technology attractive and replicable for residents and local authorities. It seeks to incorporate a social and intercultural approach in the design and implementation of urban infrastructure, generating alternatives to excessively technocratic views that result in infrastructure that is not appropriate for the socio-cultural and environmental context where they are located.

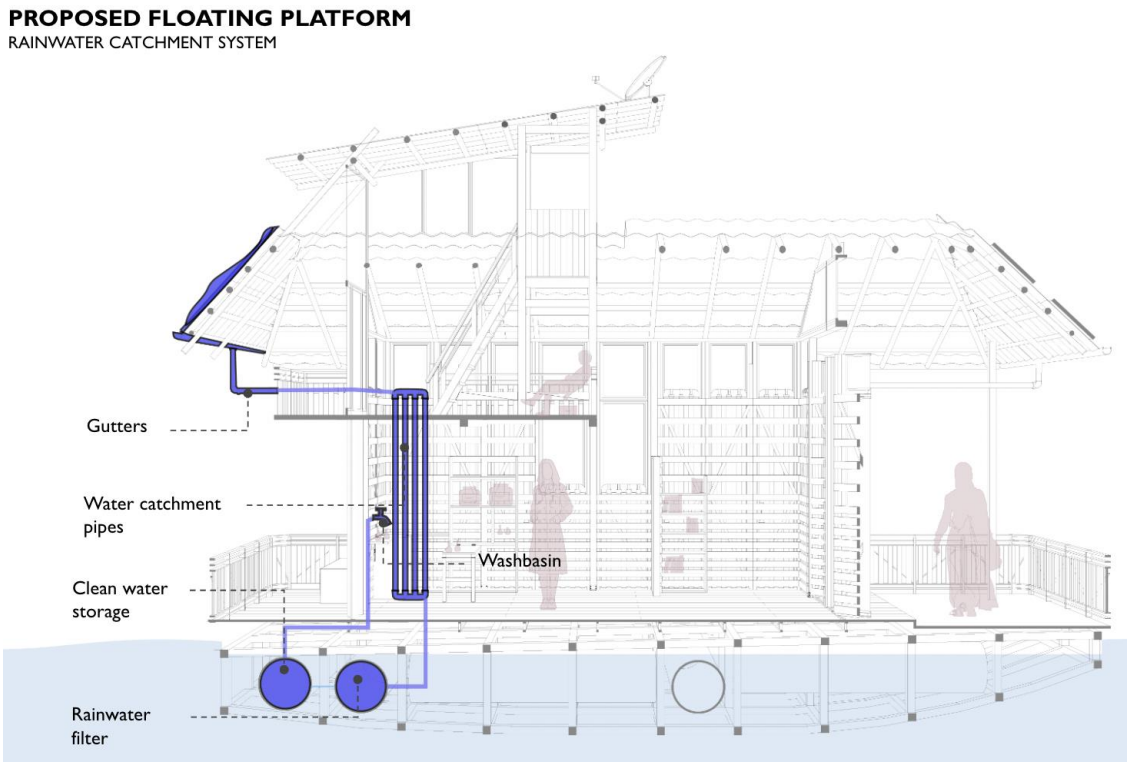

Rainwater catchment, storing, and treatment system proposed for the floating platform
Source: CASA Team, 2023

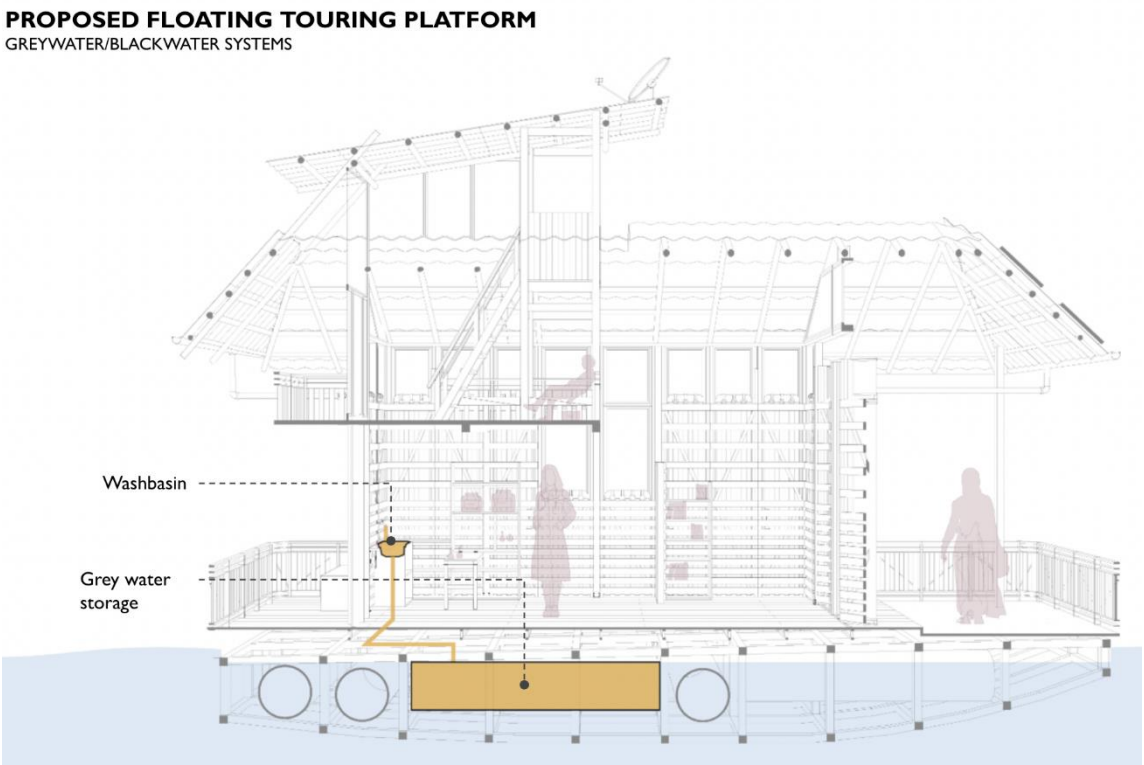

Grey and black water treatment systems proposed for the floating platform
Source: CASA Team, 2023

The grey and black water storage system is connected to the toilet and sinks. For now, it will only have the function of accumulating and when it is full, it can be pumped into a treatment unit outside the ship. The design of this platform component is still under development.

3.4 Step 4: Presentation of proposal to local authorities and universities

For the sustainability of the floating platform, we had to identify users with the capacity to use and maintain the platform. Originally, this project was intended to be a collective community space. However, after identifying the difficulties of service delivery faced by public institutions and local academia, in addition to a clearer idea of the possible costs of the platform, the team thought it more appropriate to find ways in which the platform could be collectively managed and used by public institutions to improve service delivery, including disaster management and response.

Costs for maintaining the platform include fuel, sailors and personnel's salaries, maintenance of the floating platform, maintenance of the infrastructure and maintenance of the equipment (CST rainwater system, electrical system and telecommunications system). These costs exceed the capacity of individual communities and could create an additional challenge in capacity-building for the proper use of the different technological systems put in place. As Arboleda (2022) explains, participatory or social architecture should consider maintenance costs to make sure the project does not add unmanageable burdens to communities which are oftentimes already struggling to make ends meet.

Hence, the second round of presentations involved exploring, together with representatives of public institutions and the local university, what kind of uses and activities could be held in the platform as well as pathways towards collaborative work for its use and maintenance. These exchanges provided the team of designers with sufficient material to adjust the proposal.

Additionally, around this time (late 2022), the team of researchers were able to secure funding for the continuation of the project through the Peruvian Research Council (CONCYTEC being its Spanish acronym). This funding allowed the implementation of the prototype as well as monitoring and evaluation of its use. With this, two decisions were made: doing a series of virtual simulations of the floating platform, to be able to test its floatability with licensed local naval engineers and adjusting the proposal for it to be constructed with the available funds.

Presentation to local authorities in Nauta, Loreto, Peru.
Credits: Kleber Espinoza, 2023

3.5 Step 5: Adjusting the proposal

After the exchanges with local authorities, the team of researchers continued to refine the design of the platform, articulating different components with each other and researching technologies and methods to treat grey and black water on and off site.

The platform has a flexible space and four nuclei in the corners where laboratory services, energy storage, satellite station and hygienic services (toilet, sink and shower) are concentrated.

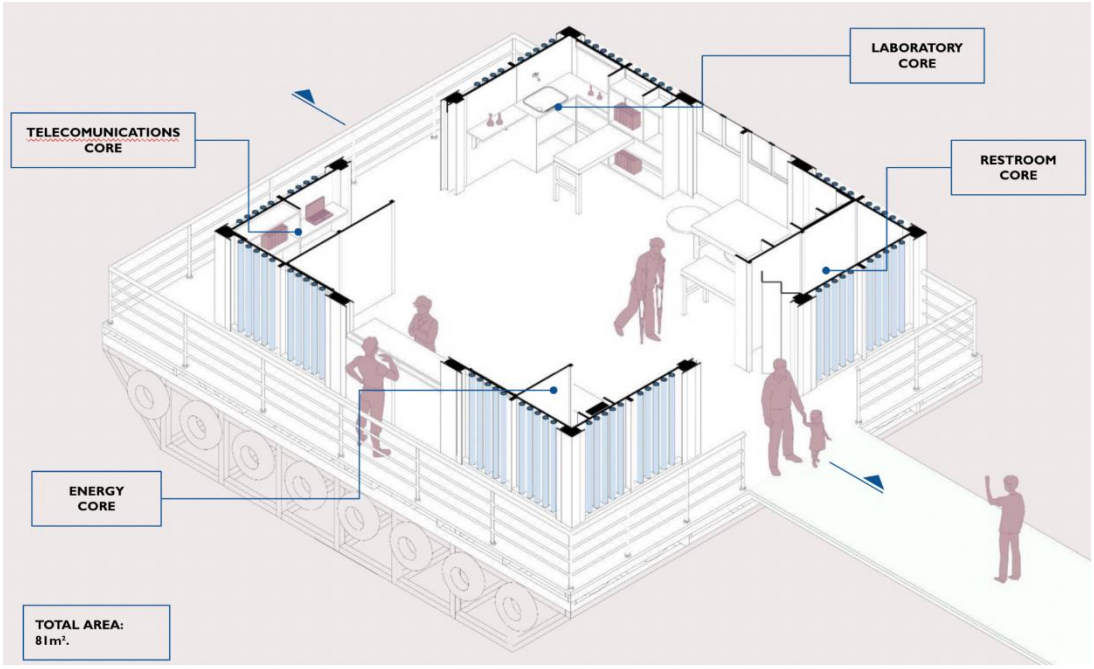

Axonometric view of the main floor of the floating platform with the four service nuclei detailed
Source: CASA Team, 2023

Access to the interior of the platform is through sliding doors on the front that, when fully open, allow the integration of external and internal activities. On the main level, below the mezzanine, are the restroom and laboratory cores. Each one has the basic necessary furniture to be able to carry out both cleaning and hygiene activities as well as carry out sample collection, experiments, research and scientific or technical work.

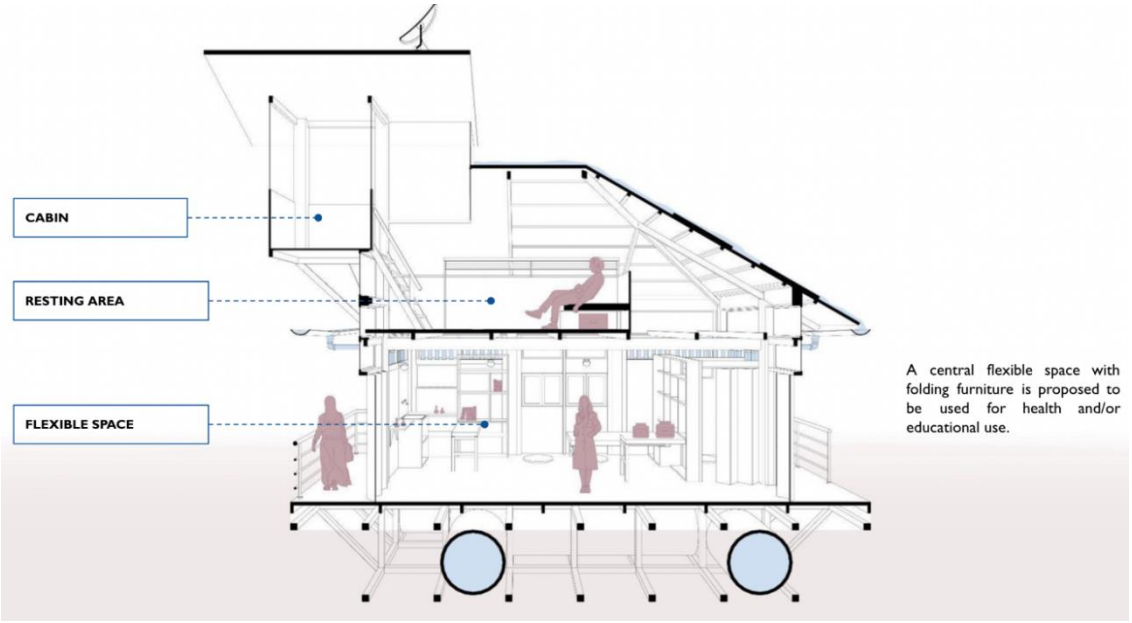

A section view of the main floor of the floating platform details the main floor, resting and cabin area
Source: CASA Team, 2023

With a better idea of available funds for the implementation of the platform, and after conversations with naval engineers about costs of construction services and materials, the overall size of the floating platform had to be reduced considerably. It went from having an area of over 80m^2 to 60m^2, of which 15m^2 are exterior spaces and 45m^2 are within the platform's walls. However, this reduction in area does not significantly alter the flexibility of uses of the platform as it mainly affects the platform's weight-bearing capacity and reduces the maximum number of users.

The base of the floating platform is the result of an integration of the rainwater and river water treatment systems, the grey and black water storage and the necessary structure to maintain the flotation and stability of the vessel.

Water treatment consists of the storage companies removing and reducing the degree of contaminants from the source water through conventional and sophisticated treatment processes, such as coagulation, flocculation, sedimentation, filtration, disinfection and reverse osmosis. producing treated water suitable for human use and

free of impurities and contaminants, in accordance with water quality standards and regulations.

The rainwater catchment system functions by means of the coverage and the gutters in the direction of the first filters. When these filters are full, the water would leave the first contaminated water tank to flow into the storage tank where it would be treated. Subsequently, it will be pumped into the treated water storage partitions for use in the boat.

Main floor plan of the floating platform with the four service nuclei detailed
Source: CASA Team, 2023

Second floor plan of the floating platform showing the crew's sleeping area
Source: CASA Team, 2023

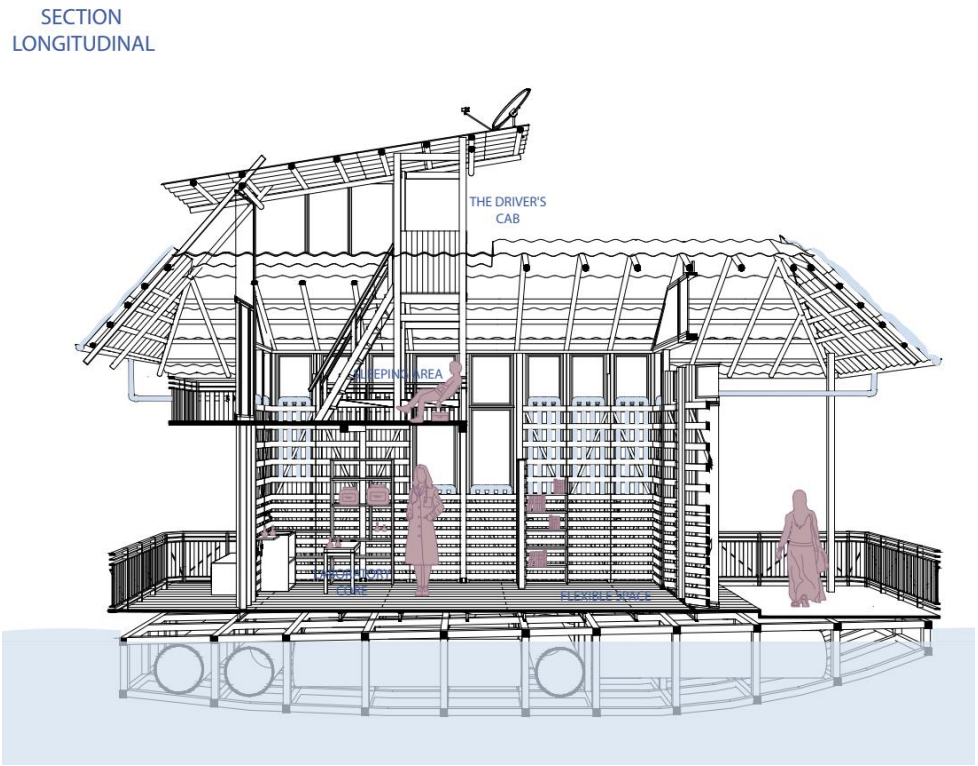

Longitudinal section of the floating platform showing the driver's cabin, crew's sleeping area and the main floor's flexible space
Source: CASA Team, 2023

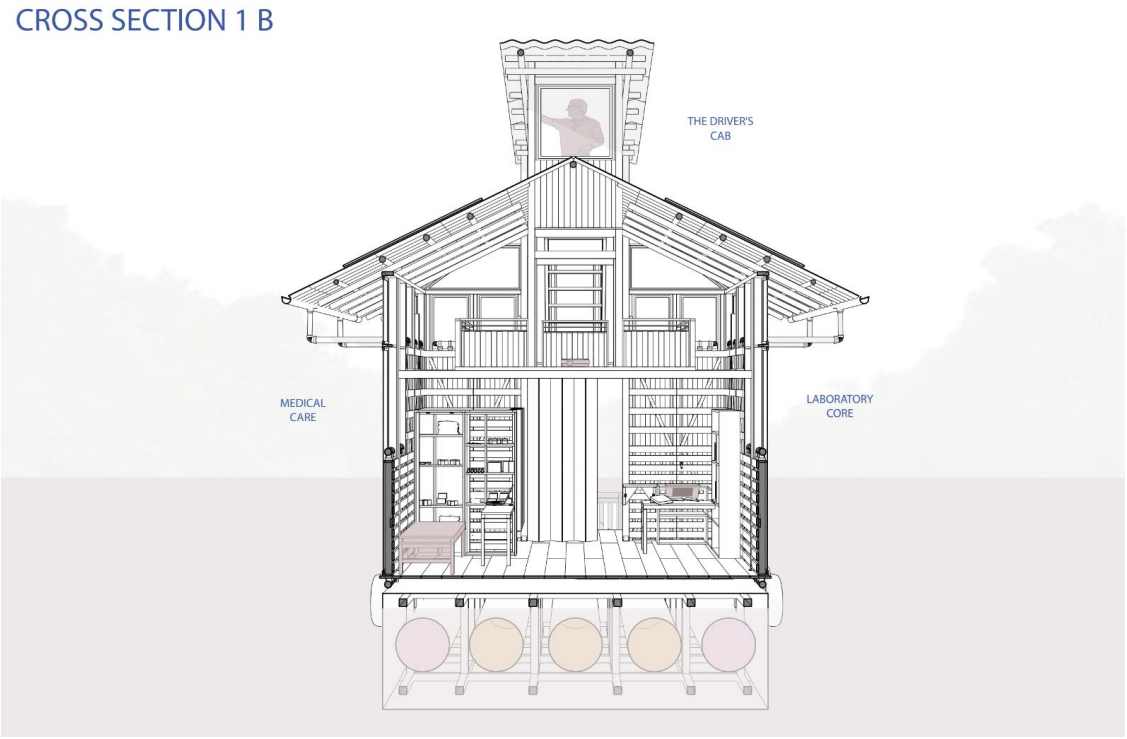

Cross section of the floating platform showing the driver's cabin, crew's sleeping area and the main floor's flexible space
Source: CASA Team, 2023

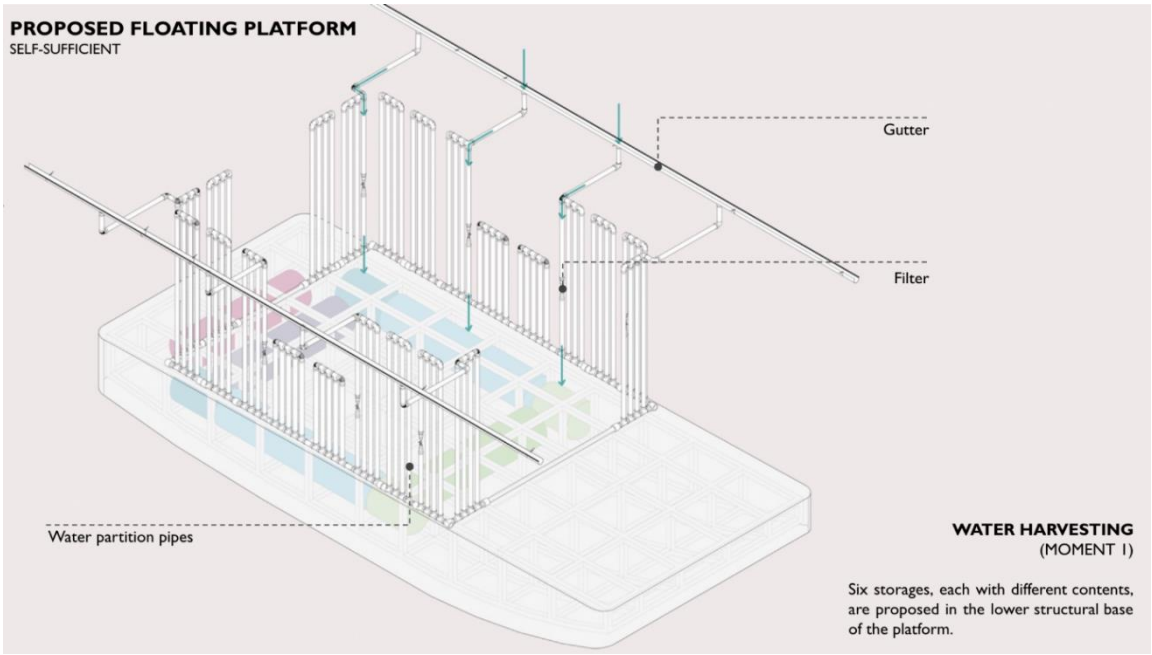

The river water catchment system is carried out at the base in a storage and after its sedimentation it is transferred to another storage where it is distributed to the toilet tank and works when there is no rainwater. The river water will be an alternative during months with low rainfall since it can be pumped towards the storage walls.

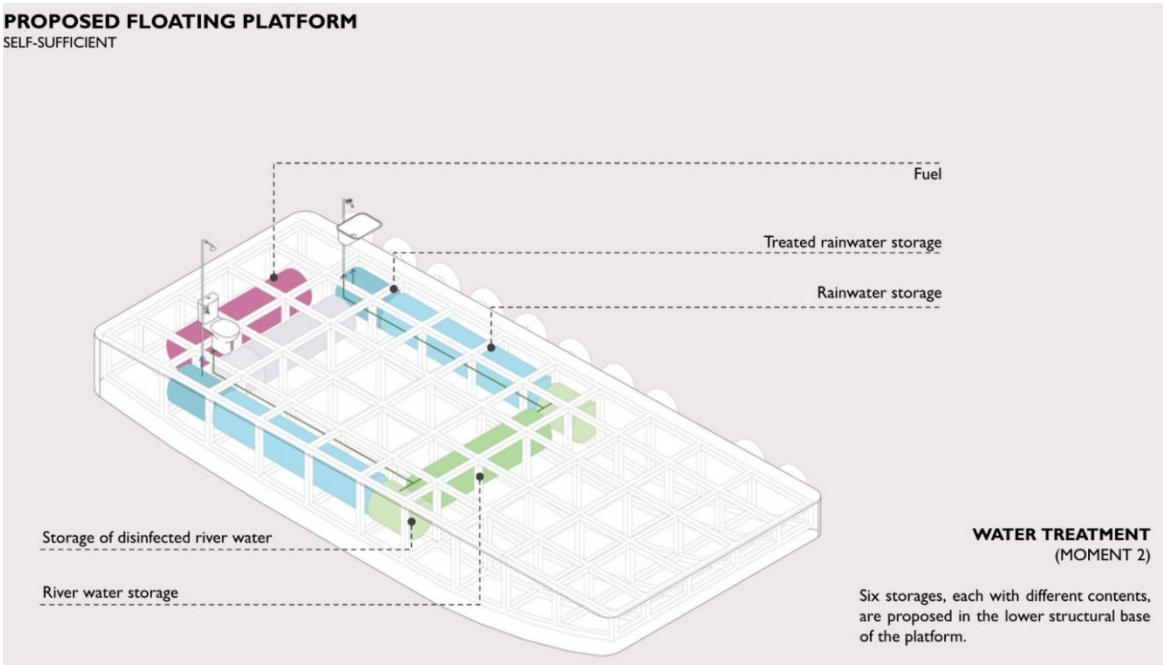

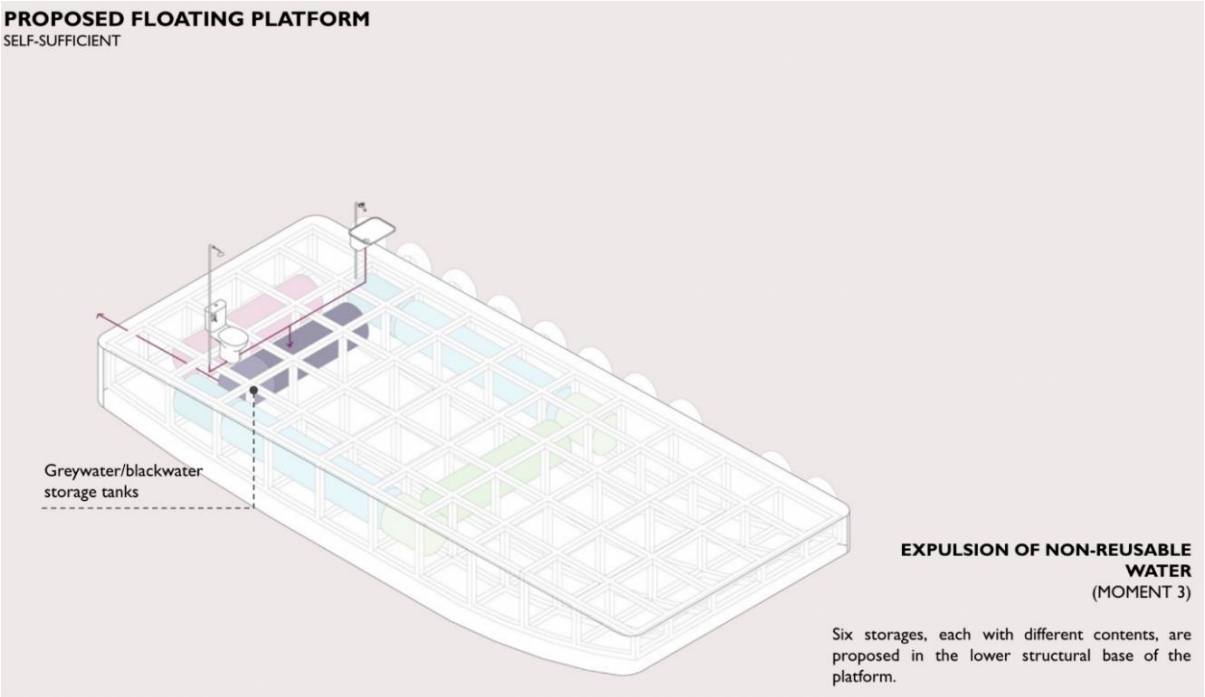

3.6 Step 6: Naval engineering calculations

Note: These calculations were undertaken by naval engineers Luis Fernando Concha Figueroa, Mariano Moscol Proaño and Leonar Llacctahuaman Hinostroza, who mentored the design of the platform.

The scantling is the dimensional calculation of the structure of the vessel, to ensure the structural integrity of the vessel in operation. This calculation is made based on the operating condition. For this case, the platform will operate in fluvial waters. Therefore, navigation range and height will be estimated based on this. Additionally, the platform is a water collector, due to this, the design of the tanks will be based on the stored water.

On the other hand, this platform will not be used as cargo transportation, which is an important factor for the estimation of the roof structure.

We present a summary of the structural calculation process. It should be noted that the calculations of the minimum dimensions that the vessel must have will be based on the standard for naval design NR 217 Part B of the classification society BUREAU VERITAS (“Rules for the Classification of Inland Navigation Vessels – PART B: Hull Design and Construction - 2021”). This standard is used due to its high reliability in naval design.

Structural Element	Minimum measurement
Cover Plate	4.76 mm
Longitudinal Deck Reinforcements	2"X2" X 1/4"
Beams	4"X4" X 1/4"
Side Plates	4.76 mm
Longitudinal Side Reinforcements	2"X2" X 1/4"
Frames	4"X4"X1/4"
Bottom plates	6.34 mm
Longitudinal background reinforcements	2"X2" X 1/4"
Floor timber	4"X4"X1/4"
Transverse bulkhead plate	4.76 mm
Transverse bulkhead vertical reinforcements	2"X2"X1/4"
Longitudinal bulkhead plate and tanks	4.76 mm
Longitudinal reinforcements of longitudinal bulkhead	2"X2" X 1/4"

4. Results and Discussion

4.1 Findings from planning documents

The unique characteristics of the dynamic Amazonian territory and the mobility and dispersion of amphibian communities throughout the lowland Amazon rainforest calls for alternative forms of service delivery, both in terms of infrastructure and of bringing social programmes closer to communities (Desmaison et al, 2021). The difficulties of reaching these communities are striking when analyzing national statistics. The population of Loreto performs lower than the national average across multiple indicators of social and sanitary wellbeing, such as access to education, malnutrition, anaemia, and teenage pregnancy, among others.

4.2 Disaster and climate-related planning responses

Novel methods of service delivery for amphibian communities are already in place, as seen in the PIAS platform promoted by the Peruvian government. However, due to the size of the ship, it cannot reach communities located near tributary rivers and it only reaches the communities every 2 to 3 months. Hence, smaller boats with more frequent visits are

needed, so that local levels of government can visit the communities more often to provide access to education and health, and to be able to better respond to risk situations (i.e. flooding and fires).

4.3 Findings from interviews

Discussion meetings were held with academics for the dissemination and generation of scientific knowledge between the Pontifical Catholic University of Peru (PUCP) and the National University of the Peruvian Amazon (UNAP). One possible use for the itinerant floating platform is for it to become a laboratory or space for exchange workshops between professionals from various disciplines of the university and inhabitants of riverside communities.

We consider that these meetings are essential for the sustainability of the project, both for the use and maintenance of the prototype to be implemented and for its possible replicability. Another important component in the development of the prototype is the work of recognition of the specificities, needs and capacities of the riverside communities for which the proposal will be implemented. We understand that we cannot add the economic and labour burden of maintaining the prototype to communities which already face difficulties in meeting their basic needs. Therefore, collaborative work with public institutions is fundamental. Working closely with the communities is essential for the proposed prototype to provide relevant and pertinent solutions capable of adjusting to their ways of living.

5. Enablers and Barriers

Enablers of this research include a common understanding of the urgency of coming up with novel solutions to attend to the necessities of amphibian communities in the lowland rainforest. Communities, local public institutions and researchers alike recognise the enormous barriers (temporal, economic and cultural) that limit and affect service delivery and the necessity to transform current ways of operating as they are perceived as inefficient, eroding trust between communities and public institutions. This common understanding enables, in turn, political will, interest and commitment in continuing to participate in the research.

Similarly, the broader team of multidisciplinary researchers participating in this project have shown high levels of commitment and participation, so that the design of the platform could consistently evolve and be improved. The design of the platform allows the exploration and emergence of technological innovation, taking into account the necessity

for these technologies to be “appropriate”, i.e. relevant to their geographic and socioeconomic context, so that they are easy to use and maintain and can be appropriated by the users. These include technologies and methods for water treatment.

As for barriers, the main barrier identified is rising costs of travel and of construction materials which limit the number of days we can be on the site as well as the distances we can travel to engage with amphibian communities. This also limits the overall size of the platform and could eventually limit the number of services it can offer, as the local public institutions have limited budget available for travel. Another important barrier is building relationships of trust between multiple stakeholders, as past experiences have eroded the relationships between public institutions and communities which feel abandoned.

6. Key Takeaways from CDRI Fellowship Programme

Based on the observations made in exchanges with the various actors related to the project, a series of conclusions emerge that provide clarity about the considerations to be considered for the continuous development of the project, both in its design aspect and in anticipating its proper use and maintenance.

The first theme that arises is the need to have an intercultural approach and openness to dialogue to understand realities and ways of living specific to riverside communities. Instead of imposing certain worldviews while discrediting others or making recommendations that are hardly applicable in these communities, the intercultural approach advocates a more empathetic understanding of lifestyles, needs and desires, and seeks integration and/or consensus between different worldviews. Vertical imposition of the provision of services and lack of recognition of diversity, particularly in cases where the exchanges are not continuous, create difficulties for the provision of services and their sustainability over time. In this sense, it was identified that local authorities have been developing programs and training for public representatives to develop strategies to improve the provision of services and strengthen relations between the public sector and riverside communities.

Regarding the limitations in reaching remote riverside communities, representatives of both the municipality and the health network expressed that they do not have their own boats and must rent them at high prices to be able to make the visits, making them infrequent and expensive. Maintaining and sustaining their own distinct

boats would be difficult for both institutions due to their limited budgets. Both institutions expressed interest in the possibility of sharing responsibilities and costs, in order to have a platform that could potentially increase the frequency of visits.

Likewise, UNAP also agreed that the high costs of boats and transportation limit both research and interactions with remote communities. Professors from a variety of faculties expressed interest in integrating the platform into their activities, such as research, laboratories (with sample collection and sharing of results via satellite), workshops, and health and nutrition campaigns, in which both professors and students could participate and strengthen their relationships with the broader environment.

We believe that these exchanges are essential for the sustainability of the project beyond its established term, both for the use and maintenance of the prototype to be implemented and for its possible replicability. We understand that we cannot add an economic and labour burden to maintain the prototype for communities with difficulties to meet these expenses. Therefore, collaborative work with public institutions becomes essential since they have greater capabilities to invest the necessary resources, especially if it is done in a tripartite manner. This learning does not mean stopping work and conversations with the riverside communities of the Marañón River. Working closely with the communities is essential for the proposed prototype to provide solutions relevant to their ways of life.

7. Conclusion

The possibility of having mobile infrastructure capable of providing service delivery, capacity building and emergency response to dispersed communities is a valuable lesson applicable not only in the Amazon rainforest but in other areas of the world with similar amphibian settlements. The flexibility of the floor plan allows it to be adapted for different uses and programmes.

Collaborative work between multiple disciplines as well as between academia, public institutions, and communities becomes fundamental for the proposal to be pertinent and responsive to unique cultural and territorial circumstances. This kind of work requires openness, empathy and willingness to learn from each other while prioritizing the needs and worldviews of historically marginalized populations.

8. Way Forward

The design of the platform is still a work in progress. We continue to adapt the structure in coordination with the different specialists involved, to comply with naval regulations and safety protocols. Additionally, we continue to make adjustments to the architectural components to ease maintenance as well as ensure the durability of the materials, as much as possible, by protecting them from sun and heavy rainfall (which involves changing the design of the roof as currently proposed).

In parallel, we will now engage in negotiations with UNAP, the Municipality and the Sanitation Network, towards a cooperation agreement for the use and maintenance of the platform, which will include further research to determine the costs involved in operating the platform with greater specificity.

Until August 2023, the team of researchers plans to hold exchange workshops and collect comments and appreciations from both government institutions allied to the project and the riverside communities of Nauta. With these workshops, we seek to continue to incorporate their comments in the project proposal. These exchanges also allow contemplating the sustainability of the prototype over time, beyond the deadlines established for the execution of the project and through the formation of alliances to explore possible routes towards the insertion of the proposal in public policies.

Implementation of the platform is scheduled for August 2023, which may extend until October 2023. The prototype is expected to be launched towards the end of October or the beginning of November 2023, leaving enough time (seven months until June 2024) for the stages of monitoring, evaluation and adjustments to the prototype, and the continuous strengthening of alliances with the main social agents and identified politicians. In July and August 2024, we will develop dissemination products of the project as well as participate in national and international seminars and conferences.

References

1. Arboleda, G. (2022). *Sustainability and Privilege: A Critique of Social Design Practice.* Charlottesville: University of Virginia Press.
2. Desmaison, B., Boano, C., & Espinoza, K. (2021). Towards an Amazonian Urbanism: Collective Infrastructures of Care. *Contesti*, 81–96. https://doi.org/10.13128/contest-12982
3. Desmaison, B. & Espinoza, K. (Eds). (2021). *Agua y Comunidad en la Amazonía: Guía de diseño, implementación, uso y mantenimiento del modelo de captación, almacenamiento y tratamiento de lluvia*. Lima, Fondo Editorial PUCP.
4. Fausto, C. (2008). Too many owners: Mastery and ownership in Amazonia. *Mana*, *14*(2), 329-366. doi: 10.1590/S0104-93132008000200003
5. Fernandes, D. y Ramírez, M. (2019a). Mi casa pequeña, mi corazón grande. Política territorial y cosmológica del pueblo Kukama. *Mundo Amazónico*, *10*(1), 157-184. doi: 10.15446/ma.v10n1.73980
6. Fernandes, D. y Ramírez, M. (2019b). Geografías afectivas del pueblo kukama, Amazonía peruana. *Espacio y Desarrollo,* (33), 47-65. doi: 10.18800/espacioydesarrollo.201901.003
7. Pérez, C. (2010). "Dinamismo Tecnológico e Inclusión social en América Latina: Una estrategia de desarrollo productivo basado en los recursos naturales" in Revista CEPAL n.100, pp. 124-125. Santiago de Chile
8. Pérez-Foguet, A. (2006). "Tecnología para el desarrollo humano. Propuestas de Educación para el desarrollo en los estudios de ingeniería" in Energía, Participación y Sostenibilidad, pp. 31-42. Barcelona: Ingeniería sin Fronteras.
9. Piccini, L. M. (2023) *Ukakana kukama: La casa las y las relaciones socioespaciales en la Amazonía contemporánea* [Unpublished Masters Thesis]. Escuela de Posgrado de la Pontificia Universidad Católica del Perú.
10. Pile, S. (2009). Emotions and affect in recent human geography. *Transactions*, *35*(1), 5-20. doi: 10.1111/j.1475-5661.2009.00368.x
11. Ramírez-López, A., Beuchelt, T., Velasco-Misael, M. (2013). "Factores de adopción y abandono del sistema de agricultura de conservación en los valles altos de México" en ASyD 10, pp. 195-214. 2013
12. Roca-Servat (2019). 'Sí a la vida, al agua y al territorio. Relaciones hidrosociales alternativas en Colombia . European Review of Latin American and Caribbean Studies Revista Europea de Estudios Latinoamericanos y del Caribe.

13. Tello Imaina, L. (2016). “Introducción” in L. Tello Imaina, y S. Boyd (Eds.), J. Huaymacari Tamani, y M. Nieves Nashnato (Trads.), *Karuara: la gente del río*. Asociación Quisca; Radio Ucamara; Wainakana Kamatawarakana.
14. Tello Imaina, L. (2018, July). (Seminar Intervention). *Simposio llevado a cabo en Conferencia Ingeniería con Propósito: Ciencia y Cosmovisión Amazónica*. Universidad de Tecnología e Ingeniería, Lima, Perú.
15. Viveiros de Castro, E. (2002). *Perspectivismo y multinaturalismo en la América indígena. A inconstância da alma selvagem* (Sao Paulo, Cosac y Naify, 2002, pp. 345-400

Constructed Wetlands for Wastewater Treatment Plant Resilience

Cayla Anderson
The University of British Columbia
Vancouver, Canada

Research supported by:
Dr Rachel Scholes
Assistant Professor,
Department of Civil Engineering
The University of British Columbia
Vancouver, Canada

Under CDRI Fellowship Programme 2022-23

Disclaimer: The views expressed in this paper reflect the opinions of the author and not necessarily the official views of CDRI.

Abstract

The increasing frequency and intensity of extreme storms and flooding events due to climate change threaten traditional wastewater treatment infrastructure capacity. In the North American Pacific Northwest, large flooding events have resulted in untreated and partially treated municipal wastewater bypassing treatment infrastructure and polluting local water bodies. As a result, there is a need to improve the resilience of wastewater treatment infrastructure. Constructed wetlands for wastewater treatment are an attractive addition to traditional wastewater treatment trains as they can provide additional treatment capacity during high intensity storm and rain events. Vertical flow constructed wetlands have been used successfully to treat shock loads of wastewater from combined sewer overflows.

To further investigate the resilience of vertical flow constructed wetlands against shock loads of partially treated wastewater, we constructed nine model wetland columns in the laboratory that were fed with synthetic, secondary municipal effluent wastewater. Twice over the four-month experimental duration, three columns were subjected to high intensity flooding events, modelling a one-in-100-year extreme rain event for the city of Vancouver, British Columbia. Under baseline conditions (i.e. not flood flow rates), the column wetlands operated with an average hydraulic retention time of 2.35 days. During high load simulations, the retention time was decreased to 0.24 ± 0.1 days in the three high load columns. Under baseline conditions, the wetlands removed 85 ± 14% of the influent ammonia concentration.

All other parameters measured remained relatively constant with no observable removal of other nutrients like phosphates and sulphates. The high loading events produced no observable effect on pH measurements, dissolved oxygen, electrical conductivity, dissolved organic carbon, and phosphates and sulphates measured in the effluent. Ammonia removal efficiency decreased to 78 ± 14% during the high loading events. However, treatment performance resumed shortly after the shock event.

Results from the study indicate that vertical flow constructed wetlands are resilient to changes in influent-loading due to flooding and high intensity storm events. Mass removal rates of ammonia based on the column data were calculated per square metre to estimate treatment performance during a high loading event in a larger, full-size system. However, caution is advised when extrapolating data. The vertical flow constructed wetland systems studied are a resilient technology that can potentially improve the resilience of municipal wastewater treatment trains.

Acknowledgments

I would like to first and foremost thank my supervisor, Dr Rachel Scholes, for her guidance and constant support in the design and execution of this project, from the very first stages of writing the application. This work and my ability to conduct scientific research could not have been possible without her. I would also like to acknowledge the team at UBC that made the setup possible: Bill and Doug in the Civil Engineering workshop, and Felix Shuen and Brad Wishart in the laboratory. I would also like to acknowledge the dedicated team of undergraduates and fellow graduate students who have assisted in sample collection – Ayesha Mushtaq, Aishwarya Das and Mackenzie Leckie.

I would like to express my deepest gratitude to Dr Rama Pandey and Dr Anne Gibbs for their mentorship during the fellowship. It has been a pleasure to share this project with you both, and your advice has been invaluable. Finally, I would like to acknowledge the CDRI Fellowship team for all their work in making this programme possible.

Funding

This research was supported by the 2022–2023 Fellowship of the Coalition for Disaster Resilient Infrastructure (CDRI), Application ID: 210922626, and the Department of Civil and Environmental Engineering at the University of British Columbia, Vancouver.

1. Introduction

The intensification of extreme weather events due to climate change has the potential to overwhelm wastewater treatment plants (WWTPs), releasing untreated or partially treated wastewater in local environments, posing serious environmental and human health concerns (Singh & Tiwari, 2019). Urban wastewaters contain high concentrations of human-derived pathogens, heavy metals, pesticides, pharmaceuticals and nutrients (nitrogen and phosphorus) which threaten aquatic ecosystems (Cantinho et al., 2016; Rizzo et al., 2020; Sarkar et al., 2019). Heavy metals, such as copper, can be toxic to fish which may adversely impact the local fishing industry (Rubalingeswari et al., 2021). High concentrations of pathogens present in local waters are dangerous to swimmers and transmit infectious diseases, while emerging contaminants such as pharmaceuticals and pesticides have adverse effects on aquatic organisms in trace concentrations.

In North America, the release of wastewater is of concern in the Pacific Northwest, where the intensity of precipitation events is predicted to increase in severity (US EPA, n.d.). In 2017, following heavy rains, Seattle's largest WWTP malfunctioned, discharging 30 million gallons of raw wastewater into the Puget Sound (*Plant Failure […] Seattle*, 2017). A similar event occurred at two other plants in early 2021, resulting in no-swim ordinances and a moratorium on shellfish harvesting for two weeks (*Heavy Rain Sends Untreated Wastewater into Puget Sound*, 2021). In Vancouver, Canada, authorities and residents express concern over the release of wastewater-derived pollutants in the Fraser River and Salish Sea (*Treated Wastewater and Aquatic Environment*, n.d.). As the local wastewater utility, Metro Vancouver, proceeds to upgrade the Iona Island WWTP, mitigating the release of raw sewage is pertinent (Hornor, 2020).

Wastewater treatment plants are constructed with a number of safeguards to build resilience against system failure (Jackson & Ferris, 2013). However, extreme weather events can cause even these precautions to fail. Constructed wetlands (CW) for wastewater treatment have the potential to act as the last line of defence after WWTP failure, to protect ecosystems from contaminants present in untreated wastewater. Figure 1 demonstrates this concept.

Constructed wetlands are widely used to polish domestic and industrial wastewaters by reducing concentrations of nutrients, organic carbon and emerging contaminants such as pharmaceuticals, pesticides and heavy metals (Khan et al., 2009; Vymazal, 2011). CWs are low cost, low energy technologies engineered to enhance aspects of natural wetland ecosystems to optimize water treatment. However, despite the

wealth of studies on constructed wetland feasibility and efficiency, the resilience of these systems for wastewater treatment following large flooding and storm events is poorly understood.

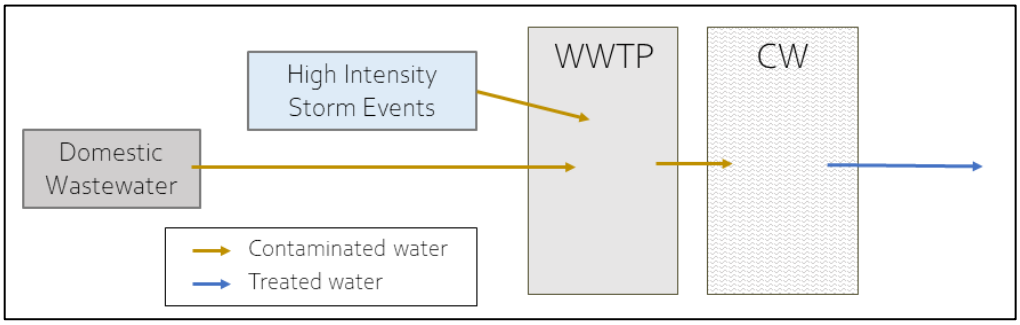

Figure 1. Conceptual Image of constructed wetlands (CW) used to buffer WWTPs during high intensity storm events

The hypothesis that CWs will improve resilience in WWTPs following extreme events is supported by successful CWs in Europe and the US, constructed to treat a combination of raw sewage and stormwater from combined sewer overflows (CSOs) (Rizzo et al., 2020; Tao et al., 2014; Tondera et al., 2019). CSOs are the primary source of pollution in local water bodies that prevent swimming and fishing after storms (Rizzo et al., 2020). CWs for CSOs prove to effectively reduce pathogen and micropollutant concentrations in CSO waters (Tondera et al., 2019). CWs are also an attractive solution because they mimic natural wetlands' ability to mitigate the impacts of flooding by slowing runoff (Brady et al., 2021). CWs for wastewater treatment have further been proven to be resilient to certain changes in inflow quantity (Sukias et al., 2018).

While the use of CWs as resilient wastewater treatment infrastructure is promising, some studies have identified potential limitations. For example, flooding had a negative impact on the treatment efficiency of an open-water treatment wetland for wastewater polishing in Orange County, California (Brady et al., 2021). There is, therefore, a lack of consensus as to how constructed wetlands will respond to high intensity storm and flooding events. This research aims to answer that question by directly characterizing the response of CWs during extreme events to understand their potential for building infrastructure resilience.

2. Aim, Objectives and Scope of the Research Study

This research aims to provide evidence to support the implementation of CWs as a polishing step following conventional wastewater treatment trains. When implemented in

this context, CWs may enhance resilience during extreme events by providing treatment capacity when conventional wastewater treatment systems are overwhelmed. This project investigated the potential resilience benefits of CWs by assessing the resilience of these technologies following shock inputs of partially treated wastewater. This research will be broadly used to inform municipalities, city planners and developers of the structural resilience of natural systems, which will in turn eliminate a barrier to their widespread adoption.

The objective of the research is to evaluate resilience to system disruptions through wetland column experiments in the lab, using them as a proxy for estimating resilience in full-scale CW systems. The scope of the research is limited to monitoring lab-scale, column wetlands fed with synthetic secondary wastewater treatment plant effluent runoff, under controlled flow conditions. The shock loading events are based on extreme precipitation data for the city of Vancouver. The results collected from the columns represent four months of operation, representing the initial maturation phase and early stabilization period. Resilience in this study is measured by observing the changes in effluent concentration of certain key parameters during and following the high load simulation. We have measured two types of resilience: 1) when there is minimal change in effluent concentrations of the parameter during the high load event, and 2) when there are significant changes in effluent concentrations of the parameter during the high load event, but treatment performance returns to pre-loading efficiency once flow returns to normal.
This research evaluated the effects of simulated flooding events on CW performance and the ability of CWs to mitigate disruptive events. The experiments were used to assess the feasibility of CW operation and removal rates of identified parameters. The findings may inform future research on removal mechanisms and pilot-scale CW studies.
The objectives of the study are as follows:

1. The construction of model constructed wetland columns in the lab that can efficiently remove common wastewater pollutants under normal flow conditions.
2. Evaluation of column wetland response under increased loading periods resembling conditions associated with high intensity storm events.
3. Estimation of wetland column resilience to the high loading events and its extrapolation for full scale systems.

3. Methodology

The study primarily comprised the construction and operation of model wetland columns. The design of the columns and subsequent high loading experiments were informed by a comprehensive review of literature related to constructed wetlands for wastewater treatment. Section 3.1 summarizes the relevant literature and provides background information regarding wastewater treatment by constructed wetlands. Section 3.2 is dedicated to the experimental setup, analytical methods and parameterization of the wetland column setup. Figure 2 summarizes the research methodology.

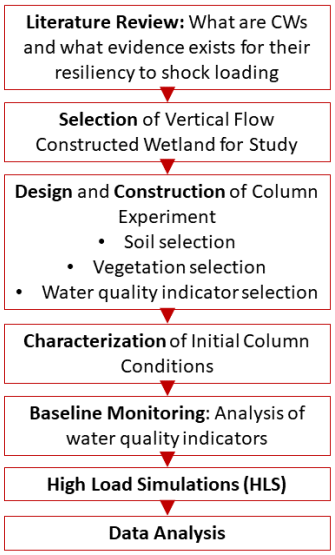

Figure 2. Methodology flow chart

3.1 Relevant Literature Summary

3.1.1 Constructed Wetlands and Wastewater Treatment

Natural wetland systems have historically been used as disposal sites for human waste for centuries (Vymazal, 2011). However, with growing populations and increases in large urban centres, natural wetland ecosystems were degraded under the influx of wastewaters. Around 1950, the development of constructed wetlands to treat and contain wastewaters began with the first pilot-scale study in Germany (Vymazal, 2022). By the 2000s, these systems were in operation worldwide with different configurations serving to treat industrial effluents, agricultural runoff, reverse osmosis concentrate, combined sewer overflows and both partially treated and raw domestic wastewaters (Cecchetti et al., 2020; Healy et al., 2007; Khan et al., 2009; Rizzo et al., 2020; Scholes et al., 2021; Vymazal, 2014).

Wetland systems are effective for water treatment due to the myriad of treatment processes that can occur in parallel in the saturated subsurface. “Wetland” refers to any area of land that is fully saturated during all or part of the year (US EPA, 2015). Complete saturation results in high rates of biological activity which can actively transform many common pollutants. Further, pollutants can be adsorbed to subsurface constituents, be taken up by plants or be transformed by photodegradation in open-water configurations

(Kadlec & Wallace, 2009). The beauty of constructed wetlands is in the versatility of their design. Different configurations of hydrology, vegetation and substrate can be optimized to meet treatment goals. What follows is a brief overview of one type of wetland design: subsurface flow wetlands.

Subsurface flow wetlands: Subsurface flow wetlands consist of fully saturated soil or gravel areas in which water flows completely underground. The ample contact time between water and the subsurface allows for filtration, sorption and biotransformation of wastewater pollutants in the subsurface (Kadlec & Wallace, 2009). Subsurface flow systems can be either planted or unvegetated. Wetland vegetation contributes to contaminant removal via filtration in the root zones and uptake of organics and nutrients (Kadlec & Wallace, 2009). Subsurface flow systems can further be divided into horizontal flow (HF) and vertical flow (VF) systems. In a HF system, the water flows horizontally along the wetland bed before being discharged through an outlet pipe into the environment. In VF systems, water flows top down, driven by gravity (Stefanakis, 2019). HF systems tend to need larger areas than VF systems and operate with longer hydraulic retention times to achieve similar treatment efficacy. For instance, Akratos and Tsihrintzis (2007) observed the adequate removal of biochemical oxygen demand (BOD) and total nitrogen at retention times of eight days or longer in a HF system. In contrast, VF systems have smaller areas and shorter hydraulic retention times (HRTs) (Saeed & Sun, 2012) ranging from a few hours to 3-4 days (Ghosh & Gopal, 2010). VF systems, therefore, perform better for aerobic degradation of contaminants, which is a faster process than the anaerobic degradation in HF systems (Vymazal, 2011). Further, HF systems are more prone to clogging than VF systems (Saeed & Sun, 2012).

3.1.2 Constructed Wetland Resilience

While the performance of constructed wetlands to treat a variety of wastewaters is well documented, few studies have directly monitored system resilience to extreme weather events. Table 1 summarizes studies on constructed wetlands for wastewater treatment that consider effects on performance related to disturbances. These disturbances range from changes in hydraulic loading to changes in influent water quality. While most are not directly related to system resilience under a changing climate, many of the disturbances studied are possible due to climate change, such as the flooding and drought conditions investigated by Brady et al. (2021). It is of note that the studies summarized in Table 1 do report variable resilience depending on the type of wetland and the type of disturbance. For example, the subsurface flow systems investigated by Sukias et al. (2018) reported full recovery following an increase in hydraulic loading, whereas the floating wetland

which also received an increase in hydraulic loading, investigated by Saeed et al. (2016), did not recover during the study period. While more research is needed to draw a stronger conclusion, these papers indicate that subsurface flow systems may be more resilient to shock loading than free water systems.

Table 1. Summary of studies investigating constructed wetland resilience to various disturbances

Wetland Type(s) / Experiment Scale	Disturbance	Effect of Disturbance	Wastewater Type	Author
Recirculating VF wetland / lab scale	High/low pH; interruption of recirculation; increased pollutant concentrations	Little observable effect after 24 hours	Synthetic domestic wastewater	Zapater et al., 2011
Shallow, free water surface (FWS) wetland / pilot-scale; microcosm experiments	Drought Flooding	Nitrate removal rates returned to pre-drought conditions within a week of rehydration Nitrate removal rates never returned to pre-flooding conditions	Secondary treated wastewater effluent	Brady et al., 2021
HF, VF and recirculating VF wetlands / pilot scale	Increased hydraulic loading	Complete recovery of pre-disturbance treatment performance within 0-3 days following disturbance	Primary treated wastewater effluent	Sukias et al., 2018
FWS wetland / pilot-scale	Increased hydraulic loading	Reduction of ammonia removal during and following shock loads	Polluted river water	Saeed et al., 2016
HF / lab-scale	Increased organic loading	Reduction in COD removal efficiency during and following the high loading	Synthetic domestic wastewater	Galvão & Matos, 2012

The studies summarized in Table 2 investigate the impacts of high loading on constructed wetland systems. The high loading in these studies is held constant for the duration of the experiment and, in some studies, compared to parallel systems with smaller inflows. While, strictly speaking, these are not resilience studies, the evidence that adequate treatment performance is possible even under high loading (short HRT) conditions is promising when applied to the conditions of this project.

Table 2. Summary of studies investigating variable influent loading rates

Wetland Type / Experiment Scale	High Loading Rates Studied	Effect of Different High Loads	Wastewater Type	Author
HF/pilot	6, 8, 14 and 20 days HRT	Efficient removal efficiency observed at HRT of eight days or longer	Synthetic domestic wastewater	Akratos & Tsihrintzis, 2007
VF/pilot	6, 12 and 24 hours HRT	Efficient removal of monitored pollutants was observed at each HRT with maximum removal efficiencies observed at 12 hours	Dairy wastewater	Minakshi et al., 2022
Upflow VF / pilot	1, 2, 3 and 4 days HRT	Best removal of monitored pollutants was observed at the 4-day HRT, however adequate removal was observed at 2, 3 and 4 days	Secondary treated wastewater effluent	Ghosh & Gopal, 2010

Finally, evidence that constructed wetlands for wastewater treatment will be resilient to high loading events resulting from large storm events, is supported by evidence of constructed wetlands used in the context of stormwater and flooding. Cecchetti et al., 2020 studied the treatment performance of a HF constructed wetland that functions as both a coastal levee and tertiary treatment for municipal wastewater. The authors found near complete removal of nitrate, trace organic contaminants and F+ coliphage in the subsurface flow system. Further, Rizzo et al., 2020 and Tao et al., 2014 have published comprehensive reviews summarizing the use of constructed wetlands to treat effluent from CSOs. CSO effluent flows are episodic and occur during storm events. Both reviews indicate positive treatment performance of a vast array of constructed wetland configurations to treat CSO effluents despite the stochastic nature of CSO events. Predominately, variations on VF constructed wetlands are used to treat CSO effluents due to their ability to hold the flood waters, slow peak flows and adequately remove wastewater pollutants of concern. Further, these systems require less area than HF systems or free water systems, making VF wetlands a more versatile treatment option. The literature reviewed in Tables 1 and 2 also indicate that VF systems may be more resilient to high loading events and short retention times. This project, therefore, focused on assessing the resilience of VF subsurface wetlands.

3.2 Experimental Design

To study the effects of high hydraulic loading on constructed wetlands in a controlled environment, we constructed nine soil columns in the lab to model full-scale constructed wetlands (Figure 3.D). Each column was filled with the following in sequence (adapted from You et al., 2019): 12.5cm coarse gravel, 2.5cm quartz sand (0.45 – 0.55cm mesh) and 30 cm of soil, planted with Carex elata 'Aurea' (golden sedge). Overflow valves enabled the columns to be operated with constant hydraulic head values of 40cm during normal operation and 45cm during flooding events. Effluent flow rates were controlled by a needle valve at the base of each column.

During normal flow conditions, synthetic wastewater was pumped into the columns by peristaltic pumps, maintaining an effluent flow rate of approximately 0.1 – 0.3 mL/minute (for the full spectra of effluent flow rates, see Section 4.1.1). The synthetic wastewater recipe was adapted from Osachoff et al., 2014 to mimic the constitution of secondary effluent from domestic wastewater treatment plants and is found in Table 3.

Table 3. Synthetic Wastewater Recipe

Compound added to Synthetic Wastewater	Concentration (mg/L)
Monopotassium phosphate	12
Sodium bicarbonate	155
Ammonium chloride	52
Magnesium chloride	25
Calcium chloride	37
Zinc Sulphate	0.2
Bovine Serum Albumin	9
Sodium alginate	7
Humic acid	18
Carbamazepine	0.01
Fipronil	0.01
Atenolol	0.01
Sulfamethoxazole	0.01
Trimethoprim	0.01

3.2.1 Column Construction

The inspiration for the column design came from the work of Pritchard et al., 2023 with soil columns modeling stormwater bioretention systems, specifically the effluent control features and mid-column sampling ports. The columns for this experiment were constructed in November and December of 2022, with assistance from the UBC Civil Engineering Department Workshop. Figure 3 shows the full setup.

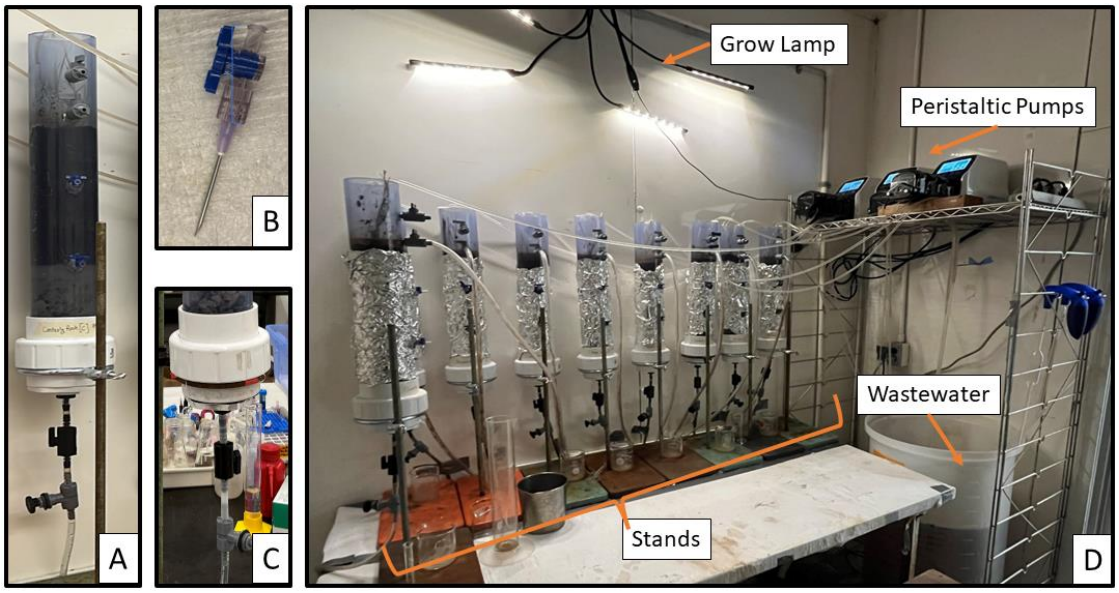

Figure 3. Experimental setup. A) Close-up photo of a single column; B) in-column sample port; C) close-up of the end fittings and effluent valves; D) full experimental setup with labels.

The tinfoil on the columns prevents photodegradation on the outer edges. Each column was given an ID letter as shown in Figure 4. For the duration of the experiment, the columns were grouped into sets of three, running in parallel, to serve as replicate samples of each other. The sets were:

Control #1: Columns W, E, R

Control #2: Columns B, V, K

High Loading Simulation (HLS): Columns C, H, Q

Figure 4. Photo of each column with their respective IDs. The colour of the label indicates to which group each column belongs. Blue: Control #1, Green: Control #2, Orange: HLS

The two control groups never experienced high loading conditions and the three columns in the HLS group received the same extreme flooding conditions. We chose to run the columns in sets of triplicates to account for the heterogeneity of environmental experimental models. While many controls are in place to ensure the columns function similarly to one another, soil characteristics and flow rates are subject to difference among columns due to differences in microbial growth and preferential flow paths. Therefore, by having many replicates, we can capture the range of wetland responses.

3.2.2 Vegetation and Soil Selection

Carex elata Aurea (golden sedge) was chosen as the model wetland vegetation in the columns. It is a hardy wetland plant native to North America that thrives in water saturated environments (*USDA Plants Database*, n.d.). As a perennial, the sedge undergoes periods of dormancy. Over the course of the experiment, it was observed that the plants became dormant, likely due to a lack of natural light. Therefore, the plants served as ornamental parts of the system and are assumed to have contributed little to treatment performance.

The columns were intended to model subsurface flow constructed wetlands, so it was important to choose a substrate representative of wetland soils. Since the data from this experiment is intended to be shared with Metro Vancouver to promote the adoption of nature-based systems within city infrastructure, we chose to work with soil that the city of Vancouver currently uses in their bioretention basins and other green stormwater infrastructure in the city. The city sources their soil from the British Columbia-based company Veratec Engineered Products Inc. Veratec supplied a sample bag of their product ECOmedia for use in this project. The parameters of this soil are displayed in Table 4.

Table 4. Soil Options and Parameters

Soil Source	EC (µS/cm)	pH	Moisture Content (%)	g Soil Organic Matter (SOM) / kg of soil	Clay (%)	Silt (%)	Sand (%)	Classification (USDA)
Veratec ECOmedia	0	6.93 ± 0.05	3%	114.87 ± 22.9	19%	28%	53%	Sandy Clay Loam

3.2.3 Column Characterization

Table 5 reports the masses of each layer of the substrate and pore space estimation. Pore space was estimated by first saturating the filled columns with carbon dioxide (CO_2) gas for one hour in an up-flow configuration. CO_2 is used to displace air in the pore space as it dissolves faster in water than air, thus allowing for more complete saturation (Pritchard et al., 2023). Following CO_2 saturation, the columns were massed and saturated with deionized water. The saturated mass was recorded and the difference of the two masses divided by the water density was taken as the volume of the pore space for each column.

Table 5. Column Substrate Mass and Pore Volumes

Group	Column	Gravel (kg)	Sand (kg)	Soil (kg)	Pore Space (cm^3)*
Control #1	W	1.1	0.2	0.6	800
	E	0.9	0.1	1.2	600
	R	0.8	0.1	1	700
Control #2	B	0.9	0.1	1.1	500
	V	0.9	0.2	1	600
	K	0.9	0.2	1	600
HLS	C	0.8	0.1	1.3	500
	H	1	0.1	0.9	800
	Q	0.6	0.2	1.2	500

*Pore space was estimated as the volume of water needed to completely saturate the dry column. 1g water = $1cm^3$

Tracer tests were then conducted to determine the hydraulic residence time and residence time distribution for each column. Bromide was used as a conservative tracer at an effluent flow rate of ~0.25 mL/minute. The tracer was spiked at the top of the columns and 50mL of composite effluent samples were collected every 3.5 hours. Bromide concentrations in each sample were measured using ion chromatography (IC) (see Section 3.2.5 for more on the IC method). The tracer test was conducted in deionized water. During this time, samples were also collected for dissolved organic carbon (DOC) analysis. Figure 9.C and 9.D display the initial soil organic carbon leaching that occurred during the startup phase of the experiment. Due to the high SOM content (Table 4), we expected to see high levels of DOC at the beginning of column operation.

The tracer results in Figure 5 indicate one-dimensional flow through the columns. While some columns yielded broader residence time distributions – specifically W and Q – the tracer concentration profiles indicate that most of the tracer exited the columns around 40-60 hours after injection. The peaks also indicate there is no observable short

circuiting within the columns however the long tails on the peaks may indicate some stagnation within the columns.

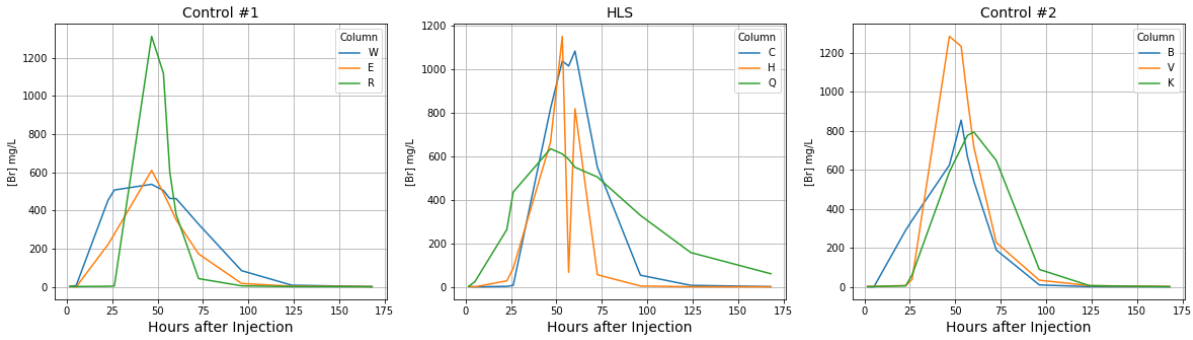

Figure 5. Effluent bromide concentrations following injection of tracer solution. Graphs separate individual column data into their respective groups. Note: Except for column H, all columns yield a single peak around 40-60 hours after injection, corresponding to a hydraulic retention time of 1.67-2.5 days.

3.2.4 Baseline Monitoring

Synthetic wastewater was introduced to the columns on January 25, 2023. Between January 25 and April 25, 50-mL composite samples were collected from the effluent valve 2-3 times per week. The effluent flow rate in the columns was maintained between 0.1–0.3 ml/minute. Influent samples were also collected on a weekly basis. After sample collection, the pH, electrical conductivity (EC), temperature and dissolved oxygen (DO) were measured (Section 3.2.5 for methods). Samples were then filtered by either 0.45-µm polyether sulfone syringe filters or 0.2-µm polyether sulfone syringe filters and prepped for further analysis. These monitoring samples allowed for determination of baseline conditions in the columns before and after the high load simulation events.

3.2.5 Water Quality parameters

pH, electrical conductivity and temperature were measured in each sample immediately after collection using a calibrated Environmental Express Oakton PC 100 Portable pH and conductivity meter. DO was also measured immediately using a Hach HQ30d portable DO probe.

Concentrations of nitrate, nitrite, phosphate, sulphate and chloride were measured in each sample by ion chromatography on a Thermo Fisher Dionex Aquion System. Dissolved organic carbon, inorganic carbon and total carbon were measured by combustion on a TOC-L Shimadzu Total Organic Carbon Analyzer and ammonia concentrations were measured by flow injection analysis using a Lachat QuickChem 8500 series 2. For each analysis, quality controls and blanks were analysed with each set of

samples to ensure data quality and accuracy.

3.2.6 High Load Simulation

When simulating flooding events associated with extreme weather conditions, we chose to model the events based on extreme rainfall data relevant to the city of Vancouver, BC. We accessed Intensity-Duration-Frequency (IDF) curves measured at the rain gauge station: VANCOUVER INTL A ID:1108395. These IDF curves are accessed on the Computerized Tool for the Development of Intensity-Duration-Frequency Curves under Climate Change – Version 6.5 (Simonovic et al., 2015). Briefly, an IDF curve reports the likelihood of a range of extreme rainfall events for a given location. For example, on the IDF curve for the Vancouver station (Figure 6), the most extreme rain event in a 60-hour period with a one-in-100-year frequency has an intensity of 29.81 mm/hour. This was the rain event we chose to model in the columns, approximating the intensity to 30 mm/hour for ease of calculation.

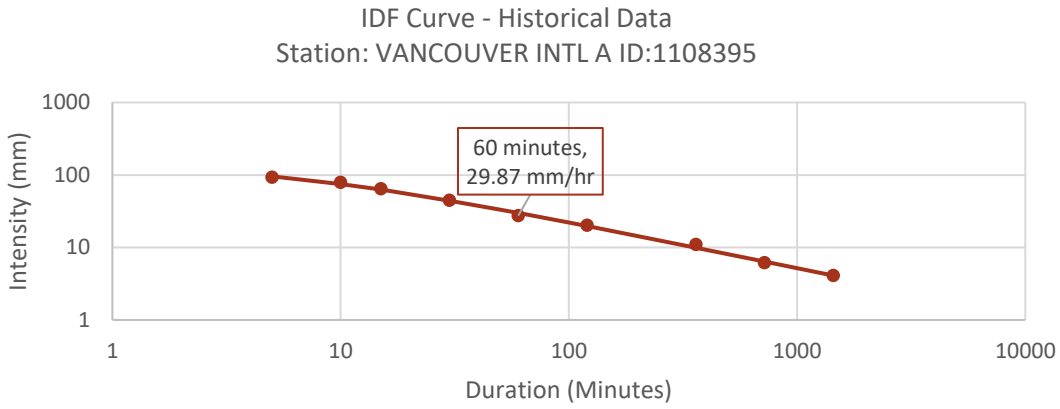

Figure 6. One-in-100-year IDF curve of Vancouver, BC based on historical precipitation data. The data and chart layout are adapted from Simonovic et al., 2015.

The model wetlands were constructed in 3-inch inner diameter pipes with a soil surface area of approximately 45.6 cubic centimetres. A 30 mm/hour intensity rainfall scaled to the size of the columns corresponds to a flow rate of roughly 2.2 mL/minute. To simulate the high load event, columns C, H and Q effluent flow rates were increased from 0.25 mL/minute to 2.2 mL/minute for one hour. Further, the columns were flooded to the second overflow valve to maintain a constant head of 45 cm for the duration of the high load event. This increase in hydraulic head simulated overland flooding of the wetland during an extreme rain event. During the 1-hour event, 50-mL composite effluent samples were collected after 30 minutes of flooding. The HLS samples were processed following the procedure discussed in sections 3.2.4 and 3.2.5.

Over the course of the column operation, two separate HLSs were initiated. The

first, here designated as HLS1, occurred in the early stages of column operation on February 27, 2023, March 1, 2023, and March 3, 2023. On each date, the three HLS columns' flow rates were increased for one hour. Samples at the normal flow rate were collected before and after the HLS to differentiate between baseline and HLS conditions, and to enable us to observe the ability of the columns to resume normal treatment efficacy. The second round of HLSs (HLS2) occurred in the late stages of column operation, on April 17 and April 19, 2023.

4. Results and Discussion

4.1 Baseline column performance

4.1.1 Hydraulics and Physicochemical Parameters

During the four months of operation, under normal flow conditions, the columns sustained an overall average flow rate of 0.23 mL/minute at the effluent. This flow rate corresponds to an average HRT of 2.35 days, where HRT for each column is computed as

$$HRT\ (days) = \frac{Volume\ of\ pore\ space\ (ml)}{Effluent\ flow\ rate\ (\frac{ml}{day})}$$

The columns were designed to maintain an HRT of approximately 2.5 days. In the literature, vertical subsurface flow systems have been reported to have successful removal of common wastewater pollutants when operated with HRTs ranging from 12 hours (Minakshi et al., 2022) to four days (Ghosh & Gopal, 2010). Longer HRTs are generally considered to enhance pollutant removal due to the extended contact time between contaminants and soil surfaces (Minakshi et al., 2022). Longer HRTs also provide more time for microbial communities to degrade contaminants. However, longer HRTs require larger systems to treat a given volume of water. Therefore, for our systems, we chose to operate within the middle of the range of commonly reported HRTs.

In practice, fluctuations around average values for HRT and flow rate were common, as observed in Figures 7.A and 7.B. Effluent flow rate is a function of soil porosity, hydraulic head and the effluent valve position on a given day. Small fluctuations in these parameters are responsible for the variety of flow rates. Table 6 reports the average flow rates and corresponding HRTs for each of the column groups.

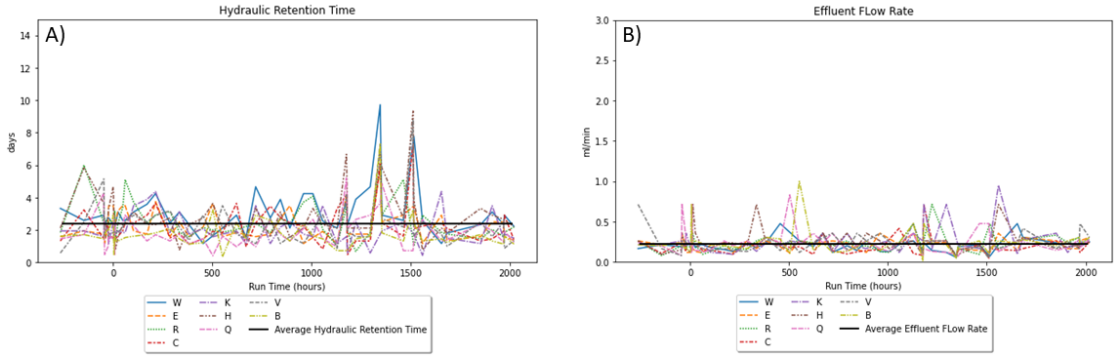

Figure 7. A) Plot of HRT values and B) flow rates for individual columns over the initial tracer period and monitoring period

Table 6. Effluent Flow Rates and Hydraulic Retention Times (mean ± standard deviation)

Group	Flow Rate (ml/minute)	HRT (days)
Control #1	0.215 ± 0.092	2.66 ± 1.26
Control #2	0.243 ± 0.146	2.06 ± 1.18
HLS Columns	0.232 ± 0.140	2.33 ± 1.38

DO and pH effluent values remained relatively stable throughout the column operation with both exhibiting a slight decrease over time as the columns matured. There was an average decrease of 1 pH unit following column treatment, with an average of 7.62 in the influent and an average of 6.62 in all column effluents. Fluctuations in individual columns were relatively small (Figures 8.A and 8.B). There was significantly more variability in the effluent concentrations of DO, which ranged from approximately 10 mg/L in early samples (i.e. in January) to less than 3 mg/L in later samples (i.e. in April). The wide range can be attributed to variations in the effluent flow rate at the time point of the samples. In general, samples that had a slower flow rate contained higher DO concentrations. This observation could be attributed to the sample collection process; as samples were collected at a slower rate, there was more contact time for atmospheric diffusion of oxygen into the composite samples prior to sample analysis. Further, because flow rates were inconsistent, some samples were collected when the columns were filled below their saturation level, i.e. there was more aeration in the columns than at full saturation, which may have contributed to the variability in DO measurements.

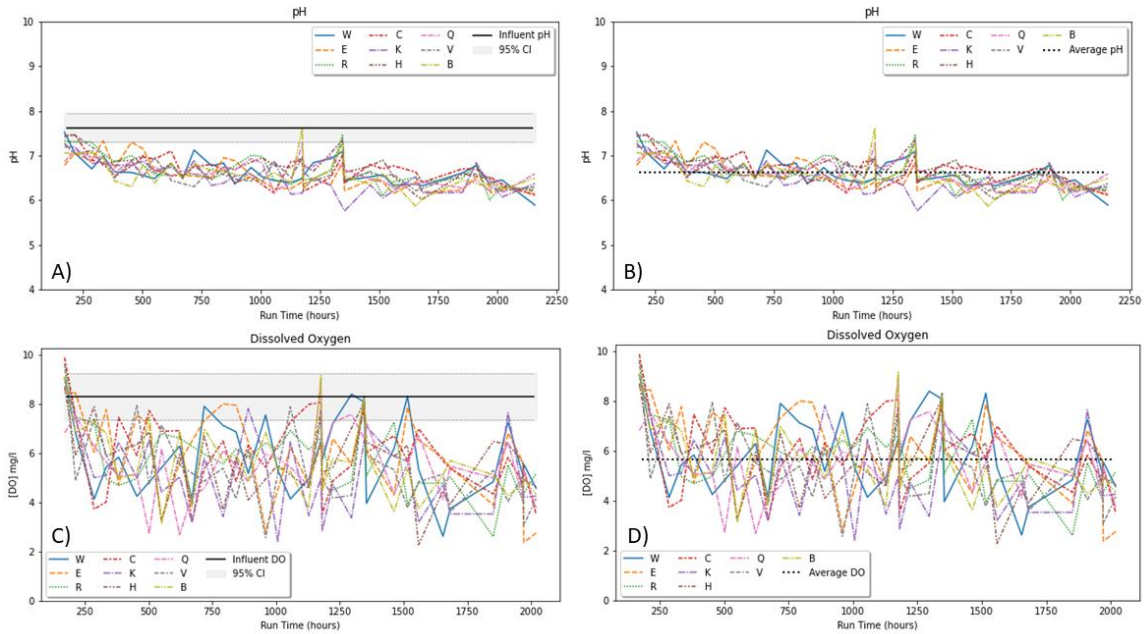

Figure 8. A) pH values for each of the nine columns and average influent pH value with its 95 percent confidence interval; B) pH values for each of the nine columns plotted with the average value of all columns over the entire column operation; C) DO concentrations measured at the effluent for each sample point of each of the nine columns and the influent concentrations with 95 percent confidence interval; D) individual column DO levels plotted with the average value of all columns over the entire column operation

Table 7. Wetland Physicochemical Parameters (mean value ± standard deviation)

Group	pH	DO (mg/L)	EC (µS/cm)	DOC (ppm)
Influent	7.62 ± 0.15	8.30 ± 0.46	423.67 ± 11.78	7.82 ± 4.50
Effluent: All Columns	6.62 ± 0.33	5.67 ± 1.52	511.28 ± 100.94	47.15 ± 59.40
Effluent: Control #1	6.61± 0.34	5.88 ± 1.53	496 ± 88.59	35.46 ± 49.64
Effluent: Control #2	6.57 ± 0.34	5.40 ± 1.56	490.33 ± 96.42	41.84 ± 70.28
Effluent: HLS	6.68 ± 0.29	5.73 ± 1.43	519.26 ± 113.46	52.75 ± 56.55

Trends for electrical conductivity and DOC indicate a clearer stabilization period than the pH and DO data. Effluent values for electrical conductivity primarily remained higher than the influent values for the first 750 hours of runtime, indicating there was likely leaching of salts and other dissolved solids from the soil during the startup phase. After this startup phase, electrical conductivity of the samples approached the influent values. We expect effluent electrical conductivity to stabilize at or near influent levels after further operation, as has been observed previously in treatment wetlands (Kadlec & Wallace, 2009).

As discussed in Section 3.2.3, prior to initiating wastewater flow in the system, the columns were first run with deionized water. During this time, samples were taken for DOC analysis. Figures 9.C and 9.D show the initial leaching of organic matter in the soil

during the pre-wastewater flow (indicated as the negative run time hours on the figure). After this first period of leaching, effluent values remained greater than influent DOC. This observation is likely the result of continued, gradual leaching from the soil as well as biomass produced by microbial communities within the soil columns.

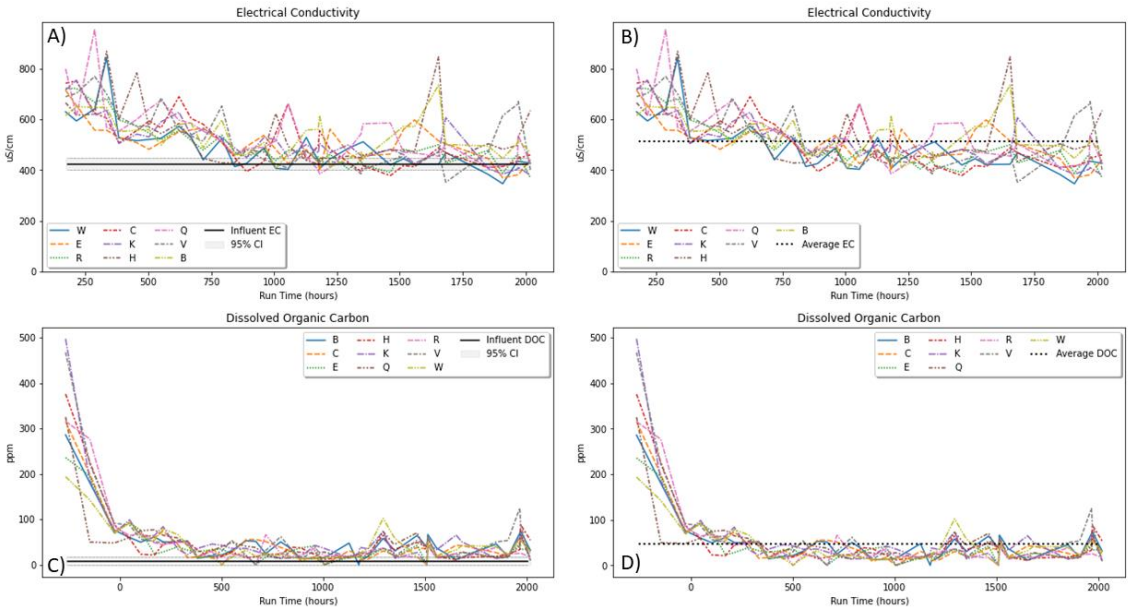

Figure 9. A) EC values for each of the nine columns and the influent EC average value with its 95 percent confidence interval; B) EC values for each of the nine columns plotted with the average value of all columns over the entire column operation; C) DOC concentrations measured at the effluent for each sample point of each of the nine columns and the influent concentrations and 95 percent confidence interval; D) Individual column DOC levels plotted with the average value of all columns over the entire column operation

4.1.2 Nitrogen

Nitrogen was introduced to the systems exclusively as ammonia (Table 3) because the synthetic wastewater was formulated to resemble un-nitrified secondary municipal wastewater effluent. In VF constructed wetland systems, it is expected that the aerobic subsurface conditions produce ample nitrification and very little denitrification (Saeed & Sun, 2012; Vymazal, 2011). The effluent nitrogen speciation in the columns supported this hypothesis. In Figure 10.A, we observed low effluent concentrations of ammonia with an average across all columns of 1.5 ± 1.41 mg-N/L, which represents an average percent removal of 85 ± 14% (Figure 10.B). These results are consistent with other studies on VF systems. For instance, Stefanakis & Tsihrintzis, 2012 reported ammonia removal efficiencies of 58 ± 13% and Tanner et al., 2012 reported up to 99.8 percent reduction in ammonia concentrations from hybrid and amended vertical flow systems. The high concentrations of nitrate and nitrite (cumulatively NO_x) found in the effluent are consistent

with ammonia removal via nitrification (Table 9 and Figure 10). Influent NO_x concentrations were approximately zero, indicating that all NO_x in the effluent was produced within the columns.

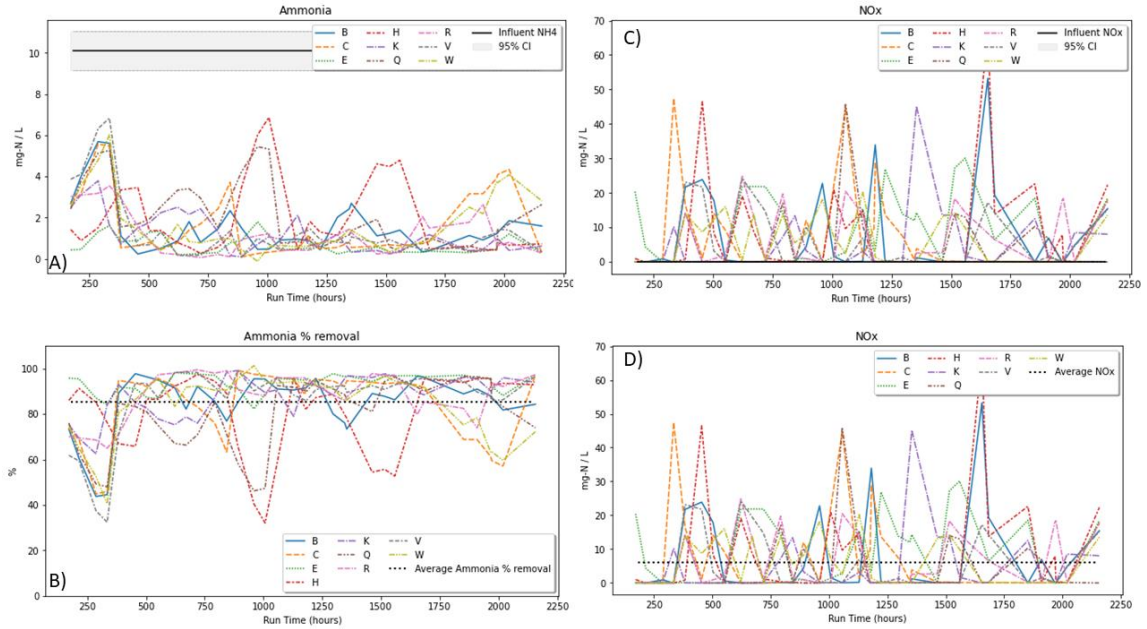

Figure 10. A) Effluent ammonia concentrations in individual columns and average influent value with 95 percent confidence interval; B) percentage removal of ammonia in each column; C) effluent NO_x concentrations for each column and average influent value; and D) effluent NO_x concentration for each column and average concentration for all columns

Table 9. Nitrogen Analysis (mean value ± standard deviation)

Group	NH_4 mg-N/L	% Removal NH_4	NO_x* mg-N / L
Influent	10.11 ± 0.45		0.05 ± 0.05
All Columns	1.50 ± 1.41	85.18 ± 13.93	6.07 ± 10.20
Control #1	1.16 ± 1.14	88.51 ± 11.28	6.88 ± 8.35
Control #2	1.40 ± 1.3	86.15 ± 12.92	5.27 ± 9.79
HLS Columns	1.92 ± 1.63	81.02 ± 16.12	6.07 ± 12.08

*NO_x = sum of NO_3 and NO_2 concentrations

Over the course of the wetland runtime, individual column effluent samples contained a wide range of NO_x concentrations. On average, all columns reported an average effluent NO_x concentration of 6.07 ± 10.2 mg-N/L (Table 9). The large standard deviation is a result of concentrations in the effluent spiking for one sample and disappearing in the next. This variance can be indicative of portions of the column where ammonia is sorbed and retained prior to microbial degradation, releasing NO_x in pulses (Kadlec & Wallace, 2009).

4.1.3 Phosphate and Sulphate

Effluent samples from the columns do not indicate any removal of phosphate, which is consistent with previous observations in VF systems (Kadlec & Wallace, 2009; Saeed & Sun, 2012). Phosphorus is predominantly removed from the water column through adsorption, precipitation and plant uptake, all of which occur primarily in systems with longer HRTs, systems with substrate amendments that enhance sorption or systems with plants specifically grown for phosphorus uptake (Ji et al., 2021; Shang et al., 2022). The average phosphate concentration in the effluent samples closely resembled that of influent concentration (Table 10). The large variability in effluent phosphate concentrations could be indicative of nonideal flow patterns in the columns, such as short circuiting or dead zones (Figure 11.A & 11.B).

Table 10. Phosphate and Sulphate Analysis (mean value ± standard deviation)

Group	PO_4 mg-P/L	SO_4 mg/L
Influent	2.32 ± 0.22	0.06 ± 0.08
All Columns	2.48 ± 2.01	1.66 ± 2.31
Control #1	2.43 ± 2.07	1.70 ± 1.79
Control #2	2.33 ± 1.88	1.63 ± 2.54
HLS Columns	2.68 ± 2.07	1.66 ± 2.55

Average effluent sulphate concentrations were consistently higher than the influent concentrations for the duration of the monitoring period when detected in the sample (Table 10). While sulphate is not directly a pollutant of concern (drinking water standards are < 250 mg/L), sulphur in wetlands plays a role in the immobilization of certain metals and can be an indicator of redox zones and biological activity (Kadlec & Wallace, 2009). The effluent sulphate concentrations were highly variable throughout this experiment. The occasional higher effluent concentrations compared to the influent may indicate areas of pooling within the column as other samples would indicate no sulphate. Alternatively, microbial activity and the degradation of the plants in the column may be releasing sulphate into the pore water.

4.2 High Load Simulations

4.2.1 Statistical Analysis

To assess the impact of the high loading events on wetland treatment performance, we first determined whether the high loading values were significantly different than results collected under normal flow conditions. A series of Student's T-tests were run between the different groups of samples reported in Table 11. Further, the HLS values were plotted alongside the grouped normal flow values for each of the water quality parameters of interest (Figure 12).

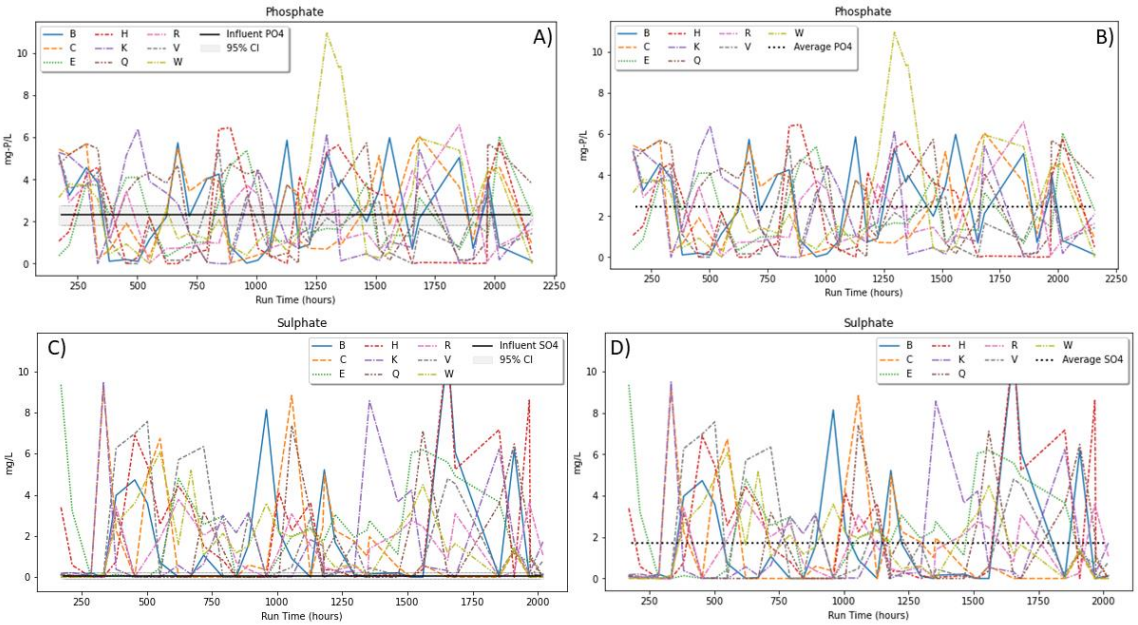

Figure 11. A) Effluent phosphate concentrations in individual columns and average influent value; B) effluent phosphate concentration by column compared to average column concentration; C) effluent sulphate concentration by column compared to average influent value; D) effluent sulphate concentration by column compared to average column concentration

Table 11. Summary of sample groups compared using the Student's T-Test. The mean(s) of those in Group #1 are compared with the mean(s) of those in Group #2

Group #1	Group #2
HLS – all events	1. Control #1 2. Control #2 3. HLS Normal Flow
HLS – 1st event	1. Control #1 2. Control #2 3. HLS Normal Flow
HLS – 2nd event	1. Control #1 2. Control #2 3. HLS Normal Flow
1. Column C – all HLS events 2. Column C – 1st HLS event 3. Column C – 2nd HLS event	Column C – normal flow values
1. Column H – all HLS events 2. Column H – 1st HLS event 3. Column H– 2nd HLS event	Column H – normal flow values
1. Column Q – all HLS events 2. Column Q – 1st HLS event 3. Column Q – 2nd HLS event	Column Q – normal flow values

4.2.2 Hydraulics and Physicochemical Parameters

As expected, there was a significant difference ($p < 0.05$) for both HRT and flow rate between each permutation of high load simulation values and normal flow values. Interestingly, there was also a significant observable difference ($p < 0.05$) between normal

A flow values of the two control groups with p = 0.03 and p = 0.04 for flow rate and HRT, respectively. However, as shown in Figure 12.A and 12.B, this difference is likely the result of occasional spikes in flow rate due to sampling anomalies, rather than a systematic difference between groups. This difference in the controls can serve to enhance the study, because it indicates that the control columns are representative of the heterogeneity observed in larger systems.

The average flow rate and corresponding HRT for the high loading events were 1.90 ± 0.48 ml/min and 0.24 ± 0.10 days. During flooding events, the HRT in the flooded columns decreased by approximately two days. It is generally assumed that lower HRTs result in reduced treatment efficiencies, however Minakshi et al., 2022 evaluated the effects of HRTs as low as six hours in VF constructed wetland systems and found treatment performance to be sustained for removal of BOD, total suspended solids (TSS) and nutrients from dairy wastewater. However in Akratos & Tsihrintzis, 2007 work and others on a HF constructed wetland, the authors concluded that shorter HRTs do not provide enough contact time between the wastewater and the subsurface for adequate treatment.

The DO concentrations under HLS conditions were generally within the range of the concentrations observed under normal flow conditions. The high load simulations did not have a significant impact on pH. Overall, the average HLS pH value was similar to normal flow rate column average; 6.42 ± 0.20, as compared to 6.62 ± 0.33, and both values are within a standard deviation of each other. This difference is more likely a result of the subtle decrease in pH values over time as observed in Figure 12.C.

Predominantly, the high loading did not significantly affect DOC or EC. Figures 11.E and 11.F support these findings, as the HLS values resemble the average normal flow values of both parameters. Interestingly, for both parameters there was a significant difference ($p < 0.05$) reported between the two control columns, similar to what was observed for the flow rates and HRTs. This correlation may indicate that effluent concentrations of DOC and EC are closely related to the effluent flow rate.

4.2.3 Nitrogen

The high loading events had the greatest effect on effluent ammonia concentrations. The average effluent ammonia concentration under HLS conditions was 2.23 ± 1.42 mg-N/L compared with an average normal operation column effluent of 1.50 ± 1.41 mg-N/L. During the high loading events, the ammonia removal efficiency decreased to 77.91 ± 14.03% a decrease of almost 8 percent removal compared to the full column performance (Table 9).

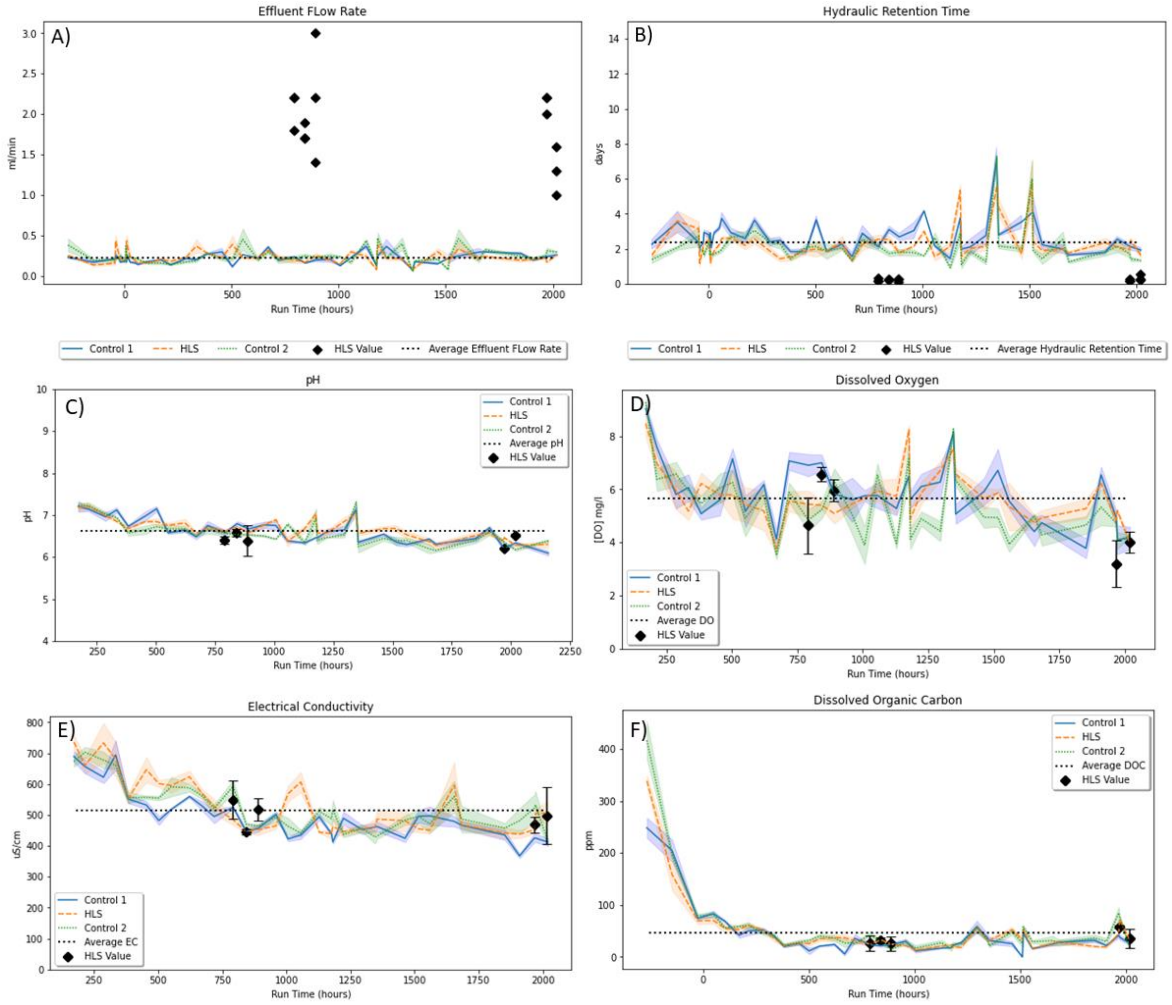

Figure 12. High load values for the parameters (diamonds with error bars) and column group averages under normal flow (lines). A) Effluent flow rate; B) HRT; C) pH; D) DO; E) EC; F) DOC

There was a significant difference between the cumulative HLS values and both control groups (p values of 0.0007 and 0.0017 for Control #1 and Control #2, respectively). Further, there was a significant difference between ammonia concentrations under normal flow conditions in the HLS columns and the two control columns. As there is no significant difference between the HLS concentrations and the HLS columns under normal flow conditions (p=0.45), it can be concluded that the introduction of the high loading events altered overall column performance even after the normal flow rate was resumed. Figure 13.A supports this conclusion as we can see a large spike in the HLS column effluent ammonia concentrations immediately after HLS1 (around hour 1000). This trend, however, was not observed in the aftermath of HLS2 and after the spike, ammonia concentrations in the HLS columns resembled those in the control columns.

There is a similar effluent NO_x peak to the one observed after the first high loading event for ammonia (around hour 1000). One possible explanation for these dual nitrogen peak effluent loads could be that the high flow rate changed some of the preferential flow

paths within the column and dislodged a pocket of nitrogen. The experiment did not continue long enough after HLS2 to see if this pattern would have been repeated.

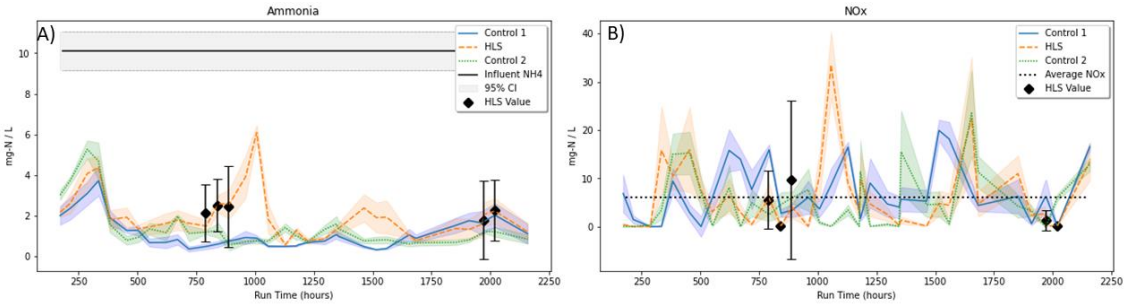

Figure 13. A) Ammonia and B) NO_x HLS concentrations and column averages under normal flow

4.2.4 Phosphate and Sulphate

The high loading events did not significantly impact effluent concentrations of phosphate or sulphate. As figures 14.A and 14.B show, the HLS values are within a standard deviation of the column average under normal flow conditions. As there was no evidence of removal of these parameters under normal flow conditions, it was not expected to see a significant effect under faster flow conditions.

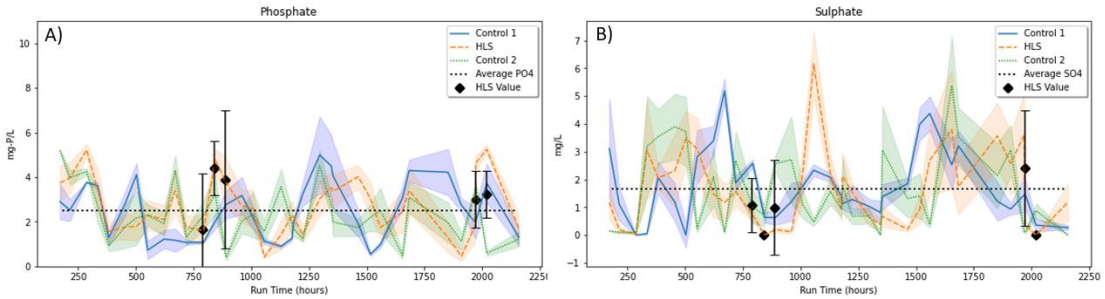

Figure 14. A) Phosphate and B) Sulphate HLS concentrations and column averages under normal flow

4.2.5 Summary

1) HRT reduced from 2.3 days to ~5.7 hours during high loading simulations; literature is conflicting if we should expect to see significant treatment reduction
2) The second round of HLS experiments (mid-April) resulted in a significant reduction in DO in the samples. Low DO levels indicate less aerobic microbial activity
3) The high load simulations had essentially no effect on pH, DOC, EC, phosphate and sulphate

4) There was a significant effect on ammonia removal due to the high loading events. The removal rate decreased from 85 ± 14% to 78 ± 14% during the HLSs and to as low as 40 percent in the sample following the events

4.3 Extrapolation to Full Scale Systems

When scaling the results from small system studies to full scale systems, it is important to exercise caution. Wetlands are heterogenous ecosystems, each comprising a unique microbial community defined by local climate, vegetation and substrate (Kadlec & Wallace, 2009). Therefore, while we can infer trends from the data collected by small, controlled systems, the removal rates observed here may not be found in fully operational systems due to variations in water flow, vegetation, influences from the outside environment, etc. It is, therefore, recommended that pilot scale studies be conducted to confirm the results found in the laboratory setting and make suggestions regarding design considerations.

As identified in Sections 4.1.2 and 4.2.3, the model wetlands performed best for the removal of ammonia from the influent wastewater and the high load events decreased the concentration of ammonia removed by the systems. Therefore, we will use the ammonia data to illustrate how the lab conditions can be extrapolated to a larger system. In the control columns under normal flow conditions, the average effluent ammonia concentrations were 1.61 ± 1.14 mg-N/L and 1.40 ± 1.31 mg-N/L in Control #1 and Control #2, respectively. These effluent concentrations correspond to average removal efficiencies of 88.5 ± 11.3% and 86.2 ± 12.9%, respectively. We can further calculate the mass removal rate and mass discharge rate of ammonia in the wetlands using equations 1 and 2, respectively. These rates can be further used to estimate the predicted removal of ammonia in wetlands of different sizes if all other parameters are consistent with the model experiment.

$$MRR_i\left[\frac{mgN}{day * m^2}\right] = \Delta C_{NH4_i}\left[\frac{mgN}{L}\right] * \frac{Q_i\left[\frac{L}{day}\right]}{SA\ [m^2]} \qquad (1)$$

$$MDR_i\left[\frac{mgN}{day * m^2}\right] = C_{NH4_i}\left[\frac{mgN}{L}\right] * \frac{Q_i\left[\frac{L}{day}\right]}{SA\ [m^2]} \qquad (2)$$

Where MRR_i is the mass removal rate of ammonia in mg of nitrogen for sample 'i'; MDR_i is the mass discharge rate (mass of ammonia exiting the wetland); ΔC_{NH4_i} is the difference in ammonia (mg-N) concentration between the influent and effluent in sample 'i', C_{NH4_i} is the effluent concentration of ammonia (mg-N), Q_i is the effluent flow rate of

sample 'i' and SA (= 0.0046 m^2) is the cross-sectional surface area of the soil column. Figures 15.A and 15.B show the mass removal rate and mass discharge over the course of column operation for the column groups. Equation 2 was adapted to calculate the influent mass loading rate for each column. The average influent mass loading rate was 798.1 ± 35.6 mg-N d^{-1} $m^{2\ -1}$ (graphed in Figure 15.B). Table 12 summarizes the average mass removal rates and discharge rates for each of the column groups. The removal rates can be used to infer the treatment efficiencies of systems with larger surface areas by simply multiplying the rates here by square metre. Caution is recommended when making these calculations and it is recommended that empirical data also be collected for large scale systems.

Table 12. Summary of Ammonia Mass Removal Rates and Discharge Rates (mean value ± standard deviation)

Group	Mass Removal Rate (mg-N d^{-1} $m^{2\ -1}$)	Discharge Rate (mg-N d^{-1} $m^{2\ -1}$)
All Columns	641.9 ± 388.3	108.8 ± 118.0
Control #1	632.6 ± 307.1	80.7 ± 81.2
Control #2	705.9 ± 477.8	100.4 ± 85.3
HLS Columns	588.7 ± 354.6	144.0 ± 160.0

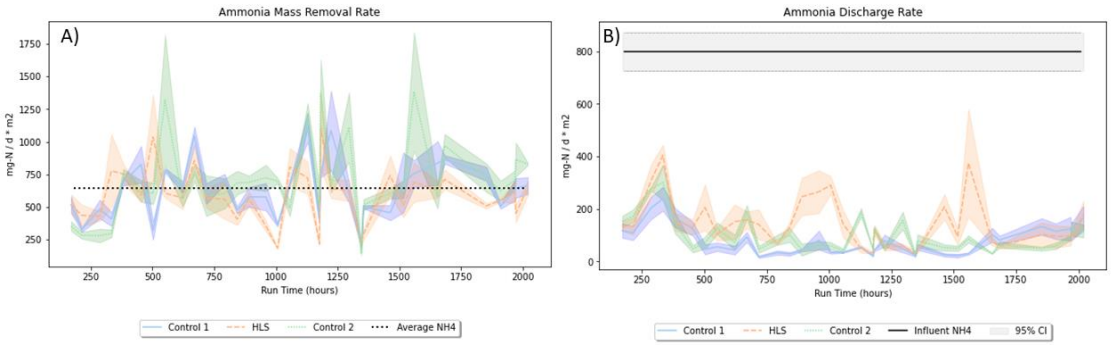

Figure 15. A) Ammonia mass removal rate and B) ammonia discharge rate

Under the high load simulations, we observe significantly higher mass removal rates than under normal flow conditions; 4749.6 ± 1736.8 mg-N d^{-1} $m^{2\ -1}$. However, this corresponds to a proportionally high effluent discharge rate of 1294.6 ± 871.8 for the average across both HLSs. Figure 16 displays the spread of the removal rates and discharge rates for ammonia under normal flow conditions and the high load simulation. While the high loading did result in a high mass removal rate, this is not expected to be sustained in the long term. Further, the average effluent mass of ammonia under the high load event was almost double that in the control columns. The mass removal rate and mass discharge rate can be used to estimate the effects of a short term (~1 hour) flooding event on a wetland column to predict the mass of ammonia discharged during these conditions.

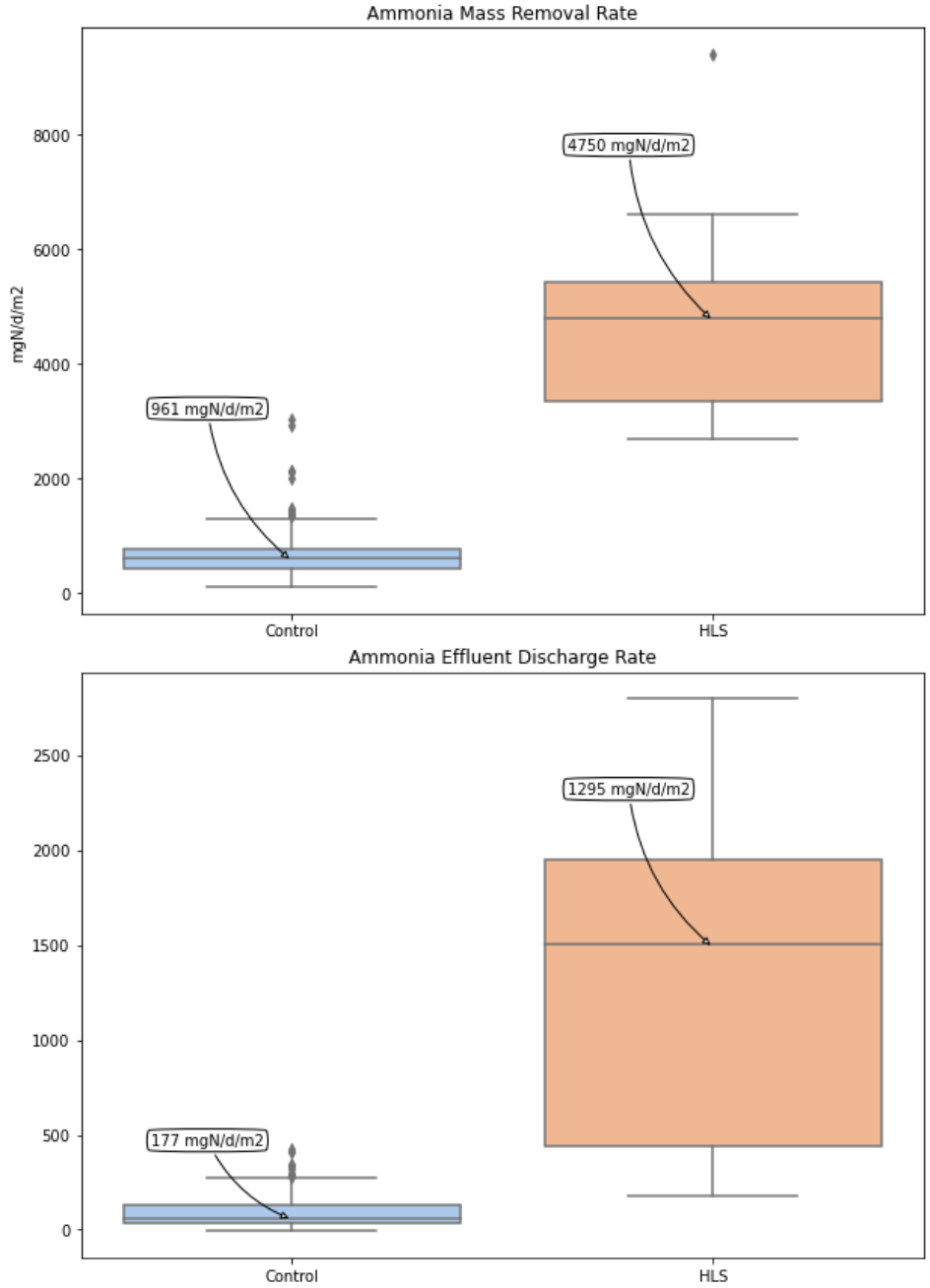

Figure 16. Box and Whisker plots of the high load simulation and control columns mass removal rate and effluent discharge rate for ammonia

Figure 17 shows that following the high loading simulations, the ammonia discharge rate in HLS columns under normal operation fluctuate slightly more than the control columns and overall, the HLS columns report a lower average mass removal rate (Table 12). When extrapolating these findings to a larger system, these fluctuations may also increase. However, overall, the column study shows almost complete ammonia removal rates during and following the shock events that can be used to infer how larger systems will respond to similar shock loading events.

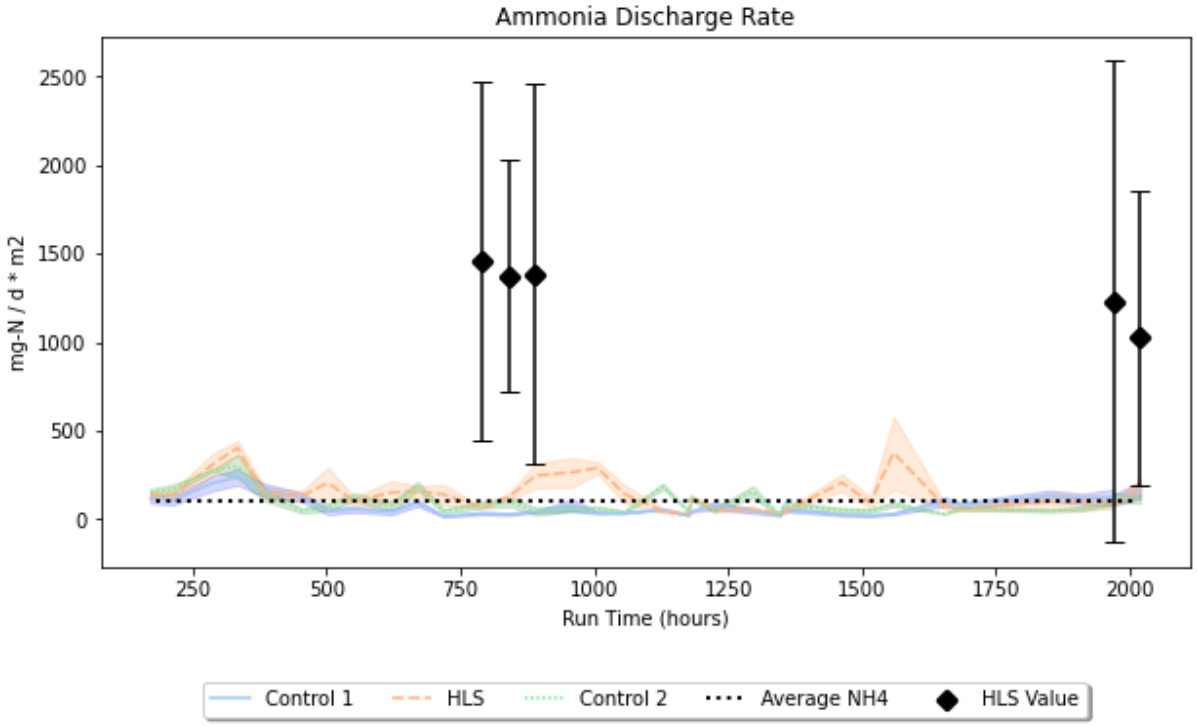

Figure 17. Ammonia discharge rate during the HLS events and normal flow conditions

5. Enablers and Barriers

The experimental design for this study passed through many iterations before the columns could be built. Initially, we expected to be able to build large scale systems fed with wastewater from the buildings at the UBC campus. However, construction delays arose for that setup and we had to adapt our experimental setup. Despite this barrier, the column experiments opened new avenues to run multiple controls and collect a robust set of data. The objectives of the study were met as originally proposed and we were able to collect evidence to further support the implementation of constructed wetlands as buffers against the impacts of a changing climate.

6.Key Takeaways from CDRI Fellowship Programme

The CDRI Fellowship Programme has made this project possible. The technical experts provided guidance from different perspectives that have helped guide this research. The inclusion of this work within the international community of scholars and practitioners of CDRI has provided a unique platform for dissemination of the knowledge produced during this research project. Further, it brings the question of constructed wetland resilience to prominence within the conversation regarding infrastructure resilience to withstand a

changing climate. We are grateful to CDRI for providing this platform to conduct quality research that can be accessed by researchers and industry partners globally.

Locally, this research will be presented at the Canadian Water Resources Association Regional Conference in October 2023, to representatives from the local water utilities (including Metro Vancouver), industry partners and academics engaging with themes of resilience and flood management in British Columbia.

Key takeaways/lessons from the project are as follows:

- The experimental setup designed for this project can be adapted to include other substrates, vegetation and influent wastewaters. The modularity and relative simplicity of the system can be utilized by other researchers to investigate variations on VF constructed wetland systems without the need for investment in large pilot projects.
- Under the experimental conditions, the simulated flooding events did not significantly alter the wetland treatment performance (except for ammonia). Following the flooding events, the wetlands quickly resumed normal performance. These results agree with the literature referenced in Section 3.1.2 which suggests that VF systems are uniquely apt to withstand stochastic and high intensity loads. In regions where high intensity storm events are expected to increase in frequency, we encourage decision makers to highly consider VF constructed wetlands along with their existing wastewater treatment infrastructure.
- Constructed wetlands are a proven wastewater treatment technology that requires less capital investment and energy than traditional wastewater infrastructure. Further, the results from this study and others referenced in Section 3.1.2 argue that these systems may also be more resilient to flooding than traditional infrastructure. Widespread adoption is encouraged in regions where climate and land area allow for development.

7. Conclusion

VF constructed wetlands have the potential to improve wastewater treatment infrastructure resilience during high intensity rain events due to their inherent resilience to shock loads. This research project aimed to describe what that resilience would look like in a controlled system. When subject to the high load simulation, measurements of pH, dissolved oxygen, dissolved organic carbon, electrical conductivity, sulphate and phosphate were not significantly different from measurements recorded during normal flow conditions in both controls and the high load columns when operated under normal

flow conditions. The high loading events, therefore, did not significantly impact wetland treatment performance for the six parameters mentioned above. These results are evidence that the VF wetland exhibits the first type of resilience identified in Section 2 – minimal effect of effluent concentrations of the measured parameter during the shock event.

The high load events did significantly impact ammonia removal within the HLS columns. Baseline column removal efficiency of ammonia under normal flow conditions was 85 ± 14% which dropped to 77 ± 14% during the high loading events. Immediately after the first high load event, HLS1, the HLS columns under normal flow conditions reported a spike in effluent ammonia concentrations (Figure 13). However, after the spike, the effluent concentrations in the HLS columns resembled those of the control columns. Ammonia removal in these systems necessitates adequate contact time between the ammonia rich influent water and nitrifying bacteria in the soil. The shock loading reduced this contact time, likely causing the lower ammonia removal efficiency. The wetland column ammonia performance is indicative of the second type of resilience identified in Section 2 – observed impact of the shock loading on treatment performance followed by recovery to pre disturbance performance.

The results from this study indicate that VF constructed wetlands recover quickly after a flooding event and many operational parameters of these constructed wetlands were not significantly impacted by the shock loading events. While these results are promising for large scale systems, it is recommended that pilot systems be tested as well to confirm the translation of the column scale results to larger systems.

The literature summarized in Section 3.1.2 combined with the results of this study indicate that constructed wetlands are a resilient type of wastewater treatment infrastructure. They can play a versatile role in protecting local ecosystems from overflows of municipal wastewater during high intensity storm events. Constructed wetlands are a robust, resilient technology that we encourage decision makers to adopt in their climate resilience strategies.

8.Way Forward

Next steps for the study are as follows:

1) Testing different intensities of flooding on column performance.
2) Testing on real wastewater as opposed to synthetic.
3) Expanding the methodology to larger scale systems to model response in less controlled environments.

References

1. Akratos, C. S., & Tsihrintzis, V. A. (2007). Effect of temperature, HRT, vegetation and porous media on removal efficiency of pilot-scale horizontal subsurface flow constructed wetlands. *Ecological Engineering*, *29*(2), 173–191. https://doi.org/10.1016/j.ecoleng.2006.06.013

2. Brady, A. R., Vega, M. A., Riddle, K. N., Peel, H. F., Lundeen, E. J., Siegmund, J. G., & Sharp, J. O. (2021). Biomat Resilience to Desiccation and Flooding Within a Shallow, Unit Process Open Water Engineered Wetland. *Water*, *13*(6), Article 6. https://doi.org/10.3390/w13060815

3. Cantinho, P., Matos, M., Trancoso, M. A., & dos Santos, M. M. C. (2016). Behaviour and fate of metals in urban wastewater treatment plants: A review. *International Journal of Environmental Science and Technology*, *13*(1), 359–386. https://doi.org/10.1007/s13762-015-0887-x

4. Cecchetti, A. R., Stiegler, A. N., Graham, K. E., & Sedlak, D. L. (2020). The Horizontal Levee: A Multi-Benefit Nature-Based Treatment System That Improves Water Quality and Protects Coastal Levees from the Effects of Sea Level Rise. *Water Res. X*, *7*, 100052.

5. *Climate change and wastewater infrastructure | WSP*. (n.d.). Retrieved September 11, 2021, from https://www.wsp.com/en-CA/insights/ca-can-we-incorporate-climate-change-principles-into-wastewater-infrastructure-design

6. *Determine pH of Soil Samples—How To Test & Measure—Cole-Parmer Canada*. (n.d.). Retrieved May 24, 2023, from https://www.coleparmer.ca/tech-article/soil-samples-ph-testing

7. Food and Agriculture Organization of the United Nations. (n.d.). *6. Soil Texture*. Retrieved May 31, 2023, from https://www.fao.org/fishery/docs/CDrom/FAO_Training/FAO_Training/General/x6706e/x6706e06.htm

8. Galvão, A., & Matos, J. (2012). Response of horizontal sub-surface flow constructed wetlands to sudden organic load changes. *Ecological Engineering*, *49*, 123–129.https:/doi.org/10.1016/j.ecoleng.2012.08.033

9. Ghosh, D., & Gopal, B. (2010). Effect of hydraulic retention time on the treatment of secondary effluent in a subsurface flow constructed wetland. *Ecological Engineering*, *36*(8), 1044–1051. https://doi.org/10.1016/j.ecoleng.2010.04.017

10. Healy, M. G., Rodgers, M., & Mulqueen, J. (2007). Treatment of Dairy Wastewater Using Constructed Wetlands and Intermittent Sand Filters. *Bioresour. Technol.*, *98*, 2268.

11. *Heavy rain sends untreated wastewater into Puget Sound*. (2021, January 14). AP NEWS. https://apnews.com/article/puget-sound-seattle-wastewater-0bb510eecd47996aec096f83e6dd2958

12. Hornor, L. B. (2020). *How Upgrading the Iona Island Wastewater Treatment Plant to "True Tertiary" Would Fulfill a Legacy*. Fraser Riverkeeper. https://www.fraserriverkeeper.ca/how_upgrading_the_iona_island_wastewater_treatment_plan_to_true_tertiary_would_fulfill_a_legacy

13. Jackson, S., & Ferris, T. L. J. (2013). Resilience principles for engineered systems. *Systems Engineering*, *16*(2), 152–164. https://doi.org/10.1002/sys.21228

14. Jasper, J. T., Jones, Z. L., Sharp, J. O., & Sedlak, D. L. (2014). Nitrate Removal in Shallow, Open-Water Treatment Wetlands. *Environmental Science & Technology*, *48*(19), 11512–11520. https://doi.org/10.1021/es502785t

15. Ji, M., Zhang, J., Wang, S., Liang, S., & Hu, Z. (2021). Enhanced phosphorus removal of constructed wetland through plant growth-promoting rhizobacteria (PGPR) addition. *Environmental Science and Pollution Research*, *28*(37), 52124–52132. https://doi.org/10.1007/s11356-021-14364-w

16. Kadlec, R. H., & Wallace, S. (2009). *Treatment Wetlands* (2, Ed.).

17. Khan, S., Ahmad, I., Shah, M. T., Rehman, S., & Khaliq, A. (2009). Use of constructed wetland for the removal of heavy metals from industrial wastewater. *Journal of Environmental Management*, *90*(11), 3451–3457. https://doi.org/10.1016/j.jenvman.2009.05.026

18. Minakshi, D., Sharma, P. K., Rani, A., Malaviya, P., Srivastava, V., & Kumar, M. (2022). Performance evaluation of vertical constructed wetland units with hydraulic retention time as a variable operating factor. *Groundwater for Sustainable Development*, *19*, 100834. https://doi.org/10.1016/j.gsd.2022.100834

19. Osachoff, H. L., Mohammadali, M., Skirrow, R. C., Hall, E. R., Brown, L. L. Y., van Aggelen, G. C., Kennedy, C. J., & Helbing, C. C. (2014). Evaluating the treatment of a synthetic wastewater containing a pharmaceutical and personal care product chemical cocktail: Compound removal efficiency and effects on juvenile rainbow trout. *Water Research*, *62*, 271–280. https://doi.org/10.1016/j.watres.2014.05.057

20. *Plant failure dumps millions of gallons of sewage in Seattle*. (n.d.). Retrieved September 11, 2021, from https://www.cbsnews.com/news/seattle-sewage-treatment-plant-electrical-failure-pugent-sound/

21. Pritchard, J. C., Hawkins, K. M., Cho, Y.-M., Spahr, S., Struck, S. D., Higgins, C. P., & Luthy, R. G. (2023). Black Carbon-Amended Engineered Media Filters for Improved Treatment of Stormwater Runoff. *ACS Environmental Au*, *3*(1), 34–46. https://doi.org/10.1021/acsenvironau.2c00037

22. Rizzo, A., Tondera, K., Pálfy, T. G., Dittmer, U., Meyer, D., Schreiber, C., Zacharias, N., Ruppelt, J. P., Esser, D., Molle, P., Troesch, S., & Masi, F. (2020). Constructed wetlands for combined sewer overflow treatment: A state-of-the-art review. *Science of The Total Environment*, *727*, 138618. https://doi.org/10.1016/j.scitotenv.2020.138618

23. Rubalingeswari, N., Thulasimala, D., Giridharan, L., Gopal, V., Magesh, N. S., & Jayaprakash, M. (2021). Bioaccumulation of heavy metals in water, sediment, and tissues of major fisheries from Adyar estuary, southeast coast of India: An ecotoxicological impact of a metropolitan city. *Marine Pollution Bulletin*, *163*, 111964. https://doi.org/10.1016/j.marpolbul.2020.111964

24. Saeed, T., Paul, B., Afrin, R., Al-Muyeed, A., & Sun, G. (2016). Floating constructed wetland for the treatment of polluted river water: A pilot scale study on seasonal variation and shock load. *Chemical Engineering Journal*, *287*, 62–73. https://doi.org/10.1016/j.cej.2015.10.118

25. Saeed, T., & Sun, G. (2012). A review on nitrogen and organics removal mechanisms in subsurface flow constructed wetlands: Dependency on environmental parameters, operating conditions and supporting media. *Journal of Environmental Management*, *112*, 429–448. https://doi.org/10.1016/j.jenvman.2012.08.011

26. Sarkar, B., Mandal, S., Tsang, Y. F., Vithanage, M., Biswas, J. K., Yi, H., Dou, X., & Ok, Y. S. (2019). 24—Sustainable sludge management by removing emerging contaminants from urban wastewater using carbon nanotubes. In M. N. V. Prasad, P. J. de Campos Favas, M. Vithanage, & S. V. Mohan (Eds.), *Industrial and Municipal Sludge* (pp. 553–571). Butterworth-Heinemann. https://doi.org/10.1016/B978-0-12-815907-1.00024-6

27. Scholes, R. C., Stiegler, A. N., Anderson, C. M., & Sedlak, D. L. (2021). Enabling Water Reuse by Treatment of Reverse Osmosis Concentrate: The Promise of Constructed Wetlands. *ACS Environmental Au*. https://doi.org/10.1021/acsenvironau.1c00013

28. Shang, Z., Wang, Y., Wang, S., Jin, F., & Hu, Z. (2022). Enhanced phosphorus removal of constructed wetland modified with novel Lanthanum-ammonia-modified hydrothermal biochar: Performance and mechanism. *Chemical Engineering Journal*, *449*, 137818. https://doi.org/10.1016/j.cej.2022.137818

29. Simonovic, S.P., A. Schardong, R. Srivastav, and D. Sandink (2015), *IDF_CC Web-based Tool for Updating Intensity-Duration-Frequency Curves to Changing Climate – ver 6.5*, Western University Facility for Intelligent Decision Support and Institute for Catastrophic Loss Reduction, open access https://www.idf-cc-uwo.ca.

30. Singh, S., & Tiwari, S. (2019). Climate Change, Water and Wastewater Treatment: Interrelationship and Consequences. In R. P. Singh, A. S. Kolok, & S. L. Bartelt-Hunt (Eds.), *Water Conservation, Recycling and Reuse: Issues and Challenges* (pp. 203–214). Springer. https://doi.org/10.1007/978-981-13-3179-4_11

31. Stefanakis, A. I. (2019). The Role of Constructed Wetlands as Green Infrastructure for Sustainable Urban Water Management. *Sustainability*, *11*(24), Article 24. https://doi.org/10.3390/su11246981

32. Sukias, J. P. S., Park, J. B. K., Stott, R., & Tanner, C. C. (2018). Quantifying treatment system resilience to shock loadings in constructed wetlands and denitrification bioreactors. *Water Research*, *139*, 450–461. https://doi.org/10.1016/j.watres.2018.04.010

33. Tanner, C. C., Sukias, J. P. S., Headley, T. R., Yates, C. R., & Stott, R. (2012). Constructed wetlands and denitrifying bioreactors for on-site and decentralised

wastewater treatment: Comparison of five alternative configurations. *Ecological Engineering*, *42*, 112–123. https://doi.org/10.1016/j.ecoleng.2012.01.022

34. Tao, W., Bays, J. S., Meyer, D., Smardon, R. C., & Levy, Z. F. (2014). Constructed Wetlands for Treatment of Combined Sewer Overflow in the US: A Review of Design Challenges and Application Status. *Water*, *6*(11), Article 11. https://doi.org/10.3390/w6113362

35. Tondera, K., Ruppelt, J. P., Pinnekamp, J., Kistemann, T., & Schreiber, C. (2019). Reduction of micropollutants and bacteria in a constructed wetland for combined sewer overflow treatment after 7 and 10 years of operation. *Science of The Total Environment*, *651*, 917–927. https://doi.org/10.1016/j.scitotenv.2018.09.17

36. *Treated Wastewater and Aquatic Environment*. (n.d.). Retrieved September 14, 2021, from http://www.metrovancouver.org/services/liquid-waste/environmental-management/treated-wastewater/Pages/default.aspx

37. US EPA, O. (n.d.). *Climate Impacts in the Northwest* [Overviews and Factsheets]. Retrieved September 13, 2021, from https://19january2017snapshot.epa.gov/climate-impacts/climate-impacts-northwest

38. US EPA, O. (2015, September 18). *What is a Wetland?* [Overviews and Factsheets]. https://www.epa.gov/wetlands/what-wetland

39. *USDA Plants Database*. (n.d.). Retrieved June 29, 2023, from https://plants.usda.gov/home/plantProfile?symbol=CAAU3

40. Vymazal, J. (2011). Constructed Wetlands for Wastewater Treatment: Five Decades of Experience. *Environmental Science & Technology*, *45*(1), 61–69. https://doi.org/10.1021/es101403q

41. Vymazal, J. (2014). Constructed Wetlands for Treatment of Industrial Wastewaters: A Review. *Ecol. Eng.*, *73*, 724.

42. Vymazal, J. (2022). The Historical Development of Constructed Wetlands for Wastewater Treatment. *Land*, *11*(2), Article 2. https://doi.org/10.3390/land11020174

43. You, Z., Zhang, L., Pan, S.-Y., Chiang, P.-C., Pei, S., & Zhang, S. (2019). Performance evaluation of modified bioretention systems with alkaline solid wastes for

enhanced nutrient removal from stormwater runoff. *Water Research*, *161*, 61–73. https://doi.org/10.1016/j.watres.2019.05.105

44. Zapater, M., Gross, A., & Soares, M. I. M. (2011). Capacity of an on-site recirculating vertical flow constructed wetland to withstand disturbances and highly variable influent quality. *Ecological Engineering*, *37*(10), 1572–1577. https://doi.org/10.1016/j.ecoleng.2011.03.033

Risk Assessment and Hazard Mapping of Bhutan's Power System Infrastructure

Cheku Dorji,

Namgay Tenzin,

Nima Dukpa

College of Science and Technology
Royal University of Bhutan

Research supported by:
Sangay Wangdi

Bhutan Power Corporation Limited

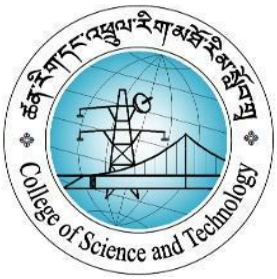

Under CDRI Fellowship Programme 2022-23

CDRI
Coalition for Disaster Resilient Infrastructure

Disclaimer: The views expressed in this paper reflect the opinions of the author and not necessarily the official views of CDRI.

Acronyms and Abbreviations

AHP	-	Analytic Hierarchy Process
AWS	-	Automatic Weather Stations
CDRI	-	Coalition for Disaster Resilient Infrastructure
BPC	-	Bhutan Power Corporation Limited
DGPC	-	Druk Green Power Corporation
DHI	-	Druk Holding and Investment Limited
GDP	-	Gross Domestic Product
GNH	-	Gross National Happiness
NDRMF	-	National Disaster Risk Management Framework
NAPA	-	National Adaptation Programme of Action
NEC	-	National Environment Commission
NCHM	-	National Centre for Hydrology and Meteorology
GLOF	-	Glacial Lake Outburst Flood
RCP	-	Representative Concentration Pathways
NREL	-	National Renewable Energy Laboratory
NTGMP	-	National Transmission Grid Master Plan
NTMP	-	National Transmission Master Plan
SHDP	-	Sustainable Hydropower Development Policy
RoW	-	Right of Way
AIS	-	Air Insulated Substation

Abstract

Human endeavours are subject to risks due to unforeseen uncertainties and risks posed by natural forces, ecosystems and various human and technological hazards. Therefore, effective hazard risk assessment and management are crucial components of any undertaking. This investigative research attempted to assess the impact of climate change on the power infrastructure and networks of the Bhutan Power Corporation, identifying probable hazards and suggesting a framework for risk management through careful planning, preparedness, prevention and mitigation. The methods employed in this research were both qualitative and quantitative and were carried out in phases, each of which built upon findings from precedents.

The first phase involved understanding the historical and current status of the power system infrastructure, networks and operations to establish a foundation for investigative questions. In the second phase, the probing questions generated from the first phase were used to assess hazard risk and potential impacts in relation to the past and present management processes of the power system. The third phase emphasized evaluating the hazards to Bhutan's power system by using a hazard probability matrix.

The major outcomes of the analysis were: (i) climatic variables, particularly temperature and precipitation, pose potential risks to the power system infrastructure through lightning, flash floods, landslides and windstorms; (ii) Bhutan Power Corporation requires well-defined policy and coherent procedures regarding the operation and maintenance of power systems, which can effectively address hazards and implement prevention and mitigation techniques; (iii) infrastructure such as power stations, transmission lines, towers and substations are vulnerable due to ageing and climate change-exacerbated hazards; (iv) plans and resources are not optimally integrated in the operation and management of the power system; and (v) hazards related to climate change need to be considered to improve the reliability and sustainability of electricity supply.

Ultimately, this research emphasizes the need to develop comprehensive hazard risk management strategies to combat the challenges posed by climate change, upgrade the resilience of power infrastructure, and ensure reliable and sustainable electricity supply.

Acknowledgments

We, the research team, wish to express our sincere appreciation and thank every individual who has assisted us with their invaluable contributions and support to the success of this research project. First of all, we express our gratitude to the CDRI Fellowship Programme for the financial support and thank the CDRI executive team for their constant guidance and for connecting us with technical experts.

Secondly, with our true gratitude, we would like to honour Dr Kampanart Silva and Dr Sai Bhaskar Reddy, the technical experts, for mentoring us with their valuable wisdom and insights through comments and constructive suggestions, which were instrumental in shaping the quality of this research project.

Thirdly, we wish to thank Dr Cheki Dorji, the president of the College of Science and Technology, Royal University of Bhutan, for his encouragement and unwavering support in enabling an environment and the necessary resources in carrying out our research work. Importantly, this study would not have been possible without the participation of the Bhutan Power Corporation (BPC), our key stakeholder. We remain indebted to the R&D department of BPC for allowing us easy access to information, field engineers and technicians in obtaining feedback and opinions in the process of collecting data. Their cooperation and candid feedback were of inestimable value to our research work.

Further, we truly acknowledge the assistance received from Ms Lily Gurung of the Civil Engineering Department in applying GIS tools and Mr Kamal Kumar Chapaigai of the Electronics and Communication Engineering Department for assisting us with the drone survey.

Finally, we express our sincere appreciation to the Electrical Engineering Department staff for letting us use their time to collect survey data from all units of the power sector across 20 districts. Given the limited time frame of the project, data collection would not have been possible without your services.

Funding

This research was supported by the 2022–2023 Fellowship of the Coalition for Disaster Resilient Infrastructure (CDRI), Application ID: ID 210909468

1. Introduction

Bhutan is a landlocked country with an area of 38,394 square kilometres located in the south-eastern part of the Himalayas, between China and India. It is about 300 kilometres wide from east to west and about 170 kilometres from north to south. The geographical terrain of Bhutan is complex; its elevations range from 100 metres in the south to over 7,500 metres towards the north. With its population slightly more than 700,000, Bhutan is one of the smallest countries in South Asia (R W Saaty, 1987) (NSB, 2022). Besides hydroelectricity, agriculture and tourism are means which the people of the country depend on for their livelihoods. Bhutan has a unique approach to measure its economic progress. It is measured not only through Gross Domestic Product (GDP), but also through the 'Gross National Happiness Index' (GNHI) where priority is also given to the well-being and happiness of the people.

Hydropower sector is the backbone of Bhutan's economy. There is 23,760 MW of untapped potential capacity which is techno-economically feasible. Till date only 2,326 MW has been installed with an average domestic load of 720 MW and the rest is exported to Bhutan’s neighbouring country, India, contributing 25 percent of the country's exchequer (DGPCL, 2022). Bhutan has acknowledged its vulnerability to climate change due to the fragile mountainous environment and its economy being dependent on hydropower and agriculture (UNDP, 2023). Bhutan is considered highly vulnerable to climate change and its consequences. The country relies heavily on subsistence agriculture and hydropower, and its fragile mountain ecosystem makes it particularly vulnerable (Jamtsho, 2011). The most important impact of climate change in Bhutan is the likelihood of melting glaciers as global temperatures rise, creating an unprecedented threat to people and livelihoods because the majority of settlement, urban expansion and communities are located along river basins and valleys (UNDP, 2023). The diversification of renewable resources outside of hydropower, such as solar and wind, is essential to complement hydroelectric power production during the dry season and to increase power supply resilience to seasonal variations and extremes (Corjan et al, 2021).

Therefore, Bhutan has developed policies to minimize the impact of climate change. Applicable policies and guidelines include the National Adaptation Program of Action (NAPA), passed in 2006, and the Disaster Management Act, passed in 2013. In 2017, the National Disaster Risk Management Framework (NDRMF) was implemented according to the Sendai Framework for Disaster Risk Reduction 2015-2030, and Bhutan

also formulated a mitigation policy in 2020 (WB, 2021 & NEC & RGOB, 2020). In addition to protecting 60 percent of its forest cover, Bhutan is committed to ensuring that the country remains carbon neutral. The country adopted the Alternative Renewable Energy Policy in 2013, which has led to the diversification and use of renewable energy. Further, Bhutan has adopted the Sustainable Hydropower Development Policy 2020, which reassesses the sustainability and future of hydroelectric power plants.

In addition to the hazard of climate variables, Bhutan lies in one of the earthquake prone zones of the world. Although there were records of huge destruction caused by earthquakes, the country has been the victim of climatic variables in many forms. Due to erratic rainfall and the rise in temperatures, flash floods, GLOFs, landslides and windstorms pose recurring annual risks to property and livelihoods in the country. Flash flooding is the greatest threat to the inhabitants who have settled along river sides and hydroelectric dams. Some of the extreme incidents include the GLOF in 1994, the outburst of Luggye Tsho (lake) which caused the loss of 21 lives and losses of many houses and properties along the downstream valleys in Punakha. The country has had 32 extreme weather events in the last seven years, including flash floods, landslides and snowfall during both the pre- and post-monsoon seasons. These events resulted in loss of life and damage to agriculture and property (Dema, 2023). The Cyclone Aila in May 2009 cost 12 lives. The damages to property and cost recovery loss were of the tune of USD 17 million (NCHM, 2017).

Power supply reliability has become more and more important as customers and services are interdependent. A manual inspection of overhead transmission poles caused a delay in fault tracing after power was restored between Trongsa and Bumthang in 2015. A technical failure was cited as the primary cause (Wangdi, 2015). Many fire incidents over the past few years, such as devastating forest wildfires and house fires have been blamed on power lines and electrical shorts (Dorji, 2020). Unreliable power supply has unnerved residents, offices and businesses in Lingmithang, Mongar. The power utility citing annual maintenance works was the cause of the outage (BBS, 2019). The power outage disrupted water supply in Phuentsholing. It took more than 15 hours to restore the water supply after a switchgear failure at the substation (Rai, 2018). About 80 households in Bjoka village, Zhemgang district, were left without electricity for a month due to flash floods and landslides caused by the heavy monsoon rain that damaged utility poles (BBS, 2019). Residents of Thimphu were frustrated by frequent power outages, mainly due to overloaded distribution transformers (Yuden, 2020). Bhutan Power System is, therefore, hampered by climate change and technical

glitches and service delivery.

Considering Bhutan's rapid socio-economic development, increasing energy consumption, expanding renewable energy portfolios and vulnerability to climate-related hazards, this research would provide timely and valuable input for policymakers and relevant sectors. Therefore, this project includes a climate change review in Bhutan, a risk assessment of the power system infrastructure and the development of spatial hazard maps as a case study for transmission lines in the Chukha region. Overall, it provides a conceptual framework for assessing risks due to climate change-related hazards to the power system infrastructure. Finally, the study focuses on preparedness and mitigation measures to improve the reliability of the power system.

2. Aim, Objectives, and Scope of the Research Study

2.1 Aim

The aim of this research is to assess likely climate change-induced hazards and their impact on the power system infrastructure of Bhutan Power Corporation. Consequently, we suggest appropriate solutions to increase system reliability and manage it efficiently.

2.2 The specific objectives of this research are to:

i. Identify climate-induced natural, human-induced and technological hazards to the power system from climate change
ii. Assess the impact of potential hazards on power generation, transmission and distribution lines, and substations
iii. Identify and evaluate vulnerabilities of power system infrastructure
iv. Carry out the risk assessment, evaluation and analysis of power systems and create multi-hazard spatial maps for the pilot study area
v. Develop a framework for climate hazard-related risk assessment of Bhutan's power system and its preparedness and mitigation measures for climate change

2.3 Scope of Research

This research focuses on conducting a hazard risk assessment of Bhutan's power system such as generation power stations, transmission and distribution lines, in collaboration with Bhutan Power Corporation. The development of spatial multi-hazard

mapping was limited to a pilot study in Chukha region, where there are two large hydropower plants – 336 MW Chukha Hydropower Plant and 1020 MW Tala Hydropower Plant – along with high-voltage substations and international transmission lines.

3. Research Methodology

The research was implemented in three major steps as shown in Figure 1.

In the first stage, a desk review was conducted followed by correspondence with the utility company, BPC. The second phase involved data collection whereby a comprehensive power system hazard risk assessment questionnaire was developed based on the National Renewable Energy Laboratory's "Guidelines for Power Sector Resilience Planning" (Stout et al., 2019).

In the third phase, data analysis, site visits and drone visual survey in the pilot study area were carried out, followed by hazard risk analysis and development of multi-hazard spatial maps using the Analytic Hierarchy Process (AHP) for the pilot study area.

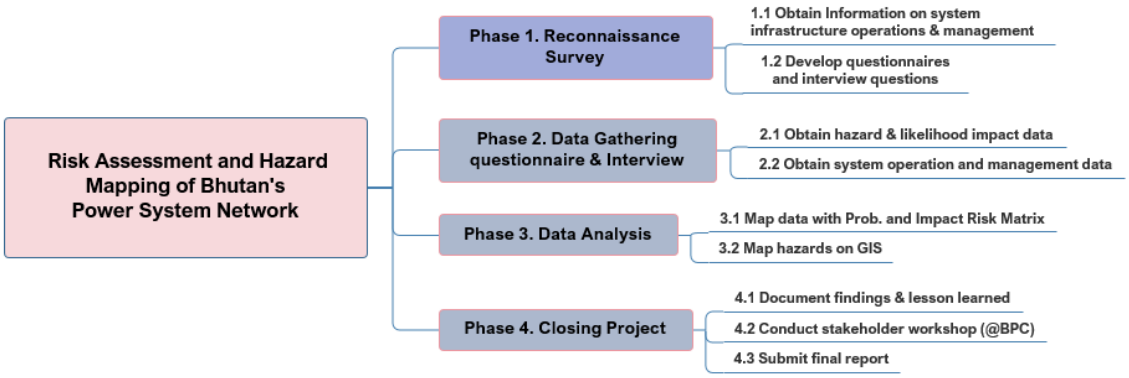

Figure 1. Schematic Illustration of the Research Method

3.1 Historical Climate of Bhutan

Bhutan's climatic conditions are influenced by its diverse topography resulting in three distinct climatic zones: subtropical, alpine and temperate. The subtropical zone, in the southern foothills ranging from 150 to 2000 metres above sea level, is characterized by high humidity, abundant rainfall and average temperatures ranging from 15°C to 30°C throughout the year (NCHM, 2019). Figure 2 provides a visual depiction of these climatic conditions.

Moving towards the Inner Himalayas, spanning from 2000 to 3000 metres, the climate is characterized by cool winters, hot summers and moderate rainfall (WBG & ADB, 2021). Finally, the alpine region, ranging from 3000 metres and reaching up to 7500 metres on the northern side, is marked by snow cover and experiences cold

winters and cool summers.

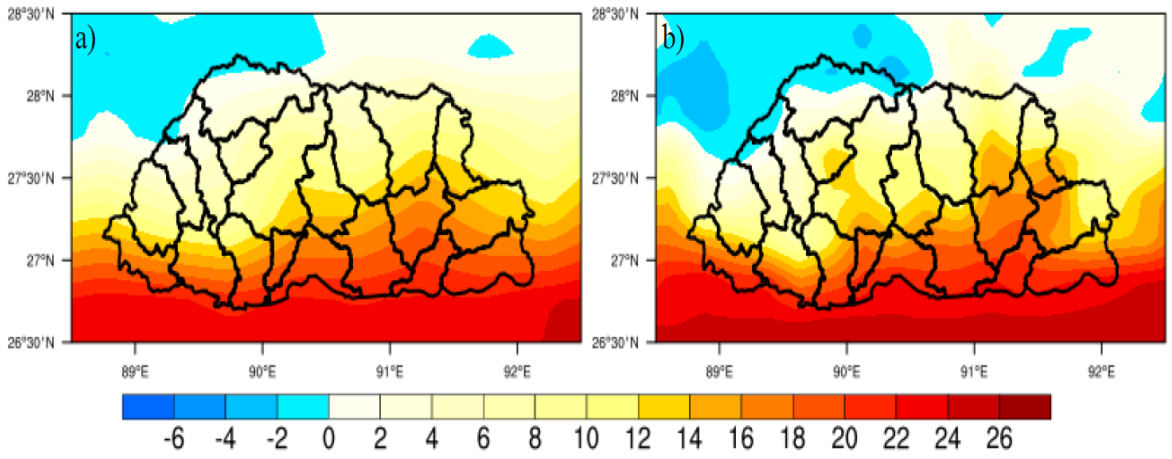

Figure 2. Spatial Distribution of Annual Mean Temperature (1975-2005) (NCHM, 2019)

3.1.1 Precipitation and Temperature profile

The analysis of data collected over a period of 21 years (1996-2017) indicated an increasing temperature trend in Bhutan (NCHM, 2019). According to the Climate Hazard Profile of Bhutan, there is a significant seasonal variation in temperatures. The summer months of June through August have average temperatures ranging from 24°C to 29°C, while the winter months of December through February experience colder temperatures, with averages close to 0°C based on the most recent climatology from 1991 to 2020.

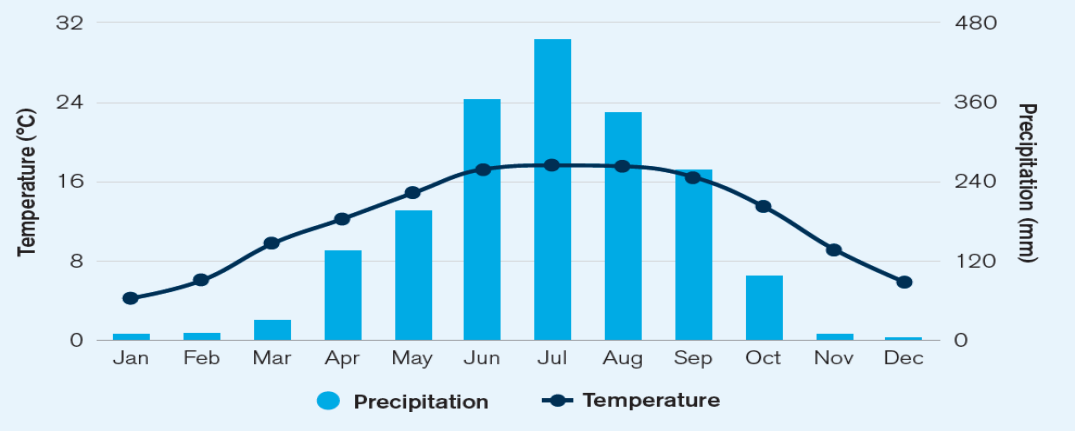

Figure 3. Average Monthly Temperature and Rainfall in Bhutan (NCHM, 2019)

In terms of rainfall, there is a noticeable difference between seasons. The summer months, June to September, receive a much higher amount of rainfall, averaging around 240 mm. On the other hand, the winter months of December to February receive comparatively less rainfall (ADB & WB, 2021). A visual representation of these rainfall forecasts can be seen in Figure 3.

According to the projections, Bhutan's annual average temperature rise will be 4.5°C more than the global average by the 2090s, as compared to 3.7°C. Similarly, the annual average maximum and minimum temperatures will rise by 4.7°C and 4.6°C, respectively, as shown in Figure 4 (WBG & ADB, 2021).

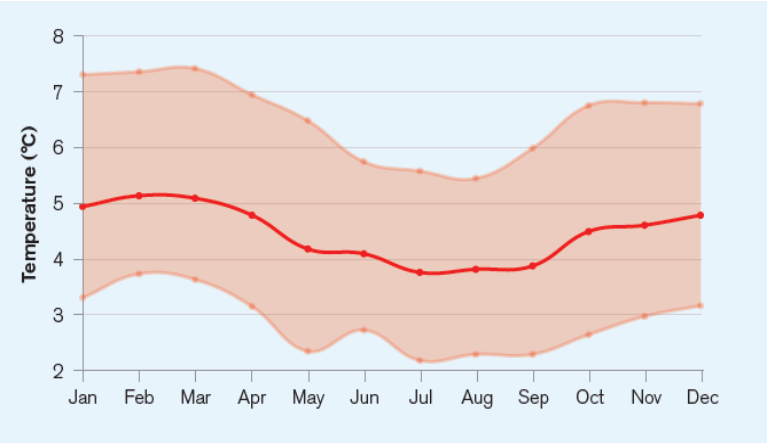

Figure 4. The Monthly Average Temperature Projections of Bhutan (WBG & ADB, 2021)

The National Centre for Hydrology and Meteorology (NCHM) started the installation of weather stations across the country in early 2010, and currently there are 20 weather stations covering the country as shown in Figure 5. Since the beginning of 2017, NCHM has started monitoring and forecasting of weather information, broadcasting daily weather information and even recording and compiling daily, monthly and annual weather events and climate induced disaster events across the country.

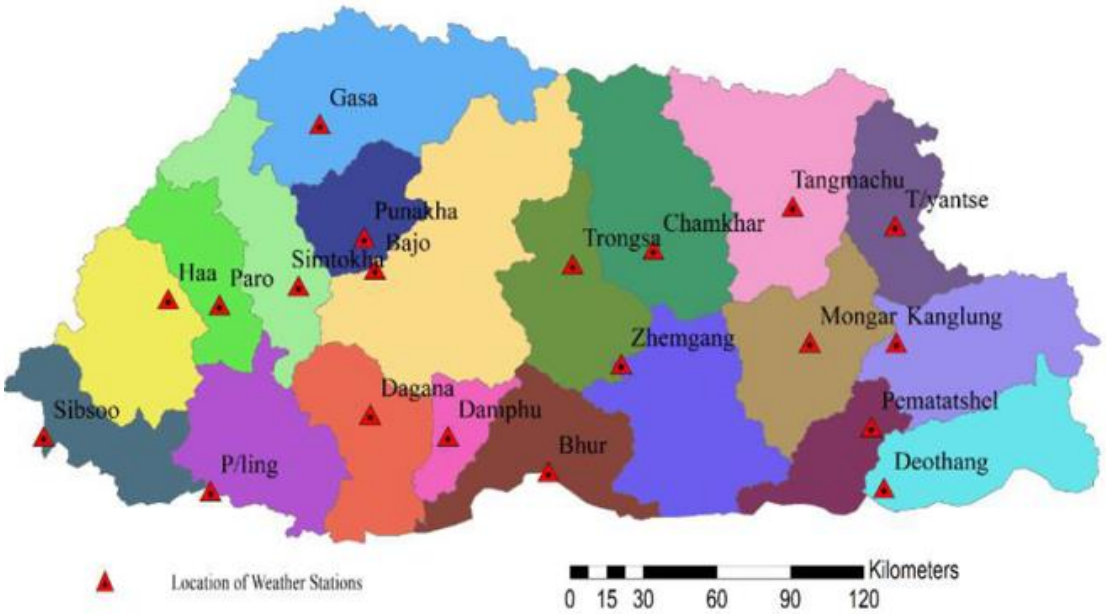

Figure 5. Location of Agro-Meteorological Stations Across the Country (NCHM)

Due to limited historical climate data, precipitation and temperature data are recorded only from 1996. There is not much record of climate hazard events except the

compendium of flash flood events across the country from 1968 to 2022 (NCHM, Vol 2, 2017). It can be seen in Figure 6 that the number of flash floods is on the rise, aggravating the cascading effect every year.

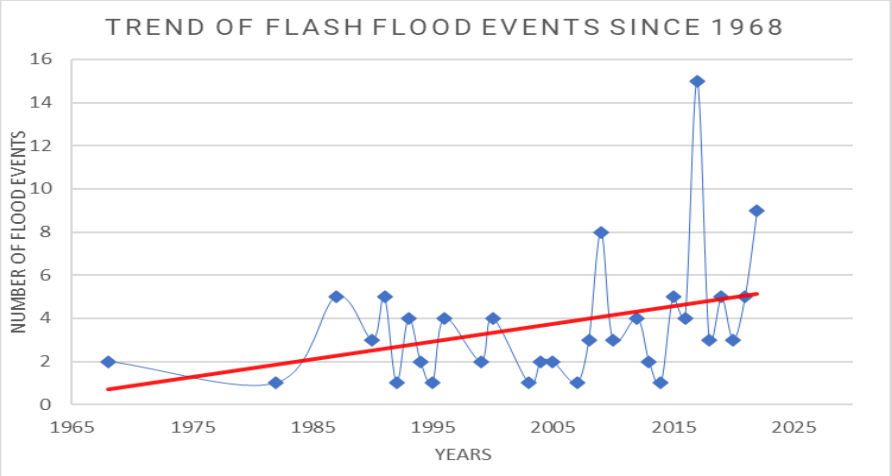

Figure 6. Trend of Flash Floods Since 1968

3.2 Energy Sources and Power Transmission Networks of Bhutan

Hydropower development in Bhutan began in 1988 with the commissioning of the 336 MW Chukha hydropower plant, and a few other hydropower plants have been added over the decades bringing the total installed capacity to 2,326 MW (DGPC Report, 2021). Figure 7 shows the 720 MW Mangdechhu power plant commissioned in 2019. Currently, three hydropower plants, namely Punatsangchhu-I as shown in Figure 8, Punatsangchhu-II and Nikachhu are under construction and are expected to increase hydropower capacity to 4,664 MW. Hydropower plants, however, are facing sustainability challenges due to global warming and glaciers that provide water for run-of-river dams.

Figure 7. 720 MW Mangdechhu Hydroelectric Project (Source: The Bhutanese, July 17, 2021)

Figure 8.1020 MW Punatsangchhu- I, Under Construction(Source: Business Bhutan, August 5, 2020)

Figure 9. 600 kW Wind Plant and 180kW Solar Farm at Wangdue Phodrang (Source: Kuensel, March 27, 2023)

According to the Renewable Energy Master Plan (2017), 12,000 MW of solar energy and 76 MW of wind energy are mentioned as technically feasible (IRENA, 2019). The current installed capacity of renewable energy including small hydropower is about 9.25 MW, and Figure 9 indicates 600 kW wind turbines commissioned in 2016 and the 180 kW solar farms installed in 2021.

There are two state-owned companies; Druk Green Power Corporation (DGPC) was established in December 2007 to develop, operate and maintain the power station. Established in July 2002, BPC is responsible for the transmission and distribution of reliable electricity to customers. Both the companies later became a part of Druk Holding and Investment Limited (DHI), established in 2007 with the mandate 'to hold and manage existing and future investments of the Royal Government for the long-term benefit of the people of Bhutan'.

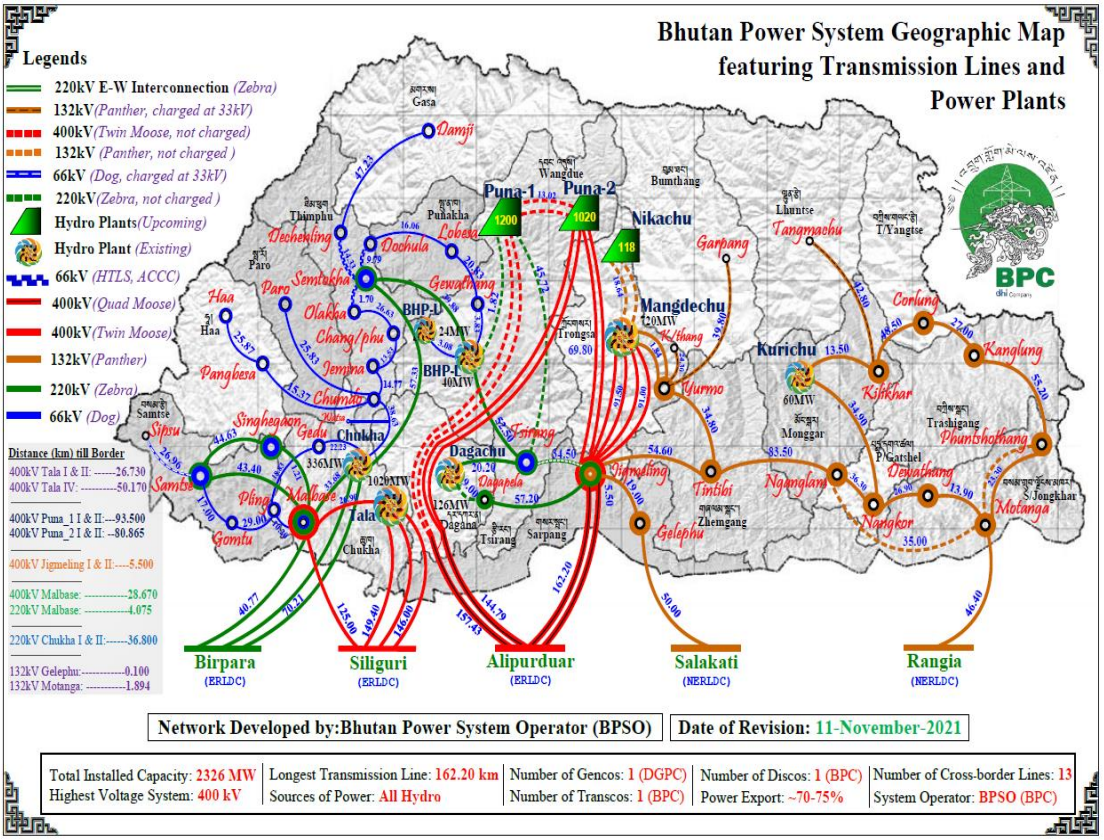

Figure 10. The Existing and Planned Power System Networks of Bhutan (DHPS, 2018)

BPC has completed the Rural Electrification Project accomplishing the milestone of 100 percent electrification in 2018 covering all rural and remote households in the country (JICA, 2022). In parallel, BPC continued the expansion of the high-voltage transmission network (DHPS, 2018) and also with the increase in domestic demand they initiated the Distribution System Master Plan (2020-2030), aiming for an adequate and optimal distribution system expansion and enhancement plan for all distribution systems in 20 districts (DSMP 2020-2030). The high voltage transmission lines consist of high voltage levels of 66kV, 132kV, 200kV and 400kV, with a total line length of more than 1300 km routed through deep forests and topographical hills, as shown in Figures 10 and 11. The low voltage distribution networks with voltage levels of 33kV, 11kV and 6.6 kV stretched more than 1700 kilometres, supplying power to the entire country (BPC, 2022).

According to the National Transmission Master Plan 2040 (NTMP, 2040), BPC has plans to expand domestic lines and include international feeders in the Indian power grid. This is to facilitate the diversification of energy sources and hydropower under development. Figure 12 (NTMP 2040) shows the planned connection of five 400 kV double circuit links and two main power pool (High-Voltage Direct Current) substations to the Indian power grid.

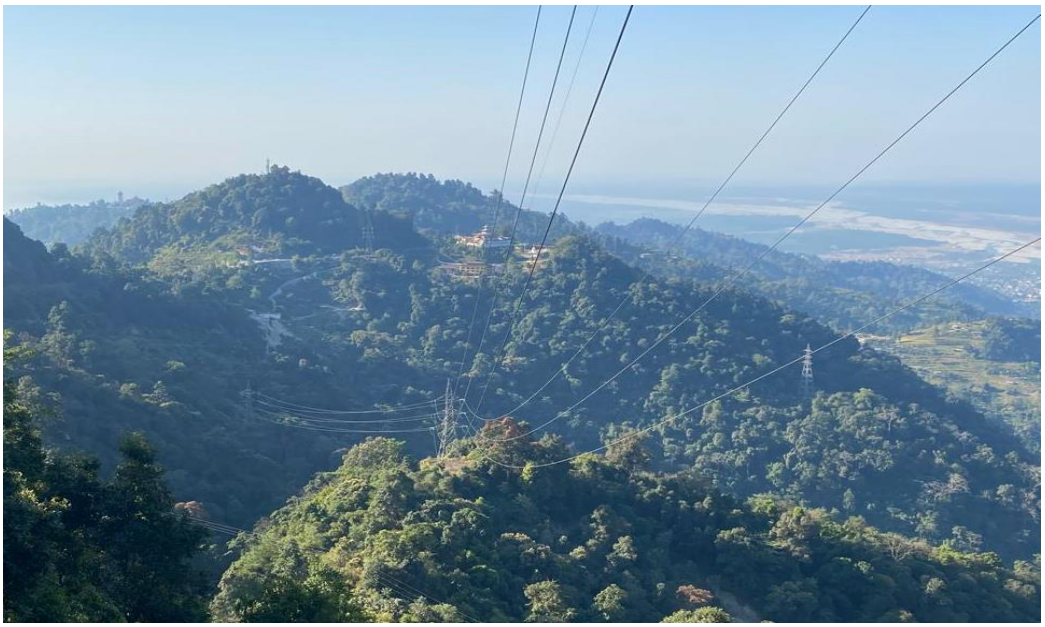

Figure 11. Transmission Lines Running through a Fragile Environment

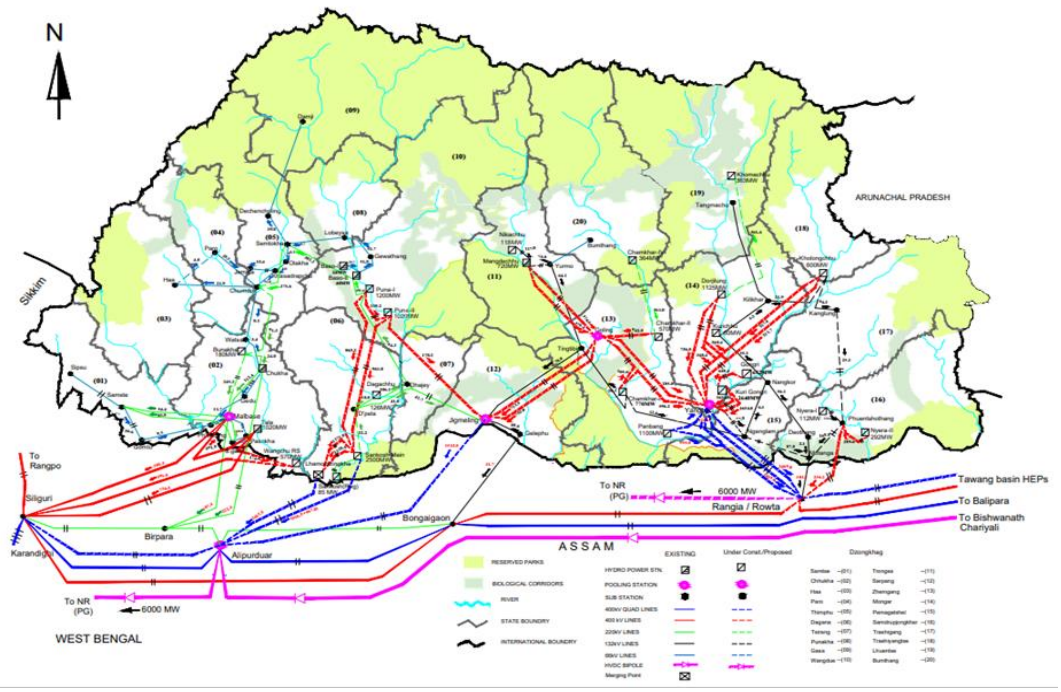

Figure 12. National Power Transmission Network (MoEA, 2018)

Although it is commendable that the BPC has accelerated its transmission grid expansion efforts and electrified all homes in Bhutan in line with the growth and diversification of energy supply and demand, there have been many reports of frequent power outages and erratic power supply throughout country. This underscores the fact that there are serious issues with energy security and reliability of the current power distribution system that require urgent and immediate attention.

While there appears to be no proper record of bookkeeping of the weather-related incidents of power outages and disruptions, numerous examples of pictures

posted on online forum of transmission lines, towers and distribution systems that have been damaged by the monsoon havoc of flash floods, windstorms, lightning and landslides could be observed. The following Figures 13 - 18 show disruptions in power infrastructure caused by climate-related hazards.

Figure 13. 66kV Tower and Optical Line Damaged at Wanakha, Chukha (BPC-FB, 2023)

Figure 14. Power Outages, Jomotshangkha, Samdrupjongkhar (BPC-FB, 2022).

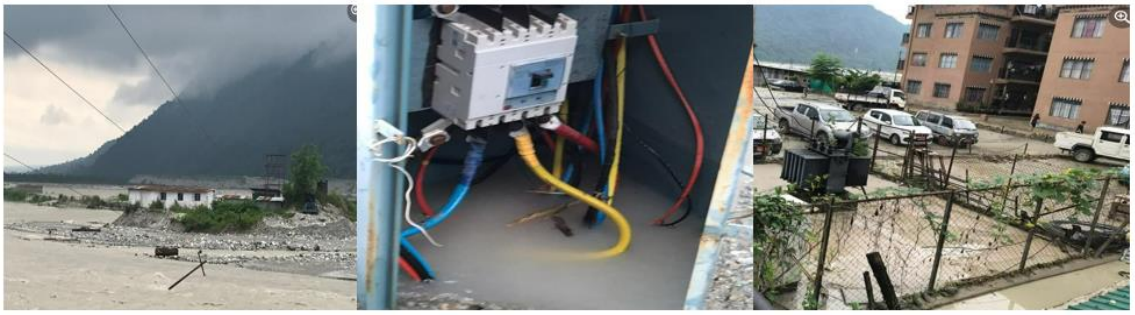

Figure 15. Flash Floods in Phuentsholing Region (BPC-FB, 2022)

Figure 16. Damages to Power Infrastructures, Wangdue Phodrang (BPC-FB, 2022)

Figure 17. Punatshangchhu-I, Dam under Construction (The Bhutanese, 2021)

Figure 18. MHPA Remains Shut after Chamdey Gangchhu Flood (Kuensel, 2020)

3.3 Risk Assessment and Development of Survey Questionnaires

In general, hazard is described as the possibility of an adverse impact, however, hazard risk in the power system is defined as the potential for damage or loss to power system infrastructure because of exposure to hazard. It is the product of the likelihood of hazards and the severity of the vulnerability (Stout et al., 2019).

According to the NREL guidelines, the potential hazards posing risks to the power system were first identified and classified into natural hazards, man-made hazards and technology-related hazards, followed by defining the impacts at which intensity hazards could affect the power system infrastructure. Subsequently, a conceptual framework for assessing the hazards associated with climate change was developed to improve power system resilience.

Identifying the potential hazards which pose risk to electrical systems is critical, as subsequent processes rely on a thorough understanding of all potential hazards. The assessment began with desk literature reviews and correspondence with our key stakeholder (BPC), sharing the objectives of this research and requesting access to data and support for the field survey.

Initially, a preliminary purposeful sample survey was conducted among BPC executives, field managers, transmission system operators and planners to assess the level of climate change awareness, preparedness and implementation measures, as well as to gather first-hand information on the current state of the power system, hazard log records, prevention and critical hazards related to power systems.

Based on the preliminary results, a comprehensive questionnaire was developed covering all important components of power system infrastructure, climate-related variables and associated risks related to natural, anthropogenic and technological hazards. This detailed survey aims to collect hazards, impacts and vulnerabilities of all substations and their regional offices in 20 districts across the country through field visits and one-on-one interviews, as shown in Figure 19.

Figure 19. Data collection from various power sector units across the country

The site visits and drone survey were also carried out in the pilot area at Chukha to visually inspect the transmission line routes and identify potential hazards in the vicinity of the transmission lines and the right of way (RoW).

3.4 Development of the conceptual framework

A comprehensive framework for conducting the envisaged study is presented in Figure 20. The process begins with understanding the current state of the power system network, its infrastructure and operational process, and management of probable associated risks.

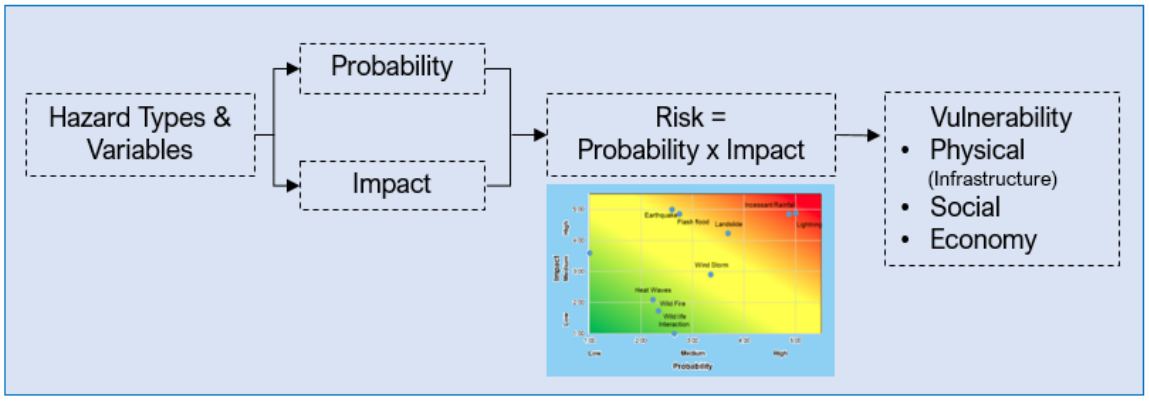

Figure 20. Conceptual Framework.

The instruments such as interviews and questionnaires were used in obtaining the data/information on the situations and circumstances. A number of critical variables, both dependent and independent, were scrutinized based on the responses obtained for analysis.

The results of the data analysis are aggregated as “risk factors” that manifest the vulnerabilities of physical infrastructure, social and economic. Subsequently, necessary prevention and mitigation measures including capacity building of the system management are spelled out as recommendations.

4. Results and Discussion

This chapter presents the results of the preliminary survey of likely hazards, the results of the hazard risk assessment survey and the GIS analysis of the selected site. The preliminary survey focused on identifying potential hazards and hazard risk assessment practices in Bhutan's power system, which includes power generation stations, power substations, power transmission and distribution lines. The results of the risk assessment survey highlight the potential risks for the power grid, possible remedial

measures and disaster preparedness. The GIS analysis focuses on the spatial analysis of case study site in the Chukha region.

According to a preliminary analysis, although employees are aware of the hazards, there is a lack of clearly defined policies for the operation and maintenance of power systems to effectively manage risks and implement remedial actions. In addition, there is a lack of a risk log or central repository to systematically catalogue disaster events and measures to prevent or minimize recurrence. Therefore, a second phase of a comprehensive survey and walk-in interviews were conducted to assess the risks and vulnerabilities of the power system. In addition, a multi-hazard analysis was carried out using AHP to create spatial hazard maps for the pilot study area using the GIS tool, as described in Sections 4.2 and 4.3.

4.1 Findings from Risk Assessment and Hazard Evaluation Survey

A comprehensive questionnaire for assessing power system hazards was developed using NREL guidelines and inputs from technical experts to assess the risks associated with natural, anthropogenic and technological hazards related to the climate change. The assessment survey was carried out on major sections of power systems such as generation, transmission, distribution, operation and control, and system management. The walk-in survey was conducted in 20 districts across the country and 321 responses were noted.

4.1.1 Survey Response Analysis

A comprehensive analysis was conducted on a dataset consisting of 321 respondents, which were scrutinized, reviewed and cleaned to identify hazards, impacts and vulnerabilities arising from climate change. Figure 21 shows the percentage of respondents from all 20 districts. The highest percentage of respondents were from Samtse and Chukha Dzongkhags at 14.6 percent and 14.3 percent, respectively. This might be due to the proximity and location of Chukha's two power stations and two high voltage substations – 400/220/66 kV Air Insulated Substation in Chukha and 220/66 kV Gas Insulated Substation. Also, Samtse is one of the largest and most populous Dzongkhags with six substations and about 23 distribution lines (DSMP Samtse, BPC, 2020).

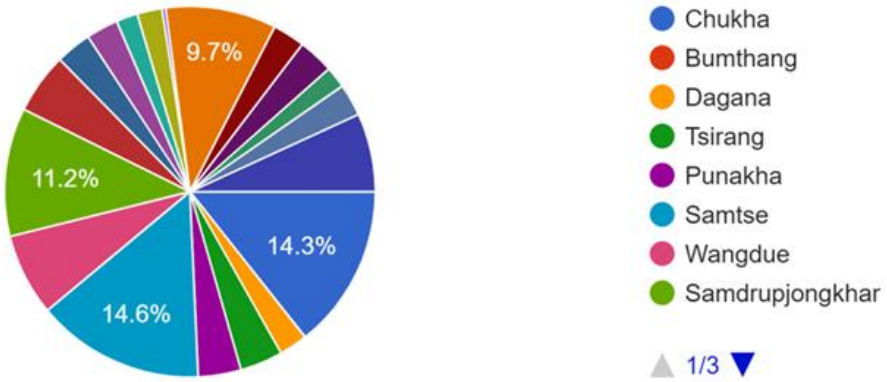

Figure 21. Breakdown of Respondents in 20 Districts

4.1.2 Phase 1: Identifying Hazards to Power Systems

The primary goal of Phase 1 is to identify potential hazards to the power system. Figures 22 and 23 show the results of this phase of hazard risk assessment in two distinct categories of hazards: (i) natural-induced hazards and (ii) anthropogenic and technological hazards. As shown in Figure 22, the survey revealed the significant hazards associated with lightning. An overwhelming 78 percent of respondents consider lightning to be one of the top natural hazards to energy systems. Likewise, 77 percent of respondents cited sustained rainfall as the primary cause of other related disasters.

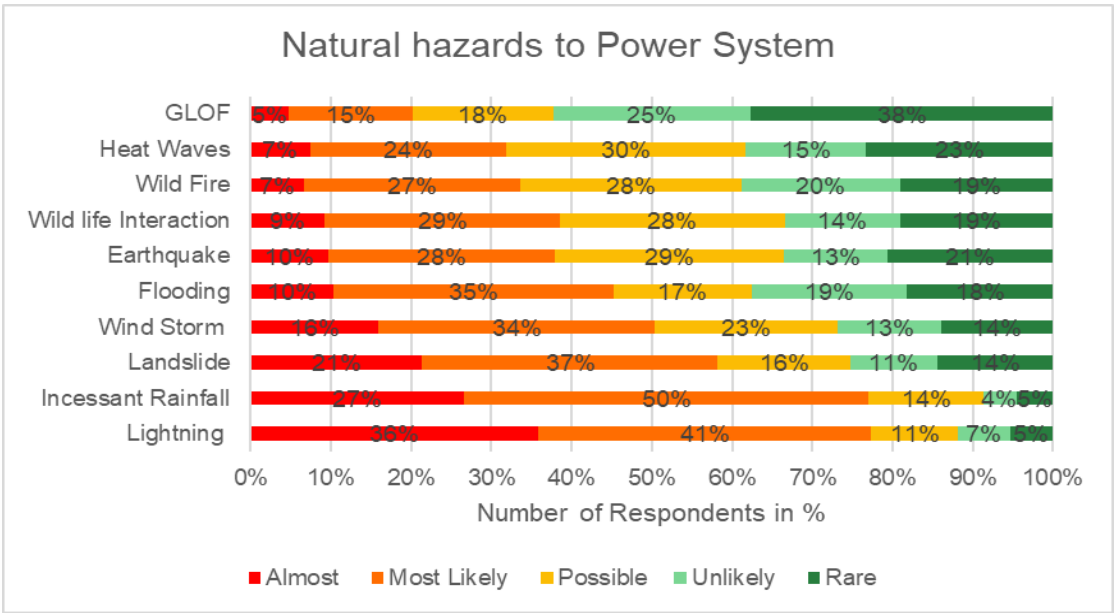

Figure 22. Natural Threats to Power Systems

Furthermore, 58 percent of respondents identified landslides as a significant hazard affecting the power system, while 50 percent identified storms as a significant hazard.

Other natural hazards, such as floods, earthquakes, wildfires, heatwaves and glacial lake outburst floods (GLOFs), however, have relatively lesser or no impact on Bhutan's power system.

An analysis of technical and human hazards revealed that ageing equipment, a lack of technical experts and poor execution (infrastructure failures) pose potential risks. Figure 23 show that equipment ageing is one of the main risks to Bhutan's power system for more than 64 percent of respondents. This is followed by accidents at 44 percent and poor quality of work at 39 percent. The results suggest that the power system infrastructure needs to be replaced with new equipment to ensure efficient operation and disaster resilience. Accidents are identified as the second most significant human-induced and technological hazard, indicating that good occupational and safety practices must be enhanced in power systems operation.

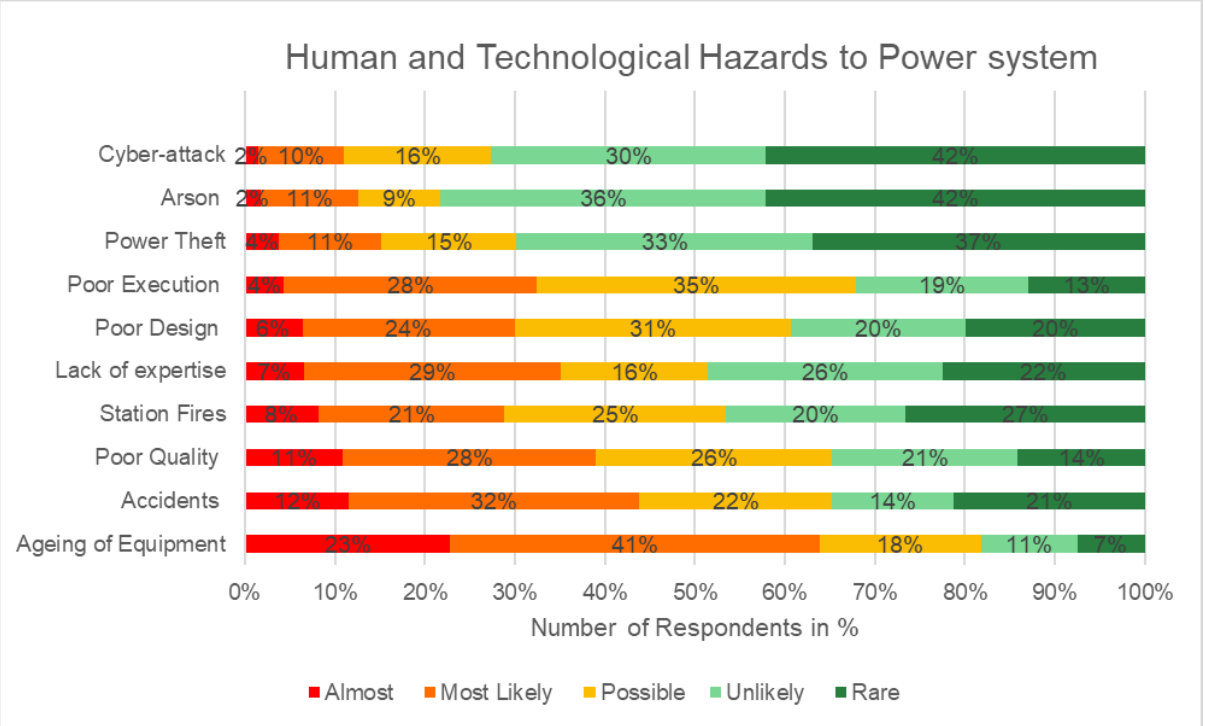

Figure 23. Human-induced and Technological Hazards

4.2 Phase 2: Identification of Potential Impacts

Phase 2 of the investigation entails analyzing the potential impact of various natural, man-made and technological hazards on different parts of the power system. The potential hazards identified from Phase 1 were used as variables in the risk assessment for each category.

Risk assessment, defined as the product of probability and its impact, is calculated graphically using weighted cumulative scores for each hazard and its impact variables for five different parts of the power system. In all cases, survey data were normalized using the maximum and minimum method, with the maximum set at 5 and the minimum at 1 and scored on a 5-point Likert scale.

$$Risk\ Assessment = Probability\ of\ Hazard\ \times Its\ Impact$$

4.2.1 Risk Assessment of Power Generating Stations

The risk assessment revealed that, among natural hazards, lighting, incessant rainfall and landslides are the hazards that have the greatest impact on power generation stations. Hazards such as earthquakes, flash floods and windstorms have moderate impacts on power generation stations while heatwaves, wildfires and wildlife interactions have little to no impact, as indicated in Figure 24.

4.2.2 Risk Assessment of Power Transmission Lines

The power transmission lines in Bhutan are routed across steep terrain and valleys until they reach the Indian plains. Figure 25 shows the hazard matrix for transmission lines most affected by lightning strikes, probably because lines are passing across the top of hills where lightning can easily touch.

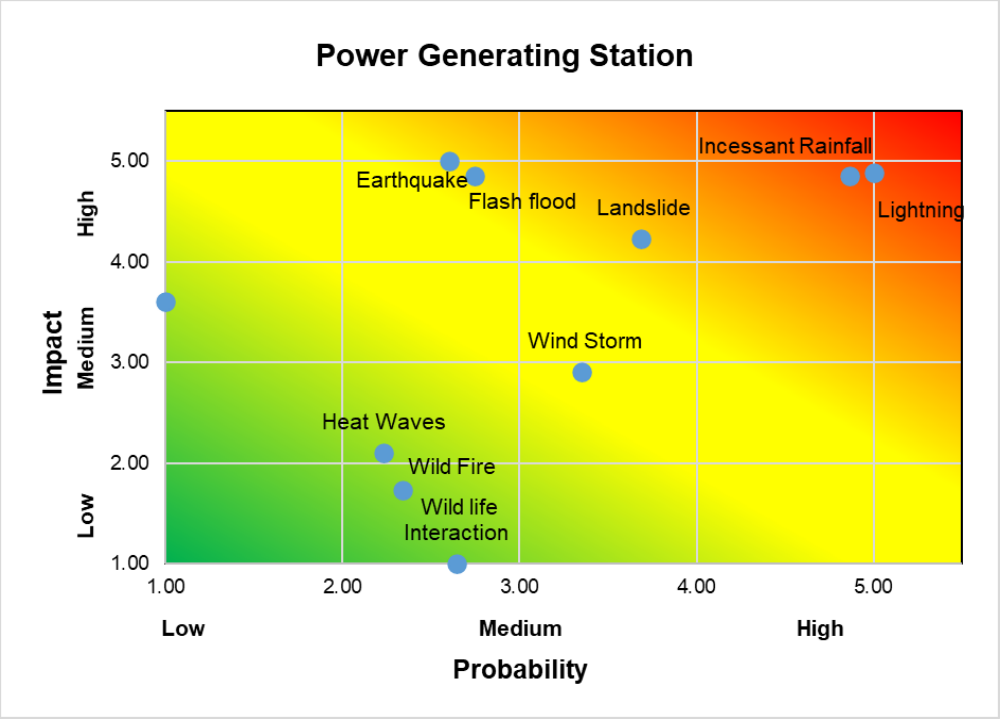

Figure 24. Risk Assessment of Power Generating Stations

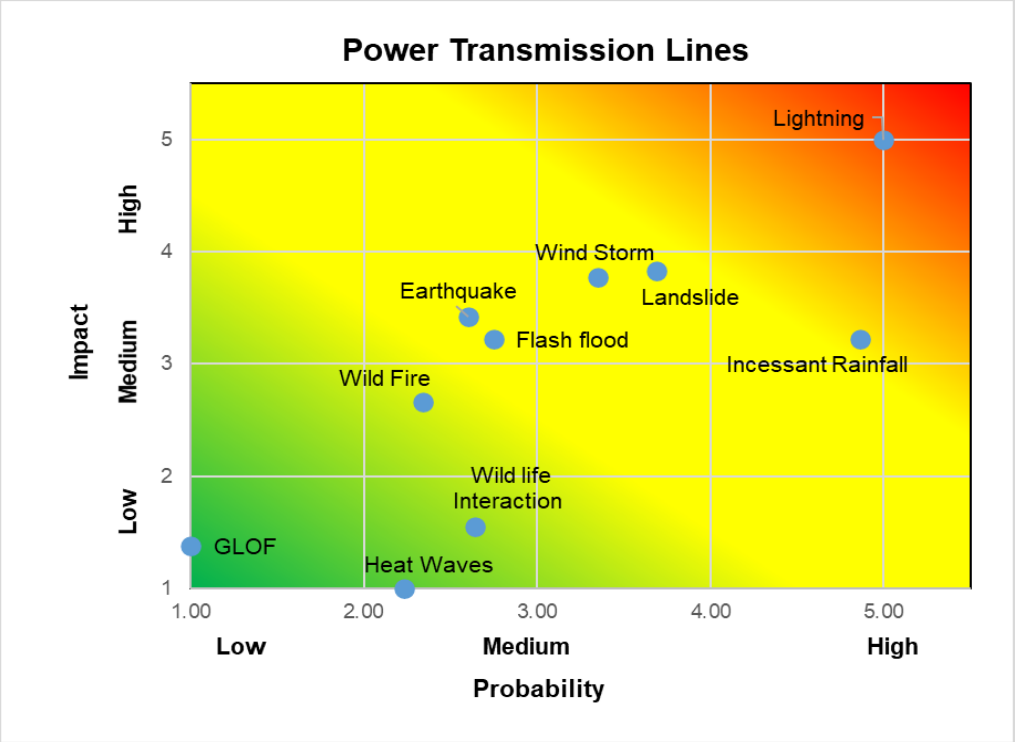

Figure 25. Risk Assessment of Power Transmission Line

As shown in Figure 26, Bhutan receives around 10 to 32 lightning strikes per square kilometre per year and the southern belt is the most affected area (Vaisala, 2022).

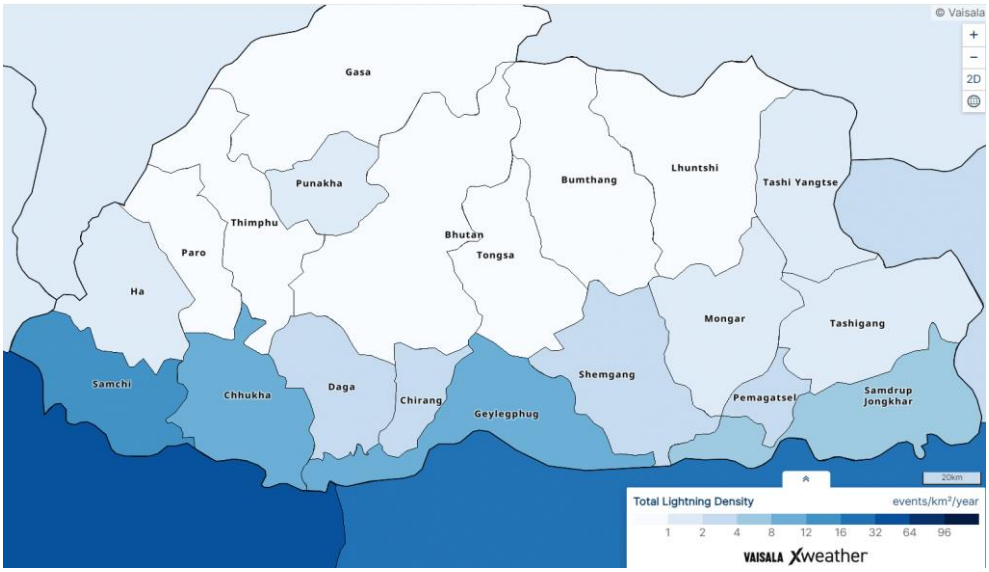

Figure 26. Lightning Density Map of Bhutan (Vaisala, 2022)

Hazards like windstorm, landslides, incessant rainfall, earthquakes and flash floods have medium impact on power transmission lines, while wildfires, wildlife interactions, heat waves and GLOF have very low impact on power transmission lines.

4.2.3 Risk Assessment of Power Transmission Towers

Transmission towers are most severely affected by lightning, landslides and incessant rainfall. Subsequently, hazards such as earthquakes, flash floods, storms and wildfires have moderate impact, while heat waves or rise in temperature, interaction with wildlife and GLOFs have little or very low impact, as shown in Figure 27.

4.2.4 Risk Assessment of Power Substations

Most substations are air-insulated and only a few substations are gas-insulated. Lightning is the most severe hazard in a substation due to thunderstorms with incessant rainfall. Windstorms, landslides, earthquakes and flash floods have medium impact, while wildfires, heat waves, wildlife interactions and GLOFs have very low impact as shown in Figure 28.

4.2.5 Risk Assessment of Power Distribution Systems

The distribution system of Bhutan's power system network consists of AIS substations. The typical voltage distribution for Low Voltage consumers is at 230 V Single Phase, 415 V three phase and 11 kV three phase systems. The distribution substations and systems are located near the load centres and serve as an important point for customers since most of the billing is done at this stage. The distribution system is also most severely impacted by lightning which is mostly induced by incessant rainfall and followed by other hazards as shown in Figure 29.

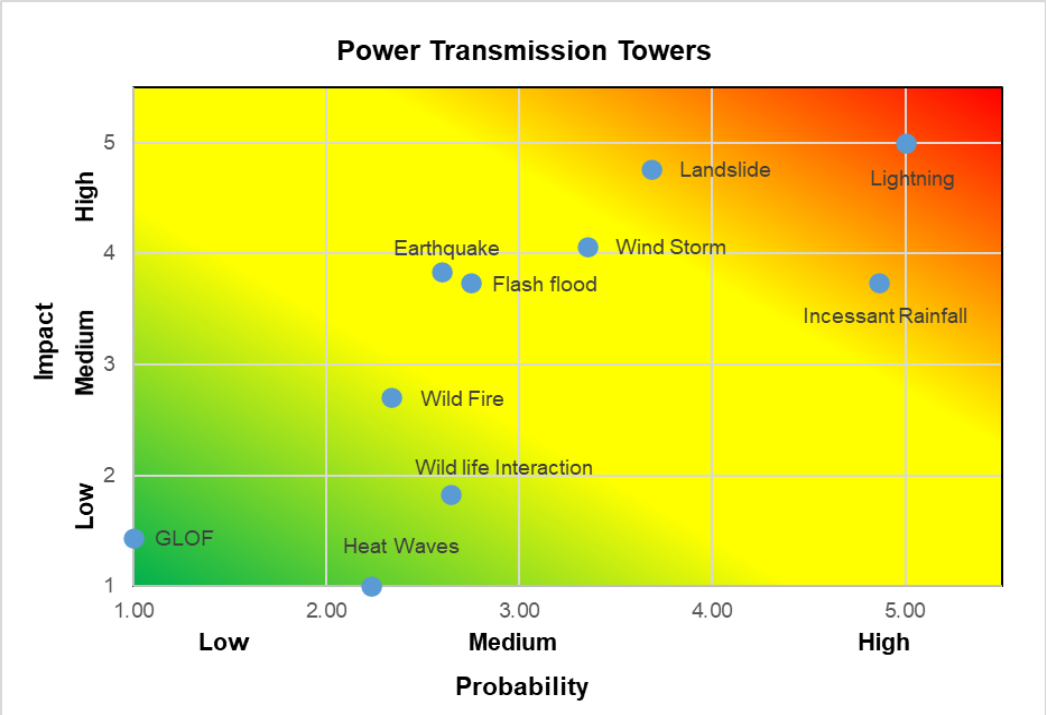

Figure 27. Risk Assessment of Power Transmission Lines

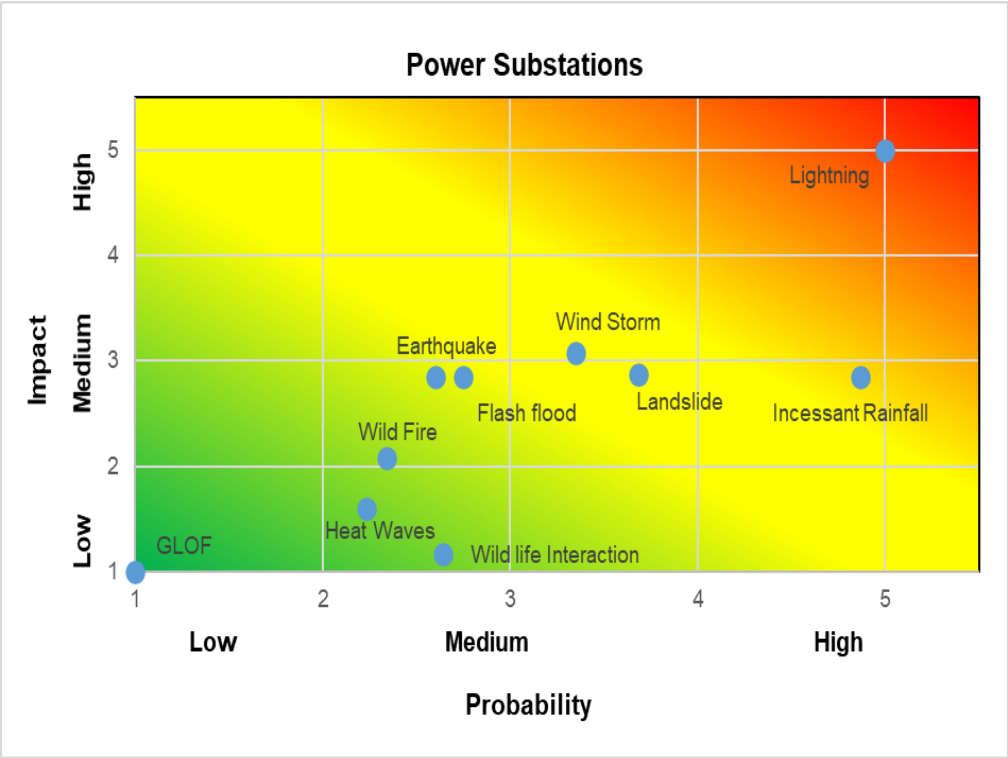

Figure 28. Risk Assessment of Substations

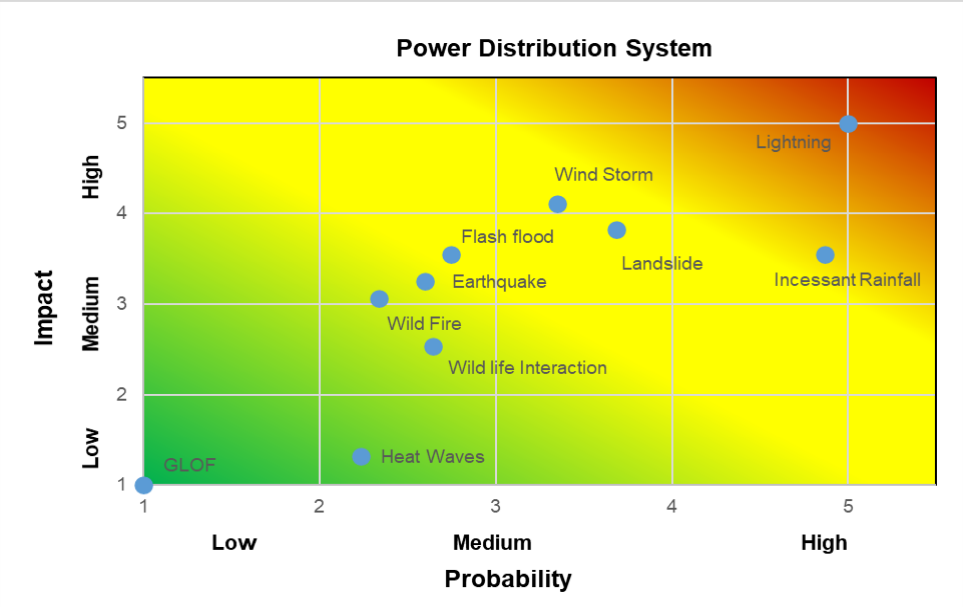

Figure 29. Risk Assessment of Substations

4.2.6 Impact Analysis Due to Different Hazards

Along the x-axis of Figure 30, analyzing the impact of various disasters on various parts of the power system, lightning has the greatest impact on all parts of the power system.

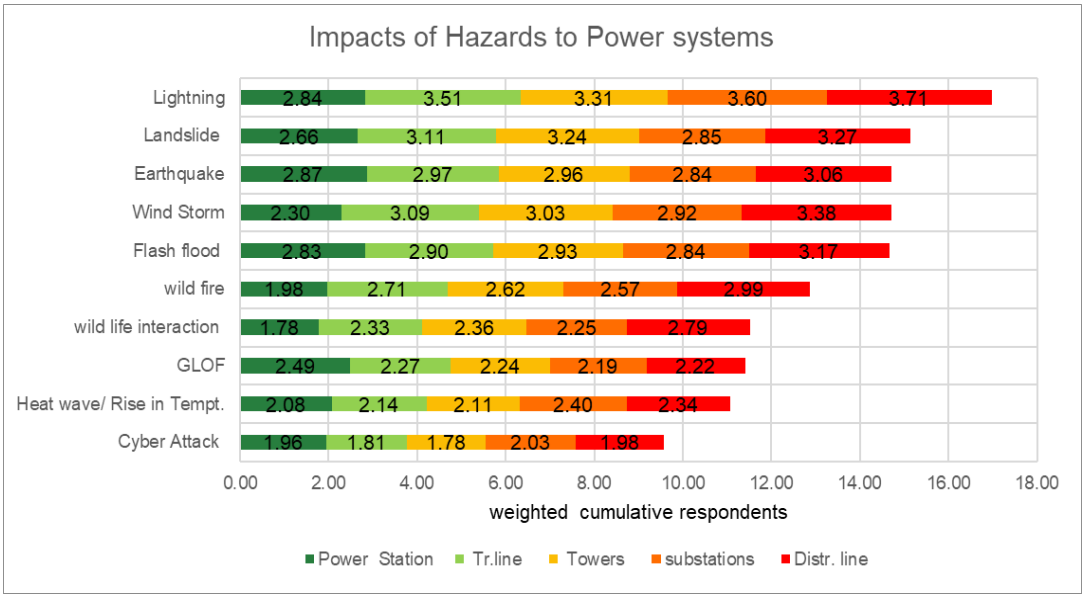

Figure 30. Impact of Hazards to Power Systems

While landslides, earthquakes, storms, flash floods and wildfires have equally high impact on all parts of the power system, wildlife interactions, GLOF and heat waves have significant impact and cyberattacks have minimal impact on all parts of the power system.

Going by the vertical y-axis impact analysis of various hazards, power stations are exposed to earthquakes, followed by lightning, flash floods and GLOF. In the case of transmission lines, the most impactful hazard seems to be lightning followed by landslides and windstorms. Similarly in transmission towers the most impactful hazard seems to be lightning followed by landslide, windstorms and flash floods. In the substations, the most impactful hazard by far seems to be lightning with a score of 3.6 followed by windstorms, landslides and flash floods. The power distribution system is impacted most by lightning followed by landslides, windstorms and earthquakes.

The results indicate that lightning has the most significant impact on the power system, followed by landslides, earthquakes, windstorms, flash floods and other factors. Among the hazards identified in Phase 1, lightning was found to have the highest impact on power stations, transmission lines and towers, substations and distribution lines, followed by landslides, earthquakes, windstorms and flash floods.

However, hazards such as wildlife interactions, cyber-attacks, GLOF and heat waves were found to have minimal impacts. This may be due to the nature of the respondents, as many of them were from the power transmission and distribution sectors, where GLOF is not a significant concern. Additionally, most of the substations in the country are not digitized and still operate on manual operating principles, which may have resulted in low impact due to cyber-attacks.

4.3 Vulnerability Assessment of Bhutan's Power System Network

The vulnerability assessment is carried out after risk assessment to assess the weakness of power system infrastructures against the various hazards identified for each of the five categories. The vulnerability assessment is carried out using a 5-point Likert scale with the percentage of respondents under each scale and the data normalized for easy analysis.

4.3.1 Vulnerability Assessment of Power Generating Stations

From Figure 31, it is seen that the power generating stations which consist of run-of-river hydropower stations are vulnerable to ageing infrastructure, followed by poor geology, windstorms and flash floods. Hydropower generating stations in Bhutan are mostly underground and due to its location in the Himalayan mountains, which are young, they are prone to slope stability issues and flash floods.

Power Generating Stations Risk Evaluation		Water inflow	Restrictricted Supply Chain	Undersized Capacity	Poor Design	Damage to Dams and Intakes	Damage to Power House and Strucutures	Ageing Infrastructure
		1	2.5347	2.7633	3.1061	3.55	3.6122	5
Lightning	5.00	5.00	12.67	13.82	15.53	17.73	18.06	25.00
Incessant Rainfall	4.87	4.87	12.33	13.44	15.11	17.26	17.57	24.33
Landslide	3.69	3.69	9.34	10.18	11.45	13.07	13.31	18.43
Wind Storm	3.35	3.35	8.49	9.26	10.41	11.89	12.10	16.75
Flash flood	2.75	2.75	6.96	7.59	8.53	9.74	9.92	13.74
Earthquake	2.60	2.60	6.59	7.18	8.08	9.22	9.39	13.00
Wild life Interaction	2.64	2.64	6.70	7.30	8.21	9.38	9.55	13.22
Wild Fire	2.34	2.34	5.93	6.47	7.27	8.30	8.45	11.70
Heat Waves	2.23	2.23	5.66	6.17	6.93	7.92	8.06	11.16
GLOF	1.00	1.00	2.53	2.76	3.11	3.55	3.61	5.00

Figure 31. Vulnerability Assessment of Power Generating Stations

Undersized capacity is also found as one of the vulnerabilities since Bhutan imports electrical energy from India during winter months where low water discharges are observed, and hydropower stations do not have any reservoirs. The ageing infrastructure is one aspect which power generating companies need to look into since the

hydropower plants such as 336 MW Chukha Hydropower Plant was commissioned in 1980s and 1020 MW Tala Hydropower Plant was commissioned in 2007. The result analysis shows that older power plants are now in need of reassessment and revamp to be disaster resilient. In the vulnerability assessment of different power systems, the generating plants are vulnerable to poor geology, flash floods, ageing infrastructure and undersized capacity.

4.3.2 Vulnerability Assessment of Power Transmission Line and Towers

The vulnerability assessment of power transmission and towers against various hazards shows that ageing infrastructure is one of the major areas of concern, followed by slope stability and undersized capacity of transmission lines and towers as shown in Figure 32. The transmission towers become susceptible to power outages due to poor reliability of ageing power system components during disasters such as lightning and switching surges, which are prominent in Bhutan.

Power Transmission Lines and Towers Risk Evaluation		Snow loading	Susceptible human interference	Expose to heat waves/Rise in Temperature	Susceptible wild life interaction	Exposure to windstroms and faults	Lack of Redundancy (under sizeand lines)	RoW Clearance	Slope Stability and restricted supply chain	Prone to Flash Floods	Ageing Infrastructure
		1.00	1.34	1.52	2.33	2.46	2.69	2.80	3.52	3.56	5.00
Lightning	5.00	5.00	6.70	7.59	11.67	12.28	13.44	13.98	17.59	17.79	25.00
Incessant Rainfall	4.87	4.87	6.52	7.38	11.35	11.95	13.07	13.60	17.11	17.31	24.33
Landslide	3.69	3.69	4.94	5.59	8.60	9.05	9.90	10.30	12.96	13.11	18.43
Wind Storm	3.35	3.35	4.49	5.08	7.82	8.23	9.00	9.37	11.79	11.92	16.75
Flash flood	2.75	2.75	3.68	4.17	6.41	6.75	7.38	7.68	9.66	9.77	13.74
Earthquake	2.60	2.60	3.48	3.94	6.07	6.38	6.99	7.27	9.14	9.25	13.00
Wild life Interaction	2.64	2.64	3.54	4.01	6.17	6.49	7.10	7.39	9.30	9.40	13.22
Wild Fire	2.34	2.34	3.14	3.55	5.46	5.75	6.29	6.54	8.23	8.32	11.70
Heat Waves	2.23	2.23	2.99	3.39	5.21	5.48	6.00	6.24	7.85	7.94	11.16
GLOF	1.00	1.00	1.34	1.52	2.33	2.46	2.69	2.80	3.52	3.56	5.00

Figure 32. Power Transmission Lines and Towers

Due to the poor geology of the region, slope stability issues are also common, especially during peak monsoon months from June to August every year when incessant rainfalls and cloud burst phenomena result in landslides and flash floods. The transmission

towers and lines are routed through thick subtropical vegetation, in most cases through undulating hills and mountains. Therefore, during monsoons with windstorms and cyclones, transient faults due to lightning and ground faults due to vegetation are common. Overall, the transmission lines and towers are vulnerable to lightning, ageing equipment, slope stability, vegetation and right-of-way clearance.

4.3.3 Vulnerability Assessment of Power Substations

The hazard map shown in Figure 33 indicated that substation areas are also most vulnerable to ageing infrastructure and insufficient capacity, as well as lightning strikes due to inadequate lightning protection systems. The substation is located near the load centre, and due to the topography, there is a high density of lightning strikes, especially in southern Bhutan where the main substation, load centre and international feeder are located.

Power Transmission Substations		Snow loading	Prone to urban flooding	Expose to heat waves/Rise in Temperature	Susceptible to Poor design	Prone to Flash Floods	Inadquate Switch gear, Control gear and Protection	Undersized Capacity	Ageing Infrastructure
		1	2.0971	2.1771	2.2343	2.52	2.5543	3.628571	5
Lightning	5.00	5.00	10.49	10.89	11.17	12.60	12.77	18.14	25.00
Incessant Rainfall	4.87	4.87	10.20	10.59	10.87	12.26	12.43	17.65	24.33
Landslide	3.69	3.69	7.73	8.02	8.23	9.29	9.41	13.37	18.43
Wind Storm	3.35	3.35	7.03	7.30	7.49	8.44	8.56	12.16	16.75
Flash flood	2.75	2.75	5.76	5.98	6.14	6.92	7.02	9.97	13.74
Earthquake	2.60	2.60	5.45	5.66	5.81	6.55	6.64	9.43	13.00
Wild life Interaction	2.64	2.64	5.54	5.75	5.91	6.66	6.75	9.59	13.22
Wild Fire	2.34	2.34	4.91	5.09	5.23	5.90	5.98	8.49	11.70
Heat Waves	2.23	2.23	4.68	4.86	4.99	5.63	5.70	8.10	11.16
GLOF	1.00	1.00	2.10	2.18	2.23	2.52	2.55	3.63	5.00

Figure 33. Power Substations

4.3.4 Vulnerability Assessment on Power System Operation and Management

Power system operation management is an important part of power infrastructure, involving power grid management, measurement and control of power system equipment. In order to ensure the efficient operation of the power system, experienced human resources, good management and efficient equipment are needed. As illustrated in Figure 34, power system operations are vulnerable to hazards due to a lack of technical expertise and poor resource integration and planning. According to the findings, there is a lack of capital investment in upgrading critical power system infrastructures (44%) and capacity building (46%). The findings also indicate a lack of

power system resilience planning with integrated resources such as renewable energy sources, as well as a lack of cooperation among different stakeholders.

Power System Operation and Maintenance		Unauthorized Self Generation	Unauthorized Connections	Lack of cyber and physical security measures	Lack of demand side management	Installation of Non Complaint Equipment	Lack of updated codes/standards	Lack of coordination with other government agencies	Lack of Backup power on operation centres	Limited generation forcasting	Limited Operational Flexibility	Inaccurate predictions or forecasting both generaton and load	Lack of short, mid and long term plans/Maintenance	Under-resourced /trained workforce	Integrated Resource and Resilience Planning
Threats	Score	1.00	1.32	1.97	2.54	3.21	3.26	3.33	3.54	3.60	3.63	3.85	4.04	4.29	5.00
Ageing Infrastructure	5	5.00	6.62	9.87	12.68	16.07	16.29	16.66	17.69	17.99	18.14	19.24	20.20	21.46	25.00
Technological Materials	3.563	3.56	4.72	7.03	9.03	11.45	11.61	11.87	12.61	12.82	12.92	13.71	14.40	15.29	17.81
Unpredictable Accidents	3.539	3.54	4.69	6.99	8.97	11.37	11.53	11.79	12.52	12.73	12.84	13.62	14.30	15.19	17.69
Technological Workmanship	3.347	3.35	4.43	6.61	8.49	10.76	10.91	11.15	11.85	12.04	12.14	12.88	13.53	14.37	16.74
Technological Design	3.012	3.01	3.99	5.95	7.64	9.68	9.81	10.04	10.66	10.84	10.93	11.59	12.17	12.93	15.06
Imcompetence	2.844	2.84	3.77	5.62	7.21	9.14	9.27	9.48	10.07	10.23	10.32	10.95	11.49	12.21	14.22
Cyber Attack	1.16	1.16	1.54	2.29	2.94	3.73	3.78	3.87	4.11	4.18	4.21	4.47	4.69	4.98	5.80
Human Action (Arson, Power Theft)	1	1.00	1.32	1.97	2.54	3.21	3.26	3.33	3.54	3.60	3.63	3.85	4.04	4.29	5.00

Figure 34. Combined Hazard Matrix for Bhutan's Power System Network

4.4 Results from Walk-in Survey of Selected Locations in Chukha Region

Transmission lines and towers face a variety of hazards and aerial photography is one of the most effective ways to identify them. A drone survey was conducted in the pilot study area in December 2022 and January 2023 to analyze the risks posed by hazards such as flash floods, slope instability and landslides, particularly during monsoons. The investigation included Malbase 400/220/66kV AIS substation, Singyegoan Samtse 220kV feeder and Chukha 66kV transmission lines (Phuentsholing region).

Figure 35 shows the drone footage of the 400/220/66 KV AIS Malbase Substation, one of the largest substations in Bhutan with domestic feeders connected to the international feeders to India. Drone surveys of the substation and adjacent areas revealed that flash flooding occurred in the substation in 2007. It was claimed that the substation was mostly inundated with debris and the entire substation was flooded. It was also observed that the substation is located between two natural drainage channels, which puts the substation at risk of landslides and flash floods.

Figure 35. Drone Footage of the 400/220/66 KV AIS Malbase Substation

Figures 36 and 37 depicts that the lithology of the area is not stable and the hilltop transmission towers are subject to hazards such as landslides, particularly during monsoons. The Land Use Land Cover (LULC) mapping shows that apart from a sparse cover of bushes and grasses along the hills, not many trees could be seen. The area was found to be dry with poor water retention.

Figure 36. Drone Footage of Landslides Hazard to Towers and Malbase Substation

Figure 37. Drone Footage Showing Hazard of Flash Floods and Landslide

Figure 38. North-East of Malbase Substation Showing Landslide and Flash Flood

Figures 38 shows the north-east side of the substation with 220 kV input lines from Chukha Hydroelectric Power Station as well as 400 kV lines from Tala Hydroelectric Power Station. Examining the drone images, there appear to have been landslides and flash floods on the hillside. The area appears to have sparse vegetation cover and dry soil, making it vulnerable to hazards such as landslides and flash floods.

Figure 39. North-West Side of Malbase Substation Showing Fragile Environment

Figure 39 shows that stability appears to be better north-west of the substation, with more vegetation and settlements. However, as compared to the north and east sides, there are new landslide traces and the lithology appears to be similar.

Figure 40 depicts the south side of the substation facing the Indian plains where two adjacent drainage channels converge, posing an erosion hazard to the Malbase substation and the international line connecting to the Indian side. In addition, it has been observed that existing drainage systems are clogged or damaged and require repairs to accommodate discharges that may occur during monsoons and cyclones.

When interacting with substation personnel, it was confirmed that lightning is the most common hazard for damaging power system components. A lightning strike also

damaged two lightning rods in the substation, likely due to inadequate safety precautions during civil excavation.

Figure 40. South side of Malbase substation showing hazard of erosion

4.5 Aerial Inspection of Transmission Towers and Lines in Chukha Region

The investigation of the transmission lines focused on lines connecting the 400/220/66 kV Malbase and 220/66 kV Singyegoan substations located in the same area. Several landslides and flash floods occurred along the transmission lines. As shown in Figure 41, one of the towers required immediate action as its foundation could be lost at any time due to erosion. It was also noted that the horizontal headroom was comparable to the standard, but the vertical headroom was not met in many places due to the terrain or steep slopes.

Figure 41. Aerial view of 220 kV Singyegoan, Samtse feeder

Figure 42 shows the 66 kV line and the distribution poles and lines where vegetation clearance was not carried out frequently, compared to the high voltage lines that could

potentially cause ground faults.

Figure 42. Vegetations and bushes along the right of way of distribution lines

4.6 Spatial Analysis Using Analytical Hierarchy Process

4.6.1 Multi-Hazard Risk Assessment

A multi-hazard risk assessment map was created using thematic maps. Different thematic maps were used as input to assess the impact of different hazards. The hazard zone maps were created by classifying the scores using ArcGIS's Jenks Natural Break Classification capability.

4.6.2 Flood Risk Assessment

The flood risk map is shown in Figure 43, where it is observed that flood risk is distributed almost equally in the region. However, it is observed that the flood risk is higher near power-generating stations and near river channels. There have been previous floods and flash floods in the Wangchu river basin as well as adjoining tributaries, especially in the lower regions of Chukha. Along the transmission lines and towers, the flood risk is moderate to high.

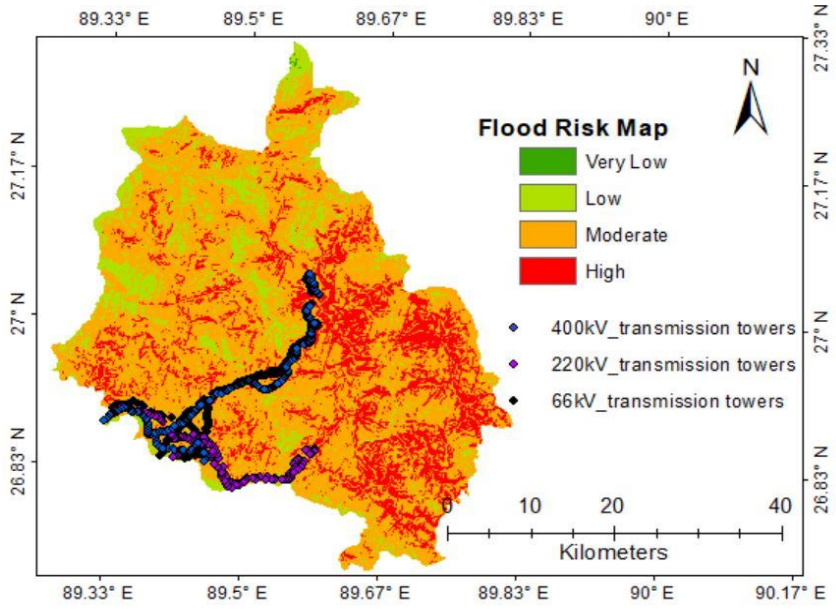

Figure 43. Flood risk map and transmission lines

4.6.3 Landslide Risk Map

Figure 44 entails the landslide risk map at the region which in general, is exposed to moderate and high risk due to the floods. Along the transmission lines and towers the landslide risks are mostly moderate and few regions with high hazard. The risk due to the landslide hazard is more in the lower regions of Chukha compared to the upper regions. There have been past landslides that are very common along the roads and in the built-up areas.

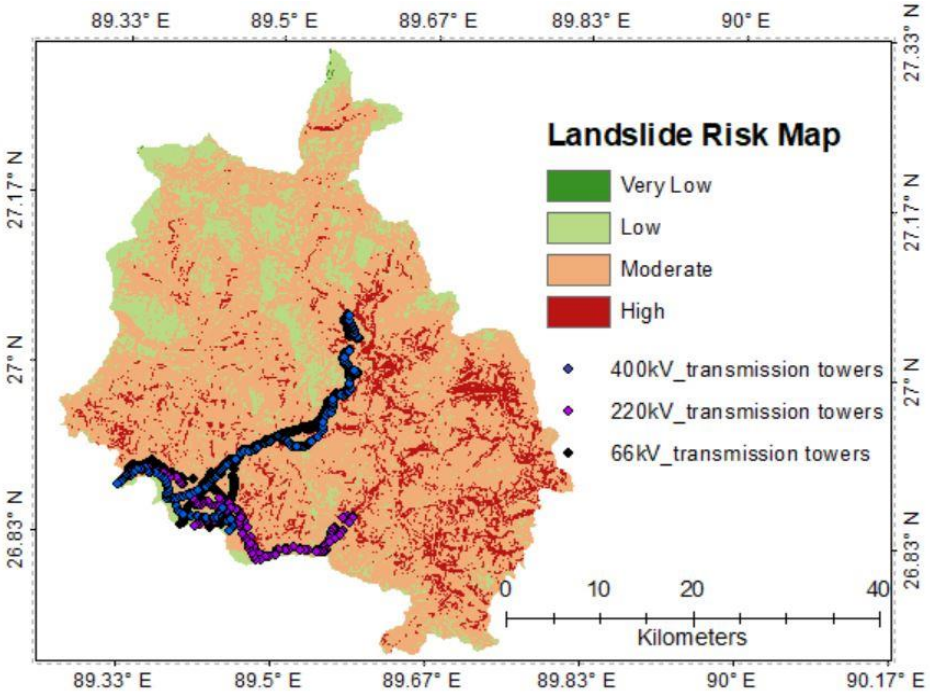

Figure 44. Landslide hazard map and transmission lines

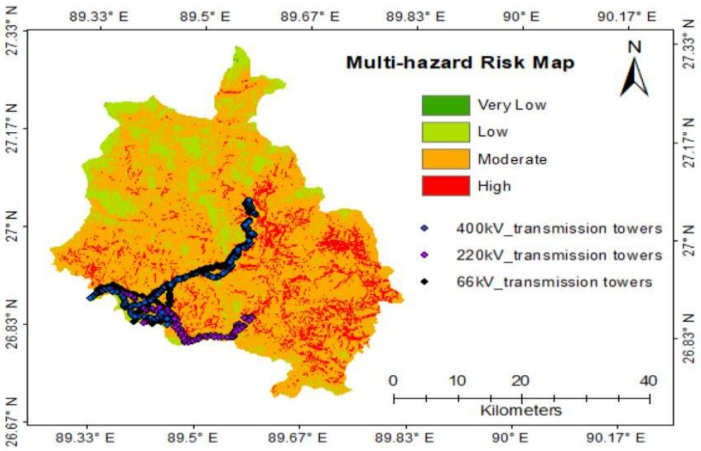

Figure 45. Power system infrastructure's exposure to multi hazards in Chukha

4.6.4 Multi-Hazard Risk Map

The multi-hazard risk map depicts the risks of landslides, floods and earthquakes along transmission lines and towers, which pose moderate to high risk as shown in Figure 45. The upper regions of the Chukha are depicted to be low risk zones compared to the lower regions. This could be due to several parameters such as lithology not being stable in lower regions, very high slope, higher precipitation and being situated nearer to faults.

4.7 Combined Hazard or Hazard Analysis

The risk assessment of the Bhutanese power grid is analysed using three different approaches - quantitative survey questionnaire for hazard analysis, qualitative analysis for walk-in surveys and spatial analysis. It is observed that hazards such as landslides, flash floods and earthquakes occur more frequently in the region. Through the questionnaires and walk-in surveys, it becomes clear that lightning, incessant rainfall, landslides and storms are more likely to occur with high impact. Hazards such as GLOF, wildlife interaction and wildfires have the lowest probability of occurrence and minimal impact.

The vulnerability assessment revealed that ageing infrastructure is one of the most common vulnerabilities, followed by undersized capacity, insufficient human resource training, poor geological conditions and the lack of redundant backup systems.

5. Key Findings of Risk Assessment and Analysis

Following are some of the cutting-edge findings which emerged from this study:

1. The historical climate review of Bhutan revealed that rise in temperatures and precipitation are the two prominent climatic variables posing potential risks to the power system infrastructure through flash floods, lightning, landslides and windstorms.
2. The historical meteorological data is unavailable. The efforts to record such data to monitor and forecast weather have started very recently.
3. The hazard analysis revealed that power stations, transmission lines, towers and substations are vulnerable due to the ageing of infrastructure exacerbated by natural hazards such as lightning, landslides, flash floods, windstorms and earthquakes.
4. There is a lack of integration of plans and resources into the operation and management of energy systems besides development of human resource capacities including adequate capital investments.
5. There is a need to adopt new technologies, change operational practices and update regulatory frameworks on the technical and policy fronts. The impact of climate change on power infrastructure could pose significant economic and financial risks.
6. While the employees of BPC were aware of impactful hazards, there is a lack of well-defined policy and procedures regarding the operation and maintenance of power systems to effectively address hazards and implement preventive and mitigation techniques.
7. There is a lack of timely intervention to prioritize plans for improving reliability, power quality, network redundancy and resilience in response to climate change. Much more efforts were seen towards expanding the corporate business

6. Recommendations

Following are the key recommended implementation strategies and procedures for minimizing exposure to hazard risks to improve reliability, efficiency and resilience of the power system:

1. Maintain hazard log as a tool to capture likely impacts of climatic hazards including identified risk owners. Also, build a system of regularly monitoring the identified hazards including potential new hazards that might emerge
2. Regular inspections and maintenance of critical components of the power system is needed since ageing of infrastructure can pose risks.

3. Invest in upgrading ageing components or systems, which may involve replacing obsolete equipment, upgrading control systems or implementing advanced technologies
4. Assess the stability of transmission line towers and substation sites located in areas prone to slope instability and implement engineering measures such as suitable foundation design, retaining walls or slope stabilization methods
5. Develop flood management strategies to prevent and mitigate the impact on electrical infrastructure, which may include improving drainage, raising critical equipment above flood level or constructing flood barriers
6. Have clear right of way (RoW) to prevent vegetation growth, encroachment or obstacles blocking transmission lines and towers. The RoW should be regularly monitored and maintained so that maintenance and repair work can be carried out efficiently
7. Conduct a full capacity assessment of substations to ensure that they can handle the increased demand and, if necessary, upgrade the capacity of substations to meet anticipated load requirements
8. Build technical capacity and competencies and prepare for emergencies by developing robust contingency plans to address potential infrastructure failures due to natural disasters. Establish communications protocols, providing timely and meaningful training to employees and coordinating with relevant authorities for rapid response and recovery efforts
9. The installation of lightning protection devices and their coverage needs to be re-examined to ensure that no part of the power system is missed within the protected area
10. Introduce redundancy in the transmission and distribution lines by building alternate routes for lines or backup substations to ensure uninterrupted power in the event of a failure

7. Enablers and Barriers

Performing investigative research into real-world problems and issues is challenging, particularly when the necessary information and related support is sought from key stakeholders and other ancillary institutions in the ecosystem.

BPC was the key stakeholder with which the investigative research was carried out. The corporation’s operational management and staff extended their enthusiastic support in conducting this research by giving easy access to the infrastructure sites and

by providing relevant information. Their keen gesture and support enabled us to conduct the investigations at our convenience.

While the investigation process and activities were anticipated to flow smoothly as desired, certain obstacles were also experienced. Firstly, time was a cause for concern since the involved faculty members had limited time to spare due to academic workload. Secondly, some sections of the respondents did not have a clear picture about the risks caused by hazard events. Thirdly, the stakeholder organization did not have sufficient historical data concerning the hazards and their impacts.

8. Key Takeaways from CDRI Fellowship Programme

The hazard risk assessment and investigative research carried out under this fellowship programme has been received well by the relevant stakeholders, particularly BPC. The research outcomes have been seen to enable decision makers in the process of preventing and monitoring impactful hazards which were not uncovered earlier though severe impacts were experienced.

From the research team's perspective, the CDRI Fellowship Programme provided the opportunity to enrich our research outlook and capabilities including avenues for networking with the scientific research community around the globe.

From the institutional perspective, the fellowship programme is found to be successful in bridging the institutions and stakeholders in the power sector in terms of partnering, research linkages and other future collaborations. Such opportunities are expected to bring about innovations and quality change in future service deliveries.

9. Conclusion

The analysis of data on climate-induced hazards indicates that they pose serious risks to power system infrastructure, resulting in significant income loss, disruption of the workplace and discomfort for household members. A significant finding of the study was the absence of a coherent operational protocol and a strategic outlook for the management of infrastructure and technology.

Through this research, the project envisages increased awareness about the benefits of the key findings for the power sector to proactively engage in long-term sustainability by promoting reliable, resilient and environment-friendly power supply that addresses climate change issues.

The solutions concluded thereof for the power company are:

1. Regularly monitor and have in place a strategic plan to avert or manage threats posed by the climate variables. One of the tools suggested to have in place is hazard logs including meteorological data which will allow effective management of hazards
2. Maintain records of the installation, maintenance and operation of power system components and infrastructure in order to reduce hazards associated with ageing and inadequate technical response
3. Regularly enhance the competencies and skills of operational personnel
4. Reassess the foundation designs, slope stabilization structures and drainage systems to enhance the stability of transmission line towers and substations including raising critical equipment above flood level or constructing flood barriers
5. Regularly maintain adequate “right of way” to prevent vegetation growth, encroachment or obstacles blocking transmission lines and towers

10. Way Forward

1. As a part of dissemination and publication, we will hold a workshop with the R&D unit of our stakeholder, BPC, to validate research findings and discuss possible training scale-ups.
2. The spatial multi-hazard map generation is carried out only for the pilot study area (Chukha) in this project. However, it could be extended to the entire power system, including generation and transmission networks, in collaboration with the power sector stakeholders such as BPC and DGPC.
3. In addition, we intend to submit the manuscript, titled "Sustainability and Resilience: A Futuristic Vision from Asia," to the Springer Journal of Energy.

References

1. BBS. (2019). *Power Outages in Bjoka Stretching to a Month*. Bhutan Broadcasting Service. http://www.bbs.bt/news/?p=118784
2. Corjan, N, & Lutz, A. (2021). *Renewable Energy for Climate Resilience Climate Hazard and Adaptation Assessment* (Issue April). www.futurewater.eu
3. Dema, C (2023). *Flash floods and landslides, Bhutan's common weather extreme events*. Kuenselonline. https://kuenselonline.com/flash-floods-and-landslides-bhutans-common-weather-extreme-events/
4. DGPCL. (2022). Annual Report 2021. In *Druk Green Power Corporation Limited* (Vol. 8, Issue 1). https://doi.org/10.3934/microbiol.2022009
5. DHPS. (2018). *National Transmission Grid Master Plan (NTGMP) of Bhutan-2018* (Issue June). http://www.moenr.gov.bt/wp-content/uploads/2018/11/National-Transmission-Grid-Master-Plan-2018.pdf
6. Dorji, T. (2020). Fire Situation in Bhutan. In *International Forest Fire News (IFFN)* (Issue 34). https://doi.org/10.1079/cabicompendium.33170448
7. Evrin, V. (2021). Hazard Assessment and Analysis Methods: Qualitative and Quantitative. *ISACA Journal*, *2*, 1–6. http://anale.feaa.uaic.ro/anale/resurse/06_Mazareanu_V_-_Hazard_management_and_analysis-hazard_assessment.pdf
8. Gorsevski, P. V., Jankowski, P., & Gessler, P. E. (2006). An heuristic approach for mapping landslide hazard by integrating fuzzy logic with analytic hierarchy process. *Control and Cybernetics*, *35*(1), 121–146.
9. IRENA. (2019). *Renewables Readiness Assessment: Kingdom of Bhutan* (Issue December). International Renewable Energy Agency. www.irena.org
10. Jamtsho, T. (2011). *Saving Shangri-la : Bhutan in the Wake of Climate Change and Disasters* (Vol. 1).
11. JICA. (2022). *Rural Electrification in Bhutan*.
12. NCHM. (2017). *Compendium of Climate and Hydrological Extremes in Bhutan*.
13. NCHM. (2019). Compendium of Climate and Hydrological Extremes in Bhutan since 1968 from Kuensel. In *Compendium of Climate and Hydrological Extremes in Bhutan since 1968 from Kuensel* (Vol. 53, Issue 9). National Centre for Hydrology and Meteorology.
14. NSB. (2022). *Statistical Yearbook of Bhutan 2022* (2022nd ed., Issue October). National Statistics Bureau.

15. Pourghasemi, H. R., Jirandeh, A. G., Pradhan, B., Xu, C., & Gokceoglu, C. (2013). Landslide susceptibility mapping using support vector machine and GIS at the Golestan province, Iran. *Journal of Earth System Science*, *122*(2), 349–369. https://doi.org/10.1007/s12040-013-0282-2
16. Rai, R. (2018). *Power supply resumes in Phuentsholing*. Kuenselonline.
17. https://kuenselonline.com/power-supply-resumes-in-phuentsholing/
18. Saaty, R. W. (1987). The analytic hierarchy process—what it is and how it is used. *Mathematical Modelling*, *9*(3–5), 161–176. https://doi.org/10.1016/0270-0255(87)90473-8
19. Saaty, T. L. (1977). A scaling method for priorities in hierarchical structures. *Journal of Mathematical Psychology*, *15*(3), 234–281. https://doi.org/10.1016/0022-2496(77)90033-5
20. Stout, S., Lee, N., Cox, S., Elsworth, J., & Leisch, J. (2019). *Power Sector Resilience Planning Guidebook*. National Renewable Energy Laboratory. https://www.nrel.gov/resilience-planning-roadmap/
21. UNDP. (2023). *Bhutan | UNDP Climate Change Adaptation*. UNDP Website. https://www.adaptation-undp.org/explore/bhutan
22. Vaisala. (2022). *Vaisala Lightning 2016-2021*. https://interactive-lightning-map.vaisala.com/?_ga=2.21860984.2118494780.1641071852-1633878486.1617010121
23. Valis, D., & Koucky, M. (2009). Selected overview of hazard assessment techniques. *Problemy Eksploatacji*, 19–32
24. Wangdi, T. (2015). *Power restored after 20 hours | Kuensel Online*. Kuenselonline. https://kuenselonline.com/power-restored-after-20-hours/
25. WBG, & ADB. (2021). *Climate Hazard Country Profile Bhutan*
26. Yuden, K. (2020). *Frequent power outages leave residents in the capital frustrated*. The Bhutanese. https://thebhutanese.bt/frequent-power-outages-leave-residents-in-the-capital-frustrated/
27. Zangpo, T. (2023). Construction of first mega solar plant to begin soon. Kuenselonline. https://kuenselonline.com/construction-of-first-mega-solar-plant-to-begin-soon/

Real-time Scour Detection and Prediction for Structural Performance and Safety

Daigo KAWABE;
Kyoto University, Japan

Vasilis SARHOSIS;
University of Leeds, U.K.

京都大学
KYOTO UNIVERSITY

UNIVERSITY OF LEEDS

Under CDRI Fellowship Programme 2022-23

CDRI
Coalition for Disaster Resilient Infrastructure

Disclaimer: The views expressed in this paper reflect the opinions of the author and not necessarily the official views of CDRI.

Abstract

This study aims to propose scour depth estimation method in real-time by means of long-term vibration monitoring and eigenvalue analysis of numerical model of an in-service railway bridge pier as a case study. Many bridge authorities make decisions on occurrence of scour by using direct measuring methods or indirect methods after a high flood event has occurred. In particular, the Japanese railway company has conducted vibration-based assessment method to identify changes in frequencies to evaluate the stability of the bridge piers. However, it is time and laborious method and inapplicable during swollen river water periods. Therefore, this study builds the remote sensing system that deploy accelerometers on top of the pier across a river and identify natural frequency in real-time during swollen river water period. To enhance a fast and easy understandable condition of the pier, this study investigates a way of estimating scour depth in real-time using eigenvalue analysis of Finite Element model of the pier. To deal with the uncertainty of identified frequency due to signal noise derived from weak signal, a novel sampling method is introduced to model the uncertainty of interaction with soil. A scour depth estimation method was applied to the time-series of identified frequencies during swollen river water period and the feasibility of the method is discussed.

Acknowledgments

We would like to thank our academic mentors, Professor Chol Woo KIM for his advice, guidance and support, which he had given us at the right time for the perfect conduct of the project.

We would like to extend our gratitude towards Dr Ranit Chatterjee, and Dr Harold Aquino, technical experts assigned by CDRI for their valuable and constructive comments, and for all the help that they have rendered through the course of time.

We would also like to thank fellowship coordinators from CDRI for their support at various stages of the work.

Funding

This research was supported by the 2022–2023 Fellowship of the Coalition for Disaster Resilient Infrastructure (CDRI), Application ID: 210827290

1. Introduction

Scour is the localized erosion that undermines bridge foundations during flooding and is considered as one of the most critical threats for bridges crossing rivers around the world. Nearly 21,000 bridges are reported to be susceptible to have their foundations undermined during extreme storm events (ASCE, 2021). It is particularly difficult to visually determine the scour risk of a bridge over a river, as the condition of the ground beneath the water surface of a pier cannot be directly visualized. Heavy rainfall disasters, especially in recent years due to climate change, have led to the need to address scour risk in more areas. Furthermore, even in areas where scour risk did not originally need to be considered like dry area, it has become necessary to examine its potential. In order to sustain older bridges as sustainable structures in the future, methods are required that allow the condition to be properly assessed and the stability to be quantitatively evaluated each time the river rises.

Bridge authorities have conducted several inspection methods for assessing the condition of the bridge foundation to help to manage such risk. For example, diving underwater observation and sinking length of the measure are the most basic inspection as direct methods. Sonar and radar and pulse devices have also potential use from the aspect of accuracy as nondestructive methods (De Falco & Mele, 2002; Fisher et al., 2013). Indirect methods to identify the state of the pier from dynamic responses has also been studied. In Japanese railway companies, a vibration-based method, called impact test that performs to hit the weight to the pier, excite the vibration, and identify natural frequency, has been commonly used for assessing the condition of the target pier because it can also evaluate damages of pier itself due to seismic events (Bao & Liu, 2017; Prendergast & Gavin, 2014; Lee et al., 2020). However, these are laborious and time-consuming methods, while they are inapplicable for real-time monitoring during heavy rainfalls to make a proper decision on the traffic operation of the bridge. As a result, once the water level in the river increases, authorities suspend the traffic for safety reasons. With a sophisticated logistics network already in place, a long-term suspended traffic would result in a very large economic loss and user disruptions.

A real-time monitoring scheme utilizing accelerometers installed on top of piers, thus, has been studied as an alternative method for scouring assessment during flooded rivers. In addition, a cloud based remote sensing system using Internet of Things (IoT) has been developed to enable high precision and structural identification to provide information on natural frequency of monitored pier in real-time. Kim et al (Kim et al., 2017,

2021) demonstrated the real-time scour monitoring by developing remote sensing system in real railway bridge pier as a practical application of indirect method.

Although monitoring of frequency is already useful, providing real-time information on structural performance e.g. scour depth, is also important for the purpose of even faster and more precise decision making of traffic suspension or resumption under uncertainty prediction. The data about frequency, therefore, is expected to use for estimating structural performance supporting to the numerical analysis. However, it is still limited to propose the real-time scour assessment method providing information on structural performance and safety.

2. Aim, Objectives, and Scope of the Research Study

This study proposes to estimate the scour depth around the vibration-monitored bridge pier for real-time scour assessment during high flood events. Since the concept of Digital Twins is compatible with real-time estimation for critical parameters of structural performance, the frequency data is shared with digital twin models to be developed for informed performance-based assessments methods to be undertaken. Firstly, FEM is updated using observation frequencies. Secondly, marginal distribution of soil spring stiffness is identified by MCMC Simulation since observed frequency has non-negligible variance. Then, relationships between scour depth and natural frequency are obtained by eigenvalue analysis including the effect of pier footing resistance.

This study demonstrates the feasibility of the proposed method using the long-term vibration-monitored data of a railway bridge pier. As you would see in Chapter 3 the principal technologies that use in this study are explained. Chapter 4 presents a case study of a railway bridge pier with long-term monitoring. Enables and barriers, key approaches and technologies, and conclusion are summarized at the end.

3.Methodology

3.1 System identification: Fast Bayesian FFT for scour identification

For a higher performance system identification, fast Bayesian FFT (Au, 2012a, 2012b; Au et al., 2013) is well known method and has already been reported and this paper only briefly introduces the basic concept of the fast Bayesian FFT. Assume that the acceleration was collected under ambient condition. Let $\{\hat{\mathbf{x}}_j \in R^n : j = 1, \ldots, N\}$ denote the

measured acceleration data at *n* degrees of freedom (DOFs) of a structure, abbreviated as $\{\hat{\ddot{\mathbf{x}}}_j\}$, where N is the number of samples collected in the time domain. The *j*th acceleration response can be modelled as follows:

$$\hat{\ddot{\mathbf{x}}}_j = \ddot{\mathbf{x}}_j + \mathbf{e}_j \tag{1}$$

where $\ddot{\mathbf{x}}_j \in R^n$ denotes the model acceleration response; $\mathbf{e}_j \in R^n$ denotes the prediction error between the measured and theoretical responses, mainly consisting of the electronic noise of the data acquisition system, environmental noise and modelling error.

The FFT of $\{\hat{\ddot{\mathbf{x}}}_j\}$ is defined as follows:

$$\hat{F}_k = \sqrt{\frac{2\Delta t}{N}} \sum_{j=1}^{N} \hat{\ddot{\mathbf{x}}}_j \exp\left[-2\pi i \frac{(j-1)(k-1)}{N}\right] \qquad (k = 1,2,\dots N) \tag{2}$$

where the FFT corresponds to the frequency $f_k = (k-1)/N\Delta t$ for $k = 2,3,\dots N_q$, with $N_q = int[N/2] + 1$, being the frequency index at the Nyquist frequency, and $int[\cdot]$is the integer part; Δt denotes the sampling interval; $i^2 = -1$.

For well-separated or closely spaced modes, they should be included in a series of specified frequency bands. Let D denote the FFT data in the ith selected frequency band containing the possible modes. According to Bayes' Theorem, the posterior PDF of $\boldsymbol{\theta}$ for a given data, where $\boldsymbol{\theta}$ denotes the modal parameters in the selected frequency band including natural frequency, damping ratio and mode shape, etc., can be expressed as follows:

$$p(\boldsymbol{\theta}|D) = \frac{p(D|\boldsymbol{\theta})p(\boldsymbol{\theta})}{p(D)} \tag{3}$$

where $p(D|\boldsymbol{\theta})$ denotes the likelihood function; $p(D)$ is a constant; $p(\boldsymbol{\theta})$ denotes a prior PDF. Assume uniform prior information, the posterior PDF is directly proportional to the likelihood function as follows.

$$p(\boldsymbol{\theta}|D) \propto p(D|\boldsymbol{\theta}) \tag{4}$$

The likelihood function can be constructed as follows: Define a vector $\hat{\mathbf{Z}}_k = [\mathrm{Re}\hat{F}_k; \mathrm{Im}\hat{F}_k] \in R^{2n}$ consisting of the real and imaginary parts of the FFT data in the ith selected frequency band at frequency f_k; Let $D = \{\hat{\mathbf{Z}}_k\}$ which includes all the FFT data in the selected frequency band. For large *N* and small Δt, the vector $\hat{\mathbf{Z}}_k$ is shown to be independent at different frequencies and follow a Gaussian distribution with zero means and covariance matrix $\mathbf{C}_{ik}$ (Yuen & Katafygiotis, 2003). Therefore, the likelihood function $p(D|\boldsymbol{\theta})$ in the ith frequency band can be constructed by a Gaussian distribution, i.e.,

$$p(D|\boldsymbol{\theta}) = \prod_k \frac{1}{(2\pi)^n \det(\mathbf{C}_k)^{0.5}} \exp[-\frac{1}{2}\hat{\mathbf{Z}}_k^T \mathbf{C}_k^{-1} \hat{\mathbf{Z}}_k] \quad (5)$$

in which, $\det(\cdot)$ denotes the determinant; $\mathbf{C}_k$, the covariance matrix of $\hat{\mathbf{Z}}_k$, is given by

$$\mathbf{C}_k = \frac{1}{2}\begin{bmatrix} \boldsymbol{\Phi} & \\ & \boldsymbol{\Phi} \end{bmatrix} \begin{bmatrix} \mathrm{Re}\mathbf{H}_k & -\mathrm{Im}\mathbf{H}_k \\ \mathrm{Im}\mathbf{H}_k & \mathrm{Re}\mathbf{H}_k \end{bmatrix} \begin{bmatrix} \boldsymbol{\Phi}^T & \\ & \boldsymbol{\Phi}^T \end{bmatrix} + \frac{S_e}{2}\mathbf{I}_{2n} \quad (6)$$

where $\boldsymbol{\Phi} = [\boldsymbol{\Phi}_1, \boldsymbol{\Phi}_2, \ldots, \boldsymbol{\Phi}_m] \in R^{n \times m}$ denotes the mode shape matrix in a selected frequency band; $\mathbf{I}_{2n}$ is an $2n \times 2n$ identify matrix; $S_e \in R$ is the PSD of prediction error in the frequency band; $\mathbf{H}_k$ is a transfer function, whose element can be expressed as:

$$\mathbf{H}_k(i,j) = S_{ij}[(1-\beta_{ik}^2) + i(2\zeta_i\beta_{ik})]^{-1}[(1-\beta_{jk}^2) - i(2\zeta_j\beta_{jk})]^{-1} \quad (7)$$

where $\beta_{ik} = f_i/f_k$; S_{ij} denotes the cross spectral density between the ith and jth modal excitation; $f_i \in R$ denotes the ith natural frequency in the frequency band; $\zeta_i \in R$ denotes the ith damping ratio in the frequency band. It is more convenient to write the likelihood function in terms of the log-likelihood function for the purpose of optimization, i.e.,

$$L(\boldsymbol{\theta}) = -ln\ p(D|\boldsymbol{\theta}) \quad (8)$$

The MPVs of modal parameters can be determined by minimizing the log-likelihood function $L(\boldsymbol{\theta})$. If directly performing the optimization, there will be some computational problem. To solve these problems, a fast algorithm has been developed (Au, 2012a, 2012b) so as to calculate the MPVs of modal parameters and the associated posterior uncertainties efficiently.

3.2 Bayesian model updating and MCMC

The stability of bridge pier due to scouring can be treated as changes in soil condition that reduces structural performance. If the updated model can fit actual structural conditions, then changes in the model parameters can indicate the severity of scouring.

Bayesian model updating is a popular model updating approach that considers uncertainties of model parameters attributable to measurement noise or modeling error (Beck & Katafygiotis, 1998; Katafygiotis & Beck, 1998). Uncertain parameters are assumed to follow a certain distribution based on experimentally obtained data. In other words, the Bayesian model updating process is fundamentally an optimization problem for which the criterion is the posterior distribution based on the level of the difference between the simulation and experiment. For Bayesian model updating, sampling procedures are invariably necessary because obtaining analytical solutions to describe a PDF of uncertain parameters is difficult. Among many sampling algorithms, the MCMC sampling algorithm (Tierney, 1994; Mosegaard, 1995) has received the most attention, especially for the MH

algorithm (Metropolis et al., 1953; Hastings, 1970). When the bridge scour is considered, only a change in a rotational soil spring stiffness is generally critical because rocking mode of the target pier is most sensitive to scouring (Abe et al.,2016). Since only a rotational soil spring stiffness is considered as an uncertain parameter, not much attention needs to be paid to sampling frequency. Therefore, this study uses MH algorithm for model updating.

In Bayesian model updating, the formulation of the posterior PDF of the uncertain parameter θ under given system response D is expressed as:

$$P(\theta|D,M) = \frac{P(D|\theta,M)P(\theta|M)}{P(D|M)} \tag{9}$$

Where M is the assumed probabilistic model for the structure, $P(D|M)$ denotes evidence of model M, and $P(D|M)$ is a normalized constant. Also, $P(\theta|M)$ is the prior PDF. For convenience, it is usually assumed as a uniform distribution. finally, $P(D|\theta,M)$ is the likelihood function, which denotes the conditional probability of D given θ. Since $P(\theta|M)/P(D|M)$ is normalizing constant, the posterior PDF, $P(\theta|D,M)$, is proportional to the likelihood function $P(D|\theta,M)$, eq. (9) is rewritten as:

$$P(\theta|D,M) \propto P(D|\theta,M) \tag{10}$$

As discussed before, the complexity of posterior PDF makes it difficult to calculate the probability and describe the probability distribution directly. Consequently, Monte Carlo Simulation is used to approximate and estimate the posterior distribution by the generated samples. This study briefly explains MH algorithm that is a commonly used as MCMC solutions in the Bayesian model updating sampling problems. Presuming that the PDF of the target distribution is $P(\theta)$, θ_k is the *k*th sample, and θ^*_{k+1} is the candidate sample generated from $q(\theta^*_{k+1}|\theta_k)$, which is the PDF of proposed distribution with given θ_k. The θ^*_{k+1} is then accepted with probability α_k given by follow:

$$\alpha_k = \alpha(\theta_k, \theta^*_{k+1}) = \min\{1, \frac{p(\theta^*_{k+1})q(\theta^*_{k+1}|\theta_k)}{p(\theta_k)q(\theta_k|\theta^*_{k+1})}\} \tag{11}$$

Therein, α_k is a constant to ensure that the stationary distribution of the Markov chain is the target distribution. if the candidate sample θ^*_{k+1} is accepted, then it would be set as the next sample of Markov chain, $\theta_k = \theta^*_{k+1}$; otherwise, the present sample is to be the next one: $\theta_{k+1} = \theta_k$. Then, this process can be repeated to generate the Markov chain samples $\theta_0, \theta_1, \ldots, \theta_n$. The symmetric random-walk Metropolis (RWM) algorithm is an important special case of the MH method in which the Markov chain will jump with a symmetric proposed distribution, as $q(\theta_{k+1}|\theta^*_k) = q(\theta_k|\theta^*_{k+1})$. It is taken to be the

sampling algorithm in this study. Eq. (11), therefore, can be simplified as follow:

$$\alpha_k = \alpha(\theta_k, \theta^*_{k+1}) = \min\{1, \frac{p(\theta^*_{k+1})}{p(\theta_k)}\} \quad (12)$$

3.3 Scour depth estimation

For the purpose of scour depth estimation, this chapter considers the relationship between scour progress and soil resistance. Usually, the types of footing of old railway bridges are spread footing which is high risk for rotation and collapsing due to scour. Since a large proportion of scour damage is spread footing type, this study considers such types of foundations. The analysis of the stability of bridge piers is considered 4 categories: sinking, sway motion, roll motion and destruction. Based on the findings of a survey of past disaster cases in Japan, this study only considers roll motion.

According to the Japanese guideline for railway bridge design document (RTRI, 2012), the modeling of soil resistance for bridge pier with spread footing type can be expressed as four soil springs as shown in **Figure 1**. Here, $\boldsymbol{k_v}$, $\boldsymbol{k_s}$, $\boldsymbol{k_h}$, and $\boldsymbol{k_r}$ represent vertical, shear, horizontal and rotational soil springs, respectively. The equation of estimating each value is explained below. In order to facilitate the discussion, the progress of scouring is distinguished from 2 stages as shown in **Figure 2**. Stage 1 and 2 are defined when scour depth is still above of the bottom of the footing and it erodes under the bottom of the footing, respectively.

- $\boldsymbol{k_v}$: vertical soil spring

  Vertical soil spring stiffness can be expressed as:

$$k_v = \rho A_v^{\frac{3}{4}} \quad (13)$$

Where ρ is the modified coefficient that is determined by soil properties and the soil penetration test, A_v denotes area at the bottom of the footing. Since k_v is a function of the area of the bottom of the footing, k_v does not change during stage 1, while it rapidly declines at stage 2. The diagram that denotes the relationship between scour depth d and k_v is shown in **Figure 3a)**.

- $\boldsymbol{k_s}$: shear soil spring

  Shear soil spring stiffness can be expressed as:

$$k_s = \lambda k_v \quad (14)$$

Where λ is conversion factor that has obtained around one third by theoretical and

experimental investigation in the past. As well as k_v, k_s does not change during stage 1, while it rapidly declines at stage 2. The diagram that denotes the relationship between scour depth d and k_s is shown in **Figure 3b)**.

- $\boldsymbol{k_h}$: horizontal soil spring

  Horizontal soil spring stiffness can be expressed as:

$$k_h = \rho A_h^{-\frac{5}{8}} \tag{15}$$

Where ρ is the modified coefficient that is determined by soil properties and the soil penetration test, A_h denotes area at the front of the footing. Since lateral movement is resisted by backfill soil above the bottom of the footing, k_h decreases at stage 1 and it reaches 0 when the backfill soil is fully eroded. The diagram that denotes the relationship between scour depth d and k_h is shown in **Figure 3c)**.

- $\boldsymbol{k_r}$: rotational soil spring

  Rotational soil spring stiffness can be expressed as:

$$k_r = k_v I_v = \frac{k_v L B^3}{12} \tag{16}$$

Where I_v is a moment of inertia of the bottom of the footing, L and B denote side and front length of the footing, respectively. As well as k_v, k_r does not change during stage 1, while it rapidly declines at stage 2. The diagram that denotes the relationship between scour depth d and k_r is shown in **Figure 3d)**.

Since the identified frequency can be obtained by remote vibration monitoring of the bridge pier, eigenvalue analysis using a numerical model with varying soil spring stiffness according to the depth of the scour is conducted to identify the natural frequency of the bridge pier. Finally, the diagram that denotes the scour depth and frequency of the pier can be estimated as shown in **Figure 4**. At stage 1 shown in **Figure 4**, the decreased trend of natural frequency occurs due to k_h, while the rapid changes in natural frequency emerges at Stage 2 due to k_v, k_s, and k_r.

Also, it should be noted that the identified frequency in real space varies due to environment of variance and signal noises, which is the reason why sampling method is introduced to assess the variables of soil springs.

3.4 Selection of a target bridge

The critical role of bridges in contributing to urban resilience is currently recognized worldwide, and exemplified through relevant research initiatives such as Climate Resilient

Infrastructure (World Bank), Climate Resilient Cities and Infrastructures (RESIN, European consortium). However, the implications of bridge failures and the disruptive impact from a functional point of views (e.g., rerouting, business interruption, evacuation routes) are not being addressed. Therefore, it is very important to apply the proposed monitoring and physical modelling scheme on real bridges. Most bridges built before 1950 or bridges in developing countries have been constructed using spread foundations.

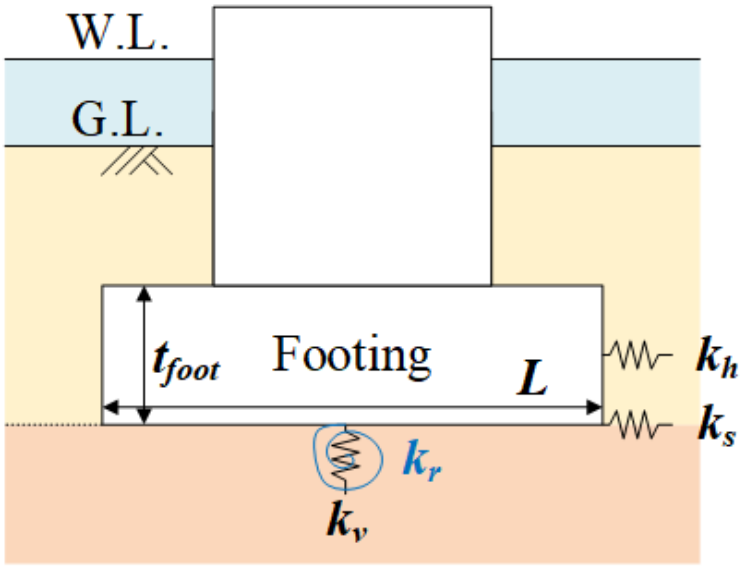

Figure 1 Four soil springs to illustrate the soil resistance based on Japanese design document.

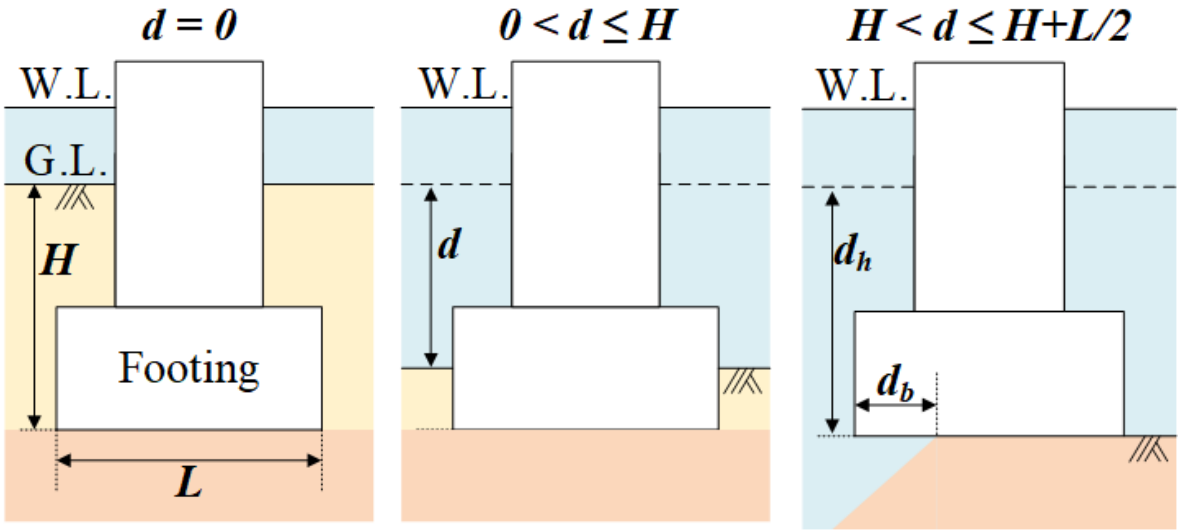

a) Initial condition (no scouring).

b) Stage 1: Scour depth above the bottom of footing.

c) Stage 2: Scour erodes under footing.

Figure 2 Scour process flow.

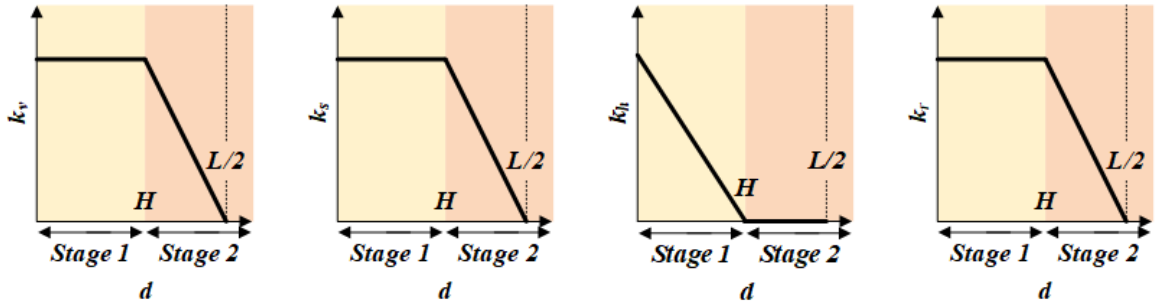

a) Vertical soil spring stiffness b) Shear soil spring stiffness c) Horizontal soil spring stiffness d) Rotational soil spring stiffness

Figure 3 Diagrams for scour depth progress with each soil spring stiffness.

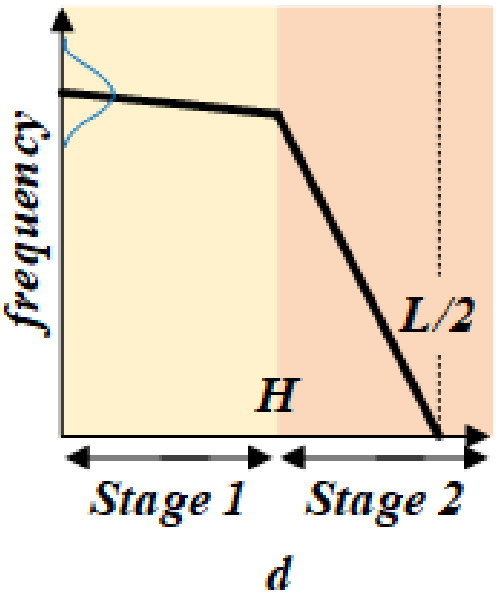

Figure 4 Diagrams for scour depth progress with natural frequency of the pier.

To select a target bridge as a case study, a high scour risked bridge should be done. According to the summarized report from Ministry of Land, Infrastructure, and Transport in Japan, bridge piers with spread foundation are the most vulnerable to the risk of scour. Most bridges built before 1950 or bridges in developing countries have been constructed using spread foundations. Although there are cases where the soundness of bridge piers with piled foundation and caisson foundation have been affected by scour mainly due to ground sinking, target bridge piers with spread foundation should be selected at first. Furthermore, riverbed protection from being scoured by the rapid flow of water using blocks can reduce the likelihood of scour effects. Therefore, bridges without riverbed protection should be selected.

This research mainly focuses on railway bridges which their impact of temporary closure due to scour effects is higher due to constrains in re-routing trains.

3.5 Methodology for estimating scour depth in real time

This chapter briefly explains the methodology for estimating the real-time estimation of scour depth. Figure 5 illustrates the flowchart of this study to assess the scour depth in real-time. Firstly, FEM is being built following design document. Since high risk bridges are relatively old where they might be lack of design information, capturing geometrical shape using laser scanner is also available. Since there is variance of identified frequency in site, the rotational soil spring stiffness with uncertainty is identified utilizing MCMC method to fit the variance of observed frequency. Then the relationship between soil spring stiffness and scour depth are deployed to the updated DEM and eigenvalue analysis to obtain the diagram between scour depth and frequency is conducted. Finally, the probability that scour depth given observed frequency f_t can be estimated.

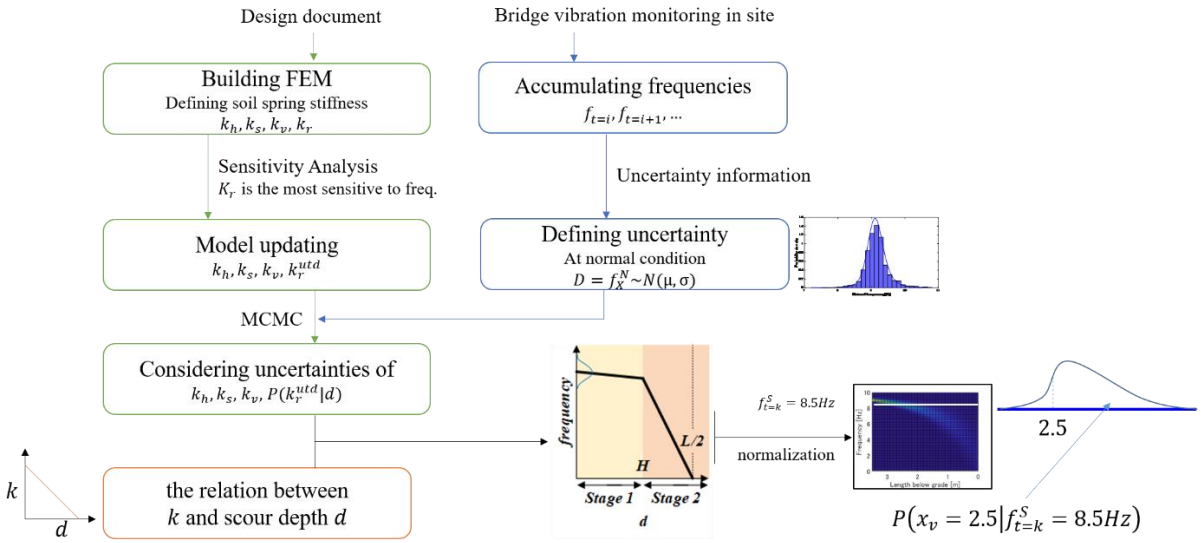

Figure 5 Flowchart of the numerical model and vibration monitoring campaign to quantify scour depth in real-time.

4.Results and Discussion: case study

4.1 Background

The monitoring bridge is a steel plate girder railway bridge with a span length of 22.5 m and an overall width of 9 m, designed for single railway track. The overview of the target pier is shown in **Figure 6**. The material of the target pier whose height and width are 9 m and 3 m respectively is concrete. The depth in river water in **Figure 6** is around 0.5m from the bottom of the ground, which is the standard water height at the normal period. The Railway company has categorized three train operation control based on the water level considering the scouring risks and the damages derived from debris; 2.5m (operation

suspended), 3.0m (slow passing), and 3.5m (caution). It should be noted that water level represents the distance between water surface and lower flange of the bridge girder: i.e. as the water surface goes up, the water level gets smaller.

According to the impact test conducted in 2006, natural frequency of transverse axis is identified in 9.1Hz, which is called target frequency from now on. Also, local scour did not progress according to the measured inspection during dry season.

Figure 6 Target bridge pier.

4.2 Field vibration

4.2.1 Monitoring-based campaign to detect scour

The tri-axial accelerometers are installed on top of the bridge pier for long-term monitoring to assess the stability of the pier. Sensors are MEMS-type accelerometers with a capacity of about 14.71 m/s^2, an optical resolution of $2 \times 10^{-4} m/s^2$ in the bridge axis and perpendicular direction, and an optical resolution of $7 \times 10^{-4} m/s^2$ in the vertical direction. The sampling frequency is 200 Hz. It can transmit and receive data wirelessly whose whole scheme is shown in **Figure 7**.

This research considers five years long-term monitoring information from 2017 in September to 2021 in June. Measurement were taken over a 24-hour period, and the vibration characteristics are identified using a minute measurement data. This study uses 25 days from 12th in June to 6th in July in 2021 including swollen river water period for applying the proposed method because the scour had not progressed during monitoring period according to the measured inspection.

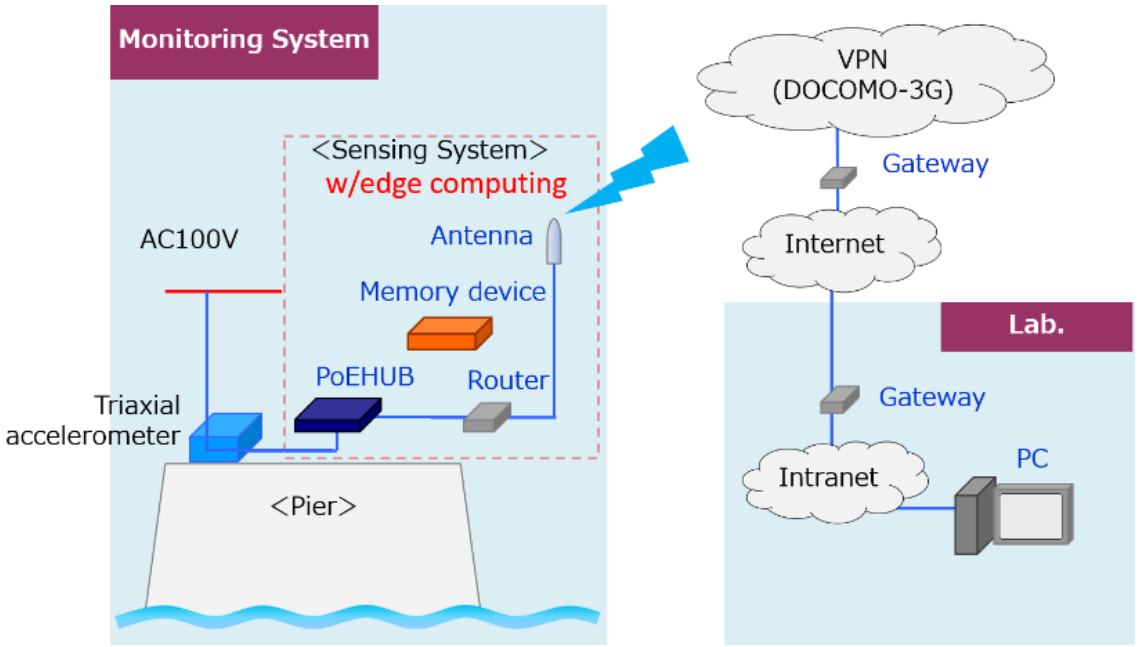

Figure 7 Remote sensing system.

4.2.2 Data collection and characteristics from the long-term monitoring of the bridge

Time series of identified target frequency by use of fast Bayesian FFT is shown in **Figure 8**. Each dot represents the identified frequency at every minute, and error bars do coefficient of variance that divides standard deviation of posterior distribution into most probable value. Although identified frequencies scattered in several days, many of them are converged around target frequency (9.1Hz). When identified frequencies less than 8Hz are focused, it has a tendency that the error bars are relatively large. In order to reduce the variance of identified frequency, identified frequencies with large coefficient of variance are to be ignored. This study applies the threshold, $\mathrm{c.o.v.} = 0.02$ that is equal to mean value plus 2 standard deviation of parameter to the identified frequencies and the results are shown in **Figure 9**. It is clearable that variances are well improved so that identified frequencies less than 8Hz are well deleted.

However, there is ineligible variances in **Figure 9**, statistical modeling is considered. **Figure 10** represents histogram of identified target frequencies of **Figure 9**. Frequency varies from 8 to 12Hz. Probability density function (PDF) at normal distribution is also shown in **Figure 10** as blue breaking line. The PDF is expressed as:

$$freq \sim \mathcal{N}(9.47, 0.56) \tag{17}$$

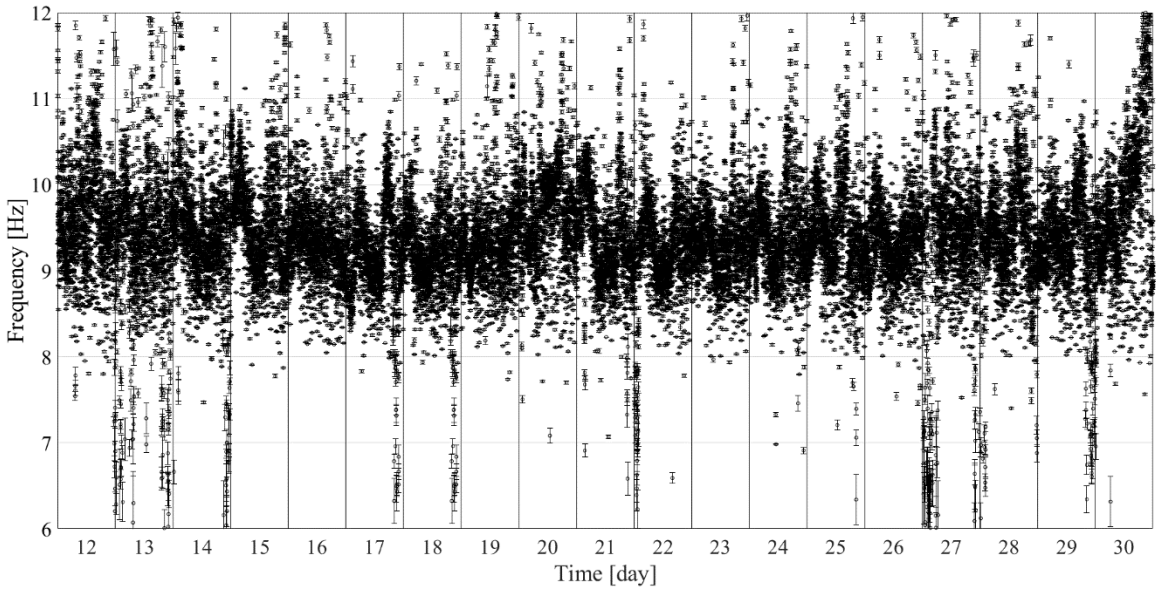

Figure 8 Time-series of identified target frequencies.

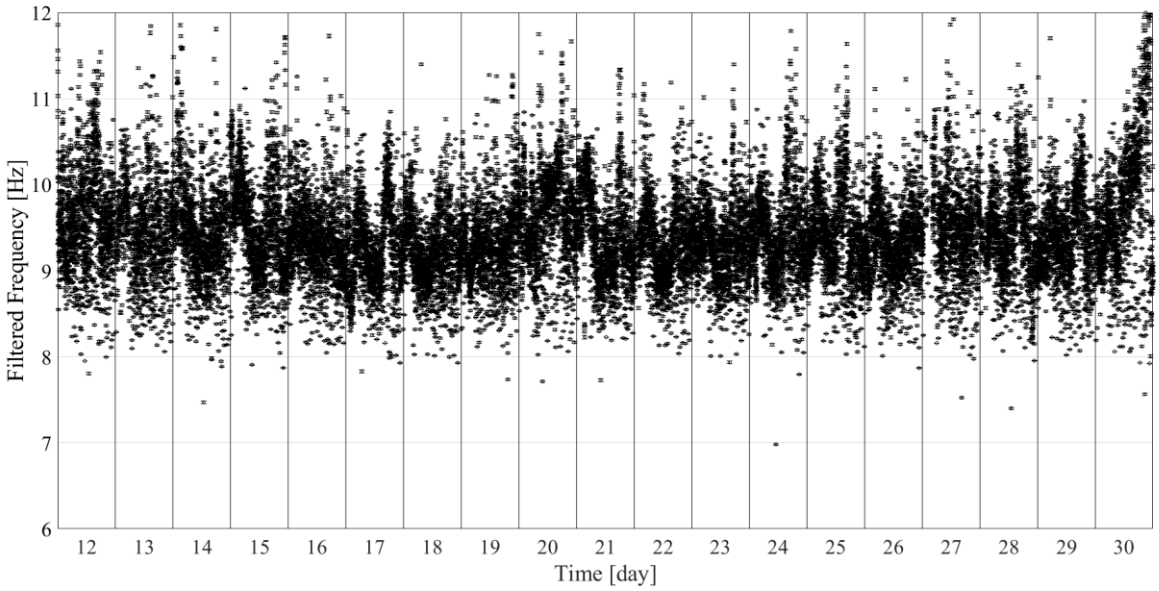

Figure 9 Revised Figure 8 by deleting those with large coefficient of variance.

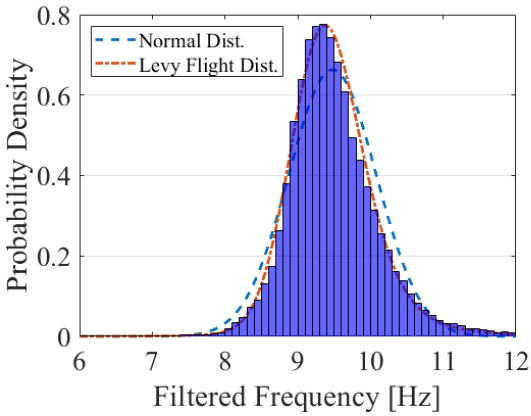

Figure 10 Statistical modeling of filtered frequencies.

4.3 Development of the numerical model for the bridge pier

This chapter presents a numerical method to identify the change of scour depth utilizing the identified frequency of the target pier through scour monitoring. The ABAQUS finite element analysis software suite was used for this study. In the FE model, the target pier is modeled with three-dimensional beam elements. Material properties are assigned to the model based on the given design code of materials. The superstructure is simplified as a point mass and attached to the pier top. The footing is modeled as a rigid body.

4.3.1 Soil spring stiffness

Adding springs are common modeling and analyzing method of the soil-structure interaction. In most cases, the foundation soil has a finite stiffness and springs can be applied in appropriate positions of the structure in order to present the finite stiffness of foundation soil. Vertical, shear, horizontal, and rotational springs are added on points of the model written as k_v, k_s, k_h, and k_r. Location in the soil springs and the information on the size of structures are illustrated in **Figure 11** and **Table 1**, respectively. k_v and k_r are set at the center of the bottom of the footing, while k_h whose height is the same as gravity point of footing and k_s are done at the side of the footing. Finally, each value was calculated and shown in **Table 2**, based on the Japanese design document and standard penetration test implemented in 2015 as written in chapter 2. 3.

The rocking mode and the relevant frequency obtained from the eigenvalue analysis are shown in **Figure 8**. Natural frequency is around 9.57Hz that is higher than the impact test results in 2009 and long-term monitoring results. Model updating is conducted for physics model to fit the observation results.

Table 1 Key size of structures

Soil spring		Value	Unit
Footing length	L	7.8	m
Footing width	B	4.5	m
Footing height	t_{foot}	2.0	m
Length below grade	H	3.5	m

Table 2 *Soil spring stiffness*

Soil spring		Value of Stiffness	Unit
Vertical	k_v	8.528×10^6	N/mm
Shear	k_s	2.842×10^6	N/mm
Horizontal	k_h	7.225×10^4	N/mm
Rotational	k_r	4.324×10^{14}	Nmm

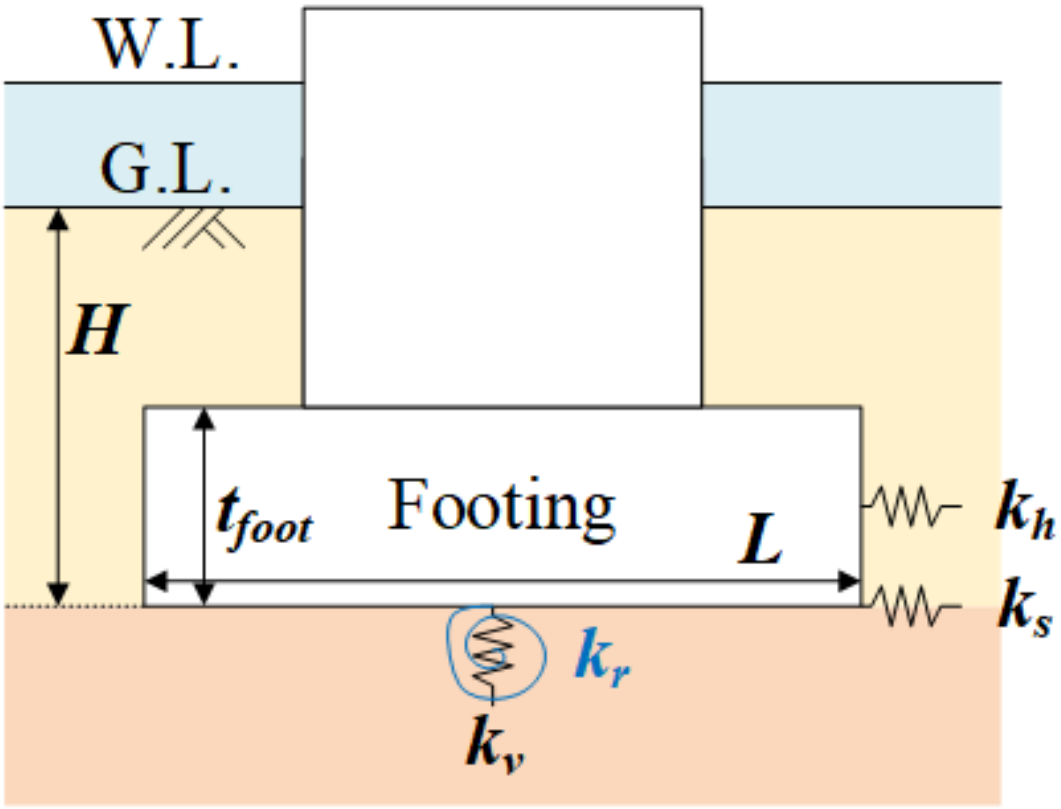

Figure 11 Location in the soil springs.

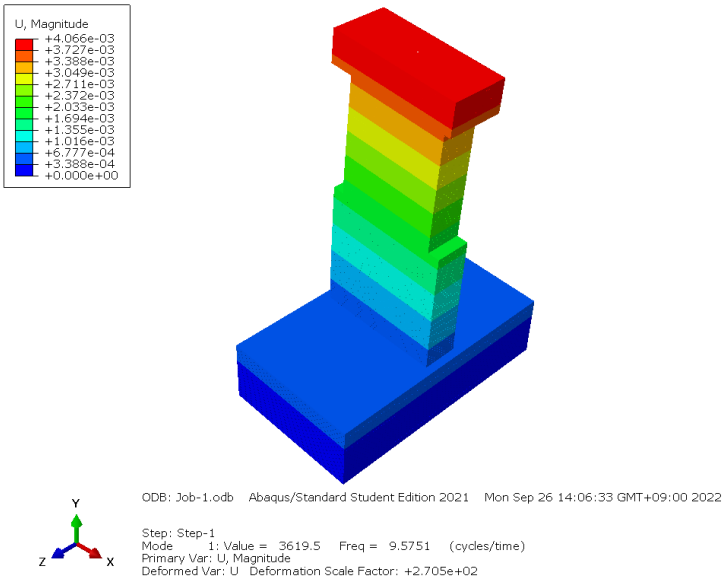

Figure 12 Eigenvalue analysis result.

4.3.2 Sensitivity analysis

Time series Sensitivity analysis is used to determine how independent variable values will affect a particular dependent variable under a given set of assumptions. In other words, sensitivity analyses studies how various sources of uncertainty in a numerical model

contribute to the overall uncertainty of the model. One soil spring stiffness is changed assuming all of the other springs remain constant, then conduct eigenvalue analysis and the change in identified natural frequency is observed. The sensitivity analysis results are shown in **Figure 13**. In conclusion, in comparison to the sensitivity of the rotational spring, sensitivities for the other springs can almost be neglected. Consequently, only the rotational spring stiffness is updated initially, and the result is shown in **Table 3**.

Table 3 Updated soil spring stiffness

Soil spring		Value of Stiffness	Unit
Vertical	k_v	8.528×10^6	N/mm
Shear	k_s	2.842×10^6	N/mm
Horizontal	k_h	7.225×10^4	N/mm
Rotational	k_r^{upd}	5.600×10^{13}	Nmm

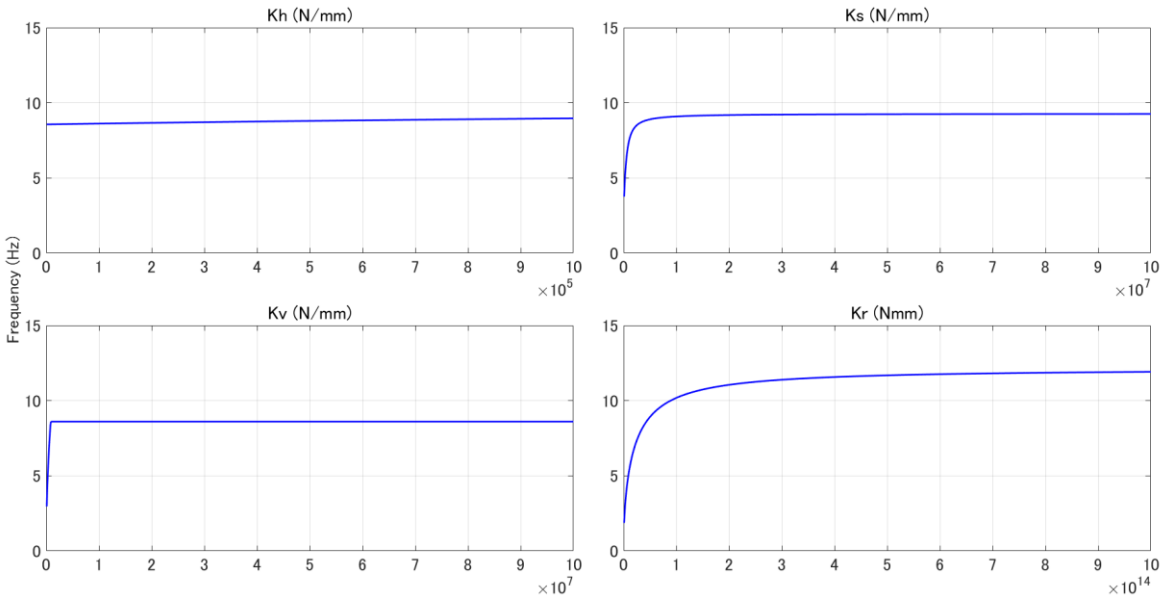

Figure 13 Sensitivity analysis result.

4.3.3 Model updating for real-time scour identification

Since identified frequencies obtained in real space have uncertainty due to signal noise etc., this chapter models it by use of sampling method as introduced in chapter 2.2. Rotational soil spring stiffness were considered in model updating. The samples generated at the last sampling step could form a posterior distribution of model parameters. The posterior distribution of frequency after the last sampling step is expressed as:

$$freq \sim \mathcal{N}(9.50, 0.24) \tag{18}$$

Figure 14 portrays the marginal distribution of updated rotational spring. Red line

represents PDF of normal distribution. Consequently, the updated spring stiffness with uncertainty are summarized in Table 4.

Table 4 *Updated soil spring stiffness with uncertainty.*

Soil spring		Value of Stiffness	Unit
Vertical	k_v	8.528×10^6	N/mm
Shear	k_s	2.842×10^6	N/mm
Horizontal	k_h	7.225×10^4	N/mm
Rotational	k_r^{upd}	$\mathcal{N}(6.72 \times 10^{13}, 7.21 \times 10^{12})$	Nmm

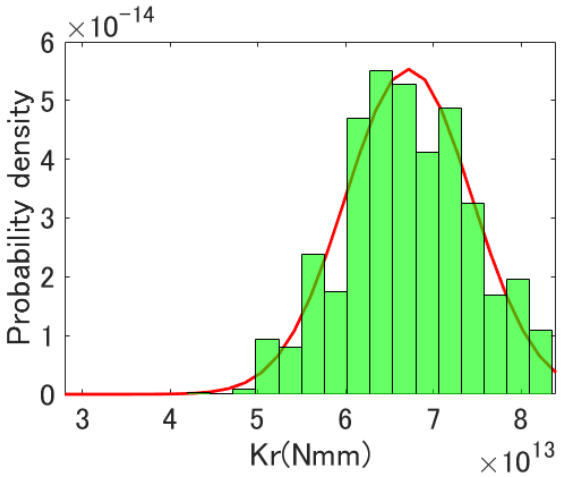

Figure 14 Marginal distribution of rotational spring stiffness.

4.4 Relationship between scour depth and spring stiffness

Based on the updated values of soil stiffness in Table 4, eigenvalue analysis was carried out with gradually decreasing stiffness followed as the relationship between soil spring stiffness discussed in chapter 2.3. The result performed normalization is shown in **Figure 15** whose horizontal axis represents scour depth. 3.5m indicates that the scour depth reaches the bottom of the footing since the ground layer length from the bottom of footing is 3.5m. **Figure 15** expresses the relationship between scour depth and identified frequency. The peaks of identified frequency are gradually decreased until 3.5m of scour depth due to decreased horizontal spring stiffness, while they are rapidly decreased since the effects of other springs.

Using the diagram in Figure 15, probability of scour depth can be estimated. For example, assuming that the identified frequency in real space f_t is obtained, the probability of scour depth $d = 3.5$ can be expressed as $\mathrm{P}(d = 3.5|f_t)$ which corresponds to the cumulative density function at $f = f_t$.

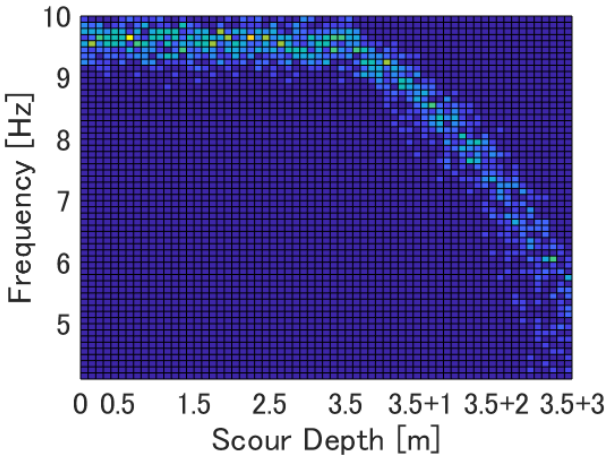

Figure 15 Relationship between scour depth and identified frequency with uncertainty.

4.4 Results and discussion

This study investigated the ambient vibration monitored from 1st of July 2019 to 4th of July 2019 to identify dominant frequency of the monitoring pier when there was intensive rainfall around the region. In particular, water level raised during 3rd of July, which is called swollen river water period (SRW period). Figure 16(a) shows the time-series of identified target frequency by means of fast Bayesian FFT method with time-series of water level written as blue line. Each dot and red line represent the identified frequency at every minute and 2 hours moving average line. There is the tendency that the identified frequencies were converged during SRW period. This is because the river water force makes the bridge pier excite, whereby the signal to noise ratio would improve. Therefore, the accuracy of identified modal parameters was improved due to the large signal to noise derived from exciting vibration.

Figure 16(b) shows the probability that scour depth reaches bottom of the footing of the target bridge pier expressed as $\mathrm{P}(d = 3.5|f_t)$. As well as time-series of identified frequency, 2 hours moving average line is added as red line. Focusing on the dots during low water level period, the probability converged to near zero although the plots scatted. On the contrary, probability plots shifted a little higher during SRW period. There is a possibility that the trend of decreasing identified frequency would be expressed as the probability of scour depth during SRW period.

Focusing on the red line through the 4 days monitoring, however, significant change in estimated probability cannot be found although the probability was recorded the highest just after the peak of water level. Furthermore, the value of probability is quite high. This derives from the coaster resolution of the set frequency in **Figure 15** as empirical cumulative distribution. Fitting two dimensional probability density curve might

improve the accuracy of estimated probability.

5. Enablers and Barriers

The critical role of bridges in contributing to urban resilience is currently recognized worldwide and exemplified through relevant research initiatives such as Climate Resilient Infrastructure (World Bank), Climate Resilient Cities and Infrastructures (RESIN, European consortium). This research mainly focuses on railway bridges which their impact of temporary closure due to scour effects is higher due to constrains in re-routing trains. To realize the proposed solution, it is important to use high accuracy and reliability sensors for modal identification, otherwise anomaly detection might be disturbed due to enhanced noise effects. This research will utilize tri-axial microtremors which have already confirmed the performance of modal identification and noise density. For this reason, the performance of each sensor will not be evaluated herein.

As discussed in chapter 3.4, spread foundation which are the most vulnerable to the risk of scour. Therefore, piers with spread foundation should be prioritized. Also, riverbed protection from being scoured by the rapid flow of water using blocks can reduce the likelihood of scour effects at bridge piers. In this research, bridges where riverbed protection has been included will not be considered. Moreover, extreme flood events in which the water level exceeds the top of the bridge pier cannot work in this system because sensors would be submerged in water and deformations obtained will not be representative. Finally, this research will focus on railway bridges only since these are the most vulnerable during flooding and could result to higher economic losses and passenger disruptions.

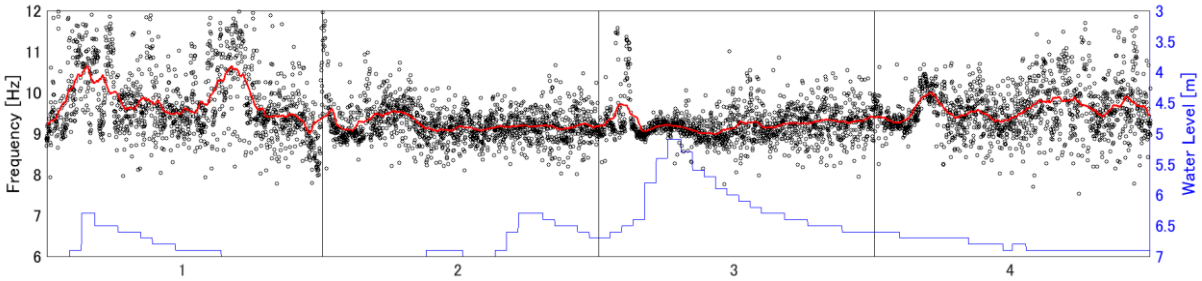

a) Time-series of identified target frequency by means of fast Bayesian FFT method.

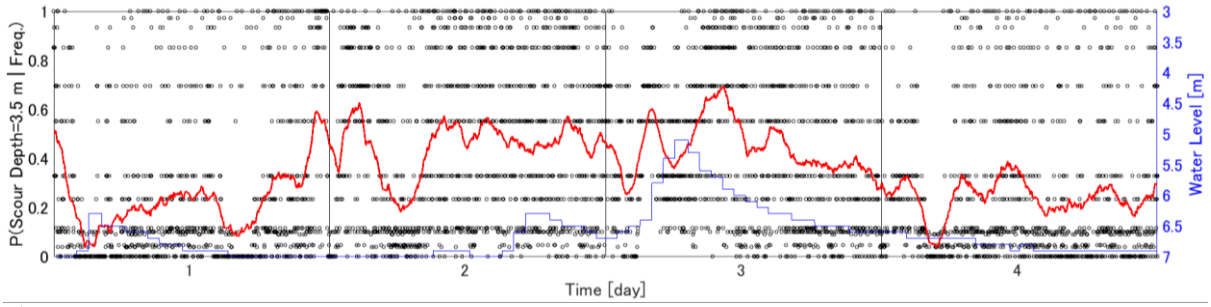

b) Time-series of probability that scour depth reaches bottom of the footing of the target pier ($\mathrm{P}(d = 3.5|identified\ frequency)$).

Figure 16 Applied proposed estimation of probability of scour depth method to the Swollen River Water period.

6. Key Takeaways from CDRI Fellowship Programme

The key technologies of this study are listed below.

1. High performance sensing system: Since the dynamic amplitude of the bridge pier consisted of high rigidity materials such as concrete and bricks is slight, high performance sensors and system identification method to obtain the modal parameters are required. This study explains the concept of frequency domain system identification method called fast Bayesian FFT method for the purpose of detection scouring of the bridge pier.
2. Sampling method: For the purpose of identifying soil spring stiffness of the bridge pier, MCMC simulation that is the widely used sampling method is introduced in this study. Since only rotational spring of the target bridge pier is sensitive to the natural frequency at transverse direction according to the sensitivity analysis, this study utilizes MCMC for assessing the uncertainty of rotational spring stiffness to lead to the uncertainty of identified frequency in real space.
3. Footing resistance effect: To deal with the spread footing type of bridge pier, resistance of footing against rotational movement cannot be avoided. This study explains the relationship between scour depth and values of each soil spring stiffness. Consequently, utilizing eigenvalue analysis of Finite Element Model, this study estimates the diagram expressing relationship between identified frequency and scour depth.
4. This study applies the proposed real-time scour depth estimation method to the real-time monitoring data. Although the accuracy of estimation still needs to investigate and improve, the output is much easier to utilize for decision-making

whether the traffic operation should stop or whether it should resume than providing information on natural frequency of bridge pier in real-time. Therefore, this method supports to install the monitoring system to bridges where the traffic is huge and economical effects is intensive.

7. Conclusion

This study investigates a way of real time scour depth estimation by means of ambient vibration monitoring of the bridge pier and eigenvalue analysis of Finite Element Model (FEM) during swollen river water (SRW) period. As a case study, a remote monitoring system including installment of accelerometers to the top of the railway bridge pier under operation and identification of the frequency in real time was conducted for real time scour assessment during SRW period. Fast Bayesian FFT method that is high accurate system identification method was used to estimate the frequency of the pier. According to the long-term monitoring results in investigating modal parameters of the target pier, the rocking mode of the pier toward bridge transverse direction was identified around 9.5Hz, whereas there were significant variances. Therefore, filtering process using coefficient of variance of identified posterior distribution was added to reduce the variance of long-term monitoring. Since there are still non-negligible variance due to weak dynamic responses of the target bridge pier, probability density function of normal distribution is modeled to illustrate the uncertainty of identified frequency in real space.

In order to estimate the relationship between scour depth and identified frequency of the pier, this study built the FE model and conducted model updating. To deal with the scouring around the pier, four soil spring stiffness is set to express the interaction with the soil. The sensitivity analysis results show that the rotational soil spring affects the natural frequency of the pier, while other springs had less influence. Therefore, only rotational soil spring was updated. Furthermore, this study conduct MCMC sampling method to model the uncertainty of rotational soil spring leading to that of identified frequency in real space. Based on the information with uncertainty of rotational soil spring stiffness, a diagram illustrating the relationship between scour depth and identified frequency was built.

This study showed one case of time-series probability that scour depth reaches bottom of the footing of the pier using time-series of identified frequency during SRW period. The tendency that probability is increased with decreasing identified frequency during SRW period was observed. However, estimated probabilities plotted specific values because of the coaster resolution of the set frequency as empirical cumulative

distribution. Fitting two dimensional probability density curves might improve the accuracy of estimated probability.

8. Way Forward

Proposed scour assessment system that has high performance but is expensive might not be acceptable as practical application in some areas. The way that can assess the safety of bridge easily and inexpensively by using the smartphone as the device although the accuracy and real time detection would be reduced can be thus proposed. The scalability is high because the proposed solution for new areas has the same anomaly detection scheme, while the replicability would not be enough unless sensitivity of sensors built-in smartphone that could identify the vibration characteristics of bridge pier were investigated. However, these schemes will be expected to benefit developing countries.

References

1. ASCE's 2021 Infrastructure Report Card. (2021, May 31). https://infrastructurereportcard.org/wp-content/uploads/2020/12/Bridges-2021.pdf
2. Abe, K., Natori, T., Kominato, Y., Sekiguchi, T., Yamano, A., Wang, L. (2016). Monitoring method of soundness of railway bridge by using soundness diagnosis indices correlated with natural frequency. *Journal of Japan Society of Civil Engineers Ser. A1(Structural Engineering & Earthquake Engineering)*. 72(1), 21-30.
3. Au, S.-K. (2012a). Fast Bayesian ambient modal identification in the frequency domain, Part I: Posterior most probable value. *Mechanical Systems and Signal Processing*, *26*, 60-75.
4. Au, S.-K. (2012b). Fast Bayesian ambient modal identification in the frequency domain, Part II: Posterior uncertainty. *Mechanical Systems and Signal Processing*, *26*, 76-90.
5. Au, S.-K., Zhang, F.-L., & Ni, Y.-C. (2013). Bayesian operational modal analysis: theory, computation, practice. *Computers & Structures*, *126*, 3-14.
6. Bao, T., & Liu, Z. (2017). Vibration-based bridge scour detection: a review. *Structural Control and Health Monitoring*, *24*(7), e1937.
7. Beck, J. L., & Katafygiotis, L. S. (1998). Updating models and their uncertainties. I: Bayesian statistical framework. *Journal of Engineering Mechanics*, *124*(4), 455-461.
8. De Falco, F., & Mele, R. (2002). The monitoring of bridges for scour by sonar and sedimetri. *NDT & E International*, *35*(2), 117-123.
9. Fisher, M., Chowdhury, M. N., Khan, A. A., & Atamturktur, S. (2013). An evaluation of scour measurement devices. *Flow Measurement and Instrumentation*, *33*, 55-67.

10. Hastings, W. K. (1970). Monte Carlo sampling methods using Markov chains and their applications.
11. Kim, C. W., Kawabe, D., Kitagawa, S., Shinoda, M., Nakamura, T., & Yao, H. (2017). Remote vibration monitoring for scour detection of a railway bridge. In SMAR2017.
12. Kim, C. W., Yoshitome, K., Goi, Y., Zhang, F. L., Kitagawa, S., Shinoda, M., & Hamada, Y. (2021). Scour Detection of Railway Bridges by Microtremor Monitoring. In *EASEC16* (pp. 97-107). Springer.
13. Lee, M., Yoo, M., Jung, H.-S., Kim, K. H., & Lee, I.-W. (2020). Study on dynamic behavior of bridge pier by impact load test considering scour. *Applied Sciences*, *10*(19), 6741.
14. Metropolis, N., Rosenbluth, A. W., Rosenbluth, M. N., Teller, A. H., & Teller, E. (1953). Equation of state calculations by fast computing machines. *The journal of chemical physics*, *21*(6), 1087-1092.
15. Mosegaard, K., & Tarantola, A. (1995). Monte Carlo sampling of solutions to inverse problems. *Journal of Geophysical Research: Solid Earth*, *100*(B7), 12431-12447.
16. Prendergast, L. J., & Gavin, K. (2014). A review of bridge scour monitoring techniques. *Journal of Rock Mechanics and Geotechnical Engineering*, *6*(2), 138-149.
17. Railway Technical Research Institute (2012). Design Standards for Railway Structures and Commentary (Bridge substructures): Maruzen shuppan.
18. Tierney, L. (1994). Markov chains for exploring posterior distributions. *the Annals of Statistics*, 1701-1728.
19. Yuen, K.-V., & Katafygiotis, L. S. (2003). Bayesian fast Fourier transform approach for modal updating using ambient data. *Advances in Structural Engineering*, *6*(2), 81-95.

Evaluation of Cyclonic Disaster Resilience of Coastal Healthcare Infrastructure in Bangladesh: A Special Comparison with Japan

Dr Gulsan Ara Parvin
Researcher, College of Policy Science,
Ritsumeikan University, Osaka Ibaraki Campus, Japan

Dr Md Anwarul Abedin
Professor
Laboratory of Environment and Sustainable Development
Department of Soil Science, Bangladesh Agricultural University, Bangladesh

Dr Nina Takashino
Associate Professor,
College of Policy Science,
Ritsumeikan University, Japan

Under CDRI Fellowship Programme 2022-23

Disclaimer: The views expressed in this paper reflect the opinions of the author and not necessarily the official views of CDRI.

Acronyms and Abbreviations

CyDRI	Cyclonic Disaster Resilience Index
UHC	Upazila Health Complex
WMI	Weighted Mean Index

Abstract

Efforts to understand cyclonic disaster resilience of critical infrastructure, especially healthcare infrastructure, are rare in Bangladesh and Japan – the two most cyclone-vulnerable countries in the world. This study evaluates the cyclonic disaster resilience of Bangladesh's coastal healthcare infrastructure through a special comparison with Japan. An intensive and systematic literature review was done to determine cyclonic disaster resilience evaluation's dimensions, parameters and indicators. Incorporating all these selected dimensions, parameters and indicators, a structured questionnaire was prepared, where a three-point Likert Scale (poor, moderate and good) was used to assess the level of resilience of the healthcare infrastructure. Cyclonic disaster resilience was evaluated using the Weighted Mean Index (WMI) method and the Cyclonic Disaster Resilience Index (CyDRI) was developed for five studied healthcare infrastructures. In Bangladesh, three Upazila Health Complexes (UHCs) in the coastal district of Satkhira and, in Japan, two coastal hospitals of Miyagi Prefecture were studied.

CyDRI scores denote that all five healthcare infrastructures have moderate (2 out of 3) levels of cyclonic disaster resilience. However, the resilience levels vary in dimensions and parameters. In the case of Bangladesh, occupational safety of all UHCs has a poor score (ranging from 1 to 1.67) in resilience evaluation, while this is in moderate condition in Japanese hospitals. Debhata UHC of Bangladesh has the highest CyDRI score in overall resilience (2.5) and structural resilience (2.7) among the five studied healthcare infrastructures. Conversely, this UHC has relatively low (1.9) resilience in the non-structural dimension. These outcomes reveal that cyclonic disaster resilience varies in structural and non-structural dimensions and even in different parameters. Therefore, this type of study is essential for precise resilience evaluation of healthcare infrastructure to allow effective budget allocation and action planning for disaster preparedness, risk reduction and, finally, building resilient critical infrastructure to serve during and after disaster.

Acknowledgements

Members of this research team would like to extend their deepest gratitude to the Coalition for Disaster Resilient Infrastructure (CDRI) for funding this important study. This team is thankful to all the CDRI staff members who were very sincere and cooperative in supporting this research in various ways. We are grateful to Dr Ranit Chatterjee and Dr Harold Aquino, the two highly efficient technical experts, who provided very useful and important guidance throughout the whole research period. The support of mentor Dr Tahsina Sharmin Hoque and Professor Dr Shofiqul Islam are highly appreciated. We are obligated to the Department of Soil Science, Bangladesh Agricultural University for supporting us as the endorsing institution. Ritsumeikan University, Osaka Ibaraki Campus is duly acknowledged for its support to conduct surveys in Japan. Support and cooperation of the authorities and staff of the five studied hospitals in Bangladesh and Japan is also highly appreciated.

Funding

This research was supported by the 2022–2023 Fellowship of the Coalition for Disaster Resilient Infrastructure (CDRI), Application ID: 210909454.

1. Introduction

Resilience is a widely used term in different disciplines, especially in climate change and disaster related research. Over a decade ago, while addressing climate change and society, Adger et al., 2011 defined the term 'resilience' as "the ability of a system to absorb change while retaining essential function; to have the ability for self-organization; and to have the capacity to adapt and learn". The United Nations Office for Disaster Risk Reduction (UNDRR, 2017) defined resilience as:

"The ability of a system, community or society exposed to hazards to resist, absorb, accommodate, adapt to, transform and recover from the effects of a hazard in a timely and efficient manner, including through the preservation and restoration of its essential basic structures and functions through risk management."

In the case of hospitals, Zhong et al., 2014 define resilience as "the ability of hospitals to resist, absorb and respond to the shock of disasters while maintaining and surging essential health services, and then to recover to their original state or adapt to a new one." Considering healthcare infrastructure, resilience refers to the ability of a healthcare system to withstand and recover from disasters while continuing to provide essential healthcare services to the population. It involves the capacity of healthcare facilities, personnel, supply chains and information systems to absorb, adapt and respond effectively to adverse events or challenges. Resilient healthcare infrastructure is essential to identify vulnerabilities, assess preparedness, improve response capabilities, allocate resources effectively, enhance coordination and communication, and promote continuous improvement to guide policy and decision-making (Olu, 2017). It helps to ensure that healthcare systems are well-prepared to withstand and recover from disruptions, ultimately safeguarding the health and well-being of the population. According to the World Health Organization's (WHO) guidance for climate-resilient and environmentally sustainable healthcare facilities (Prats, 2020), health systems and facilities include hospitals, clinics and community-care centres. Further, healthcare facilities provide health services to patients and vary in size from small healthcare clinics to very large hospitals.

Healthcare infrastructure resilience has assumed enormous importance after the Covid-19 pandemic. Covid -19 situation. For example, UN Secretary General has emphasized two critical issues of the present world, COVID-19 and climate change in UN general assembly on September 21, 2021. To combat with COVID-19 or such other health crises and climate change induced consequences to human health, healthcare infrastructures (HI) are the most crucial. Nonetheless, accessing necessary healthcare remains a challenge for the people of coastal Bangladesh that are highly vulnerable to climate change induced disasters (Mallik et al., 2017) and health impacts. The coastal belt of Bangladesh is experiencing several disasters and have very limited access to health care facilities. According to Kabir et al., (2014), among the total population in the coast Bangladesh, only about one third have access to the health facility. People of these areas suffer from a lack of appropriate health facilities and skilled healthcare providers (Huda et al., 2021). Bangladesh is a low-lying country with a long coastline, and it is highly vulnerable to various climate change impacts, including sea-level rise, cyclones, storm surges and flooding. With these poor healthcare facilities, lives and health status of coastal people is aggravating with the extreme weather events, especially cyclonic disasters (cyclone and storm surges) that are the most common in coastal areas and affecting almost every year (Gazi, 2019). Therefore, evaluating the resilience of healthcare infrastructure is crucial for coastal Bangladesh, considering its vulnerability to various natural hazards, particularly cyclones.

Similar to Bangladesh, Japan is highly prone to different kind of disasters such as typhoons, floods and earthquakes. From physical infrastructure to rapid recovery, Japan has made disaster-proofing into an exact science with its unique expertise and skills (Cabinet Office Japan, 2021). In Japan, healthcare facilities always receive the highest priority in disaster safety and resilience. Both the Hyogo Framework for Action 2005–2015 and Sendai Framework for Disaster Risk Reduction 2015–2030 prioritize disaster safety and resilience of hospitals and healthcare facilities. As a part of the 'Fundamental Plan for National Resilience, 2014' (Miyazawa & Kikuchi, 2021), Japan has proposed disaster-resilient healthcare and welfare functions. To the best of our knowledge, very limited

information is available regarding healthcare system resilience with a special focus on health infrastructure facilities and their resilience to disasters in Japan.

Healthcare infrastructure plays a crucial role in ensuring the resilience of the overall healthcare system. In the past, researchers highlighted the importance of healthcare system resilience as a whole (Biddle et al., 2020). While infrastructure is an essential component of a resilient healthcare system, it has received relatively less attention in certain discussions. Thus, very limited information is available for the healthcare infrastructure resilience in both Bangladesh and Japan. Comparing the healthcare infrastructure resilience in Bangladesh with Japan can provide valuable insights and learning opportunities for both countries. A comparative analysis of the healthcare infrastructure resilience in Bangladesh with Japan can help identify gaps, highlight successful strategies and facilitate knowledge exchange to strengthen healthcare systems in both countries. It is important to adapt the lessons learned to the specific context and resources available in each country while promoting cooperation for better disaster preparedness and response. Furthermore, Japan has a long history of providing development assistance to Bangladesh, and this comparison can further strengthen their partnership.

2. Aim, Objectives, and Scope of the Study

2.1 Aim of the study

Considering the vulnerabilities and risks of health care facilities of coastal Bangladesh, this study aims to evaluate cyclonic disaster resilience of coastal healthcare infrastructure in Bangladesh and Japan. Here a special focus is given to compare the level of resilience of both countries and to identify the factors that are playing role to determine the level of resilience.

2.2 Objectives of the study

In order to achieve the aim, specific objectives of this study are as follows.

- To develop a non-engineering, relatively easy methodological approach to evaluate cyclonic disaster resilience of healthcare infrastructure

- To evaluate the structural and non-structural cyclonic disaster resilience of coastal healthcare infrastructure of Bangladesh and Japan
- To identify the responsible factors contributing to structural and non-structural resilience of health care infrastructures
- To compare the overall resilience level of healthcare infrastructure between Bangladesh and Japan
- To propose policy recommendations to enhance cyclonic disaster resilience of healthcare infrastructures

2.3 Scope and limitations of the study

Scope of this study are listed as follows:

- Rather than considering different disasters this study addresses only cyclonic disaster (cyclone, typhoon, storm surge and flood caused by heavy rainfall during cyclone) resilience evaluation of healthcare infrastructures
- Rather than any other area, only coastal areas that are cyclone or typhoon vulnerable are within the scope of this study and healthcare infrastructures of coastal areas are the targeted infrastructures

2.3 Main limitations of this study are

2.3.1 Perception-based

Respondents of each specific studied healthcare infrastructure determined as a team, the resilience level on a 3-point rating scale based on their own evaluation and perception. As the teams are serving the healthcare infrastructures for several years and are well-versed in every aspect of healthcare infrastructures their evaluation of cyclonic disaster resilience level was considered to be accurate. Further, cross-cultural perception could not be calibrated. Respondents of Bangladesh and Japan have their own standard of evaluation, and they have used that to evaluate the resilience level of their respective healthcare infrastructure considering the general situation of their country. Due to the lack of baseline data, it was hard to carry out standardization. As an alternative, reliable quantitative

data was not possible to use here due to the unavailability of updated quantitative data for all the resilience indicators used in this study.

2.3.2 Equivalent weightage

Even though equivalent weightage was recognised as a limitation, it is challenging to establish the relative importance between different dimensions of resilience. During data collection, all dimensions, parameters and variables were given weight by using a three-point rating scale. This was an equal weightage approach. Ignoring the measures of relative importance, equivalent weightage was given.

3. Study Areas and Healthcare Infrastructures

3.1 Study Area and Healthcare Infrastructure selected in Bangladesh

Coastal belt of Bangladesh is highly vulnerable to cyclonic disasters (Afroz et al., 2018). Among all 19 coastal districts, Satkhira district of southwestern Bangladesh is identified as one of the most cyclone prone districts of Bangladesh (Hoque, et al., 2021, Islam et al., 2015). This district is categorized as the high cyclone hazard prone area (Hossain, et al., 2019). There are many studies addressing cyclone vulnerabilities and resilience of south-western coastal areas. But studies focusing infrastructures and cyclone, especially critical infrastructure and cyclonic disasters are rare in Bangladesh. Therefore, this study has selected Satkhira district, which is a bit remote in location and vulnerable to cyclonic disasters.

Satkhira district is consists of seven Upazilas (sub-districts), two pourasavas (Municipality) and seventy-eight unions. Sundarbans is the largest single block of tidal halophytic mangrove forest in the world, a world heritage site is located at the southern part of the district. However, despite, having importance of this district, its resources and population is often suffered by devastating cyclones. Moreover, basic services and facilities, especially, standard and condition of healthcare infrastructure of this district are very poor. Table 1 (MoHFW, 2021) denotes the basic utility sources and number of beds of Upazila

Health Complexes (UHCs) of Satkhira district. The shaded rows are the studied UHC.

Table 1. Status of health care facilities in different Upazilas of Satkhira districts of Bangladesh

	Number of beds	Electricity	Waste management	Water sources	Toilet facility
Satkhira					
Assasuni	31	National grid	Not available	Tubewell	Adequate
Debhata	50	National grid	Standard	Tubewell	Adequate
Kalaroa	50	National grid	Not available	Tubewell	Inadequate
Kaliganj	31	National grid	Non-standard	Pond	Adequate
Shyamnagar	50	National grid	Not available	Tubewell	Inadequate
Tala	50	National grid	Not available	Tubewell	Inadequate
Sadar	70	National grid	Standard	Tubewell	Inadequate

Source: MoHFW, 2021

The Government of Bangladesh provides healthcare services to its rural people (about 62% of national population) through health facilities called Upazila Health Complex (UHCs) at the sub-district or upazila level (Ahmed, et al., 2010). However, health complexes are not equipped with adequate infrastructural facilities and the number of doctors is limited considering the number of patients. The condition of electricity supply, waste management facility, water sources and toilet facilities varied in different health complexes. However, the common problem is health facility system is at below the required standard (Huda et al., 2021). Considering cyclonic disaster vulnerabilities and poor healthcare facilities, UHC of Satkhira district are selected for this study to evaluate cyclonic disaster resilience evaluation of healthcare infrastructure. There are six UHCs in Satkhira district. Among these six, three UHCs are randomly selected. However. During selection it was tried to select UHC from different parts of the districts. Therefore, Tala UHC (northern part), Debhata UHC (central part) and Shyamnagar UHC (southern part) are selected for this study (Fig 1).

Tala Upazila Health Complex is situated at Tala Upazila, which is 26 km away from Satkhira sadar (centre) of Satkhira district. Debhata Upazila Health Complex is situated at Debhata Upazila and it is 19 km away from Satkhira sadar. Shyamnagar Upazila Health Complex is 51 km away from Satkhira sadar.

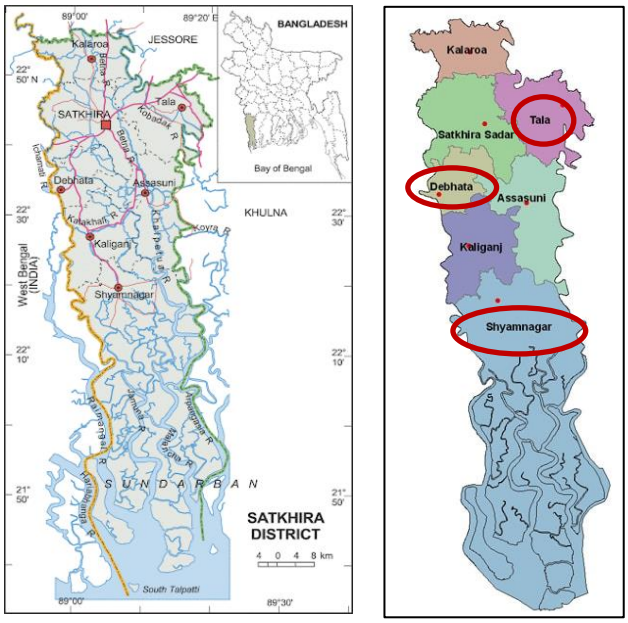

Figure.1 (a) Map of Satkhira District (left one); (b) Location of studied UHC (right one)

Study Area and Healthcare Infrastructure Selected in Japan

Japan in one of the most disaster-prone countries in the world. Among different region Tohoku is one of the most disaster-prone regions of Japan. Cyclonic disaster, which is known as typhoon in Japan is the most common in Tohoku region. After Great East Japan Earthquake in 2011, this region was affected by a number of typhoons. Therefore, during selecting study area and typhoon vulnerable healthcare infrastructures literature review and web searched were conducted focusing this region. Based on the typhoon vulnerabilities a list of different healthcare infrastructures was prepared. From the list communications were made with different hospital personnel. Among different hospitals two healthcare facilities of Marumoi town were willing to participate in this study. Considering their typhoon vulnerabilities and their damage during recent devastating typhoon/cyclone name Hagibis two hospitals are selected for this study. In this study, as the Japan's hospitals authorities did not permit to disclose their names, here studied healthcare infrastructures are named as Japan Hospital A and Japan Hospital B (Fig. 2).

Hospital A, Marumori Town, Miyagi

In Japan, two healthcare infrastructures are studied. Among these two, one is a psychiatric hospital located. As the hospital authority have not allowed to disclose

their identity, here in this study it is named as Japan Hospital A. This healthcare infrastructure is located in A-town (given name) at the southern part of Miyagi Prefecture. The hospital is located approximately 40 Km. south of the centre of Sendai city that is the prefectural capital. The hospital is a five-minute walk from the nearest train station and about 50 minutes by car from the Sendai city. Shiroishi River is located within 1 Km. of the hospital and that causes flooding during typhoon season. During recent severe typhoon Hagibis (No. 19 in Japanese) the hospital faced devastating impacts and the first floor of the building was fully flooded.

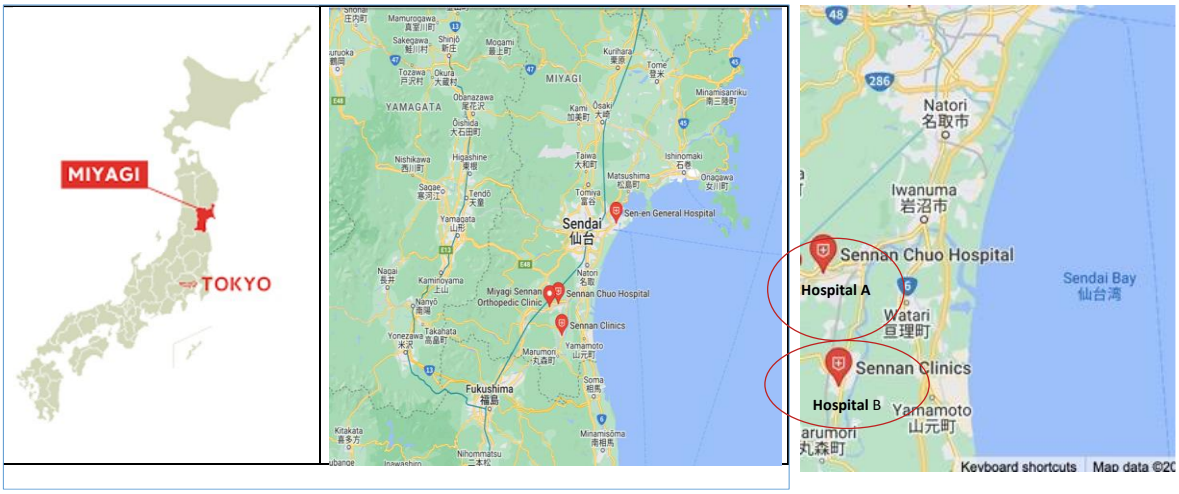

Figure. 2 Location of healthcare infrastructure studied in Japan.

Hospital B, Marumori, Miyagi

The hospital is located in the southern part of Miyagi Prefecture. The east and west sides of the B city are mountainous, and the Abukuma River flows nearby the hospital from south to north. The hospital is located approximately 50 Km. south from the centre of Sendai, the prefectural capital and it is about 70 minutes from the hospital by car. The hospital is located in the centre of the town, in the vicinity of Town Hall, a civic centre, banks, agricultural cooperatives, and other major buildings, and in a favourable environment with little noise. It is about 20-minute walk or 5-minute cab ride from the nearest train station.

During the last severe typhoon (typhoon Hagibis, known as typhoon no. 19 in Japan) the first floor was flooded. Dialysis machines were inundated and were not in the condition of operation. So, emergency transfer of dialysis patients was

carried out. During typhoon Hagibis in 2019 approximately 100 inpatients, 12 inpatients requiring dialysis and 22 kidney outpatients were transferred. Due to flooding, approximately 120 patients were evacuated to the second floor by the flood prevention (firefighting) team. Dialysis function was restored within 3 days, and all patients returned to the Hospital within one week.

4. Methodology

The main goal of this research is to evaluate cyclonic disaster resilience of healthcare infrastructures of coastal Bangladesh with a special comparing with typhoon affected Japanese coastal healthcare infrastructures. To achieve this goal a systematic and sequential methodological approach is followed. Methodological approaches of this study are briefly described here.

4.1 Step 1. Selection of Study Area and Healthcare Infrastructures

Since this study aims to evaluate cyclonic disaster resilience of healthcare infrastructures, coastal zones were selected for the study both in case of Bangladesh and Japan. Literature review, discussion with relevant academics and key informants were done to identify the specific areas or districts from coastal zone.

In case of Bangladesh, Upazila Health Complex (UHC) is the main healthcare facility at the lowest administrative territory of Bangladesh Government. Rural people are mainly dependent UHC for their all health services. Therefore, for this study UHCs were targeted to evaluate healthcare infrastructure resilience. Email and telephonic communications were made with the Chief Medical Officer (Doctor) of a number of UHCs located in the selected coastal districts. From different UHCs three were selected considering their vulnerability, location and overall willingness to response.

Similarly, in case of Japan, through literature review a list of 14 hospitals that are located in coastal areas and vulnerable to cyclone or typhoon was made. From this list officials of different healthcare infrastructures were contacted and requested for their cooperation for resilience evaluation field survey. Among a number of different hospitals two hospitals from Miyagi prefecture that are vulnerable to typhoon and were severely affected by typhoon in 2019 were

selected for resilience evaluation. In Section 2 about the selected study areas and the healthcare infrastructures are briefly discussed. For initial field visit communication was made with different healthcare personnels.

4.2 Step 2. Literature search for Cyclonic Disaster Resilience Evaluation Indicators for Healthcare Infrastructures

Systematic and intensive literature review was conducted to select cyclonic disaster resilience evaluation indicators for healthcare infrastructures. Fig. 3 is a diagrammatic explanation of sequential steps followed to get relevant literatures, to select relevant and important literatures and finally to prepare a final list of cyclonic disaster resilience evaluation dimensions, parameters and indicators. Table 2 also presents detail about the literature review for finalizing resilience evaluation indicators.

Table 2. Systematic Literature Review Approach

Search Engine and time period	Key Words for searching	Literature found	Literature Included	Dimensions and Parameters found from Literature	Indicators found from Literature
Scopus Indexed Journals, Scholarly Articles, Scientific Reports and WHO Standards, National Standards etc. from PubMed, Web of Science, SCOPUS, Google and Google Scholar From Year 2003 to 2023 (20 years)	1st phase Health system disaster resilience evaluation indicator	19,300	Included after Title screening: 370 documents Included after abstract screening: 97 documents Included after whole paper, methodology and relevance screening: 46 documents Finally, Resilience evaluation indicators are picked and listed: 32 documents	2 Dimensions for Healthcare Infrastructure Resilience Evaluation 6 parameters for Structural resilience 4 parameters for Non-Structural resilience	54 indicators
	2nd phase Hospital disaster resilience evaluation indicator	19,000			
	3rd phase Healthcare infrastructure cyclonic disaster resilience evaluation indicator	6,480			
	4th phase Healthcare infrastructure cyclonic disaster resilience evaluation indicator, Bangladesh	2,960			
	5th phase Healthcare infrastructure cyclonic disaster resilience evaluation indicator, Japan	2, 830			

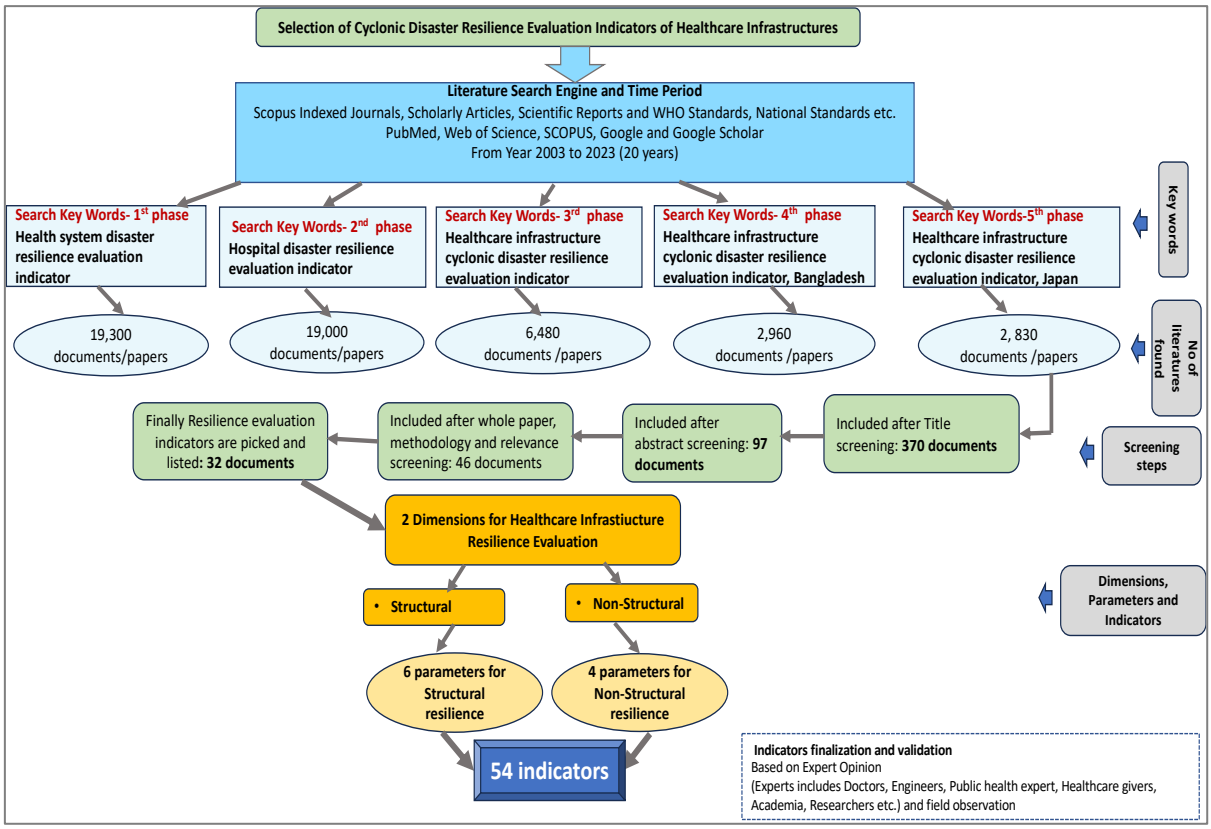

Figure .3 Methodological Diagram of intensive literature search, review and finalization of cyclonic disaster resilience evaluation dimensions, parameters and indicators

4.3 Step 3. Systematic and Intensive Literature Review to Select Resilience Evaluation Dimensions, Parameters and Indicators

With a systematic and intensive review of total 32 documents and journal papers two broad dimensions, 10 parameters and 54 indicators are listed to evaluation of cyclonic disaster resilience of coastal health care infrastructure in Bangladesh and Japan. These selected dimensions named as a) Structural and b) Non-Structural Dimension (Luke et al., 2021, Ryan et al., 2016, WHO, 2015, WHO, 2019)

Literature review denotes that there are five different domains of resilience or resilience frameworks applied for hospital/health system adopted by different scholars (Bruneau et al, 2007, Zhong et al, 2014, WHO, 2015, Blanchet et al, 2017, Kruk et al, 2017 and WHO, 2019). Considering these five domains following 10 parameters are adopted to evaluate cyclonic disaster resilience of healthcare infrastructures.

A. Building condition and Furniture

B. Location and surrounding

C. Water, Energy, Waste Management

D. Hygiene and Sanitation

E. Information and communication facilities and Management (availability and quality)

F. Cyclonic Disaster Preparedness and Management

G. Manpower and Human Recourses

H. Facilities

I. Occupational Safety

J. Financial affordability, audit and transparency

The dimensions, parameters and indicators that are listed to evaluate cyclonic disaster resilience of healthcare infrastructure are show in table 3. Relevant references are cited at the right most column.

Table 3 Resilience Assessment Dimensions and Indicators (tentative) will be used for calculating WMI.

Dimensions	Parameters	Indicators	References of literature
Structural	**Building condition**	1. Age of the building 2. Construction material 3. Building codes 4. Regular inspection and maintenance of the building and facilities 5. Availability of spaces to maintain social distancing and isolation during epidemic/pandemic along with cyclone	Nekoie-Moghadam, et al., (2016), WHO, (2015 a), WHO, (2019), Luxon, L. (2015), Fallah et al., (2020), World Bank, (2018), Prats, E. V. (2020), Kaji and Lewis (2006), Ali et al., (2021)
	Location and surrounding	1. Location and land type of the building 2. Surrounding land use and topography 3. Distance from the coast 4. Catchment area (area coverage) 5. Condition of access road 6. Accessibility during disaster	Guenther and Balbus, (2014), WHO (2015), WHO, (2019), Luxon, L. (2015). Luxon, L. (2015). Fallah et al., 2020, JICA, 2017, World Bank, (2018), Prats, E. V. (2020), Bianchi and Malki (2021)
	Water, Energy, Waste Management	1. Water supply condition (availability and quality) 2. Alternative and emergency water supply 3. Energy supply condition 4. Alternative and emergency energy (electricity supply) 5. Waste management condition	Guenther and Balbus, (2014), WHO (2015), WHO, (2019), Gupta et al., (2021), Zhong et al, (2014), Back and Kim, (2010), Nuzzo et al., (2019), Fallah et al., (2020), Prats, E. V. (2020), Al-Maruf (2021)
	Hygiene and	1. Toilet facilities	Guenther and Balbus,

	Sanitation	(availability and quality) 2. Hygiene in the building, facilities, utilities 3. Hygiene maintenance level and ability during pandemic	(2014), WHO (2015), WHO, (2019), Gupta et al., (2021), Fallah et al., (2020), Prats, E. V. (2020), Al-Maruf (2021)
	Information and communication facilities and Management (availability and quality)	1. Telecommunication and network availability, quality 2. Data recording and management 3. Computer and IT facilities for healthcare system operation and management 4. Professional for ITC operation and management	WHO, (2015), WHO (2019), ASPR TRACIE, (2022), Back and Kim (2010), Luxon, L. (2015). Fallah et al., (2020), Thomas, et al., (2020), Prats, E. V. (2020), WHO, (2010)
	Disaster Preparedness and Management	1. Emergency and Hazard management facilities 2. Disaster preparedness, disaster drill, risk assessment, monitoring 3. Facilities to manage epidemic/pandemic like COVID-19 along with cyclone 4. Condition of emergency supply chain (food, water, medicine and medical facilities) 5. Disable and gender friendly facilities during disaster 6. Availability and efficiency of disaster management action plan (preparedness, response, recovery) 7. Emergency response team 8. Evacuation plan and route 9. Warning system 10. Emergency response and recovery budget	Hanefeld et al., (2018), Stone et al., (2020), Guenther and Balbus, (2014), Zhong et al, (2014), Back and Kim, (2010), Sharma and Sharma (2020), Nuzzo et al., (2019), Fallah et al., (2020), Thomas, et al., (2020), Prats, E. V. (2020), Maria (2021), Kaji and Lewis (2006), Ali et al., (2021), ADB, (2021)
Dimensions	**Parameters**	**Indicators**	
Non-Structural	**Manpower/Human resources**	1. Doctor/Physician and Population Ratio 2. Nurse and Population Ratio 3. Presence and Effectiveness of Hazard management team 4. Manpower Having	Kruk, et al., (2015), WHO, (2015a), WHO (2019), Back and Kim (2010), Nuzzo et al., (2019), Luxon, L. (2015). Fallah et al., (2020), Thomas, et al., (2020), Maria (2021), WHO, (2010)

		disaster training 5. Availability of alternative chain of command during emergency 6. Mental health support staff	
	Facilities	1. ICU and NICU (for newborn babies) and Population Ration 2. Hospital Bed and Population Ratio 3. Availability and quality of surgery facility 4. Availability and quality of pathological facility 5. Oxygen cylinder and supply availability 6. Xray, MRI, CT scan and such other diagnostic facilities 7. Efficiency of the facilities to serve emergency situation during disasters 8. Number of ambulances and condition of that	Back, M. H., & Kim, H. J. (2010), Who, (2015a), WHO, (2019), Nuzzo et al., 2019, Luxon, L. (2015). Fallah et al., (2020), Prats, E. V. (2020), Maria, (2021), Kaji and Lewis (2006)
	Occupational Safety	1. Availability of incentives for emergency workers and working hours 2. Availability of insurance during emergency duties 3. Availability of adequate PPE	Back and Kim (2010), Luxon, L. (2015). Fallah et al., (2020), Prats, E. V. (2020), Maria (2021)
	Financial affordability	1. Availability of fund and budget to maintain regular operating and maintenance cost of Hospital 2. Auditing system 3. Adequacy of Financial condition 4. Availability and adequacy of additional fund required to manage disaster	Grimm et al., 2021, Fallah et al., (2020), Thomas, et al., 2020, Prats, E. V. (2020), WHO, (2010), ADB, (2021)

4.4 Step 4. Literature Review and Secondary Data Collections

At the initial stage of this study intensive literature review was done to select study area, healthcare infrastructure and to formulate the list of resilience evaluation dimensions,

parameters and indicators. In addition to this, secondary data related to the basic information and facilities of healthcare infrastructures of Japan and Bangladesh were collected from different papers, documents and web sites of the hospitals or healthcare facilities. WHO standards for healthcare facilities were searched and collected from secondary sources.

For this study data collection is done at four different stages. These stages and different tasks related to data collection are described in Step 5, 6 and 7.

4.5 Step 5. Questionnaire Development

After secondary data collection and finalizing the indicators, questionnaire was developed. Considering two dimensions, 10 parameters and 54 indicators, a questionnaire was prepared. This questionnaire comprises about 100 questions addressing each indicator.

At the initial part of the questionnaire, there was a table to know the quantity and availability of all basic facilities in a hospital.

To evaluate the level of resilience each of the question was needed to answer using Likertrating scale ranges from 1 to 3 that denote 1 = poor, 2 = Moderate and 3 = Good in terms of resilience. In the index calculation these scores or choices will indicated as $X_1..X_3$.

The last part of questionnaire was consisted of two parts. First was to weigh each of the 10 parameter considering their current level of resilience in the studied healthcare infrastructure (from 1 to 10 any score). Second part was to prioritize the parameters by ranking from 10 to 1 means the highest to lowest priority for resilience. No duplication of score was allowed in this second part. This last part is to understand overall present level of resilience of each parameter at present and to understand which parameter is more important than other one to enhance future resilience.

In case of Bangladesh, a brief questionnaire was prepared to conduct survey among the patients of the healthcare facility to judge their satisfaction level associated with 10 parameters of hospital resilience. However, this was not possible for Japan hospitals, since it was not possible to get approval from the hospital authority to interview their patients.

4.6 Step 6. Preliminary Field Visit

After selection of the healthcare infrastructures an initial filed visit was made to do rapport building and understanding about the study area and its healthcare infrastructure. During this preliminary survey indicator validation and questionnaire

pre-testing were conducted.

4.7 Step 7 Questionnaire Survey and Data Collection for Resilience Evaluation

After preliminary survey and pre-testing of questionnaire some necessary minor revisions were done. Field survey preparation and communication were made (Fig. 4).

In case of Bangladesh Upazila Health Complex- names as UHCs were the targeted healthcare infrastructure. Therefore, Upazila Executive Official, who is named as UNO (Upazila Nirbahi Officer) was contacted and approval was taken before starting field visit and data collection for this study. After receiving approval from the UNO office, officials of Ministry of Health and Family Welfare (MoHFW), Local Government and Engineering Department (LGED) and Public Health and Engineering Department (PHED) and Chief Medical Official (chief of UHC) and his/her team were contacted for questionnaire survey. A team consists of these different experts and lead by Chief Medical Official of UHC provided answers to the questions.

Figure 4 Photos of field survey and data collection from the officials (top two photos are in Bangladesh and bottom two are in Japan).

In case of Japanese healthcare infrastructure (hospital), before questionnaire survey, communications were made for receiving approval from hospitals authority. After having approval appointment for field survey were made. During questionnaire survey a team

consisted of chief administrative official and his team and chief medical official and his team responded to all questions. Hospital officials accompanied this research team and made hospital tour to show and explain different issues of vulnerabilities and initiatives for resilience enhancement.

4.8 Step 8. Data Processing and Analysis- resilience evaluation by indexing

After data collection, it is processed by using Excel and Statistical package for Social Science (SPSS). Indexing calculations are done by using excel. Calculation steps and formulas are revealed below.

First steps: calculation of resilience for each parameter

There are different approaches of indexing in the different academic fields. However, considering disaster and health infrastructure this study has follow an adopted methodological approach as demonstrated by Parvin et al. 2021, Jovanović, et al., 2020 and Parvin et al., 2011.

As mentioned before, each question addressing resilience indicator was scored as 1 (poor) or 2 (Moderate) or 3 (Good resilience) to indicate the present level of resilience of the indicator/variable. In the calculation of the resilience index for each parameter these scores or choices are indicated as $X_1..X_3$.

$$X = \frac{\sum_{i=1}^{n} X_i}{n}$$

Here,

x = values of the indicator/variable (here response of each question related to the resilience indicator)

n = total number of questions addressing the indicators under each parameter

X =*average of the parameter*

Second steps:

In the last part of the questionnaire respondents gave weight to each parameter considering the existing level of resilience of the parameter. This weight ranges from 1 to 10 denoting the lowest to the highest level of resilience. Average score of each parameter was multiplied by this weight. In the calculation of the overall resilience index of each healthcare infrastructure these scores or choices are indicated as $W_1..W_{10}$. Finally, Weighted Mean Index (WMI) method was used to compute cyclonic disaster resilience index of healthcare infrastructure. The formula used for WMI method is

$$\text{WMI} = \frac{\sum_{i=1}^{n} Xi * Wi}{\sum_{i=1}^{n} Wi}$$

Weighted Mean:

$$\frac{\sum_{i=1}^{n} w_i x_i}{\sum_{i=1}^{n} w_i} = \frac{w_1x_1 + w_2x_2 + w_3x_3 + w_4x_4 + w_5x_5}{w_1 + w_2 + w_3 + w_4 + w_5}$$

In simple terms, WMI = Σwx/Σw, where w = the weights and x = the value of the parameter. This WMI score of each healthcare infrastructures denotes its level of cyclonic disaster resilience level. This score is named as Cyclonic Disaster Resilience Index (CyDRI) of the respective healthcare infrastructure.

4.9 Step 9 Graphical presentation, Comparison and Analysis of issues and parameters related to resilience

After completion of resilience score calculation and indexing graphical presentations in the form of spider diagram, bar diagram and tables were developed. All these graphs and tables imply the comparative level of resilience of different parameters of a healthcare infrastructure in case of cyclonic disaster. These graphs and tables also present comparative resilience level of Bangladesh and Japan's healthcare infrastructures.

4.10 Step 10. Reports Writing, Submission and Dissemination

After completion of data collection and analysis main focus was given to write a comprehensive report. This report comprises background of this important research, its aims, implication, approach of works, present level of resilience of studied healthcare infrastructures of Bangladesh and Japan. Comparative level of cyclonic disaster resilience level of the healthcare infrastructures of Bangladesh and Japan. This reports also indicated the factors that are responsible for the level of resilience. As one of the outcomes of this study, policy guidelines are also part of this report.

Outcomes of this research are started to disseminate among the authorities of relevant healthcare facilities. Dissemination will be continued in the forms of pursuing and motivating for resilience enhancement initiatives. Reporting to the relevant officials, public communication and publications will be continued. Fig. 5 shows whole steps of work

conducted for the completion of this study.

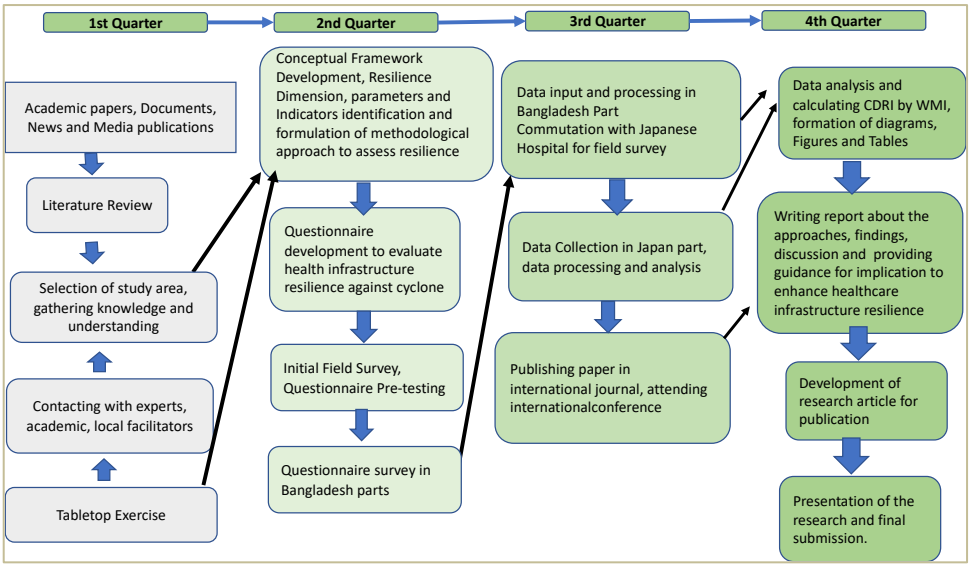

Figure. 5 Basic steps of works in this study in different quarters

5.Results and Discussion

Study argues that critical infrastructures share the same space and mutual dependencies, and consequently contribute to city's overall resilience (Serdar et al., 2021). Among different critical infrastructures hospitals are expected to continue to provide medical care during disasters. However, during any severe disasters they often fail to function due to critical circumstances (Djalali, et al. 2013). Therefore, during discussing about future hospital, Luxon (2015) indicates that healthcare infrastructure needs to consider built environment, medical equipment, access, technology, governance, staff structure etc. to develop a resilient community.

Considering the definition of resilience and the facilities, manpower that are needed to have a resilient healthcare system or healthcare infrastructure, in this study an inventory was made to understand the availability of facilities and manpower of the studied healthcare infrastructures. Further, cyclonic disaster resilience evaluation approach that is developed in this study is applied to evaluate the resilience level of studied healthcare infrastructures in Japan and Bangladesh. In this results and discussion part cyclonic disaster resilience, facilities and manpower and their comparative positions in Bangladesh and Japan are discussed under different sub-sections.

5.1 Facilities and Manpower of Healthcare Infrastructure

According to WHO guideline, for a healthcare facility adequate number of skilled human resources with decent working conditions, empowered and informed to respond to challenges and facilities for the efficient functioning are key to provide safe and quality healthcare (Prats, 2020). Therefore, this study has collected information related to available manpower including doctors, nurses, different medical machineries and equipment operators, technicians and such others. Information related to all basic facilities and medical equipment, healthcare infrastructure construction year, material and utilities are collected to understand the condition and affordability of the studied infrastructure to provide quality and safe care during normal and disaster or emergency time as well.

Table 4 is the list of available basic facilities and manpower of five different healthcare infrastructures studied in Bangladesh and Japan. In case of Bangladesh, analysing the number of health care manpower (doctors, nurses) and population of the area it is found that the ratio is one of the worst compare to the other parts of the world, even to the neighbouring countries. In the study area, in each Upazila, the Upazila Health Complex (UHC) is the only healthcare facility of the Government. Further, being rural area private hospital or clinic are not so available. Therefore, people mostly need to depend on Upazila Health Complex. However, table 5 denotes the severe situation by showing the number of people per doctor, nurses and per hospital bed. In every aspect this situation is one of the worst in the world.

Table 4. Facilities and Manpower of healthcare infrastructure

Aspects	Bangladesh			Japan	
	Tala UHC	**Shyamnagar UHC**	**Debhata UHC**	**Hospital A**	**Hospital B**
Construction Year of the Building	2005	1968	1987	2012	1967 Retrofitting: 1990
Building Material	Concrete	Brick and Cement	Brick and Concrete	Steel Frame	Reinforced Concrete
Number of Doctors	13	13	17	4 full time and 10 part-time	18 part-time
Number of Nurses (male and female)	30 (1 male)	33 (3 male)	30 (no male)	85 (38 nurses,16, assistant nurses and 31 nursing assistants)	40
Number of Cleaner	1	3	4	5	4

Number of technicians or other supporting staffs	6	6	1	34	24
Number of ICT facility operator	0	2	1	0	3
Physiotherapists	0	0	0	0	4
Psychiatrist	0	0	0	3 full time and 4 part-time	0
Number of beds	50	50	50	185	95 (general bed 30, long time care bed 60)
Average number of Outpatients per day	200-250	400-450	125-130	0	
Number of ICU bed	0	0	0	0	0
Number of NICU beds	0	0	0	0	0
Number of toilets	38	23	12	59	18
Average number of users per toilet	7	20	10-12		14
Number Drinking water sources (Tap/tube-well/other)	7	1	3	136 filters	10 water serve points
Number of operation/surgery room	1	1	2	0	1
Capacity of drinking water storage facility (tank size in liter)	1000L	1000L	200L and 2 Deep Tube-wells	60,000 L	102,000L
Capacity of regular using water storage facility (tank size in liter)	1000L	1000L	200L and 2 Deep Tube-wells	60,000L	102,000L
Number of Oxygen cylinder	20-25	40-45	15	Big 12 and small 2	10
Number of automated external defibrillator /AED	0	1	1	5	4
Number of generator (for emergency electricity supply) and capacity (how many hours back up possible)	2	1	1	1 (310 KVA)	2 (capacity 3 day to about a week)
Number of land phone	1	1	1	43	50
Number of cell	0	1	2	20	20

phone					
Number of X-Ray,	3	1	1	Fix 1 and Portable 2	3
MRI, CT scan machine	0	0	0	0	CT 1

Table 5. Population per doctor, nurse and hospital bed in studied UHC in Bangladesh

Healthcare Infrastructure Names	No. of Doctor	No. of Nurses	No. of Bed	Total Population of the Area	Population per one doctor	Population per one nurse	Population per Hospital bed
Tala UHC	13	30	50	299,820	23,063	9,994	5996
Shyamnagar UHC	13	33	50	3,18,254	24,481	9644	6,365
Debhata UHC	17	30	50	1,25,358	7374	4179	2,507
Japan Hospital A	14	84	185	80,853	5775	962	439
Japan Hospital B	18	40	95	27,976	1554	699	294

Note: Population data of the studied Upazilas of Bangladesh are from BBS 2011(the available latest one) and Population data of Japan Hospital are from City population website (2020).

According to WHO (2021) estimation, Bangladesh has 6.7 doctors per 10,000 population. Another report of WHO (2015b) estimated that in Bangladesh the ratios of doctors to nurses to technologists are 1:0.4:0.24, which is a stark contrast to WHO recommended ratio of 1:3:5. During describing the medical manpower or health workforce, Bangladesh health system review report prepared by WHO (2015b) stated that "shortage, inappropriate skill mix and inequitable distribution". This situation is clear from table 4 and table 5. The situation in studied healthcare infrastructures on Bangladesh is more severe compared to the national situation of Bangladesh.

Considering WHO standard, per 1000 population there should have 1 doctor, 5 nurses and 3.5 hospital beds, which is not available in case of both Japan and Bangladesh (except the number of beds in Hospital B. There are about 26.4 doctors and 130 nurses per 10,000 population in Japan. While this number is about 6.7 and 4 or 5 in case of Bangladesh (WHO, 2021). Even though, the situation is far better than Bangladesh, comparing with the national average number of doctor, nurse and hospital beds are low in the studied Japanese healthcare infrastructure (table 5). According to the estimation in 2020 (https://tradingeconomics.com/japan/medical-doctors), in Japan per 1000 population the numbers of doctor, nurse and hospital bed are 2.67, 12.85 and 12.63 respectively. However, unlike Bangladesh, there are other alternative hospital or clinic in the area of both Hospital A and Hospital B. Therefore, this shortage of manpower is not

so acute in case of Japanese healthcare infrastructure.

In the aspect of availability of some basic facilities, there are no significant differences between Bangladesh and Japanese healthcare infrastructures. However, it is regretting that some of the equipment that are considered as must needed during any emergency, like Automated External Defibrillator (AED), land and mobile phone and water storage facility are seriously inadequate or even absent in case of studied UHC of Bangladesh.

In contrast, amazingly there are some special facilities in Shyamnagar UHC of Bangladesh. Among these special facilities, Basic Emergency Obstetric Care (BEOC), Comprehensive Emergency Care (CEMC), Breast feeding corner, Diarrhoea corner and HIV screening facility are mentioned worthy.

5.2 Cyclonic Disaster Resilience Index (CyDRI) of Healthcare Infrastructures of Bangladesh and Japan

5.2.1 Overall, structural and Non-Structural Resilience

According to US Department of Health and Human Service (2020), public health infrastructures prevent disease, promote health and help to prepare for both acute (emergency) threats and chronic (ongoing) challenges to health. These threats and challenges include all hazards and disasters. As the preparation, irrespective of public and private, health infrastructures are needed to enhance resilience. In the context of critical infrastructures, Smart Resilience Project (2016), define resilience as "*the ability to anticipate, prepare for, and adapt to changing conditions and withstand, respond to, and recover rapidly from disruption*". In this study, 10 parameters of resilience evaluation include the issues and indicators associated with preparation, response and recover. Considering all parameters Weighted Mean Index of resilience is calculated to evaluate the overall cyclonic disaster resilience level of studied healthcare infrastructures. Figure 6 depicts the overall resilience level of studied healthcare infrastructures.

It is interesting to notice that the weighted scores of overall CyDRI for all five studied healthcare infrastructure are ranges from 2 to 2.4 out of 3, which denote moderate or medium level of resilience. Irrespective of Bangladesh or Japan the resilience level is medium. It should be noted that during scoring each of the resilience indicator respondents gave their evaluation score considering the situation in respect to the whole respective country.

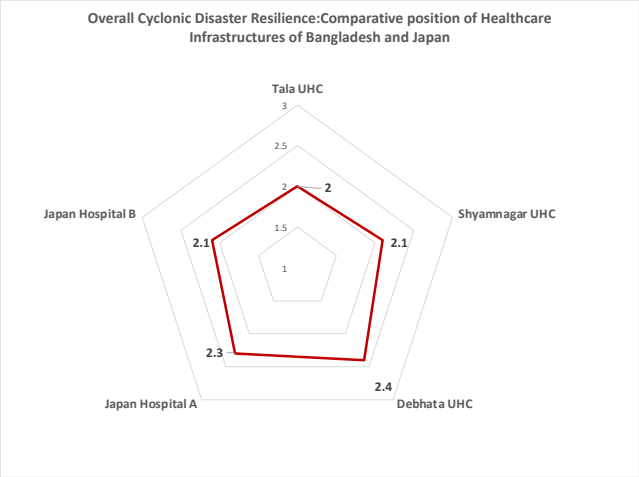

Figure 6. Overall Cyclonic Disaster Resilience Index (CyDRI) of Healthcare Infrastructure of Bangladesh and Japan

More engrossing is Debhata UHC of Bangladesh has obtained the highest overall resilience score among all five studied healthcare infrastructures. In the contrary to the overall resilience, the resilience level in non-structural dimension is the lowest (1.95) in case of Debhata UHC. So, it is clearly understood that overall resilience index or score of any healthcare infrastructure does not denote its full resilience level in all structural and non-structural dimensions and in all parameters. Therefore, detail resilience evaluation in different dimensions and parameters are essential. Fig. 7 implies the comparative information and understanding of the overall, structural and non-structural resilience level of five studied healthcare infrastructure in Bangladesh and Japan. Figure 7 that is presented in Bar diagram to provide clear and comparative view. This figure is an important one, since it presents the comparative resilience level of all five healthcare infrastructures, and the comparative resilience level in all dimensions including structural, non-structural and overall.

Except Debhata UHC, other healthcare infrastructures have not much differences in their overall, structural and non-structural resilience level. Japan Hospital A has same resilience level (score 2.3) in overall, structural and non-structural dimension. In case of Japan Hospital B, weighted resilience scores for the overall, structural and non-structural dimension are also almost same that are 2, 2.1 and 2.1 respectively. Overall resilience level of Japan Hospital B is same as the overall score obtained by Shyamnagar and Tala UHC of Bangladesh.

In Bangladesh Debhata UHC has remarkably different resilience level in structural and non-structural dimension. Calculating the obtained scores in different dimensions it can be said that non-structural resilience level of Debhata UHC is 27% lower than its structural resilience level. Similarly, not only the dimensional aspect, but there are also

variations in the resilience level in case of different parameters under each dimension. Therefore, this study attempted to evaluate the resilience level of different parameters associated with structural and non-structural dimensions of healthcare infrastructure.

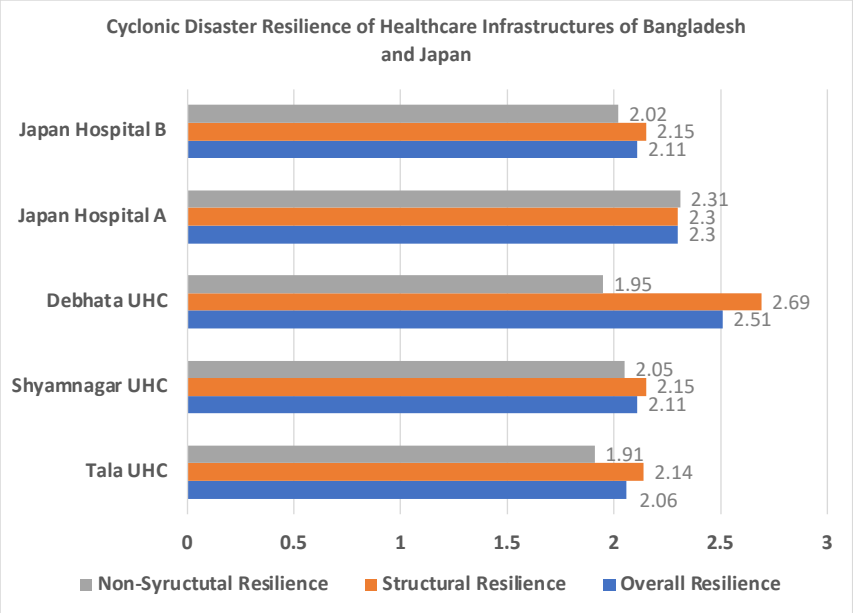

Figure 7. Overall, Structural and Non-Structural Resilience level of Healthcare Infrastructures

5.2.3 Level of Cyclonic Disaster Resilience in Different Parameters

Overall resilience scores that are calculated by considering individual score of each parameter have not very high deviation among the studied healthcare infrastructures. However, resilience level of 10 different parameters is different from each other in case of different healthcare infrastructures. Fig. 8 reveals that despite having medium level of overall cyclonic disaster resilience, there remain wide variations in the resilience score of different parameters.

In Fig. 8, five different colours denote five different studied healthcare infrastructures and the 10 corner points of the radar diagram reveal the 10 parameters considered during resilience evaluation. From the figure it is vividly clear that for different healthcare facilities different parameters have widely different resilience scores.

For instance, in case of Debhata UHC, information and communication facility and management have good resilience level by having the highest score (2.88); while this score is 1.4 for hygiene and sanitation and for occupational safety it is 1.33 (out of 3). This low score in hygiene and sanitation is also proved during field visit, by surprisingly noticing cats and dog freely moving around near the accommodation place of hospital patients. Similarly, occupational safety that includes incentive, insurance, transportation

and personal protection equipment are the lowest in Debhata UHC. This occupational safety parameter has the low score for all healthcare infrastructure in Bangladesh.

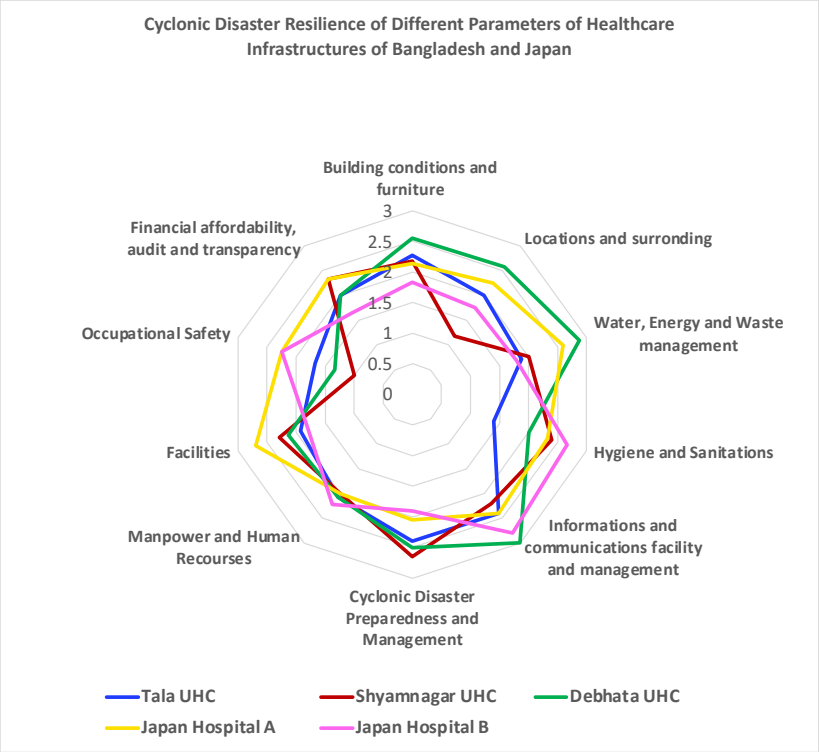

Figure 8. CyDRI of different parameters of healthcare infrastructures

Despite having low score in hygiene and sanitation and occupational safety, Debhata UHC has modern WiFi modem for all time internet connection, it has skilled professional for the operation and management of Information and Communication Technologies necessary for the hospital operation. Further, data recording facilities and computer facilities are good in Debhata UHC. Two deep tube-well are installed to ensure all time pure water supply to the hospital. Solar panel and generator for alternative and emergency power supply are available in Debhata and waste are managed separately and properly.

Debhata UHC is located far from the coast and relatively on high land. Among different parameters of resilience, locational suitability, building condition, water supply, energy and waste management, information and communication facilities and management are relatively good in Debhata that have boosted its level of resilience among all five studied healthcare infrastructures. However, its hygiene and sanitation condition are not as good as some other parameters of resilience.

In case of Shyamnagar UHC, resilience score for location and surrounding is 1.18 out of 3. This UHC is relatively close to coast and surrounded by rivers that enhanced its locational vulnerabilities. This locational parameter is one of the key determinants of its

cyclonic disaster resilience level. Since the location and surrounding and building condition are not so good, Shyamnagar UHC has given priority to disaster preparedness and it has the highest score (2.65 out of 3) among all five healthcare infrastructures in case of cyclonic disaster preparedness and management.

Figure 8 is another important outcome in this study. Identification of the variation of resilience level in different parameters are crucial for effective action planning and budget allocation to enhance cyclonic disaster resilience and disaster preparedness of a healthcare infrastructure. For detail information and CyDRI scores in different parameters table 6 is provided.

Table 6. Weighed scores of CyDRI of different Healthcare Infrastructures in 10 different Parameters

Parameters	**Name of the Healthcare Infrastructures**				
Structural	**Tala UHC**	**Shyamnagar UHC**	**Debhata UHC**	**Japan Hospital A**	**Japan Hospital B**
Building conditions and furniture	2.27	2.18	2.55	2.14	1.83
Locations and surrounding	2	1.18	2.57	2.25	1.75
Water, Energy and Waste management	1.88	2	2.88	2.6	1.8
Hygiene and Sanitations	1.4	2.4	2	2.33	2.67
Information and communications facility and management	2.4	2.2	3	2.4	2.8
Cyclonic Disaster Preparedness and Management	2.4	2.65	2.5	2.05	1.9
CyDRI score for Structural Parameters	**2.1**	**2.1**	**2.7**	**2.3**	**2.1**
Non-Structural Parameters					
Manpower and Human Recourses	2.07	2	2.07	2	2.22
Facilities	1.93	2.29	2.14	2.7	1.79
Occupational Safety	1.67	1	1.33	2.25	2.25
Financial affordability, audit and transparency	2	2.33	2	2.33	1.66
CyDRI score for Non-Structural parameters	**1.9**	**2.0**	**1.9**	**2.3**	**2.0**
Overall CyDRI score	**2.0**	**2.1**	**2.5**	**2.3**	**2.1**

For better understanding the comparative level of resilience of different parameters under structural and non-structural dimensions Fig. 9 and Fig. 10 separately presenting the level

of resilience by Bar diagram. Five different colours of the bar in Fig. 9 imply five different studied healthcare infrastructures.

From the figure it is distinctly understood that in different parameters different healthcare infrastructure has the low level of resilience irrespective of Bangladesh or Japan. For instance, in Building condition and furniture surprisingly Japan Hospital B has the low level of resilience compared to the other infrastructures. In fact, this healthcare infrastructure is 56 years old a private hospital. Retrofitting was done in 1990, which is 33 years before. Therefore, in their present condition of building and furniture they judge it as poor in cyclonic disaster resilience. Further, the hospital authority claimed about not having adequate support from the Government for disaster risk reduction and resilience enhancement of the building. Cyclonic disaster preparedness, water, energy and waste management parameters also have relatively low resilience in case of Japan Hospital B.

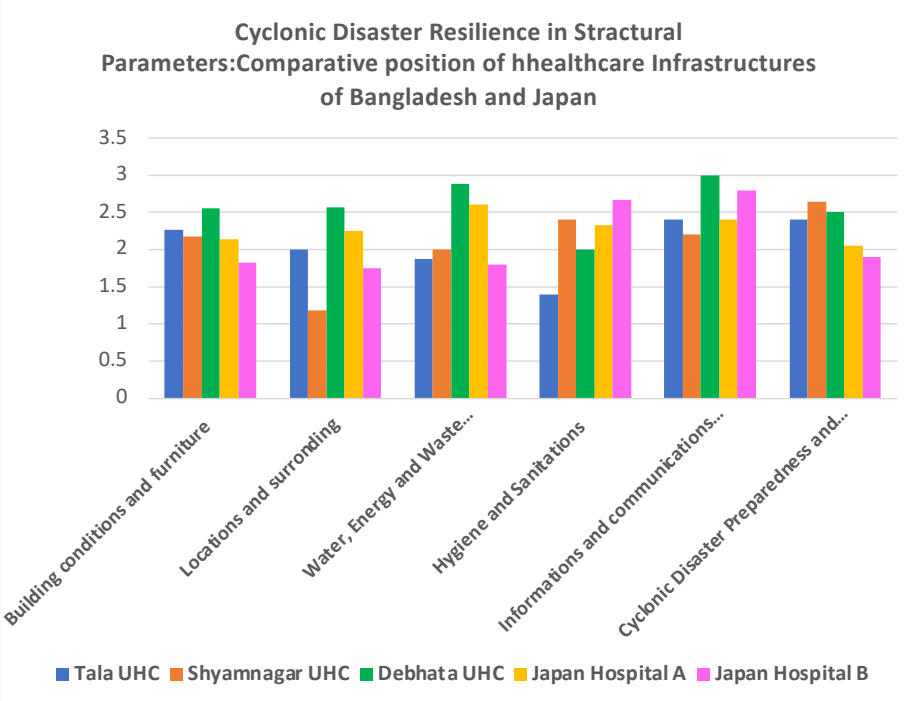

Figure 9. Variation of Cyclonic Disaster Resilience in Structural Parameters

Figure 10 denotes that all non-structural issues are not having same level of resilience in case of all healthcare infrastructures. In case of Bangladeshi UHC, resilience level of occupational safety is very low, while this is not so low in case of Japanese hospital. Emergency work incentive, insurance, transportation and PPE that are associated with occupational safety are poor in Bangladesh in contrast with Japan. In case of manpower all healthcare infrastructures have similar level of resilience. However, there remain variations in non-structural resilience level between two Japanese hospitals and among the five studied hospitals.

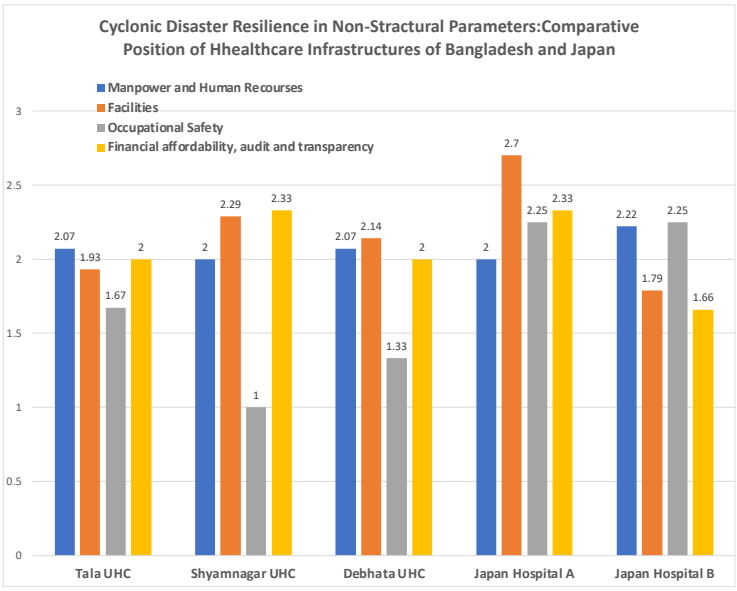

Figure 10. Variation of Cyclonic Disaster Resilience in Non-Structural Parameters

Despite locating in the cyclonic disaster-prone coastal belt and within 1 Km of Abukuma river of Japan, hospital B is not putting the highest score in disaster preparedness. Further its resilience level in different structural and non-structural parameters is also relatively low. Building and furniture, disaster preparedness, facilities and financial affordability in these four parameters Japan Hospital B is having low resilience score among all other healthcare infrastructures (Fig. 9 and Fig. 10). As mentioned before, Japan Hospital B is the oldest healthcare infrastructure among five studied hospitals. However, in the Marumori town Hospital B is one of the main hospitals to provide dialysis services to kidney patients and presently there are about 30 patients depending to the hospital for dialysis.

Being a small private hospital, it has not that much financial affordability to enhance its resilience in different parameters. Furthermore, in 2019 the devastating cyclone Hagibis had severe impact to this hospital. At the ground floor electric cable of all emergency machineries and medical equipment were under water at that time. With small support from the Government the hospital has tried to recover to some extent. However, their efforts to enhance resilience and reduce disaster risk are sluggish due to availability of fund and poor affordability. Figure 11 shows some of the efforts for their resilience enhancement.

Explanation of Figure:

A. Water storage and water supply facilities at Shyamnagar UHC. During COVID- 19 hand wash and water supply facilities are installed at the entrance of the hospital.

B. During COVID- 19 hand wash and wat.er supply facilities are installed at the entrance of Tala UHC. Ramp is set for the easy movement of patient with wheelchair. And to ensure easy access during emergency and disaster.

C. Greening and hospital beautification project to enhance ventilation and refreshment of patient and to cool the microclimate of UHC.

D. Electric cable of emergency medical equipment and machineries of Hospital B that were inundated during 2019 typhoon and associated flooding are now covered with metal box and elevated to 20cm from the floor level. This is done to protect these emergency cables from future flooding. However, due to funding problem it is not done for whole hospital.

E. In Hospital B, few air conditioners and generators are lifted up to protect from future flooding during cyclone and heavy torrential rain time. But many of the facilities are still at the ground level that could not lifted, as there is no fund to do that.

F. Poor road condition of the hospital B is repaired by hospital authority.

A. Shyamnagar UHC

B. Tala UHC

C. Debhata UHC

D. Hospital B

E. Hospital B

F. Hospital B

G. Hospital A

H. Hospital A

I. Hospital A

Figure 11. Resilience enhancing initiatives of different healthcare infrastructures

G. In hospital A the emergency cables that were under the floor and inundated during typhoon Hagibis are removed and shifted to the elevated place and covered with water proofing system.

H. Height of chair, desk, emergency cables and switch board of hospital A are elevated and cables are covered with metal box to protect from inundation and damage during typhoon and flooding.

I. Water barriers for doors and passage to prevent flood water to enter into the hospital. Backside of the photo shows storage of some emergency material to use during typhoon time.

Japan Hospital A of has relatively better resilience level compared to Hospital B and two other UHC in Bangladesh. This Hospital A is the newest one among all five studied healthcare infrastructures. After the Great East Japan Earthquake in 2011, Hospital A is constructed 11 years before with modern building construction technology of Japan. However, this hospital is located within 200 metres of a big river named Shiroshi river. The building is located within a bowel shaped topography, surrounded by mountain and hilly areas. Therefore, during typhoon, due to associated heavy rainfall this area become flooded. During latest severe cyclone Hagibis (in Japan named as typhoon no.19) in 2019 this hospital faced devastating impacts (Fig 11). After that Government lunched a huge drainage project for the area and supported the hospital to recover. Due to huge investment for disaster recovery and enhancing disaster resilience Hospital A is having relative better position is cyclonic disaster resilience.

6. Enablers and Barriers

This study is blessed to have different enablers. Among these the mentality and environment of coordinated team works have enabled to conduct this study in two different countries and focusing five healthcare infrastructures. Facilities in Bangladesh Agricultural University and Ritsumeikan University, Japan enabled the team to complete this study within one year, which is not so enough time to do such a study. Periodic and systematic guidance from the staffs of CDRI and technical experts have facilitated to maintain sequential steps in the completion of the study. The IT team of CDRI is an important enabler by helping reporting, uploading and sharing all information on CDRI Portal. Apart from these, several scholars, key informants and hospital staffs are the main enablers of this study.

This research has faced different barriers too. Having timely consent and approval of field survey was a barrier in case of hospital survey in Japan. It passed long time to select cyclone vulnerable coastal hospitals that are willing to participate in this research. This time gap imposes huge pressure in the last quarter of the research time period. However, after having approval, Japanese hospitals extended very good supports and cooperation. In the Bangladesh side, main barrier was to have adequate time from all respondents. Further, literature addressing healthcare infrastructures and cyclonic disaster resilience is almost absent in case of Bangladesh and even Japan. So having access to appropriate literatures and secondary materials was a barrier for this study. Despite all these barriers, the enablers and dedication of the team have made it possible to complete this important study timely.

7. Key Takeaways from CDRI Fellowship Programme

This research has contributed to several key aspects of learning and understanding associated with healthcare infrastructure cyclonic disaster resilience. This approach of cyclonic disaster resilience evaluation of healthcare infrastructure is not any high technology-based engineering approach. Therefore, it is easily applicable and relatively cost effective for decision makers for policy and action planning. Following are four main practical implications.

- ***Periodical assessment of resilience level and monitoring of progress***

Formulation of Cyclonic Disaster Resilience Index (CyDRI) of healthcare infrastructure require a simple but systematic methodological approach. This similar methodological approach is applicable to determine levels of resilience of other infrastructures with an adjustment. This approach is useful for periodical resilience assessment of an infrastructure. This periodical assessment would facilitate monitoring of the progress of any infrastructure management and disaster resilience initiative.

- ***Preparation of micro-level action plans to enhance resilience***

Resilience level of different healthcare infrastructures is different. Further, structural, and non-structural resilience are not same for all infrastructures. This type of resilience evaluation helps to understand structure specific strength and weakness and thus to formulate need oriented action plan for specific infrastructure.

- ***Comparative analysis and budget allocation***

The Sendai Framework for Disaster Risk Reduction (SFDRR, 2015–2030) has prioritised investment in disaster risk reduction for resilience (UN/ISDR, 2015, cited in Weichselgartner & Pigeon, 2015). Therefore, limited budgets and financial resources need to be used efficiently. In this context, this resilience evaluation approach would facilitate an effective budget allocation process and financial planning for enhancing healthcare infrastructures' disaster resilience.

- ***Database to facilitate city decision making, planning, and development works***

Parameters and indicator based this resilience analysis of different healthcare infrastructure will provide detailed information that will serves as an important database for decision makers, planners, and others seeking to implement development projects addressing healthcare facilities.

All these implications and take away from this study is briefly presented in Fig.12.

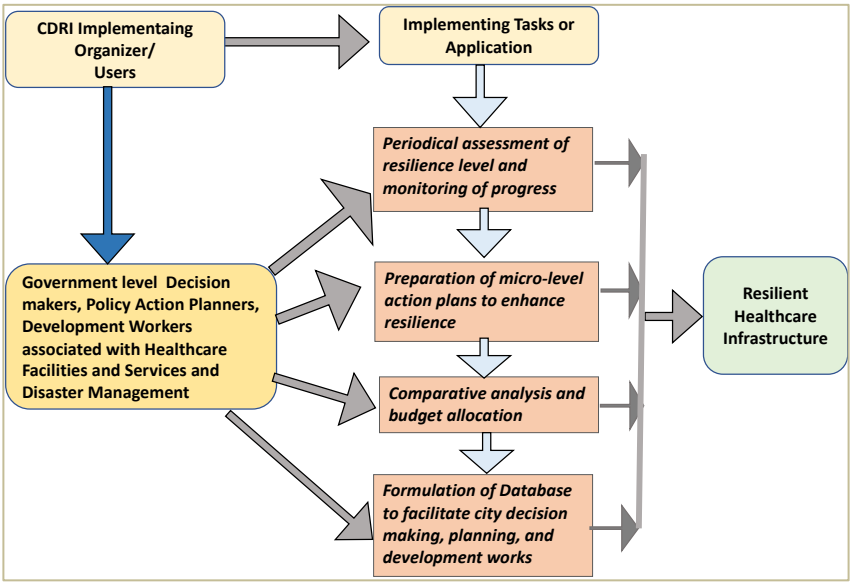

Figure 12. Implication of CyDRI (cyclonic disaster resilience index) to enhance healthcare infrastructure resilience.

8. Conclusion

The book titled as 'WHO guidance for climate resilient and environmentally sustainable health care facilities' written Prats (2020) claimed health care facilities as the first and last line of defence to climate change impacts and to provide the needed services and care to people harmed by extreme weather and other long-term climate hazards and disasters. Therefore, it is necessary to build resilient healthcare infrastructures so that it can defend from the first to last during any emergency and disasters. Building disaster resilience of any healthcare infrastructure require proper evaluation of current resilience level of healthcare infrastructure in different dimensions including both structural and non-structural, as well as different parameters. From the outcomes of this research, it is distinctly understood that better score in overall CyDRI (e.g., Debhata) is not the indication of its full resilience and good condition in all parameters of resilience, since resilience levels of hygiene and sanitation and occupational safety are poor in Debhata UHC. Further, CyDRI or Cyclonic Disaster Resilience Index of any health care infrastructure is not always same in case of structural dimension or non-structural dimension or even different parameters. So, it is important to evaluate and understand all these different level of disaster resiliences of any infrastructure. CyDRI calculated by this study also indicate that it is not always the fact that the healthcare infrastructure in develop countries like Japan will have the high level of resilience compared to the other less developed or developing countries like Bangladesh. Here it is found that even being healthcare infrastructure of a developed country, hospital of Japan has low level of

resilience. There are different factors and issues that are associated with this low level of resiliences. So, these factors and issues should be addressed during resilience evaluation and thus in action planning and budget allocation in future resilience building approach.

In Bangladesh and Japan there is no such non-technical perception-based approach used or developed to examine cyclonic disaster resilience level of any critical infrastructure. Comparison between Bangladesh and Japan has provided a direction to understand what matters to have better resilience in health care infrastructure in both countries. Although it is an empirical based analysis to explore the level of resilience, the findings will help the policy makers for site specific future intervention in health care infrastructure through microlevel planning to develop resilient community considering the context of Japan. The findings from this research project will provide better understanding of present disaster resilience level of healthcare infrastructure and factors associated with that. This understanding and evaluation will facilitate policy action planning and budget allocation for enhancing cyclonic disaster resilience of coastal healthcare infrastructure of Bangladesh and Japan as well. This type of research and implication of that are essential for all critical infrastructure to withstand and serve during and after disaster.

9.Way Forward

This study is conducted in three coastal healthcare infrastructures of Bangladesh and two coastal hospitals of Japan. It has provided valuable outcomes by providing methodological approach of evaluating and formulating Cyclonic Disaster Resilience Index (CyDRI). However, further research is needed including large number of samples that would allow different statistical analysis to find correlations between different variables. Due to small sample size, statistical analysis like Principal Component Analysis, Factor Analysis and such other suitable analyses were not possible to apply in this study. It is recommended to do this kind of study in different countries, in different parts of the country with adequate samples, time and financial support.

References

1. ADB (2021), Disaster Resilient Infrastructure, Unlocking Opportunities for Asia and pacific, Asian Development Bank
2. Adger, W.N.; Brown, K.; Waters, J. (2011). Resilience. In Dryzek, J.S., Norgaard, R.B., Schlosberg, D., (Eds.). *The Oxford handbook of climate change and society*.; Oxford University Press: Oxford, UK; New York, NY, USA, pp. 696–710, ISBN 978-0-19-956660-0.
3. Afroz, S., Cramb, R., & Grünbühel, C. (2018). Vulnerability and Response to Cyclones in Coastal Bangladesh: A Political Ecology Perspective. *Asian Journal of Social Science*, *46*(6), 601–637. https://www.jstor.org/stable/27073534
4. Ahmed, S., Siddique, A. K., Iqbal, A., Rahman, F. N., Islam, M. N., Sobhan, M. A., ... & Sack, R. B. (2010). Causes for hospitalizations at upazila health complexes in Bangladesh. *Journal of health, population, and nutrition*, *28*(4), 399.
5. Ali, H. M., Desha, C., Ranse, J., & Roiko, A. (2021). Planning and assessment approaches towards disaster resilient hospitals: a systematic literature review. *International Journal of Disaster Risk Reduction*, *61*, 102319.
6. Al-Maruf, A., Jenkins, J. C., Bernzen, A., & Braun, B. (2021). Measuring household resilience to cyclone disasters in coastal Bangladesh. *Climate*, *9*(6), 97.
7. ASPR (Assist. Secr. Prep. Response), TRACIE. **2022**. *Climate change resilience and healthcare system considerations*. Rep., US Dep. Health Hum. Serv., Washington, DC. **https://files.asprtracie.hhs.gov/documents/aspr-tracie-climate-change-resilience-and-healthcare-system-considerations-508.pdf**
8. Back, M. H., & Kim, H. J. (2010). Analysis of hospital disaster in South Korea from 1990 to 2008. *Yonsei medical journal*, *51*(6), 965-970
9. Bianchi, E., & Malki-Epshtein, L. (2021). Evaluating the risk to Bangladeshi coastal infrastructure from tropical cyclones under climate change. *International Journal of Disaster Risk Reduction*, *57*, 102147.
10. Biddle, L., Wahedi, K., & Bozorgmehr, K. (2020). Health system resilience: a literature review of empirical research. *Health policy and planning*, *35*(8), 1084-1109.
11. Bruneau, M., & Reinhorn, A. (2007). Exploring the concept of seismic resilience for acute care facilities. *Earthquake spectra*, *23*(1), 41-62.
12. Blanchet, K., Nam, S. L., Ramalingam, B., & Pozo-Martin, F. (2017). Governance and capacity to manage resilience of health systems: towards a new conceptual

framework. *International journal of health policy and management*, *6*(8), 431.

13. Cabinet Office, Japan (2021). White Paper, Disaster Management in Japan, available https://www.bousai.go.jp/en/documentation/white_paper/pdf/2021/R3_hakusho_english.pdf
14. Djalali, A., Castren, M., Khankeh, H., Gryth, D., Radestad, M., Öhlen, G., & Kurland, L. (2013). Hospital disaster preparedness as measured by functional capacity: a comparison between Iran and Sweden. *Prehospital and disaster medicine*, *28*(5), 454-461.
15. Fallah-Aliabadi, S., Ostadtaghizadeh, A., Ardalan, A., Fatemi, F., Khazai, B., & Mirjalili, M. R. (2020). Towards developing a model for the evaluation of hospital disaster resilience: a systematic review. *BMC health services research*, *20*(1), 1-11.
16. Gazi, A. K. (2019). People With Vulnerabilities to Cyclone in The Coastal Area of Bangladesh: An Overview. *International Journal of Social Sciences and Economic Review*, 80-91.
17. Grimm, P. Y., Merten, S., & Wyss, K. (2021). Evidence of health system resilience in Myanmar during Cyclone Nargis: a qualitative analysis. *BMJ open*, *11*(9), e050700.
18. Guenther, R., & Balbus, J. (2014). Primary protection: enhancing health care resilience for a changing climate. *US Department of Health and Human Services*.
19. Gupta, N., Dewan, A., & Mathur, M. (2021). Estimating relative importance of resilience indicators for large-scale hospital buildings to withstand hydrological. disasters. *Int J Stud Res Technol Manag*, *9*, 24-33.
20. Hanefeld, J., Mayhew, S., Legido-Quigley, H., Martineau, F., Karanikolos, M., Blanchet, K., ... & Balabanova, D. (2018). Towards an understanding of resilience: responding to health systems shocks. *Health policy and planning*, *33*(3), 355-367.
21. Hossain, M. S., Karlson, M., & Schmid Neset, T. S. (2019). Application of GIS for cyclone vulnerability analysis of Bangladesh. *Earth Science Malaysia*, 25-34.
22. Hoque, M. A. A., Pradhan, B., Ahmed, N., Ahmed, B., & Alamri, A. M. (2021). Cyclone vulnerability assessment of the western coast of Bangladesh. *Geomatics, Natural Hazards and Risk*, *12*(1), 198-221.
23. Huda, F. Akhter, Hassan R. Mahmood, Aniqa Tasnim Hossain, Jasmin Khan, Omar Faruk, Zahed Shafiqur Razzak, Kazi Tamara Binta Kamal, Shams El Arifeen (2020) Health Needs and Health System Response in the Coastal Districts of Bangladesh. International Centre for Diarrhoeal Disease Research, Bangladesh

24. Islam, M. A., Griffin, A. L., Paull, D. J., & Murshed, S. (2022). Assessing critical infrastructure resilience in terms of its service-providing capacity in coastal Bangladesh: A synthesis of geospatial techniques and social responses. *International Journal of Disaster Risk Reduction*, *67*, 102633.
25. Islam, Didar-Ul, Bhuiyan AH., Ramanathan AL (2015). Climate change impacts and vulnerability assessment in coastal region of Bangladesh: a case study on Shyamnagar Upazila of Satkhira District. *Journal of Climate Change*, *1*(1, 2), 37-45.
26. JICA (2017), Disaster Resilient Society for All, Integrating Disaster Risk Reduction Challenges with Sustainable Development, Japan International Cooperation Agency, Ver 3.1, 2017
27. Jovanović, A., Klimek, P., Renn, O., Schneider, R., Øien, K., Brown, J., ... & Chhantyal, P. (2020). Assessing resilience of healthcare infrastructure exposed to COVID-19: emerging risks, resilience indicators, interdependencies and international standards. *Environment Systems and Decisions*, *40*, 252-286.
28. Kabir, R., et al. (2014) Climate change and public health situations in the coastal areas of Bangladesh. International Journal of Social Science Studies. 2: 109.
29. Kaji, A. H., & Lewis, R. J. (2006). Hospital disaster preparedness in Los Angeles County. *Academic emergency medicine*, *13*(11), 1198-1203.
30. Kruk, M. E., Ling, E. J., Bitton, A., Cammett, M., Cavanaugh, K., Chopra, M., & el-Jardali, F. (2017). Constructing Resilient Well-being Programs: A Proposal for a Resilience Index. *BMJ*, *357*, j2323.
31. Luke, J., Franklin, R., Aitken, P. and Dyson, J., 2021. Safer hospital infrastructure assessments for socio-natural disaster–a scoping review. Prehospital and disaster medicine, 36(5), pp.627-635.
32. Luxon, L. (2015). Infrastructure–the key to healthcare improvement. *Future hospital journal*, *2*(1), 4.
33. Mallick, B., Ahmed, B., & Vogt, J. (2017). Living with the risks of cyclone disasters in the south-western coastal region of Bangladesh. *Environments*, *4*(1), 13.
34. Maria, Rodrigues Leal Moitinho De Almeida, (2021). Fostering hospital resilience to disasters: lessons from a tertiary hospital in Nepal.
35. Miyazawa, H., & Kikuchi, H. (2021). Integrated Care Systems Established to Strengthen Community Disaster Resilience. *Community-Based Integrated Care and the Inclusive Society: Recent Social Security Reform in Japan*, *12*, 241.
36. MoHFW (2021) Facility registry. Government of People's Republic of Bangladesh, Ministry of Health and Family Welfare.

https://facilityregistry.dghs.gov.bd (Accessed on: 13 September 2021).

37. Nekoie-Moghadam, M., Kurland, L., Moosazadeh, M., Ingrassia, P. L., Della Corte, F., & Djalali, A. (2016). Tools and checklists used for the evaluation of hospital disaster preparedness: a systematic review. *Disaster medicine and public health preparedness*, *10*(5), 781-788.
38. Nuzzo, J. B., Meyer, D., Snyder, M., Ravi, S. J., Lapascu, A., Souleles, J., ... & Bishai, D. (2019). What makes health systems resilient against infectious disease outbreaks and natural hazards? Results from a scoping review. *BMC public health*, *19*, 1-9.
39. Olu, Olushayo. (2017). Resilient health system as conceptual framework for strengthening public health disaster risk management: an African viewpoint. *Frontiers in public health*, *5*, 263.
40. Prats, E. V. (2020). *WHO guidance for climate-resilient and environmentally sustainable health care facilities*. World Health Organization.
41. Parvin, Gulsan Ara, Ahsan Reazul, S.M., Yusop, Azalia, bt.M, Abedin, Anwarul, Md., Gordon, Jessica, and Ahmad, Hamdan, M., (2021), Kampung (Village) Flood Resilience: An Empirical Analysis in Malaysia, Environmental Hazards, Taylor and Francis Eprint link: https://www.tandfonline.com/eprint/UAHAG9FAXRSIUPDQ6HEP/full?target=10.1080/17477891.2021.1887800
42. Parvin, G. A., & Shaw, R. (2011). Climate disaster resilience of Dhaka city corporation: an empirical assessment at zone level. *Risk, Hazards & Crisis in Public Policy*, *2*(2), 1-30.
43. Ryan, B. J., Franklin, R. C., Burkle Jr, F. M., Aitken, P., Smith, E., Watt, K., & Leggat, P. (2016). Reducing disaster exacerbated non-communicable diseases through public health infrastructure resilience: perspectives of Australian disaster service providers. *PLoS currents*, *8*. World Health Organization. (2019). Hospital safety index: Guide for evaluators.
44. Sendai Framework for Disaster Risk Reduction (SFDRR) 2015–2030. (2015). United Nations. Retrieved September 4, 2020, from https://www.preventionweb.net/files/43291_sendaiframeworkfordrren. pdf Smart Resilience: Smart resilience indicators for smart critical infra- structures. EU H2020 project Nr. 700621. https://www.smartresil ience.eu-vri.eu/
45. Stone, T., Banks, J., Brant, H., Kesten, J., Redfern, E., Remmers, A., & Redwood, S. (2020). The introduction of a safety checklist in two UK hospital emergency

departments: A qualitative study of implementation and staff use. *Journal of clinical nursing*, *29*(7-8), 1267-1275.

46. Sharma, S. K., & Sharma, N. (2020). Hospital preparedness and resilience in public health emergencies at district hospitals and community health centres. *Journal of Health Management*, *22*(2), 146-156.
47. Thomas, S., Sagan, A., Larkin, J., Cylus, J., Figueras, J., & Karanikolos, M. (2020). Strengthening health systems resilience: key concepts and strategies.
48. United Nations Office for Disaster Risk Reduction (UNDRR). (2017). Terminology. Online Glossary. Retrieved September 15, 2022, from https://www.undrr.org/terminology
49. World Bank. (2018). *Converting Disaster Experience into a Safer Built Environment: The Case of Japan*. World Bank.
50. World Health Organization. (2019). Hospital safety index: Guide for evaluators.
51. World Health Organization. (2015a). *Operational framework for building climate resilient health systems*. World Health Organization.
52. WHO (2015b). Bangladesh health system review, WHO Library Cataloguing-in-Publication Data, Health Systems in Transition, Vol. 5 No.
53. Weichselgartner, J., & Pigeon, P. (2015). The role of knowledge in disaster risk reduction. International Journal of Disaster Risk Science, 6(2), 107–116. https://doi.org/10.1007/s13753-015- 0052-7
54. World Health Organization. (2010). *Monitoring the building blocks of health systems: a handbook of indicators and their measurement strategies*. World Health Organization.
55. Zhong, S., Clark, M., Hou, X. Y., Zang, Y., & FitzGerald, G. (2014). Validation of a framework for measuring hospital disaster resilience using factor analysis. *International journal of environmental research and public health*, *11*(6), 6335-6353.
56. Zhong, S., Clark, M., Hou, X. Y., Zang, Y. L., & Fitzgerald, G. (2014). Development of hospital disaster resilience: conceptual framework and potential measurement. *Emergency Medicine Journal*, *31*(11), 930-938.
57. https://www.who.int/data/gho/data/indicators/indicator-details/GHO/medical-doctors-(per-10-000-population)
58. https://www.citypopulation.de/en/japan/admin/miyagi/04320__shibata/
59. https://tradingeconomics.com/japan/medical-doctors

Development of a Distributed Optical Fibre Sensor Network-Based Condition Monitoring System to Alert Road Collapses

Dr Madhubhashitha Herath
Senior Lecturer
Department of Engineering Technology
Faculty of Technological Studies, Uva Wellassa University, Badulla, Sri Lanka

A/Prof Jayantha Epaarachchi
Associate Professor,
School of Engineering,
Faculty of Health, Engineering and Sciences,
University of Southern Queensland, Toowoomba, QLD 4350, Australia.

Under CDRI Fellowship Programme 2022-23

Disclaimer: The views expressed in this paper reflect the opinions of the author and not necessarily the official views of CDRI.

Abstract

Road infrastructure is a crucial public asset as it contributes to economic development and growth while bringing critical social benefits. It connects communities and businesses and provides access to education, employment, social, and health services. Heavy rain, floods and hurricanes cause road collapse that results in life-threatening catastrophes and road closure. The cost of emergency repair is estimated to be ten times that of planned maintenance. Therefore, condition monitoring and preventive maintenance will have significant cost and safety advantages for road infrastructure. The rapid rise in pore water pressure can be adduced as the key root cause for a road collapse.

This research introduces a monitoring technique based on distributed optical fibre sensors that will facilitate early warning for road infrastructure. Laying subterranean distributed optical fibre sensors along a road offers unique advantages for spatially distributed measurements for hundreds of kilometres. By analyzing the dynamic strains, real-time road conditions can be measured. The evolution of the strain fields can relate to road collapse dynamics with an unprecedented resolution for early warning.

The proposed sensor system is designed in segments to measure the porewater pressure and vertical and horizontal ground movements. The concept and the mechanical design were developed with the aid of computer simulations and CAD software. The key component of the sensor assembly, the pore water pressure sensitive diaphragm was made from silicon rubber. In order to enhance the durability and long-term behaviour of the silicon diaphragm under subterranean conditions the silicon matrix was reinforced with carbon-based nanomaterials. The pore water pressure sensors were fabricated by embedding a bare optical fibre into the silicon diaphragm. Initially, the first version of a porewater pressure sensor array has been tested under laboratory conditions to investigate the water pressure measuring performance by measuring strain readings through an Optical Backscatter Reflectometer. Afterwards, the second version of a porewater pressure sensor array has been tested systematically to calibrate and build the relationship between water pressure and strain readings. The third version of the sensor consisted of all three components including the porewater pressure sensor, and vertical and horizontal ground moment sensing components. The performance of the entire sensor system will be demonstrated in a physical model that has been constructed to date.

It was proven that proposed sensor has the potential to precisely measure pore

water pressure and was revealed that the measured strain readings are proportional to the applied hydrostatic pressure. The real-time measurements indicating the combined subterranean conditions of the roads can be obtained frequently from a remote location as the optical fibres can transmit the measured data for long distances. The established system will be introduced to road development authorities for condition monitoring and to alert road collapses at the early stage. A model combined with water pressure sensing and land properties can be developed in the future to address any developing geohazards in water prone areas. Moreover, the scientific findings will be published in an esteemed journal and presented at an international conference. The developed condition monitoring and early warning system will be proposed for implementation in a high-risk road section in Sri Lanka and Australia

Acknowledgments

This research was supported by the 2022-2023 Fellowship of the Coalition for Disaster Resilient Infrastructure (CDRI). The constructive comments provided by the two technical experts Dr Kampanart Silva and Dr Dilip Patel are greatly appreciated. We are grateful for their experience and providing numerous suggestions, valuable comments, thoughtful guidance, and motivation. The mentor, Professor Kolitha Wijesekara has always been incredibly supportive, and we are thankful for his prompt responses, easy access and open-door policy that helped us to carry out the research smoothly.

We express our sincere gratitude to Uva Wellassa University for generously providing a research grant to expand the research activities and providing access to their research facilities as the host institution. We are indebted to the to the Centre for Future Material of the University of Southern Queensland for providing with invaluable testing facilities and a world class research environment.

This research might not have been possible without the dedicated work of Ms Kusumi Anjana the Research Assistant who actively contributed to the success of the project. She played a leading role throughout this research. We would like to express our sincere appreciation to Mr Minol Jayawikrama and Mr Sandaruwan Jayalath for their invaluable support in conducting the experiments of this project. We also express our sincere appreciation to Dr Nadeej Priyankara and Mr Osura Ayodhya for their technical support and valuable comments.

Funding

This research was supported by the 2022–2023 Fellowship of the Coalition for Disaster Resilient Infrastructure (CDRI), Application ID: 210921613 and Uva Wellassa University Research Grant UWU/RG/2022/39.

1. Introduction

Road infrastructure is a crucial public asset as it contributes to economic development and growth while bringing critical social benefits. It connects communities and businesses and provides access to education, employment, social, and health services. Heavy rain, floods and hurricanes cause road collapse that results in life-threatening catastrophes and road closure. The cost of emergency repair is estimated to be ten times that of planned maintenance(Begum et al., 2019; Glendinning et al., 2014). Therefore, condition monitoring and preventive maintenance will have significant cost and safety advantages for road infrastructure. The rapid rise in pore water pressure can be adduced as the key root cause for a road collapse. However, the mechanisms that initiate and propagate the failures are not adequately investigated to date (Igwe, 2015). The municipalities and road authorities seek to implement automated evaluation of road damage. The smart sensors and real-time condition monitoring systems intended for damage detection, localization, classification, quantification and prognosis of road infrastructure are crucial requisites for climate and disaster-resilient transport(Sony et al., 2019). Currently, (Cigna et al., 2017) devices such as smartphones containing high-resolution digital cameras, sensors, and powerful processors are being researched for road inspection. Fully automated evaluations often employ vehicles equipped with sophisticated and expensive sensors. Satellites and unmanned aerial vehicles also detect ground movements (Cigna et al., 2017). However, these types of discrete and noncontact sensors are incapable of accurately estimating the physical fields with spatial continuity for a long distance (Schenato, 2017). The lack of technology, know-how, and funds to afford state-of-the-art equipment for data collection and analysis have hindered road damage detection, localization, classification and quantification by using contact and spatially distributed sensors, which are promising for early warning (Arya et al., 2021).

2. Aim, Objectives, and Scope of the Research Study

2.1 Objectives

The research project is intended to develop a distributed fibre optic-based condition monitoring system to alert road collapses. The project will continue for two years with the funding support from the host institution. The entire project will aim at the following objectives.

- Design, develop and test distributed optical fibre sensor arrays to integrate into subterranean road layers.
- Measure the ground motions of a road model and the pore water pressure along the sensor arrays using the DOFS sensors.
- Develop the relationship between pore water pressure and ground displacement.
- Investigate the damage type and extent by using the strain field variations for early warning.

The first phase of the project, funded by the CDRI, is aimed at the following objectives.

- Design and develop an optical fibre sensor array to integrate into subterranean ground levels.
- Enhance the long-term behaviour and durability of the sensor.
- Evaluate the performance of the sensor system through laboratory experiments.

Measure the ground motions of a road model and the pore water pressure in the subterranean using a DOFS sensor array.

2.2 Research Gap

- The real-time condition monitoring of soil using inclinometers is limited to slope stability and embankment monitoring and is geographically tested only in Chinese soil conditions.
- The improvements which are to be fulfilled when DOFS are applied to roads are not well addressed.
- The simultaneous measurement of pore water pressure and ground displacement has not been comprehensively tested yet.
- The cross relationship between the pore water pressure and the pore water pressure-induced ground motion is not examined. Thus, the type of damage is not specified.

2.3 Scope of the Research Study

The search study includes the design and development of a DOFS-based sensor system. The performance of the sensor is initially tested in laboratory experiments. A working prototype of the sensor is fabricated and tested using a physical model of a road. The proposed research will be developed upon the model which would mimic the soil conditions of mountainous areas and thus will be directly advantageous for the countries like Sri Lanka, Nepal, and Bhutan. But it is not limited to a particular country and the

solution is applicable worldwide.

3. Methodology

3.1 Literature Review

The ground consists of soil, soft sediment and hard rocks that tend to lose stability due to a lack of friction and cohesion. The presence of groundwater reduces the shear strength of the earth's materials. If fluid pressures rise significantly, they can completely neutralize friction forces [1]. The effect of moisture on the soil properties has been examined and it has been found that there is an exponential decrease in the soil properties: uniaxial compressive strength, tensile strength and young's modulus in the presence of moisture while there is a linear decrease in the Point load index as depicted in the **Figure 2.** Behaviour of uniaxial compressive strength, tensile strength, point load index and young modulus in the presence of moisture (Verma et al., 2014)Figure 2. The effective shear strength also visibly decreases in high moisture conditions (Verma et al., 2014).

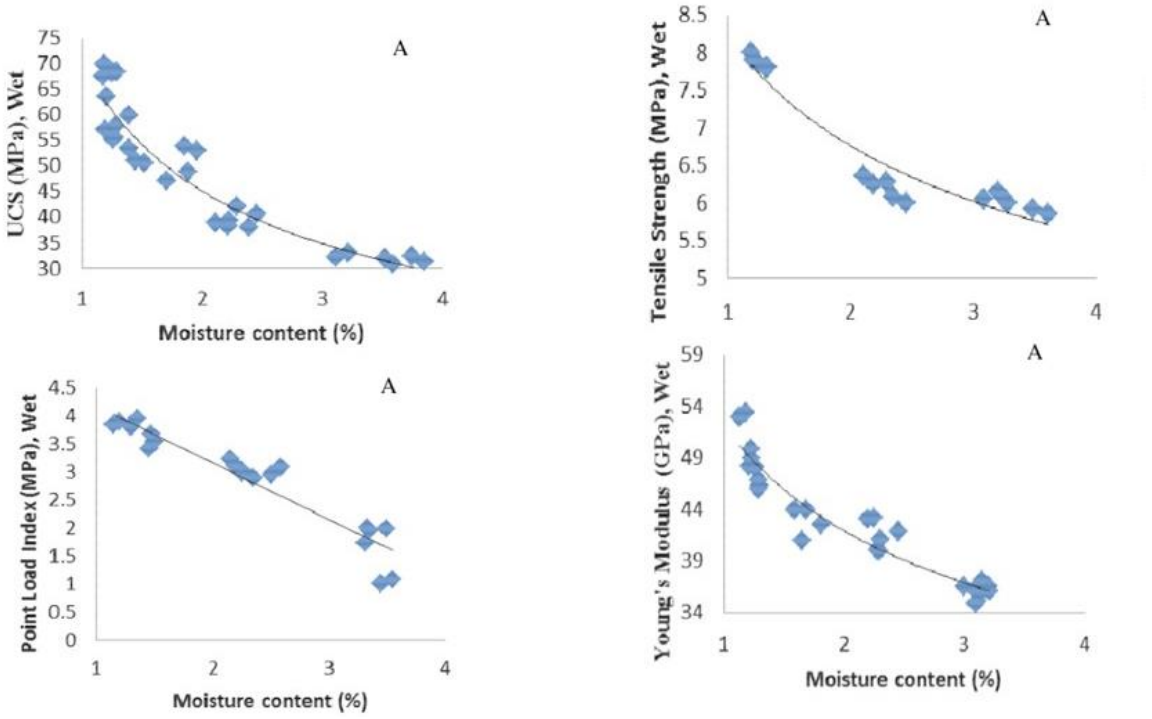

Figure 2. Behaviour of uniaxial compressive strength, tensile strength, point load index and young modulus in the presence of moisture (Verma et al., 2014)

Due to this behaviour of soil, the stability might lose in diverse ways: soil liquefaction, soil erosion, subsidence and slope instability. The soil stability can be evaluated by measuring the water content in the soil concerning the type of soil (Deng, n.d.). In the current context,

there are plenty of methods that monitor the presence of water in the underground conditions, which include automated sensing vehicles, ultrasonic sensors, and satellites, while innovative technologies are emerging. Optical fibre sensing is a such a new emerging technology which can be modified according to the sensing needs, parameters and environment.

The optical fibre cables are capable of monitoring temperature and strain with the exact location along the cable, while the cable acts as both the sensing element and the transmitting element. When the light encounters the point of strain, some of it is reflected back towards the source due to backscattering. The reflected light contains information about the location and magnitude of the strain along the cable. This information is extracted by analyzing the reflected light using the technique of time-domain reflectometry (TDR) (Wijaya et al., 2021). TDR works by measuring the time delay between the transmitted and reflected light signals. By knowing the speed of light in the optical fibre cable, the distance to the point of strain can be calculated. The magnitude of the strain can be determined from the amount of backscattered light and its intensity. The optical fibre cable that is being used for underground geotechnical monitoring can come in different types as pointed, quasi-distributed and distributed (Gong et al., 2019). Furthermore, the commercially available, well-developed distributed sensors are of two types as in Table 1 (Künzel & Petryna, 2016).

Table 1. Performances of Some Commercial Optical Fibre Sensing Systems

Type	Spacial Resolution (m)	Sensing Range (km)	Temperature Resolution (^{0}C)	Strain Resolution (με)
BOTDR	5	45	0.1	2
	11	55	-	1
	22	80	-	1
	80	70	0.005	0.1
	110	80	-	1
BOTDA	1.5	10	0.1	2
	4	60	0.1	2
	20	30	0.1	2

Due to the harsh conditions underneath the soil, it is essential to increase the survivability of the sensor thus a protective layer must be used. Corrugated outer cable sheath, attaching to the rods/inclinometer or embedded in geotextile is the most frequent method

of protecting cables (Hong et al., 2016).

Since the cables are directly exposed to aqueous conditions the water there can cause the optical fibre cable to swell or expand, which can reduce its sensitivity to external strain. Figure 3 shows the shift of frequency of an optical fibre in the presence of water. When the cable is exposed to strain, the water inside it can move and deform, which can cause the cable to absorb some of the strain energy and reduce the amount of strain that is transmitted to the optical fibre. To minimize the impact of water on optical fibre cables, various measures can be taken, such as using waterproof coatings, protective casings, and moisture-resistant connectors. In addition, some optical fibre cables are designed to be highly resistant to water, making them suitable for use in wet or humid environments (HAUSWIRTH, 2014).

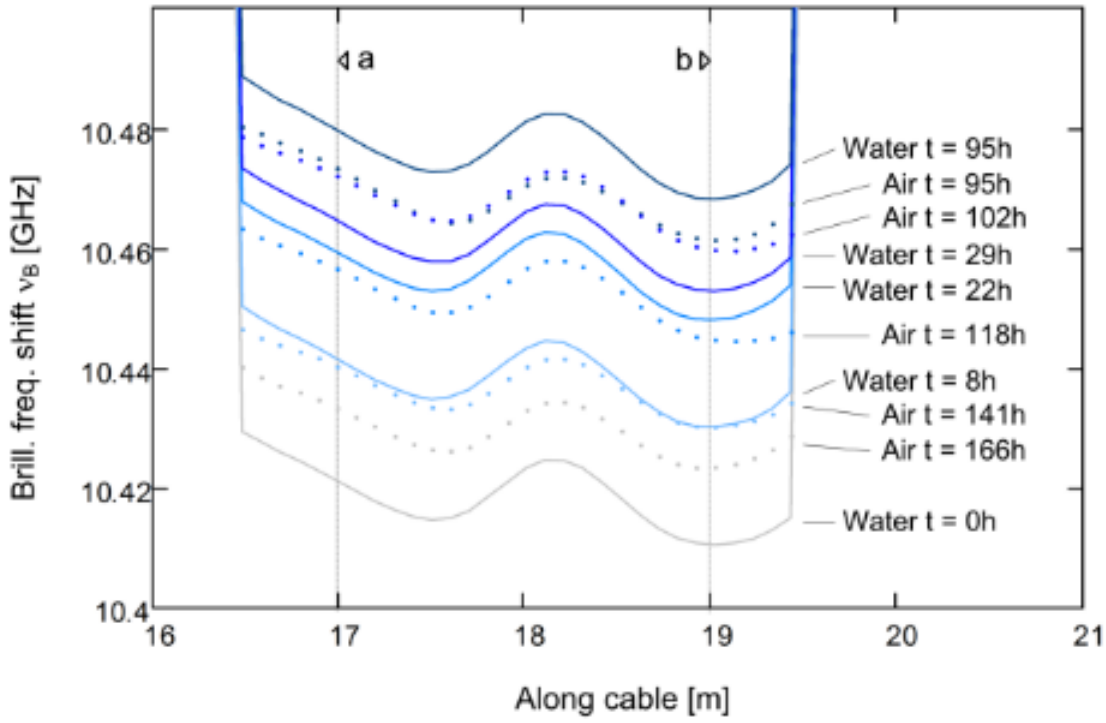

Figure 3. Frequency shift of optical fibre cable in the presence of water.

Traditionally, pressure is measured using gauges. But they include the limitations: frequent calibration, low tolerance in harsh environments (high-temperature, high-pressure, corrosive conditions), and single-point sensing. Distributed Pressure sensing comes with expressing the pressure acting on a surface in terms of strain that are induced because of pressure. The Brillouin pressure sensitivity of standard single-mode fibres has been characterized by several Authors, with slightly varying results as summarized in Wong et al. have been comparing the dynamic response and the magnitude of the pressure monitored through an optical fibre cable with a pressure

transducer to validate the performance of the optical fibre liquid pressure sensing.

Table 2. Distibuted Pressure Sensors Extracting the Measurement of Pressure-Induced Strain

Type	Fibre	Coating	Pressure Sensitivity (MHz/MPa)	Pressure Resolution (MPa)	Pressure Range (MPa)	Reference
BOTDR	SMF	Nylon	-0.74	0.467	34.5	(Méndez & Diatzikis, 2006)
	SMF	Silicone	-3.34	0.103	-	
	-	ETFE	-1.27	1.57	24	(Zhang et al., 2013)
	SMF	-	-0.91	-	25	(Le Floch & Cambon, 2003)
DAS	SMF	Tight Buffer	0.81 nε /kPa @ 0.1 Hz	40 Pa	1 KPa	(Becker et al., 2017)

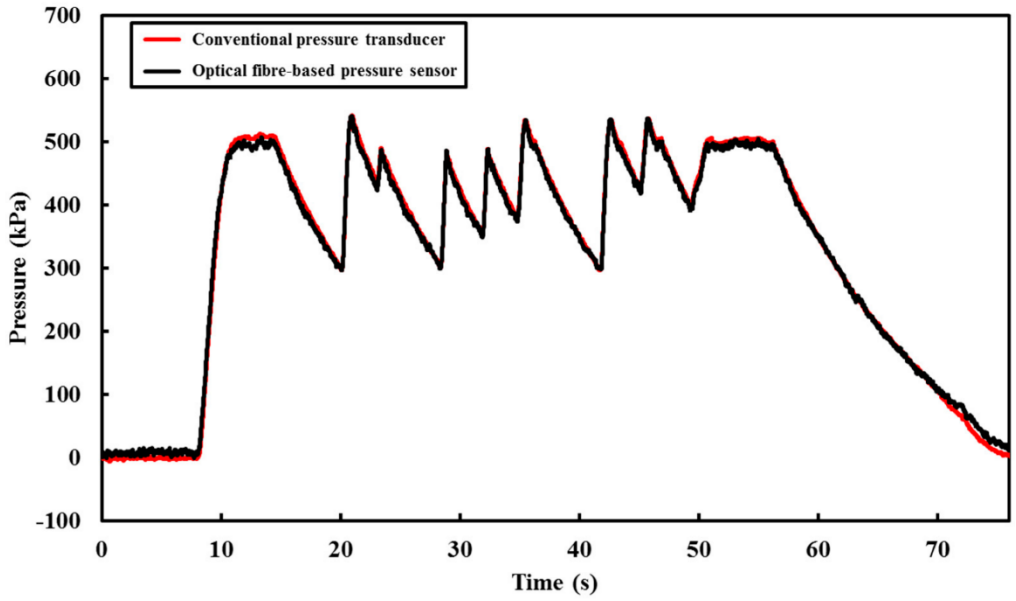

Figure 4. Comparison between the optical fibre-based pressure sensor and the traditional pressure transducer.

The results shows that the optical fibres are capable of mimicking the performance of the optical fibre cables (Wong et al., 2018). When the fibre is pre-tensioned before pressurization, the sensitivity decreases to –0.412 MHz/MPa. However, according to the studies by Wright et al., it was cleared out that this pre-strained condition would not affect the accuracy. The group has been testing water pressure using optical fibre cables which are stained with two different values yet achieved the accuracy (Wright et al., 2019).

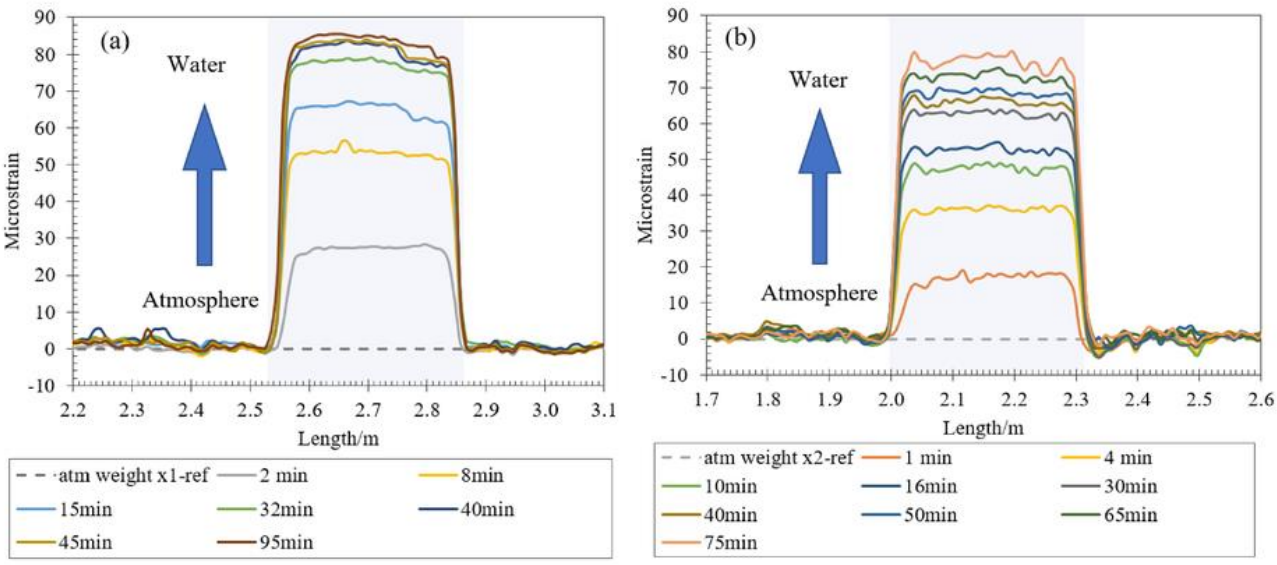

Figure 5. Strain-based water detection using fibres measured with OBR. (a): the strain of the cable with controlled strained conditions (b) the strain of the cable when the strain is twice as the previous condition.

The fibre optic cable may expand or contract as a result of temperature variations, which may alter how much strain is distributed along the cable's length. Variations in temperature might modify this distribution, resulting in mistakes or inaccurate data. A recent study shows the decrease in sensitivity when temperature increases (Aime et al., 2021).

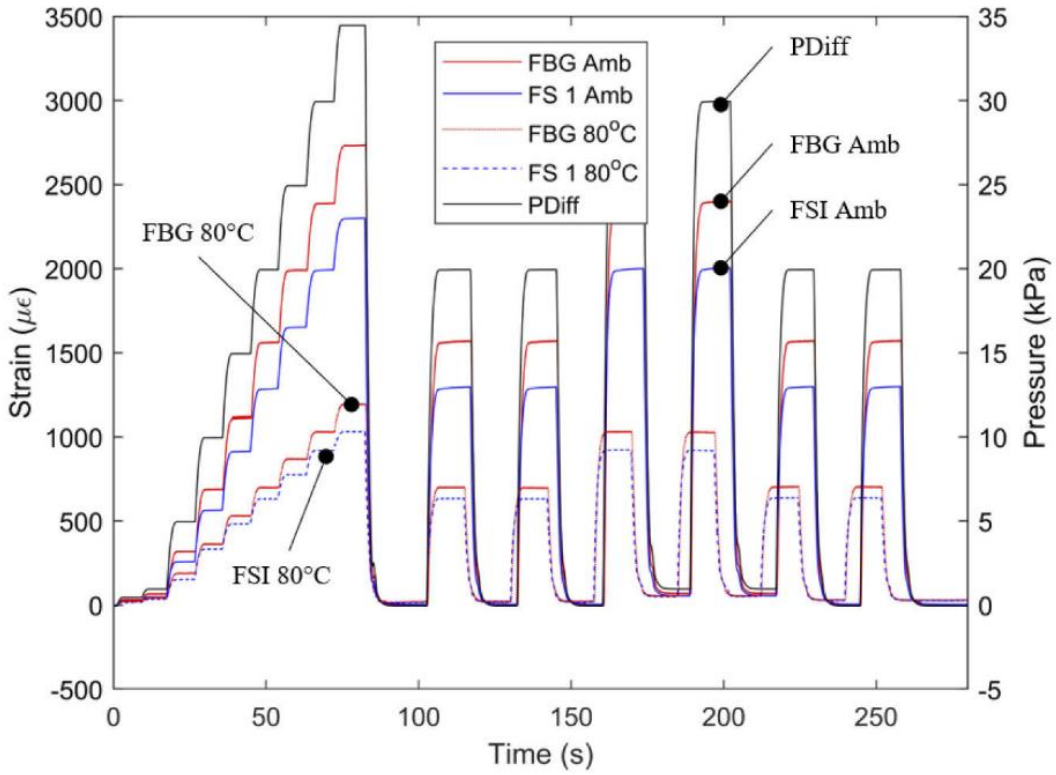

Figure 6. Pressure sensitivity measured at ambient temperature and at 80 ^{O}C.

Since the elevated temperatures and pre-strained situations have been affecting the sensitivity (not the accuracy) low strained conditions must be maintained while temperature compensation is necessary

Using of distributed optical fibres for ground motion monitoring includes,

- Soil Levees and Embankments Monitoring
- Pressure
- Temperature
- strain
- Slopes and Landslides Monitoring
- Ground Subsidence and Earth Fissure Monitoring

The possibility of using optical fibre sensors for ground motion motoring can be extracted through some recent applications. The installation of optical fibre cables along an embankment by Becker et al. has validated the use of optical fibre by identifying failure zone using the strain measurement.

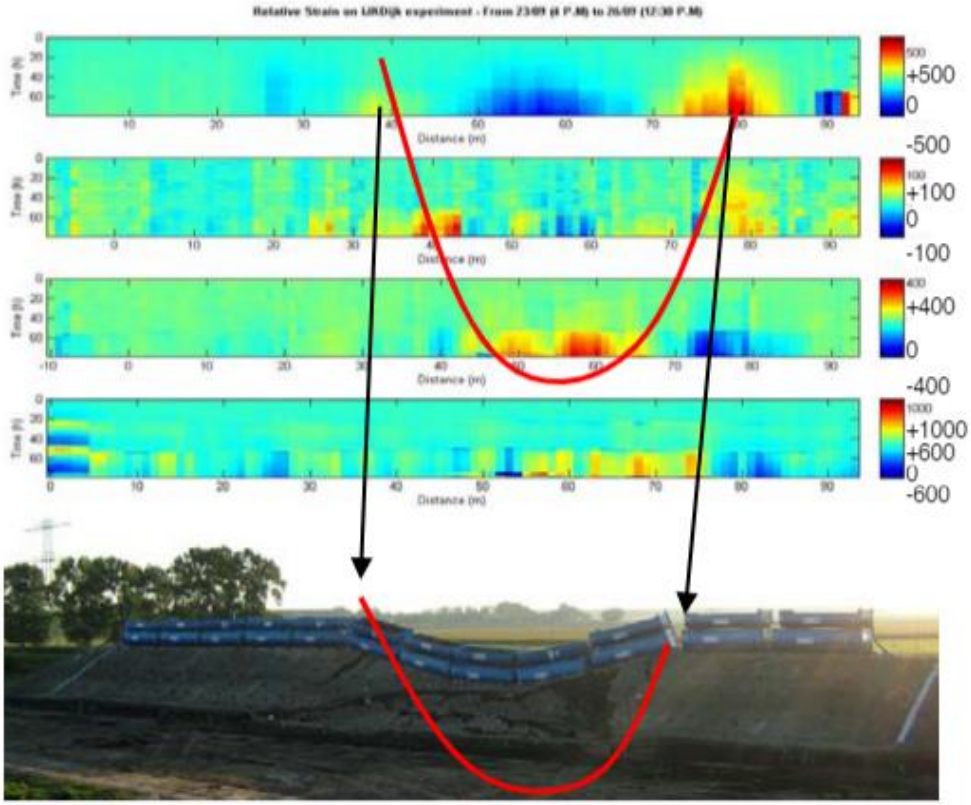

Figure 7 .The relative strain was measured on the cable 1 day before the collapse.

Furthermore Liehr et al. and Song et al. tried using optical fibres in laboratory-scaled slope models to identify the capability of forecasting slope failures (Liehr et al., 2009; Song et al., 2017).

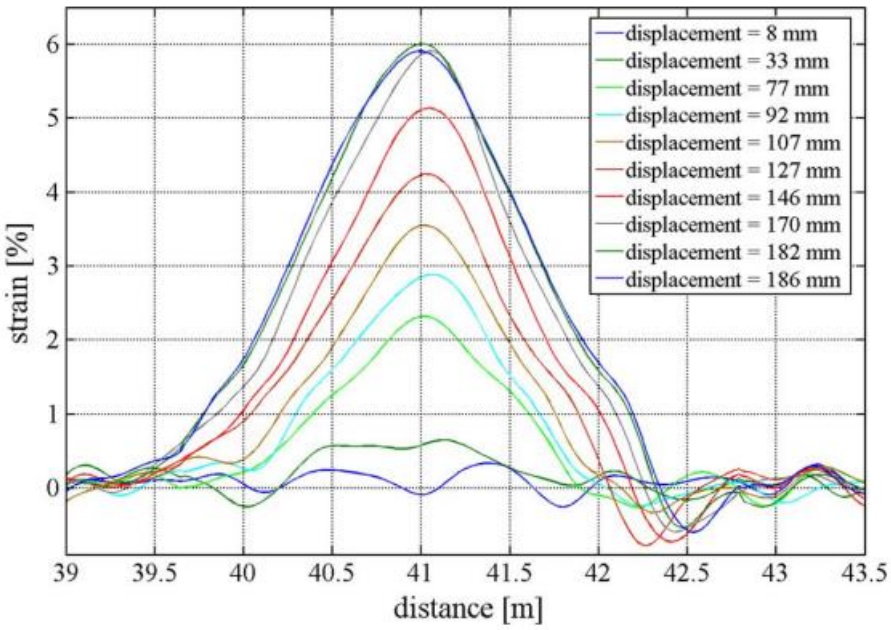

Figure 8. Calculated strain distribution for different displacements along the slope.

The most reliable implementation is the use of inclinometers together with optical fibre cables. Bednarski et al. have placed two independent lines (A and B) of 3DSensors along the 48 m section with a spacing of approximately 200 cm. Along section B, the longitudinal inclinometer was installed as a reference technique. Data from distributed optical fibre displacement sensors were analysed with 10 mm spatial resolution, The obtained raw strain data were averaged from two bottom fibres and two top fibres to increase the final accuracy (Bednarski et al., 2021).

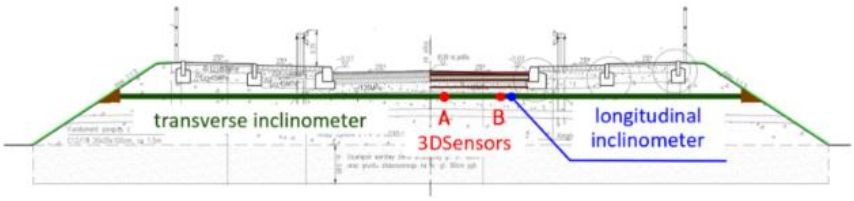

Figure 24. Cross-section of the embankment at the location of transverse inclinometer.

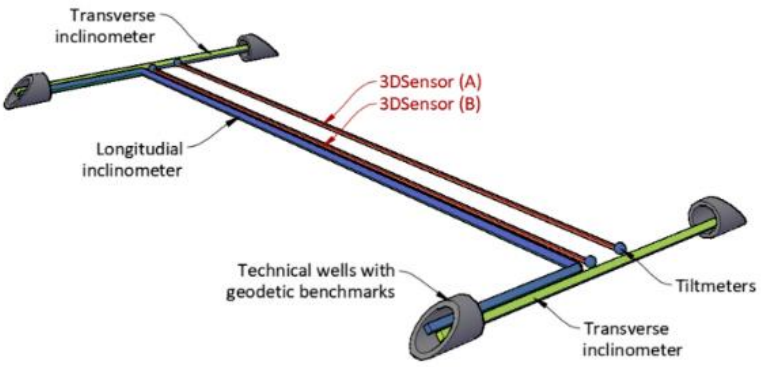

Figure 9. Visualization of the monitoring system with 3DSensors, inclinometers and technical wells.

The instances where the optical fibres are successfully identified ground motions can be summarized as in the Table 3.

Table 3. examples for optical fibres used in ground condition monitoring.

Parameter	Location/ suggested location	Measured parameter	Technology	Reference
Ocean-solid earth interactions	Buried for 2 km offshore on sea floor (a 2500 m-deep oceanic plain) 41.5 km long	Strain/strain rate	Fibre optic-based distributed acoustic sensing (DAS) Electro-optic telecommunication cable	(Sladen et al., 2019)
Earthquake	1 to 2 m below ground	Strain rate	Fiber optic-based distributed acoustic sensing (DAS)	(Lindsey et al., 2017)
volcanic earthquakes	depth of approximately 50 cm	Dynamic strain	Fiber optic-based Distributed Acoustic Sensing (DAS)	(Nishimura et al., 2021)
Landslides	60 cm below ground (in a large-scale physical model of a slope)		Distributed Optical Fibre Sensing (DOFS)	(Schenato et al., 2017)
Landslides	On the retaining wall block	Displacement and temperature	FBG and BOTDR	(Huntley et al., 2014)
Landslides	On anti-slide piles	Strain and Temperature	DOFS-BOTDA	(Wei et al., 2022)

However, the installation of fibres can be quite difficult, and it must be done with the least amount of disruption possible to the site to preserve its stability. The OFS method can be extended to simultaneous monitoring of vertical, and horizontal motion using a single cable up to a distance of 50 km with a special resolution of 5 m, while precision can be enhanced with a low diameter and lengthy inclinometers.

3.2 Experimental Plan

The experiment was developed upon the literature review. Initially a conceptual design was developed. The conceptual design was subjected to CAD simulations to identify the feasibility of each design. Upon identification of the proper design the sensor preparation was carried out with silicone rubber. The intention of the sensor preparation was to have a pressure sensing membrane with an optical fibre embed in it, so that change of curvature of that certain membrane induce a strain in the fibre. The strains were supposed to measure by backscattered spectrometer. Secondly the land motion was to convert to a

strain in an optical fibre which was mounted on a rigid structure which will follow the ground motion. To enhance the properties of the membranes nano fillers was used while making the sensors. There properties are tested with tensile testing and TGA after a certain period of exposure to underground conditions.

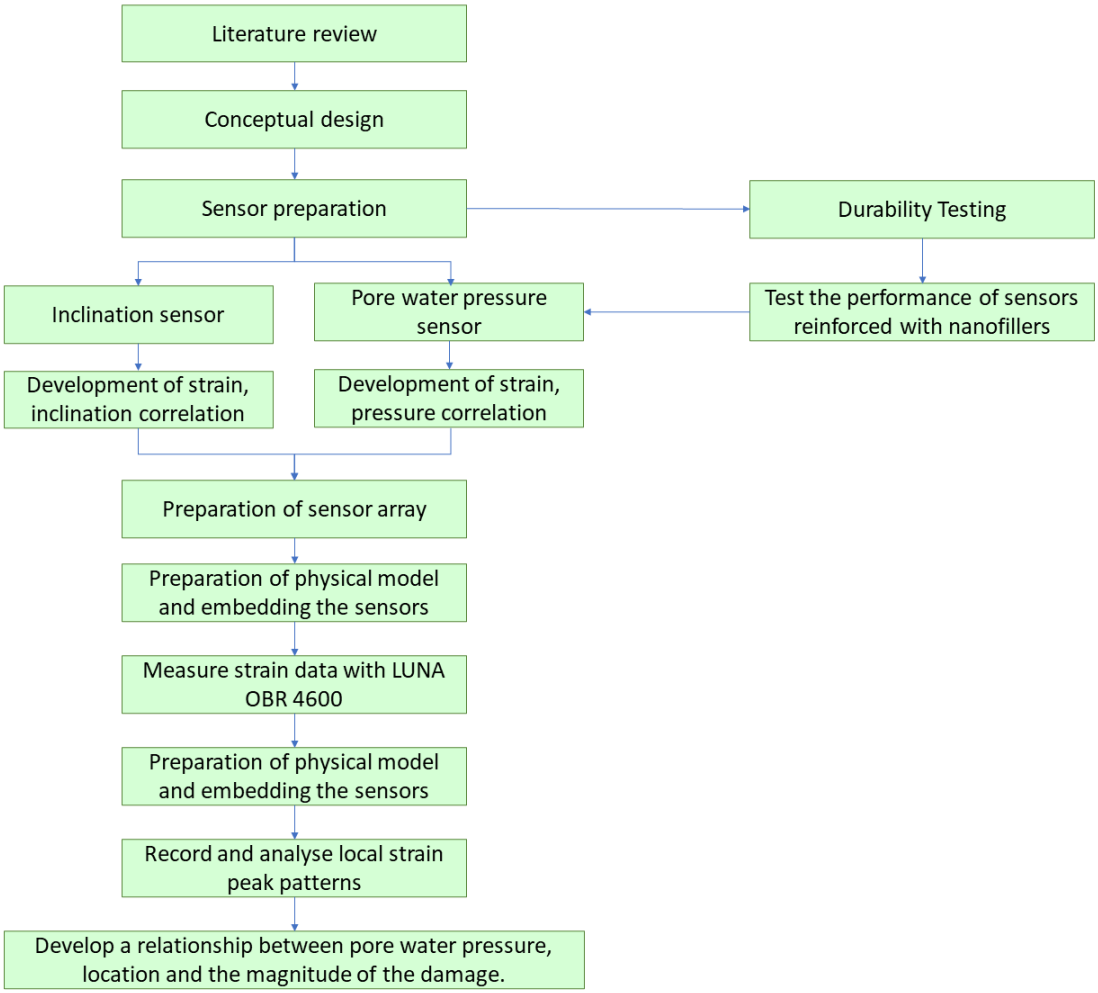

Figure 10. Experiment plan.

Three versions of sensors were built to different purposes. Sensor version 01 was to develop the corelation between pressure and the strain while the second sensor was to observe the pressure performance of membranes with different nano reinforcements and different thicknesses. The third version was to deploy in underground to measure water pressure and the ground motion.

Completing the ground implementation and the experiment the relationship between pore water pressure, location and the magnitude of the damage has been extracted.

3.3 Development of the Conceptual Framework

According to th literature the research gap was decided as:

- The real-time condition monitoring of soil using inclinometers is limited to slope stability and embankment monitoring and is geographically tested only in Chinese soil conditions.
- The improvements which are to be fulfilled when DOFS are applied to roads are not well addressed.
- The simultaneous measurement of pore water pressure and ground displacement has not been comprehensively tested yet.
- The cross relationship between the pore water pressure and the pore water pressure-induced ground motion is not examined. Thus, the type of damage is not specified.

Accordingly, two conceptual designs were drafted. The design includes simultaneous measurement of pore water pressure and deformation.

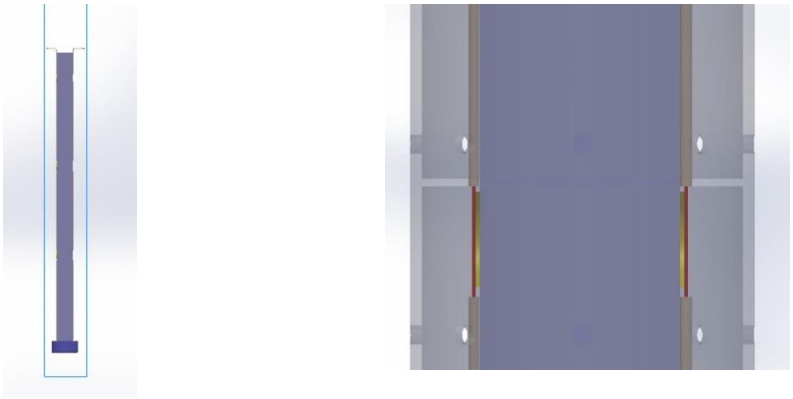

Figure 11. Conceptual Design 01

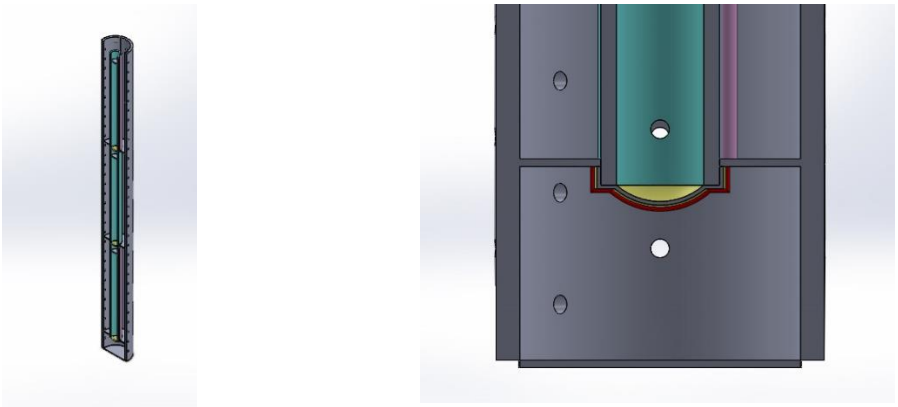

Figure 12: Conceptual Design 02

The two designs compromise optical fibre cables embedded into silicone membranes, but the pressure acting on two different ways. The conceptual design 01 compromise of vertical membranes where water pressure acts horizontally on the membrane. In design 02 the water pressure acts on the membrane in the vertical direction.

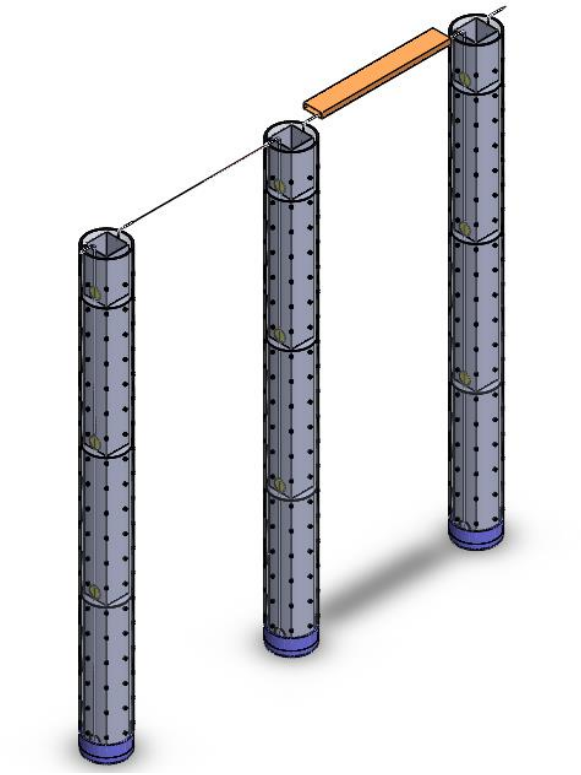

Figure 13.: Sensor Array

The sensors are decided to be placed in series. The optical fibre will measure the water pressure and the inclination simultaneously. This is achieved as fibre runs through both membranes and outer pipes.

3.4 Step 4: Real Data Assessment

3.4.1 Membrane simulation

An investigation was carried out utilizing Creo Parametric 3D CAD software to examine the correlation between strain of a silicone membrane and pressure applied in the direction of the optical fibre cable placement. The simulation was carried out on a 35 mm diameter membrane that was restrained and subjected to pressure on its mid-section (22 mm, the same diameter as the hole of the aluminium bar in the actual experiment setup). The pressure exerted on the membrane was gradually increased from 1 kPa to 10 kPa, with a step of 1 kPa; this is equal to a hydrostatic pressure of a water column of 1 m to 10 m, with a step of 1 m. The outcome of the study will enable a better understanding of the

strain and pressure relationship in silicone membranes and thus will facilitate the design of more efficient and accurate optical fibre cables.

3.4.2 Membrane preparation

To create the pressure sensing membrane, we mixed a 2-part silicone (RTV 586) with 2% curing agent by weight. This type of silicone is highly elastic, meaning it can stretch and deform under stress but will return to its original shape when the load is removed. This elasticity allows the membrane to withstand repeated compression and elongation without permanent deformation. By adding 2% hardener, we maintained the membrane's tensile strength at 2.28 MPa. We then placed SMF 28 125 µm single-mode bare optical fibres in moulds, positioning them in the midplane of the membrane, and poured the silicone into the mould.

To remove any trapped air, the moulds were placed in a vacuum oven at -0.08 bars for two minutes at room temperature. The silicone-filled moulds were then sandwiched between two glass plates and left to press for 24 hours.

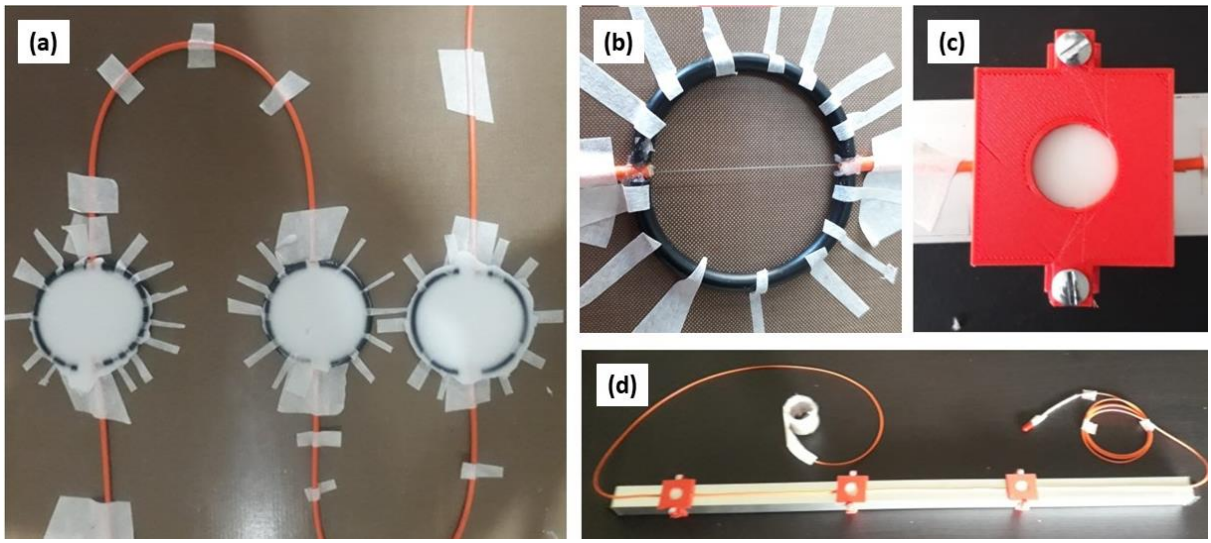

Figure 14. Fabrication process of sensors (a) dried silicone rubber membranes in the moulds (b) bare optical fibre cable before pouring silicone rubber (c) silicone rubber membrane tightened to the aluminium bar (d) fully fabricated sensor array.

Following this, sensors were affixed to a hollow aluminium box bar. The bar has a 22mm hole located behind the membrane to allow for expansion, and the edges of the box bar were sealed to keep atmospheric pressure consistent and prevent water leaking in.

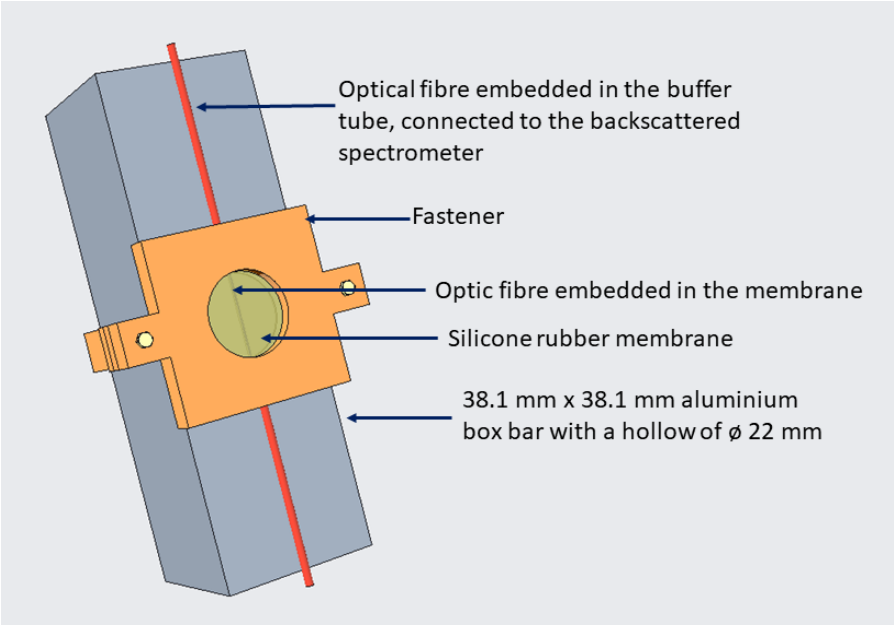

Figure 15. Pressure sensing element mounted on the aluminium box bar

Sensor versions

Three different types of sensors were developed to examine the performance of the silicone membranes in the presence of water pressure. The sensor version 01 consists of 100% silicone membranes fixed 300 mm apart. The sensor was developed to identify the variation of strain induced due to the water pressure at different heights. A hollow aluminium box bar (38.1 mm x 38.1 mm x 1000 mm) was used as the mounting surface. Hollows of 20 mm diameter were drilled 300 mm apart. The silicone membranes (ø35 mm x 3 mm) with optical fibre cable embedded in it was mounted and fastened.

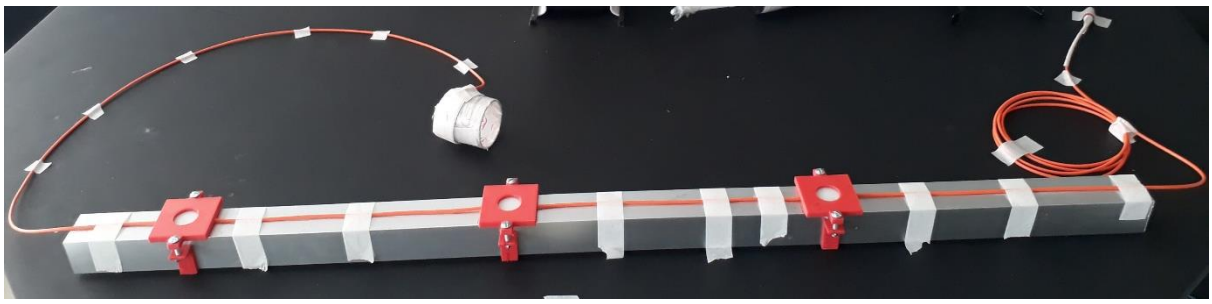

Figure 16. Sensor Version 01

Th sensor version 02 was developed to examine two factors: the strain behaviour of the membrane.

i. when it is reinforced with a nano material.
ii. when the thickness of the membrane is changed

The nano materials used as reinforcing materials are:

i. Graphene oxide

ii. Reduced Graphene Oxide

iii. Graphite

iv. Carbon Black

The process of making the nano material reinforced membranes started with measuring 2% of nanofiller by weight. For each gramme of silicone addition of 1 ml of ethanol to the nanofillers. Then the mix of nanofillers and ethanol were sonicated for 30 minutes. In the next stage silicone rubber was added and mixed for 1 hour. The well mixed sample was placed in the vacuum oven at 80 ^{0}C and at -0.08 bars for 3 hours. It is expected that all the ethanol to be evaporated at the end of that period. Taking out of the oven it was let to cool down overnight to the room temperature. Reached the desired temperature 2% of the hardener was added and mixed well.

Meanwhile the membrane moulds (ø 3.5 mm x3 mm and ø 3.5 mm x 1.5 mm) were placed on PTFE adhesive clothing secured glass plates. The Optical fibre cable is placed across the mould. Then the prepared silicone rubber was poured into the moulds. The silicone filled moulds were placed in the vacuum oven for 2 mins at -0.08 bars, so that any trapped air bubbles will explode, and the liquid silicone rubber would spread evenly. Taking out of the oven they were Compressed with the other glass plate.

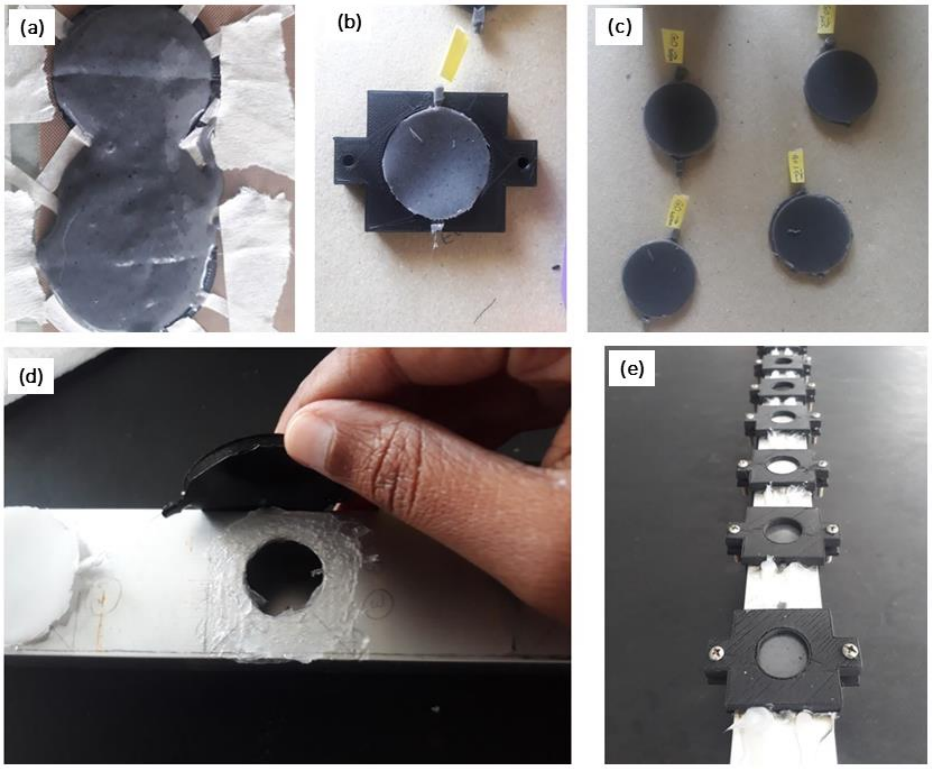

Figure 17. Fabrication of sensor version 02. (a) silicone rubber with nano fillers poured into moulds. (b) cured silicone membrane fixed into a fastener (c) silicone membrane with 2 thicknesses (d) membranes before fixing in to the aluminium box bar (e) fixed membranes to the aluminium box bar.

The aluminum bar was then enclosed in a ø 90 mm PVC tube. The pipe can be fixed to a vertical water column that can cause a water pressure. Since the sensor is placed horizontally the same pressure would be affecting on each membrane.

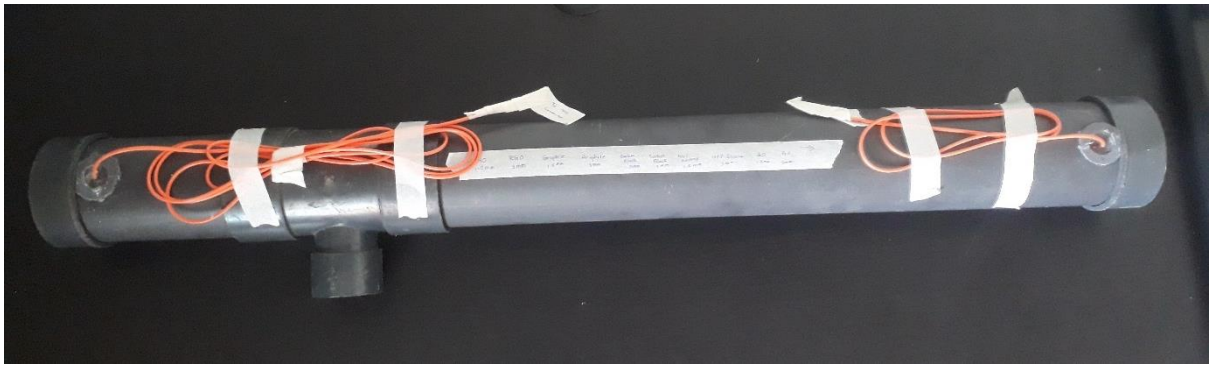

Figure 18. *Completed sensor version 02.*

The sensor fabrication was followed by the tensile test and TGA conducted each sample and 100% silicone. The sensor version 3 was designed for the final field testing. This was extended to measure both inclination of soil and underground water pressure. The preparation of the water pressure of the sensor version 03 follows the procedure followed by the sensor version 01. After analysis of the elasticity of each membrane material for the final sensor membranes were made from 100% pure silicone rubber and silicone rubber reinforced with 2% graphite.

In the sensor version 03 the membranes were mounted on the aluminium hollow cubes and those cubes were mounted again on ø 25 mm PVC pipe (as mentioned in the annex). It was designed such to follow any deformation that can happen due to soil motion. The array of sensors was later placed inside ø 90 mm PVC tube. The tube is drilled at certain intervals to water to seep inside and from inside it is separated into several compartments. So that water filled in each compartment does not flow to another.

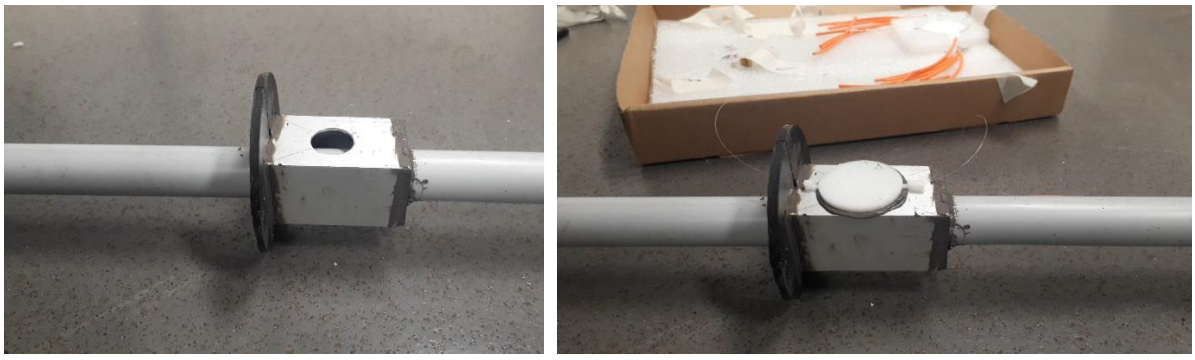

Figure 19. Preparation of the sensor version 03.

3.4.4 Durability Test

Since the literature suggested that the behaviour of silicone rubber can get affected by underground conditions, their changes in those conditions were to be monitored. Accordingly, the silicone rubber reinforced with nano materials and pure silicone were exposed to ground conditions. The nano fillers used as reinforcement were:

i. Graphite

ii. Carbon Black

iii. Reduced graphene oxide

iv. Graphene oxide

Figure 20. (a) Silicone Rubber with 2% Reduced Graphene Oxide

Figure 21. Silicone Rubber with 2% Carbon Black

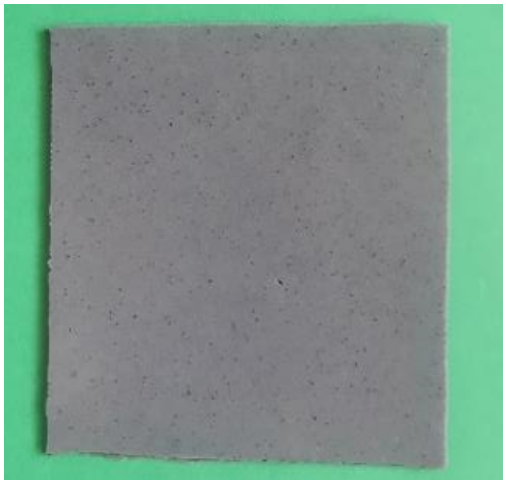

Figure 22. Silicone Rubber with 2% Graphene Oxide

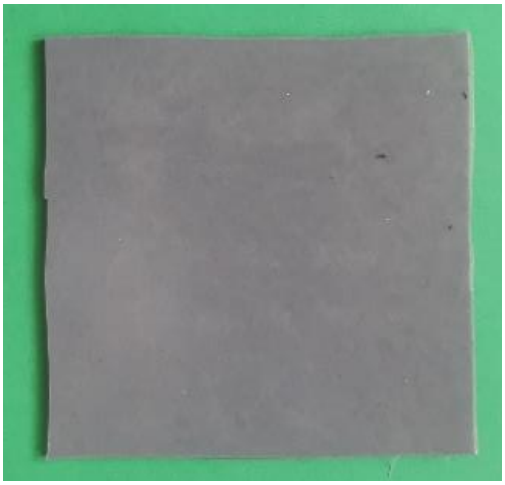

Figure 23. Silicone Rubber with 2% Graphite

The preparation of each sample included following steps:

- Measuring 2% of nanofiller by weight

- For each gramme of silicone addition of 1 ml of ethanol to the nanofillers
- Sonicating for ½ hour
- Addition of silicone rubber and mixing for 1 hour
- Placing in the vacuum oven at 80 ^{0}C and at -0.08 bars for 3 hours.
- Taking out of the oven letting it cool down overnight.
- Adding 2% of the hardener and mixing well
- Pouring silicone rubber into the glass plate in between moulds
- Compress between two glass plates and curing of 24 hours.

The prepared samples underwent the tensile test and TGA analysis. The tensile test was carried out according to IS0 37 standards. The rubber samples were cut in to dumbbell shapes and used as specimens. The test was carried out using universal test machine with a 5 Kn load cell. The investigated properties include 100% modulus and the elongation at break.

A thermogravimetric analyzer (Perking-Elmer TGA 4000, USA) was used to study the thermal stability of the Silicone rubber samples. The experiment involved heating the samples under nitrogen purging from 50 ºC to 550 ºC, followed by switching to oxygen purging at 550 ºC and heating up to 800 ºC. The temperature ramp remained consistent at 100 ^{0}C/min throughout the entire temperature range.**Table 4.** Concentrations of the Solutions Made

Chemical	Solubility in Water (g/l)
$CaSO_4$	10
$MgSO_4$	10
$CaCO_3$	10 (A saturated solution)
$MgCO_3$	10 (A saturated solution)
$CaCl_2$	10
NaCl	10

Table 5. Conditions of the Solutions Made

Solution		pH value
High pH	NaOH	10
Low pH	H_2SO_4	3
Neutral	Deionized water	7

Once the samples were prepared, they were exposed to selected compounds which were frequently found in ground water, microbial environment of soil and different Ph conditions. To mimic those conditions several solutions are made.

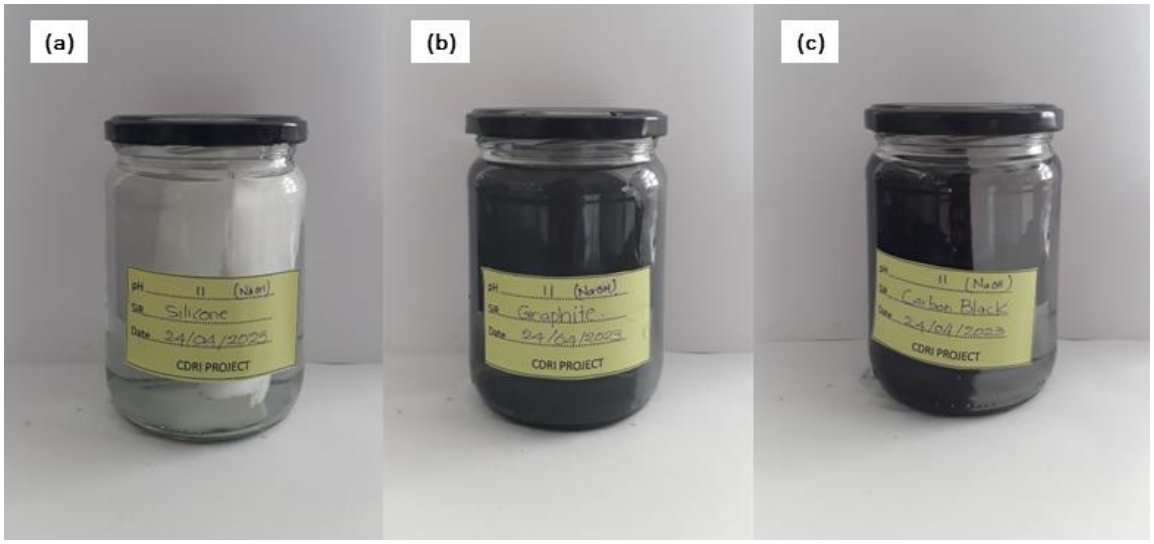

Figure 24. Silicone rubbers exposed to high pH conditions(a) pure silicone rubber (b) silicone rubber reinforced with Graphite (c) silicone rubber reinforced with carbon black.

The above samples are expected to be kept in artificial soil conditions for 100 days and will be followed by tensile test, TGA, and SEM imaging.

3.4.5 Laboratory scale testing

The silicone samples and silicone rubbers with nano fillers were tested for tensile tests and TGA at the laboratory facilities od Rubber research institute of Sri Lanka. The sensor version 01 was tested to examine the behaviour of it against water pressure. The array of sensors is placed in a vertical tube and water was filled at 1 litre a time, meanwhile the respective strain measurements are recorded.

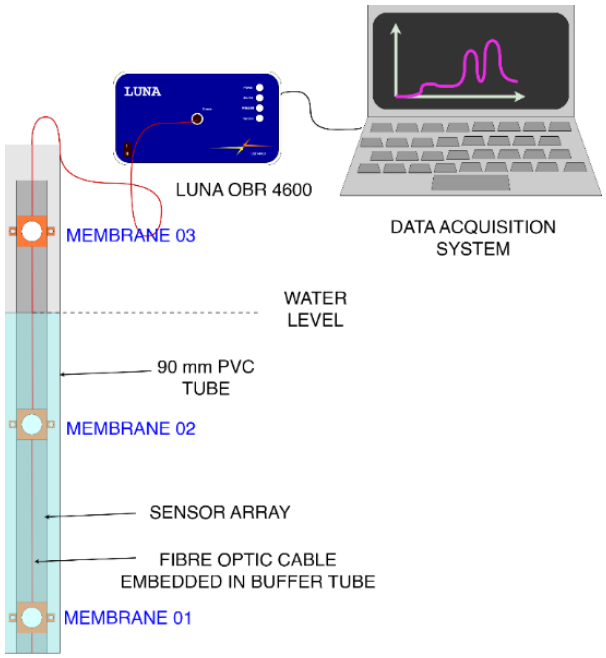

Figure 25. Test setup used to examine the strain behaviour of silicone membranes at different heights.

In the process of acquiring data, the Luna OBR 4600 was set to a scan range of 1555.870 - 1577.155 nm. The system specifications feature a group index of 1.5, spatial resolution of 1 mm, and a gauge length of 10 mm.

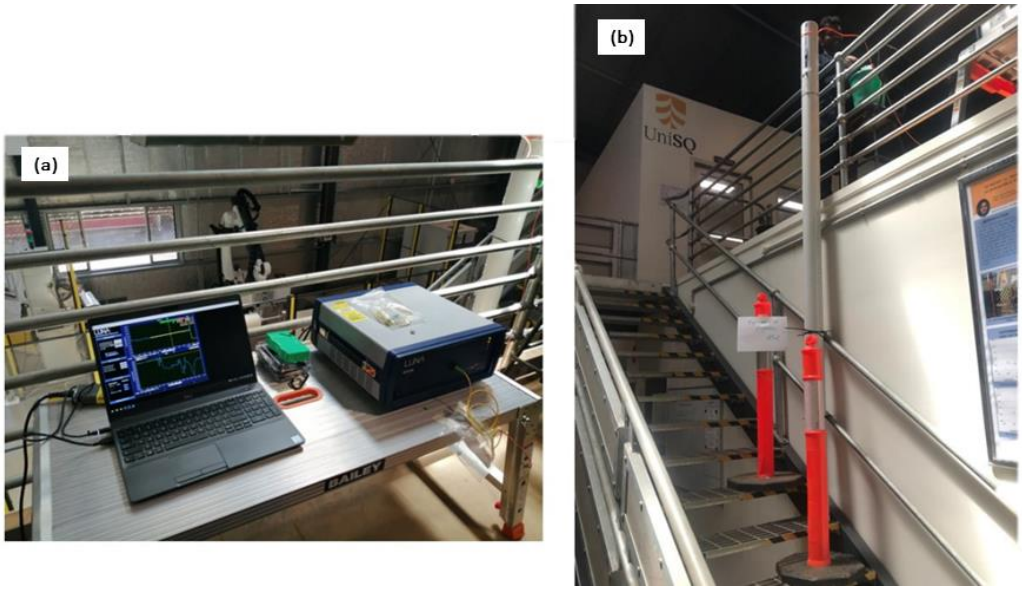

Figure 26. Laboratory testing of sensor version 01 (a) data acquisition system (LUNA OBR 4600 and the software interface) (b) sensor version 01 enclosed in the PVC tube.

The outer casing of the sensor version 03 is to be tested to correlate the strain and the deformation. The pipe will be fixed at one end and will be loaded on one end so that it will mimic the field setup. Then the fibre along the pipe will be connected to the LUNA OBR 4600 and then the deformation will be measured against the stain.

Physical Model Preparation and Testing

To examine the behaviour of the sensors in the real environment the sensor version 03 will be implemented in the ground conditions. Accordingly, the ground has been excavated as depicted in the annex.

Figure 27. Before and during excavation (8th June 2023)

Figure 28. After excavation and bore hole drilling (8th June 2023)

The sensors will be deployed in the two bore holes which are 200 mm diameter and 2 m deep. The fibres are mounted on the pipe and for the horizontal placement, the fibres will be mounted on adhesive bituminous tapes. The end of the fibre will be connected to the LUNA OBR 4600.

The sensors will be fixed at the end of the bore hole with concrete and the space between the sensor and the bore hole will be filled with gravels. The water lines will be placed along the borehole to water pressure.

The bore holes are enclosed at a height of 2 m so that the water will be kept pressured in the bore hole. Filling the soil back to the excavated area the soil will be compressed with a plate compressor. During the process, the strain readings will be recorded.

4. Results and Discussion

4.1 Development of the Conceptual Framework

4.1.1 Simulation Results

Using the CAD simulation, the corelation between the pressure and the strain was extracted. The figure below depicts strain variation along the membrane in YY direction. The negative values stand for compressions which are expected around the constrained area while the maximum positive strain in achieved in the midpoint of the membrane.

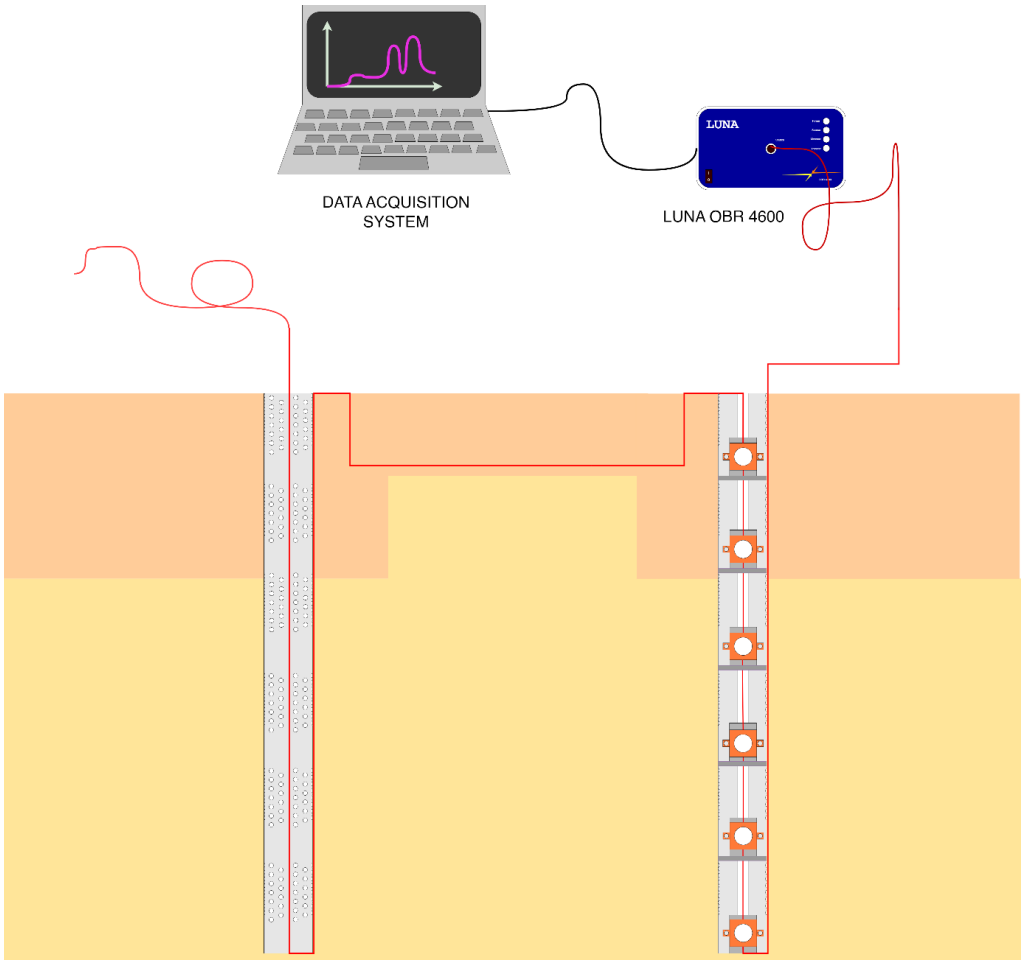

Figure 29. Experiment setup for field testing of sensor version 03.

To extract the relation between the pressure and the strain the pressure at the midpoint of the membrane was graphed against the respective strain. As depicted in the following figure, the strain experienced by the material exhibited a linear relationship with the applied pressure. This highlights the potential of using optical fibres to sense pressure based on strain.

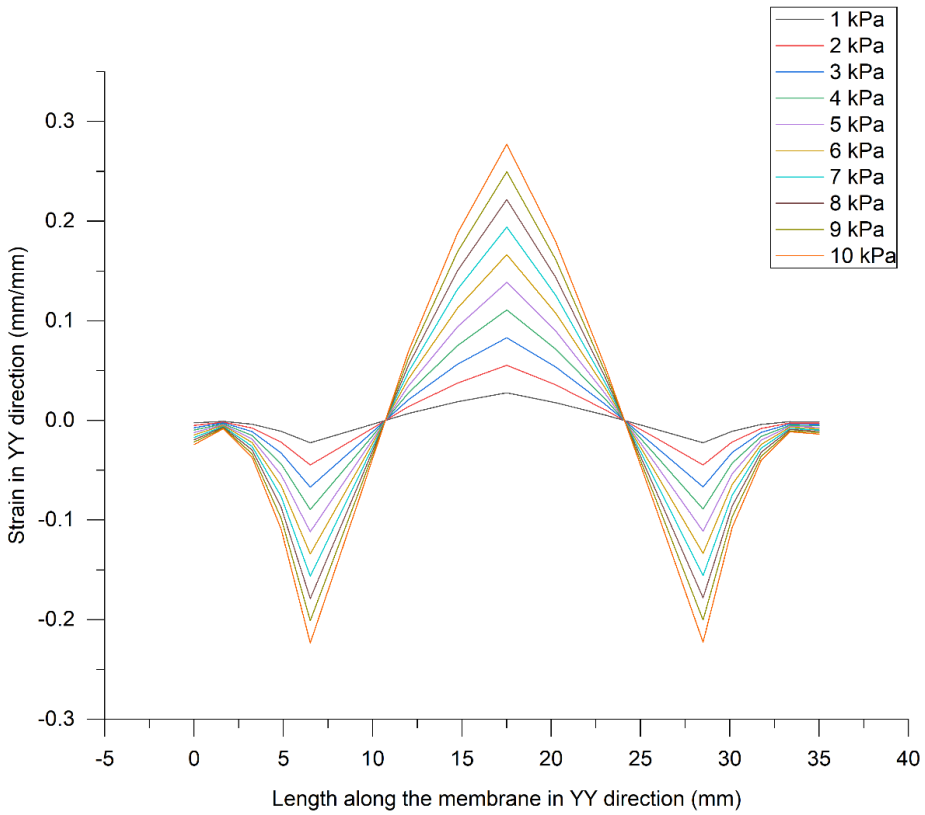

Figure 30. Simulated pressure variation along the membrane from 1 kPa to 10 kPa.

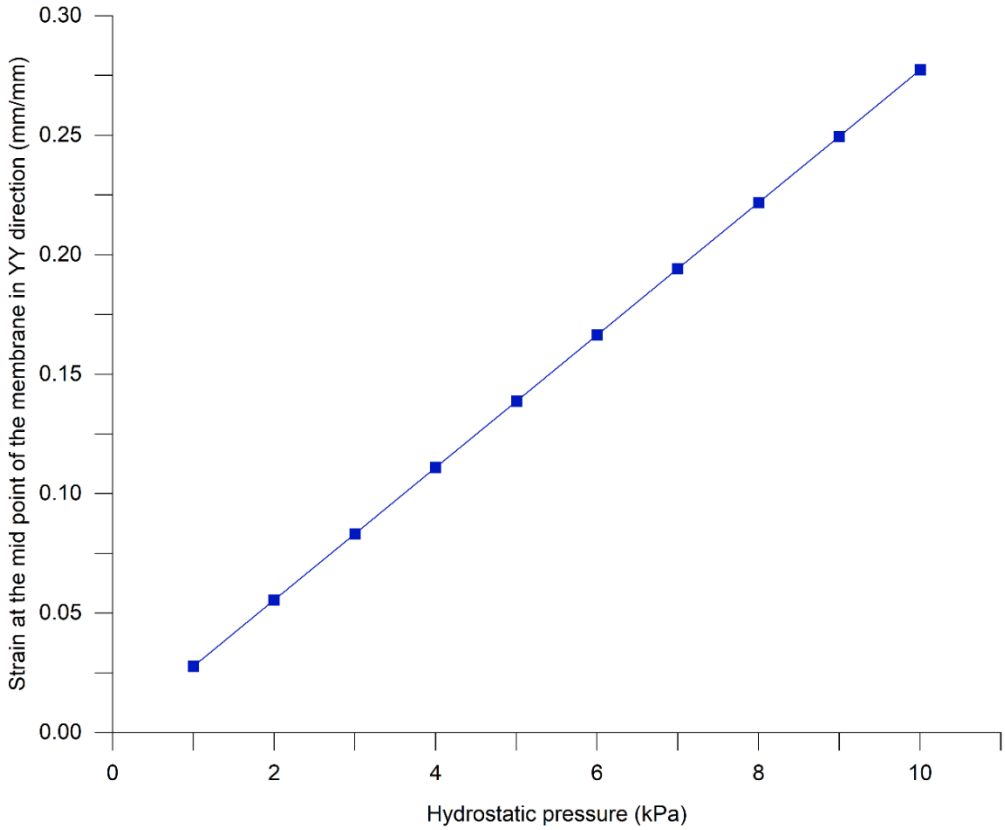

Figure 31. Correlation between pressure and the midpoint strain.

4.1.2 Durability Test

As discussed in section 3.4.4 silicone samples reinforced with nano materials were tested for their durability in underground conditions. Their initial properties were recorded before the exposure to underground conditions was given.

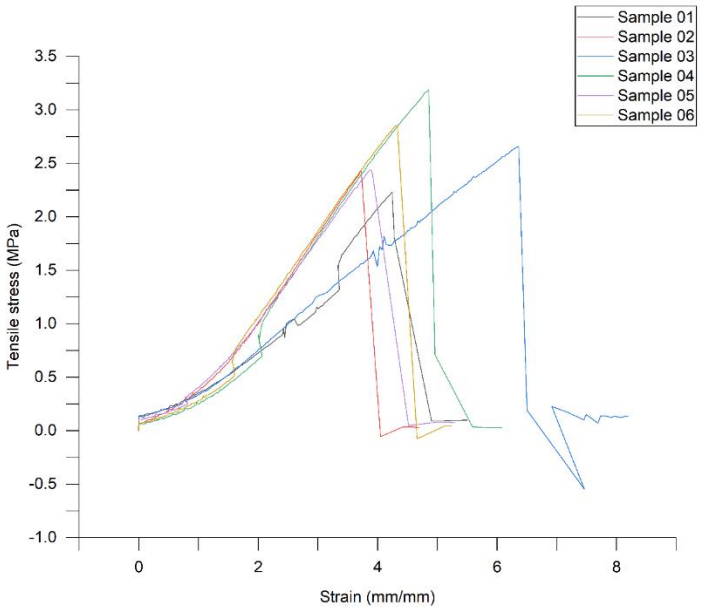

Figure 32. Tensile test result for silicone rubber.

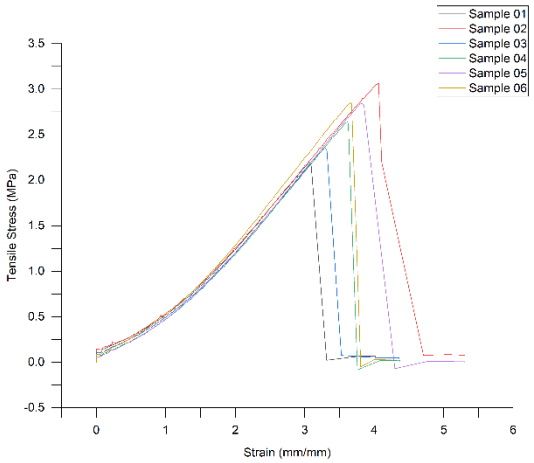

Figure 33. Tensile test result for silicone rubber with graphene oxide as the filler material

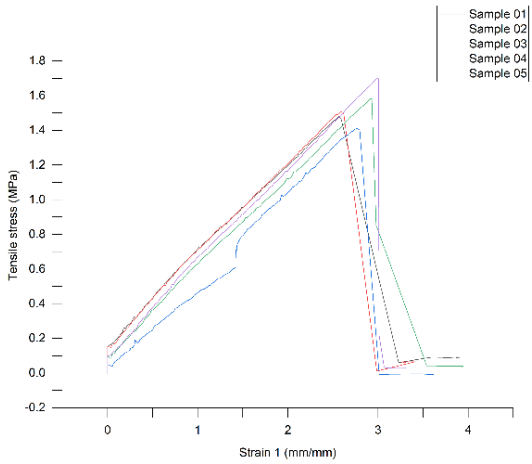

Figure 34. Tensile test result for silicone rubber with reduced graphene oxide as the filler material

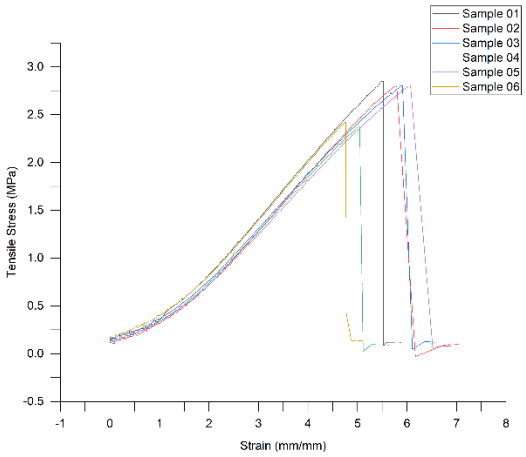

Figure 35. Tensile test result for silicone rubber with carbon black as the filler material

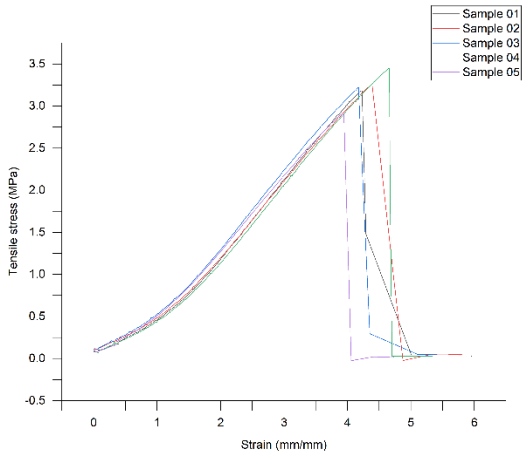

Figure 36. Tensile test result for silicone rubber with graphite as the filler material

The tensile properties for each sample of silicone rubber can be summarized as in the Table 6. As the table indicates Silicone rubber reinforced with graphite nano fillers demonstrates the best performance with a tensile strength of 3.2 MPa other than all the other sample with similar amount of filler loading. That exhibits the potential of using graphite as a reinforcement material for silicone rubber when high tensile strength is expected. It justifies the assumption that the addition of nanofillers except reduced graphene oxide has increase the tensile properties of silicon rubber since all the samples has increased their tensile strength more than neat silicone rubber sample.

The thermal stability of the silicone rubber samples was investigated with TGA. The results of the test are as illustrated in the **Figure *37.*** TGA results for silicone rubber and silicon rubber reinforced with nano *Figure 37*. As mentioned in the Figure *37* the TGA curve exhibit two main weight loss events. The initial weight loss up to 300 ^{0}C represent the initial weight loss of moisture. The weight loss between 300 0C and 500 0C stands for the thermal decomposition of silicone rubber samples. Through the TGA curve the decomposition temperature and the subsequent weight loss for each sample was extracted as mentioned in the *Table 7*.

Table 6. Tensile Properties of nanofiller loaded silicone rubber.

Silicone Rubber	Tensile strength (MPa)	Modulus at 100% (M100) (MPa)	Elongation at break (EB) (%)
SiR-CB	2.68	0.35	550.36
SiR-RGO	1.54	0.64	277.19
SiR-GO	2.66	0.50	358.57
SiR-G	3.20	0.48	427.15
SiR	2.63	0.33	456.48

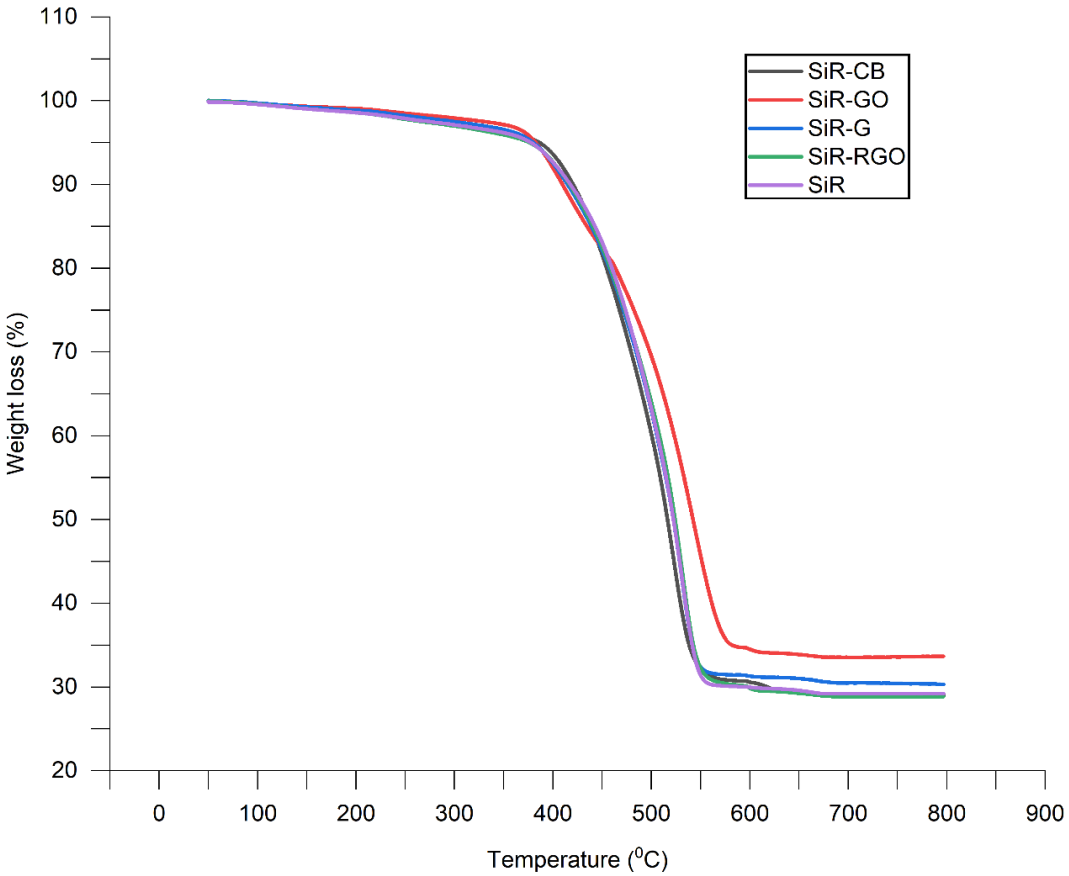

Figure 37. TGA results for silicone rubber and silicon rubber reinforced with nano fillers.

Based on the TGA data, it can be stated that SiR-GO possesses the highest thermal stability among the silicone samples tested. This can be proven by its highest onset degradation temperature. However, SiR-GO also exhibited a relatively high weight loss at the onset temperature, exhibiting a rapid initial degradation.

Table 7. Summary for the thermogravimetric analysis of silicone rubbers

Silicone Rubber	Onset Degradation temperature (^{0}C)	Weight loss at onset temperature (%)
SiR-CB	456.76	93.893
SiR-RGO	466.84	94.68
SiR-GO	459.41	95.047
SiR-G	465.72	93.383
SiR	465.76	94.044

SiR-CB and SiR-G demonstrated lower thermal stability compared to SiR-GO, meanwhile SiR-G showing the lowest onset degradation temperature. However, the weight loss percentages for SiR-CB and SiR-G were comparatively lower, indicating a slower degradation rate at the initial stages. SiR-RGO and SiR exhibited intermediate thermal

stability, with moderate onset degradation temperatures and weight loss percentages. The time period of 100 days will be reached on 02nd August 2023. So that the samples can be examined under tensile test, TGA and SEM imaging.

4.1.3 Laboratory Scale Testing

During the lab experiment to identify the pressure strain behaviour the strain data was extracted with the backscattered reflectometer while filling the water in the outer tube. From the long fibre the optical fibre span was reduced to the length of the sensor array and the strain induce on the optical fibre cable by the water column was extracted. The extracted data is depicted in the graphed as below. The peaks can be clearly seen form three discrete points as the water column height was increased.

When the water column height rises, the pressure on the membrane also increases. Each subsequent peak has a higher value than the previous one for that reason. The membrane 01 displayed the largest elongation due to maximum hydrostatic pressure compared to others.

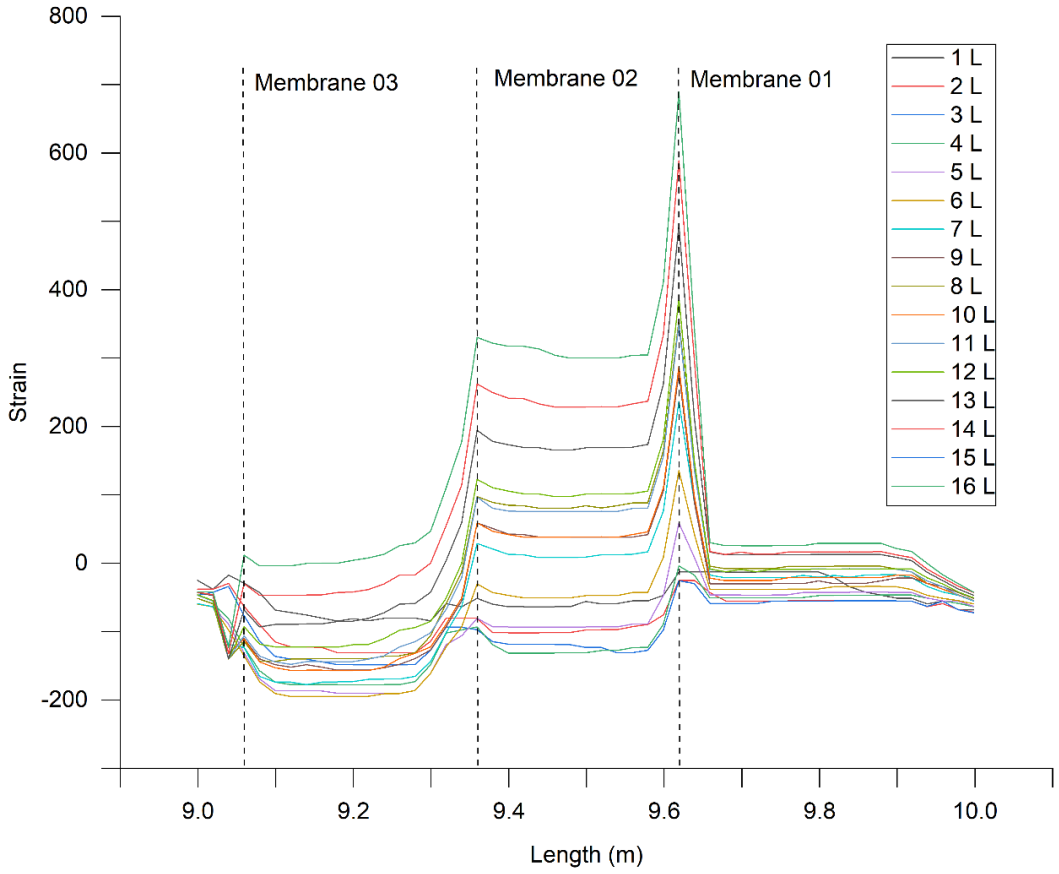

Figure 38. The strain induced in each membrane with respect to the volume of water filled.

The tension experienced during hikes is caused by the stretching of the fibre between two adjacent membranes. The pressure at each membrane was calculated by converting the

volume of the water column to its corresponding height. Considering the midpoint of the membrane 01 in YY direction, readings for the strain behaviour with respect to the hight is graphed in the figure 34. As the height and the hydrostatic pressure shows a linear relationship for fluid with constant density the, the pressure follows the same curve for fluids with constant density and gravitation acceleration, relationship between height and hydrostatic pressure is linear. Hence the pressure follows a consistent curve as height at all point.

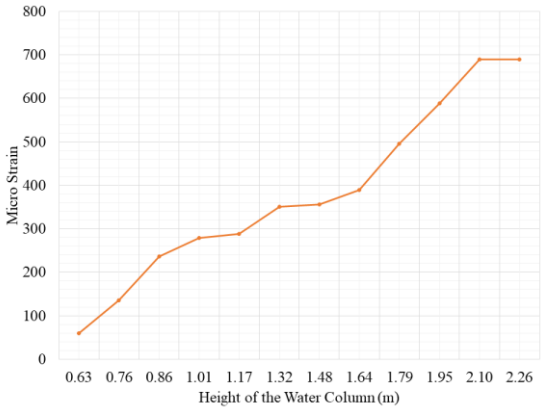

Figure 39. The relationship between the height and the strain.

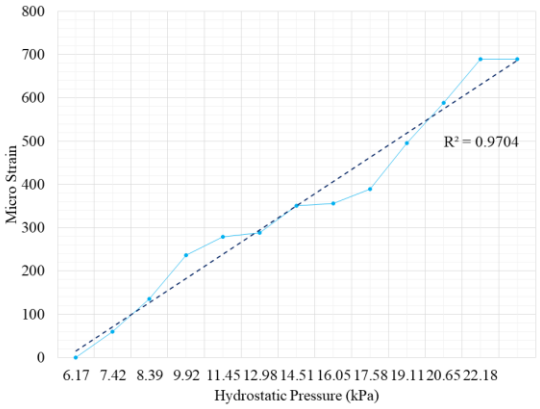

Figure 40. The relationship between the hydrostatic pressure and the strain.

Considering the strain induced in the optical fibre cable as the independent variable and the magnitude of the pressure as the independent variable a linear regression model has been developed as depicted in the figure 9. According to the linear regression model the R^2 being equal to 0.9704; approximately 97.04% of the variance in the dependent variable is explained by the independent variables in the model. The model has demonstrated a remarkable ability to capture a substantial portion of the data's variability and exhibit powerful predictive capabilities, as evidenced by the high degree of goodness of fit.

4.1.4 Field experiment

The field experiment will be conducted on 5th July 2023 and the behaviour of sensors in the presence of ground water pressure will be measured simultaneously with the inclination.

5. Enablers and Barriers

Table 8. Enablers and barriers for the project

Enablers	Barriers
The DOFSs have the ability to lay in the subterranean, along a road for long distances and measure spatially distributed sensor data accurately.	Laying of DOFSs can be simply done during the construction of a road and it is challenging to install the sensors in existing roads without interrupting the traffic.
Optical fibre cables a light weight and easy to handle. If a cable breaks during installation and under operation it is possible to splice and repair.	Installing sensor system and laying the cables are delicate works that required trained professionals for road development.
The protected optical fibre is resistive to soil conditions and those are also being used at telecommunication cables at present. The materials used to fabricate the sensors are selected by considering their performance during their operation.	During the long service life, the sensors can be degraded as optical fibres and critical components such as diaphragms and protection tubes will be exposed to various geological conditions.
The proposed sensors are designed in modules and therefore it is simple to replace the sensors during a malfunction.	The replacement of sensors required time to install and make the connection to existing optical fibre.
The operational cost of the proposed system is significantly low compared to the alternative methods. Once the sensors are installed the measurements can be obtained from a remote location. Optical fibre cables and other materials are readily available in the market to fabricate sensor.	Capital investment for the optical backscatter reflectometer is high compared to the alternative measuring equipment.

6. Key Takeaways from CDRI Fellowship Programme

The smart sensors and real-time condition monitoring systems intended for damage detection, localization, classification, quantification and prognosis of road infrastructure are crucial requisites for climate and disaster-resilient transport. The CDRI fellowship programme directly benefited to provide an advanced engineering solution to an exciting challenge face by the highway engineers and researchers.

The proposed distributed optical fibre-based sensor system can acquire data throughout the road for a long-distance, which is incapable of discrete sensing systems. The optical fibre sensors can be located underneath the road during its construction and a

continues optical fibre cable can be used measure multiple parameters such as porewater pressure and horizontal and vertical ground motions. Variations to the road's condition and potential failure modes can be identified at the early stage of a collapse. The technical feasibility of the proposed solution has been proven through laboratory and field experiments. The proven technology can be scaled up and be implemented for newly constructing roads.

The CDRI fellowship program benefited both Uva Wellassa University, Sri Lanka and University of Southern Queensland, Australia enhance the research and development on disaster and climate resilient infrastructure. Moreover, fellowship supported a postgraduate degree in the field of disaster resilient infrastructure and that enabled an academic exchange programme between the two universities. The team members could enhance their research carrier perspectives towards DRI.

7. Conclusion

This research provided an engineering solution for condition monitoring of roads that are probable to collapses due to pore water pressure and ground movements. Herein a distributed optical fibre based three in one sensor was designed and developed. The sensor consisted of three key segments that can measure pore water pressure, horizontal and vertical ground motions. The porewater pressure measuring performance and calibrations were tested under the laboratory. The performance of the entire sensor will be tested under the physical model that is constructed to date. The following conclusions are made.

- The silicon diaphragm embedded DOFS has the potential to precisely measure pore water pressure, and it was revealed that the measured strain readings are proportional to the applied hydrostatic pressure.
- Incorporation of graphite has enhanced the tensile strength and elastic modulus compared to the parent silicon material. Three different sample are exposed to nine different geo-based conditions and the degradation and tensile property reduction due to long term exposure is yet to be studied.
- The real-time measurements indicating the combined subterranean conditions of the roads can be obtained frequently from a remote location as the optical fibres can transmit the measured data for long distances.

8. Way Forward

Herein a series of experiments were conducted in laboratory and by using a physical model of a road. A limited number of experiments will be insufficient to introduce a rigorous decision-making system. Therefore, it is essential the carryout a pilot project by introducing the proposed solution to an actual road section that is probable to damage. Although the early warning is achievable, advanced post-processing algorithms and deep-learning-based decision-making systems are crucial. Big data collection from the roads for a longer period and damage prognosis need to carry out and several iterations will be required to improve the systems up to a commercialized product. The proposed research will be directly advantageous for the countries having roads through wetlands and mountain rejoins. But it is not limited to a particular country and the solution is applicable worldwide.

References

1. Aime, L. F. J., Kissinger, T., James, S. W., Chehura, E., Verzeletti, A., & Tatam, R. P. (2021). High sensitivity pressure measurement using optical fibre sensors mounted on a composite diaphragm. Optics Express, 29(3), 4105. https://doi.org/10.1364/OE.416715

2. Arya, D., Maeda, H., Ghosh, S. K., Toshniwal, D., Mraz, A., Kashiyama, T., & Sekimoto, Y. (2021). Deep learning-based road damage detection and classification for multiple countries. Automation in Construction, 132, 103935. https://doi.org/10.1016/j.autcon.2021.103935

3. Becker, M., Coleman, T., Ciervo, C., Cole, M., & Mondanos, M. (2017). Fluid pressure sensing with fiber-optic distributed acoustic sensing. Https://Doi.Org/10.1190/Tle36121018.1, 36(12), 1018–1023. https://doi.org/10.1190/TLE36121018.1

4. Bednarski, Ł., Sieńko, R., Grygierek, M., & Howiacki, T. (2021). New Distributed Fibre Optic 3DSensor with Thermal Self-Compensation System: Design, Research and Field Proof Application Inside Geotechnical Structure. Sensors 2021, Vol. 21, Page 5089, 21(15), 5089. https://doi.org/10.3390/S21155089

5. Begum, S., Jaisankar, G., Boyidi, S., Kumar, B., Ganesh, K., Sridevi, T., Anil, N., Sailaja, U., & Dileep, K. (2019). Road Network for Disaster Guide in Rural Area, East Godavari District, AP, India—A Case Study of Spatial Approach. In Springer Series in Geomechanics and Geoengineering (pp. 683–691). https://doi.org/10.1007/978-3-319-77276-9_60

6. Cigna, F., Banks, V. J., Donald, A. W., Donohue, S., Graham, C., Hughes, D., McKinley, J. M., & Parker, K. (2017). Mapping Ground Instability in Areas of Geotechnical Infrastructure Using Satellite InSAR and Small UAV Surveying: A Case Study in Northern Ireland. Geosciences, 7(3), Article 3. https://doi.org/10.3390/geosciences7030051

7. Deng, X. (n.d.). Land Quality: Environmental and Human Health Effects.

8. Glendinning, S., Hughes, P., Helm, P., Chambers, J., Mendes, J., Gunn, D., Wilkinson, P., & Uhlemann, S. (2014). Construction, management and maintenance of embankments used for road and rail infrastructure: Implications of weather induced pore water pressures. Acta Geotechnica, 9(5), 799.

9. Gong, H., Kizil, M. S., Chen, Z., Amanzadeh, M., Yang, B., & Aminossadati, S. M. (2019). Advances in fibre optic based geotechnical monitoring systems for underground excavations. International Journal of Mining Science and Technology, 29(2), 229–238. https://doi.org/10.1016/J.IJMST.2018.06.007

10. HAUSWIRTH, D. (2014). A STUDY OF THE NOVEL APPROACHES TO SOIL DISPLACEMENT MONITORING USING DISTRIBUTED FIBER OPTIC STRAIN SENSING.

11. Hong, C. Y., Zhang, Y. F., Zhang, M. X., Leung, L. M. G., & Liu, L. Q. (2016). Application of FBG sensors for geotechnical health monitoring, a review of sensor design, implementation methods and packaging techniques. Sensors and Actuators, A: Physical, 244, 184–197. https://doi.org/10.1016/J.SNA.2016.04.033

12. Huntley, D., Bobrowsky, P., Qing, Z., Sladen, W., Bunce, C., Edwards, T., Hendry, M., Martin, D., & Choi, E. (2014). Fiber optic strain monitoring and evaluation of a slow-moving landslide near Ashcroft, british columbia, canada. Landslide Science for a Safer Geoenvironment, 1, 415–421. https://doi.org/10.1007/978-3-319-04999-1_58

13. Igwe, O. (2015). The causes and mechanisms of rain-induced highway and pavement collapse in Obolo-eke, Southeast Nigeria. Arabian Journal of Geosciences, 8(11), 9845–9855. https://doi.org/10.1007/s12517-015-1899-z

14. Künzel, A., & Petryna, Y. S. (2016). Parameter Identification based on quasi-continuous strain data captured by high resolution fiber optic sensing. https://www.researchgate.net/publication/311182451

15. Le Floch, S., & Cambon, P. (2003). Study of Brillouin gain spectrum in standard single-mode optical fiber at low temperatures (1.4–370 K) and high hydrostatic pressures (1–250 bars). Optics Communications, 219(1–6), 395–410. https://doi.org/10.1016/S0030-4018(03)01296-3

16. Liehr, S., Lenke, P., Wendt, M., Krebber, K., Seeger, M., Thiele, E., Metschies, H., Gebreselassie, B., & Munich, J. C. (2009). Polymer optical fiber sensors for distributed strain measurement and application in structural health monitoring. IEEE Sensors Journal, 9(11), 1330–1338. https://doi.org/10.1109/JSEN.2009.2018352

17. Lindsey, N. J., Martin, E. R., Dreger, D. S., Freifeld, B., Cole, S., James, S. R., Biondi, B. L., & Ajo-Franklin, J. B. (2017). Fiber-Optic Network Observations of Earthquake Wavefields. Geophysical Research Letters, 44(23), 11,792-11,799. https://doi.org/10.1002/2017GL075722

18. Méndez, A., & Diatzikis, E. (2006). Fiber Optic Distributed Pressure Sensor Based on Brillouin Scattering. Optical Fiber Sensors (2006), Paper ThE46, ThE46. https://doi.org/10.1364/OFS.2006.THE46

19. Nishimura, T., Emoto, K., Nakahara, H., Miura, S., Sugimura, S., Ishikawa, A., & Kimura, T. (2021). Source location of volcanic earthquakes and subsurface characterization using fiber-optic cable and distributed acoustic sensing system. Scientific Reports. https://doi.org/10.1038/s41598-021-85621-8

20. Schenato, L. (2017). A Review of Distributed Fibre Optic Sensors for Geo-Hydrological Applications. Applied Sciences 2017, Vol. 7, Page 896, 7(9), 896. https://doi.org/10.3390/APP7090896

21. Schenato, L., Palmieri, L., Camporese, M., Bersan, S., Cola, S., Pasuto, A., Galtarossa, A., Salandin, P., & Simonini, P. (2017). Distributed optical fibre sensing for early detection of shallow landslides triggering. Scientific Reports, 7(1). https://doi.org/10.1038/s41598-017-12610-1

22. Sladen, A., Rivet, D., Ampuero, J. P., De Barros, L., Hello, Y., Calbris, G., & Lamare, P. (2019). Distributed sensing of earthquakes and ocean-solid Earth interactions on seafloor telecom cables. Nature Communications, 10(1). https://doi.org/10.1038/s41467-019-13793-z

23. Song, Z., Shi, B., Juang, H., Shen, M., & Zhu, H. (2017). Soil strain-field and stability analysis of cut slope based on optical fiber measurement. Bulletin of Engineering Geology and the Environment, 76(3), 937–946. https://doi.org/10.1007/S10064-016-0904-4

24. Sony, S., Laventure, S., & Sadhu, A. (2019). A literature review of next-generation smart sensing technology in structural health monitoring. Structural Control and Health Monitoring, 26(3), e2321. https://doi.org/10.1002/stc.2321

25. Verma, D., Thareja, R., & Singh, T. N. (2014). Influence of water content on Geotechnical Properties of Deccan Basalt, Maharashtra, India. International

Research Journal of Geology and Mining, 4(4). https://doi.org/10.14303/irjgm.2014.024

26. Wei, C., Deng, Q., Yin, Y., Yan, M., Lu, M., & Deng, K. (2022). A Machine Learning Study on Internal Force Characteristics of the Anti-Slide Pile Based on the DOFS-BOTDA Monitoring Technology. Sensors 2022, Vol. 22, Page 2085, 22(6), 2085. https://doi.org/10.3390/S22062085

27. Wijaya, H., Rajeev, P., & Gad, E. (2021). Distributed optical fibre sensor for infrastructure monitoring: Field applications. Optical Fiber Technology, 64. https://doi.org/10.1016/j.yofte.2021.102577

28. Wong, L., Deo, R., Rathnayaka, S., Shannon, B., Zhang, C., Kong Chiu, W., Kodikara, J., & Widyastuti, H. (2018). Leak Detection in Water Pipes Using Submersible Optical Optic-Based Pressure Sensor. Sensors (Switzerland). https://doi.org/10.3390/s18124192

29. Wright, R., Badar, M., Egbu, J., Lu, P., Buric, M., Ruishu Wright, al F., Egbu, J. C., Ohodnicki Jr, P. R., Wright, R. F., & Ohodnicki, P. R. (2019). Fully distributed optical fiber sensor for water and humidity monitoring. Https://Doi.Org/10.1117/12.2519239, 11000(14), 33–42. https://doi.org/10.1117/12.2519239

30. Zhang, G., Gu, H., Dong, H., Li, L., & He, J. (2013). Pressure sensitization of brillouin frequency shift in optical fibers with double-layer polymer coatings. IEEE Sensors Journal, 13(6), 2437–2441. https://doi.org/10.1109/JSEN.2013.2255270

Resilience of Power Grid Infrastructure with Renewables to Extreme Events in a Changing Climate

Prateek Arora
Ph.D. Candidate
New York University, USA

Research supported by:
Dr Luis Ceferino
Assistant Professor
Civil and Urban Engineering
Center for Urban Science and Progress,
New York University, USA)

Under CDRI Fellowship Programme 2022-23

Disclaimer: The views expressed in this paper reflect the opinions of the author and not necessarily the official views of CDRI.

This report has been prepared based on the findings reported in the following manuscripts during the fellowship period.

Arora, P., & Ceferino, L. (2023a). A performance-based probabilistic framework to model risk to power systems from hurricanes. *14th International Conference on Applications of Statistics and Probability in Civil Engineering*.

Arora, P., & Ceferino, L. (2023b). Could rooftop solar panels and storage have enhanced the electricity resilience during Hurricane Isaias (2020)? *14th International Conference on Applications of Statistics and Probability in Civil Engineering*, *2020*.

Arora, P., & Ceferino, L. (2023c). Probabilistic and machine learning methods for uncertainty quantification in power outage prediction due to extreme events. *Natural Hazards and Earth System Sciences*, *23*(5), 1665–1683. https://doi.org/10.5194/NHESS-23-1665-2023

Acronyms and Abbreviations

GLM – Generalized Linear Models

GAM – Generalized Additive Models

SAIFI – System Average Interruption Frequency Index

SAIDI – System Average Duration Frequency Index

Abstract

Strong hurricane winds damage power grids and cause cascading power failures, resulting in critical service disruption and major economic losses. A Resilient power system should minimize the extent of prolonged power disruptions. In this project, we present two different aspects to enhance power grid resilience to power disruptions from hurricanes (a) predicting the extent of power outages before the arrival of a hurricane to allow utilities to prepare for an emergency response to rapidly recover from power outages and develop a probabilistic method to understand the expected performance of power systems to future hurricanes (b) investigating the potential of solar power to sustain through the power outages during a hurricane.

Statistical and machine learning models have been proposed to predict the extent of power disruptions due to hurricanes. Existing outage models use inputs including power system information, environmental parameters, and demographic parameters. This paper reviews the existing power outage models, highlighting their strengths and limitations. Existing models were developed and validated with data from a few utility companies and regions, limiting the extent of their applicability across geographies and hurricane events. Instead, we train and validate these existing outage models using power outages from multiple regions and hurricanes, including hurricanes Harvey (2017), Michael (2018), and Isaias (2020), in 1910 US cities. We discuss the limited ability of state-of-the-art machine learning models to (1) make bounded outage predictions, (2) extrapolate predictions to high winds, and (3) account for physics-informed outage uncertainties at low and high winds. Our findings suggest that further developments are needed for power outage models for proper representation of hurricane-induced outages.

Additionally, Utilities must make risk-informed decisions to prioritize their limited resources (e.g., for grid hardening) in cities expected to experience larger and longer hurricane-induced outages. We investigate the expected performance of power systems to future hurricanes. This paper presents a generalized probabilistic framework coupling the expected frequency of future hurricane hazard levels and probabilistic outage predictions to understand the frequency of power system performance indices, namely the System Average Interruption Frequency Index and System Average Interruption Duration Index, from hurricanes. Results show that factors other winds, such as land use patterns, influence the risk of power outages across cities in New Jersey from future hurricanes.

Hurricane Isaias (2020) caused more than two million power outages in the U.S. that, in several cases, lasted more than four days. This large-scale electricity loss demonstrated a lack of grid resilience, especially in New Jersey. This paper evaluates the contribution of solar panels and behind-the-meter batteries in microgrids to the resilience of an electricity distribution network. We present a what-if case study for New Jersey during Hurricane Isaias in 2020. We analyze an extensive power outage dataset at the building level for 9,267 households from a large utility company in Marlboro Township, New Jersey, during Hurricane Isaias to determine unserved power demand. We use historical irradiance in New Jersey for the duration of outages during Hurricane Isaias (2020) to determine the potential of solar electricity for resilience. We observe that solar panels on each rooftop would have improved resilience for electric energy in the aftermath of Hurricane Isaias.

Acknowledgments

We acknowledge the support of the Coalition for Disaster Resilient Infrastructure (CDRI) Fellowship for this research. This research is also supported by the New York University Tandon School of Engineering Fellowship. We also thank Jersey Central Power & Light (JCPL) for providing power outage data in New Jersey, USA, during Hurricane Isaias (2020).

Funding

This research was partially supported by the 2022–2023 Fellowship of the Coalition for Disaster Resilient Infrastructure (CDRI), Application ID: 210924669.

1. Introduction

Hurricanes can cause significant damage to the power distribution systems, resulting in large power failures and losses of billions of US dollars (Smith, 2020). Strong winds from hurricanes can destroy the exposed overhead distribution lines in a power grid and cause cascading power failures. For example, Hurricane Isaias (2020) damaged old power infrastructure and caused over 2 million power outages across the US. More than a million outages occurred in New Jersey (Zaveri & Shanahan, 2020) even though Hurricane Isaias had transitioned to a tropical storm when it hit New Jersey, reducing its sustained winds to 25 m s^{-1} (Latto et al., 2021). Power outages caused by storms can last for several hours to weeks and even months (Rivera et al., 2022). To address this issue, the US Department of Energy (DOE) has prioritized investing in enhancing power infrastructure resilience (National Academies of Sciences, 2017).

In this project, we present two different aspects to enhance power grid resilience to power disruptions from hurricanes (a) predicting the extent of power outages before the arrival of a hurricane to allow utilities to prepare for an emergency response to rapidly recover from power outages (b) investigating the potential of solar power to sustain through the power outages during a hurricane.

2. Aim, Objectives, and Scope of the Research Study

The first part of this paper describes the input features, data sources, and data pre-processing used in the model development for power outage prediction. We further explain the selection of important and uncorrelated input features for model development. We highlight the limitations of existing state-of-the-art power outage prediction models. Finally, we suggest improvement with quasi-binomial regression to predict power outages before the arrival of a hurricane.

Additionally, we probabilistically quantify power system performance indices, SAIFI and SAIDI, across multiple cities in the US to Hurricanes using power outage models to assess the risk of outages to future hurricanes. We combined distribution on outages with the return period of future hurricanes to estimate the return period of different levels of performance determined by SAIFI and SAIDI. These indices can be determined for all types of system-wide power interruptions around the year. However, this study considers only hurricane-caused power interruption to determine SAIFI and SAIDI, as extreme

weather events have been the major causes of large-scale, sustained outages (Ankit et al., 2021; Brown, 2002).

In the second part of the paper, we formulate and analyze a what-if case study for New Jersey during Hurricane Isaias in 2020 to evaluate the value of solar panels and behind-the-meter batteries in microgrids for resilience to supply uninterrupted power during hurricanes.

As this paper focuses on two aspects of resilience, we have divided the methodology, results and discussion, and conclusion section into two major subdivisions (a) power outage model and risk quantification to future hurricanes (b) solar potential during hurricane Isaias (2020) in New Jersey, USA.

3. Methodology

3.1 Power Outage Model and Risk Quantification to Future Hurricanes

3.1.1 Literature Review

Utilities must first assess the vulnerabilities in their power system infrastructure to enhance their resilience to hurricanes. Outage prediction models can assist utilities in planning and placing their resources before and during an extreme event for an emergency response to rapidly recover the failed power distribution systems (Arab et al., 2016).

Liu et al., (2005) developed a negative binomial generalized linear model (GLM) to predict power outages in North and South Carolina. This model used hurricane parameters such as maximum wind speeds and duration of wind speeds over 20 ms^{-1}; environmental parameters including land cover, tree type, soil drainage properties, and precipitation; and utility information on the number of transformers and customers. The model included only a specific utility, which limited the use of the outage model in other regions. The model also included a storm indicator, making the model not applicable to hurricanes with different characteristics than the ones in the training data.

Han, Guikema, Quiring, et al., (2009) also developed a negative binomial GLM to predict outages in the Gulf Coast. This model did not include any specific utility and storm indicators and instead used only generalizable features (e.g., wind speed, precipitation) to make the model applicable to any hurricanes. Han, Guikema, & Quiring, (2009) also developed generalized additive models (GAMs) with the same input features as GLMs.

GAMs showed an improved accuracy over GLMs in power outage predictions because GAMs can effectively model the highly non-linear behaviour of outages and the input parameters, e.g., precipitation and soil moisture can have non-linear effects on power outages (Han, Guikema, & Quiring, 2009).

More recently, researchers developed decision trees-based machine learning methods, which are robust to outliers and noise, called random forest (L, 2001), to predict power outages caused by storms. Guikema et al., (2014) used only publicly available data to develop a hurricane outage prediction model, independent of utility-specific input parameters, with random forest regression. Maderia, (2015) improved accuracy in power outage predictions with random forest models by including information on tree species). McRoberts et al., (2018) and Shashaani et al., (2018) developed multistage zero-inflated power outage prediction models to better account for zero outages. The first stage of such a model is classification to predict outages or no outages. The further stages of the model predict the count of outages on the point classified as having an outage.

GLM (Liu et al., 2005), GAM (Han, Guikema, & Quiring, 2009), and random-forest-based power outage prediction models (Guikema et al., 2014; McRoberts et al., 2018; Shashaani et al., 2018) provide outage predictions at a coarser level compared to predictions at component. However, these models are mostly based on open-source, publicly available data and can be generalized at a larger scale to the coastal cities in the United States. Hence, for this paper, we focus on GLM, GAM, and random-forest-based power outage prediction models. As the power outage data are generally not made publicly available by the utilities, the previous models are primarily calibrated to data from a few regions. For example, Liu et al., (2005) developed the outage prediction model for North and South Carolina. Guikema et al., (2014), Nateghi et al., (2014) and Shashaani et al., (2018) developed the outage prediction models for the Gulf Coast. This paper addresses this gap by calibrating and validating existing models to extensive outage data from New Jersey, New York, Florida, and Texas at the city level. Thus, we investigate the generalized behaviour of power outage models across the United States and focus on publicly available input variables to make our calibrated models widely applicable.

To further allow utilities in pre-storm planning, we present a probabilistic performance-based engineering approach to couple these methods with hurricane hazard models to inform planners on risk hotspots, i.e., where communities can face the largest and longest power outages from hurricanes. Krawinkler, (1995) first introduced the performance-based engineering approach to characterize earthquake risks and assess if buildings would achieve a satisfactory level of performance in future earthquakes. The

existing probabilistic approaches for the reliability of power systems against hurricanes have focused mostly on winds as the reliability-reducing factor (Brown, 2002). However, these methods (Lu et al., 2021; Zhang et al., 2022) require extensive data on power systems that are not easily accessible, and factors other than winds, such as grid topology, can affect the reliability of power systems (Petersen, 1982). Hence, we need a standard measure to compare the risk profile of power systems from hurricanes at a large scale. The performance of power systems is generally measured based on the Institute of Electrical and Electronics Engineers (IEEE) defined performance indices, namely System Average Interruption Frequency Index (SAIFI) and System Average Interruption Duration Index (SAIDI) (IEEE SA - IEEE 1366-2022).

Utilities need informed decision-making to protect and prioritize the areas more vulnerable to extreme weather events. We combined distribution on outages with the return period of future hurricanes to estimate the return period of different levels of performance determined by SAIFI and SAIDI. These indices can be determined for all types of system-wide power interruptions around the year. However, this study considers only hurricane-caused power interruption to determine SAIFI and SAIDI as extreme weather events have been the major causes of large-scale sustained outages (Ankit et al., 2021).

3.1.2 Data Description

We acquired power outage data from PowerOutage (https:// poweroutage.us/), an organization that tracks and records outages from utilities at the city level across the US. PowerOutage (https: //poweroutage.us) regularly gets updates from utilities to keep the outage count close to actual outages. The data covered the power outages for Hurricane Isaias (2020) for 11 utilities in New York and 5 in New Jersey, for Hurricane Michael (2018) for 5 utilities in Florida, and for Hurricane Harvey (2017) for 39 utilities in Texas. Our dataset has about 3.6 million outages in total. Figure 1 shows outages caused by Hurricane Isaias in New Jersey in 2020.

We calibrated outage models at the city level resolution, comparable to the most recent models by McRoberts et al., (2018) and Shashaani et al., (2018). Here, we used data with reported outages for 1910 cities in New York, New Jersey, Texas, and Florida. Following the previous literature, we use the covariates, listed in Table 1, at the city level. Further description of the availability, resolution, and methods to obtain each variable at the city level is provided in the subsequent subsections. The total number of data points available is 1910 (cities). The dataset has been divided into train and test datasets with a ratio of 80:20

3.1.2.1 Response Variable

We focused on two response variables: the number of outages which are equivalent to the number of customers without power in a city and the fraction of customers without power. GLM and GAM use Poisson and negative binomial distributions to assess the count of outages as they model discrete and non-negative variables. Random forests can model the fraction of households without power in a city, which is important to compare impact levels across cities.

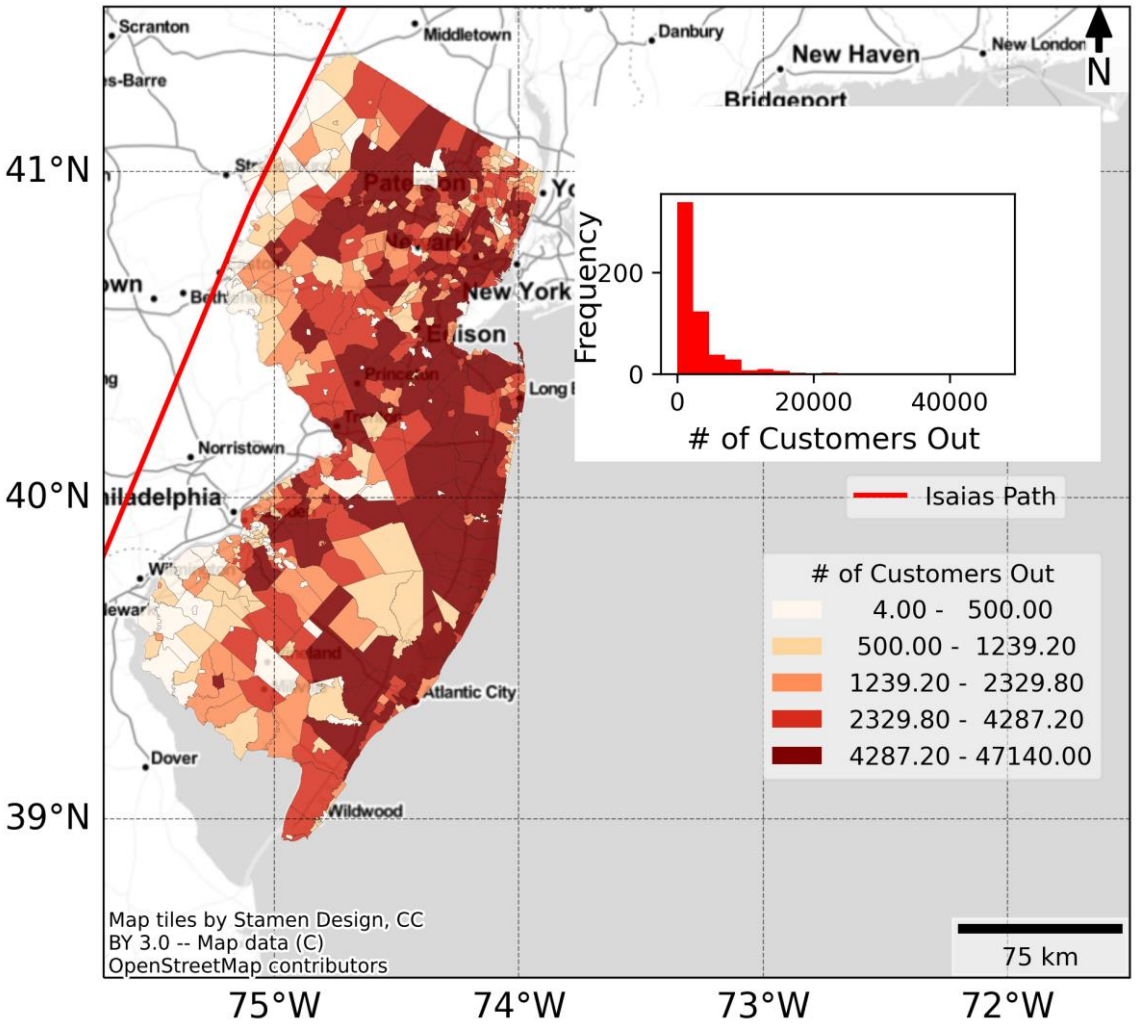

Figure 1. Power outages in aftermaths of Hurricane Isaias (2021) in New Jersey at the city level. (extracted from (Arora & Ceferino, 2023c))

3.1.2.2 Hurricane Parameters

The hurricane parameters considered for this stdy are 3 s gust wind speed and duration of strong winds over 20 ms^{-1}, as in previous research (Guikema et al., 2014; Han, Guikema, Quiring, et al., 2009; Liu et al., 2005; Shashaani et al., 2018). The overhead distribution system is the most vulnerable component of a power grid to high hurricane winds (National Academies of Sciences, 2017). The poles are designed to sustain wind speeds

of around 20 ms^{-1} (IEEE Standard, 2007). Thus, winds above 20 ms^{-1} could substantially damage the electric poles. The 3-s gust wind speed and duration of strong winds for the three hurricanes in the dataset were calculated based on a complete wind profile model for tropical cyclones by Chavas et al., (2015). We determined the wind speed for each city at its centroid. Figure 2 illustrates the variation of 3-s wind gusts in New Jersey during Hurricane Isaias.

Table 1. Parameters to build the power outage prediction models: all variables are rescaled at the city level. Parameters are grouped into categories separated by horizontal lines. We selected one variable from each category of each group to minimize correlation across parameters. * denotes the final selected parameters.

Feature	Abbreviation	Data Source
3 s gust wind speed Duration of strong winds	Vmax* Duration	(Chavas et al., 2015)
Percent developed area Percent water area Percent barren area Percent forest area Percent scrub area Percent grassland area Percent pasture area Percent crops cultivated area Percent wetlands area	Developed Water Barren Forest Scrub Grassland Pasture Crops Wetlands	(*MRLC Viewer*, n.d.)
Standard precipitation index 1 month Standard precipitation index 3 months Standard precipitation index 6 months Standard precipitation index 12 months	SPI1 SPI3 SPI6* SPI12	(Xia, 2012)
Soil moisture first layer Soil moisture second layer Soil moisture third layer	CDF1* CDF2 CDF3	(Xia, 2012)
7 d precipitation	Precip*	(Xia, 2012)
Root zone depth	Rzone*	((dataset) Soil Survey Staff, n.d.)
Percent treed area	Trees*	(Krist Jr. et al., 2014)
Mean elevation Median elevation	Mean_Ele Median_Ele	(Danielson & Gesh, 2011)
Population density	Pop_Den*	(*Geography & ACS*, n.d.)

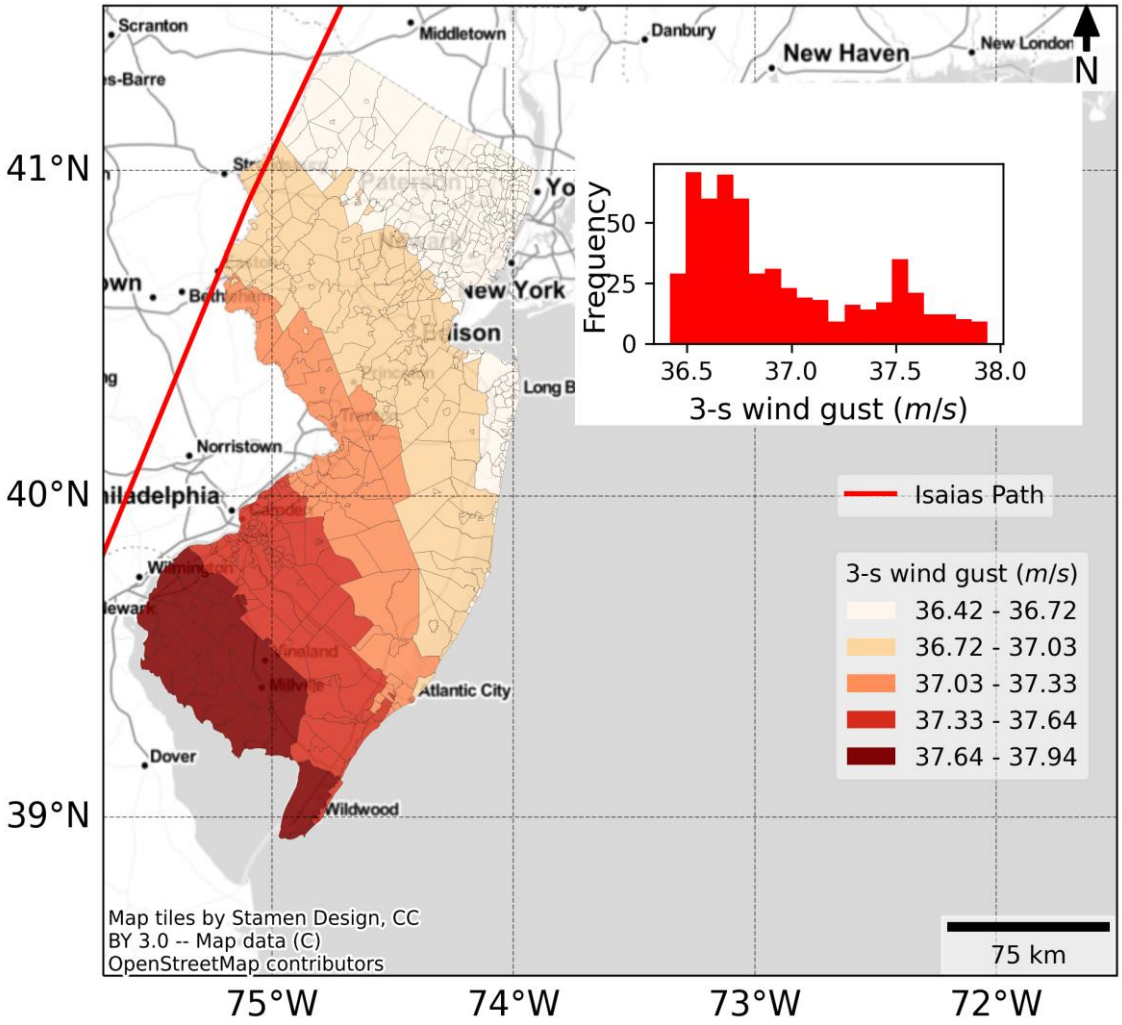

Figure 2. Distribution of 3 s wind gust at the city level (mean: 36.95 m s−1, standard deviation: 0.41 m s−1) across New Jersey before the arrival of Hurricane Isaias. (extracted from (Arora & Ceferino, 2023c))

3.1.2.3 Land Cover Data

Power grid patterns vary for different land use classes, resulting in different outage mechanisms. For example, rural areas can suffer larger power outages since they have radial grid patterns where component failures can propagate more than in cities with gridded patterns (Petersen, 1982). We obtained National Land Cover Data (NLCD) at a resolution of 30 m x 30 m classified into 20 different classes available from the Multi-Resolution Land Characteristics Consortium, which is maintained by the United States Geographical Survey (USGS) (https://www.mrlc.gov/viewer/). We have reclassified the NLCD into nine classes (Table 1). We utilized the spatial analyst in ArcGIS (a tool for geographic information systems) (ESRI 2019, n.d.) to clip the 30 m × 30 m land cover raster for each city to determine the percentage of area covered by these cover classes

3.1.2.4 Precipitation and soil moisture data

Precipitation and soil moisture data are available from the variable infiltration capacity

(VIC) model from the National Land Data Assimilation System Phase 2 (NLDAS2) (Xia, n.d.; Xia et al., 2012) for each hour since 1979 with a resolution of 0.125◦ × 0.125◦. The poles and overhead distribution lines in the vicinity of trees are susceptible to falling trees due to strong hurricane winds. The wet soil conditions from high precipitation and soil moisture increase the likelihood of trees and electric poles uprooting from strong hurricane winds (Han, Guikema, Quiring, et al., 2009). Also, persistent drought conditions, e.g., low precipitation in the months before a hurricane, can weaken the roots of trees because of gaps in the soil layer, making trees more susceptible to strong winds (McRoberts et al., 2018).

Soil moisture from NLDAS2 is available for three depths: 0–10, 10–40, and 40–100 cm. We calculated daily soil moisture for these depths by taking the average hourly readings. We normalize the soil moisture, as it can vary because of different soil types in different regions, by evaluating the percentile for three layers. We denote the soil moisture percentiles for three layers of soil at 0–10, 10–40, and 40–100 cm depth as CDF1, CDF2, and CDF3, respectively.

For the current study, we calculated the standard precipitation index (SPI) (Guttman, 1998; Wu et al., 2007) for durations of 1, 3, 6, and 12 months by adding hourly time series data for precipitation. Fig. 3 illustrates the variation of SPI 1 month in New Jersey before the arrival of Hurricane Isaias. We also included the expected precipitation after the hurricane makes landfall for the next 7 d, as heavy rain can lead to flooding resulting in clustered outages (McRoberts et al., 2018). We used nearest-neighbour interpolation to obtain soil moisture and precipitation at the city centroid by taking the value available at the nearest point.

3.1.2.5 Root zone depth

The effective root zone depth is defined as the depth of the soil from which plants and trees can effectively extract water and nutrients for growth (http://www.wood-database.com). The more effective the root zone depth for trees, the less likely they will fail from strong hurricane winds (McRoberts et al., 2018). We add average root zone depth as an input parameter for outage predictions because it could indicate the hazard from falling trees to the power lines. Root zone data are available from the United States Department of Agriculture (USDA) under Gridded Soil Survey Geographic ((dataset) Soil Survey Staff, n.d.) at 30 m × 30 m resolution as raster data.

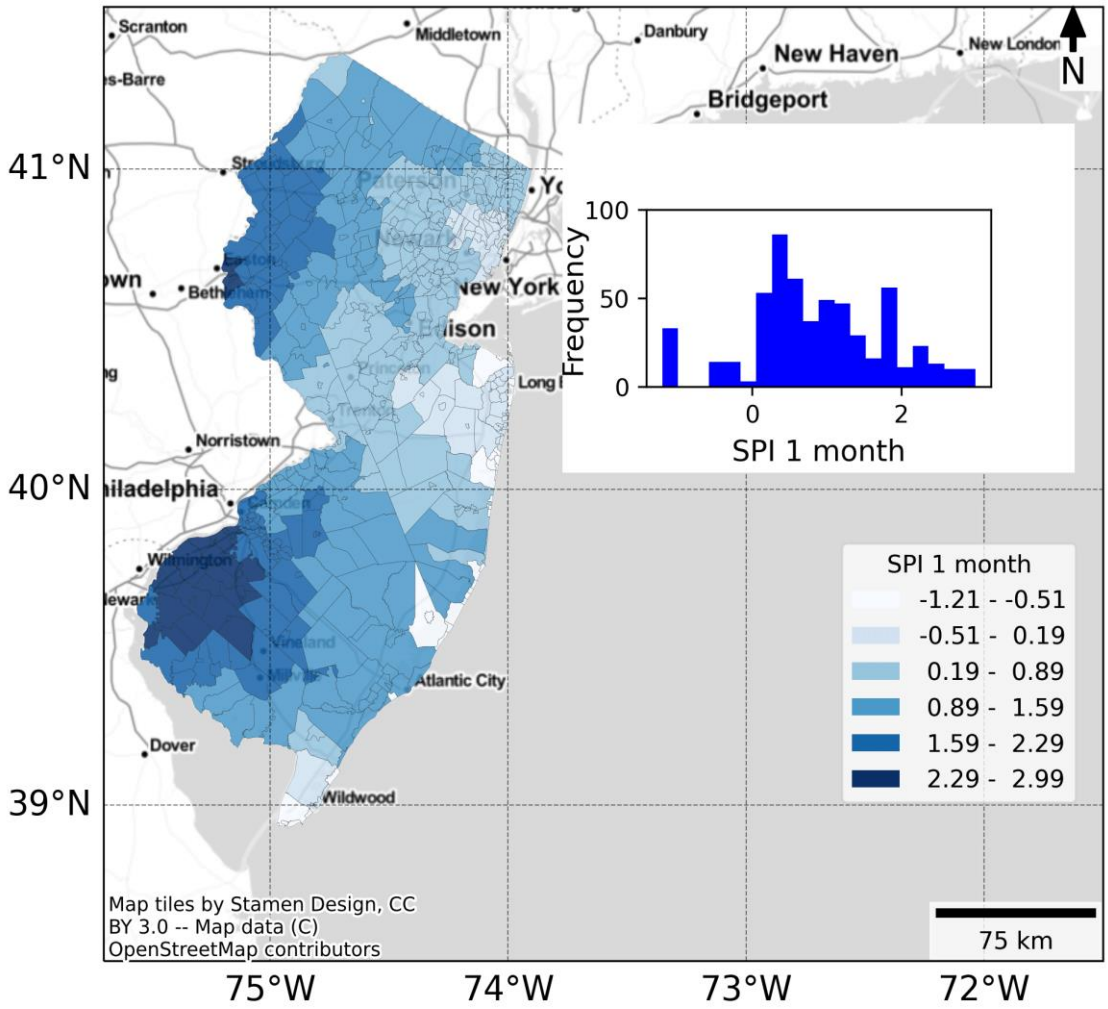

Figure 3. Distribution of SPI 1 month (mean: 0.88, standard deviation: 0.93) across cities in New Jersey before the arrival of Hurricane Isaias. (extracted from (Arora & Ceferino, 2023c))

3.1.2.6 Percentage treed area

USDA created National Insect and Disaster Risk Maps (Krist Jr. et al., 2014) in 2012, with the area covered by trees at 240 m × 240 m as raster data. The raster tree data are used to calculate the percent of the area covered by trees at the city level using the spatial analytic tool in ArcGIS (ESRI, 2019). Figure 4 illustrates the distribution of percent treed area in New Jersey.

3.1.2.7 Elevation

Previously, researchers have found that hurricane wind speeds (and thus damages) vary with surface topography (Chapman, 2000; McRoberts et al., 2018; Miller et al., 2013). Thus, we use the median and mean elevation at the city centroid, using nearest neighbour interpolation, as topographic variables to capture the changes in elevations across the cities. We obtained these parameters from the digital elevation model (DEM) at a 30 arcsec resolution scale developed by USGS as part of the DEM: Global Multi-resolution

Terrain Elevation Data (GMTED2010) (Danielson & Gesh, 2011).

3.1.2.8 Density Data

Demographics data are available from the American Community Survey (ACS) (https://www.census.gov/ programs-surveys/acs). The ACS collects different demographic data for each US census tract. The ACS started data collection in 2010, and we have considered data from 2019. We obtained the population density as it indicates the number of distribution poles and system components exposed to winds (Brown, 2002).

3.1.3 Model Development: Feature Selection

Machine learning models with high-dimensional input data can be hard to train, especially when datasets are sparse, as in the case of infrastructure failures (Verleysen & François, 2005). Feature selection, also called variable selection, is an essential step in machine learning model development to select relevant variables and discard redundant and highly correlated ones (Cai et al., 2018). We performed the feature selection for outage prediction in two steps. First, we performed a forward selection with a linear regression (Kohavi & John, 1997) for an initial rank on feature importance (Fig. 5). We started with a set of empty features and added features one by one. At each step, we selected the variable that led to the largest increase in the R^2. Our results show that, as expected, wind speed and duration of strong winds affect the power outages most. We found that precipitation and soil moisture are important for outage prediction, even for linear regression, suggesting that their relevance could be even higher for non-linear regressions. We also found that population density is critical for outage prediction, which could be explained by a positive correlation between density and the density of transformers, as described in (Liu et al., 2007).

In the second stage, we analyzed the correlations between the input parameters. We found that input features within the same category in Table 1 are highly correlated. For example, the maximum wind speed and duration of strong winds, which are at the top of the ranking in forward selection (Fig. 5), have a correlation coefficient of 0.89. Hence, we kept only maximum wind speed as an input feature since it is better ranked than the duration of strong winds in the forward selection. We conducted a similar analysis for the different categories listed in Table 1 to select the input variable with the strongest predictive power. Due to their lower importance in our results, we did not include parameters from the elevation and land cover categories, as they contribute less than 1% to R^2. Finally, we selected the following seven variables that will be used:

– 3 s gust wind speed

– 7 d precipitation

– standard precipitation index 6 months

– soil moisture first layer

– population density

– percent treed area

– root zone depth

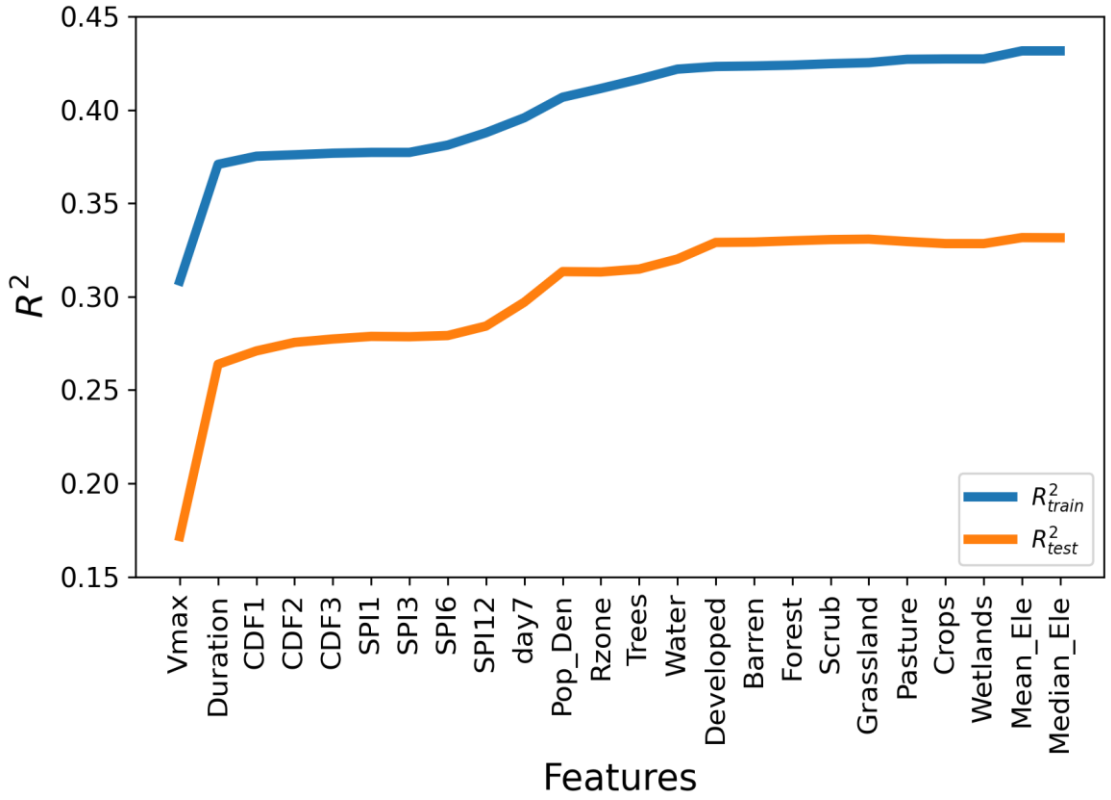

Figure 5. Forward selection: selection of important input parameters based on importance to explain the variability in outage predictions. Feature descriptions are shown in Table 1. (extracted from (Arora & Ceferino, 2023c))

3.1.4 Generalized Linear Models

Generalized linear models (GLMs) are a generalization of ordinary linear regression. GLMs allow us to use a flexible link function to relate a linear model (of the input variables) to the response variable (Dunn & Smyth, 2018). Unlike ordinary linear regressions, GLMs do not assume homoscedasticity, i.e., when the variance of the response variable is constant across the values of the input variables. The assumption of homoscedasticity fails for the number of customers without power since this output variable has positive counts, and when damage to power infrastructure is negligible (e.g., little storm), the variable's variance (and mean) should change and approach zero (Dunn and Smyth, 2018).

In addition, GLMs can utilize multiple statistical models to represent the data instead of

the only normal distribution as in ordinary linear regressions. Outages have a lower bound of zero counts that normal distributions cannot capture. Thus, previous researchers have used the following distributions to represent outages with GLMs.

3.1.4.1 Poisson GLMs

Poisson regression models, a category of GLMs, are applicable for positive count data where observations are independent. Outages are modelled as a Poisson random variable:

$$P(y;\mu) = \frac{e^{-\mu}\mu^{y}}{y!} \qquad (1)$$

where y is the number of outages in a city. The Poisson distribution is described by the parameter μ, the mean number of outages in a city. A log link connects the parameter μ to the input variables, which assures that μ is greater than zero.

$$ln\ ln\ (\mu)\ = \beta X(\qquad 2)$$

where β is learned from the historical outages from extreme events, often through maximum likelihood estimation (MLE). We use glm package in R studio (https://www.rdocumentation.org/packages/stats/ versions/3.6.2/topics/glm) to fit the Poisson GLM to our power outage data.

The variance in a Poisson distribution is equal to the mean, i.e., Var(y) = μ. Thus, the variance grows as μ increases. However, previous research has found that outage variance from historical data is significantly bigger than the mean (Han, Guikema, Quiring, et al., 2009; Liu et al., 2005) a phenomenon that is known as overdispersion in Poisson regressions (Dunn and Smyth, 2018).

3.1.4.2 Negative Binomial GLMs

Negative binomial GLM is a hierarchical model which can account for overdispersion effects in power outage count predictions (Dunn and Smyth, 2018). Negative binomial GLMs are based on a Poisson–gamma mixture distribution, i.e., the outage count y is distributed as a Poisson random variable

$$P(y;\mu,\tau) = \frac{e^{-\mu\tau}(\mu\tau)^{y}}{y!} \qquad (3)$$

where μ is a factor that when multiplied by τ equals the mean of the Poisson distribution. τ is an additional random variable to account for extra variance, with a mean equal to 1 and distributed as gamma

$$P(\tau;\ k) = \frac{\left(\frac{1}{k}\right)^{\frac{1}{k}}}{\Gamma\left(\frac{1}{k}\right)}\ \tau^{\frac{1}{k}-1}e^{-\tau/k} \qquad (4)$$

where k is the overdispersion parameter and $\Gamma()$ is the gamma function; thus, the variance

of τ equals k. After marginalizing the random variable τ ,

$$P(y;\ \mu, k) = \frac{\Gamma\left(y+\frac{1}{k}\right)}{\Gamma(y+1)\Gamma\left(\frac{1}{k}\right)}\left(\frac{\mu}{\mu+\frac{1}{k}}\right)^{y}\left(1-\frac{\mu}{\mu+\frac{1}{k}}\right)^{\frac{1}{k}} \quad (5)$$

which is equivalent to a negative binomial distribution with a variance of $\mu + k\mu^2$. This variance is higher than the one in the Poisson GLM with one term that is proportional to μ^2. Thus, negative binomial GLMs account for significantly higher variances. μ is parameterized as in Eq. (2). Then, β and k are estimated through MLE using the glm package in R studio (https://www.rdocumentation.org/packages/stats/versions/3.6.2/topics/glm).

Researchers have also developed zero-inflation outage prediction models to improve statistical performance for unbalanced data, e.g., when there are a lot of data points with no outages (McRoberts et al., 2018; Shashaani et al., 2018). In this paper, we do not fit zero-inflated models, as our data are balanced, i.e., we observe at least one outage in each city.

3.1.5 Generalized Additive Models

GLM models assume a linear relationship between the logarithm of the mean number of outages and input parameters (Eq. 2). However, previous research has shown that they have non-linear relationships (Han, Guikema, Quiring, et al., 2009), which can be modelled with non-parametric extensions of GLMs. Generalized additive models (GAMs) capture non-linear relationships using smoothing functions

$$ln\ ln\ (\mu)\ = \beta_0 + \sum_{j=1} \quad \beta_j f_j(x_j) \quad (6)$$

where μ is the mean outages for a city, $x_j \in X$ is the individual input parameter, β_0 is the intercept, and $f_j(x_j)$ are the smoothing functions for each input parameter. Some examples of smoothing functions are regression splines, B splines, and P splines. We used quartic-order polynomials for all input variables (Yee, 2012) except for maximum wind speeds. For this variable, we reduced the order of the polynomial to 1 to always obtain a monotonically increasing relationship between winds and outages, as we would expect from the structural behaviour of infrastructure against extreme loads. We used MLE to estimate GAMs' parameters through iteratively reweighted least squares (IRLS) (Wood, 2017) using the MGCV library in R studio. Poisson GAM assumes the Poisson distribution on the number of outages as described in Eq. (1), with link function equal to Eq. (6). Similarly, negative binomial GAMs assume the Poisson–gamma distribution mixture for the number of outages as mentioned in Eq. (5), with link function equal to Eq. (6).

3.1.6 Random Forest

Random forest regressions (L, 2001) are non-parametric ensembles of decision trees that do not assume any underlying probability distribution for the decision variable. Tree-based methods are easy to build and powerful machine learning tools. Decision trees split at each node based on some criteria involving the value of a particular input variable. For regression trees, binary splits at each node are performed for each variable (Fig. 6) (Hastie et al., n.d.). The split with the largest reduction of squared errors is selected at each step. The splitting stops once there is no performance gain for the regression analysis. For the prediction, the decision tree will point to a final leaf node based on the criterion for the splitting of feature space, and the output for the decision tree is the average of the predicted variable,

$$\hat{y_i} = average\ (y_i | x_i \in L_m) \qquad (7)$$

where L_m is the final leaf node (Fig. 6).

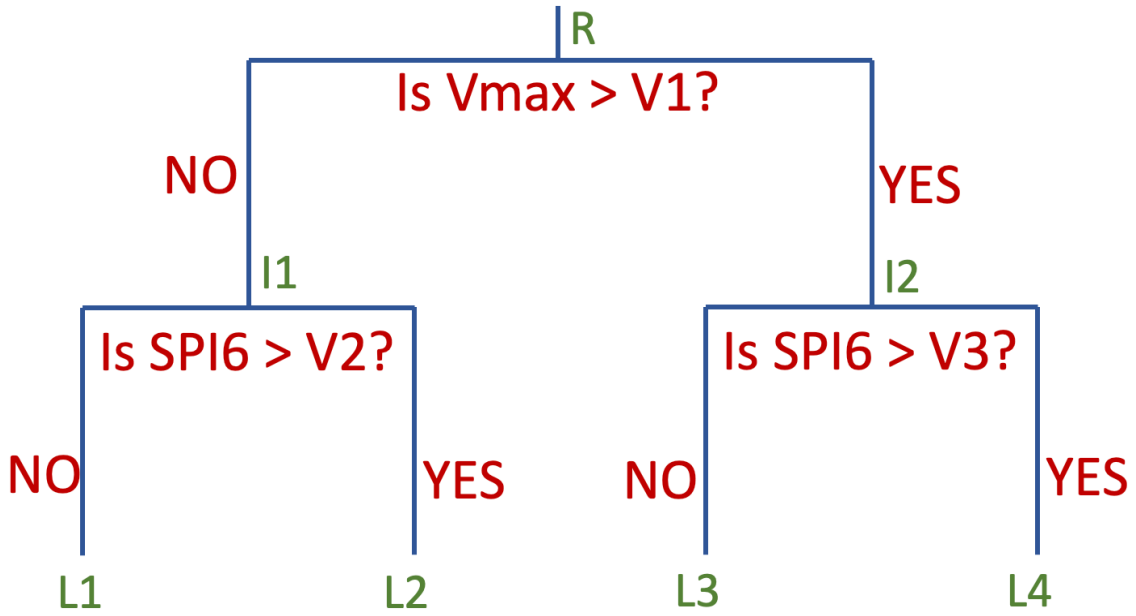

Figure 6. Example of a simple decision tree with two input features, maximum wind speed (ΩVmax) and precipitation (SPI6), to predict outages. The split at the root node (R) is done with Vmax. Thus, if the wind speed value is greater than the value V1, the points will belong to the right interior node (I2), otherwise they belong to the left node. Similarly, interior nodes are further divided into leaf nodes L1, L2, L3, and L4 using values of SPI6. (extracted from (Arora & Ceferino, 2023c))

Random forests "grow" a large number of parallel decision trees and bag new samples for each decision tree (L, 2001). The final output is the average of outputs from each decision tree modelled in parallel. The random selection of features results in the development of uncorrelated trees, reducing the variance in predictions (Hastie et al., 2001). In this paper, we use the sci-kit learn module in Python to fit the random forest model. We also use the

GridSearchCV module in Python (Pedregosa et al., 2011) to tune for the parameters and select the model with the least error on out-of-bag samples.

3.1.7 Probabilistic framework to model future risk to hurricanes.

Next, we combined distribution on outages with the return period of future hurricanes to estimate the return period of different levels of performance. Negative Binomial power outage model can account for larger dispersions and capture outages at all wind levels (Arora & Ceferino, 2023). Hence, this paper uses the Negative Binomial GAM-based power outage model to demonstrate how outage models can be used to quantify power system performance probabilistically. We are not able to determine all the input parameter in the power outage model for future. So, we use a reduced model with three input parameters: wind gust, population density, percent developed land cover.

Utilities are assigned performance ratings based on reliability indices defined by IEEE. Although utilities often exclude storm events while determining reliability indices (Brown, 2002) as old power systems are not designed to withstand shocks from extreme weather.

3.1.7.1 System Average Interruption Frequency Index (SAIFI)

SAIFI measures the number of sustained outages (outages more than a minute) a consumer will experience during a year given as:

$$SAIFI = \frac{Total\ Customer\ Interruptions}{Total\ Customers\ Served} /yr \qquad (8)$$

For outages caused by one storm during a year, SAIFI will represent a fraction of customers without power during the storm. Cities with higher SAIFI are at more risk for power interruptions from storms.

3.1.7.2 System Average Interruption Duration Index (SAIDI)

SAIDI measures the number of sustained outages hours (outages more than a minute) a consumer will experience during a year given as:

$$SAIDI = \frac{Total\ Customer\ Interruptions\ Duration}{Total\ Customers\ Served} hr/yr \qquad (9)$$

To determine the total unserved power system supply (Brown, 2002), information on both the duration and the number of outages is required. A high SAIDI value for a city is indicative of longer sustained power outages.

3.1.7.3 Modelling Total Customer Interruption Duration

According to the definition of SAIDI (Eq. 2), we need the total customer power interruption duration. (Liu et al., 2007) modelled the time to recover the storm-induced power outages as a function of outage size since cities with more outages recover more slowly. Similarly,

we model total customer power interruption duration as a function of outages.

$$ln\ ln\ (CD) = a * ln\ ln\ (O)\ + b \quad (10)$$

where CD is the total customer power interruption duration and O is the number of outages. We use scikit library in python (Pedregosa et al., 2011) to obtain coefficients a and b in Eq. 10. We used the log link in Eq. 10 as total interruptions will always be greater than zero for an outage event. We used historical data for Hurricane Isaias (2020), obtained from (poweroutage.us), for outages and total customer interruption duration to perform regression in Eq. 10. We show the regression line for total interruption duration and number of outages in Fig. 7.

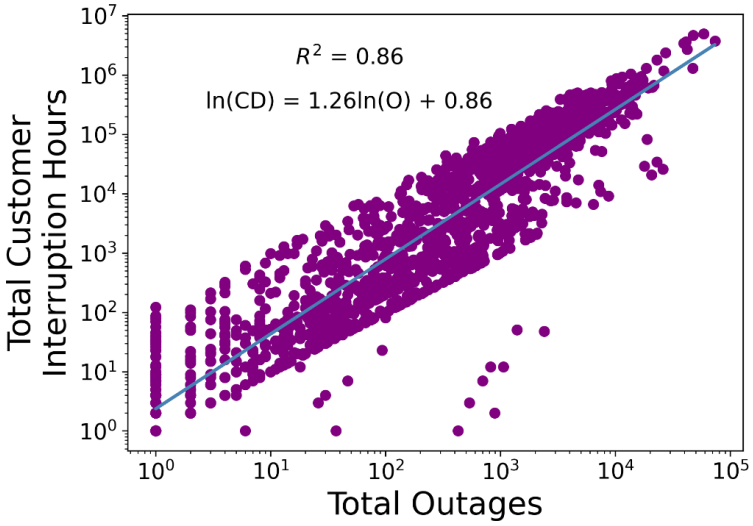

Figure 7. Regression between total customers interruption hours and total outages. (extracted from (Arora & Ceferino, 2023a))

R^2 of 0.86 in Fig. 7 represents a good fit between total interruption duration and outages, as more outages would require more time to recover, resulting in more total hours of customer interruptions. From Eq. 10, $ln\ (CD)$ is normally distributed as

$$ln\ ln\ (CD) \sim N\ (a * ln\ ln\ (O)\ + b, \sigma^2) \quad (11)$$

3.1.7.4 Probabilistic Framework

Utilities mostly design their power systems to reduce the number of power interruptions under normal operating conditions. Utilities are rated based on their performance to reduce SAIFI, and SAIDI (*IEEE SA - IEEE 1366-2022*, n.d.). Performance based engineering can give the rate of observing performance indices for extreme events (Krawinkler, 1995).

$$\lambda(DV > x) = \int (P(H) d\lambda_H \quad (12)$$

where DV in performance engineering is the decision variable (DV) (i.e., performance indices in this study), $\lambda(DV > x)$ is the rate of DV exceeding a value of x, λ_H is the hazard rate whose intensity H affects the decision variable, and $P(H))$ is the probability of

exceeding the decision variable given hazard. We adopted this methodology to assess the performance of power systems of cities in New Jersey, US. prone to hurricane hazards.

3.1.7.5 Wind Hazard

Strong hurricane winds devastate power systems, so the hazard for this study is wind speeds. We obtained 3-s wind speeds for return periods for 10, 25, 50, 100, 300, 700, 1700, and 3000 years from ASCE 7-16 wind maps (*ASCE 7 Standard | ASCE*, n.d.). Fig. 8 presents the 3-s gust wind speeds for 10-year return period for cities in New Jersey. The reader should note that ASCE 7-16 wind maps include all types of wind hazards, not limited to hurricanes.

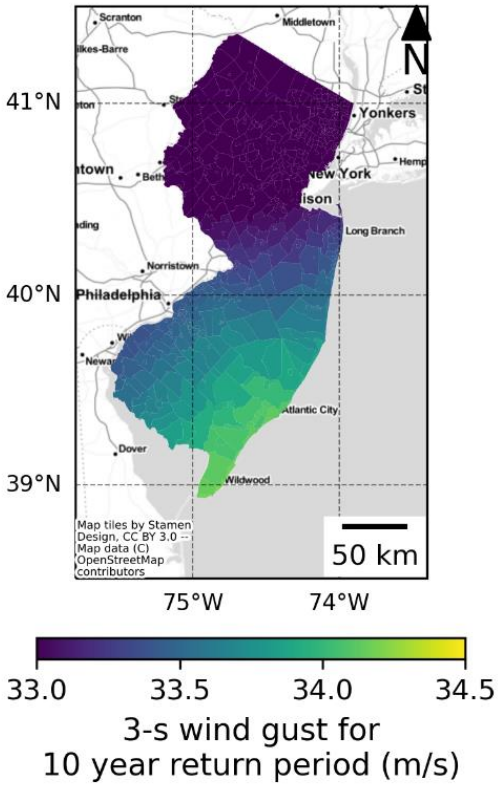

Figure 8. 3-s wind gust for 10-year return period in New Jersey. (extracted from (Arora & Ceferino, 2023a))

3.1.7.6 Rate of SAIFI

Using the probabilistic framework in Eq. 12, we can obtain the rate of outages.

$$\lambda(O > x) = \int (P(w) d\lambda_w \qquad (13)$$

here $\lambda(O > x)$ is the rate of exceeding x outages, $P(O > x|w)$ is the proabability of exceeding x outages given a wind speed of w obtained from Eqs. 5 and 6 and is the rate of exceeding a particular wind speed which is the inverse of the return period obtained from ASCE 7-16 wind maps. Eq. 6 gives the link between mean outages and winds, and

Eq. 5 gives the probability distribution of outages. However, ASCE 7-16 wind maps provide wind speeds at discrete return period intervals, so we perform a linear regression between the log of λ_w and w to obtain λ_w at all winds. A closed form is not available for integral Eq. 13, but a discretized sum can be performed to obtain $\lambda(O > x)$.

$$\lambda(O > x) = \sum P(w) \left|\frac{d\lambda_w}{dw}\right| dw \qquad (14)$$

Where $\frac{d\lambda_w}{dw}$ is the slope of best fit line between $ln\ ln\ (\lambda_w)$ and w multiplied with λ_w. In Eq. 14, we can obtain outages x for a particular $\lambda(O > x)$. From Eq. 8, SAIFI is the fraction of total outages, and total customers served. Since the number of customers served is constant, we can find the rate of SAIFI as

$$\lambda(SAIFI) = \frac{\lambda(O>x)}{Total\ Customers\ Served} \qquad (15)$$

For decision-making and prioritizing the upgrade of the power grid, utilities can compare the $SAIFI$ of different cities for a fixed $\lambda(SAIFI)$.

3.1.7.7 Rate of SAIDI

Similar to the rate for total outages, we can get the rate of total customer interruption duration. From Eq. 13, we can get $\lambda(O)$ (also, $\lambda(O > x)$). Further, Eq. 11 represents the distribution of total customer interruptions duration as a function of O. Hence, we can obtain the rate of total customer interruptions duration.

$$\lambda(CD > x) = \int (P(O) d\lambda_o \qquad (16)$$

where is $P(CD > x|O)$ is the probability of exceeding x total customer interruption hours given outages (O) obtained from Eq. 11. Similar to Eq. 14, we can discretize Eq. 16

$$\lambda(CD > x) = \sum P(O) \left|\frac{d\lambda_o}{dO}\right| dO \qquad (17)$$

we perform a linear regression between $ln\ (\lambda_O)$ and O to obtain $\left|\frac{d\lambda_o}{dO}\right|$ for different outage counts. Eq. 9 gives the relationship between total customer interruption hours and SAIDI. Thus, we can find the rate of SAIDI as

$$\lambda(SAIDI) = \frac{\lambda(CD>x)}{Total\ Customers\ Served} \qquad (18)$$

We present results for $SAIFI$ and $SAIDI$ for cities in New Jersey for a 10-year return period (or $\lambda(SAIFI) = 0.1\ and\ \lambda(SAIDI) = 0.1$) in results section.

3.2 Solar potential during hurricane Isaias in New Jersey, USA

3.2.1 Literature Review

Researchers have worked on predicting hurricane-induced outages (McRoberts et al., 2018) so that utilities can coordinate (National Academies of Sciences, 2017) and arrange

for backup generators. Almost 95% of the residential and critical buildings, e.g., buildings, are backed by fossil fuel fired generators using diesel or natural gas (Phillips et al., 2016). However, these backup sources may not be reliable (*Hurricane Sandy After Action Report and Recommendations to Mayor Michael R. Bloomberg*, 2013) and does not align with renewable energy goals of reducing the impact of emissions on our climate (*Federal Sustainability Plan Catalyzing America's Clean Energy Industries and Jobs*, 2021).

Emergency planners are now considering the value of renewable energy sources in enhancing the resilience of power systems (Laws et al., 2018). Modern rooftop solar panels can sustain higher hurricane wind speeds than the old vulnerable distribution poles (Ceferino et al., 2023a), as seen in recent extreme weather events (Cortes et al., 2022). Babrock Ranch, a community in Florida located 12 miles away from coastlines, has 700,000 solar panel installations providing power to 2,000 households. The community was unaffected by the massive power outages caused by Hurricane Ian in September 2022 with no damage to solar panels (Cortes et al., 2022).

Most studies on renewables-based resiliency in power systems have focused on commercial customers or conducted at a coarse resolution of transmission level addition of renewables (Watson, 2020). (Patel et al., 2021) studied the effect of different adoption policies for solar panels in enhancing the resilience of power systems at the household level during an earthquake. However, hurricanes are very different from earthquakes as clouds during hurricanes can significantly reduce the incident solar irradiance on solar panels (Ceferino et al., 2022, 2023b). Thus, reducing the solar energy generated during a hurricane.

We formulate and analyze a what-if case study for New Jersey during Hurricane Isaias in 2020 to evaluate the value of solar panels and behind-the-meter batteries in microgrids for resilience to supply uninterrupted power during hurricanes. This study focuses on Marlboro Township, New Jersey, residential buildings, where 9,267 households lost power in the aftermath of Hurricane Isaias (2020).

3.2.2 Hurricane Isaias: power outages and solar irradiance

Hurricane Isaias reached New Jersey on August 4, 2020, (Latto et al., 2021) with high winds which snapped and downed many trees and powerlines. We show in Fig. 9 the wind fields for Hurricane Isaias in New Jersey computed using a complete wind profile model for tropical cyclones developed by Chavas et al. (2015) and the location of our study area (Marlboro Township, New Jersey). More than one million people were left without electricity in New Jersey (OE-417 Form, 2020), even though Isaias weakened to a tropical storm as it hit New Jersey with sustained winds of 57 mph. Isaias caused economic

losses of about 4.2 billion dollars and caused 15 deaths (Latto et al., 2021).

3.2.2.1 Power Outages

We obtained the power outage at the building level from Jersey Central Power & Light (JCPL), a major utility company in New Jersey. JCPL serves 1.1 million consumers in New Jersey and recorded 780,000 peak outages in the aftermath of Hurricane Isaias (2020) (Jim Giuliano, 2020). JCPL recorded their first consumer-level outage around 8 am on August 4, 2020, and the JCPL crew restored power for 90% of their consumers after 72 hours (Jim Giuliano, 2020). These prolonged power outages bring a strong need for backup power, motivating this on solar panels and behind-the-meter batteries. Outage data from JCPL includes the city number, the street address of the consumer, zip code, start and end time of power outages, and type of consumer (residential, industrial, or commercial). For the scope of this paper, we limit our study to the outages that happened in residential buildings in Marlboro Township, a municipality in New Jersey (Fig. 10).

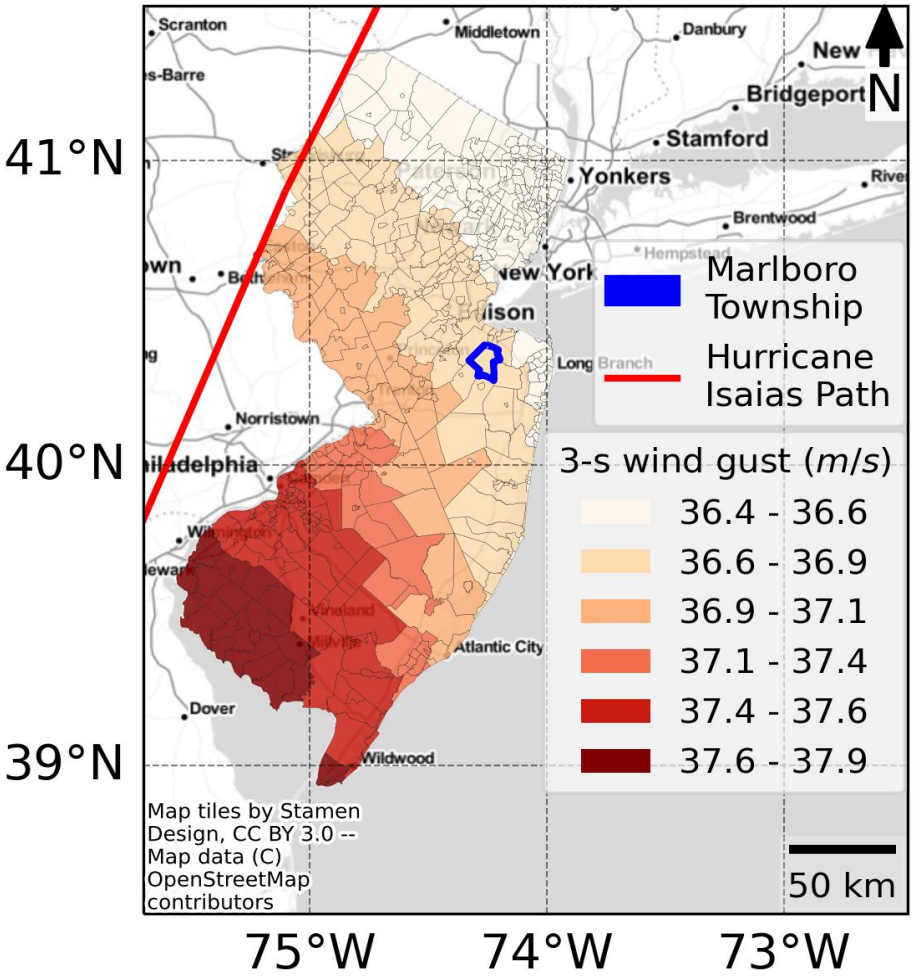

Figure 9. 3-s gust wind speed in New Jersey from Hurricane Isaias (2020) and location of selected study location (Marlboro Township, New Jersey, USA). (extracted from (Arora & Ceferino, 2023b))

3.2.2.2 Geocoding Outages, Parcel Data, and Building Footprints

We geocoded the outages using the New Jersey Office of GIS (NJOGIS) statewide geocoding services (NJ Geographic Information Network | Geocoding, 2022) with an address provided by JCPL in the outage database to get the longitude and latitude of outages in ArcGIS (ESRI, 2019). Next, we matched the geocoded outages with the New Jersey building parcels (complete area covered by a plot).

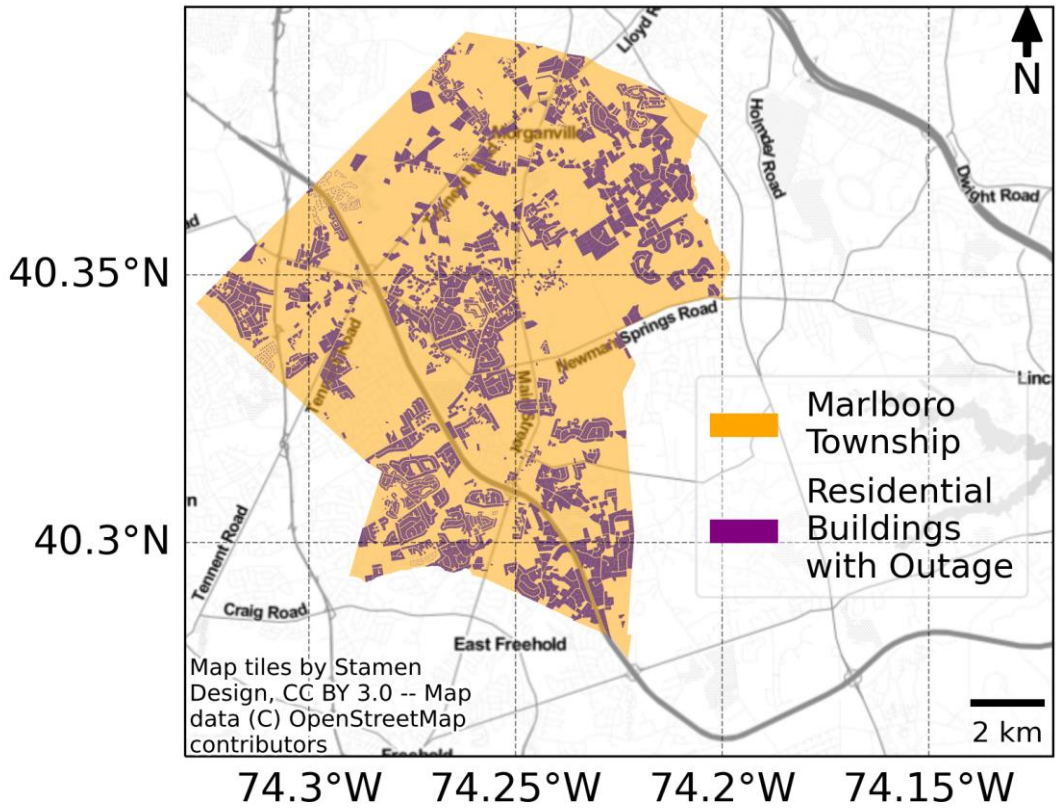

Figure 10. Location of buildings with power outages in Marlboro Township, New Jersey in the aftermath of Hurricane Isaias (2020). (extracted from (Arora & Ceferino, 2023b))

We determined the area available for solar panels for each building. For that, we obtained the building footprints from NJOGIS since footprints of the actual buildings have a smaller area than parcels, as a parcel also includes open areas, e.g., gardens, patios, and garages. Also, a parcel may contain more than one building footprint, as some parcels have separate garages or other open spaces. We took the maximum footprint area in a parcel as the roof area for solar power estimation. Fig. 10 shows the residential building with outages in Marlboro Township, New Jersey. We did not match geocoded outages to parcels as the NJOGIS geocoder allocated the latitude and longitude at the centre of parcels. We excluded 2.7% outages from our analysis that did not match any parcel as the geocoder did not match some addresses. We further selected outages for 9,267 single-family household residential buildings.

3.2.2.3 Solar Irradiance

We used global horizontal irradiance (GHI) to calculate the potential solar electricity (Patel et al., 2021). GHI is available from the National Solar Radiation Database from National Renewable Energy Laboratory (NREL) at a spatial resolution of 4km and a temporal resolution of 30 minutes (Sengupta et al., 2018). We obtained the GHI for the duration of outages caused by Hurricane Isaias (2020) in New Jersey. We used nearest neighbour interpolation to get the GHI for a building by assigning the GHI value available at the nearest distance. We averaged GHI values at 30 minutes to get the hourly GHI. Figure 18(c) shows the average GHI across Marlboro township from August 4 to August 13, 2020.

3.2.3. Measuring solar potential and resilience

The available solar irradiance at the rooftop of a building is often affected by the shadows from the adjacent buildings or trees. Thus, using the entire roof to size a solar panel is not optimal. (Lopez et al., 2012) mention about 22% and 27% of the roof area in cold and warm regions, respectively, are often available for solar electricity generation. New Jersey has moderately cold winters and warm summers. Thus, we assume 25% of the rooftop area is available for panel installation.

Also, not all points on a roof are fully exposed to the sky. The sky view factor (SVF) is used to determine the portion of a sky visible from a point on the rooftop (Redweik et al., 2013). SVF varies from zero (for a completely obstructed view of the sky) to one (for a clear view of the sky above the horizon). We use New Jersey Digital Elevation Model from NJOGIS to obtain SVF, with a relief visualization toolbox in Python, for buildings in Marlboro Township. Most of the buildings in the neighbourhood of Marlboro are single-family residential buildings with significantly less obstruction on the rooftop to the sky. We obtained a mean SVF of 0.98 across all the residential buildings. The final solar irradiance available at a rooftop is GHI multiplied by 25% of the roof area and SVF. An alternative approach to solar panel sizing (Patel et al., 2021) is based on net zero, where the energy consumed matches the energy produced by a user. In this paper, we use the maximum available area to quantify the maximum resilience potential of solar panels.

3.2.3.1. Solar panel fragility

Like overhead distribution and transmission power lines, solar panels installed on rooftops are exposed to high hurricane winds. Thus, we should understand the risk of solar panel damage from hurricane-high winds. Fragility functions are defined to represent the likelihood of solar panel failure at different wind gusts. Ceferino et al. (2023)

developed data-driven fragility models of the rooftop-mounted and ground-mounted solar panels to the hurricane winds. They used the dataset on the performance of solar panels during hurricanes Irma and Maria in 2017 and Hurricane Dorian in 2019. Their dataset consisted of 46 sites of rooftop-mounted panels and 14 large ground-mounted panels with an average capacity of 13 MW. The rooftop panels were mostly damaged from debris impact during hurricanes. Additional damage was at the connections of solar panels to the rooftop, e.g., 46% of panels experienced failures at the clamp, and about 17% experienced racking.

Ceferino et al. (2023) fitted the lognormal distribution to represent the fragility of the solar panels is given by Eq. 19 and plotted in Fig. 11. They used 3-s wind gust as the intensity measure to express the likelihood of failure of solar panels.

$$p = \phi((ln(w) - ln(\bar{w}))/\beta) \quad (19)$$

where p = probability of solar panel's failure

$\phi(.)$ = standard normal cumulative distribution

$\bar{w}$ = 80 m/s (for rooftop panel) and 90 m/s (ground mounted panels)

β = 0.32 (for rooftop panel) and 0.15 (for ground mounted panels)

w = wind speed experienced by solar panels

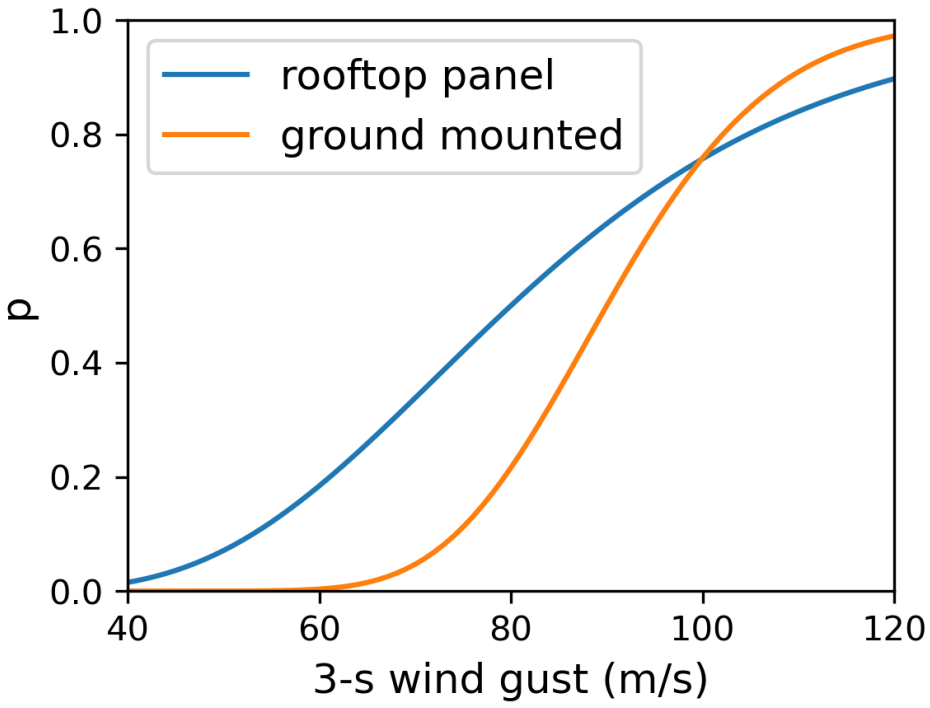

Figure 11. Fragility functions for the rooftop solar panels and ground mounted solar panels based on the parameters from Ceferino et. al (2023)

Other factors, such as rain, could affect the workability of solar panels, but considering such factors is outside the scope of this project, and we considered only winds as the damaging factor. However, solar panels are provided with strong casing to sustain rain and continue to work during rains. For example, Babcock Ranch, a community in Florida located 12 miles away from coastlines, has 700,000 solar panel installations providing power to 2,000 households. The community was unaffected by the massive power outages caused by Hurricane Ian in September 2022, with no damage to solar panels (Cortes et al., 2022). For the rest of this report, we focused on enhancing power grid resilience with solar panels mounted on the rooftops of residential buildings.

3.2.3.2. Solar generation, battery, and consumption

We assumed standard crystal silicone panels are installed for all the buildings with a solar energy conversion efficiency of 19% (Dobos, 2014). We considered 14% system losses used as default by NREL (Dobos, 2014). The system losses due to soiling, shading, mismatch, wiring, connections, light-induced degradation, nameplate rating, and availability. Finally, we assumed a DC-to-AC conversion efficiency of 96%. So, the total converted solar energy is available solar power multiplied by conversion efficiency, system losses, and DC-to-AC efficiency.

We computed the wind fields for Hurricane Isaias (Figure 9) in Marlboro Township using a complete wind profile model for tropical cyclones (Chavas et al., 2015). We observed a maximum 3-s gust wind speed close to 37 m/s. According to Ceferino et al. (2023), rooftop solar has close to zero probability of failure for 3-s gusty winds of less than 40 m/s. So, we assume no panel failure for the Hurricane Isaias scenario, and all panels generate solar energy. We assumed households have a Tesla Powerwall installed with a usable capacity of 13.5 kWh. The battery will discharge every hour by the amount of energy consumed by the user and will charge if the generated solar power exceeds the consumed power. Power consumption data at the building level is not publicly available. The U.S. Energy Information Administration (EIA) collects data on monthly sold electricity to residential consumers by utilities as part of the monthly industry report, also known as form EIA-861M (Form EIA-861M (Formerly EIA-826) Detailed Data, 2020). Since sales in the year 2020 were affected by Hurricane Isaias, we considered the average sales during August from 2019 to 2021 to get the average energy consumed by the user per hour. Thus, for this study, we considered power consumption of 1,534 kW for every household. Refinements to this study could adjust consumption depending on the building size, as bigger homes could consume more electricity (Patel et al., 2021).

3.2.3.3. Resilience Metric

Previously, researchers (Cimellaro et al., 2010; Ouyang & Dueñas-Osorio, 2014) have defined a time-dependent resilience metric to quantify the performance and responsiveness of the power systems disruption post extreme weather events. The resilience metric in Eq.20 is the ratio of the area under the actual performance curve and the area under the expected performance curve of power systems.

$$R(T) = \int_0^T P_R(t)dt / \int_0^T P_T(t)dt \qquad (20)$$

Where $P_T(t)$ is the expected percent of consumers with power under normal conditions, ideally 100%. And $P_R(t)$ is the actual percent of consumers with power disruption post-hurricane. For this paper, we compare the percent increase in resilience for power systems with solar panels compared to no backup power. To get the percentage of residential consumers with power, we set the total number of consumers equal to the peak number of outages in the aftermath of Hurricane Isaias. We perform the integrals in Eq. 19 from the onset of the first outage $(t = 0)$ to the time of restoration of the last outage $(t = T)$.

4. Results and Discussion

4.1. Power Outage Model and Risk Quantification to Future Hurricanes

In this section, we discuss the statistical performance of different outage models by comparing the R^2. We use different R^2 metrics since traditional ones, like the coefficient of determination, have many limitations for counting variables. R^2 is generallgoodness-of-fitre the goodnessof-fit for the linear regression model. Similarly, a pseudo - R^2 (also, R^2_{DEV}) is used to measure the goodness-of-fit for non-linear GAM models.

$$R^2_{DEV} = 1 - \frac{D(y,\hat{y})}{D(y,\underline{y})} \qquad (21)$$

where $D(y,\hat{y})$ is the deviance for the fitted model, and $D(y,\underline{y})$ is the deviance for the null model. The output for the null model is the average of observed historical outages. Deviance measures the amount of variance explained by the fitted model, as explained in (Dunn & Smyth, 2018).

We also compare the performance of developed models for our generalized data covering the southeast, southwest, and northeast regions in the US, with the results from previous models applied to a particular region.

4.1.1. Generalized Linear Models

We trained Poisson and negative binomial GLMs to predict the outage counts. The predictions are based on the seven input features mentioned in the feature selection section. All the input features are significant at a p-value of 2×10^{-6}. We compared the statistical performance of the Poisson and negative binomial GLMs (Table 2). We have a total of 1528 training data points with seven input variables and one additional slope constant. Thus, the residual degree of freedom for each model is 1520. The high value of residual deviance, relative to the degree of freedom, in the Poisson GLM shows large overdispersion (Liu et al., 2005; Han et al., 2009b; Dunn and Smyth, 2018). Thus, using this new outage dataset, we confirm that the variance in historical outages largely exceeds the mean value. A negative binomial GLM has a low residual deviance value compared to the Poisson model and is more similar to the degrees of freedom, indicating that a negative binomial GLM can handle overdispersion in power outage predictions more satisfactorily. The R^2_{DEV} is higher for the negative binomial GLM, also suggesting the negative binomial's better statistical performance.

Table 2. Statistical performance measurements for generalized linear models.

Model	Residual Deviance	R^2_{DEV}
Poisson GLM	6038042	0.20
Negative Binomial GLM	1949	0.29

4.1.2. Generalized Additive Models

We also trained the Poisson and negative binomial GAMs. Like for GLMs, GAMs are trained with the seven input features mentioned before. All the input features are significant at a p-value of 2×10^{-6} for both models. Like for GLMs, the residual degrees of freedom for each model are 1520. The residual deviance for Poisson GAM (Table 3) is ~ 38 % less than the one in Poisson GLM (Table 2), which is a minimal improvement to overcome the large overdispersion, as the deviance is still significantly higher than the degrees of freedom. However, R^2_{DEV} shows a more significant performance improvement as its value increases to 0.53 for Poisson GAM (Table 3) over a value of 0.20 for Poisson GLM (Table 2). The negative binomial GAM has a low value of residual deviance, which indicates that the negative binomial GAM can handle overdispersion. Additionally, non-linear shapes from spline functions (Eq. 6) for GAMs improve the outage predictions. The R^2_{DEV} for the negative binomial GAM improves significantly to a value of 0.62 (Table 3) over the 0.29 in the negative binomial GLM (Table 2). The R^2_{DEV} for GAMs is not available in the previous literature, so further comparisons with previous work could not be made.

Table 3. Statistical performance measurements for generalized linear models.

Model	Residual Deviance	R^2_{DEV}
Poisson GAM	3565948	0.53
Negative Binomial GAM	1866	0.62

4.1.3. Random forest

We calibrated the random forest model to predict the fraction of customers without power. We performed the hyperparameter tuning using the GridSearch tool in Python (Pedregosa et al., 2011) with cross-validation to select the best input parameters for the random forest. We tuned the model parameters by reducing the maximum depth. We obtained a cross-validation R^2 of 0.48 and training R^2 of 0.63. Finally, we obtained an R^2 of 0.48 on the hold-out test. The number of randomly grown trees in the selected random forest model is 500. Fig. 12 shows the predicted fractional outages against the observed outages using a tuned random forest (RF). RF does not generalize well to the outages due to Hurricane Isaias, which had low wind speeds ($\sim$ 36 $m\,s^{-1}$) in New Jersey but still caused outages to 60 % of consumers in 213 cities (out of 565) in New Jersey. This effect is visible in Fig. 12, where RF underestimated the fractional outages for severely affected cities in New Jersey.

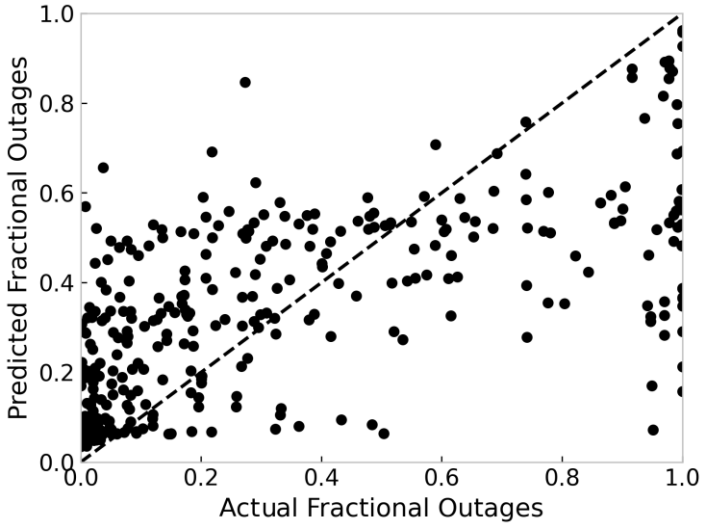

Figure 12. Random forest outage predictions on the 20% holdout test. (extracted from (Arora & Ceferino, 2023c))

The R^2 for the random forest model cannot be compared to different R^2 statistics calculated for GLM and GAM models, as the output for random forest (fraction of outages) differs from GLM and GAM models (outage counts). Also, we cannot calculate R^2_{DEV} statistics for random forest as there is no underlying probability distribution assumed for random forest predictions.

We present the variable importance in the random forest model in Fig. 13. We ranked importance by finding the variable that leads to the largest difference in the mean squared error between the base (full) model and the permuted (reduced) model. We present the normalized importance factors in decreasing order of importance (Fig. 13). We found that maximum wind speed is the most important parameter in the random forest model (Fig. 13), which coincides with our findings from a simple linear regression in Fig. 5. Precipitation is the second most important variable, with a relative importance of 0.33, as trees can more easily be torn out from wetter soil. Population density is the third most important variable in outage predictions since it is a proxy for cities' density of transformers exposed to winds.

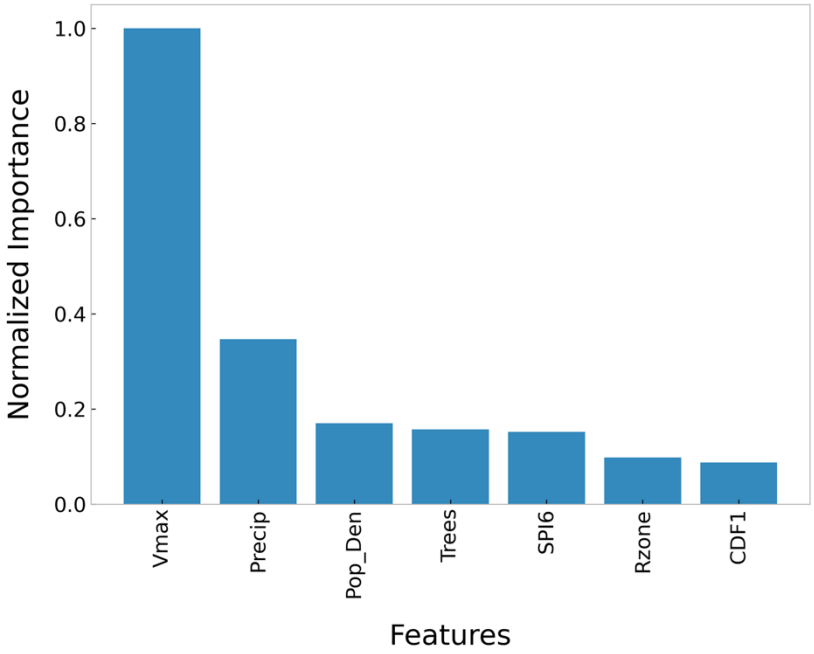

Figure 13. Random forest variable importance in decreasing order of importance. All importance factors are normalized by the highest value, i.e., the factor for Vmax. (extracted from (Arora & Ceferino, 2023c))

Random forest and negative binomial GAMs show superior performance in predicting the power outages caused by a hurricane. We rescale the negative binomial GAM predictions by the total number of customers to compare the Mean Squared Error (Wallach & Goffinet, 1989) MSE values of negative binomial GAM and RF models at the same scale as fractional outages. MSE for the negative binomial GAM is 45.13, and MSE for RF is 0.06. Researchers should be careful in making the direct comparison for MSE values of the fraction-based RF model and the count-based negative binomial GAM model, as these models are optimized for a different set of response variables. The high MSE for the negative binomial arises from overestimating outages, which we discuss next.

4.1.4. Limitations to the state-of-the-art outage models

Different machine learning models discussed in previous sections can predict power outages for a hurricane-stricken city. Here, we discuss the limitations of state-of-the-art machine learning models for power outage predictions.

4.1.4.1. GLM and GAM's predictions are unbounded.

GLM and GAM regressions can predict the mean number of outages in the city. The models have a lower bound of zero as both Poisson and negative binomial distributions predict the count of outages. However, there is no upper bound on the predicted number of outages. Hence, GLM or GAM models can predict more outages than the number of customers, resulting in an overestimation of power outages.

For illustration, we present the power outage predictions on 20 % hold-out test data for the negative binomial GAM (Fig. 14). For 76 cities out of 382 (19.8 %) in test data, predicted outages are more than the number of customers, and the overestimation can be significant. Modelers could impose an upper bound on the predictions using the total number of customers as the maximum possible outage. However, this adjustment would violate the assumptions in the Poisson–gamma mixture model (Eq. 5) and GAM link function (Eq. 6).

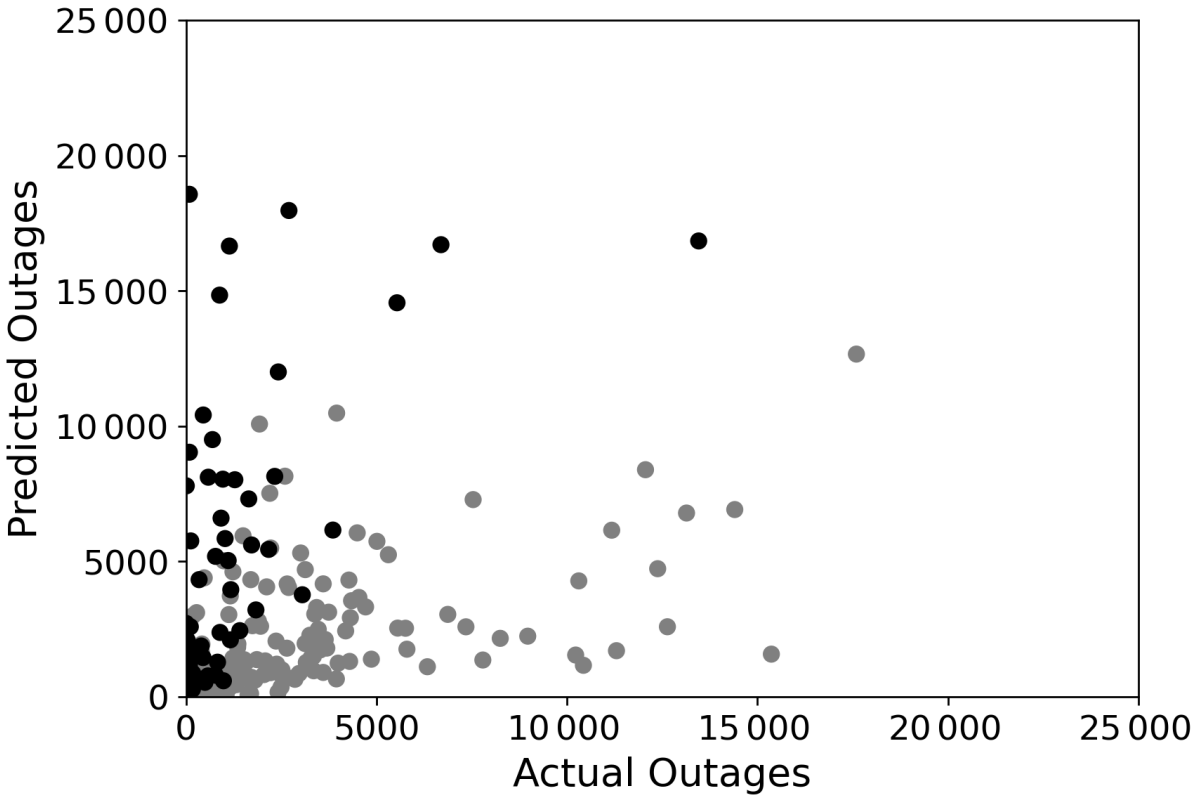

Figure 14. Outage predictions on 20 % holdout test data using the negative binomial GAM outage model. Black dots represent the cities with predicted outages larger than the number of customers. Grey dots represent the cities with predicted outages less than or equal to number of customers. (extracted from (Arora & Ceferino, 2023c))

4.1.4.2. Random forest's lack of extrapolability for high winds

Random forest predictions are an average value of the outages in the training data (Eq. 7). Thus, unlike GLMs, random forest predictions are bounded by the minimum and maximum values of power outages in training data. Based on simple physics, one would expect more damage and more outages from higher wind speeds. We plotted the partial dependence of the fraction of customers without power against wind speed. The partial dependence, $g(x_j)$ (Hastie et al., n.d.; Nateghi et al., 2014) of the input variable x_j is given by

$$g(x_j) = \frac{1}{N}\sum_{i=1}^{N} \hat{y}(x_j, x_{ic}) \quad (22)$$

where N is the total number of observations, x_{ic} are the variables other than x_j , and $\hat{y}_i$ is outage prediction (Eq. 7) for the ith data point.

For this assessment, we trained the random forest model on a reduced dataset, with only New York and New Jersey, and on a complete dataset, including Florida and Texas. We present the partial dependence of wind speed in Fig. 15, also including the distribution of wind speeds in the training data. Hurricanes of category 3 or higher bring wind speeds above 40 ms^{-1} that can significantly damage electric poles (Bjarnadottir et al., 2013). However, they are significantly less observed in inland cities, especially in the northern United States, as storms often weaken in their transition to higher latitudes and after leaving the ocean. For example, only tropical storms with wind speeds of less than 33 $m\,s^{-1}$ have impacted New York City for the past 20 years (https: //coast.noaa.gov/hurricanes/#map). As per ASCE 7–10 wind hazard maps (https: //hazards.atcouncil.org/) wind speed of 43 ms^{-1} has a return period of 100 years for New York City. Thus, it is very unlikely, and evident from Fig. 15, to get outage data in New York and New Jersey for winds above 43 ms^{-1} .

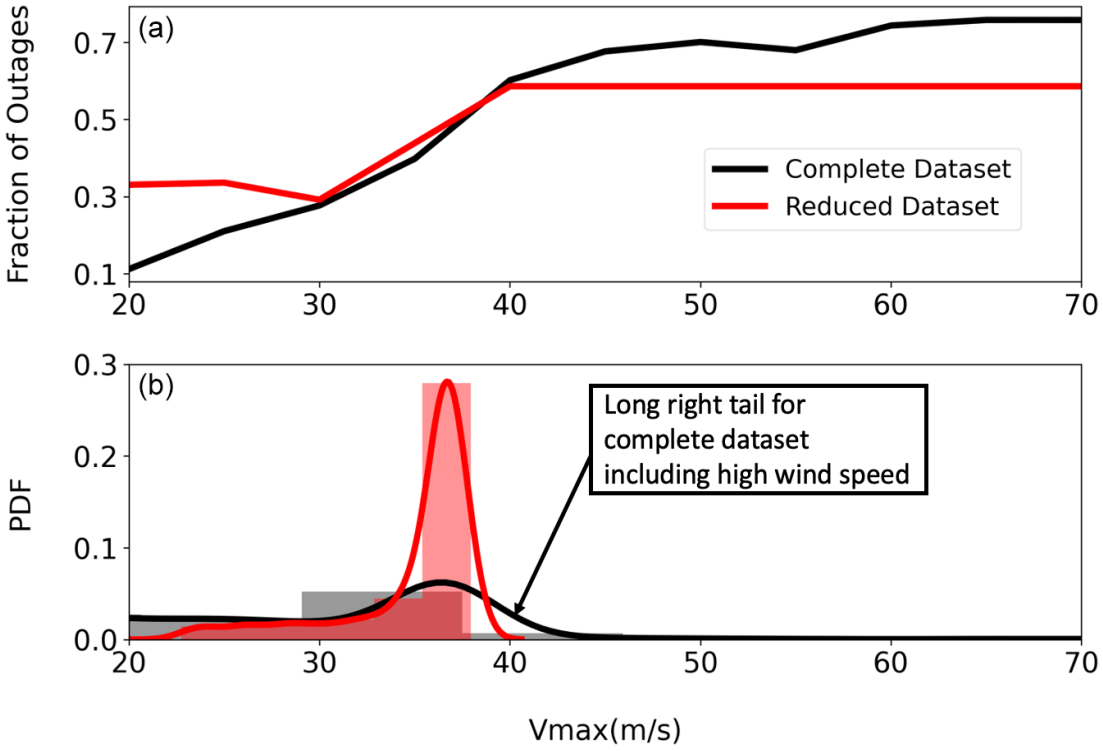

Figure 15. (a) Partial dependence of wind speed on power outages. (b) Distribution of wind speed in the complete and reduced dataset. The random forest model does not extrapolate for the wind speeds and outages not in the range of training data. (extracted from (Arora & Ceferino, 2023c))

These limited outage datasets have strong implications for the validity and extrapolability of outage models based on random forest regressions. Under the reduced dataset, i.e., with only New Jersey and New York, outage predictions increase as the wind speed increases from 20 to 40 $m\,s^{-1}$. However, the fraction of outages reached a maximum of 0.58 at wind speeds of 40 ms^{-1} and does not increase with higher wind speeds. Under the complete dataset, results improve by including outages in Florida and Texas. These states experience higher winds; e.g., their 100-year return-period winds are ~70 ms^{-1} in contrast to the 43 ms^{-1} in New York (https://hazards.atcouncil.org/). While these results show improvement, they also show that the data are still insufficient to make the random forest model follow the physics of infrastructure failure and extrapolate predictions for high winds causing outages close to 100 %.

4.1.4.3. Lack of physics-based variance shape

In catastrophic storms, we expect large outages with higher certainty, e.g., Hurricane Ida (2021) in Louisiana (Elamrouss, 2021) and Tropical Storm Fiona (2022) in Puerto Rico (Rivera et al., 2022), close to 100 %. Structural models for power poles estimate failure probabilities close to 95 % for winds of 70 $m\,s^{-1}$ (Bjarnadottir et al., 2013; Ouyang & Dueñas-Osorio, 2014). Thus, the physics of infrastructure failure suggests that variance in

outages should be smaller for catastrophic winds. To evaluate if existing models follow these principles from the physics of power infrastructure failure, we quantified the variance in predictions for Jersey City by varying the wind speed and keeping the other input variables unchanged (Fig. 16).

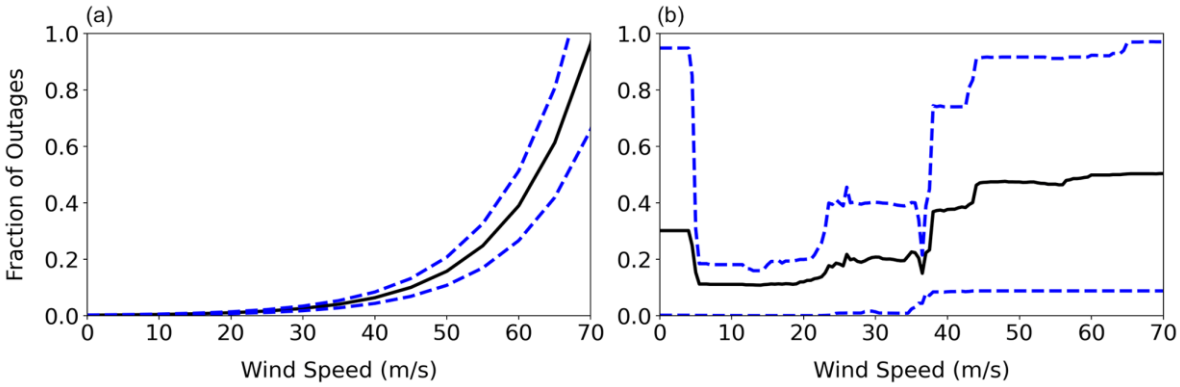

Figure 16. Prediction ranges of power outage as a function of wind speed for (a) the negative binomial GAM and (b) random forest. For GAM, mean and standard deviations are based on Eq. (5). For random forest, we use quantile random forest to determine percentiles and assume normal distribution to find comparable intervals of the mean plus and minus the standard deviation. Black lines indicate the mean outage predictions. Blue dashed lines indicate the 1 standard deviation interval for outage predictions. (extracted from (Arora & Ceferino, 2023c))

As discussed previously, negative binomial GAMs capture the variability of outages better than Poisson models. Thus, we focus on the former models and estimate the variance according to Eq. (5). Figure 16a show the mean and 1 standard deviation interval for outage predictions with varying wind speeds. We normalized the GAM's predictions to show fractions and compare them to the random forest model. GAM's predictions go beyond 1, as discussed previously, but we truncated the y axis at 1 for comparison purposes. The linear relationship in the link function ensures that the variance (function of the square of mean outages from Eq. 5) grows with wind speed. The variance shows higher values as the predicted outage fraction approaches to 1. In fact, the variance is also unbounded in the negative binomial GAM and goes to infinity.

The random forest model can only predict the mean number of outages. Thus, it cannot evaluate variances. However, the quantile regression forest (QRF) (Meinshausen, 2006) can predict the outages at different confidence intervals, and we use it to quantify variance. We presented random forest prediction intervals in Fig. 16b. The random forests had a standard deviation of 0.45 for high winds (>70 $m\,s^{-1}$), departing from the expected value of zero for catastrophic winds. Additional data could improve these random forest variance estimates. However, as mentioned earlier, infrastructure failure data are sparse. Moreover, structural models predict no damage to power infrastructure at wind speeds

lower than 10 $m\,s^{-1}$), (IEEE, 2007; Bjarnadottir et al., 2013). Thus, we expect outage predictions closer to 0 with a higher degree of certainty. Negative binomial (and Poisson) GAMs handle this case well, as the variance is zero when the mean outage is zero (Eqs. 1 and 5). In contrast, we found that random forests had a standard deviation of 0.66 for zero wind speeds, showing that they also have limitations to represent physics-informed variance at low wind speeds.

4.1.5. SAIFI and SAIDI for 10-year return period in New Jersey, USA

Based on the reduced negative binomial based power outage model, we present the results for SAIFI and SAIDI for 10-year return period in New Jersey, USA. We present in Fig. 17, SAIFI for cities in New Jersey for a 10-year return period (or λ(SAIFI) = 0.1). Thus, in 10 years, cities will exceed the SAIFI presented on Fig. 16.

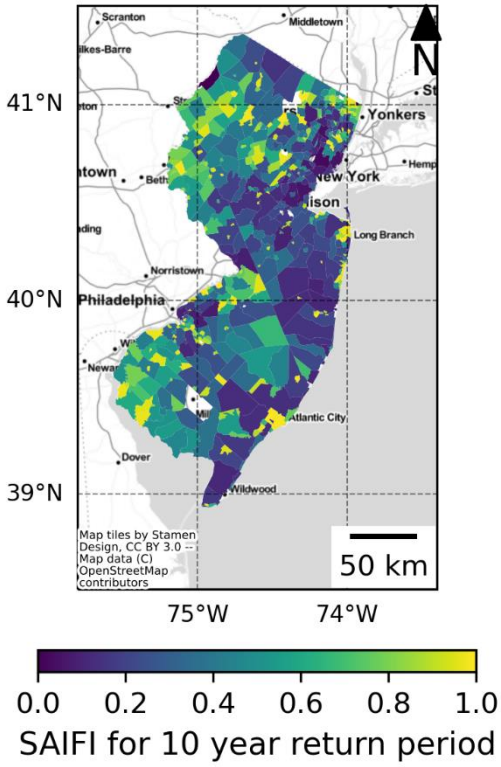

Figure 17. SAIFI for 10-year return period in New Jersey, USA (extracted from (Arora & Ceferino, 2023a))

SAIFI distribution in Fig. 17 does not follow a pattern as such for winds in Fig. 8. This is counterintuitive, as high-value SAIFI is expected for high winds. The power outage model developed to obtain SAIFI is also a function of the percent area covered by the developed area and population. The winds for the same return period have a low variation of only from 33m/s to 34.5 m/s within New Jersey, so other input features have more impact on the spatial variations of SAIFI. Therefore, we investigated the correlation between SAIFI

and other input parameters. We found a small negative correlation (Pearson coefficient = −0.1) between SAIFI and the percent developed area in a city. The negative correlation can be attributed to varying grid patterns between rural and urban areas, as rural areas generally have radial grids which can have more power outages compared to gridded patterns in urban areas (Petersen, 1982; Brown, 2002). Also, we found a negative correlation (Pearson coefficient = −0.3) between SAIFI and population density, as low population density can indicate the low density of transformers in a city (Brown, 2002). The sparsity of components in power grids can reduce the resilience and lead to more outages (Brown, 2002).

We present in Fig. 18 SAIDI for cities in New Jersey for a 10-year return period (or λ (SAIDI) = 0.1). We found a negative correlation (Pearson coefficient = −0.22) between SAIDI and percent developed area and a negative correlation (Pearson coefficient = −0.20) between SAIDI and population density. Both SAIFI and SAIDI are negatively correlated with the percent developed area and population density, showing that the presented framework can capture the behaviour of power systems in large regions without using extensive information on power system components.

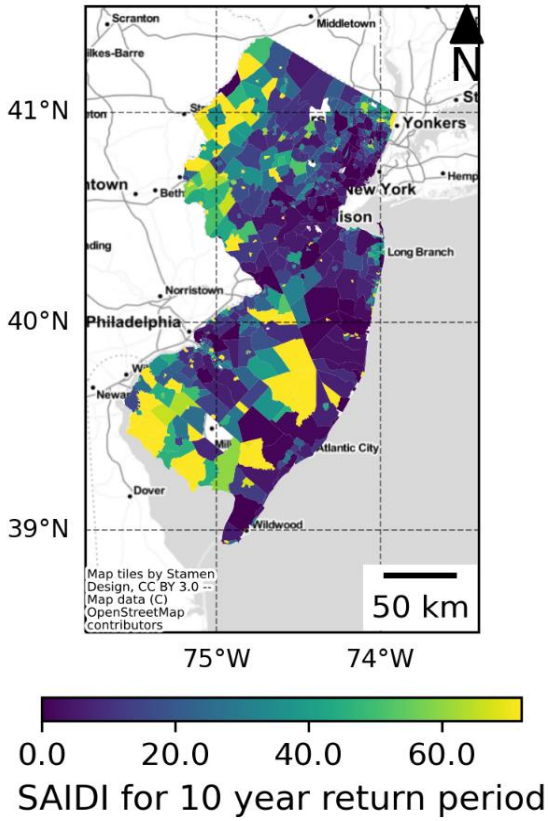

Figure 18. SAIDI for 10-year return period in New Jersey, USA (extracted from (Arora & Ceferino, 2023a))

4.2 Solar potential during hurricane Isaias in New Jersey, USA

Given National Oceanic and Atmospheric Administration provide weather forecast 3-7 days ahead of a storm (Squitieri & Gallus, n.d.), we assume in response to pre-disaster planning for outages, households keep their battery charged. We consider two scenarios for the state of the battery, (a) fully charged battery and (b) half-charged battery.

Considering solar panels could provide limited backup power, households may choose to reduce their power consumption post-hurricane. We consider three scenarios for consumption, (a) no reduction in power consumption, (b) 25% reduction in consumption, and (c) 50% reduction in consumption. Thus, we present results for six combinations based on the state of the battery and reduction in consumption in Fig. 19.

Rooftop solar panels installed under all scenarios show a resilience gain compared to the base case of actual outages with no backup power. The resiliency gain for the 50% consumption scenario for a battery fully and half charged at the onset of outages is 37.3% compared to no backup power. The resiliency gain for a 75% consumption scenario for battery fully and half charge is close to 35%. And, for 100% consumption, resiliency gain is close to 30%. From Fig. 19, we can observe all the households will have no outage if they curtail their consumption to 50%. For scenarios with 75% and 100% consumption, consumers only depend on battery storage for supply at night, and outages occur once the battery is completely drained. However, battery charges during daytime, and households recover from the outage. This cycle continues until the main grid supply is restored.

5. Enablers and Barriers

The research has been supported by the essential power outage data during Hurricane Isaias (2020) provided by the Jersey Central Power & Light. The additional availability of power outage data from poweroutage.us has enabled the development of power outage models.

The constant support from project mentor Dr Luis Ceferino and his expertise in disaster risk analysis have been vital to the success of this project. Further discussions with the technical experts, Dr Kampanart Silva and Dr Paris Kloss during mid-quarterly and quarterly check-in meetings have allowed to explore different aspects of the project.

The presented data-driven for power outage modelling currently utilizes only publicly available input parameters. However, more data is needed to develop a high-resolution

model, which more extensive outage dataset for different regions, e.g., for other summer and winter storms. In addition, other infrastructure data can also improve outage prediction by including additional power system information e.g., location of circuit breakers, number of poles, and structural specification of poles such as type of material, height, and radius of the pole.

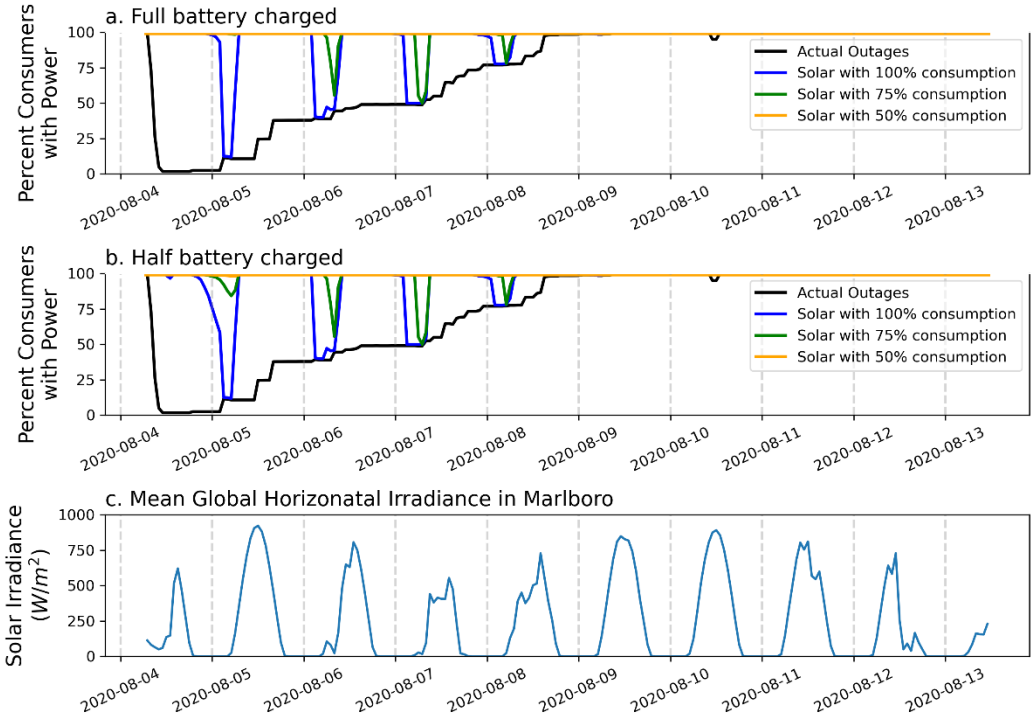

Figure 19. (a) Power Outage scenarios when the battery is fully charged at the onset of power outages. (b) Power Outage scenarios when the is half charged at the onset of power outages. (c) mean solar irradiance in Marlboro Township. (extracted from (Arora & Ceferino, 2023b))

6. Key Takeaways from CDRI Fellowship Programme

The data-driven methods can help understand the risk to infrastructure from extreme weather events. For example, power outage models can assist utilities in preparing and rapidly recovering from hurricane induced power failures. The data-driven approach based on historical outages can guide utilities to identify the sections of the power grid most vulnerable to hurricanes. Additionally, transitions in complex energy systems are often slow because of reliability, capital investments, and the involvement of many stakeholders. Hence, it is an excellent opportunity to build a resilient power grid when transitioning towards cleaner energy sources.

The 2021 United Nations Climate Change Conference, also called COP 2021, saw

participation from 197 countries making pledges to reduce carbon emissions to limit the temperature rise by 1.5℃. Renewable energy has always been the centre of focus towards the goal of reducing the impact of emissions on our climate. However, renewable energy sources, such as solar panels, can also be vulnerable to impact from extreme weather events (Fig. 20). A comprehensive risk assessment can enable the better adoption of new technologies in the energy sector toward a resilient power grid. This paper presented the methods to determine the solar potential during a hurricane in New Jersey, USA. The presented methods are generalizable and could be extended to determine solar potential in different geographies with minimal information on solar exposure and topography information.

Figure 20. Failure of clip attachment between solar panels and roof in aftermaths of hurricane Ian (2022) in Florida, USA. (credits: Dr Luis Ceferino)

7. Conclusion

7.1 Power Outage Model and Risk Quantification to Future Hurricanes

This paper summarized existing power outage prediction models, (a) GLMs and (b) GAMs based on Poisson and negative binomial distributions and (c) random forest regressions. Power outages depend on several factors, including hurricane, environmental, and demographic conditions. We combined the outages from four different states in US to develop a generalized power outage model across different regions, improving previous efforts that only calibrated outage models to a particular region or utility companies in the US. We calibrated the state-of-the-art outage models using seven input parameters: 3-s wind gust speed, 7 d precipitation after the storm, standard precipitation index for 6 months before the storm, soil moisture for a depth between 0 and 10 cm, population density, the percent area covered by trees, and trees' root zone depth.

First, we found that Poisson regressions are unsuitable for modelling outages, as historical outages have larger variances than the mean, resulting in overdispersion. We found that negative binomial regressions account for these larger variances better than Poisson regressions. We demonstrated that the random forest could also capture this non-linear behaviour, as we found a value of 0.48 for the R^2 in the cross-validation.

However, each model has its own merits and demerits in predicting outages. Poisson and negative binomial estimates are unbounded and can overestimate power outages. The negative binomial GAM failed to account for low uncertainty in outage predictions at high winds. We found that random forest also fails to account for low uncertainty at low winds. Overestimated power outages could result in prioritizing a less affected city, placing more resources on that city than required. Erroneous power outage estimates with high uncertainty can result in the non-optimal placement of resources, as optimal resource allocation algorithms will use predicted outages (Brown, 2002).

We suggest beta (Ferrari & Cribari-Neto, 2010) and binomial regressions (Dunn and Smyth, 2018) to model power outages in future research. While testing their performance is not covered in this paper, beta and binomial distribution can help overcome existing limitations due to their fundamental properties. For example, beta and binomial regressions are upper-bounded, unlike negative binomial GLM and GAM regressions. Thus, beta or binomial GAMs can model the fraction of outages in a city, i.e., directly in the case of beta since it goes from 0 to 1, or after normalizing the total number

of outages by the maximum number of customers in the case of the binomial regressions. Also, beta and binomial GAMs can extrapolate outages for the extreme (low and high) values of winds since they can model monotonically increasing outages as a function of environmental parameters. Finally, beta and binomial GAMs have variances closer to zero at outage fraction observation values of 0 and 1, better representing the physics or power infrastructure failures.

We also suggest including the parameters that could capture the potential flooding along the coastal regions. The significant storm surges can also extensively damage the power grid resulting in compounding of risk along with high winds (Poudyal et al., 2022). Thus, we suggest including parameters such as

We also presented a probabilistic framework that couples a probabilistic outage model and wind hazard to estimate the rate of observing power system performance indices, SAIFI and SAIDI. We presented the results for SAIFI and SAIDI in New Jersey, US, for a return period of 10 years. We observed that including parameters such as land cover and population density could capture the behaviour of power systems to hurricanes. For future work, a comprehensive power outage model could be adopted to consider the uncertainty not only in winds but also in other environmental parameters such as precipitation and soil moisture. The presented performance-based probabilistic study can inform stakeholders, such as utilities and regulatory bodies, like the Board of Public Utilities in New Jersey, about the expected performance of a system for different hazard levels.

7.2 Solar potential during hurricane Isaias in New Jersey, USA

We presented a what-if scenario of resilience to power outages in the aftermath of Hurricane Isaias (2020) with solar panel adoption by residents of Marlboro Township, New Jersey. We observed that all the houses gain resilience with solar panels compared to no backup. Moreover, by intentionally reducing their consumption, households can sustain themselves throughout power outages with solar panels and energy stored in the battery even more effectively. This study presented the importance of solar panels for electric grid resilience. However, the study was limited to certain conditions.

For future studies, more practical considerations could be considered when studying the resilience of solar energy to hurricanes. For example, solar panels and batteries could be sized based on the net-zero energy consumption of the user. Furthermore, during disasters, community members with undamaged solar panels could

share energy with households with no source of power, as the adoption of solar panels could be limited, given the socio-economic conditions of the neighbourhoods (Wang et al., 2022). Thus, methods presented in this study could be extended to a more comprehensive study on resilience with solar panels.

8. Recommendations and Way Forward

We plan to test an improved power outage model for the upcoming hurricane season in the USA. We are developing a web interface to forecast power outages (Fig. 21) that could assist utilities and inform the community member to arrange for backup power. The continuous power supply is essential for the undisrupted functioning of critical facilities, e.g., hospitals, and fire stations, for emergency response post-disaster.

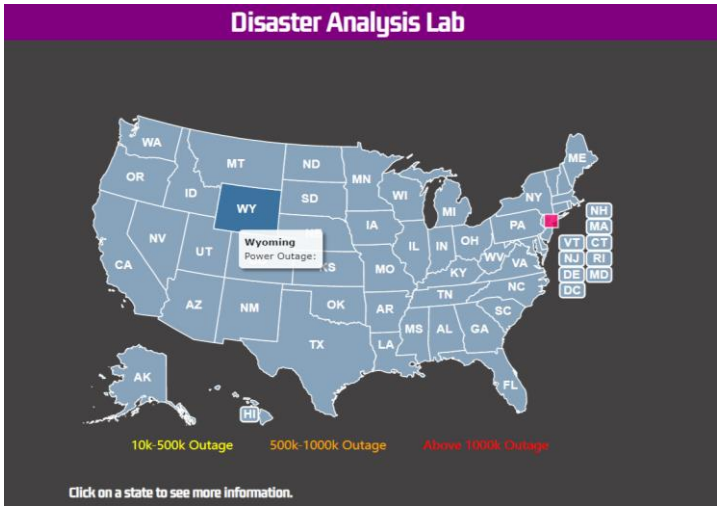

Figure 21. Web layout interface for the deployment of power outage model.

Strong winds from hurricanes damage the power grid infrastructure, including long power lines or transmission towers that serve power to many residential, commercial, and industrial customers. Grid hardening techniques such as undergrounding power lines or replacing wooded poles with steel poles could improve the resilience of power systems to hurricanes. Furthermore, adopting distributed energy resources, such as solar panels (presented in this paper), could also provide the necessary power supply when the primary grid is off, resulting in increased resilience to extreme weather events. We presented a probabilistic method to identify vulnerable sections of the power grid. The presented method could be further extended to understand possible economic losses from outages and the cost-benefit analysis of adopting different measures to enhance the resilience of power infrastructure. These methods can guide underlining an optimal strategy for choosing economically practical measures and increasing the power grid's resilience.

This paper considered the solar potential only through rooftop solar panels for Marlboro township in New Jersey, USA. The analysis can also extend to consider the solar potential

in the facades of residential buildings (Redweik et al., 2013). The measures could include installing clear glass window solar panels. However, this would require testing the glass window panels against extreme winds to understand their reliability during hurricanes comprehensively. Solar panels can be irreparably damaged from debris during hurricanes that could be possibly handled by designing solar panels with small replaceable parts to avoid losing power for a longer period (Majdi et al., 2021). Other damage modes for rooftop panels include clip failures, racking failures, roof attachment failures, and rack or connection, roof attachment failures (Ceferino et al., 2023a). Thus, attention should also be given to connections of solar panels to rooftops, as any such failure could result in losing possible backup power from solar panels. Understanding the performance of solar panels post-disaster through field visits in areas with more frequent hurricanes (e.g., Florida) could give a better understanding of the failure modes of solar panels, which would be beneficial to implement structural upgrades to future solar panel design. Finally, electricity consumption would increase in response to the electrification of households (e.g., for cooking and heating) to reduce emissions from fossil fuels. As indicated in this paper, user consumption also determines resilience. Therefore, increased electricity consumption should be considered in the final resilience calculation of power grid infrastructure to future natural hazards.

Climate change can exacerbate the vulnerabilities of power grid infrastructure to extreme weather events. The methods presented in this paper to evaluate the vulnerabilities of the primary grid and solar panels did not consider any increased risk from climate change. However, climate change would result in a global 13% increased frequency of strong (category 4 or 5) hurricanes (Knutson et al., 2019). Thus, we plan to assess the resilience of power grid to increased risk from increased frequency of strong hurricanes under future climate.

References

1. Ankit, A., Liu, Z., Miles, S. B., & Choe, Y. (2021). *U.S. Power Resilience for 2002--2017*. http://arxiv.org/abs/2103.15859
2. Arab, A., Khodaei, A., Khator, S. K., & Han, Z. (2016). Electric Power Grid Restoration Considering Disaster Economics. *IEEE Access*, *4*, 639–649. https://doi.org/10.1109/ACCESS.2016.2523545
3. Arora, P., & Ceferino, L. (2023a). A performance-based probabilistic framework to model risk to power systems from hurricanes. *14th International Conference on Applications of Statistics and Probability in Civil Engineering*.
4. Arora, P., & Ceferino, L. (2023b). Could rooftop solar panels and storage have enhanced the electricity resilience during Hurricane Isaias (2020)? *14th International Conference on Applications of Statistics and Probability in Civil Engineering*, *2020*.
5. Arora, P., & Ceferino, L. (2023c). Probabilistic and machine learning methods for uncertainty quantification in power outage prediction due to extreme events. *Natural Hazards and Earth System Sciences*, *23*(5), 1665–1683. https://doi.org/10.5194/NHESS-23-1665-2023
6. *ASCE 7 standard | ASCE*. (n.d.). Retrieved August 16, 2022, from https://www.asce.org/publications-and-news/asce-7
7. Bjarnadottir, S., Li, Y., & Stewart, M. G. (2013). Hurricane Risk Assessment of Power Distribution Poles Considering Impacts of a Changing Climate. *Journal of Infrastructure Systems*, *19*(1), 12–24. https://doi.org/10.1061/(asce)is.1943-555x.0000108
8. Brown, R. E. (2002). *Electric Power Distribution Reliability*.
9. Cai, J., Luo, J., Wang, S., & Yang, S. (2018). Feature selection in machine learning: A new perspective. *Neurocomputing*, *300*, 70–79. https://doi.org/10.1016/j.neucom.2017.11.077
10. Ceferino, L., Lin, N., & Xi, D. (2022). Stochastic modelling of solar irradiance during hurricanes. *Stochastic Environmental Research and Risk Assessment*, *36*(9), 2681–2693. https://doi.org/10.1007/S00477-021-02154-2/FIGURES/6
11. Ceferino, L., Lin, N., & Xi, D. (2023a). Bayesian updating of solar panel fragility curves and implications of higher panel strength for solar generation resilience. *Reliability Engineering and System Safety*, *229*. https://doi.org/10.1016/J.RESS.2022.108896
12. Ceferino, L., Lin, N., & Xi, D. (2023b). Bayesian updating of solar panel fragility

curves and implications of higher panel strength for solar generation resilience. *Reliability Engineering & System Safety*, *229*, 108896. https://doi.org/10.1016/J.RESS.2022.108896

13. Chapman, L. (2000). Assessing topographic exposure. *Meteorological Applications*, *7*(4), 335–340. https://doi.org/10.1017/S1350482700001729
14. Chavas, D. R., Lin, N., & Emanuel, K. (2015). A model for the complete radial structure of the tropical cyclone wind field. Part I: Comparison with observed structure. *Journal of the Atmospheric Sciences*, *72*(9), 3647–3662. https://doi.org/10.1175/JAS-D-15-0014.1
15. Cimellaro, G. P., Reinhorn, A. M., & Bruneau, M. (2010). Framework for analytical quantification of disaster resilience. *Engineering Structures*, *32*(11), 3639–3649. https://doi.org/10.1016/J.ENGSTRUCT.2010.08.008
16. Cortes, M., Arora, P., Ceferino, L., Ibrahim, H., Istrati, D., Reed, D., Roueche, D., Safiey, A., Tomoczek, T., Zisis, I., Alam, M., Kijewski-Correa, T., Prevatt, D., & Robertson, I. (2022). *StEER - Hurricane Ian | DesignSafe-CI*. StEER. https://www.designsafe-ci.org/data/browser/public/designsafe.storage.published/PRJ-3709/#details-4421495110974640621-242ac118-0001-012
17. Danielson, J. J., & Gesh, D. B. (2011). *Global multi-resolution terrain elevation data 2010 (GMTED2010): U.S. Geological Survey Open-File Report 2011–1073*. Terrain. https://www.usgs.gov/publications/global-multi-resolution-terrain-elevation-data-2010-gmted2010
18. (dataset) Soil Survey Staff. (n.d.). *Gridded Soil Survey Geographic Database (gSSURGO) | Ag Data Commons*. Retrieved September 20, 2022, from https://data.nal.usda.gov/dataset/gridded-soil-survey-geographic-database-gssurgo
19. Dobos, A. P. (2014). *PVWatts Version 5 Manual*. www.nrel.gov/publications.
20. Dunn, P. K., & Smyth, G. K. (2018). Generalized Linear Models with Examples in R, https://link.springer.com/book/10.1007/978-1-4419-0118-7. In *Springer New York, NY*.
21. Elamrouss, A. (2021, September 9). *75% of power outages reported in Louisiana after Hurricane Ida have been restored, governor says | CNN*. https://www.cnn.com/2021/09/09/us/hurricane-ida-aftermath-louisiana-thursday/index.html
22. ESRI 2019. (n.d.). *ArcGIS Desktop: Release 10.8*.

23. *Federal Sustainability Plan Catalyzing America's Clean Energy Industries and Jobs*. (2021).
24. Ferrari, S. L. P., & Cribari-Neto, F. (2010). Beta Regression for Modelling Rates and Proportions. *Http://Dx.Doi.Org/10.1080/0266476042000214501*, *31*(7), 799–815. https://doi.org/10.1080/0266476042000214501
25. *Form EIA-861M (formerly EIA-826) detailed data*. (n.d.). Retrieved January 29, 2023, from https://www.eia.gov/electricity/data/eia861m/
26. Guikema, S. D., Nateghi, R., Quiring, S. M., Staid, A., Reilly, A. C., & Gao, M. (2014). Predicting Hurricane Power Outages to Support Storm Response Planning. *IEEE Access*, *2*(September 2015), 1364–1373. https://doi.org/10.1109/ACCESS.2014.2365716
27. Guttman, N. B. (1998). Comparing the palmer drought index and the standardized precipitation index. *Journal of the American Water Resources Association*, *34*(1), 113–121. https://doi.org/10.1111/j.1752-1688.1998.tb05964.x
28. Han, S. R., Guikema, S. D., & Quiring, S. M. (2009). Improving the Predictive Accuracy of Hurricane Power Outage Forecasts Using Generalized Additive Models. *Risk Analysis*, *29*(10), 1443–1453. https://doi.org/10.1111/J.1539-6924.2009.01280.X
29. Han, S. R., Guikema, S. D., Quiring, S. M., Lee, K. H., Rosowsky, D., & Davidson, R. A. (2009). Estimating the spatial distribution of power outages during hurricanes in the Gulf coast region. *Reliability Engineering and System Safety*, *94*(2), 199–210. https://doi.org/10.1016/j.ress.2008.02.018
30. Hastie, T., Tibshirani, R., & Friedman, J. (n.d.). *Springer Series in Statistics the Elements of Statistical Learning Data Mining, Inference, and Prediction*.
31. *Hurricane Sandy After Action Report and Recommendations to Mayor Michael R. Bloomberg*. (2013).
32. *IEEE SA - IEEE 1366-2022*. (n.d.). Retrieved February 8, 2023, from https://standards.ieee.org/ieee/1366/7243/
33. Knutson, T., Camargo, S. J., Chan, J. C. L., Emanuel, K., Ho, C. H., Kossin, J., Mohapatra, M., Satoh, M., Sugi, M., Walsh, K., & Wu, L. (2019). Tropical cyclones and climate change assessment. *Bulletin of the American Meteorological Society*, *100*(10), 1987–2007. https://doi.org/10.1175/BAMS-D-18-0189.1
34. Kohavi, R., & John, G. H. (1997). Wrappers for feature subset selection. *Artificial Intelligence*, *97*(1–2), 273–324. https://doi.org/10.1016/S0004-3702(97)00043-X
35. Krawinkler, H. (1995). *New trends in seismic design methodology*.

36. Krist Jr., F. J., Ellenwood, J. R., Woods, M. E., Mcmahan, A. J., Cowardin, J. P., Ryerson, D. E., Sapio, F. J., Zweifler, M. O., & Romero, S. A. (2014). *2013–2027 National Insect and Disease Forest Risk Assessment*. *January*.
37. L, B. (2001). Random forests. *Machine Learning*, 45:5–32.
38. Latto, A., Hagen, A., & Berg, R. (2021). *National Hurricane Center Tropical Cyclone Report. Hurricane Isaias*. *June* 1–32.
39. Laws, N. D., Anderson, K., DiOrio, N. A., Li, X., & McLaren, J. (2018). Impacts of valuing resilience on cost-optimal PV and storage systems for commercial buildings. *Renewable Energy*, *127*, 896–909. https://doi.org/10.1016/J.RENENE.2018.05.011
40. Liu, H., Davidson, R. A., & Apanasovich, T. V. (2007). Statistical forecasting of electric power restoration times in hurricanes and ice storms. *IEEE Transactions on Power Systems*, *22*(4), 2270–2279. https://doi.org/10.1109/TPWRS.2007.907587
41. Liu, H., Davidson, R. A., Rosowsky, D. V., & Stedinger, J. R. (2005). Negative Binomial Regression of Electric Power Outages in Hurricanes. *Journal of Infrastructure Systems*, *11*(4), 258–267. https://doi.org/10.1061/(asce)1076-0342(2005)11:4(258)
42. Lopez, A., Roberts, B., Heimiller, D., Blair, N., & Porro, G. (2012). *U.S. Renewable Energy Technical Potentials: A GIS-Based Analysis*. http://www.osti.gov/bridge
43. Lu, Q., Asce, S. M., Zhang, W., Asce, M., Bagtzoglou, A. C., & Asce, F. (2021). Physics-Based Reliability Assessment of Community-Based Power Distribution System Using Synthetic Hurricanes. *ASCE-ASME Journal of Risk and Uncertainty in Engineering Systems, Part A: Civil Engineering*, *8*(1), 04021088. https://doi.org/10.1061/AJRUA6.0001205
44. Maderia, C. M. (2015). *Importance of Tree Species and Precipitation for Modeling Hurricane-induced Power Outages*.
45. Majdi, A., Alqahtani, M. D., Almakytah, A., & Saleem, M. (2021). Fundamental study related to the development of modular solar panel for improved durability and repairability. *IET Renewable Power Generation*, *15*(7), 1382–1396. https://doi.org/10.1049/RPG2.12079
46. McRoberts, D. B., Quiring, S. M., & Guikema, S. D. (2018). Improving Hurricane Power Outage Prediction Models Through the Inclusion of Local Environmental Factors. *Risk Analysis*, *38*(12), 2722–2737. https://doi.org/10.1111/risa.12728
47. Meinshausen, N. (2006). Quantile Regression Forests. *Journal of Machine Learning Research*, *7*, 983–999.

48. Miller, C., Gibbons, M., Beatty, K., & Boissonnade, A. (2013). Topographic speed-up effects and observed roof damage on Bermuda following Hurricane Fabian (2003). *Weather and Forecasting*, *28*(1), 159–174. https://doi.org/10.1175/WAF-D-12-00050.1
49. Nateghi, R., Guikema, S., & Quiring, S. M. (2014). Power Outage Estimation for Tropical Cyclones: Improved Accuracy with Simpler Models. *Risk Analysis*, *34*(6), 1069–1078. https://doi.org/10.1111/risa.12131
50. National Academies of Sciences, E. and M. (2017). Enhancing the Resilience of the Nation's Electricity System. *Enhancing the Resilience of the Nation's Electricity System*. https://doi.org/10.17226/24836
51. *National Electrical Safety Code, ANSI/IEEE Standard C2-2007*. (2007). *552*.
52. *NJ Geographic Information Network | Geocoding*. (n.d.). Retrieved January 26, 2023, from https://njgin.nj.gov/njgin/edata/geocoding/index.html
53. *OE-417 Form*. (n.d.). Retrieved January 25, 2023, from https://www.oe.netl.doe.gov/OE417/Form/Home.aspx
54. Ouyang, M., & Dueñas-Osorio, L. (2014). Multi-dimensional hurricane resilience assessment of electric power systems. *Structural Safety*, *48*, 15–24. https://doi.org/10.1016/j.strusafe.2014.01.001
55. Patel, S., Ceferino, L., Liu, C., Kiremidjian, A., & Rajagopal, R. (2021). The disaster resilience value of shared rooftop solar systems in residential communities. *Earthquake Spectra*, *37*(4), 2638–2661. https://doi.org/10.1177/87552930211020020/ASSET/IMAGES/LARGE/10.1177_87552930211020020-FIG3.JPEG
56. Pedregosa, F., Varoquaux, G., Gramfort, A., Michel, V., Thirion, B., Grisel, O., Blondel, M., Prettenhofer, P., Weiss, R., Dubourg, V., Vanderplas, J., Passos, A., Cournapeau, D., Brucher, M., Perrot, M., & Duchesnay, E. (2011). Scikit-learn: Machine Learning in {P}ython. *Journal of Machine Learning Research*, *12*, 2825–2830.
57. Petersen, H. C. (1982). Electricity Consumption in Rural Vs. Urban Areas. *Western Journal of Agricultural Economics*, *07*(01), 13–18.
58. Phillips, J. A., Wallace, K. E., Kudo, T. Y., & Eto, J. H. (2016). *Onsite and Electric Backup Capabilities at Critical Infrastructure Facilities in the United States*. https://doi.org/10.2172/1260256
59. Poudyal, A., Wertz, C., Nguyen, A. M., Mahmud, S. U., Gunturi, V., & Dubey, A. (2022). *Spatiotemporal Impact Analysis of Hurricanes and Storm Surges on Power Systems*. https://arxiv.org/abs/2212.06047v1

60. Redweik, P., Catita, C., & Brito, M. (2013). Solar energy potential on roofs and facades in an urban landscape. *Solar Energy*, *97*, 332–341. https://doi.org/10.1016/J.SOLENER.2013.08.036
61. Rivera, I., Mckay, R., & Disavino, S. (2022). *Puerto Rico power grid no match for Fiona; residents unsurprised | Reuters*. https://www.reuters.com/business/environment/some-13-million-customers-without-power-puerto-rico-after-hurricane-fiona-2022-09-20/
62. Sengupta, M., Xie, Y., Lopez, A., Habte, A., Maclaurin, G., & Shelby, J. (2018). The National Solar Radiation Data Base (NSRDB). *Renewable and Sustainable Energy Reviews*, *89*, 51–60. https://doi.org/10.1016/J.RSER.2018.03.003
63. Shashaani, S., Guikema, S. D., Zhai, C., Pino, J. V., & Quiring, S. M. (2018). Multi-Stage Prediction for Zero-Inflated Hurricane Induced Power Outages. *IEEE Access*, *6*, 62432–62449. https://doi.org/10.1109/ACCESS.2018.2877078
64. Smith, A. B. (2020). *2010-2019: A landmark decade of U.S. billion-dollar weather and climate disasters*. www.ncdc.noaa.gov/billions
65. Squitieri, B. J., & Gallus, W. A. (n.d.). *On the Changes in Convection-Allowing WRF Forecasts of MCS Evolution due to Decreases in Model Horizontal and Vertical Grid Spacing. Part I: Changes in Cold Pool Evolution*. https://doi.org/10.1175/WAF-D-22-0041.1
66. Verleysen, M., & François, D. (2005). The curse of dimensionality in data mining and time series prediction. *Lecture Notes in Computer Science*, *3512*, 758–770. https://doi.org/10.1007/11494669_93/COVER
67. Wallach, D., & Goffinet, B. (1989). Mean squared error of prediction as a criterion for evaluating and comparing system models. *Ecological Modelling*, *44*(3–4), 299–306. https://doi.org/10.1016/0304-3800(89)90035-5
68. Wang, Z., Arlt, M. L., Zanocco, C., Majumdar, A., & Rajagopal, R. (2022). DeepSolar++: Understanding residential solar adoption trajectories with computer vision and technology diffusion models. *Joule*, *6*(11), 2611–2625. https://doi.org/10.1016/J.JOULE.2022.09.011
69. Watson, E. B. (2020). Wind Conditions with Increased Solar and Wind Power Generation. *Ieee Transactions on Power Systems*, *35*(2), 929–937.
70. Wood, S. N. (2017). Generalized additive models: An introduction with R, second edition. *Generalized Additive Models: An Introduction with R, Second Edition*, 1–476. https://doi.org/10.1201/9781315370279/GENERALIZED-ADDITIVE-MODELS-SIMON-WOOD

71. Wu, H., Svoboda, M. D., Hayes, M. J., Wilhite, D. A., & Wen, F. (2007). Appropriate application of the Standardized Precipitation Index in arid locations and dry seasons. *International Journal of Climatology*, *27*(1), 65–79. https://doi.org/10.1002/joc.1371
72. Xia, Y. (n.d.). *NLDAS VIC Land Surface Model L4 Hourly 0.125 x 0.125 degree V002*. https://doi.org/10.5067/ELBDAPAKNGJ9
73. Xia, Y., Mitchell, K., Ek, M., Sheffield, J., Cosgrove, B., Wood, E., Luo, L., Alonge, C., Wei, H., Meng, J., Livneh, B., Lettenmaier, D., Koren, V., Duan, Q., Mo, K., Fan, Y., & Mocko, D. (2012). Continental-scale water and energy flux analysis and validation for the North American Land Data Assimilation System project phase 2 (NLDAS-2): 1. Intercomparison and application of model products. *Journal of Geophysical Research: Atmospheres*, *117*(D3), 3109. https://doi.org/10.1029/2011JD016048
74. Yee, T. W. (2012). *Package "VGAM" (Vector generalized linear and additive models)*. http://www.springer.com/series/692
75. Zaveri, M., & Shanahan, E. (2020). *2.5 Million Lose Power and One Is Killed as Isaias Batters N.Y. Area*. New York Times. https://www.nytimes.com/2020/08/04/nyregion/isaias-ny.html#:~:text=More%20than%20two%20and%20a,and%20nearly%20hurricane%2Dforce%20winds..
76. Zhang, J., Asce, S. M., Zhang, W., Asce, M., Lu, Q., Zhu, J., Asce, A. M., Bagtzoglou, A. C., & Asce, F. (2022). A Fragility-Weighted Topological Network for Resilient Assessment of Overhead Power Distribution System Subjected to Hurricane Winds. *ASCE-ASME Journal of Risk and Uncertainty in Engineering Systems, Part A: Civil Engineering*, *8*(2), 04022015. https://doi.org/10.1061/AJRUA6.00012

Flood Disaster Resilient Hydraulic Design of Bridges Exposed to Climate Change

Prof Rakesh Kumar
Department of Civil Engineering
Sharda School of Engineering & Technology
Sharda University
Greater Noida (India)

Under CDRI Fellowship Programme 2022-23

CDRI
Coalition for Disaster Resilient Infrastructure

Disclaimer: The views expressed in this paper reflect the opinions of the author and not necessarily the official views of CDRI.

Abstract

India is expanding its highway and railway networks for better connectivity and to give boost to its infrastructure facilities and economy. For this purpose, safe and optimal design of the bridges incorporating the impact of climate change is of primary importance. Inadequate hydraulic design of bridges leads to their failure whereas over-design results in excessive cost of construction. A comparative study of conventional approach, which is in practice and the L-moments based flood frequency analysis is carried out and the superiority of the L-moments over the conventional approach is demonstrated. On the basis of Zi -statistic criteria as well as L-moment ratio diagram, Generalised Logistic distribution is selected as the suitable frequency distribution for the study area and design floods are estimated using this frequency distribution. The effect of climate change on the design floods and the resulting hydraulic variables of the river reach for the bridge site are simulated using the downscaled projections of climate scenarios and the defined increases in the design floods. Hydraulic modelling for the bridge site is carried out using the design floods for various scenarios for incorporating impact of climate change in the hydraulic design of the bridge.

The floods of 50 and 100-year recurrence intervals computed by L-moments method are 16.70% and 22.74% higher than the conventional method. The hydraulic modelling of reach of the river of about 1.70 km is carried out using HEC-RAS package for 24 river cross-sections obtained from the topographic survey. Based on the L-moments approach, the simulated water levels at the bridge are estimated as 255.88 m and 256.40 m for 50-year and 100-year return periods floods respectively. The velocities of flow are estimated as 3.70 m/s and 3.90 m/s for 50-year and 100-year recurrence interval floods respectively. The top width and hydraulic depth etc. are also estimated by the hydraulic modelling approach. For 15% increase scenarios of 50 and 100-year recurrence interval, water levels are estimated as 256.31 m and 256.90 m. For the downscaled climatic projections, the water levels are estimated as 253.48 m and 255.38 m for 2050 and 2100. Taking the results of various scenarios into consideration, the project authorities may take appropriate decision for flood disaster resilient design and construction of the bridge. The methodology developed in the study will serve as guideline/ manual for the organizations involved in planning, design and construction of bridges for optimal hydraulic design of flood disaster resilient bridges exposed to climate change and the departments involved in construction of highway, railway and other bridges may apply this methodology for construction of flood disaster resilient bridges exposed to climate change.

Acknowledgements

I acknowledge the scientific and financial support extended by the Coalition of Disaster Resilient Infrastructure, New Delhi. The support of the Sharda School of Engineering & Technology and Department of Civil Engineering, Sharda University, Greater Noida is also well-acknowledged. The operational support extended by the Research Development Cell and Finance Office; at Sharda University is also gratefully acknowledged.

Funding

This research was supported by the 2022–2023 Fellowship of the Coalition for Disaster Resilient Infrastructure (CDRI), Application ID: 210827291.

1. Introduction

Bridges are constructed over rivers, canals, creeks and valleys etc. for building the highways and railways and these are one of the most used types of structures by mankind, as various types of vehicles pass over the bridges. Failures of Bridges lead to loss of lives, damage to property and inconvenience to the public etc. One of the main causes of failures of the bridges is overtopping by floods because of inadequate hydraulic design of the bridge waterways. The first and foremost important factor to be decided in the design of bridges is to determine the waterway required for the bridge. Estimation of design flood at a bridge location with water level/ flow depth, flow velocity etc. are key variables to ensure the safety of bridges, which are exposed to climate change, as well. Year after year it is seen that some of the bridges are washed away in India and other parts of the world. For example, in Madhya Pradesh, six bridges were swept away in the year 2021 leading to huge economic losses and inconvenience to the people.

In this study, a methodology for design flood estimation for the bridges is developed based on the L-moments based frequency analysis and its superiority over the existing conventional method is demonstrated. Further, the estimated design flood is used in an integrated numerical hydraulic modelling framework for the determination of the highest flood level for the construction of a bridge near Roorkee in Northern India over river Solani, which is a tributary of river Ganges. The study has created a procedure for design of flood disaster resilient bridges for the road and railway networks to make the transport infrastructure more resilient considering the impact of climate change and its induced uncertainties in the extreme rainfall events.

2. Aim, Objectives, and Scope of the Research Study

2.1 Aim of the study

The study aims to carry out a comparative analysis of the conventional and advanced approaches of design flood estimation, and hydraulic modelling and consider the effect of climate change on flood disaster resilient hydraulic design of the bridges.

2.2 Objectives of the study

The main objective of the study is to review the methodologies being used for the hydrologic and hydraulic design of the highway and railway bridges, identify the gaps,

apply the advanced approaches and incorporate the effect of climate change for flood disaster resilient hydraulic design of the bridges. The objectives of the study are:

1. To carry out comparative flood frequency analysis studies using the emerging L-moments approach and the conventional flood frequency analysis techniques and identify the robust procedure for designing flood estimation for the bridges.
2. To carry out the optimal hydraulic design of the bridges based on the hydraulic modelling approach using the HEC-RAS Package.
3. To incorporate the impact of climate change into the hydraulic design of bridges using the downscaled GCM data as well as the specific percentage increases in the design floods.

2.3 Scope of the study

The study demonstrates the robust procedure of hydrological and hydraulic modelling of flood disaster resilient hydraulic design of the highway and railway bridges considering the impact of climate change and may be adopted by the engineers, academicians and other practitioners involved in planning, design and construction of the bridges as well as developing guidelines, manuals and standards for hydraulic design of bridges.

Apart from the above, estimation of floods of various recurrence intervals are also required for design of embankments, weirs, barrages, dams, nuclear and thermal power projects, spillways, drainage systems as well as for adopting various types of measures such as preparation of flood risk-zone maps, zoning of flood plains etc. The study also provides a pathway for hydrological and hydraulic analysis for such purposes, as well. =

3. Methodology

3.1 Review of literature

Estimation of floods of various recurrence intervals design of hydraulic structures as well as taking up different types of non-structural measures has been very extensively studied. Pilgrim and Cordery (1992) state the significance of estimation of flood peaks for watersheds of small and medium sizes. International Association of Hydrological Sciences (IAHS) took up an initiative on “Prediction of Ungauged Basins (PUBs)” and termed the decade from 2003 to 2012 as “Decade of PUBs” (Sivapalan, 2003). In India, studies have been carried out for estimation of design floods by different organisations (CWC, 1987). In addition, regional flood frequency analysis studies are conducted at some of research and academic organizations (e.g. Kumar et al., 1999; 2003; 2005; 2011 and Kumar, 2019 etc.).

Hosking and Wallis (1997) described L-moments approach in regional frequency analysis. Zafirakou-Koulouris et al. (1998) summarized the advantages of L-moments over the ordinary product moments. Guidance for rainfall and riverflow frequency estimation for United Kingdom is provided in the Flood Estimation Handbook (1999). Saf (2009) carried out regional flood frequency analysis using L-moments for the West Mediterranean Region of Turkey. Badreldin and Ping (2012) performed regional rainfall frequency analysis for the Luanhe Basin by using L-moments and cluster techniques. Seckin et al. (2011) presented flood frequency analysis of Turkey using L-moments. Kumar et al. (2012) conducted a study sponsored by the Nuclear Power Corporation of India on flood inundation modelling using coupled 1-D&2-D hydrodynamic model MIKE-FLOOD for estimation of safe grade elevation for nuclear power project at Gorakhpur in Haryana considering safety against design flood of the upstream catchment; at site flooding; dam break flooding of the Bhakra dam; canal breaches and design of external and internal drainage systems for the nuclear power plant site. Considering the climate change condition of an increase in design rainfall by 15%, the maximum flood level increases have been estimated as 10 cm in the safe grade elevation of the nuclear power plant. Pandey et al. (2013) discussed the essence of climate change on hydrologic extremes is studied. Mamoon and Rahman (2014) presented a new design rainfall in Qatar using L-moment based index frequency approach is derived. Keshtkar (2015) described low flow frequency analysis by L-moments method for Iranian central plateau river basin. Chang et al. (2016) compared annual maximum and partial duration series for derivation of rainfall intensity-duration-frequency relationships in Peninsular Malaysia. Khan et al. (2017) presented regional frequency analysis of extremes precipitation using L-moments and partial L-moments. Kim et al. (2017) described appropriate model selection methods for nonstationary generalized extreme value models. Elgamal et al. (2017) presented the impact analysis of satellite rainfall products on flow simulations in the Magdalena River Basin, Colombia. Hailegeorgis and Alfredsen (2017) carried out regional flood frequency analysis and prediction in ungauged basins including estimation of major uncertainties for mid-Norway.

Kumar et al. (2017) carried out hydraulic modelling for the Brahmaputra Riverfront development project for Guwahati, sponsored by the Guwahati Metropolitan Development Authority. In this study, the 100-year return period flood is estimated using the annual maximum peak flood data of the Pandu GD site. The water surface profile is simulated using the MIKE-11 model for the design of the proposed embankment of the Brahmaputra River in Guwahati. The maximum flood levels are computed at the Indian Oil Corporation

area and Guwahati gauging site. Under the climate change scenario, an increase of 15% is considered in the 100-year return period flood. The water surface profile is computed considering the impact of climate change using the MIKE-11 model. An average increase of 0.6 m has been estimated considering the impact of climate change at most of the river locations along the river reach. Kumar et al. (2018) carried out a study sponsored by NLC India Limited (NLC) (formerly Neyveli Lignite Corporation Limited) on area drainage for a 3×800 MW Odisha thermal power project. In this study, the embankments of the Bhedan River in Odisha are designed for a 50-year return period flood for a reach of about 12 km. Adequacies of the embankment level for design flood considering the impact of climate change have been evaluated. The daily rainfall values are increased by 15% to study the impact of climate change on design floods. With a 15% increase in rainfall values, the design rainfall values for a 50-year return period are estimated to be 35.7 cm. The flood peak for a 50-year return period increases by 13% for the climate change scenario. The simulated water surface profile for a 50-year return period flood is shown below. Figure 1 shows the embankment levels and water surface profile for 50-year recurrence interval flood considering the impact of climate change.

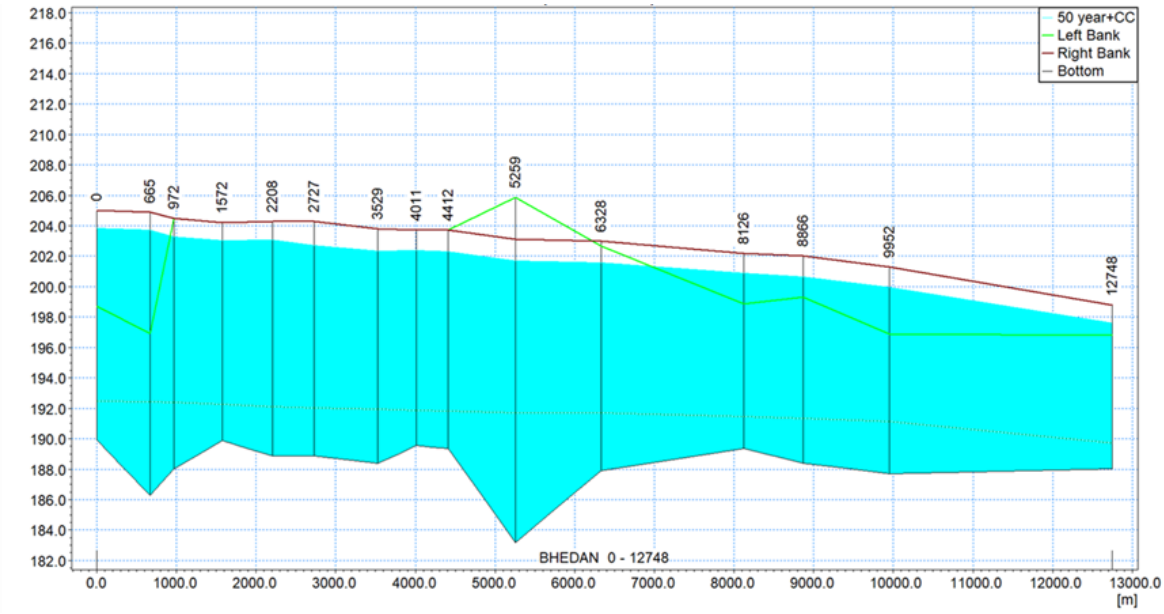

Figure 41 Embankment levels and water surface profile for 50-year return period flood considering the impact of climate change

3.2 Design flood estimation, hydraulic modelling and assessment of impact of climate change

As most of the locations of the bridges to be constructed are in the ungauged catchments, in this study daily annual maximum rainfall values of the two rain gauges

located at Dehradun and Roorkee are used for carrying out rainfall frequency analysis using the L-moments approach. The best fit distribution is identified using the L-moment ratio diagram and Zi-statistic criteria. The rainfall values of various return periods are estimated using the best fit distribution and these rainfall values are convoluted with Clark model of using the HEC-HMS package for estimation of floods of 50 and 100-year return periods.

The HEC-RAS Package is used for carrying out the optimal hydraulic design of the bridges using the various scenarios of 50 and 100-year return period floods for estimation of the depth of flow and velocity of flow for evaluating the Highest Flood Level (HFL), to which freeboard is added up for determining the height of the deck of the highway or railway bridges.

The impact of climate change on the hydrological and hydraulic design of bridges is studied using the downscaled GCM data as well as the specific percentage increases in the design floods for designing the flood disaster resilient bridges exposed to climate change.

3.3 Development of the conceptual framework

As per the objectives of the study comparative rainfall frequency analysis studies are carried out using the advance L-moments approach and the conventional flood frequency analysis techniques and differences in the estimated rainfall values of 50 and 100-year return periods are computed. These floods for 50 and 100-year recurrence intervals periods are estimated by convoluting these rainfall values with the Clark Instantaneous Hydrograph (IUH) (Kumar et al., 2007). The hydraulic modelling of the river reach of the bridge site is carried out using HEC-RAS package and impact of climate change is assessed based on the fixed percentage increases in design floods as well as the climatic projection scenarios as illustrated below.

3.4 Study area and availability

The catchment of the river Solani up to Roorkee has been selected as the study area in this study. The study area covers parts of district Dehradun and the area near Roorkee town of the district Haridwar lying in Uttarakhand, which is located in the northern part of India. This bridge site is located near the about 175 years old famous aqueduct on the river Solani over which the upper Ganga canal flowed earlier and which has been replaced by a newly constructed aqueduct some years back. Figure 2 Shows the location of the study area.

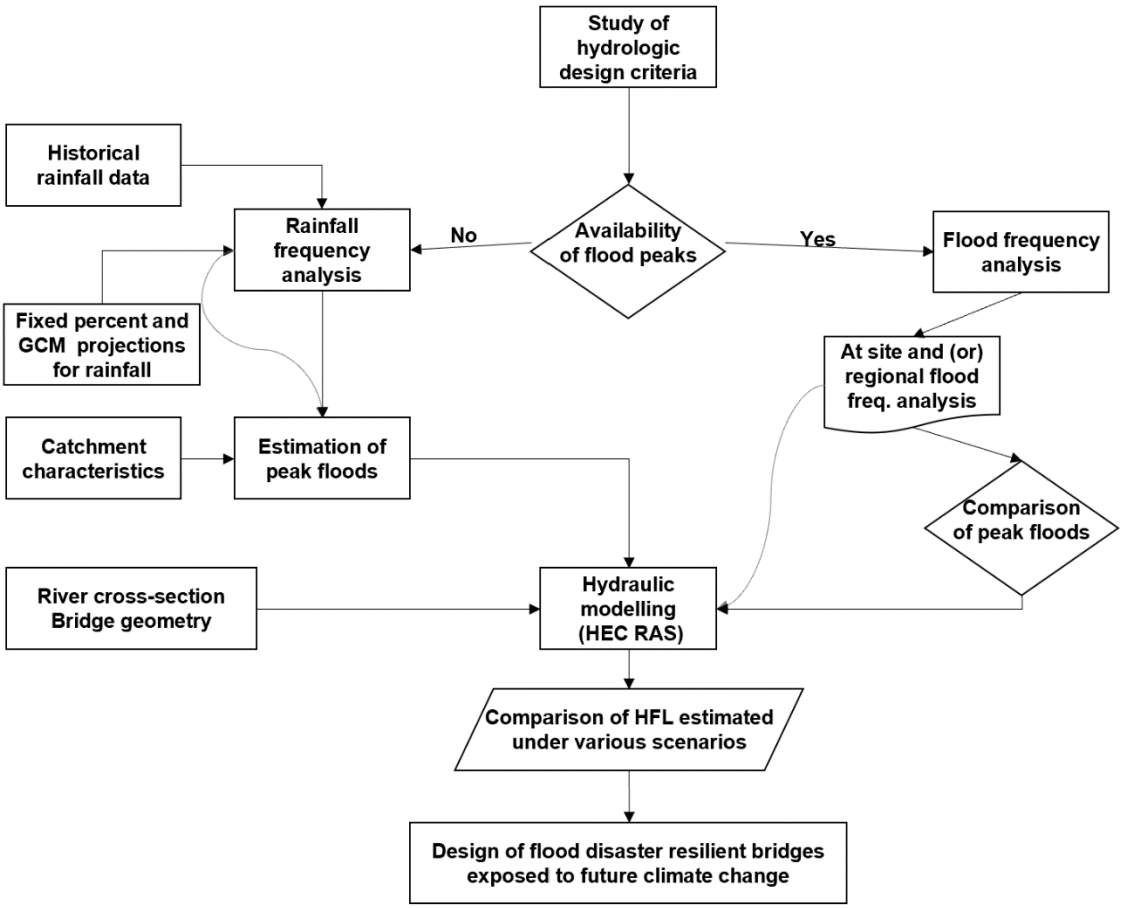

Flow diagram for methodology for flood disaster resilient hydraulic design of bridges exposed to climate change

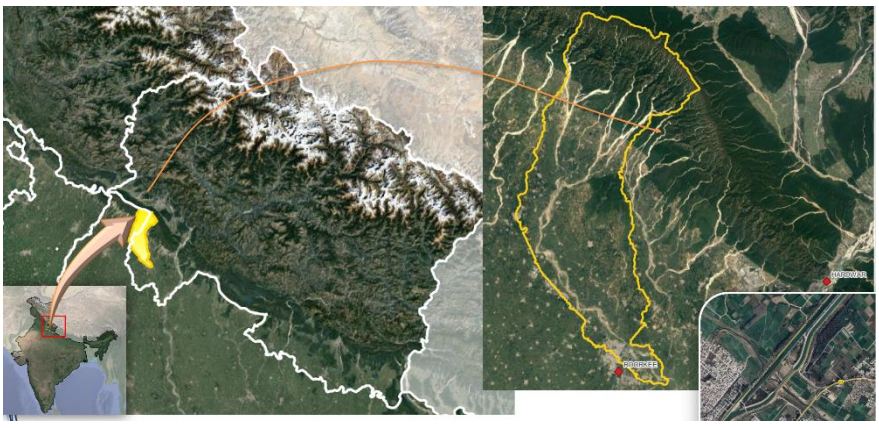

Figure 42 Location of the bridge site near Roorkee

As river flow data are not available near the bridge site, therefore, the available daily annual maximum rainfall data of the Dehradun and Roorkee rain-gauge stations are used in the study for the estimation of rainfall values for various return periods using the L-moments approach. Table-1 shows Also, rainfall values of 50- and 100-year return periods

for conventional methods based on the EV-I distribution obtained from the Atlas prepared by the India Meteorological Department (IMD), New Delhi and the] Central Water Commission, New Delhi.

Table 9 One day mean annual peak rainfall, sample statistics, sample size and discordancy measure for two rain-gauges

S. N.	Rain-gauge	Daily Mean Annual Peak Rainfall (mm)	L-CV (τ_2)	L-skew (τ_3)	L-kurtosis ($\tau 4$)	Sample Size (Years)	Discordance Measure (D_i)
(1)	(2)	(4)	(5)	(6)	(7)	(8)	(9)
1	Dehradun	162.498	.2069	.3321	.2991	60	1.00
2	Roorkee	129.624	.2132	.1918	.1290	54	1.00

The river cross-sections data for 24 cross-sections for the bridge site are obtained by outsourcing the work to an external agency and the same is used in carrying out hydraulic modelling of the river reach for the bridge site using the US Army Corps of Engineers software HEC-RAS.

4. Results and Discussion

4.1 Rainfall values for various return periods based on conventional approach

The Probable Maximum Precipitation (PMP) Atlas for Ganga River Basin Including Yamuna, published by CWC (2015) is available, in which grid Standard Project Storm (SPS) and Probable Maximum Precipitation values and isohyets of all some of the extreme storms that occurred so far in and around the basin are provided. The time distribution coefficient to estimate the hourly rainfall is also given in the PMP Atlas. The rainfall values for 50 and 100-year return periods are obtained from the PMP Atlas and given in Table 2 for the Ganga River Basin Including Yamuna, published by CWC (2015) in which rainfall values for various return periods are estimated by the conventional approach using the Extreme Value-I (EV-I) distribution based on the method of moments are available along with the SPS and PMP values. The time distribution coefficient to estimate the hourly rainfall is also available in the PMP Atlas and the same is used in the study.

Table 10: Rainfall values of various return periods for one-day duration obtained from IMD-CWC Atlas (2015)

Rain gauge	25-year	50-year	100-year
Roorkee	225	252	278
Dehradun	262	295	328

4.2 Estimation of rainfall values using L-moments

Rainfall values for various return periods are estimated using the L-moments approach (Kumar, 2019; Kumar and Chatterjee, 2005 Kumar et al., 2012). The Discordancy measure (D_i) is used to screen the annual maximum peak rainfall data of the two rain gauges. Twelve frequency distributions namely Extreme value (EV1), Normal (NOR), Generalized extreme value (GEV), Generalized normal (GNO), Uniform (UNF), Logistic (LOS), Generalized logistic (GLO), Exponential (EXP), Generalized Pareto (GPA), Pearson Type-III (PE3), Kappa (KAP) and Wakeby (WAK) are used for carrying out the study. Based on the L-moments ratio diagram and $|Z_i^{dist}|$ -statistic criteria, the robust frequency distribution is identified for the study area as discussed below.

The Discordancy measure estimated for the two rain gauges is given in Table-1. The L-moment ratio diagram shown in Figure 3 illustrates that GLO is the robust frequency distribution as per this test. The Z_i^{dist}-statistic estimated for the various distributions given in Table-3 also illustrates that its values are the minimum for the GLO distribution. Thus, both the tests illustrate that GLO is the robust frequency distribution for the study area. Regional parameters for the various distributions as well as their parameters and growth factors/ quantile estimates are given in Table-4 and Table-5 respectively. The estimated regional rainfall values for various return periods for various frequency distributions are given in Table-6. The rainfall values estimated by the GLO frequency distribution are used for the estimation of floods for 50 and 100-year recurrence intervals.

Table 11. Z_i^{dist} -statistic for various distributions

S. No.	Distribution	Z_i^{dist} -statistic
1	GLO	-0.02
2	GEV	-0.58
3	GNO	-0.89
4	PE3	-1.44
5	WAK	-2.00

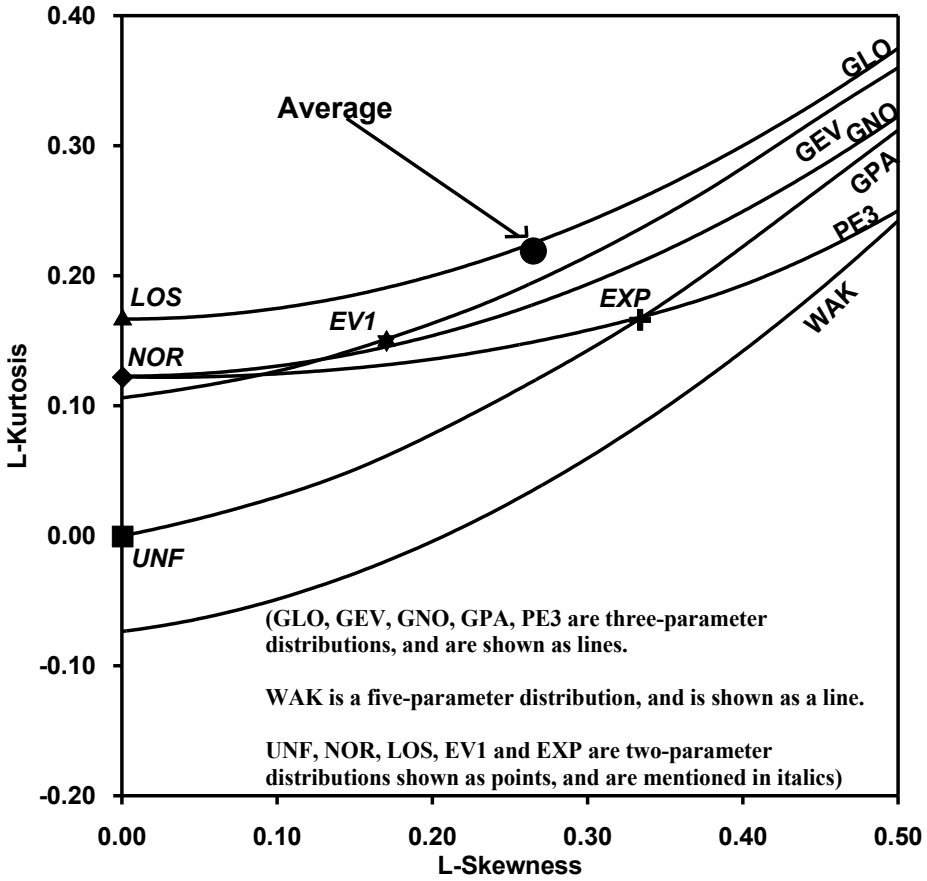

Figure 43: L-moment ratio diagram for the catchment of Solani River up to the bridge sit

Table 12 Regional parameters for the various distributions

Distribution	Parameters of Various Frequency Distributions				
GLO	ξ = 0.911	α = 0.186	k = -0.266		
GEV	ξ = 0.807	α = 0.260	k = -0.144		
GNO	ξ = 0.902	α = 0.327	K = -0.553		
PE3	μ = 1.000	σ = 0.402	γ = 1.598		
WAK	ξ = 0.429	α = 1.686	β = 6.339	γ = 0.298	δ = -0.127

4.3 Comparison of rainfall frequency estimates by conventional method and L-moments

As given in Table 7, the conventional rainfall frequency analysis method underestimated the rainfall values of the 50-year return period by 15.16% and the 100-year recurrence intervals rainfall values by 22.73%. Thus, the quite significant overestimation of rainfall values of 50 and 100-year recurrence intervals in the study establishes the superiority of L-moments in the estimation of floods of various recurrence intervals.

Table 13 Growth Factors for Various Distributions

Distribution (1)	Return Periods (Years)								
	2 (2)	10 (3)	20 (4)	25 (5)	50 (6)	100 (7)	200 (8)	500 (9)	1000 (10)
	Growth Factors								
GLO	.911	1.467	1.744	1.842	2.182	2.588	3.072	3.864	4.604
GEV	.905	1.498	1.771	1.864	2.169	2.503	2.872	3.419	3.882
GNO	.902	1.513	1.780	1.869	2.152	2.453	2.778	3.218	3.580
PE3	.898	1.535	1.789	1.870	2.118	2.363	2.605	2.922	3.160
WAK	.907	1.492	1.782	1.880	2.205	2.560	2.947	3.514	3.989

Table 14 Regional rainfall values for various return periods

Distribution (1)	Return Periods (Years)								
	2 (2)	10 (3)	20 (4)	25 (5)	50 (6)	100 (7)	200 (8)	500 (9)	1000 (10)
	Growth Factors								
GLO	133.1	214.3	254.7	269.0	318.7	378.0	448.7	564.4	672.5
GEV	126.8	209.8	248.0	261.1	303.8	350.6	402.3	478.9	543.7
GNO	131.7	221.0	260.0	273.0	314.5	358.3	404.6	470.0	522.9
PE3	131.2	224.2	261.3	273.1	309.4	345.1	380.5	426.8	461.6
WAK	217.9	260.3	274.6	322.1	373.9	430.4	513.3	582.6	217.9

Table 15 Comparison of peak flood values for 50 and 100-year return periods for conventional method and L-moments

RFA Method	50-year	Percent deviation	100-year	Percent deviation
Conventional	277.00	+15.16	308.00	+22.73
L-moments	319.00		378.00	

4.4 Flood Estimation using Rainfall of Various Return Periods

The rainfall values of various recurrence intervals are convoluted with synthetic unit hydrograph developed for the study area and floods of various recurrence intervals are estimated as discussed below.

4.4.1 Development of synthetic unit hydrograph using Clark model

The map of the Solani River catchment is shown in Figure 4 and its catchment characteristics obtained for developing the Clark unit hydrograph as discussed in the

Flood Estimation Reports-FEH-(Central Water Commission, 2018; 1994; 1987; Kumar et al., 2007) as well as the unit hydrograph are presented in Table 8. The parameter, time of concentration (Tc) is the time taken by a water drop from the hydraulically the most distant location to the outlet of the catchment. It is the time from the end of runoff generating rainfall over the catchment to the point of inflexion the recession limb of the Direct Runoff Hydrograph (DRH). An averaged value of 'Tc' from observed data should be considered for analysis. Here, three empirical equations i.e. Kirpich, Kerby and California are used for the estimation of Tc as shown in Table 9 below. Considering the time to peak about 0.7 time of time of concentration, the time to peak value is estimated. Clark unit hydrograph has been developed using HEC-HMS package for the desired time base of the unit hydrograph (TB). With the above Clark unit hydrograph parameters, the 1 cm rainfall excess and 1-hour duration unit hydrograph for the study area is given in Table-10 and the plot of unit hydrograph is presented in Figure 5.

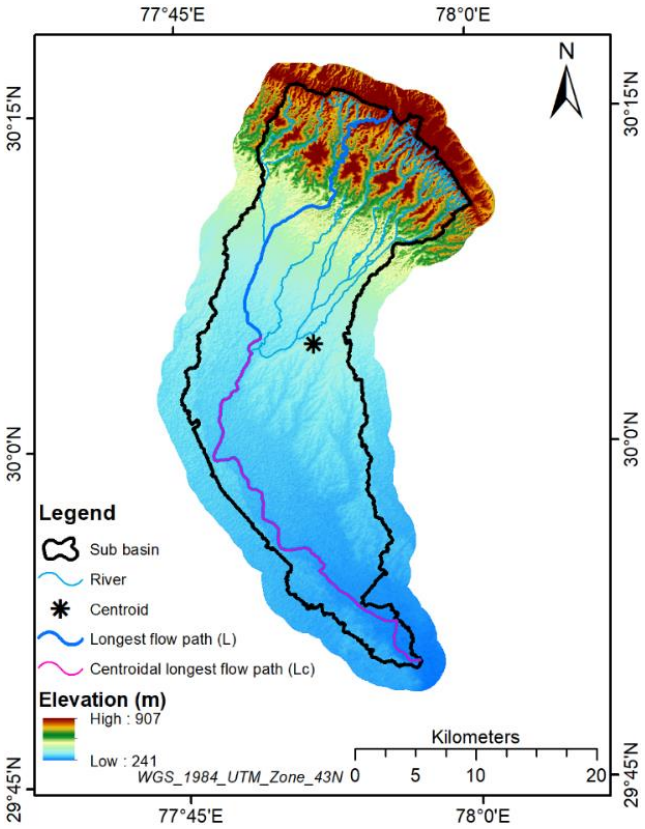

Figure 44 Map of the Solani River catchment up to the bridge site

The unit hydrograph for the study area has been developed using the Clark method provided in HEC-HMS. The Clark model uses two parameters, time of concentration, 'Tc', and storage constant, 'K', and a time-area histogram concept. The values of Tc as 14.9 and K as 3.2 were used in the study. The values of the Clark model unit hydrograph developed in the study are given in Table 10 and the unit hydrograph is shown given in

Figure 5.

Table 16 Characteristics of Solani catchment

Characteristics	Value
A: Area of the catchment (km^2)	556.7
L: Length of the main stream (km)	74.8
L_c: Centroid longest flow path (km)	43.3
S: Equivalent stream slope (m/km)	2.7

Table 17 Tc and TB as per empirical formula, which has been used to estimate Clark's K

Formula	Tc (h)	tp (0.7*Tc)	Ratio of TB/tp (FEH-7)	TB (0.7*TB/tp) (as per FEH-7)
Kirpich	17.8	12.5	2.7	33.3
Kerby	14.8	10.4	2.7	27.7
California	12.0	8.4	2.7	22.4
Average	14.9	10.4	2.7	27.8

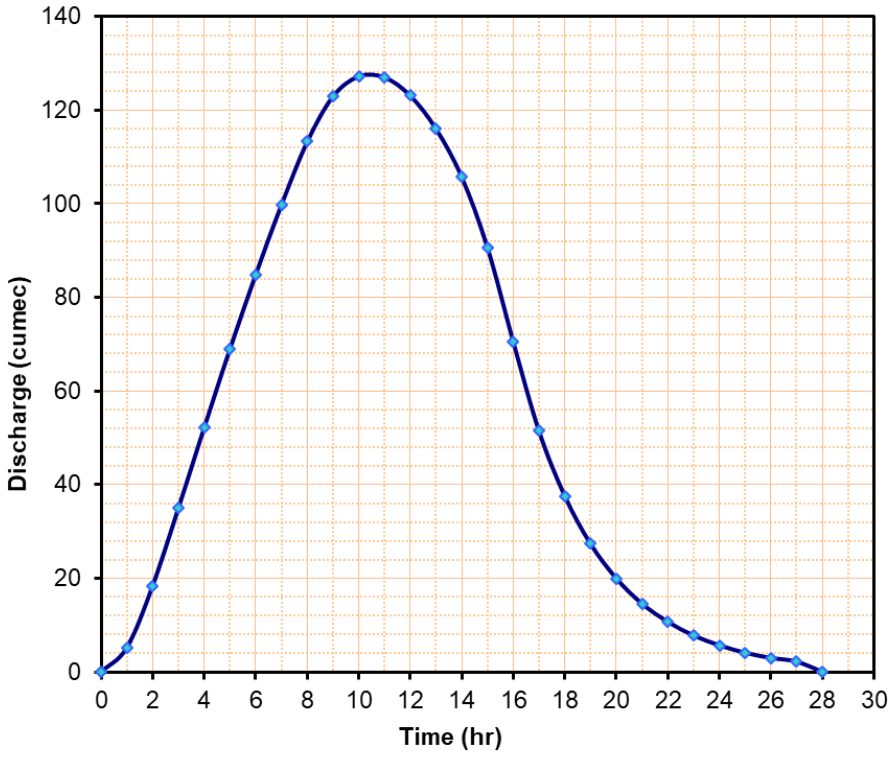

Figure 45 Plot of unit hydrograph

Table 18 Ordinates of the unit hydograph for the study area

Time (h)	1	2	3	4	5	6	7	8	9	10
Discharge (m^3/s)	0	5.2	18.4	52.2	69.0	84.9	99.8	113.3	123.0	123.3
Time (h)	11	12	13	14	15	16	17	18	19	20
Discharge (m^3/s)	127.1	123.2	116.1	105.8	90.7	70.6	51.5	37.6	27.4	20.0
Time (h)	21	22	23	24	25	26	27	28		
Discharge (m^3/s)	14.6	10.7	7.8	5.7	4.1	3.0	2.2	0		

4.4.2 Conversion of daily rainfall values of various return periods into hourly values

The rainfall values of 50 and 100-year recurrence intervals are estimated using the conventional method and the L-moments are distributed into one hourly values using the curve for time distribution of 24 h duration as provided in the India Meteorological Department (IMD)-Central Water Commission (CWC) Atlas (2015) and shown Figure 6. Figure 7 shows the rainfall hyetograph for 100-year rainfall for the study area estimated from the 100-year return period rainfall.

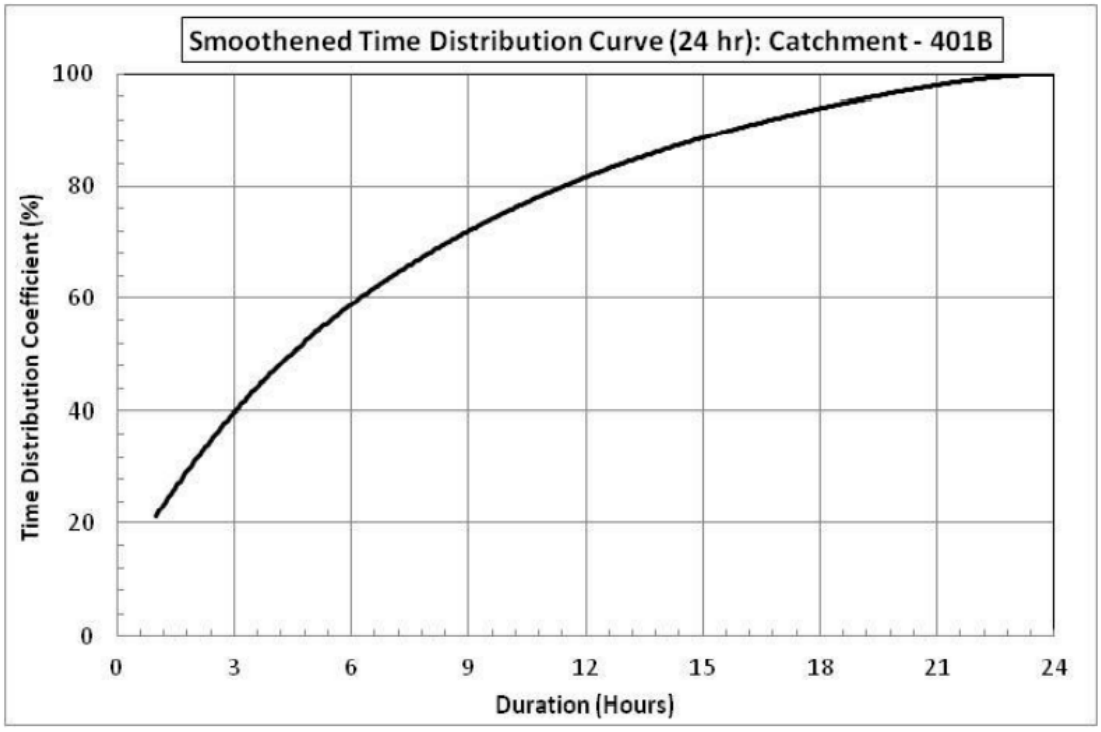

Figure 46 Time distribution curve for design rainfall for the study area

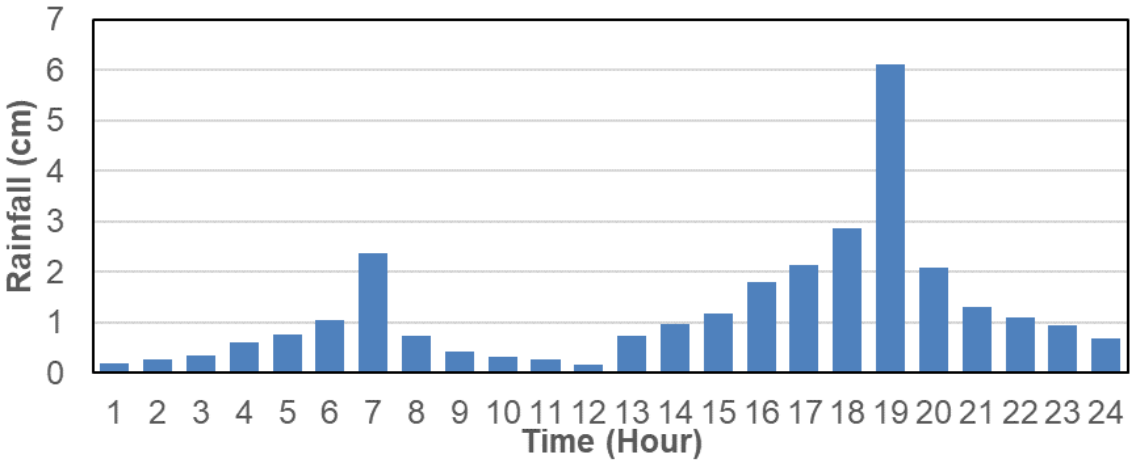

Figure 47 Rainfall hyetograph for 100-year rainfall for the study area

4.4.3 Estimation of floods of various return periods

The rainfall values of various return periods are estimated at an interval of 1 h by the conventional method and the L-moments are convoluted with the Clark unit hydrograph and converted into a flood hydrograph. The flood hydrographs for 50 and 100-year return periods are shown in Figure 8 to Figure 10.

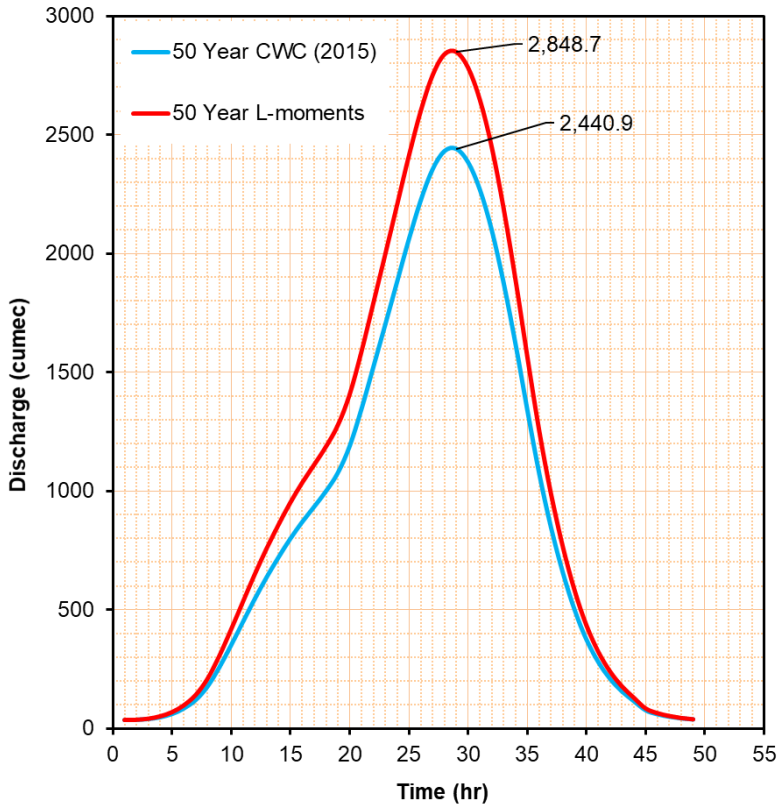

Figure 48 Flood hydrographs for the 50-year return period

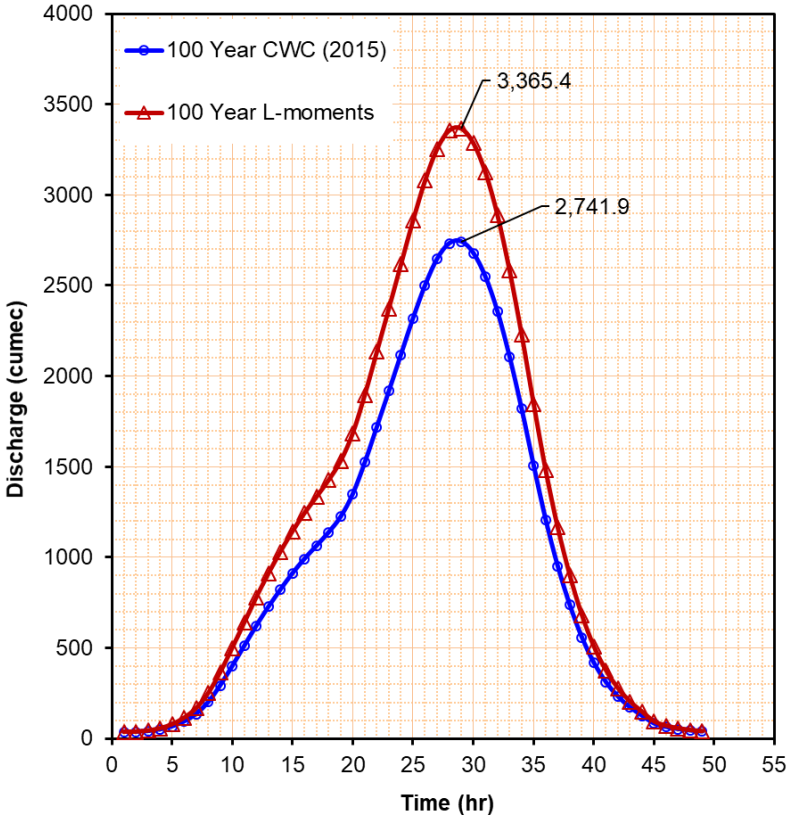

Figure 49 Flood hydrographs for the 100-year return period

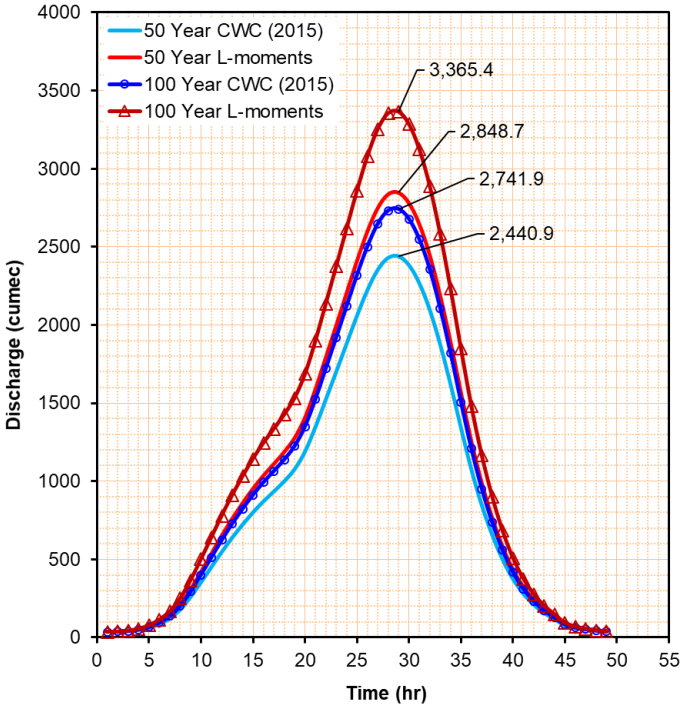

Figure 50 Flood hydrographs for 50and 100-year return periods

4.4.4 Estimation of floods of various return periods using regional flood frequency analysis

Floods of 50 and 100-year return periods are also computed for the catchment under study employing the regional flood frequency analysis method (RFFA-LMT) developed by Kumar (2019) as mentioned below.

$$Q_T = \left[-5.654 + 10.724 \left(\frac{1}{T-1} \right)^{-0.165} \right] * A^{0.771}$$

Where, Q_T is the flood in m^3/s for T year recurrence interval or the return period and A is the area of the catchment under study in km^2.

A comparison of flood estimates for this method, the conventional method (CWC,2015) and the L-moments-based method are in Figure 11.

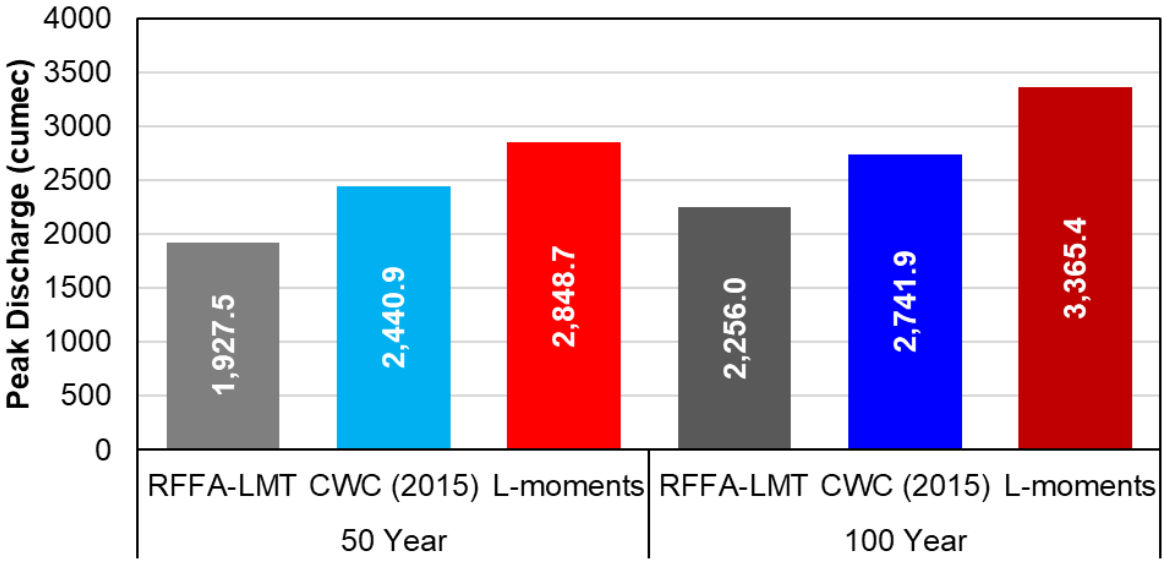

Figure 51 Comparison of design floods for various Methods

The regional flood frequency analysis method (RFFA-LMT) is developed using the annual maximum peak flood data; whereas, the Conventional method (2015) and L-moments-based methods are based on frequency analysis of rainfall, where almost the whole of the rainfall is considered to get converted into flood except some very minor infiltration loss therefore the RFFA-LMT method is excluded from further analysis. The floods of 50 and 100-year return periods estimated by the conventional and L-moments are used in the further analysis. A comparison of peak flood values for 50 and 100-year return periods for the conventional method and L-moments methods is shown in Table-11.

Table 19 Comparison of peak flood values for 50 and 100-year return periods for conventional method and L-moments

RFA Method	50-year	Per cent deviation	100-year	Per cent deviation
Conventional (2015)	2440.90	+16.70	2741.90	+22.74
L-moments	2848.70		3365.40	

4.5 Effect of Impact of Climate Change on Design floods

The analysis and results for incorporating the impact of climate change into the hydraulic design of bridges using the specific percentage increases in the design floods as well as downscaled General Circulation Model (GCM) data are discussed below.

4.5.1 Effect of climate change design floods using the fixed percentage method

As some organizations are adopting a fixed percentage increase in floods considering the impact of climate change (e.g., Kumar et al, 2012; 2017, 2018) the increases of 10%, 15%, 20%, 25% and 50% are considered in the flood and flood hydrographs for these increases are estimated as shown in Figure 12 and Figure 13 for 50 and 100-year return periods for the conventional method. A comparison of flood peaks is shown in Figure 14. The respective values obtained for the L-moments approach are shown in Figure 15 to Figure 17.

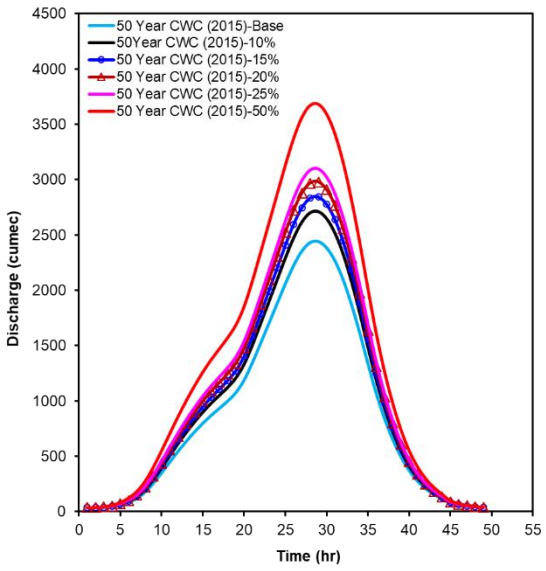

Figure 52 Comparison of flood hydrographs for fixed increases in rainfall values for a 50-year return period based on conventional method considering the effect of climate change

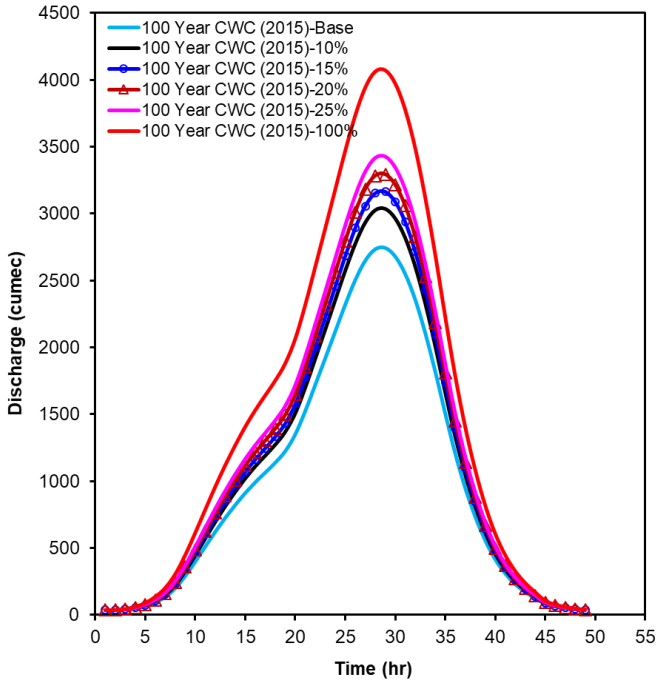

Figure 53 Comparison of flood hydrographs for fixed increases in rainfall values for a 100-year return period based on conventional method considering the effect of climate change

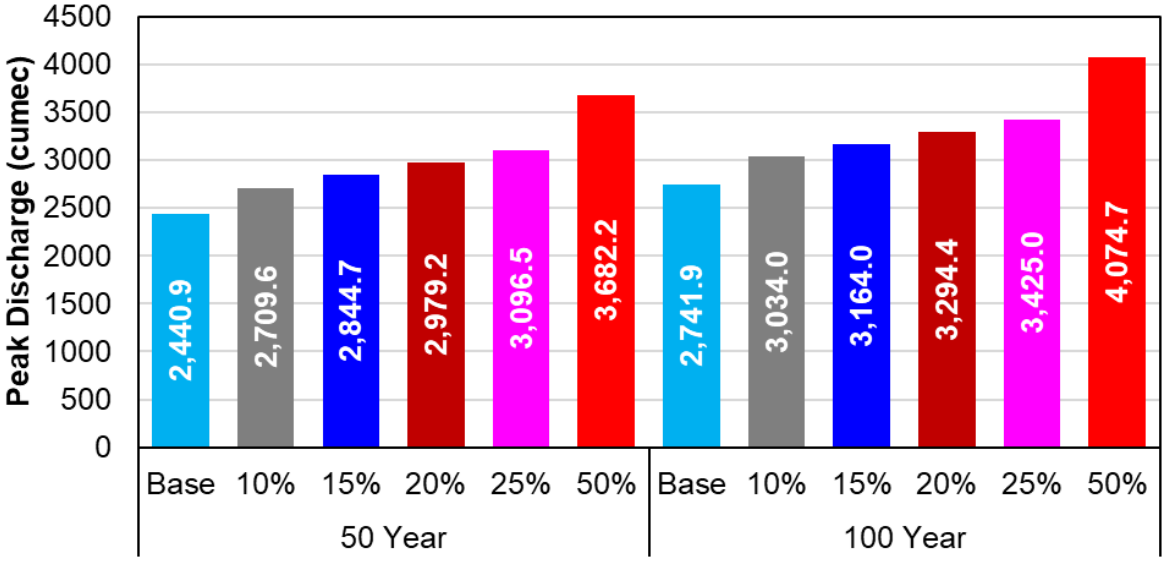

Figure 54 Increases in peak floods for fixed increases in rainfall values for conventional method considering the effect of climate change

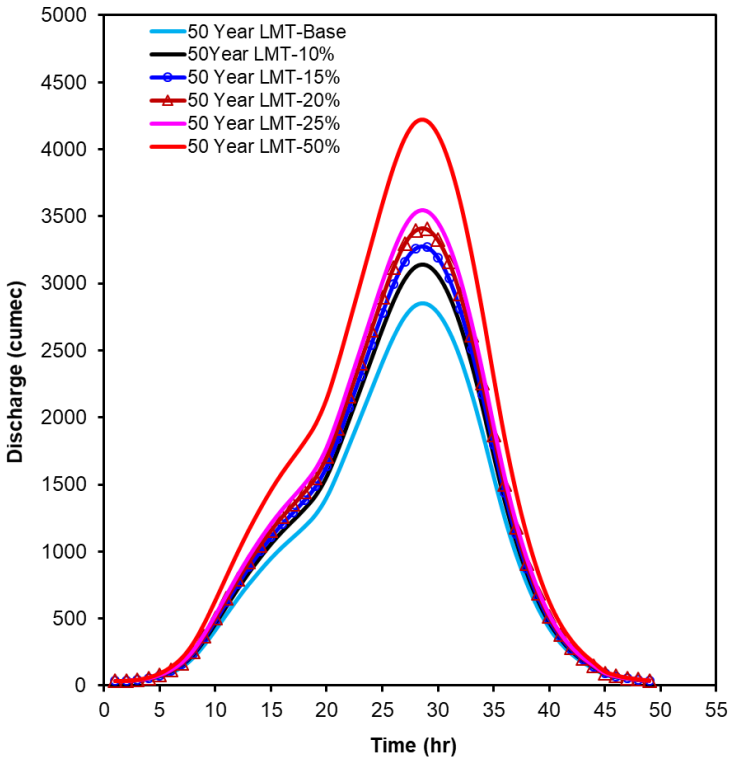

Figure 55 Comparison of flood hydrographs for fixed increases in rainfall values for a 50-year return period based on L-moments considering the effect of climate change

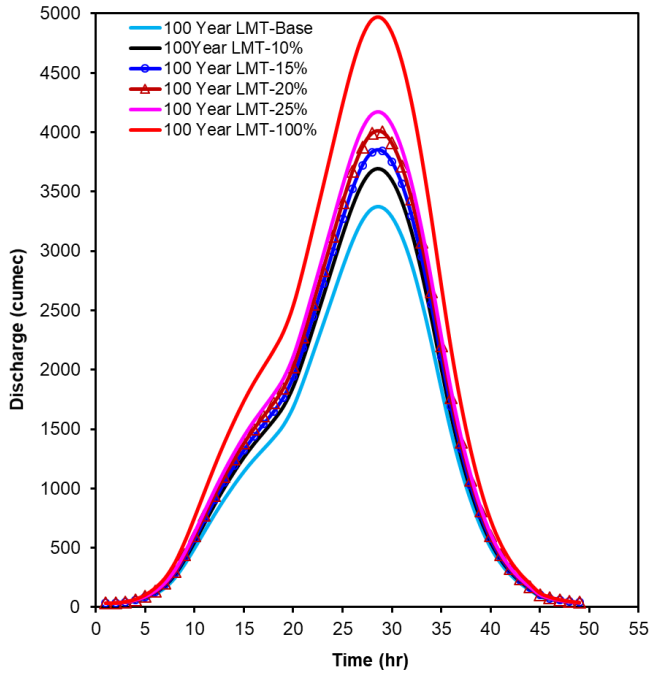

Figure 56 Comparison of flood hydrographs for fixed increases in rainfall values for a 100-year return period based on L-moments considering the effect of climate change

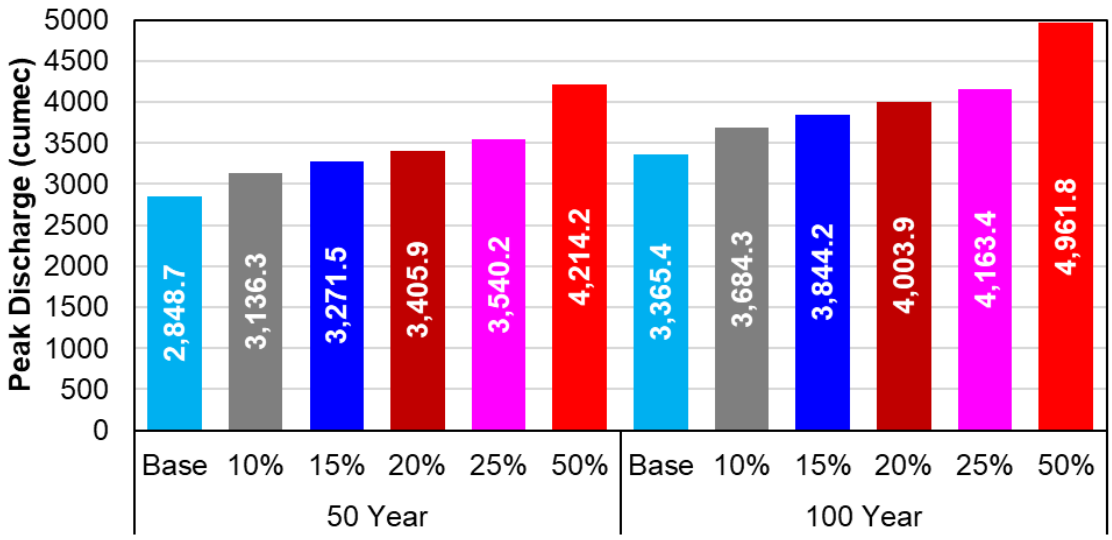

Figure 57 Increases in peak floods for fixed increases in rainfall values for the L-moments method considering the effect of climate change

4.5.2 Effect of climate change design floods using downscaled GCM data

Data for future rainfall is extracted from Bias Corrected Climate Projections dataset prepared by Mishra et al., (2020) from Coupled Model Int(comparison Project-6 (CMIP6) models for South Asia (https://zenodo.org/record/3873998#.ZE4MjnZBxPY). This contains Bias-corrected data of precipitation prepared using 13 different models prepared at 0.25° spatial resolution. From these 13 models 6 best models were selected for Haridwar region. Total of 20 grid points were identified on Haridwar district using the data of the models.

These files contain bias-corrected data of precipitation at 0.25° spatial resolution for Haridwar district (taluk: Roorkee and Haridwar) located in the south-west region of Uttarakhand. The bias-corrected dataset is developed using Empirical Quantile Mapping (EQM) for projected (2015–2100) climate for the two scenarios Shared Socioeconomic Pathways (SSPs) (SSP245 and SSP585) using output from 6 selected General Circulation Models (GCMs) from Coupled Model Intercomparison Project-6 (CMIP6). Details of models are provided below.

As the study area is covered by two rain gauges located at Dehradun and Roorkee the daily downscaled rainfall values for various GCMs for Dehradun and Roorkee are obtained for 2050 and 2100 and the same is given in Table-12 and Table-13. It is observed that rainfall for the future years shows a decrease in rainfall values, except for one of the GCMs. The average values of 1-day annual maximum rainfall for this GCM for Dehradun

and Roorkee for 2050 and 2100 are given in Table-14 and these values are convoluted with the Clark unit hydrograph for estimating the peak flood values for 20250 and 2100. The design flood hydrographs for 2050 and 2100 using the downscaled climate change projection scenarios are shown in Figure 18.

Model	Organization	Resolution	References
ACCESS-ESM1-5 (GCM1)	Commonwealth Scientific and Industrial Research Organization/Australia	1.25° × 1.875°	(Law et al., 2017)
BCC-CSM2-MR (GCM2)	Commonwealth Scientific and Industrial Research Organization/Australia	1.125° × 1.125°	(Wu et al., 2019)
EC-Earth3 GCM3)	EC–EARTH consortium/Europe	0.7° × 0.7°	(Massonnet et al., 2020)
EC-Earth3-Veg (GCM4)	EC–EARTH consortium/Europe	0.7° × 0.7°	----
INM-CM4-8 (GCM5)	Institute for Numerical Mathematics, Russian Academy of Science/Russia	1.5° × 2 °	(Volodin et al., 2018)
INM-CM5-0 (GCM6)	Institute for Numerical Mathematics, Russian Academy of Science/Russia	1.5° × 2 °	(Volodin et al., 2018)

Table 20 Daily downscaled rainfall values for various GCMs for Dehradun

S.No.	GCM	2050		2100	
		Date	Rainfall (mm)	Date	Rainfall (mm)
1	GCM1	25.06.2050	72.28	05.07.2100	72.68
2	GCM2	13.08.2050	104.21	02.08.2100	79.52
3	GCM3	27.09.2050	109.26	17.08.2100	246.69
4	GCM4	12.07.2050	140.66	04.08.2100	303.20
5	GCM5	25.06.2050	132.92	19.12.2100	128.51
6	GCM6	09.06.2050	69.35	19.02.2100	202.72

Table 21 Daily downscaled rainfall values for Roorkee

S.No.	GCM	2050		2100	
		Date	Rainfall (mm)	Date	Rainfall (mm)
1	GCM1	25.06.2050	93.67	28.07.2100	74.03
2	GCM2	01.06.2050	97.71	02.08.2100	143.94
3	GCM3	27.09.2050	108.62	17.08.2100	162.07
4	GCM4	12.07.2050	153.80	04.08.2100	250.90
5	GCM5	25.06.2050	105.43	19.12.2100	126.79
6	GCM6	09.08.2050	56.54	10.06.2100	126.68

Table 22 Average values of 1-day annual maximum rainfall for Dehradun and Roorkee

S.No.	GCM	2050		2100	
		Dehradun (mm)	Roorkee (mm)	Dehradun (mm)	Roorkee (mm)
1	GCM1	72.28	93.67	72.68	74.03
2	GCM2	104.21	97.71	79.52	143.94
3	GCM3	109.26	108.62	246.69	162.07
4	GCM4	**140.66**	**153.80**	**303.20**	**250.90**
5	GCM5	132.92	105.43	128.51	126.79
6	GCM6	69.35	56.54	202.72	126.68
	1-day max average	(140.66+153.80)/2 = **147.23**		(303.20+259.90)/2 = **277.05**	

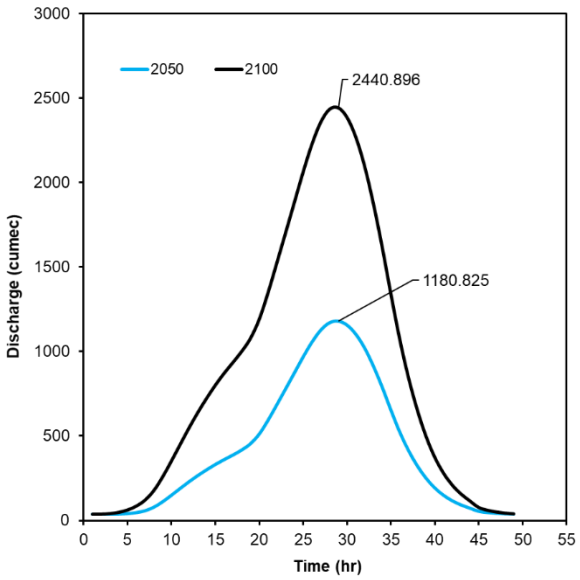

Figure 58 Design flood hydrographs fo2050 and 2100 using the downscaled climate change projection scenarios

4.6 Hydraulic Modelling for Bridge

To carry out the optimal hydraulic design of the bridges based on the hydraulic modelling approach the HEC-RAS Package is used. As discussed above, the twenty-four cross-sections of the river reach are used in the model setup. Manning's roughness coefficient value of 0.025 is adopted for the river channel and its value for banks is adopted as 0.035. As the observed river flow data are not available for the Solani River; hence, the calibration and validation of the river flow model could not be carried out and as such sensitivity analysis of the Manning's roughness coefficient could not be carried out. The longitudinal section of the reach of the river is shown in Figure 19. The results of simulations of hydraulic modelling for 50 and 100-year return periods based on the 50 and 100-year recurrence intervals for the L-moments approach using the fixed percentage increases and the downscaled 2050 and 2100-year floods are shown in Figure 20 to Figure 22.

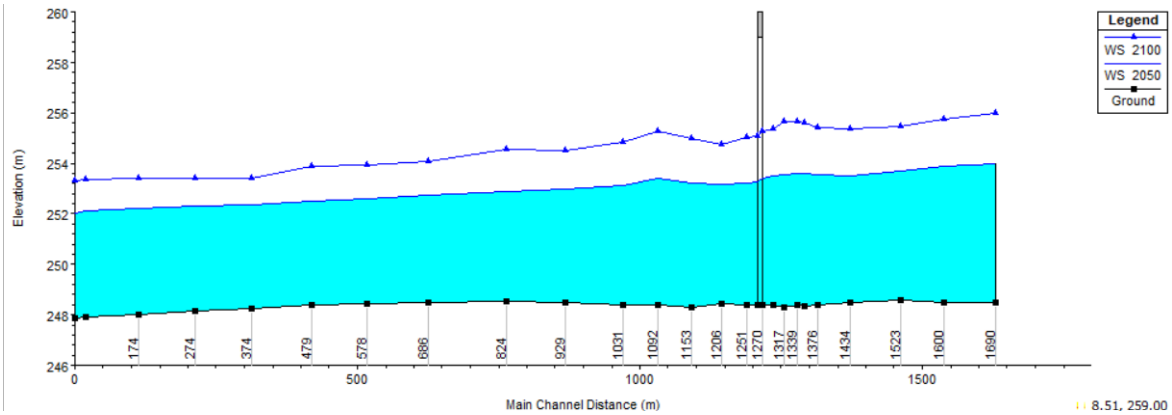

Figure 59 Highest Flood Levels (HFLs) and velocity of flown for the various fixed percentage increases in design floods for 50-year floods for L-moments

4.7 Findings from Stakeholders Workshop

As envisaged in the proposal of the study, a stakeholder's workshop was organised on 12 June 2023 and some of the stakeholders were invited for participation in the workshop. The objectives of the workshop were:

a) To present the methodology, analysis and results of the study carried out for flood disaster resilient hydraulic design for bridges exposed to climate change carried out under the CDRI-sponsored research project.

b) To obtain suggestions, comments and observations of the experts and various stakeholders for incorporating in the study and enhancing the applicability of the study.

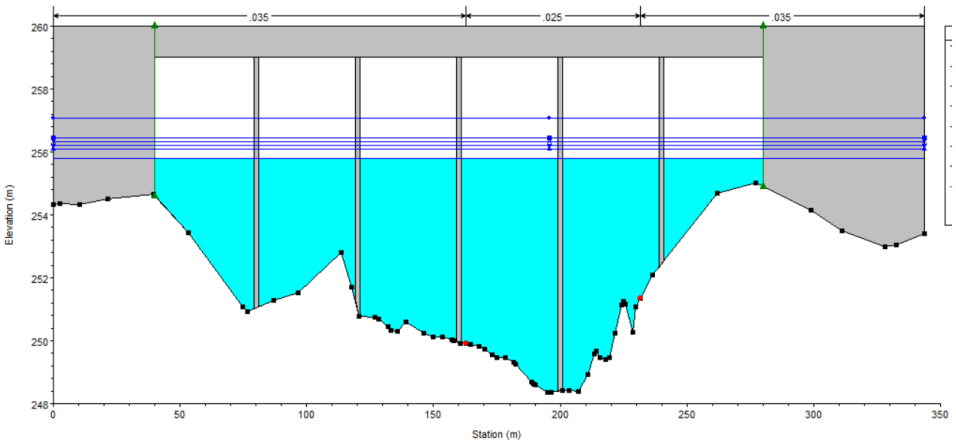

Reach	River Sta	Profile	Q Total	Min Ch El	W.S. Elev	Crit W.S.	E.G. Elev	E.G. Slope	Vel Chnl	Flow Area	Top Width	Froude # Chl
			(m3/s)	(m)	(m)	(m)	(m)	(m/m)	(m/s)	(m2)	(m)	
Reach 1	1297	base	2849.00	248.37	255.88	253.86	256.37	0.000713	3.70	1079.16	343.80	0.46
Reach 1	1297	10	3136.00	248.37	256.18	254.08	256.69	0.000712	3.81	1151.66	343.80	0.47
Reach 1	1297	15	3271.00	248.37	256.31	254.18	256.84	0.000713	3.86	1183.47	343.80	0.47
Reach 1	1297	20	3406.00	248.37	256.44	254.28	256.98	0.000716	3.91	1214.42	343.80	0.47
Reach 1	1297	25	3540.00	248.37	256.57	254.38	257.12	0.000718	3.97	1244.59	343.80	0.47
Reach 1	1297	50	4214.00	248.37	257.21	254.80	257.82	0.000711	4.18	1399.49	343.80	0.48
Reach 1	1270		Bridge									
Reach 1	1251	base	2849.00	248.40	255.57	254.01	256.28	0.001070	4.36	922.16	360.50	0.56
Reach 1	1251	10	3136.00	248.40	255.87	254.50	256.60	0.001045	4.45	994.95	360.50	0.56
Reach 1	1251	15	3271.00	248.40	256.01	254.61	256.75	0.001040	4.50	1026.45	360.50	0.56
Reach 1	1251	20	3406.00	248.40	256.13	254.72	256.89	0.001036	4.55	1057.03	360.50	0.56
Reach 1	1251	25	3540.00	248.40	256.26	254.98	257.02	0.001032	4.60	1086.81	360.50	0.56
Reach 1	1251	50	4214.00	248.40	256.91	255.40	257.72	0.000985	4.77	1242.77	360.50	0.56

Figure 60 Highest Flood Levels (HFLs) and velocity of flown for the various fixed percentage increases in design floods for 50-year floods for L-moments

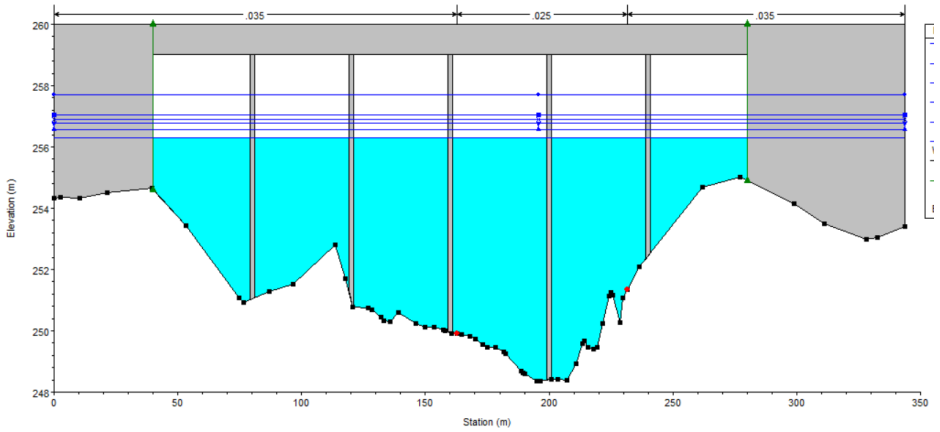

Reach	River Sta	Profile	Q Total	Min Ch El	W.S. Elev	Crit W.S.	E.G. Elev	E.G. Slope	Vel Chnl	Flow Area	Top Width	Froude # Chl
			(m3/s)	(m)	(m)	(m)	(m)	(m/m)	(m/s)	(m2)	(m)	
Reach 1	1297	base	3365.00	248.37	256.40	254.25	256.94	0.000715	3.90	1205.23	343.80	0.47
Reach 1	1297	10	3684.00	248.37	256.69	254.48	257.26	0.000726	4.03	1273.13	343.80	0.48
Reach 1	1297	15	3844.00	248.37	256.90	254.67	257.47	0.000701	4.04	1324.39	343.80	0.47
Reach 1	1297	20	4004.00	248.37	257.03	254.70	257.62	0.000708	4.11	1355.62	343.80	0.47
Reach 1	1297	25	4163.00	248.37	257.17	254.75	257.77	0.000710	4.16	1389.44	343.80	0.48
Reach 1	1297	50	4962.00	248.37	257.85	255.39	258.52	0.000714	4.41	1553.20	343.80	0.48
Reach 1	1270		Bridge									
Reach 1	1251	base	3365.00	248.40	256.10	254.69	256.84	0.001037	4.54	1048.00	360.50	0.56
Reach 1	1251	10	3684.00	248.40	256.37	255.07	257.16	0.001041	4.67	1113.88	360.50	0.57
Reach 1	1251	15	3844.00	248.40	256.60	255.17	257.37	0.000981	4.64	1169.69	360.50	0.55
Reach 1	1251	20	4004.00	248.40	256.73	255.27	257.52	0.000988	4.71	1199.59	360.50	0.56
Reach 1	1251	25	4163.00	248.40	256.87	255.37	257.67	0.000984	4.76	1233.02	360.50	0.56
Reach 1	1251	50	4962.00	248.40	257.54	255.81	258.41	0.000963	4.99	1395.23	360.50	0.56

Figure 61 Highest Flood Levels (HFLs) and velocity of flow for the various fixed percentage increases in design floods for 100-year floods for L-moments

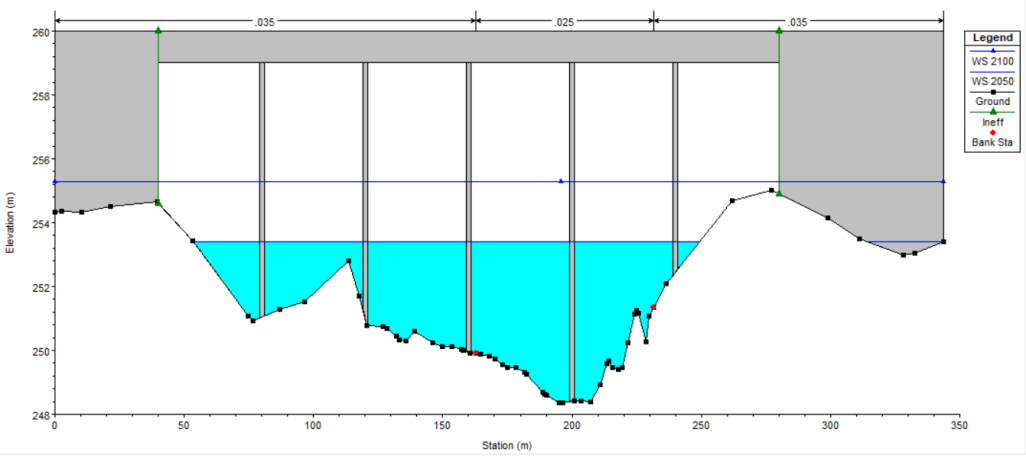

Reach	River Sta	Profile	Q Total	Min Ch El	W.S. Elev	Crit W.S.	E.G. Elev	E.G. Slope	Vel Chnl	Flow Area	Top Width	Froude # Chl
			(m3/s)	(m)	(m)	(m)	(m)	(m/m)	(m/s)	(m2)	(m)	
Reach 1	1297	2050	1181.00	248.37	253.48	252.17	253.82	0.000827	2.93	543.12	229.04	0.46
Reach 1	1297	2100	2441.00	248.37	255.38	253.52	255.84	0.000737	3.56	959.59	343.80	0.46
Reach 1	1270		Bridge									
Reach 1	1251	2050	1181.00	248.40	253.24	252.23	253.74	0.001283	3.47	434.19	177.89	0.57
Reach 1	1251	2100	2441.00	248.40	255.05	253.70	255.76	0.001169	4.30	797.56	360.50	0.58

Figure 62 Highest Flood Levels (HFLs) for the various fixed percentage increases in design floods for 50-year floods for climate change projections for 2050 and 2100

The participants of the orkshop, expressed that the study will serve as a guideline/ manual/ standard for the organizations involved in design and construction of the highway, railway and other bridges. The report of the study should be circulated to such organizations for its wider applications for flood disaster resilient optimal design and construction of the bridges. It will also serve as a reference for the Bureau of Indian Standards (BIS) for preparing the standards for hydraulic design of the bridges. Also, the CWC-IMD Atlases may be revised at based on the L-moments approaches of frequency analysis, which are found to be superior to the conventional approach, in the present study. The participants of the workshop appreciated the study and suggested that the methodology proposed in the study should be provided to the organisations involved in planning, designing and construction the bridges for its wider applications. It was also suggested that the methodology and findings of the study should be submitted to some good journal for wider circulation as well as submitted to the concerned authorities for including it in standards, manuals and guidelines for planning, design and construction of the bridges.

Stakeholders Workshop organised on 16 June 2023 at Sharda University, Greater Noida

5.Enablers and Barriers

Adequate coordinated planning, strong design standards, guidelines, manuals, cutting-edge technologies, and knowledge sharing are all necessary for construction of flood resilient bridges exposed to climate change. Considering flood resilience requires coordinated efforts from engineers, urban planners and hydrologists. It is necessary to

define and implement comprehensive design guidelines that take the effects of climate change and hydraulic pressures into account. Technology advancements have made it possible to create hydraulic designs that are resistant to flooding, such as better flood modelling software. Adopting resilient design practices requires effective knowledge exchange and collaboration between experts and stakeholders. It calls for bridging the gap between developed technologies and their applications in real life implementation for construction of the bridges.

6. Key Takeaways from CDRI Fellowship Programme

Estimation of floods of various return periods using the L-moments approach and consideration of the impact of climate change as well as hydraulic modelling of the reach of the river for the construction of bridges are immensely important and the methodology for the same has been developed in the current research. If the design flood is not correctly estimated and it is underestimated, it would result in getting the bridge washed away during the high flood. On the other hand, if the design flood is over estimated, it would lead to higher cost of its construction. Hydraulic modelling using the design flood provides the Highest Flood Level (HFL) and velocity of flow for construction of the bridge. Consideration of impact of climate change in design flood and hydraulic modelling makes the bridge flood disaster resilient under the climate change conditions in future. This methodology developed in the study may be used by the organisations involved in planning, design and construction of bridges as well as other related hydraulic structures. The standards, guidelines and manuals should include the methodology for planning, design and construction of the flood resilient bridges exposed to climate change.

7.Conclusion and Way Forward

The daily rainfall values for 50 and 100-year return periods estimated by L-moments are found to be 15.16% and 22.73% higher than the conventional approach for the catchment of Solani River near Roorkee having an area of 556.7 km^2. The Clark IUH model is used to derive synthetic unit hydrograph for the study area. The critical rainfall sequences are used for convolution with the synthetic unit hydrograph for computing the direct surface runoff hydrograph. The base flow is added to the direct surface runoff hydrograph for estimating the flood hydrograph. The design floods for a 50-year recurrence interval at the bridge site are estimated as 2440.90 m^3/s and 2848.70 m^3/s for the conventional method

and L-moments method respectively. Whereas the design floods for a 100-year recurrence interval at the bridge site are estimated as 2741.90 m^3/s and 3365.40 m^3/s for the conventional method and L-moments method respectively. Thus, the floods of 50 and 100-year return periods estimated by the L-moments method are 16.70% and 22.74% higher than the conventional method. It implies that the construction of the bridge using the conventional method would lead to an inadequate waterway as the bridge would be under-designed by the conventional method.

For consideration of the impact of climate change using fixed parentage increases in floods of 50 and 100-year recurrence intervals are considered. Also, the rainfall values obtained from the downscaled projections of the climate scenarios for the years 2050 and 2100 are used for further hydraulic modelling of the river reach of the bridge site. Amongst the downscaled scenarios the design floods are estimated as 1180.83 m^3/s and 2440.89 m^3/s for 2050 and 2100 as conservative estimates because most of the scenarios show a decrease in rainfall for the study area and still a lot of uncertainty is associated with the projections of rainfall values for the climatic projections.

The hydraulic modelling of river reach of about 1.70 km is carried out using HEC-RAS using the 24 river cross-sections obtained from the topographic survey of the river reach of the bridge site. The simulated water levels at the bridge are estimated as 255.88 m and 256.40 m for 50-year and 100-year recurrence intervals floods respectively. The velocities of flow are estimated as 3.70 m/s and 3.90 m/s for 50-year and 100-year return period floods respectively. The top width and hydraulic depth etc. are also estimated by the hydraulic modelling. For 15% increase scenarios for 50 and 100-year recurrence intervals, the water levels are estimated as 256.31 m and 256.90 m. For the downscaled climatic projections, the water levels are estimated as 253.48 m and 255.38 m for 2050 and 2100. The project authorities may consider the various scenarios and take appropriate decisions for the design and construction of the bridge.

In conclusion, ensuring the flood disaster resilience hydraulic design of bridges in the face of climate change requires a multifaceted approach. Adequate funding, integrated planning, robust design standards, guidelines, manuals, innovative technologies, and knowledge sharing all play critical roles in achieving this goal. By being vigilant about the consequences of failure of bridges and aware about the methodologies, which should be included in standards and manuals, flood disaster resilient bridges may be designed and constructed. Also, efforts should be made to bridge the gap between the developed advanced methodologies and technologies and their applications by the practitioners.

In the existing practice of design flood estimation, floods of various return periods are estimated using the Extreme Value-1 distribution based on the method of moments. In this study a comparative study of conventional approach, which is in practice and the L-moments based flood frequency analysis is carried out and the superiority of the L-moments over the conventional approach is demonstrated. On the basis of Zi -statistic criteria as well as L-moment ratio diagram, Generalised Logistic distribution is selected as the suitable frequency distribution for the study area and design floods are estimated using this frequency distribution. The effect of climate change on the design floods and the resulting hydraulic variables of the river reach for the bridge site are simulated using the downscaled projections of climate scenarios and the defined increases in the design floods. Hydraulic modelling for the bridge site is carried out using the design floods for various scenarios for incorporating impact of climate change in the hydraulic design of the bridge. The higher estimation of design floods by the L-moments approach advocates that the existing practice would under design the bridge, while the L-moments method would facilitate in the safe hydraulic design. The hydraulic modelling carried out in the report estimated the depth of flow and velocity of flow for the design floods, which are required for construction of the bridges. The various scenarios considered in the study for assessment of impact of climatic change enable to incorporate the impact climate change for design and construction of flood disaster resilient bridges exposed to climate change.

8. Limitations of the Study

As the required observed hydrological and topographical data are not available for most of the project sites, the present study has been carried out using the regional approaches of estimation of floods of various return period. Also, it is observed from the downscaled GCMs data that the future rainfall would decrease in the region of the study area. However, presently there is a lot of uncertainty associated with the future projections of the rainfall data. As observed stage-discharge data are not available for the study area, the calibration and validation of the reach of the river for the bridge site could not be carried out.

References

1. Hassan, B. and Ping, F., 2012. Formation of homogenous regions for Luanhe basin by using l-moments and cluster techniques. International Journal of Environmental Science and Development. Vol. 3, No. 2, 205-210.
2. Chang, K.B., Lai, S.H., Othman, F., 2016. Comparison of annual maximum and partial duration series for derivation of rainfall intensity-duration-frequency relationships in Peninsular Malaysia. J. Hydro. Eng. 21(1): 05015013.
3. CWC-IMD, 2015. PMP Atlas for Ganga basin including Yamuna, Prepared by Central Water Commission and India Meteorological Department, New Delhi.
4. Central Water Commission, 2018. Design flood estimation study of Daya Minor Irrigation Project, Rajasthan, Govt. of India,
5. Central Water Commission, 1987. Flood estimation report for Sone Subzone-1 (d) Report No. S/15/1987, Dote. of Hydrology (Small Catchments), New Delhi.
6. Central Water Commission, 1994, Flood estimation report for Western Himalayas - Zone 7 Report No. WH/22/1994, dote. of Hydrology (Small Catchments), New Delhi.
7. Elgamal et al., 2017. Impact analysis of satellite rainfall products on flow simulations in the Magdalena River Basin, Colombia. Journal of Hydrology: Regional Studies, 9 (2017) 85–103.
8. Guidelines for the Design of Small Bridges and Culverts, 2020. The Indian Road Congress.
9. Allegorise, T.T. and Alfredsen, K. Regional flood frequency analysis and prediction in ungauged basins including estimation of major uncertainties for mid-Norway, Journal of Hydrology: Regional Studies 9 (2017) 104–126.
10. Hosking, J.R.M., Wallis, J.R., 1997. Regional frequency analysis-an approach based on L-moments. Cambridge University Press, New York.
11. Keshtkar, A.R., 2015. Low flow frequency analysis by L-moments method (Case study: Iranian Central Plateau River Basin). Desert Management Department, International Desert Research Center (IDRC), University of Tehran, Tehran 1417763111, Iran,167-175.
12. Khan, S.A., Hussain, I., Hussain, T., Faisal, M., Muhammad, Y.S., Mohamd S.A.,

2017. Regional Frequency Analysis of Extremes Precipitation Using L-Moments and Partial L-Moments. Advances in Meteorology.

13. Kim, H., Kim, S., Shin, H., Heo, J., 2017. Appropriate model selection methods for nonstationary generalized extreme value models, Journal of Hydrology, 547, 557-574.
14. Kumar, R. 2023. Regional Flood Frequency Relationships for Indian catchments and a relook on hydrologic design criteria under climatic change". Chapter in the book by Springer publication on Proceedings of the International Conference on Water Energy Food and Sustainability, Portugal, May 10-12, 2023 (Accepted).
15. Kumar, R. 2019. Development of regional flood frequency relationships using L-moments for gauged and ungauged catchments of India, Water Utility Journal, European Water Resources Association, Vol.23, pp. 37-47.
16. Kumar, R, Mani, P and Patra, J.P. (2018). Area Drainage Study for NLC Talabira Thermal Power Project, Stage I (3x800 MW), National Institute of Hydrology, Roorkee for NLC India Limited (NLCIL), Neyveli.
17. Kumar, R, Mani, P and Patra, J.P. (2017). Flood Disaster Risk Management for a Project Site in India under the Changing Climate. Journal of Indian Water Resources Society, Vol. 37, No. 3, July, 2017, pp. 37-41.
18. Kumar, R, Mani, P and Patra, J.P. (2017). Hydraulic Modelling for Brahmaputra Riverfront Development Project for Guwahati, National Institute of Hydrology, Roorkee for Guwahati Metropolitan Development Authority (GMDA), Guwahati.
19. Kumar, R, Mani, P and Patra, J.P. (2012). Estimation of Design Basis Flood and Safe Grade Elevation for Nuclear Power Project at Gorakhpur, Haryana, National Institute of Hydrology, Roorkee for Nuclear Power Corporation of India Ltd, Mumbai.
20. Kumar, R., Chatterjee, C., 2011. Development of regional flood frequency relationships for gauged and ungauged catchments using L-moments, In the In Extremis disruptive events and trends in climate and hydrology, Edited by Kropp, J.P., Schellnhuber, H.J. Springer.105-127.
21. Kumar, R., Chatterjee, C., Kumar, S., 2003. Regional flood formulas using L-moments for small watersheds of Sone Subzone of India. Journal of Applied Engineering in Agriculture, American Society of Agricultural Engineers. Vol. 19, No. 1,47-53.
22. Kumar, R., Chatterjee, C., Kumar, S., Lohani, A.K., Singh, R.D., 2003. Development of

regional flood frequency relationships using L-moments for Middle Ganga Plains Subzone 1(f) of India. International Journal of Water Resources Management, Kluwer Academic Publishers, Netherlands. Vol. 17, No. 4, August, 243-257.

23. Kumar, R., Chatterjee, C., 2005. Regional flood frequency analysis using L-moments for North Brahmaputra Region of India. Journal of Hydrologic Engineering, American Society of Civil Engineers. Vol. 10, No. 1, 1-7.
24. Kumar, R., Singh, R.D., Seth, S.M., 1999. Regional flood formulas for seven Subzones of Zone 3 of India. J. Hydro. Eng. ASCE, 4(3), 240-244.
25. Kumar, R., Chatterjee, C., Singh, R.D., Lohani, A.K., and Kumar, S. Runoff estimation for an ungauged catchment using GIUH based Clark and Nash models". Journal of Hydrologic Processes, U.K., Vol. 21, pp. 1829-1840, May, 2007.
26. Kumar, R., Mani P., Patra, J.P., 2012. Estimation of design basis flood and safe grade elevation for nuclear power project at Gorakhpur. Haryana, Project Report, National Institute of Hydrology, Roorkee, India.
27. Kumar, R., Chatterjee, C., 2011. Development of regional flood frequency relationships for gauged and ungauged catchments using L-moments. In Extremis disruptive events and trends in climate and hydrology, Edited by Kropp, J.P., Schellnhuber, H.J. Springer, 105-127.
28. Law, R. M., Ziehn, T., Matear, R. J., Lenton, A., Chamberlain, M. A., Stevens, L. E., Wang, Y. P., Srbinovsky, J., Bi, D., Yan, H., & Vohralik, P. F. (2017). The carbon cycle in the Australian Community Climate and Earth System Simulator (ACCESS-ESM1) - Part 1: Model description and pre-industrial simulation. Geoscientific Model Development, 10(7), 2567–2590. https://doi.org/10.5194/gmd-10-2567-2017.
29. Mamoon, A.A., Rahman, A., 2014. Uncertainty in Design Rainfall Estimation: A Review. Journal of Hydrology and Environment Research, Vol. 2, No 1, Enviro. Water Sydney, 65-75.
30. Massonnet, F., Ménégoz, M., Acosta, M., Yepes-Arbós, X., Exarchou, E., & Doblas-Reyes, F. J., 2020. Replicability of the EC-Earth3 Earth system model under a change in computing environment. Geoscientific Model Development, 13(3), 1165–1178. https://doi.org/10.5194/gmd-13-1165-2020
31. Mishra, V., Bhatia, U., & Tiwari, A. D., 2020. Bias-corrected climate projections for South Asia from Coupled Model Intercomparison Project-6. Scientific Data, 7(1).

https://doi.org/10.1038/s41597-020-00681-1

32. Mani, P., Chatterjee, C., Kumar, R., 2014. Flood hazard assessment with multiparameter approach derived from coupled 1D and 2D hydrodynamic flow. Natural Hazards, Springer Publishers, January, Volume 70, Issue 2, 1553-1574.
33. Pandey, R.P., Kumar, R., Singh, R.D., Ojha, C.S.P., 2013. Essence of Climate Change on Hydrologic Extremes. Book on Climate Change Modeling, Mitigation, and Adaptation, (ed: Rao Y and others), Chapter No. 10: doi: 10.1061/9780784412718.ch10. Publisher ASCE, USA, 251-298.
34. Pilgrim, D.H., Cordery, I., 1992. Flood runoff, Handbook of Hydrology. D.R. Maidment (Ed), Chap.18, McGraw-Hill, New York, 9.1-9.42.
35. Research Design and Standards Organization., 1991. Estimation of design discharge based on regional flood frequency approach for Subzones 3 (a), 3 (b), 3 (c) and 3 (e) of India. Lucknow, India.
36. Saf, B., 2009. Frequency analysis using L-moments for the west Mediterranean region of Turkey. J. Hydro. Eng. 14(8), 783-794.
37. Seckin, N., Haktanir, T., Yurtal, R., 2011. Flood frequency analysis of Turkey using L-moments method. Hydrology Process. 25, 3499-3505.
38. Sivapalan, M., Bloschl, G., Zhang, L., Vertessy, R., 2003. Downward approach to hydrological prediction, Hydrological Processes 17, 2101–2111 Published online in Wiley Inter Science www.interscience.wiley.com. DOI: 10.1002/hyp.1425, 2101-2111.
39. The Flood Estimation Handbook, UK, 1999. Five printed volumes (Centre for Ecology & Hydrology, UK, ISBN: 9781906698003), 1999.
40. Volodin, E. M., Mortikov, E. V., Kostrykin, S. V., Galin, V. Y., Lykossov, V. N., Gritsun, A. S., Diansky, N. A., Gusev, A. V., Iakovlev, N. G., Shestakova, A. A., & Emelina, S. V., 2018. Simulation of the modern climate using the INM-CM48 climate model. Russian Journal of Numerical Analysis and Mathematical Modelling, 33(6), 367–374. https://doi.org/10.1515/rnam-2018-0032
41. Wu, T., Lu, Y., Fang, Y., Xin, X., Li, L., Li, W., Jie, W., Zhang, J., Liu, Y., Zhang, L., Zhang, F., Zhang, Y., Wu, F., Li, J., Chu, M., Wang, Z., Shi, X., Liu, X., Wei, M., … Liu, X., 2019. The Beijing Climate Center Climate System Model (BCC-CSM): The main progress from CMIP5 to CMIP6. Geoscientific Model Development, 12(4), 1573–

1600. https://doi.org/10.5194/gmd-12-1573-2019

Nature-Based Solutions for Resilient Infrastructure Systems

Robyn Alison Haggis
Environmental Change Institute
University of Oxford, *United Kingdom*

Under CDRI Fellowship Programme 2022-23

Disclaimer: the views expressed in this paper reflect the opinions of the author and not necessarily the official views of CDRI.

Abstract

Climate change hazards, such as floods, droughts and landslides, threaten infrastructure systems and the services that they provide. There is a need to increase the resilience of existing infrastructure systems and embed resilience into the design of new infrastructure. Traditionally, decision-makers have tended to focus on built infrastructure options for the provision of services including adaptation, however there is increasing recognition that nature-based solutions (NbS) can provide services relevant to infrastructure, including increased resilience to climate change.

This Fellowship aims to support the scale-up of NbS in decision-making for infrastructure resilience, with a focus on energy, transport and water sectors. Three outputs are developed through the Fellowship: (1) a conceptual framework to identify which NbS options can increase the resilience of different infrastructure sectors to a range of climate change driven hazards; (2) a database of key metrics for evaluating the costs and benefits of different NbS options, created from an extensive literature review of academic and policy documents; (3) a pilot interactive decision-making tool which can be used by decision-makers to identify and evaluate relevant NbS options to increase the resilience of their chosen sector to their relevant climate hazards, populated with data from existing studies.
Through the Fellowship, numerous data gaps relating to NbS were identified, including effectiveness at service provision, monitoring and maintenance costs. Key-informant interviews suggest that the data gaps are a consequence of factors including a lack of funding for monitoring, a lack of technical and human capacity, and reporting requirements of funders. These gaps pose a challenge to the comparison of NbS options in infrastructure decisions, and to scaling uptake of NbS through infrastructure planning and investments.

As part of the Fellowship, the pilot decision-making tool is applied to the case study of Jamaica, to identify NbS options for increasing the resilience of road transport infrastructure to two fluvial (river) flooding scenarios: one of 2m flood depth and one of 1.3m flood depth. The results show that NbS may have greater requirements in terms of space and time than built infrastructure, but can help to reduce economic damages from climate impacts, potentially reducing requirements for built adaptation infrastructure, and at the same time lead to multiple additional benefits for policy agendas such as the Paris Agreement, Sustainable Development Goals and Convention on Biological Diversity.

NbS should be considered as part of standard practice in infrastructure decisions, to ensure their broad potential benefits are maximised. The outputs developed through this Fellowship provides a starting point for identifying NbS options, assessing the various costs

and benefits, and defines the key metrics which should be reported upon to inform robust decision-making.

Acknowledgments

I am extremely grateful for the guidance, support and feedback from my mentor, Dr Raghav Pant, and my technical experts, Dr Rama Pandey and Dr Sai Bhaskar Reddy Nakka, as well as the CDRI team for all their work and inputs along the way.

Funding

This research was supported by the 2022–2023 Fellowship of the Coalition for Disaster Resilient Infrastructure (CDRI), Application ID: 210929748.

Definitions

- **Damage curve:** a curve that relates to the potential physical damage to an infrastructure asset against a given magnitude of a hazard (van Ginkel et al, 2021).
- **Economic damage:** the quantification of economic value of repairing or replacing the asset that is physically damaged by a hazard (Koks et al, 2019).
- **Exposure:** the presence of people; livelihoods; environmental services and resources; infrastructure; or economic, social, or cultural assets in places that could be adversely affected (IPCC, 2012).
- **Nature-based solutions (NbS):** building on previous work by the International Union for Conservation of Nature (IUCN), the United Nations Environment Assembly (UNEA) (res 5/5) defines NbS as "actions to protect, conserve, restore, sustainably use and manage natural or modified terrestrial, freshwater, coastal and marine ecosystems that address social, economic and environmental challenges effectively and adaptively, while simultaneously providing human well-being, ecosystem services, resilience and biodiversity benefits".
- **Resilience:** the ability of a system and its component parts to anticipate, absorb, accommodate or recover from the effects of a hazardous event in a timely and efficient manner, including through ensuring the preservation, restoration or improvement of its essential basic structures and functions (IPCC, 2012)
- **Risk:** the likelihood over a specified time period of severe alterations in the normal functioning of a community or a society due to hazardous physical events interacting with vulnerable social conditions, leading to widespread adverse human, material, economic, or environmental effects that require immediate emergency response to satisfy critical human needs and that may require external support for recovery (IPCC, 2012)
- **Vulnerability:** the degree of exposure of an infrastructure asset to a hazard, and its susceptibility to suffer physical damage (Zio, 2016).

1. Introduction

Climate change threatens the resilience of existing and future infrastructure systems such as energy, water and transport. Hazards such as flooding, drought, extreme temperatures, snowfall, sea level rise and hurricanes threaten both infrastructure assets and the resources that they depend upon. There is a need to adapt existing infrastructure systems to climate change and embed resilience into the planning and design of new infrastructure.

Traditionally, decision-makers have predominantly focused on built, 'grey' or 'hard' infrastructure options for the provision of infrastructure-relevant services including adaptation. However, a disproportionate focus on built rather than nature-based infrastructure solutions can have negative impacts for the natural environment, including through habitat fragmentation, pollution of air, water and land, and carbon emissions, as well as for societies who depend upon natural ecosystems for their livelihoods and for access to natural resources (Seiler, 2003).

There is a growing evidence base to suggest that nature-based solutions (NbS) can deliver infrastructure services in their own right, complement built infrastructure to enhance the provision of infrastructure services, and protect infrastructure from climate change, safeguarding service provision, while providing multiple additional benefits for biodiversity, communities and their livelihoods (UNEP, 2023; Haggis et al, pending publication). Studies have highlighted the potential for NbS to provide services which can help to increase the resilience of infrastructure to climate hazards, including wave dissipation, flood regulation, urban cooling, pollutant filtration, freshwater provision and erosion control (e.g., Browder et al, 2019). For example, wetlands can help to regulate water supplies to potable water reservoirs, safeguarding supplies during periods of drought (UNEP, 2014). Forests upstream of hydropower can stabilise soils and reduce the sedimentation of turbines and generators during flood events (Vogl et al, 2016). Living fences can protect transport networks such as roads and railways from snowfall (Blanken, 2018).

Proponents of NbS argue that while built infrastructure serves limited purposes at any one time, the strategic and carefully planned use of NbS offers opportunities to provide services to infrastructure and multiple additional benefits for biodiversity, societies and economies simultaneously which can help to progress development agendas such as the Sustainable Development Goals (SDGs), Paris Agreement, and Convention on Biological Diversity (Seddon et al, 2020; Seddon et al, 2021; Kapos et al,

2019). Benefits include increased flexibility, adaptability, resilience to climate change, carbon sequestration, empowered communities, reduced costs of implementation and maintenance, diversified income streams, and the provision of habitat and ecosystem connectivity for biodiversity (Cohen-Sacham et al, 2016; Blicharska et al, 2019; Fuldauer et al, 2022).

The impact of climate change on infrastructure systems is already apparent, and many future risks to infrastructure are already locked in. There is an urgent need to increase the resilience of existing infrastructure systems to climate change, and to embed resilience into the development of new infrastructure. It is estimated that almost US $100 trillion of investment in infrastructure is required globally by 2040 (Global Infrastructure Hub, 2017). Long lifespans, high costs and difficulty of reversal means that infrastructure investments lock in patterns of development for decades, whether they be positive or negative (Thacker et al, 2019). It is therefore imperative that NbS are factored into infrastructure planning from the outset, to ensure that their benefits to infrastructure and potential for multiple additional benefits for biodiversity and societies are optimised, and to minimise the further loss of nature from infrastructure development. To do so requires informed decision-making on infrastructure planning and investments.

The last decades have seen advances in formal decision-making methodologies for infrastructure planning and investment, including the long-term planning of resilient infrastructure systems under uncertainties of future climate scenarios and socio-economic development trajectories (Simpson et al, 2016). There have also been advances in methodologies for geospatial decision-making at national and supranational scales, both within the infrastructure literature and NbS discourse. For example, national infrastructure assessments have modelled vulnerability of built infrastructure networks to climate hazards to inform resilience planning (Pant et al, 2016; Thacker et al, 2017), while ecosystem services have been used to inform natural network planning for conservation in the EU (Lanzas et al, 2019; Liquete et al, 2016). Increasingly, studies are looking at the potential for NbS to increase the resilience of infrastructure systems to climate change. For example, Menendez et al (2020) and Beck et al (2018) quantified the risk reduction benefits of mangroves and coral reefs, respectively, on coastal infrastructure systems, while an Foreign, Commonwealth & Development Office (FCDO) funded project undertaken by the Oxford Programme for Sustainable Infrastructure Systems (OPSIS) assessed the potential for NbS to increase the resilience of energy, transport and water infrastructure networks in the small island developing state of Jamaica. At the same time, there are a growing number of databases, tools and platforms on NbS, including the

Nature-based Solutions Initiative (NbSI) Evidence Tool and the International Institute for Sustainable Development (IISD) database on NbS, which can support informed decision-making.

However, despite recent innovations, frameworks for understanding the applicability of different NbS options to different infrastructure sectors are mostly non-existent within the literature, and there are few standardised approaches, datasets or metrics which can be compared to built infrastructure options in decisions as part of standard practice. Equally, while the costs and benefits of NbS are recognised in principle, there is little analysis of the scale of benefits that they may provide to infrastructure in practice, or how much needs to be done to achieve those benefits. The extent to which NbS can provide benefits to infrastructure, including reduced risks associated with climate change hazards and increased infrastructure resilience, requires the development of new frameworks and methodologies, scientific information and analysis.

2. Aim, Objectives, and Scope of the Research Study

The aim of this Fellowship is to develop new frameworks and tools which can be used to inform a standardised approach to the assessment of NbS for resilient infrastructure, with the view to ultimately scale-up the systematic consideration and deployment of NbS in infrastructure planning and decision-making.

The objectives include the development of:

- A **conceptual framework** to identify which NbS options can increase the resilience of different infrastructure sectors to a range of climate change hazards.
- A **database** of key metrics for evaluating the costs and benefits of different NbS options, populated with data where available which can be compared to typical built infrastructure options during infrastructure decisions as part of standard practice.
- A pilot **interactive decision-making tool** which can be used by decision-makers to identify the relevant NbS options for their sector and selected climate hazards, and outlining relevant cost and benefit data where it is available. Following the Fellowship, it is expected that this tool will be made available through an online platform on CDRI's website and further expanded / populated with data to fill data gaps.

The duration of the Fellowship is 1 year, and therefore the scope of the project has been designed according to the timeframe, to form a pilot framework, database and decision-making tool which can be subsequently expanded, populated and refined following the Fellowship. These outputs are intended to provide decision-makers with the first building blocks for embedding NbS into projects for infrastructure resilience, to be further built upon in coming months and years.

A broad range of NbS options and climate hazards are considered within the scope of the Fellowship, as outlined in the Methodology Section below. Costs and benefit metrics are identified, and populated only where data is readily available. Three infrastructure sectors have been considered within the pilot tool to demonstrate its applicability to decision-making: energy, transport and water. The tool is tested in one applied case study: to assess the potential effectiveness, costs and benefits of NbS in order to reduce fluvial (river) flood risk to roads in Jamaica.

There is already global interest in the application of NbS for increasing the resilience of infrastructure systems to climate change. This includes CDRI's 'Infrastructure for Resilient Island States' (IRIS)[9], CDRI's DRI Dialogue Series on Implementing NbS for Climate and Disaster Resilient Infrastructure[10] and CDRI's hybrid session 'Pioneering NbS for Resilient Infrastructure' held at the 26th UN Climate Change Conference of Parties (COP26) in 2021[11]. There are ongoing projects being undertaken by other institutions including the United Nations Environment Programme (UNEP), the Green Climate Fund (GCF), the United Nations Office for Project Services (UNOPS), the Global Center on Adaptation (GCA) and the University of Oxford Environmental Change Institute (ECI). These projects face challenges of limited information and quantitative data on NbS which can be compared to built infrastructure solutions in the decision-making process. This CDRI Fellowship has enabled the development of a standardised framework, database of costs, benefits and metrics, which can be applied and replicated globally, and a decision-making tool which can be integrated immediately into the project work of these organisations to help decision-makers optimise NbS in their decisions. It is expected that the outputs of this Fellowship can help to inform infrastructure planning and investment at different spatial scales and contexts, including at the level of national-scale planning and decision-making across different countries.

[9] https://iris.cdri.world/

[10] https://www.cdri.world/events/dri-dialogue-series-implementing-nature-based-solutions-for-climate-and-disaster-resilient-infrastructure

[11] https://www.cdri.world/upload/pages/1726998552949560_202203111022cdri-cop26_outcome_document_compressed.pdf

3. Methodology

3.1 Step 1: Desk research and literature review

A desk-based literature review was conducted to gather relevant information and data. This included:

- Development of a typology of typical built infrastructure assets within the three sectors of energy, transport and water (see results section 4.1)
- Assessment of the vulnerability of each of the infrastructure sectors to a broad range of climate change hazards (see results section 4.1)
- Identification of NbS options which can support risk reduction (see results section 4.1)
- Identification of key metrics for assessment of NbS, and the gathering of quantitative and qualitative information on different NbS options where this was readily available, including their effectiveness at risk reduction and various costs and benefits, as well as relevant performance benchmarks (see results section 4.1).

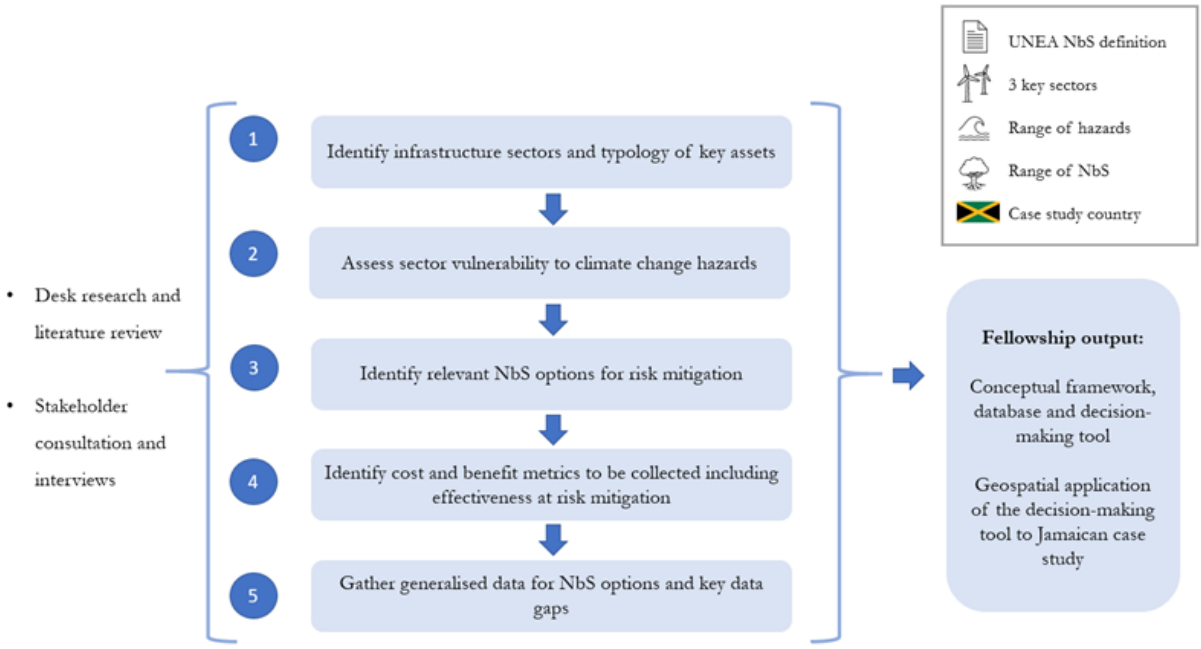

Figure 1. Flowchart of methodology

A range of data sources were consulted as part of the literature review process. This included relevant reports from international organisations including the World Bank, GCA, CDRI and UNEP, as well as various academic journal articles sourced through platforms including Google Scholar and the University of Oxford Bodleian Libraries e-resources.

3.2 Step 2: Interviews and data analysis

18 semi-structured interviews were conducted with key informant stakeholders in Jamaica. Interviewees were from organisations within the public and private sector, including USAID, Jamaican Government, the Forestry Department, and the Jamaican Conservation and Development Trust. Interview questions were designed to understand the enabling environment context to implementing NbS within Jamaica, including the key barriers and opportunities for deployment and scale-up. Semi-structured interview format enabled comparison of questions and answers across interviewees, with the opportunity to ask relevant follow-up questions and additional questions specific to individual interviewees.

3.3 Step 3: Development of the conceptual framework, database and decision-making tool

The outputs of the Fellowship include the development of a conceptual framework on NbS, database of relevant metrics, and interactive decision-making tool which can be used by decision-makers to identify and assess NbS options for infrastructure resilience. The information gathered through Step 1 (literature review) and Step 2 (interviews) informed the development of the Fellowship outputs in Step 3. These are contained within one large excel-based tool, which is structured in 5 parts:

1. A methodology page for navigating the decision-making tool.
2. An interactive, front-facing component of the tool which forms the user interface. The front-end of the tool forms what the decision-maker who uses the tool sees and interacts with, and which generates information on relevant NbS options to address their infrastructure need. Here, decision-makers can select the infrastructure sector of relevance to them (energy, transport or water) and which hazards they are affected by. The tool then provides a list of potential NbS options which can reduce risks associated with the selected hazard, and information on the potential effectiveness, costs and benefits where data was available and gathered during the literature review.
3. A data capture sheet which highlights key information to be collected from NbS projects to inform robust decision-making.
4. Back-end of the tool. This includes:
    a. Information on the three infrastructure sectors, a typology of typical built infrastructure assets and their vulnerability to the different climate hazards.

b. Conceptual framework outlining the NbS options which can reduce risks associated with the different climate hazards.
c. Database of relevant metrics on the effectiveness, costs and benefits of NbS which underpin the decision-making process. These are populated with data at levels ranging from global to national, where data is available.
d. Relevant look-up tables and calculations which are used to generate the interactive aspect of the user experience.

5. Dashboard of preliminary statistics on NbS for resilient infrastructure. This calculates statistics including the number of NbS options available for increasing resilience to each hazard, and the percentage of NbS for which data is available. This is expected to be updated in future months following the Fellowship.

The tool is not intended to be a comprehensive database of costs and benefits of different NbS options. Rather, it forms a pilot tool and generalised framework and database on the relevance of NbS to infrastructure decision-making with a view to:

- Demonstrate the applicability of such a decision-making tool to inform infrastructure planning and decision-making.
- Present a standardised set of indicators and metrics which should be routinely reported upon in NbS projects as part of standard practice, and which can inform future monitoring strategies.
- Highlight any apparent gaps in data that become visible through the literature review process.

It is expected that following the CDRI Fellowship, the decision-making tool will be expanded to other sectors, populated further as more data becomes available, and include information on the potential for NbS to directly substitute and enhance service delivery (see section 8 on the 'Way Forward'). The pilot decision-making tool will be made available online on the CDRI website for use by decision-makers and other interested stakeholders globally.

3.4 Step 4: Geospatial application of the decision-making tool

This step of the methodology involved the application of the decision-making tool to a case study, to demonstrate its potential applicability to real-world decision-making problems. The small island developing state of Jamaica was chosen for the case study. It

was selected owing to its vulnerability to a range of climate hazards, the presence of large swathes of nature, its small and contained size, and following previous work undertaken there with OPSIS as part of an FCDO-funded project. This enabled timelier access to geospatial data on climate hazards, infrastructure sectors and natural land cover, as well as relevant hazard damage curves and information on asset replacement / rehabilitation costs for use in the analysis, and was beneficial for the data gathering process given the relatively short timeframe of the CDRI Fellowship.

In order to demonstrate the tool, one hazard and one infrastructure sector and subsector was selected – fluvial (river) flood risk to road transport networks. Geospatial data in the form of hazard maps, spatial road network data and land cover maps was sourced through the previous project work from stakeholders including the Jamaican Government and the Jamaican Forestry Department. This was used in combination with the J-SRAT tool, developed by OPSIS, which enabled easy visualisation of roads, flood risk and landcover. The steps followed were:

- Selection of flooded area in Jamaica and identification of roads exposed to flood risk through geospatial visualisation. Various hazard return periods were available – initial demonstration of the tool looked at 2m flood depth and 1.3m flood depth, which some of Jamaica's roads are exposed to during 1-in-100-year and 1-in-20-year return period river floods.
- Quantification of flood risk to roads in terms of economic damages using information on projected flood depths, asset exposure extent and relevant damage curves for the asset.
    - Based on previous studies done in Jamaica (e.g., Glas et al, 2017), it is assumed that roads are damaged only when flood depth is greater than 50cm. Economic damages to the road are therefore estimated based on the depth of water which surpasses 50cm.
    - Hazard damage curves are used to determine the damage ratio, which reflects what percentage of the asset is damaged by the flood.
    - Projected economic damages to the road are calculated by multiplying the unit cost of asset replacement / rehabilitation for the extent of road exposed to the flood by the damage ratio.
- Use decision-making tool to identify relevant NbS options for flood risk reduction and their costs and benefits.
    - The tool shows that various NbS options are applicable for the mitigation of river flooding.

- Initial demonstration of the tool looked at the potential for forest-based NbS (restoration, protection, improved management) to reduce flood risk.
- The decision-making tool shows that forests can reduce flooding by 5-30% for floods of up to 1-in-100-years.
- Re-calculate projected economic damages to the road assuming corresponding reduction in flood depths.

3.5 Assumptions

This research assumes that NbS can provide ecosystem services which can substitute, complement and **protect** built infrastructure to ensure the resilience of infrastructure assets and services. This research is broad-scale rather than at the level of granular detail. Therefore, the decision-making tool provides generalised data on costs, benefits and effectiveness of service provision to guide decisions, sourced from international reports and studies, rather than country-specific data. Any decision-maker using this tool will need to undertake follow-on site-specific assessments to account for any local variations including condition, topography, soil type, slope and socio-political conditions which may impact local costs, benefits and effectiveness.

4. Results and Discussion

4.1 Findings from literature review

Through the literature review process, a typology of sectors, sub-sectors and examples of built infrastructure assets was developed. These are shown in Table 1.

Table 1 Typology of sectors and sub-sectors, along with examples of built assets, considered through the Fellowship. This typology is not exhaustive and developed from various sources including UNEP (2023).

Sector	Sub-sector	Description
Energy	Generation	Includes hydropower, solar, wind, non-renewable
	Transmission and distribution	Includes pipelines, overhead power lines, pylons, substations, underground power lines
Transport	Roads	Paved and unpaved roads, bridges
	Railways	Railway lines, stations, signal boxes
	Airports	Terminals, runways and landing strips, airport grounds
	Ports	Rivers and seaports including container terminals,

		harbours, shipping channels, inland navigation ways including rivers and canals
Water	Supply	Rivers and streams, reservoirs, rainwater harvesting systems, boreholes
	Treatment	Water treatment plants
	Distribution	Pipelines

A broad range of climate hazards were identified (building on those of Chausson et al, 2020) which can pose a risk to the three infrastructure sectors and impair their ability to function and provide services. These include:

- *Drought*
- *Surface flood (pluvial)*
- *River flood (fluvial)*
- *Urban flood*
- *Coastal flood*
- *Tsunami*
- *Storm surge*
- *Sea level rise*
- *Water quality (water purification)*
- *Water quality (erosion control)*
- *Water quality (biological control)*
- *Water quality (temperature control)*
- *Heat*
- *Urban Heat Island (UHI)*
- *Landslide*
- *High winds*
- Cyclone
- *Snowfall*
- *Avalanche*
- *Wildfire*
- *Land subsidence*
- *Rockfall*
- *Coastal erosion mitigation (shoreline stabilisation*

NbS identified for inclusion within the conceptual framework and decision-making tool include the protection / restoration / management / creation of:

- *Agricultural management: contour trenching*
- *Agricultural management: cover crops*
- *Agricultural management: drought resistant crops*
- *Agricultural management: furrow diking*
- *Green roofs*
- *Green spaces*
- *Green walls*
- Living fence

- *Agricultural management: grazing land management*
- *Agricultural management: mulch*
- *Agricultural management: no-till agriculture*
- *Agricultural management: silviculture*
- *Agricultural management: tillage*
- *Agroforestry*
- *Aquifer*
- *Beaches*
- *Bioretention areas*
- *Constructed wetlands*
- *Coral reef*
- *Dunes and vegetated dunes*
- *Floodplains*
- *Forests*
- *Gardens*
- *Mangrove*
- *Open spaces*
- *Oyster reef*
- *Ponds*
- *Rain garden*
- *Reconnection of rivers to floodplains*
- *Re-meandering of rivers*
- *Restoration of rivers banks and beds*
- *Riparian buffers*
- *Salt marsh*
- *Seagrass*
- *Street trees*
- *Terrace*
- *Urban park*
- Wetlands

Various metrics for assessing the different costs and benefits of NbS in comparison to other NbS and built infrastructure options were identified which can support the decision-making process. These include:

- **Implementation cost and cost breakdown** (US $ per square meter / linear meter): also known as capex, this is the total cost of implementing the initial solution, encompassing the purchase or rental of land, permits, site preparation, materials including seedlings, labour, machinery, etc.
- **Maintenance cost and frequency** (US $ per square meter / linear meter per unit of time required for maintenance - e.g. monthly, quarterly, annually): also known as opex, this is the total cost of maintaining and ensuring the day-to-day functioning of the solution, encompassing costs such as weeding, watering, maintenance of protective fencing, labour costs, costs associated with machinery and materials (e.g. for moving and replenishing sand in beach nourishment schemes).
- **Monitoring cost** (US $ per square meter / linear meter per unit time) - e.g. monthly, quarterly, annually): this is the cost of monitoring the costs and benefits of the NbS

solution, including effectiveness at increasing infrastructure resilience, and includes labour, materials (e.g. technical equipment) and the frequency at which monitoring is undertaken.

- **Time to achieve benefits:** the number of years required for the NbS solution to provide the required benefits. Current information suggests that some solutions may provide benefits immediately, over short timescales (<5 years), medium timescales (5-10 years), or much longer timescales (>10 years).
- **Effectiveness at service provision:** this reflects the effectiveness of the solution at increasing infrastructure resilience to climate change hazards, for example, the percentage reduction in flood depth for different return periods. Measuring effectiveness is likely to be challenging and requires technical expertise, funding for monitoring and evaluation of data collected long-term across multiple case studies.
- **Carbon storage potential** (tonnes of carbon / tonnes of CO_2 stored per square meter / linear meter): this reflects the ability of different NbS options to contribute to the temperature reduction goals of the Paris Agreement. For some NbS options this may be zero or negative, reflecting that some NbS may not sequester carbon or may even be carbon sources.
- **Sustainable Development Goals and targets**: following Fuldauer et al (2022) the Sustainable Infrastructure Partnership's SustainABLE tool, and UNEP (2023) this assesses the number of SDG goals and targets which can be influenced by different NbS options and reflects the ability of different NbS options to contribute to the 2030 Agenda of Sustainable Development.
- **Kunming-Montreal Global Biodiversity Framework:** following UNEP (2023) this assesses the number of goals and targets under the new Kunming-Montreal Global Biodiversity Framework which can be influenced by each NbS option and reflects the ability of different NbS options to contribute to the Convention on Biological Diversity.
- **Survival rate:** implementation of NbS does not guarantee their survival. Previous work (Ellison et al, 2019) has highlighted the likelihood of survival of some coastal and marine NbS options, represented in % likelihood of survival.
- **Space required** (in square meters, linear meters or % of catchment): NbS options require differing amounts of space. In the case of infrastructure resilience, many will have larger space requirements than built infrastructure options. This may be a constraining factor in locations where space is limited, such as small islands or urban areas, and must be considered within the decision-making process.

- **Threats to persistence long term:** some NbS face developmental and environmental pressures that may risk their long-term survival, such as infrastructure development, agricultural encroachment, rising sea surface temperatures and hurricanes. Identification of relevant threats in the decision-making process can be used to determine the suitability of NbS options (i.e., whether the NbS is likely to be present in the future to provide the required service) and the identification of relevant measures to mitigate the threat.
- **Lifespan** (in years / decades): the length of time that the NbS solution will persist and provide services for has the potential to be longer than that of built infrastructure options. Factoring the lifespan of NbS options versus built infrastructure into the decision-making process can help to make the case for investment in NbS.
- **Flexibility to adapt to climate change:** some NbS options can adapt naturally to climate change or regenerate following climate change impacts, unlike built infrastructure options. For example, mangroves can keep pace with sea level rise in some cases through accretion of sediments, unlike built coastal defence infrastructure (Silva et al, 2015; The World Bank, 2021). Consideration of this adaptability to climate change can help to make the case for investment in NbS.
- **Additional benefits for biodiversity, societies and the economy:** NbS options can provide multiple wider benefits, such as habitat, food and medicinal resources, sustainable livelihood options for local communities, touristic opportunities and improved mental and physical well-being. Recognising and accounting for these benefits in the decision-making process can sway investments in the favour of NbS (UNEP, 2023).

Information gathered through the literature review process suggests that the majority of climate hazards pose a risk to each of the three sectors considered within this Fellowship. The preliminary literature review suggests that the climate hazards which have the most potential NbS options for risk reduction are water-related, including water quality (water purification), drought, and flood-related hazards, as well as heat. Equally, the pilot results suggest that the NbS which have potential to support mitigation across the broadest range of climate hazards include forest-based NbS and wetlands. These results reflect existing information and therefore will need to be updated in the future as new research is undertaken.

The preliminary literature review suggests that most evidence which is readily available to decision-makers (e.g., in the form of easy-access reports rather than academic articles which are behind a paywall) is on NbS for the mitigation of water-

related hazards, and particularly floods (e.g. The World Bank, 2017; United Nations, World Water Assessment Programme, 2018; UNEP, 2014). Correspondingly, there is relatively less readily available information in the form of easy-access reports on other hazards such as landslides or wildfires. Consequently, there is a relatively greater breadth of quantitative data available on the costs and effectiveness of water related NbS, such as the water storage capacity of wetlands and green roofs, and the flood reduction benefits of forests, which is likely to increase their potential for selection in decision-making processes compared to other hazards and other NbS options.

The literature review highlighted some key information gaps. Most notable gaps on the costs of NbS relate to monitoring costs, which appear to be largely unreported, but also implementation and maintenance costs. There was also limited information on the effectiveness at service delivery for many NbS options, or timescales required to achieve benefits, which poses a key barrier to comparison against built infrastructure options and scaling the uptake of NbS in decision-making processes. Most readily available information was highlighted for implementation costs per unit area, although gaps were still notable across different NbS options. With regard to NbS types, less information was available on agricultural management NbS, such as the cost and effectiveness of cover crops, mulching, or drought-resistant crops for the provision of services that can mitigate hazards such as drought or water quality.

here information on costs or effectiveness at service provision was provided, the data recorded and corresponding unit type varied largely between projects, making comparison of different options challenging. For example, the reported effectiveness of different NbS for coastal flood mitigation varied from reduction in wave height (in cm or in %) to % reduction in wave energy. Equally, the flood reduction benefits of terrestrial forests are typically reported for units of area representing catchment proportions (e.g., 25-40% of a catchment to be forested for flood reduction benefits), but are not typically broken down by unit area to enable a comparison of different forest sizes (e.g., it is unclear from the data if there is a greater benefit if a catchment is 80% forested compared to 25-40%). Given the large breadth of projects and ongoing studies on NbS, it is expected that the evidence base on the effectiveness of NbS options will be added to over the years, however it will be important to ensure that it is reported in a way that enables comparison across different NbS types and hazards. Where cost data was found to vary within the literature, this has already been converted to a standardised unit (US $ per m^2) within the decision-making tool developed through this Fellowship.

The following section shows the results of the key informant interviews, which

assessed some of the challenges in terms of the enabling environment that form barriers to the deployment and scaling of NbS, and of the collection of the necessary data to support informed and robust decision-making.

4.2 Findings from Interviews

Interviews with key informant stakeholders highlighted key enabling environment barriers to scaling up NbS and recording data on NbS in the context of the small island developing state of Jamaica. The key barriers which were identified are shown in table 2.

Table 2. Enabling environment barriers to scaling up NbS in Jamaica, as identified through key informant interviews.

Challenge	Description	Source
Political will	Lack of commitment at all levels. Requires a bottom-up approach with local communities empowered with information and knowledge. Political will is sometimes difficult – many have bigger problems, e.g., poaching	Jamaica Environment Trust; Marine Lab
Technical and human capacity	Lack of technical capacity to undertake monitoring following implementation. Few people have expertise in NbS so there is limited human capacity to scale NbS.	UN (2018); Marine Lab
Local knowledge	Lack of awareness, communication and knowledge at all levels. Engineers would need to change their way of thinking to an integrated approach. Lack of monitoring and evaluation means projects don't start from a place of knowledge. E.g., 3 million trees initiative – risks planting trees where they are unsuitable. A lack of awareness on the value of NbS means that some NbS have been damaged or destroyed.	UN (2018); Jamaica Environment Trust
Data gaps	Data on costs and benefits are lacking – this makes it hard to apply for funding. Monitoring of effectiveness does not typically occur.	Planning Institute of Jamaica (PIOJ)
Squatters	In the rural areas, major issues within watersheds are farmers and squatters. Slash and burn agriculture leaves land bare. Rangers monitor day to day. The process to remove squatters is tedious and must be done via the courts.	National Water Commission; Marine Lab
Animals	Animals have been known to destroy new trees (e.g., cows)	National Water Commission
Forest fires	Forest fires are annual in Jamaica, sometimes caused by slash and burn. Particularly bad in	National Water Commission

	2015/16. This impacts the survival rate of NbS.	
Funding for NbS	Funding is a barrier to small islands who need funding for healthcare and other basic services too. Requires funding for permits (e.g., land permits) which are not always factored in, and longer funding timescales given the time delays, but funds are typically short-term. Funding for education / awareness raising is often missed. Funding for restoration – Jamaica is classified as middle income, so they often get loans instead of grants – hard to find complementary funding and not eligible for so many grants. Onerous reporting conditions and different requirements of funders mean that multiple different reports on NbS must be written; this typically falls on the same people who are implementing NbS, meaning human capacity is stretched. Funders typically require projects to report on metrics such as numbers of trees planted, or number of hectares restored, rather than on outcomes in terms of solution effectiveness.	British High Commission; Jamaica Environment Trust; PIOJ
Community buy-in	Average Jamaican is more concerned about basic needs. People do not like listening to government – not very responsive, lack of trust. Requires leadership. Particularly challenging with cost-of-living crisis. Some communities prefer to see built infrastructure solutions for risk reduction.	British High Commission
Condition	Invasive species, poor soils, low biodiversity hinder effectiveness. Caribbean pine is invasive which increases risk of fire as very flammable.	British High Commission
Lack of engagement	Some initiatives may be undertaken with limited consultation, e.g., of forestry department, NEPA, local communities.	British High Commission
Legislation	National Parks and Forest Reserves are under two different pieces of legislation managing the same space. Allows different management practices. The responsibility for setting the mandates for forestry move from ministry to ministry – currently in the office of the PM, not necessarily an environmental ministry.	British High Commission

Misaligned mandates	Misaligned mandates cause conflicts between agencies – while one agency may be protecting another may be giving out land for farming. E.g., million trees initiative incentivises tree planting, but some utilities (JPS) are cutting down trees along roadsides. Mangroves have been cut down in protected areas without permits to fix water pipes.	Jamaica Environment Trust
Built infrastructure focus	Focus tends to be on built projects in the case of coastal protection. More research to support the use of hard infrastructure. NbS take longer which is a deterrent.	Jamaica Environment Trust PIOJ
Land ownership	Feasibility issue is land ownership – government owned land which is neglected and used by squatters – politicians do not want to evict them for fear of losing votes	Marine Lab
Time to achieve benefits	The longer timeframes that some NbS require for service provision is a barrier to selection.	PIOJ

Monitoring the outcomes of NbS and effectiveness at service provision is hindered predominantly by a) a lack of funding for monitoring over sufficient timescales or of metrics which track solution effectiveness; b) lack of technical capacity and skills for monitoring; c) lack of human capacity in terms of availability of skilled people to conduct monitoring. Where funding is provided for monitoring outcomes, this typically lasts for project durations which are generally much shorter than NbS project lifecycles, often extending only as long as 2-3 years.

Time to achieve benefits is a hindrance to scaling NbS. The longer lengths of time required for some NbS options to reach maximum potential for service provision compared to traditional built infrastructure options poses issues in terms of:

- Service need – the time required for some options to provide services is not always aligned with the need.
- Options selection – longer timeframes do not always align with election cycles of political decision-makers who want to be seen to have impact within the timeframe of their work.
- Funding – funding provided by donors does not always extend for the duration required to maintain and manage solutions – reporting requirements typically require outcomes to be provided within short timeframes (often <5 years) which is not aligned with some NbS options.

Some stakeholders report that in some local communities, hard infrastructure solutions

are perceived as providing more effective risk reduction measures compared to NbS. General consensus amongst interviewees suggested greater awareness raising is required amongst different stakeholders to ensure the wider value of NbS in terms of benefit provision is captured, to secure buy-in from local communities, and to maximise the chance of their success long-term.

4.3 Development of the decision-making tool

The pilot decision-making tool developed through this Fellowship is provided separately. It reflects the data collected predominantly during the literature review, and supplemented through interviews where relevant information on metrics and data was provided. The decision-making tool includes the conceptual framework outlining which NbS options are applicable to mitigate each climate hazard, and a database of metrics for assessing the costs and benefits of NbS options, as outlined in section 4.1. As discussed in the previous two sections (4.1 and 4.2), there remain numerous data gaps. The collection of data for each of the metrics as part of standard practice on NbS will enable a more robust evaluation of the full range of costs and benefits of NbS options and their comparison against other NbS and built infrastructure options in infrastructure decisions

4.4 Geospatial application of the decision-making tool

The pilot decision-making tool has been applied to the case study of Jamaica. To test the functioning and applicability of the tool to real-life decisions, the tool was used to assess the potential costs and benefits of forest-based NbS for mitigating the impact of 2m and 1.3m floods on road transport networks, which are both associated with 1-in-100-year and 1-in-20-year floods. To select a relevant location for testing the tool, QGIS was used to geospatially visualise (figure 2) landcover; (figure 3) road transport networks; (figure 4) flood risk. These are shown below, along with (figure 5) the combined geospatial data layers.

Geospatial visualisation shows a given road is at risk of a 1-in-100-year flood in 2050 that has a 2m flood depth. The cost of road rehabilitation is US $1,447 per meter (J$224,000). As discussed in section 4, it is assumed that damage to the road occurs only when a flood overtops 0.5m. Without adaptation, the road is projected to incur economic damages of US $535.39 (J$82,827.30) per meter (1.5m flood depth damage ratio * cost of rehabilitation).

The decision-making tool shows that forests are applicable to reduce flood risk to infrastructure, including transport infrastructure and road networks, and can reduce

floods up to 1-in-100-year by 5-30% if 25-40% of the upstream catchment is forested (Dadson et al, 2017)[12]. This corresponds to a reduction in flood depth from 200cm to 190-140cm. Estimates suggest that this equates to economic damages of US$509.34 - $390.69 (J$78,797.24 - $60,441.54) per meter. This can lead to avoided economic damages ranging from $26.05 - $144.7 (J$4,022.32 - $22,385.76) per meter, approximately 5-27% of initial damages.

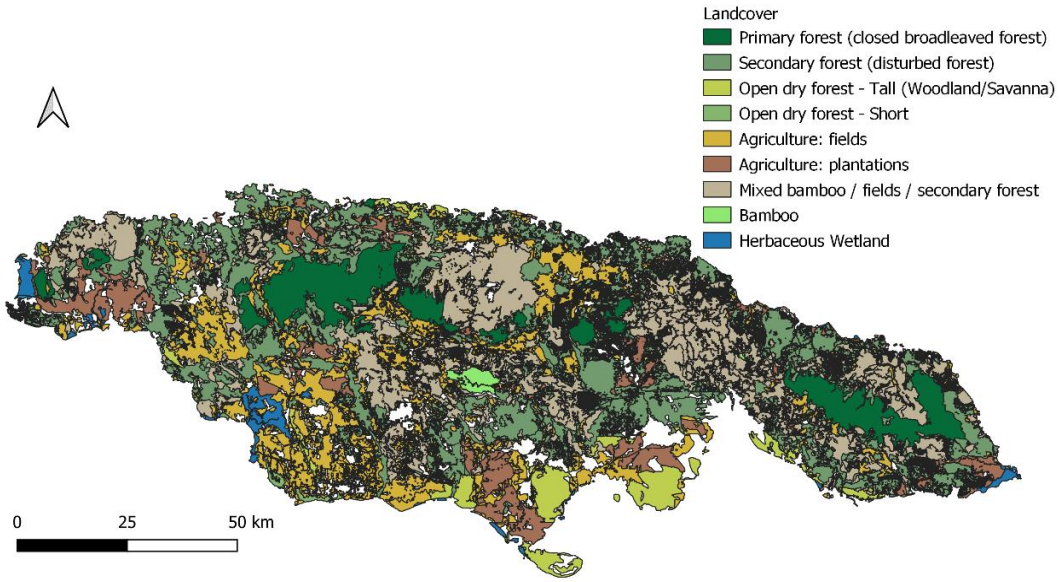

Figure 2. Natural landcover in Jamaica

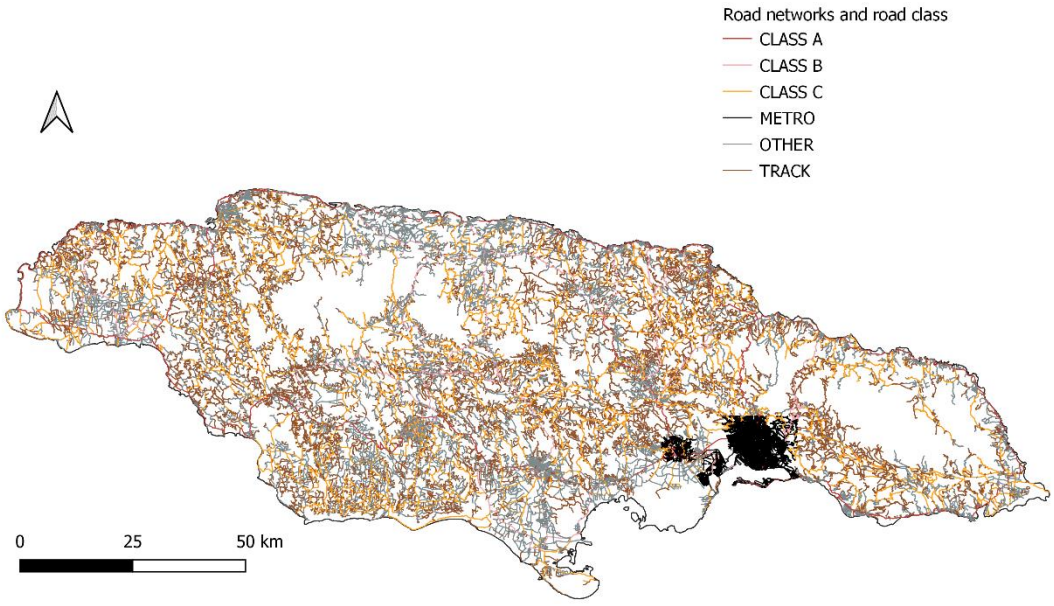

Figure 3. Jamaican road networks

[12] We acknowledge that this is a very broad range. However, at present, no detailed studies have been done for Jamaica, and therefore we are using the best data available from the literature. This could be improved through further research and site-specific studies.

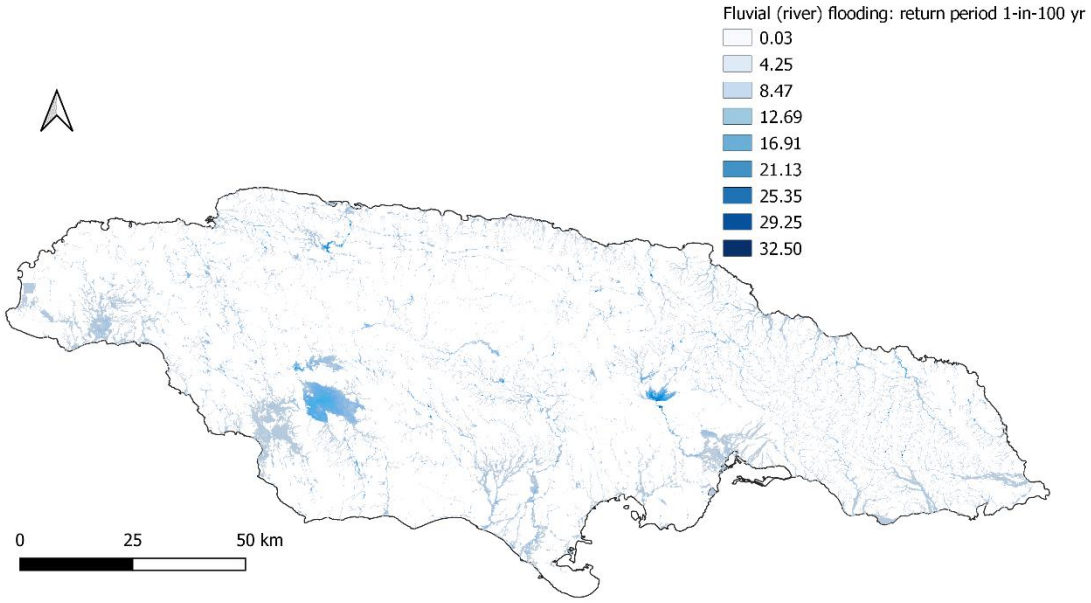

Figure 4. Fluvial (river) flooding in Jamaica, for a 1-in-100-year return period flood

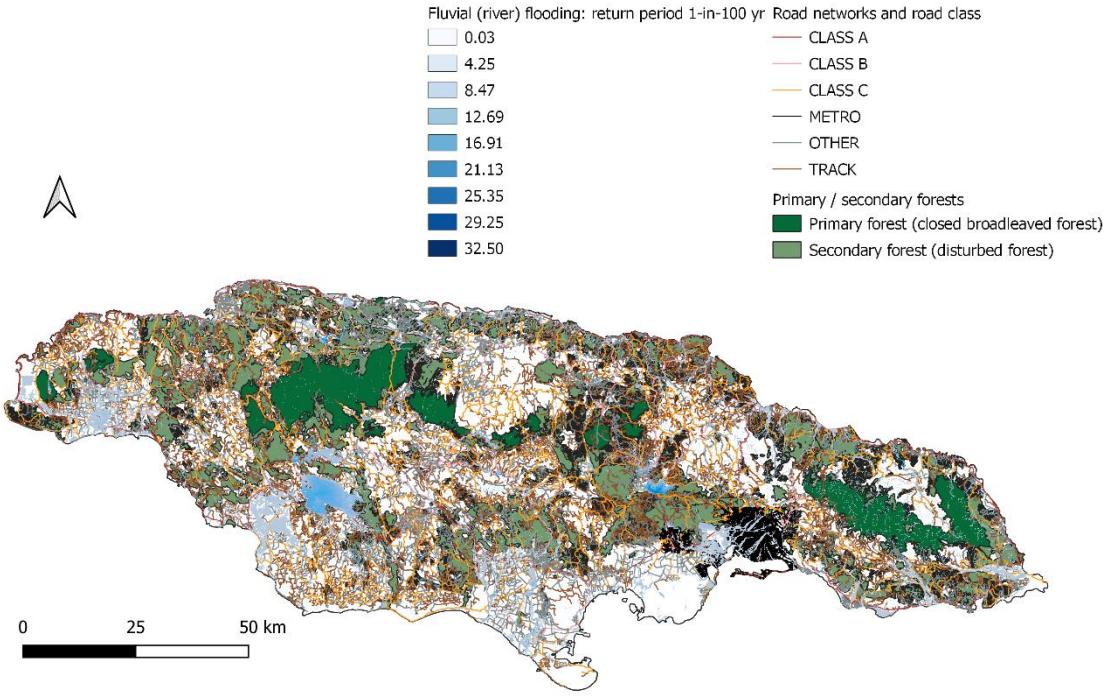

Figure 5. combined geospatial data layers showing primary and secondary forests, road networks and 1-in-100-year river flooding.

In the event of a smaller, 1-in-20-year flood, a given road is shown to be exposed to a flood of 1.3m depth. Assuming the same flood reduction benefits from forests of 5-30%, this corresponds to a reduction in flood depth to 123.5-91cm. Estimates suggest that this equates to economic damages of US$274.93 - $162.06 (J$42,532.94 - $25,071.43) per meter. This can lead to avoided economic damages ranging from US$101.29 - $214.16 (J$15,670.03 - $33,131.54) per meter, approximately 27-57%. In this scenario, it suggests that forests have greater potential for avoiding damages to infrastructure for smaller

floods compared to larger floods.

In addition to avoided economic damages, the decision-making tool shows that investment in forest-based NbS can result in multiple wider benefits. For example, in Jamaica, primary forests are estimated to store 88.22 tonnes of CO_2 and secondary forest 82.08 tonnes of CO_2 per hectare, supporting progress towards national carbon sequestration targets under the Paris Climate Change Agreement. They can also improve soil quality and lead to benefits for agriculture, while supporting recreation, air and water quality, nutrient cycling, human well-being, provide marketable products such as timber and food which can improve livelihoods, and provide habitat for biodiversity. These additional benefits mean that forests can advance progress on 93 out of 169 SDG targets (55%). By reducing flood damages to transport infrastructure, forests can also help to safeguard up to 76 SDG targets (43%). Combining the benefits in terms of safeguarded SDG targets with those influenced through additional co-benefits, forests can help to progress to up to 121 SDG targets (72%). The tool also shows that forests can play a role in contributing to the Kunming-Montreal Global Biodiversity Framework under the UN Convention on Biological Diversity - they can contribute to meeting 3 of the 4 long-term goals and 70% of the targets (16 out of 23).

The cost of implementation varies depending on the type of NbS (e.g., forest protection, restoration or improved management) and the context (e.g., tropical small island developing state compared to an urban developed context). The preliminary literature review and pilot decision-making tool highlights some information on implementation and maintenance costs, although there are outstanding gaps. For example, data on forest protection is a current gap within the tool, however forest restoration is estimated at US $0.06 / J $9.28 per m^2 in a Jamaican context, while reforestation can cost US $0.2-0.35 / J $30.94 - $54.15 per m^2 elsewhere (location undefined), and forest management is shown at US $39.32 / J $6,082.98 per m^2 (location undefined). Maintenance costs are generally lacking but have been reported for a UK study of afforestation, totalling US $0.36-0.37 / J $55.69 - $57.24 per m^2. Cost data will vary largely depending on land prices, ecosystem condition (e.g. whether it is very degraded or healthy) and other local factors, and therefore should be updated to reflect local costs in the years following the Fellowship.

As mentioned above, for flood mitigation benefits, large space requirements may be necessary, totalling as much as 25-40% of a catchment for maximum benefit (Dadson et al, 2017). The time requirements for forest-based NbS may vary depending on the condition of the forest and the type of intervention (e.g., protection versus improved

management, or restoration). For example, to maintain the protected status of an already-protected, healthy forest will take no time to implement and provide benefits, however, to put an unprotected forest under protected status may take up to 10 years for legislation to be written and passed under law. Where a forest is very badly degraded, it can take as much as 15-20 years to reach full potential for service provision through restoration (The World Bank, 2021). In Jamaica, geospatial data on protected areas can be used to identify whether a given forest that is found to be improving infrastructure resilience is protected (see Figure 6 which shows protected areas). This can help to inform decision-makers of whether a given forest should be granted protected status[13]. Ecosystem condition is fundamental to effectiveness at service provision, and can be evaluated through analysis of satellite data, site-specific assessments and interviews with local stakeholders.

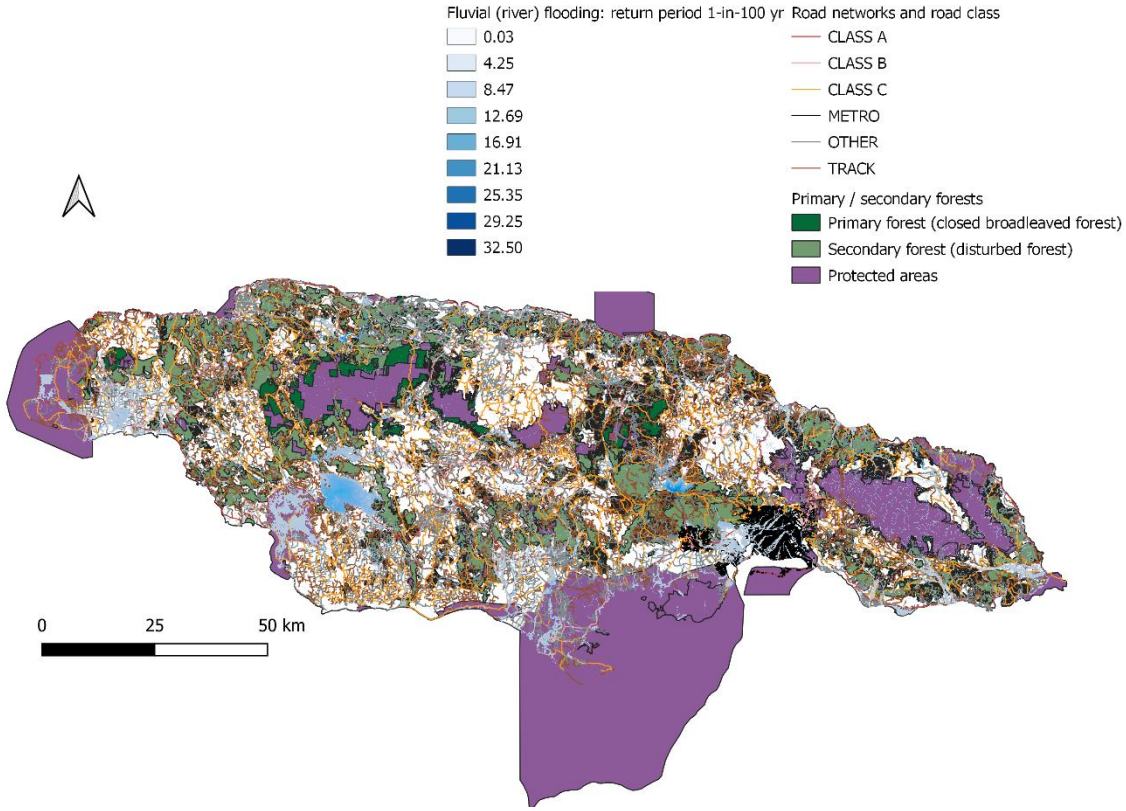

Figure 6. protected areas, shown in purple, can be used to identify if a given ecosystem that is found to be benefitting infrastructure systems is under protected status or not.

There are a broad range of costs and benefits associated with NbS; larger than for built infrastructure. The larger space and time requirements required for certain NbS options may be off-putting to some decision makers, and infeasible in some locations where available land area is a significant constraint. The applied case study suggests that

[13] Legislation on protected areas should ensure that local communities are not negatively affected by a protected area – a protected area should seek to permit sustainable use (e.g. harvesting of fruits and timber) and stewardship of natural resources by local and indigenous communities, rather than their exclusion.

forest-based NbS cannot completely prevent economic damages to road transport infrastructure from flooding of 2m or 1.3m depth, but that they can contribute to avoided economic damages, potentially reducing requirements for built infrastructure adaptation options. The ability of NbS to provide multiple additional benefits, including for national policy agendas such as the Paris Agreement, SDGs and the Convention on Biological Diversity can potentially lead to greater cost-effectiveness of investments compared to built infrastructure, and will be fundamental to achieving positive outcomes for biodiversity (Haggis et al, pending publication; UNEP, 2023). Decision-makers should therefore ensure that both NbS and combined NbS-built infrastructure options are considered alongside built infrastructure options to maximise the benefits that can be achieved and efficiency of investments. This requires that the full range of benefits and costs are reflected in infrastructure assessments and accounted for in the decision-making and investment process, and that the relevant data on costs, benefits and effectiveness is recorded across the NbS lifecycle to support future assessments.

5. Enablers and Barriers

There are several enablers for this research. These include:

- As a PhD student at the University of Oxford I have access to academic journals and relevant articles on NbS. This is complemented by the growing availability of international reports and publications on the topic, including a recently published report by the Global Facility for Disaster Reduction and Recovery (GFDRR). This has been very valuable to the literature review component of the Fellowship, the gathering of relevant data on costs and benefits of NbS, and the development of the decision-making tool.
- Membership to the Oxford Programme for Sustainable Infrastructure Systems and Nature-based Solutions Initiative has given me access to teams of people with expertise on both climate risks to infrastructure and NbS. This has proved helpful in identification of key data sources and methodologies throughout the Fellowship.
- A prior research project in Jamaica has meant that I was able to readily access key informant stakeholders for the interview component of the Fellowship, and geospatial data to which I could apply the decision-making tool.
- Access to a mentor, technical experts and the CDRI team provided useful feedback and constructive advice throughout the duration of the Fellowship, including suggestions of new publications for consideration. The process of quarterly

check-ins provided helpful milestones along the way, which ensured consistent progress, time management, and opportunities for feedback and refinement of methods.

- The selection process at the beginning of the Fellowship was valuable in terms of ensuring a realistic scope for the 12-month project which enabled a better, more detailed research project.
- The funding provided through the Fellowship ensured that I could dedicate time to this research project, which should result in an output that can be applied in real world decisions.

There are several barriers to the research:

- Although the topic of NbS is growing, there remains a general lack of data on costs and benefits of NbS, specifically relating to effectiveness at service provision, maintenance and monitoring costs. This is reflected in the data gaps within the pilot decision-making tool and is likely to remain a barrier to scaling uptake of NbS for infrastructure resilience more broadly.
- The 12-month duration meant that the scope of the research project had to be limited – this included the scope of sectors included within the decision-making tool and the granularity of data gathered for NbS options. The decision-making tool does not generally reflect country-specific data, but rather reflects data sourced from international publications.
- The effectiveness of NbS options does not distinguish across variations in contextual features such as topography, soil type, ecosystem condition. For example, the data on effectiveness of forests for flood reduction does not distinguish between healthy forests and degraded forests, despite it being understood that healthy forests are much more effective at benefit provision than those of poor condition, nor does it distinguish between forests on sloped or flat land. It is expected that as more studies are undertaken, the data within the decision-making tool can be added to to reflect an updated knowledge base.

6. Key Takeaways from CDRI Fellowship Programme

The key takeaways from this Fellowship are as follows:

- Large data gaps are a barrier to comparing NbS options against built infrastructure options in infrastructure decisions. This is particularly the case in terms of

effectiveness at service provision, time to provide benefits, monitoring and maintenance costs.

- There is potential for NbS to provide multiple additional benefits, greater than that of built infrastructure, for biodiversity, carbon storage, and communities. These broader benefits need to be fully accounted for in decisions on infrastructure to reflect the full potential of NbS options. The decision-making tool provides a standardised framework of key metrics which can be considered going forward.
- CDRI provides a very valuable Fellowship programme – opportunities in terms of constructive feedback, a platform to showcase our research, opportunities to participate in conferences and reports, and access to mentors, technical experts and the CDRI team are useful for both research and career development.
- The decision-making tool is a major outcome of this research. It is a generalised tool which has immediate applicability by decision-makers, and which can be expanded in future years to cover a broader range of sectors and services. It provides a framework for considering NbS for resilience and can be applied geospatially to hep prioritise NbS options in adaptation strategies.

7.Conclusion

This Fellowship has provided a framework, database and decision-making tool that can help to identify and compare the costs and benefits of relevant NbS options to address built infrastructure vulnerability to climate hazards within energy, transport and water sectors. A broad range of NbS options can be considered in assessments to increase the resilience of infrastructure systems to a range of climate hazards, including landslides, snowfall, heat and flooding. There remain large data gaps, particularly in terms of effectiveness of different NbS options at service provision, time required to achieve benefits, maintenance and monitoring costs. Many of these are due to factors such as lack of funding for monitoring outcomes, a lack of technical expertise and human resources, reporting requirements of funders and time delays to benefit provision which pose barriers to implementation and / or data collection. Data gaps will need to be filled and existing data updated in future months and years as more studies are undertaken. However, the tool developed through this Fellowship can be used as a starting point for decision-makers, to support decisions ranging from sub-national to national and supra-national scale and to weigh up the broad range of costs and multiple benefits that NbS can provide. Initial testing of the tool in an applied case study suggests that NbS can help to reduce economic damages of climate hazards to infrastructure, and further highlights

the importance of their consideration alongside built infrastructure options in decisions on infrastructure resilience. There is scope to continue to expand the tool in future years to encompass all infrastructure sectors and infrastructure services, beyond protective services.

8. Way Forward

This Fellowship is intended to provide the foundation for decision-makers to consider NbS more routinely in their decisions and is intended to provide the first building block to implementation. This decision-making tool has great potential for application in real life decision-making for infrastructure resilience. Further research can be undertaken to broaden and add to the tool. This includes:

- Broaden the number of infrastructure sectors considered within the tool. This may consider solid waste, digital communications, finance, retail, health, education, etc.
- Widen the scope of services provided by NbS which are considered within the tool. The current tool considers only the costs, benefits and effectiveness of NbS to **protect** built infrastructure. This may be extended to consider the ability of NbS to **deliver** the service and substitute for the asset, and to **enhance** the service and complement the asset (see UNEP, 2023). For example, NbS can enhance services provided by the education sector by improving cognitive functioning, but this is not accounted for within the current tool.
- Fill data gaps and update existing data within the tool through continuing to review existing and new literature, and through further interviews with relevant stakeholders.
- Undertake further demonstration of the tool in applied case studies, for different hazards, infrastructure sectors, and in different countries.

Following the Fellowship, there remains potential to:

- Host the decision-making tool on CDRI's website to make it available to decision-makers globally, and in a format that can be added to.
- Produce an academic paper, contribute to reports, present at conferences to disseminate the research from the Fellowship.

References

1. Beck, M. W., Losada, I. J., Menendez, P., Reguero, B. G., Diaz-Simal, P., and Fernandez, F., (2018) The global flood protection savings provided by coral reefs. Nature Communications, 9: 2186.
2. Blanken, P. D. (2018). Designing a living snow fence for snow drift control. *Arctic, Antarctic, and Alpine Research* 41 (4), 418-425. https://doi.org/10.1657/1938-4246-41.4.418.
3. Browder, Greg, Suzanne Ozment, Irene Bescos Rehberger, Todd Gartner, and Glen-Marie Lange. 2019. Integrating Green and Gray: Creating Next Generation Infrastructure. Washington, DC: The World Bank and World Resources Institute. https://openknowledge.worldbank.org/handle/10986/31430
4. Blicharska, M., Smithers, R. J., Mikusinski, G., Ronnback, P., Harrison, P. A., Nilsson, M., and Sutherland, W. J., (2019) Biodiversity's contributions to sustainable development. *Nature Sustainability* 2, 1083-1093. https://www.nature.com/articles/s41893-019-0417-9.epdf?author_access_token=bUAtn1CEDi_fMfiGJINC-NRgN0jAjWel9jnR3ZoTv0PoJkztOZ8mperjgQm6vluQZuFvzQVsoEVicNa_w66RwpslyUX3sEWPR26xuRGWuU6_olhSY3hYvHIkRgafLTTSqHRDXcW7lQuEqLDgYAE6Yw%3D%3D.
5. Chausson, A., Turner, B., Seddon, D., Chabaneix, N., Girardin, C. A. J., Kapos, V. et al. (2020). Mapping the effectiveness of nature-based solutions for climate change adaptation. *Global Change Biology* 26 (11),6134-5155. https://doi.org/10.1111/gcb.15310.
6. Cohen-Shacham, E., Walters, G., Janzen, C., and Maginnis, S. (2016). *Nature-based solutions to address global societal challenges.* Gland, Switzerland: The International Union for Conservation Nature. https://portals.iucn.org/library/sites/library/files/documents/2016-036.pdf.
7. Dadson, S. J., Hall, J. W., Murgatroyd, A., Acreman, M., Bates, P., Beven, K., Heathwaite, L., Holden, J., Holman, I. P., Lane, S. N., O'connell, E., Penning-Rowsell, E., Reynard, N., Sear, D., Thorne, C., and Wilby, R., (2017) A restatement of the natural science evidence concerning catchment-based 'natural' flood management in the UK. Proceedings of the Royal Society A, 473(2199). Available at: https://doi.org/10.1098/rspa.2016.0706

8. Ellison, G., Kaupa, S., Ozment, S., Schleifer, L., Jongman, B., and Gartner, T., (2018) Nature-Based Solutions for Disaster Risk Management: Coastal Flooding and Erosion Protection. To accompany Browder, G., Ozment, S., Bescos, I. R., Gartner, T., and Lange, G., (2019) Integrating Green and Gray: Creating Next Generation Infrastructure. Available at: https://doi.org/10.46830/wrirpt.18.00028
9. Fuldauer, L. I., Thacker, S., Haggis, R. A., Fuso-Nerini, F., Nicholls, R. J., and Hall, J. W. (2022). Targeting climate adaptation to safeguard and advance the Sustainable Development Goals. Nature Communications 13 (1), 3579. doi: 10.1038/s41467-022-31202-w.
10. Glas, H., Jonckheere, M., Mandal, A., James-Williamson, S., De Maeyer, P., and Deruyter, G., (2017) A GIS-based tool for flood damage assessment and delineation of a methodology for future risk assessment: case study for Annotto Bay, Jamaica. Natural Hazards (88) pp. 1867-1891. https://link.springer.com/article/10.1007/s11069-017-2920-5
11. Global Infrastructure Hub (2017). Global Infrastructure Outlook. Infrastructure investment needs. 50 countries, 7 sectors to 2040. Available for download at https://outlook.gihub.org/
12. Haggis., R., et al. (pending publication). A framework for informed planning and decision-making on nature-based solutions for infrastructure.
13. Kapos, V., Wicander, S., Salvaterra, T., Dawkins, K., and Hicks, C. (2019). *The role of the natural environment in adaptation, Background Paper for the Global Commission on Adaptation.* Rotterdam and Washington, D.C.: Global Commission on Adaptation.
14. IPCC (2012) Managing the risks of extreme events and disasters to advance climate change adaptation. Special Report of the Intergovernmental Panel on Climate Change. Cambridge University Press, Cambridge, UK and New York, NY, USA. https://www.ipcc.ch/site/assets/uploads/2018/03/SREX_Full_Report-1.pdf
15. Koks, E. E., Rozenberg, J., Zorn, C., Tariverdi, M., Vousdoukas, M., Fraser, S. A., Hall, J. W., and Hallegatte, S., (2019) A global multi-hazard risk analysis of road and railway infrastructure assets. Nature Communications (10:2677). https://doi.org/10.1038/s41467-019-10442-3
16. Lanzas, M., Hermoso, V., de-Miguel, S., Bota, G., and Brotons, L., (2019) Designing a network of green infrastructure to enhance the conservation

value of protected areas and maintain ecosystem services. Science of the total environment, 651, 1, 541-559.

17. Liquete, C., Kleeschule, S., Dige, G., Maes, J., Grizetti, B., Olah, B., and Zulian, G., (2015) Environmental Science and Policy 54-268-280.
18. Menéndez, Pelayo, Iñigo J. Losada, Saul Torres-Ortega, Siddharth Narayan, and Michael W. Beck. 2020. "The Global Flood Protection Benefits of Mangroves." Scientific Reports 10 (1): 4404. https://doi.org/10.1038/s41598-020-61136-6.
19. Pant, R., Thacker, S., Hall, J. W., Alderson, D., and Barr, S., (2016) Critical infrastructure impact assessment due to flood exposure. Journal of Flood Risk Management, 11, pp.22-33.
20. Seddon, N., Chausson, A., Berry, P., Girardin, C. A. J., Smith, A., and Turner, B. (2020). Understanding the value and limits of nature-based solutions to climate change and other global challenges. *Philosophical transactions of the royal society B* 375, 1794. https://doi.org/10.1098/rstb.2019.0120
21. Seddon, N., Smith, A., Smith, P., Key, I., Chausson, A., Girardin, C. et al. (2021). Getting the message right on nature-based solutions to climate change. *Global Change Biology* 27(8), 1518-1546. Available at: https://doi.org/10.1111/gcb.15513
22. Seiler, A. (2003) Effects of infrastructure on nature. Office for Official Publications of the European Communities.
23. Silva, R., Martínez, M. L., Odériz, I., Mendoza, E., and Feagin, R. A., (2015) Response of vegetated dune–beach systems to storm conditions. Coastal Engineering, 109, p.53-62. Available at: https://doi.org/10.1016/j.coastaleng.2015.12.007
24. Simpson, M., James, R., Hall, J. W., Borgomeo, E., Ives, M. C., Almeida, S., Kingsborough, A., Economou, T., Stephenson, D., Wagener, T. (2016) Decision analysis for the management of natural hazards. Annu. Rev. Environ. Resour. 41, 489-516.
25. Thacker, S., Adshead, D., Fay, M., Hallegatte, S., Harvey, M., Meller, H. et al. (2019). Infrastructure for sustainable development. *Nature Sustainability* 2, 324-331. https://www.nature.com/articles/s41893-019-0256-8.
26. The World Bank (2017). *Implementing Nature Based Flood Protection: Principles and Implementation Guidance*. Washington, DC: World Bank. *https://openknowledge.worldbank.org/handle/10986/28837*.

27. The World Bank (2021) A Catalogue of Nature-Based Solutions for Urban Resilience. World Bank, Washington, DC. Available at: http://hdl.handle.net/10986/36507
28. United Nations, World Water Assessment Programme (2018). *United Nations World Water Development Report 2018. Nature-based solutions for water*. Paris, France: UNESCO. https://www.undp.org/publications/nature-based-solutions-water#:~:text=NBS%20use%20or%20mimic%20natural,(e.g.%2C%20floodplain%20restoration%2C%20green.
29. United Nations Environment Programme. (2014) *Green Infrastructure Guide for Water Management: Ecosystem-Based Approaches for Water-Related Infrastructure Projects*. United Nations Environment Programme. https://wedocs.unep.org/bitstream/handle/20.500.11822/9291/-Green%20infrastructure%3a%20guide%20for%20water%20management%20%20-2014unep-dhigroup-green-infrastructure-guide-en.pdf?sequence=3&isAllowed=y.
30. United Nations Environment Programme (2023). Nature-based Infrastructure Solutions – assessing the role of nature-based infrastructure in addressing global sustainable development challenges. Nairobi.
31. van Ginkel, K. C. H., Dottori, F., Alfieri, L., Feyen, L., and Koks, E. E., (2021) Flood risk assessment of the European road network. Nat. Hazards Earth Syst. Sci., 21, 1011-1027. https://doi.org/10.5194/nhess-21-1011-2021
32. Vogl, A. L., Dennedy-Frank, P. J., Wolny, S., Johnson, J. A., Hamel, P., Narain, U., and Vaidya, A., (2016) Managing forest ecosystem services for hydropower production. Environmental Science & Policy, 61, pp.221-229.
33. Zio, E., (2016) Critical Infrastructures Vulnerability and Risk Analysis. European Journal for Security Research (1) pp.97-114. DOI 10.1007/s41125-016-0004-2

Framework for Evaluating Bridge Network Resilience by Considering Socio-Technical Attributes

Dr Rubel Das

Dr Masaaki Nakano

Tetsuro Goda

Nippon Koei co. ltd,

Research and development centre
Japan

Under CDRI Fellowship Programme 2022-23

CDRI
Coalition for Disaster Resilient Infrastructure

Disclaimer: the views expressed in this paper reflect the opinions of the author and not necessarily the official views of CDRI.

Abstract

Transportation bridges are the weakest element among all the components of the transportation infrastructure system. Recent experience with natural and man-made water-related disasters indicates that the current transportation systems cannot protect and prevent all disruptive events. Owing to frequent disasters, the U.S. initiated the Critical Infrastructure Protection (CIP) program. However, the focus is gradually shifting from CIP to critical infrastructure resilience (CIR) because CIP does not address all the aspects of securing the nation's critical infrastructure [Das, 2020]. In this study, structural properties are considered explicitly while the interdependency of bridges is analyzed. The failure of a bridge may not significantly influence the network-level performance. The bridge is likely to have users. However, the disruption of another bridge may produce a substantial hindrance. For example, a collapsed bridge has many users, and the users have no alternatives to reach their destination. Therefore, it is necessary to evaluate the interdependency and importance of each network section. Certain destinations can be reached via multiple routes, whereas others have only one route. Therefore, this study assesses the resilience through a network-level analysis. We combined both structural and traffic factors in a single framework by utilizing structural assessment for each bridge and the operational performance for transportation networks. The concepts presented were applied to a real transportation network in Yamaguchi, Japan, to illustrate the mathematical procedures.

We propose a method based on the concept of 4R (robustness, redundancy, rapidity, and resourcefulness). In this study, we used the location data for Yamaguchi city, which contains many transportation bridges. AGOOP data contain a time stamp and spatial location stamp in addition to an attached id. After implementing the initial OD table from AGOOP data, we performed an iteration process to match with counted data.

We have utilized return period 475 years to estimate the bridge damage levels. The damage level of bridges owing to earthquakes can be estimated using the flowchart proposed by [Kobayashi Unjoh, 2005]. According to that study, the condition of bridges can be categorized into three: damage levels A, B, and C. The result for a return period of 475 has 2 bridges with damage level "A," 17 bridges with damage level "B," and 8 bridges with damage level "C." Meanwhile, the result for a return period of 2,475 years has 6 bridges with damage level "A," 14 bridges with damage level "B," and 7 bridges with damage level "C."

The restoration strategy is crucial to minimize the effect of the hazard. The strategy of repairing damaged bridges influences individuals' convenience and

satisfaction. The rate of bridge repairing is dependent on the availability of resources. We selected the bridge with the largest number of users, thus reducing the traveller's cost. Here, three restoration strategies were analyzed: (1) Road-user priority scenario (2) Road-type priority scenario and (3) Damage-type priority strategy.

In scenario 1, the average speed after the restoration of bridges increased. The average speed for scenario 2 on the 10th day was higher than that for the other periods. The average speeds on the fifth and fifteenth days were lower than that in the base case. Without a variation in scenario 3, the average speed after the restoration of bridges was higher than the base level except on the 30th day.

We evaluated the performance of each strategy by counting the number of individuals who gained after each five-day period. The areas above the curves were computed and are presented in resilience curve. It can be observed that scenario 1 has the lowest area above the curve. Although the areas above the curves for scenarios 2 and 3 are significantly close, that for scenario 3 is the largest. Based on the area, the pre-disaster user-based scenario (scenario 1) produced a more resilient system.

Based on the above results, pre-disaster maintenance results less severe damages and the post-disaster recovery will be faster. Thus, it can make trade-off between pre-and post-disaster cost.

Acknowledgments

We would like to express our sincere gratitude to our academic mentors, Professor Shinya Hanaoka, Dr Ranit Chatterjee and Dr Bhaskar Reddy Nakka Sai for their valuable guidance and support throughout the research process. Their insightful suggestions and expertise have played a pivotal role in shaping the successful completion of this endeavour. I am truly grateful for the time and effort that they dedicated to reviewing my work, providing constructive feedback, and sharing their wealth of knowledge. Their mentorship has not only enhanced my understanding of the subject matter but has also broadened my perspective on the project's implications.

Furthermore, I would like to express my sincere thanks to the entire staff of the Nippon Koei ltd. co. for fostering an environment of intellectual growth and providing the necessary resources for my project.

Additionally, I extend my heartfelt thanks to the Coalition for Disaster Resilient Infrastructure (CDRI) for providing the necessary funding and resources that enabled the execution of this project. Your financial support has been pivotal in facilitating the experimental work and data analysis required for achieving meaningful results.

Funding

This research was supported by the 2022–2023 Fellowship of the Coalition for Disaster Resilient Infrastructure (CDRI), Application ID: #210927708

1. Introduction

Urban infrastructure is an important public resource and an essential component for urban development. It is composed of multiple types of functional infrastructure such as transportation, drainage, and sewerage infrastructure. These pieces of functional infrastructure should generate certain capacities to provide various functions to promote urban development economically, socially, and environmentally. Urban infrastructure becomes critical when its unavailability severely impacts the well-being, health, safety, and economy of the region. Although these pieces of infrastructure are becoming increasingly complex and interdependent, transportation infrastructure is still the key. Transportation bridges are the weakest element among all the components of the transportation infrastructure system.

[Gordon, Richardson, Davis, 1998] estimated that nearly one-quarter of business interruption losses could be attributed to the failure of highway bridges after the 1994 Northridge (Los Angeles) earthquake. Conventional risk-based strategies have been implemented to guide protection and prevention options that seek to mitigate or neutralize the likelihood of anticipated disruptive events and the potential adverse impact from the events. However, recent experience with natural and man-made water-related disasters indicates that the current transportation systems cannot protect and prevent all disruptive events. Moreover, these may perform unreliably because of the high uncertainty of disturbances, complex interdependence of infrastructure systems, and stochastic failures resulting from unpredictable events. Owing to frequent disasters, the U.S. initiated the Critical Infrastructure Protection (CIP) program. However, the focus is gradually shifting from CIP to critical infrastructure resilience (CIR) because CIP does not address all the aspects of securing the nation's critical infrastructure [Das, 2020].

The term resilience implies "bouncing back" from a disruption. It has been defined in various disciplines according to their objectives. The concept of resilience was first introduced in modern science by [Holling, 1973] to describe the capability of an ecological system to endure damage under stress and regain a stable state. This concept was subsequently introduced into other fields such as management and engineering, with resilience definition assessment methodologies differing between fields. Most of these definitions combine several aspects represented by the concepts of "risk management, vulnerability, reliability, robustness, flexibility, and survivability." For example, in infrastructure engineering, a resilient element such as a road can absorb an abrupt disturbance and recover its normal traffic flow capacity within a reasonable timeframe.

Although most individuals can conveniently comprehend an intuitive and qualitative meaning of the concept of resilience, it has been demonstrated to be one of the most difficult to define qualitatively and quantitatively. Therefore, resilience measures or strategies have not been applied widely.

1.1 Definition of Resilience in the transportation field:

Research has been performed on resilience in the field of transportation engineering, and a few definitions have been proposed. A few definitions are listed below:

- Resilience is the capability of the system to maintain its demonstrated level of service or to restore itself to that level of service in a specified time frame [Heaslip, 2010]
- Resilience is the characteristic that enables the system to compensate for losses and function even when infrastructure is damaged or destroyed [Battelle, 2007]
- Resilience is a characteristic that indicates the system performance under unusual conditions, the recovery speed, and the amount of external assistance required for restoration to its original functional state [Murray-tuite, 2006]
- Resilience is the capability of a system to accommodate variable and unforeseen conditions without catastrophic failure. [VTPI, 2010]
- Transportation resiliency is defined as “a system’s capability to function before, during, and after major disruptions through reliance upon multiple mobility options” [Amdal Swigart, 2010]

1.2 Resilience assessment level in transportation network

The resilience of each bridge can be measured because a bridge consists of several components (girders, pillars, joints, etc.). In general, structural analysis and seismic effects are the key aspects of interest here. However, in this study, structural properties are considered implicitly while the interdependency of bridges is analyzed. The failure of a bridge may not significantly influence the network-level performance. The bridge is likely to have users. However, the disruption of another bridge may produce a substantial hindrance. For example, a collapsed bridge has many users, and the users have no alternatives to reach their destination. Therefore, it is necessary to evaluate the interdependency and importance of each network section. Certain destinations can be reached via multiple routes, whereas others have only one route. Therefore, this study assesses the resilience through a network-level analysis.

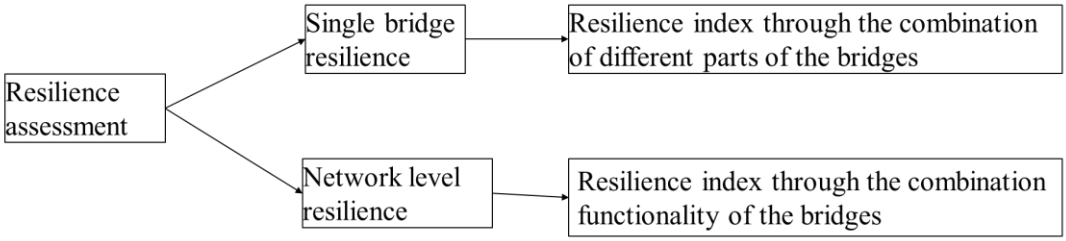

Figure 63. Level of network assessment

For the past few decades, resilience has been widely used as a performance indicator for various civil infrastructure systems including acute-care hospitals, water supply systems, power transmission systems, and transportation systems. In the majority of cases, individual hazards (i.e., earthquake, hurricane, and tornado) are considered to be the prime source of disaster. Multi-hazard events were also accounted for in estimating resilience in a few of the studies that considered seismic events in the presence of corrosion degradation of flood-induced scour at bridge foundations as multi-hazard load cases. This study considers structural properties explicitly to evaluate the health index of bridges. Subsequently, the resiliency of the transportation bridge network is computed.

2. Aim, Objectives, and Scope of the Research Study

This section describes the aim, objectives, and scope of the research study.

2.1 Novelty in this study:

Although several researchers have proposed resilience indices for transportation networks, our approach adds novelty to the knowledge domain for the following reasons:

- Our transportation network does not limited to the two extreme cases of bridge damage (working and not working). The proposed model incorporates the intermediary situations in which the maximum speed of bridges is reduced.
- Our study integrated post-disaster damage with pre-disaster interventions. In addition, the post-disaster damage was presented by reducing the maximum permissible speed. Thus, the structural and transportation properties were integrated.
- The trip properties were computed using human-cantered data (AGOOP). Here, we demonstrated a method to develop an OD table from a large database.

- This study computed the post-disaster trip properties using a traffic simulation technique. Therefore, post-disaster congestion and route options originate from network and human attributes.

2.2 Research Aim and Objective

Structural engineers analyze the performance of a bridge by modelling the different components of bridges (pillar, girder, material, and etc.). Meanwhile, traffic engineers focus on 1) the traffic performance by considering a bridge as a component of the entire transportation network and 2) the travel time, congestion, and alternative routes or transport modes. If a critical bridge collapses, the transport network may be split into two separate networks. Meanwhile, traffic users may not be affected if a non-critical bridge collapses. Therefore, it is necessary to integrate the structural properties and traffic characteristics for decision making. The research questions were formulated as follows:

- How can the structural properties and traffic characteristics be integrated for bridge network resilience?
- How can a network's performance be measured in pre-disaster and post-disaster cases?
- How can the resilience of a transport bridge network be quantified?

To answer the above-mentioned research questions, we formulated the following specific objectives:

1. Analyze the current condition of each bridge through physical property analysis. Then, predict the future damage of those bridges by integrating earthquake hazards.
2. Compute the usage rate of each link by analyzing the pre-disaster trip pattern. We propose a model to integrate the pre-disaster and post-disaster route selection patterns.
3. Finally, we evaluate the effect of the recovery pattern of bridges. The objective of this research is to demonstrate a method to quantify resilience and quantitatively discuss the properties determining the resilience of transportation networks.

The concept of resilience is essential for decision-making regarding investment in the transportation network. There is no holistic approach for integrating robustness,

redundancy, resourcefulness, and rapidity in the framework of the resilience of transportation networks. Along this line, the current study aimed to address key missing links in the evaluation and prediction of the resilience and functionality of individual bridges and bridge systems.

In this study, we combined both factors in a single framework by utilizing structural assessment for each bridge and the operational performance for transportation networks. The concepts presented were applied to a real transportation network in Yamaguchi, Japan, to illustrate the mathematical procedures. Such methods can help decision makers analyze the relative improvements in resilience because of the proposed project alternatives.

2.3 Scope

The research project aims to investigate and analyze the resilience of bridge transport network. The primary focus is to understand and evaluate the ability of bridge transport networks to withstand disruptions, adapt to changing conditions, and quickly recover from adverse events.

The scope of the project encompasses several key aspects:

- Network analysis: The project will involve studying the characteristics of bridge transport networks, including the layout, connectivity, and interdependencies of bridges, roads, and other transportation infrastructure. This analysis will provide insights into the vulnerabilities and strengths of the network.
- Damage Assessment: The project will conduct a comprehensive assessment of potential risks and threats that can impact bridge transport network resilience. This may include natural disasters (such as earthquakes, floods, or hurricanes), accidents, infrastructure failures, or deliberate attacks. This project explains the damage assessment of each bridge for earthquake with two return periods.
- Resilience Metrics and Indicators: The research will establish appropriate metrics and indicators to measure the resilience of bridge transport networks. These include 4R factors such as robustness, redundancy, resourcefulness, and recovery. Developing suitable quantitative and qualitative measures will enable the assessment of network resilience levels.
- Modelling and Simulation: The project will utilize traffic simulation tool (SUMO) for analyzing traffic characteristics. These simulations will help identify critical vulnerabilities, assess system performance, and evaluate the effectiveness of

resilience strategies and interventions.

- Resilience Enhancement Strategies: Based on the findings from the analysis and simulations, the project will propose and evaluate strategies to enhance the resilience of bridge transport networks. These strategies may include infrastructure upgrades, maintenance practices, emergency response plans, alternative routes, communication systems, and other proactive measures.
- Case Studies and Real-world Applications: The project will include case studies of specific bridge transport networks to validate the research findings and assess the practical implementation of resilience measures. Here, Yamaguchi city, Japan has been selected.

By comprehensively exploring these aspects, the research project aims to contribute to the understanding of bridge transport network resilience and provide valuable insights to policymakers, transportation authorities, and infrastructure planners. Ultimately, the project aims to improve the overall resilience and sustainability of bridge transport networks, ensuring their functionality and adaptability in the face of future challenges.

3.Methodology and results

Disruption caused by disasters initially reduces the performance of transportation networks. In the absence of external support for recovery, the user distribution onto functional routes and networks eventually attains a new equilibrium. At this point, the network maintains a new performance level depending on the magnitude of disasters and robustness of the network. With the availability of external support, the recovery processes begin at a speed dependent on the flow rate of resources external to the system. The extent of degradation of network performance caused by disasters and the speed of recovery are important in measuring resilience.

3.1 Research conceptual framework

The research methodology is based on the concept of resilience shown in Figure 64. It is based on the assumption that networks have characteristic degradation and response profiles. Here, we propose a method based on the concept of 4R (robustness, redundancy, rapidity, and resourcefulness).

- **Robustness**:

When the network functions under normal or standard conditions without being affected by any disruption, the system operates with the maximum efficiency. Robustness

measures the functionality that remains active after a disaster.

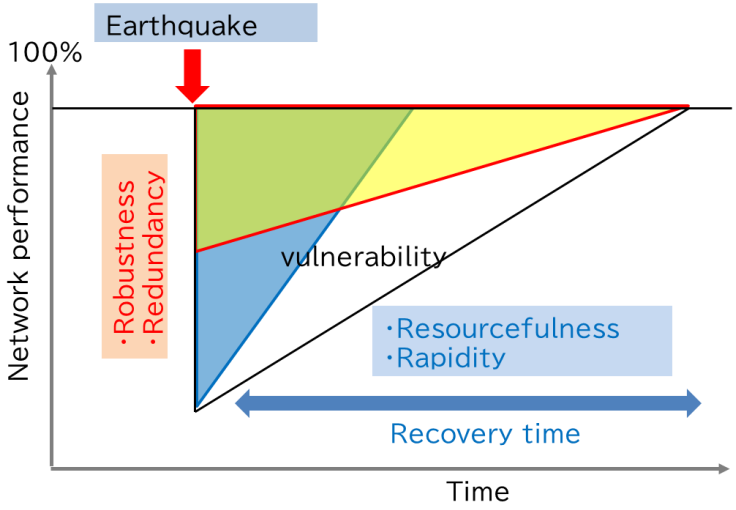

Figure 64. Typical resilience triangle used in this study.

- **Redundancy**:

Cimellaro, Reinhorn, Bruneau, (2010) stated that redundancy represents the capability to use alternative resources to maintain the functionality when major resources become insufficient or absent. In this study, we considered the network spare capacity and network route diversity as the measures of redundancy. It measures the connectivity of all the origins and destinations after a disaster. It computes the percentage of trips that could not be completed owing to the removal of a bridge.

Consider a one-link one-way freeway segment that connects origin A to destination B. This link can satisfy the hourly traffic demand. Because there is only one link between the OD pair, the entire traffic should pass through this link to reach the destinations. If the link is closed owing to an incident, the user cannot reach their destination until it reopens because there is no alternative route. Although a network may satisfy the pre-disaster traffic demand, it may fail to satisfy the post-disaster traffic demand.

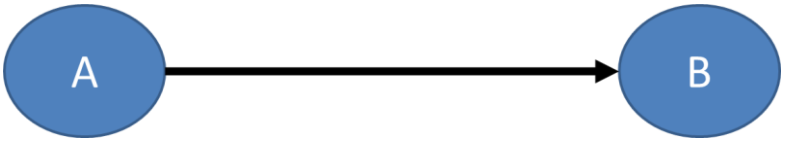

Figure 65. Simple one-road link network.

Considering the static demand, the travel time of a link defined by the Bureau of Public Road (BPR) function is given as follows:

$$t_a(x_a) = t_a(0)\left(1 + 0.15\left(\frac{x_a}{c_a}\right)^4\right) \quad (1)$$

where x_a, $t_a(0)$, and c_a are the flow, free-flow travel time, and capacity of the link, respectively. Here, the congestion and traffic signal effects are not considered explicitly. In this study, we utilized a traffic simulator to estimate the travel time on each link.

Rapidity and resourcefulness:

These are combined in one frame because these are interrelated. It is apparent that a higher resourcefulness results in a higher rapidity. Resourcefulness includes manpower, finance, materials, and equipment. Figure 66 illustrates the relationship between resourcefulness and rapidity. This relationship exists when resources are utilized optimally. In this study, the rapidity and resourcefulness were represented through scenario generation.

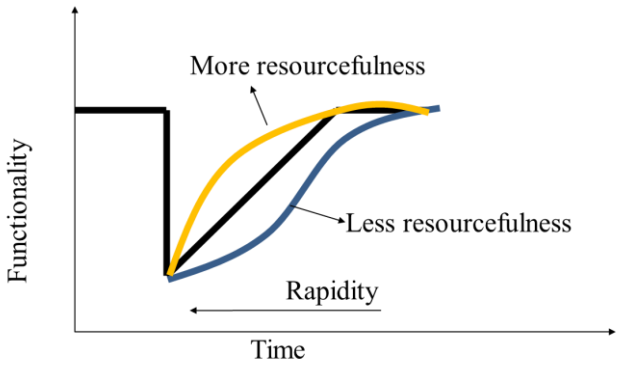

Figure 66. Interrelationship between rapidity and resourcefulness.

3.2 Case study region

Yamaguchi was selected for the case study. It has many bridges, and individuals rely on cars for their daily activities. In addition, a large area in this city is barren because it is mountainous. Certain crucial bridge-related data such as the construction year and design load in the city are available. This city was selected because it has many bridges that need to be retrofitted to prevent catastrophes.

3.3 Trip distribution computation from AGOOP data

In this section, the computation steps for the AGOOP data are explained. We obtained mobile phone location data from AGOOP Corporation in Japan. AGOOP was established in April 2009 and is owned by SoftBank Corp., a major mobile phone service company. These location data include worldwide position information logs obtained using GPS.

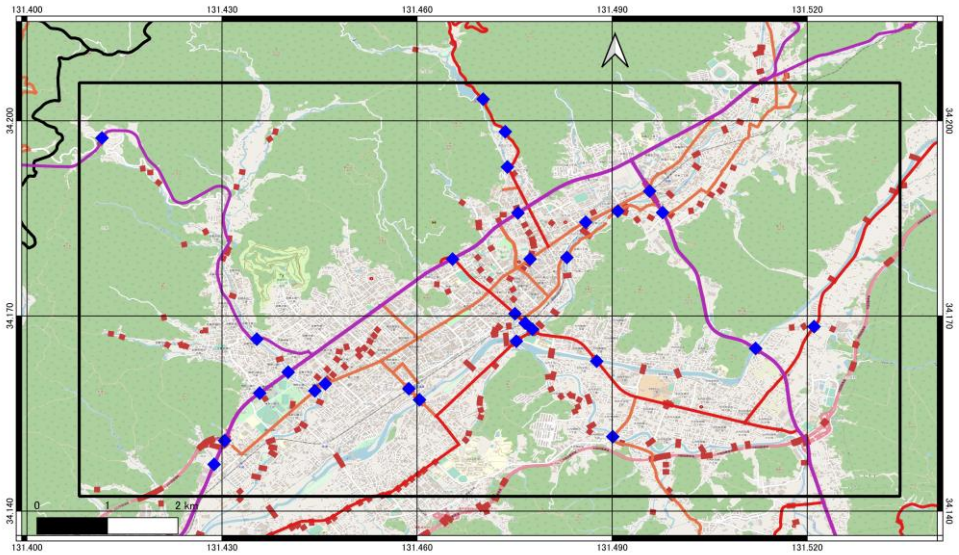

Figure 67. Blue colour represents the bridges that are considered in this study. The red colour links represent the bridges that are not considered in this study.

The GPS location information was acquired after obtaining written access-permissions from the users. In this study, we used the location data for Yamaguchi city, which contains many transportation bridges. AGOOP data contain a time stamp and spatial location stamp in addition to an attached id. Because the attached ID is generated by a computer, a researcher cannot identify the individual. Moreover, the ID varies each day. Therefore, it is infeasible to track an individual for more than a day. The recent AGOOP database contains sex and age information with missing data. The missing values in AGOOP data should be replaced.

3.3.1 Creation of OD

To simplify the model, we omitted smaller roads. In particular, we utilized trunk roads, primary roads, and secondary roads. The definition of these road types is available in OSM_wiki (2023). The results for this network are shown in Figure 68. The levels (i.e., T1, T2, etc.) in the figure represent the points where the trip was generated or ended. It also shows the locations of the selected 27 bridges. The blue dot represents the bridges where the traffic survey was conducted, and the red one represents those where it was not conducted.

Figure 69 shows the steps for assigning AGOOP data points to the selected network. The process has to be performed for each individual. Although the application of an activity-based model could be more realistic for generating an OD table, we proposed the concept of furthest distance trip. The furthest distance trip was computed based on the first location of the individual. In addition, we required a trip generator function from 250 m-mesh population density. It was assumed that 10% of individuals would undertake trips each day. A more detailed analysis of the OD table development is recommended.

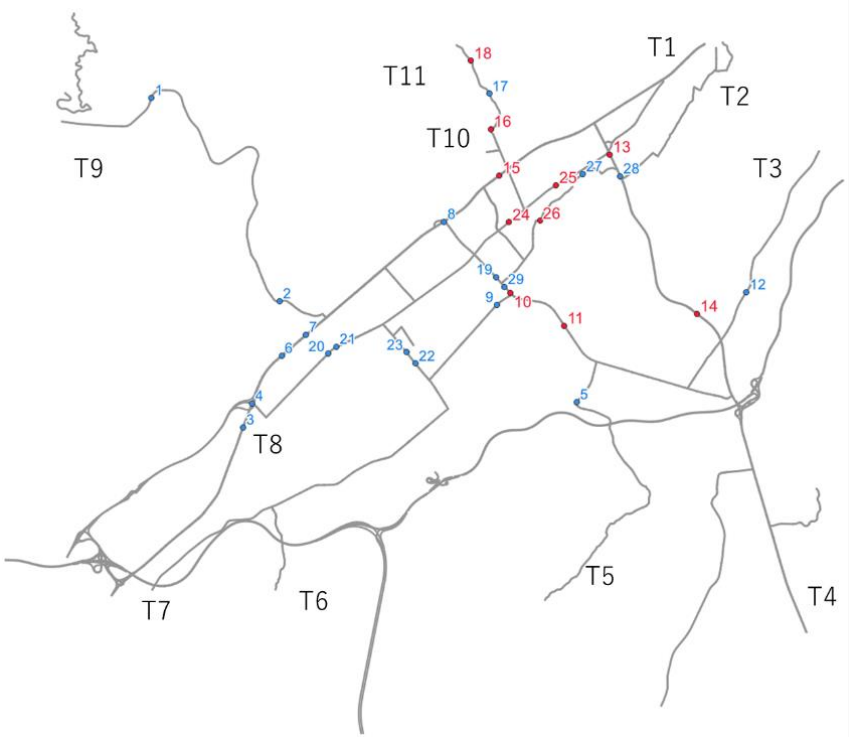

Figure 68. Traffic analysis zone (TAZ) for converting AGOOP data to trip data.

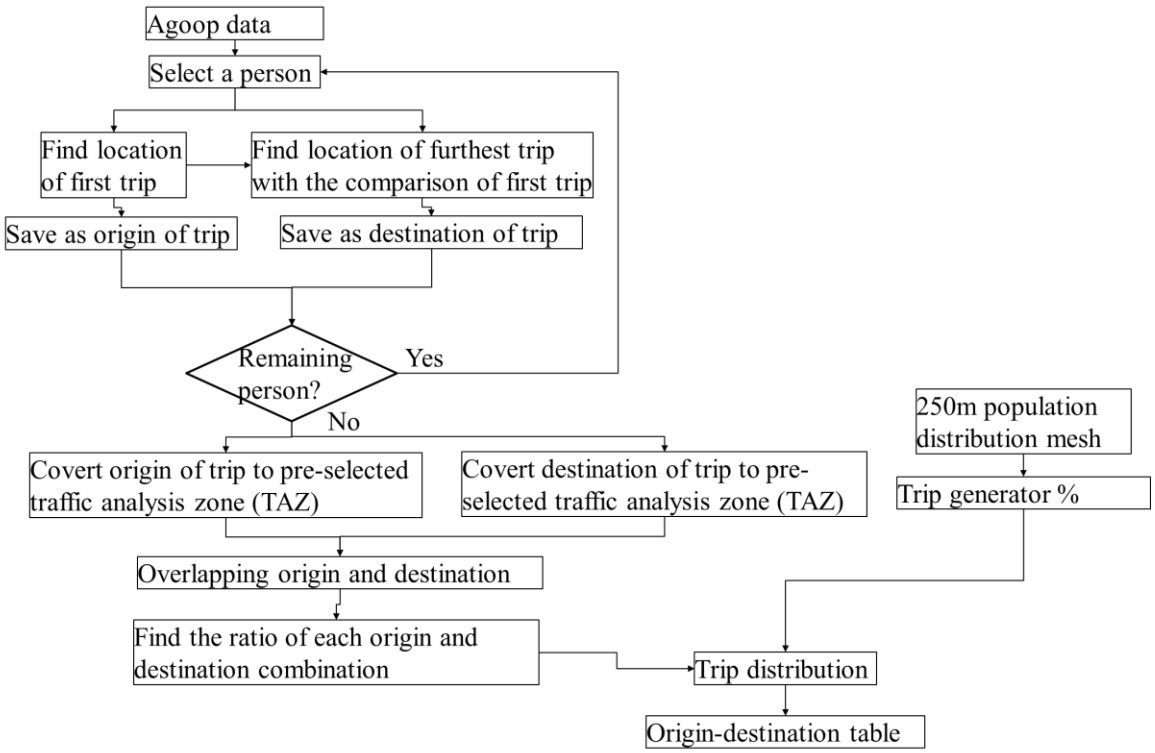

Figure 69. Creation of OD from AGOOP data.

We compared the AGOOP-originated data and our survey data as we counted the traffic in several locations. After a manual adjustment, we finalized the OD table. The final ratios are presented in Table 23

Table 23. Final trip table (percentage)

èDestination

ORIGIN	T1	T2	T3	T4	T5	T6	T7	T8	T9	T10
T1	0	1	1	16	2	2	2	4	1	1
T2	1	0	0	1	0.5	0.5	0.5	0.5	0.5	0.5
T3	0.5	0.1	0	0.5	0.3	0.1	0	0.2	0.1	0.2
T4	15.4	2.5	0.2	0	1.4	0.2	1.2	7.5	0.3	1.3
T5	3	0.1	0.1	1	0	0.1	0.1	0.1	0.1	0.4
T6	1	0.2	0.2	1	0.2	0	0.1	0.2	0	0.1
T7	1	0.1	0.2	2	0.2	0	0	0.5	0	0
T8	8.2	0.9	0.2	5	0.2	0.1	0.1	0	0	0.3
T9	0.5	0.1	0.1	0.9	0.2	0	0	0	0	0.2
T10	0.5	0	0	1.5	0	0	0	2	0	0
A very small fraction of trips goes to T11, which is not presented here.										

3.4 Structural analysis

The structural damages to our target 27 bridges were to be estimated. Two earthquake scenarios were employed considering different return periods (475 and 2,475 years). Then, the damage level of bridges owing to earthquake was evaluated. In this section, our methodology and the obtained results regarding seismic and structural analysis are described.

3.4.1 Earthquake Scenarios

The seismic intensity is employed to evaluate the damage level of bridges. Therefore, it was necessary to collect a seismic intensity map of our target area. Japan Seismic Hazard Information Station (J-SHIS) provides a map on their website as open-source data. In this research, two return periods were assumed:

475 years (10% probability of exceedance in 50 years) and
2,475 years (2% probability of exceedance in 50 years).

The seismic maps are shown in the figures below. The seismic intensity with a return period of 475 years has a maximum value of 5.9 and minimum value of 4.8. Meanwhile, the seismic intensity with a return period of 2,475 years has a maximum value of 6.4 and minimum value of 5.3. Because the seismic intensity is determined based on the condition of the surface layer of the ground, mountainous regions tend to obtain lower values of seismic intensity than urban areas.

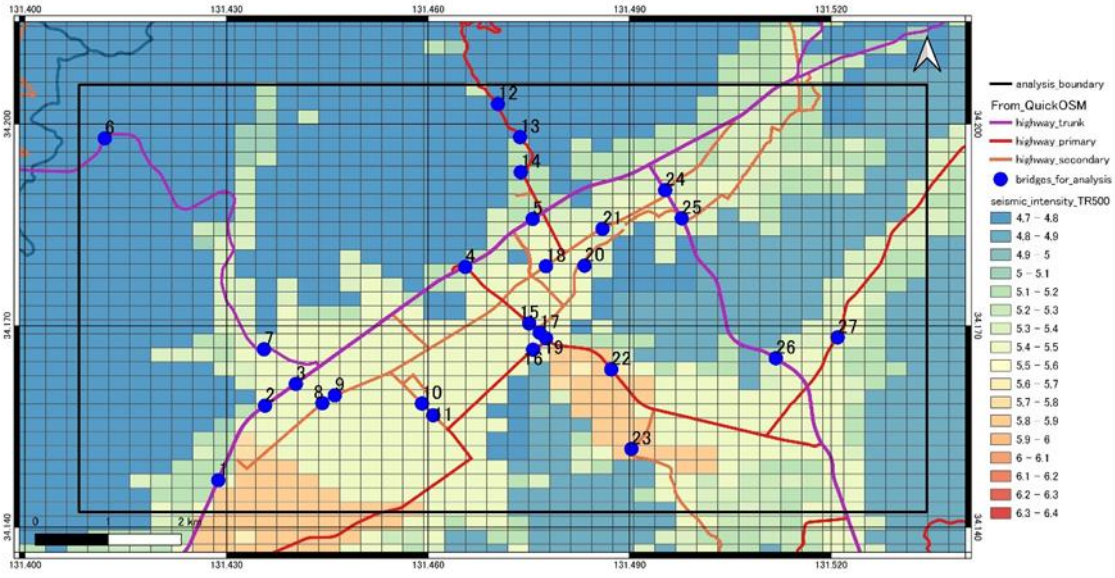

Figure 70. Seismic intensity map (return period of 475 years)

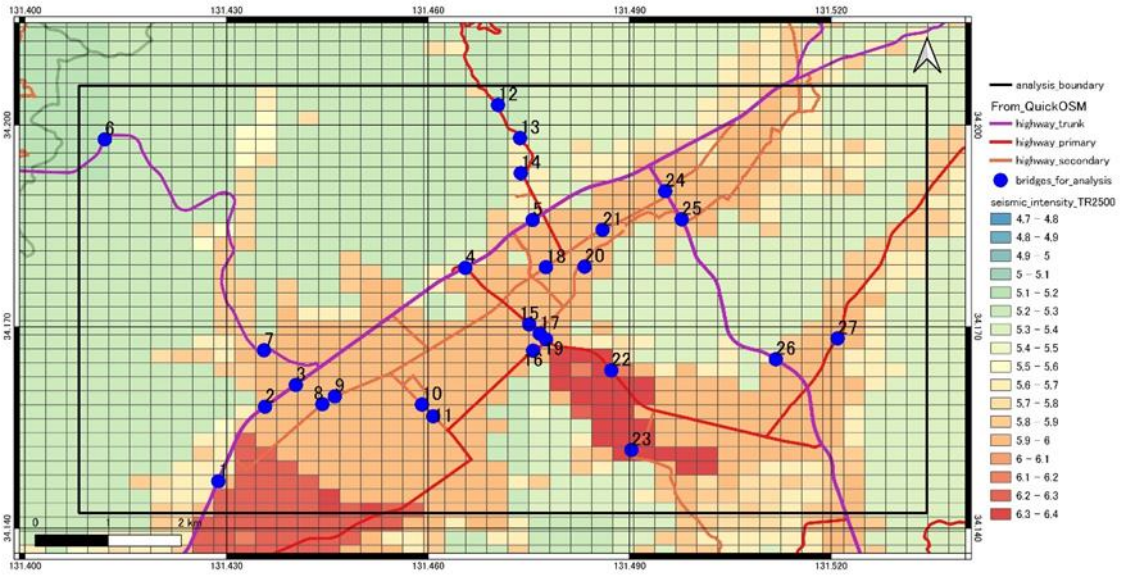

Figure 71. Seismic intensity map (return period of 2,475 years) (note that a lower return period is practical)

In general, earthquakes with return periods of 100 years (Level1 earthquakes) and 475 years (Level2 earthquake) are considered in the Japanese design standard for road bridges. Although seismic intensity maps with return periods of 2,475 years are illustrated above as an example, such large return periods are not commonly considered in Japan.

3.4.2 Structural damage evaluation

The damage level of bridges owing to earthquakes can be estimated using the flowchart proposed by [Kobayashi Unjoh, 2005]. According to that study, the condition of bridges can be categorized into three: damage levels A, B, and C.

Table 24. Definition of damage levels of bridges

Damage Category	Conditions
Damage Level 'A': Large Damage	The bridge has a severe damage that causes the deterioration of the loading capacity. Fatal damage such as superstructure collapse is likely.
Damage Level 'B': Middle Damage	The bridge has a damage that causes the deterioration of the loading capacity. However, it can be in service if the damage does not deteriorate further owing to aftershocks or live load.
Damage Level 'C': Small Damage	The bridge does not have a damage that can cause the deterioration of the loading capacity in a short time.

These parameters need to be collected to evaluate the bridge damage using the flowchart of [Kobayashi Unjoh, 2005]. Certain parameters are available as open-source databases,

whereas the remaining parameters are obtained by visual verification or on-site measurement.

Table 25. Information necessary for structural damage evaluation

Parameters	Information Source
Seismic intensity, SI value	Japan Seismic Hazard Information Station (J-SHIS)
Number of Spans	Maintenance database for road and facilities (MLIT)
Applied Design Standard	
Bridge Type	
Superstructure Type	
Shear Span Ratio	
Reduction of Main Re-bar	
Type of Bearing Support	
Length from Girder Edge to Front Surface of Abutment, Girder Fall Prevention	
Device for Preventing Girder Movement	

The figure below shows the flowchart of [Kobayashi Unjoh, 2005]. The following tendencies should be considered while examining the damage level of a bridge.

- A large seismic intensity causes severe damage on structures.
- Old bridges that are not reinforced against earthquakes tend to sustain severe damage.
- Structural features that strengthen a bridge against earthquakes, such as rubber bearings, reduce the damage level of the bridge.

Certain bridges, e.g., bridges 5 and 18, have particularly weak features against earthquakes. The embankment of bridge 5 has collapsed, and bridge 18 has a bent steel pier. The flowchart does not describe the approach for handling these types of structures. Therefore, we performed an assessment to determine the damage level from the perspective of the bridge engineer. The damage level of bridges 5 and 18 were classified as “A” without using the flowchart.

3.4.3 Analysis Results

The two figures below show the results of the evaluation of the damage level of 27 bridges. The result for a return period of 475 has 2 bridges with damage level “A,” 17 bridges with damage level “B,” and 8 bridges with damage level “C.” Meanwhile, the result for a return period of 2,475 years has 6 bridges with damage level “A,” 14 bridges with damage level “B,” and 7 bridges with damage level “C.” It was verified that a large seismic

intensity increases the number of severely damaged bridges.

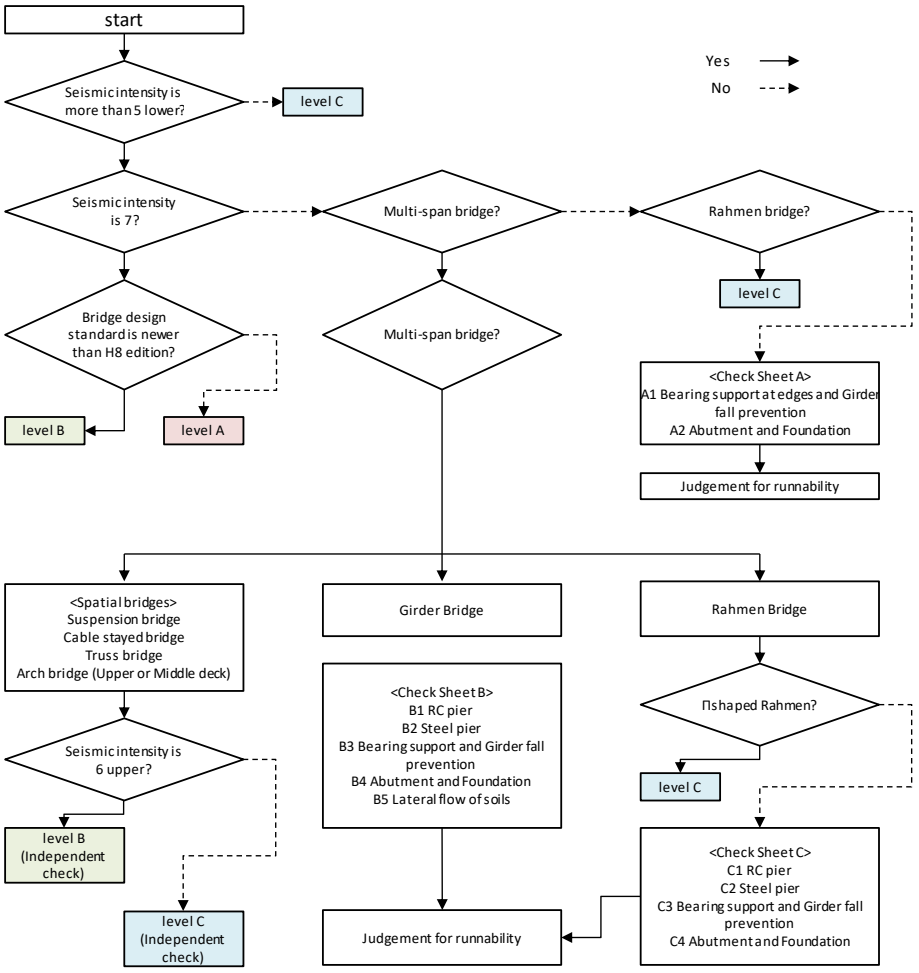

Figure 72. Flowchart proposed by [Kobayashi Unjoh, 2005]

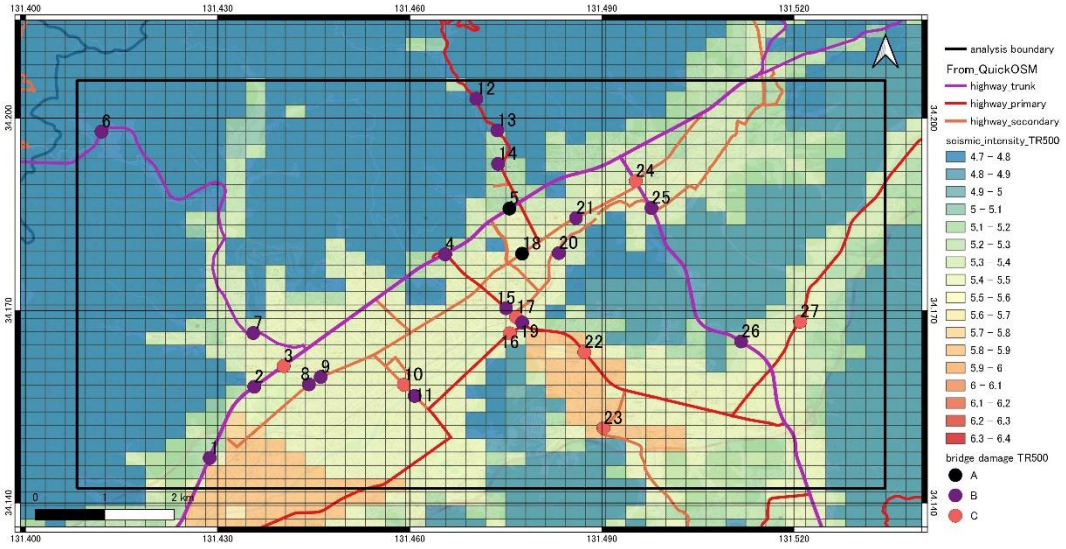

Figure 73. Damage level (return period of 475 years)

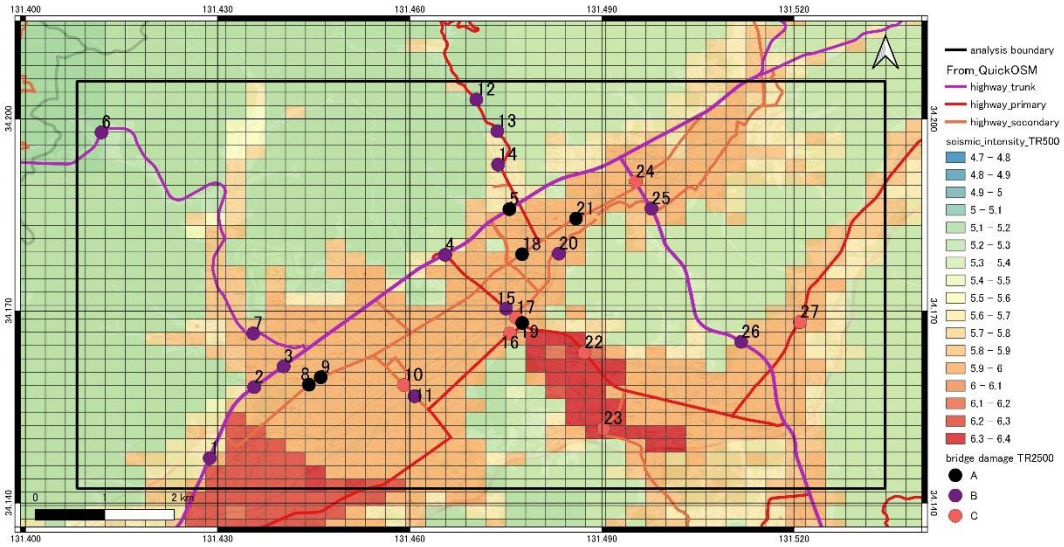

Figure 74. Damage level (return period of 2,475 years)

Table 26 presents the results of the structural analysis. Here, three damage levels are considered: A, B, and C.

Table 26. Bridge damage level and length of each bridge

Bridge ID	Bridge Damage	Bridge ID	Bridge Damage	Bridge ID	Bridge Damage
1	B	10	C	19	B
2	**B**	**11**	**B**	**20**	**B**
3	C	12	B	21	B
4	**B**	**13**	**B**	**22**	**C**
5	A	14	B	23	C
6	**B**	**15**	**B**	**24**	**C**
7	B	16	C	25	B
8	**B**	**17**	**C**	**26**	**B**
9	B	18	A	27	C

3.5 Transportation analysis

This section explains the simulation.

3.5.1 Flowchart

We employed Figure 75 to compute the resilience triangle. Based on the scenario, we generated a set of bridges that need to be repaired. We then selected the bridge with the largest number of users, thus reducing the traveller's cost. Then, the resources required to

perform maintenance work were deducted from the available resources. Subsequently, the bridge with the second highest travel cost was selected. Again, the resources required were deducted. When no resources were available, the selected bridges were updated. We computed the number of days required to repair each bridge based on its damage level and floor area. Therefore, the required days for each bridge varied. We planned to observe the transportation network improvements every day. We tracked the outcomes of the simulation every five days the transportation simulation requires a longer time to complete.

3.5.2 Road type properties

During the traffic simulation, we selected three road types: trunk road, primary road, and secondary road. This definition is available in OSM Wiki. Trunk roads are defined as the most important roads in a country's system. These roads need not necessarily be divided highways. Primary roads are the next most important roads in a country's system that are not motorways. These generally link larger towns. Secondary roads are the next most important roads in a country's system. These generally link larger towns. The maximum permitted speed of each road differs, as shown in Table 27. The speed limit was examined randomly from Google Maps. However, each vehicle agent can run at 100 km/h in the absence of a road speed limit. In the simulation, each vehicle conformed to the speed limit of each road. The speed limit of each bridge after an earthquake was reduced according to its damage level. In this study, three damage levels were examined.

Table 27. Speed range of each route type

Route type definition	Pre-disaster speed km/h (typical Japanese road speed)
Trunk road	50
Primary	40
Secondary	30

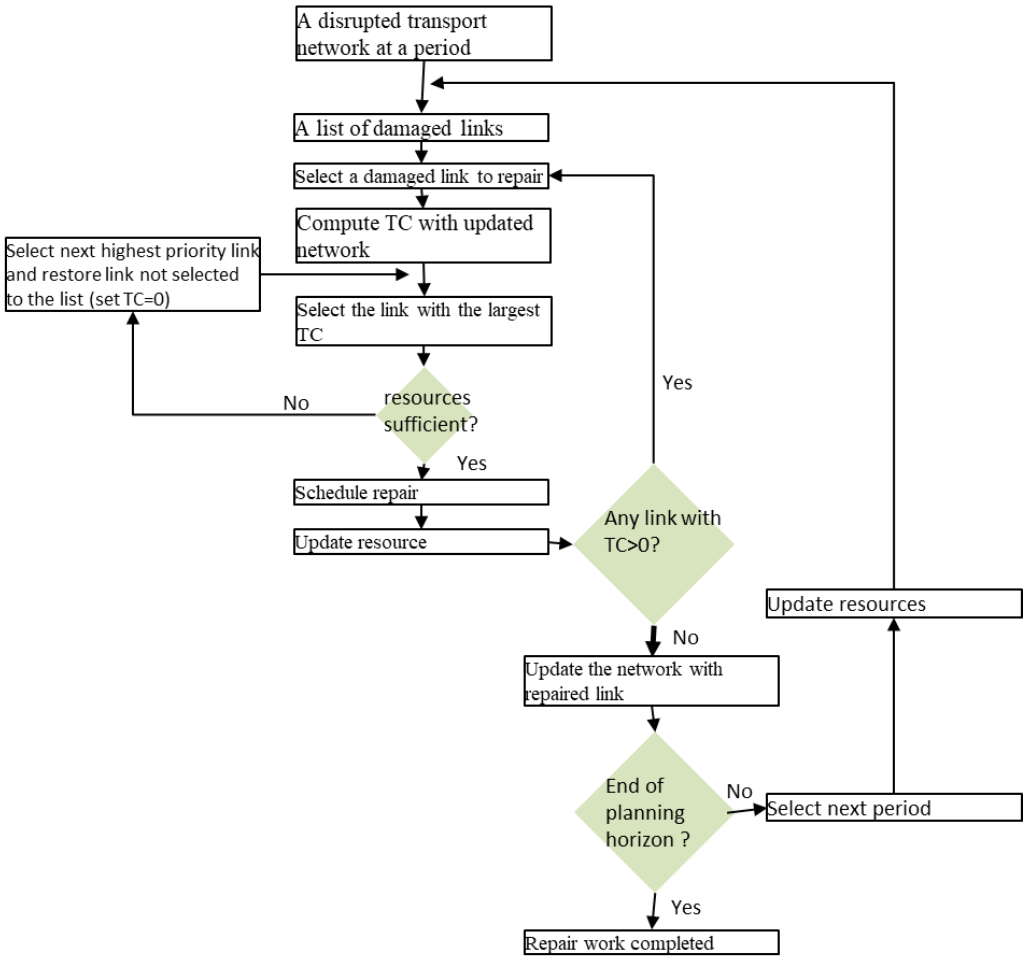

Figure 75. Post-disaster simulation strategy.

3.5.3 Scenario setting

The simulation was dynamic. That is, the network was updated after a bridge was restored. Subsequently, a traffic simulation was conducted with the updated network. The number of users was calculated based on the updated network. However, the OD table remained unaltered. The OD distribution generally varies after a disaster. There are several reasons for these variations. Because one of our research objectives was to observe the timing of recovery, we omitted the trips undertaken immediately after the disasters. In the recovery stage, the restoration strategy is crucial to minimize the effect of the hazard. Here, three restoration strategies were analyzed. Table 28 summarizes the scenario.

Table 28. Description of Scenario

Scenario 1:	*Scenario 2*	*Scenario 3*
Before disaster: Most users first	Combination of Route type and most users	Combination of damage level and most users

The strategies are explained below:

- Scenario 1 (Road-user priority scenario): This is the simplest strategy. Here, the number of pre-disaster road users is the basis.
- Scenario 2 (Road-type priority scenario): The road-type priority is the basis of this scenario. In general, each country has a unique definition of road type. In this study, we utilized the classification of road types defined by an open street map. Herein, the bridges on the trunk road are restored first. It is possible to have more than one bridge on the trunk road and budget constraints. Therefore, a strategy for selecting bridges on the trunk road is required. Here, we propose a sub-ranking of bridges based on the number of users on the trunk road. After restoring all the bridges on the trunk road, the primary road would be selected. Similarly, the number of users on the primary road is the secondary condition. After completing the restoration of all the primary roads, the affected bridges on the secondary roads are selected. As performed earlier, the bridges with more users would be selected first. To summarize, scenario 2 can be written as follows:
    - Trunk road + most users
    - Primary road + most users
    - Secondary road + most users
- Scenario 3 (Damage-type priority strategy): The damage-type priority is the basis here. In this study, we defined three damage types: damage A (super critical), damage B (critical), and damage C (sub-critical). Therefore, bridges with damage A are restored first. Considering the likelihood of having more than one bridge with damage level A and budget constraints, a strategy for selecting bridges with this damage level is required. Here, we propose a sub-ranking of bridges based on the number of users. After restoring all the bridges with damage level A, those with damage level B are selected. Similarly, the number of users is the secondary condition. Finally, the affected bridges with damage level C are selected. As performed earlier, the bridges with more users would be selected first. To summarize, scenario 3 can be written as follows:

- Damage level A + most users
- Damage level B + most users
- Damage level C + most users

After performing a pre-disaster traffic simulation, the number of bridge users was computed. Therefore, we computed the sequence of bridges with most users. The sequences of the bridges in each scenario are presented in Table 29.

Table 29. The sequence of bridge repair in each scenario

Sequence	Scenario 1: bridge id	Scenario 2: bridge id		Scenario 3: bridge id	
1	_23	_26	Trunk road	_18	Damage A
2	_15	_24		_5	
3	_17	_25		_15	Damage B
4	_19	_3		_19	
5	_22	_1		_26	
6	_26	_2		_21	
7	_18	_5		_25	
8	_21	_4		_1	
9	_24	_7		_2	
10	_25	_6		_4	
11	_1	_23	Primary road	_14	
12	_2	_15		_7	
13	_3	_17		_6	
14	_16	_19		_12	
15	_5	_22		_13	
16	_4	_16		_11	
17	_14	_14		_8	
18	_7	_27		_9	
19	_6	_12		_20	
20	_27	_13		_23	Damage C
21	_12	_21	Secondary Road	_17	
22	_13	_18		_22	
23	_10	_10		_24	
24	_11	_11		_3	

25	_20	_8		_16	
26	_8	_9		_27	
27	_9	_20		_10	

Here, the settings of manpower and rehabilitation resource are described.

- It is quite difficult to determine how much manpower is available immediately after a disaster around our target area. We made some assumption for implementing our simulation in this study. It was assumed that one group is composed of 10 workers and 1[group/day] denotes one group conducts a rehabilitation work of bridges for a day. 50groups are set as the maximum resources available per day. For instance, 1,630groups are required to fully restore all the damaged bridges after the earthquake with return period of 475years. In this situation, it takes about 33days (=1,630/50) for completion of rehabilitation.
- Also, it is difficult to individually settle the necessary manpower resource for rehabilitation of bridges. Although rehabilitation resource for each bridge should be changed considering its structural features, some assumptions are made for simplifying the problem in this study. The necessary rehabilitation resources are given dependent on the damage level: namely, 60[group/day] for damage level 'A' per 300m^2 of bridge surface, 30[group/day] for damage level 'B' per 300m^2 of bridge surface and 10[group/day] for damage level 'C' per 300m^2 of bridge surface. The required resource for recovery increases when a bridge has larger bridge surface and more serious damage, and vice versa.

3.5.4 Post-disaster impact presentation

Researchers are debating on the means to present the post-disaster effect on transportation networks. A few of them assume a zero-one game. In this case, researchers analyze whether the subject bridge has collapsed or is functioning effectively. This type of analysis is more suitable for man-made disasters such as terrorist attacks, where terrorists plan to have a larger impact on the network. Many researchers adopt a similar assumption for natural disasters as well, such as earthquakes that may destroy a bridge completely. For example, the Kumamoto (Japan) earthquake in 2016 destroyed the Aso Bridge. These incidents have received significant media attention. In this study, we focused on an eminent problem after a disaster wherein bridges are not destroyed completely and are not fully functional. Here, the capacity is neither zero nor one. Rather,

the post-disaster capacity attains a value between zero and one. The values are listed in Table 30. Here, we assume that damage level A causes the bridge to function at 20% of the pre-disaster speed. Similarly, damage level C causes it to function at 70% of the pre-disaster speed.

We conducted semi-structured interviews with structural engineers to understand the effect of earthquakes on bridges. We observed that an earthquake may cause a dramatic reduction in weight carrying capacity. Therefore, certain bridges may not carry heavy trucks. For example, 40-ton trucks may be rerouted owing to the weight limit on a bridge. Because our focus was on passenger trucks, we did not include this phenomenon in this study.

Table 30. Post-disaster speed based on road type and disaster type.

Damage level	Post-disaster speed
A	$0.2 \times predisaster\ speed$
B	$0.5 \times predisaster\ speed$
C	$0.7 \times predisaster\ speed$

3.5.5 Individuals' route selection behaviour

Now, we present individuals' behaviour in the form of a traffic assignment principal. In a pre-disaster situation, individuals attempt several routes to reach their destination. Because the congestion levels and travelled distances in routes differ, the perceived utilities also differ. Depending on their utility, a transportation network gains an equilibrium state. To analyze the equilibrium state, we performed multiple iterations for the dynamic user assignment mode. The behaviour of individuals after a disaster is crucial. It is likely that an individual would continue using the best route that was decided upon in the pre-disaster situation. We named this pattern 1, as presented in Table 31. In case pattern 2, individuals attempt to evaluate the available route options if an alternative exists. In this study, we utilized pattern 2 to represent the route selection behaviour. After a bridge is restored, the congestion level in the network would also be updated. Individuals would modify their route to obtain a higher utility. Individuals are prepared to select a route based on their experience. Therefore, we iterated the simulation 10 times to represent the selected route. This state is known as the equilibrium state.

Table 31. Route selection behaviour

	Pattern_1	Pattern_2
Pre-disaster	Equilibrium state	Equilibrium state
Post disaster	Route identical to the pre-disaster one	Route varies if alternative exists

3.5.6 Simulation software

In this study, we utilized the open-source traffic simulator "Simulation of Urban MObility" (SUMO). The version was SUMO 1.17.0. The environment was of Windows 64 bit. SUMO has a tool named "TRAffic Control Interface" (TraCI). It helps a researcher achieve real-time control of an agent. PYTHON programming language was used to integrate TraCI and other SUMO tools such as "Dynamic User Assignment" (DUA).

3.5.7 Result

This section explains the results of the traffic simulation. The average speeds of relevant users are presented below. First, we listed the bridges that were restored for each five-days. Relevant users (n) are those who utilized the restored bridges. The base case represents the scenario immediately after a disaster. Therefore, the number of relevant users is equal for the base case and each scenario corresponding to the target date. Let the number of relevant users for five days for the base case be x_{1b5} and that for five days in scenario 1 be x_{1s5}. Therefore, $x_{1b5} = x_{1s5}$. Similarly, for 10 days, $x_{1b10} = x_{1s10}$. However, the number of relevant users increases each after each period of five days. Therefore, $x_{1b5} < x_{1b10}$. Comparing the different scenarios, the number of relevant users in scenario 1 on five-day and that in scenario 2 on five-day differ. Therefore, $x_{1b5} \neq x_{2b5}$.

We collected the average speed of each user. We could not extract the average speed directly from the traffic simulator. However, the simulator provided the departure time (t_{si}), arrival time (t_{ei}), and travelled distance (l_i). Therefore, the average speed of user i was calculated by

$$v_i = \frac{l_i}{t_{ei} - t_{si}} \quad (2)$$

$$V = \frac{\sum_i^n v_i}{n} \quad (3)$$

After computing each relevant individual's average speed, the average speeds of each group were computed (eq]). Figure 76 illustrates that the average speed after the

restoration of bridges increased. In addition, the average speeds of scenario 1 on each five-day period were larger than those of the base case.

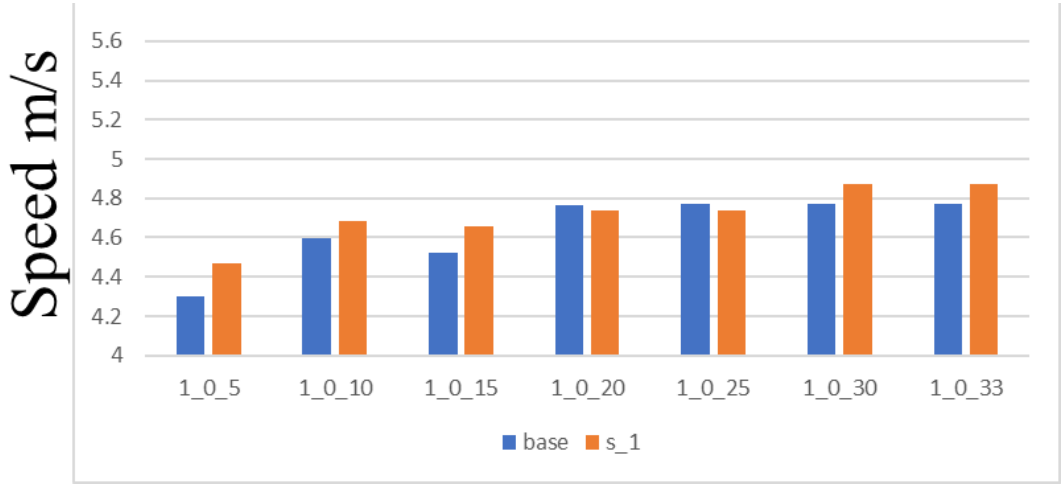

Figure 76. Average speed of bridge users (base case and scenario 1) [for days after disaster]

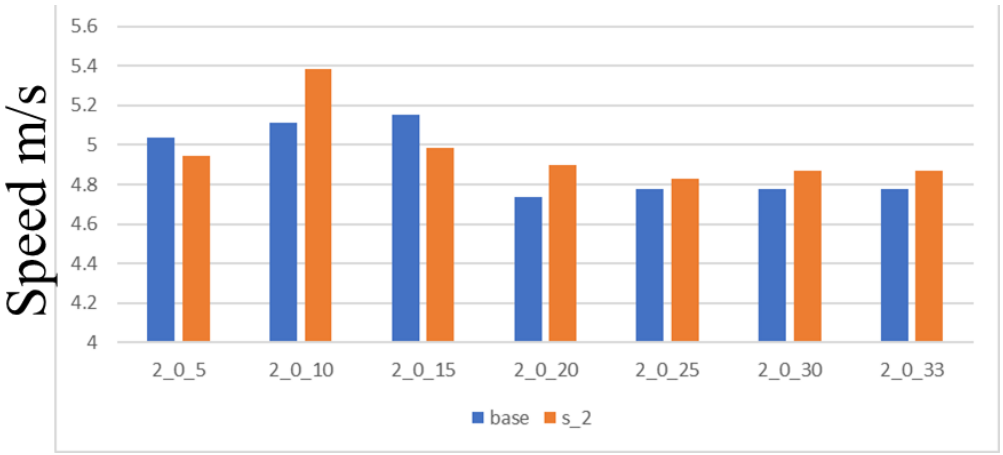

Figure 77. Average speed of bridge users (base case and scenario 2) [for days after disaster]

Figure 77 shows a different pattern. The average speed for scenario 2 on the 10th day was higher than that for the other periods. The average speeds on the fifth and fifteenth days were lower than that in the base case. A reason is that many users experienced congestion after the restoration of the bridges. Therefore, the average speed was reduced.

Figure 78 shows the results for scenario 3. Without a variation, the average speed after the restoration of bridges was higher than the base level except on the 30th day.

During that period, the speed was equal. If the scenario prioritizes the damage level, the network is likely to gain.

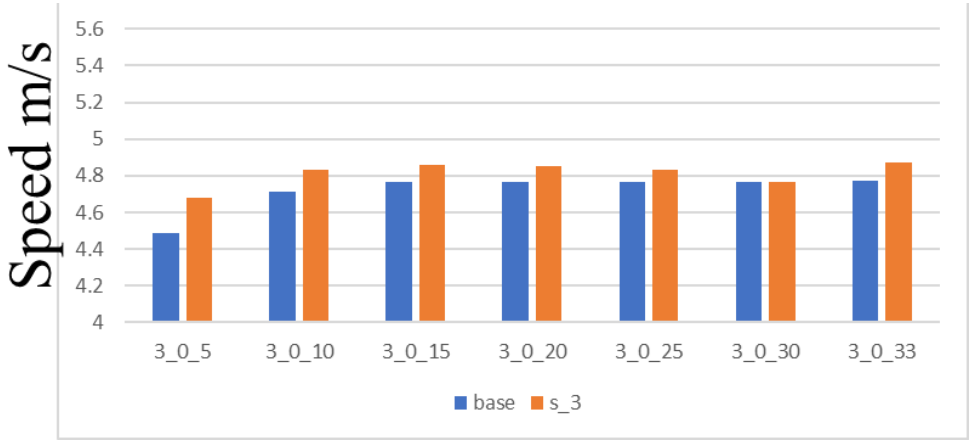

Figure 78. Average speed of bridge users (base case and scenario 3) [for days after disaster]

Figure 79 illustrates the integrated results for all the scenarios. Herein, we evaluated the performance of each strategy by counting the number of individuals who gained after each five-day period. After five days, strategy 1 outperformed. Strategies 2 and 3 had no significant difference on the fifth day. On the 10th day and 15th day, the differences among scenarios were evident. However, no scenario had a clear advantage until the 15th day. On the 20th day, the results became significantly close to each other. For scenario 3, it can be observed that the number of benefitted users within 15–25th day did not vary.

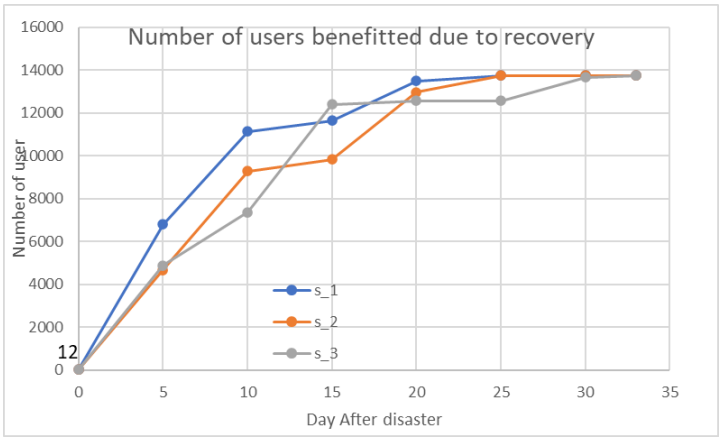

Figure 79. Generation of resilience triangle.

Figure 79 does not clearly present the performance of each scenario. The areas above the curves were computed and are presented in Figure 80. It can be observed that scenario 1 has the lowest area above the curve. Although the areas above the curves for scenarios 2 and 3 are significantly close, that for scenario 3 is the largest. Based on the area, the pre-

disaster user-based scenario (scenario 1) produced a more resilient system. Scenario 1 outperformed because the resilience was computed based on the number of total users. Because individuals' movement patterns remained fixed, they gained from the recovery of those bridges that were being used. However, several new trips generated after a hazard were excluded from this analysis. The shape of the resilience triangle may vary if those trips are included.

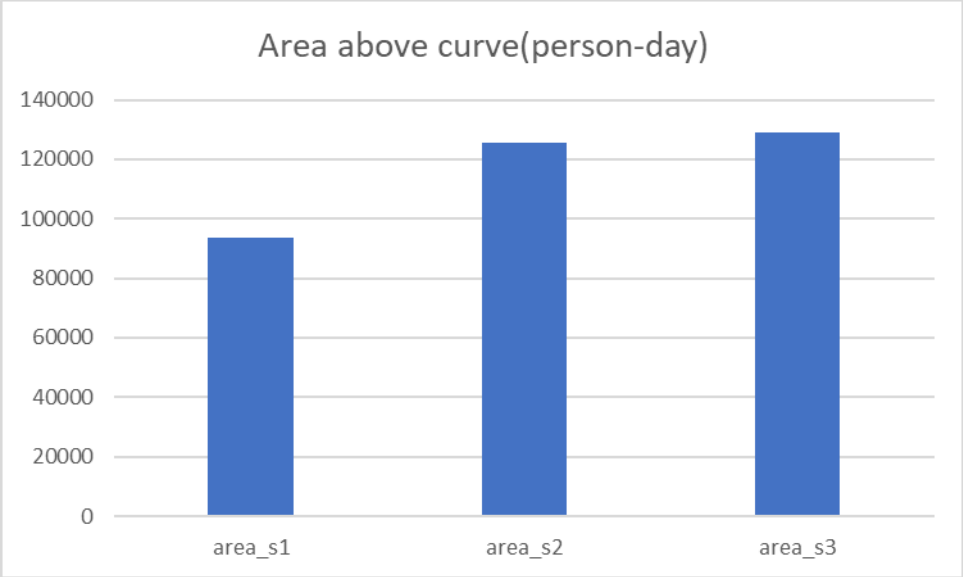

Figure 80. Comparison of area above curve.

4.Enablers and barriers

Maintenance interventions are important components to consider while assessing bridge resilience. The National Academy of Engineering in the U.S. cited the restoration and improvement of aging urban infrastructure as one of the challenging tasks. They define two major maintenance actions: corrective maintenance (CM) and preventive maintenance (PM). CM should be performed when the system performance attains a minimum threshold (or a particular failure state), whereas PM can be performed multiple times during the life cycle of a system to extend its safe service life. PM is performed to prevent the unpreventable structural failure.

For significantly degraded bridges, CM could be highly expensive owing to the probable replacement of major bridge components and higher downtime of bridges. The cost of maintenance can be reduced by performing several PMs at various stages of the bridge life span. This, in turn, circumvents the need for CM.

Preferably, an efficient maintenance plan depends on the maintenance policy, optimum

time for maintenance, and maintenance strategy (or cost of maintenance). Different maintenance policies are available in the literature to carry out maintenance programs. For PM programs, the age-replacement policy, periodic-replacement policy, failure limit policy, sequential policy, and repair limit can be categorized for single-unit systems. Several studies have also been performed over the past four decades to define optimum maintenance policies for engineering systems.

4.1 Enablers:

4.1.1 Flexibility of bridge damage modelling

One key outcome from the structural model is the prediction of bridge damage level. This model utilized static structural properties. Therefore, the model solution is fast and less data intensive. We collected historical data of each bridge in Yamaguchi city, Japan. Similarly, the model can be applied to other regions in Japan. The model can readily be transferred to other countries where similar data is available.

4.1.2 Utilizing mobile positioning data for traffic planning:

AGOOP data has been used to identify trip distribution. Since AGOOP data provides a spatial and temporal stamp, the details of the trip can be observed. Here, a traffic distribution model has been proposed. Since the application of mobile big data (i.e., AGOOP) is increasing in the domain of transportation planning and engineering, the proposed trip distribution model shows a method to integrate mobile positioning data to traffic simulation. Thus, this study makes a link between big data analysis and traffic simulation. Since mobile operators collect the data for their billing purpose, traffic engineers can benefit from the alternative usages of positional data.

4.1.3 Multi-hazard analysis:

The structural model was analysed for two return periods: 475 years and 2475 years. It is necessary to analyze the earthquake historical data. While following the American Association of Highway and Transportation Officials (AASHTO) guidelines, the return periods of 475 years are recommended. The two pillars of this study are (1) bridge damage level and (2) traffic simulation. The structural model can incorporate other hazards. Thus, the proposed model is not limited to earthquakes only.

Application of resilience index:

The outcome of this study is a resilience index of transport networks. This index integrates socio-technical attributes. Therefore, the decision making of bridge

maintenance becomes practical and comprehensive. Besides, it is possible integrated pre- and post-disaster costs. Moreover, the decision makers can observe the effect of pre-disaster maintenance. Thus, resilience can be increased.

4.2 Barriers

This section explains the limitations of the study.

4.2.1 Selection of route to reach the destination

In this study, a dynamic user assignment model was utilized to select the route to reach the destination. In this model, the travel time and congestion are explicitly considered. Other factors such as narrow road links, presence of trees, sitting benches, convenience stores, shopping arcades, or shadows are not considered (as shown in Figure 81). These factors may influence the route selection. Several studies have analyzed the effect of road-side characteristics on route selection. They determined that roadside factors have a significant influence on route selection. The results are used for improving sidewalks. However, no clear evidence was available to demonstrate that the route selection post-disaster is dependent on the road-side properties. However, it could be worthwhile to identify the influencing factors for route selection after a disaster.

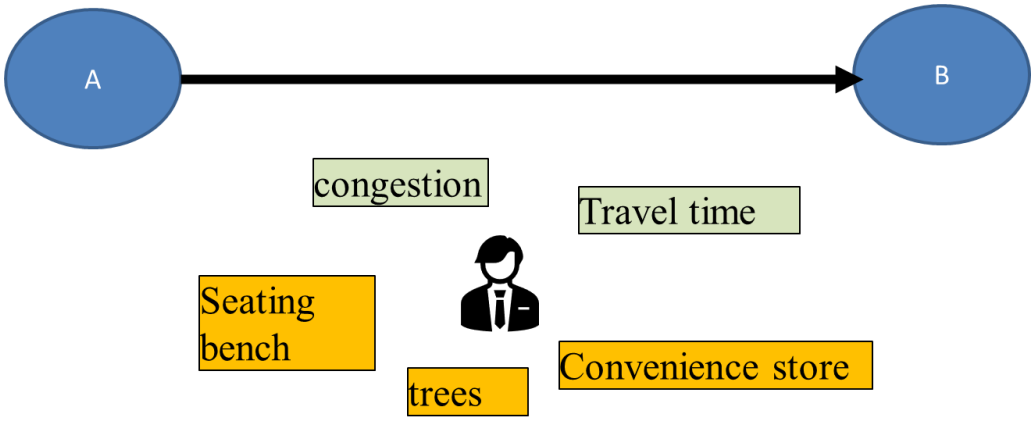

Figure 81. Influencing factors in route selection. The green colour boxes were considered in this study.

4.2.2 Multiple activities in a trip

Here, the user travels to the destination directly. However, the user may have performed multiple activities in a trip (known as trip chain). This study did not consider the trip chain, as illustrated in Figure 82. Here, the AGOOP database was utilized to estimate the OD table by comparing the longest trip. The AGOOP data source can be used to compute the trip chain. The number of users on the road link would vary because the trip chain may

use a different form of OD table.

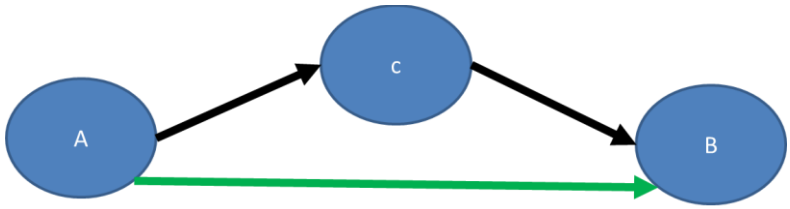

Figure 82. Concept of trip chain. In this study, only the green line (direct trip) was considered. The black line represents the trip chain.

4.2.3 Absence of modes other than road-based transportation

This study assumed that the individuals residing in Yamaguchi City would continue using road-based transportation. A city may provide alternative transportation modes such as water boats and cycles. However, this study did not consider a multi-transportation model. This limitation is crucial because road users may change dramatically if alternative transportation modes are available.

4.2.4 Absence of traffic attraction attributes

In this study, the traffic origin was computed based on the population density, and the trip distribution was computed based on the AGOOP data by considering the longest trip from the first record point. Here, we did not consider the traffic attraction attributes such as hospitals, schools, and government offices. The OD table can be updated by incorporating traffic attraction attributes.

4.2.5 Inclusion of freight flow with individual's flow

Table 30 illustrates the speed reduction caused by bridge damage. However, the analysis will be robust if freight flow is included. It could be integrated by incorporating weight limit restrictions on bridges and rerouting overweight trucks after a disaster. In addition to AGOOP data, the OD of truck trips is required. This study did not consider immediate post-disaster response. The inclusion of ambulance and other trips of first responders can make the model comprehensive.

5.Key Outcomes

This chapter explains the key outcomes of the research project supported by CDRI Fellowship Programme.

5.1 Multi-criteria decision making

Bridge restoration is a multi-criteria decision-making process. Moreover, the timing of the bridge restoration decision is crucial because a decision maker may not have access to all the data after a disaster. Therefore, the results of this research project would be helpful in deciding the sequence of restoration. This study incorporated the structural safety of bridges after analyzing the bridge properties. The social aspect was incorporated by considering accessibility. This study did not explicitly provide guidelines for the budget for bridge restoration. However, it assumed that the available budget of the network manager would be optimized. While optimizing or allocating the post-disaster budget, the restoration sequence of scenario 1 (road user priority scenario) could be utilized. Thus, our proposed model is effective for a network manager. The evidence of this action is presented in Figure 80.

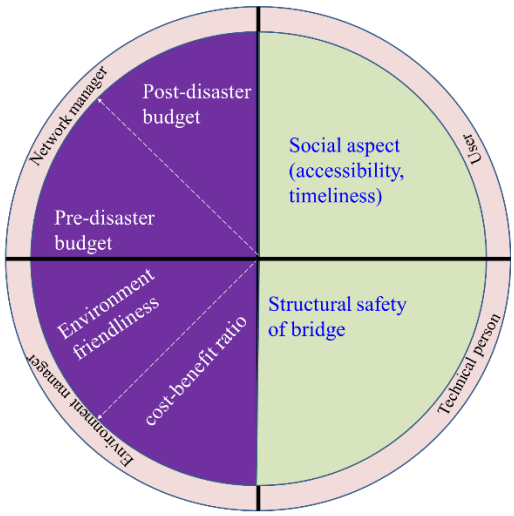

Figure 83. Multi-criteria decision making for bridge restoration (the green area is covered explicitly in this study)

5.2 Policy for balancing between pre- and post-disaster budgets

This is one of the crucial decisions made by network managers. Pre-disaster planning and investment may increase the robustness of the system. The transportation network cannot be protected completely from a hazard even with a larger amount of pre-disaster investment. These characteristics are illustrated in Figure 84. Therefore, a trade-off between pre- and post-disaster investment is necessary. Lower social costs and faster recovery can be achieved with increased robustness. Therefore, better resilience can be achieved.

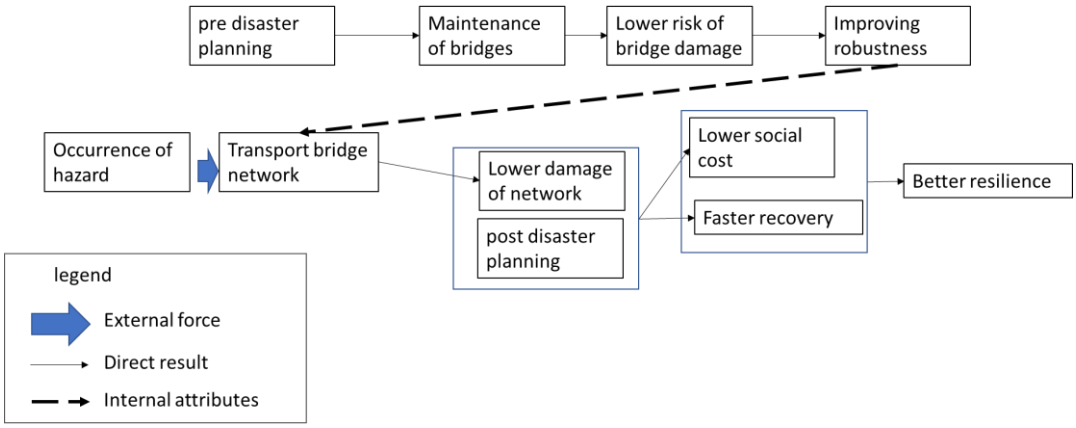

Figure 84. Trade-off between pre- and post-disaster costs.

In this study, a structural analysis was conducted. Here, we utilized several attributes. One of these is the year of the previous maintenance action. Therefore, the reduction in bridge failure can be updated by incorporating recent maintenance data. With the updated bridge damage probability, a new resilience triangle can be developed. As Table 30 illustrates, the effect of bridge damage through speed reduction can also be demonstrated by the restriction on truck weight limit. Without pre-disaster intervention, the bridge damage level could be A. After bridge maintenance, the damage level could be C. Therefore, our proposed model achieves a trade-off between pre- and post-disaster costs.

5.3 Decision making by incorporating social attributes.

Network managers generally administer a larger coverage region. Certain zones may have a higher population density, whereas others have a lower one. Meanwhile, certain roads are utilized extensively to access basic services such as hospitals, post-offices, and supermarkets. Similarly, certain specified roads may be dedicated to bus routes or emergency vehicles. Therefore, a network manager should not randomly select a bridge for restoration. The decision should be made such that the social costs are reduced. In addition, traffic generation/attraction cannot be uniform throughout the network. In this study, an OD table was generated based on the population density. Therefore, the trip generations from each TAZ are different. In addition, we utilized AGOOP data for analyzing the trip distribution. Thus, the trip attraction attributes were considered implicitly in this study. The results are presented in Table 23 where the trip ODs are presented as a percentage of the total trips. By utilizing our proposed model, a network manager can differentiate the importance of each TAZ.

5.4 Pre-disaster bridge maintenance level

A city has budget constraints, whereas a network manager needs to take judicious risks so that the impact of hazards on socio-economic domains is lower. In conjunction with our proposal, the manager needs to know the current health index and potential damage to a bridge. After selecting the weakest bridge for maintenance, a manager updates its database. Using the updated health index, the manager can apply the proposed model. Then, the difference in the results before and after maintenance is the true effect of maintenance. The manager can subsequently select another bridge for maintenance and apply our proposed model.

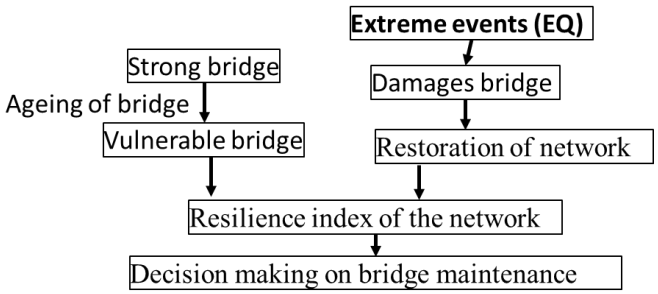

Figure 85. Application of resilience index in decision making.

The above-mentioned strategy assumes that the decision maker would make decisions the maintenance activities sequentially. However, our approach is flexible in that it adopts a set of bridges for maintenance activities. After the maintenance of this set of bridges, their health index is updated. Subsequently, our proposed model can be applied. The flow of decision making is illustrated in Figure 85. The sequence of bridges can be developed using Table 29. In this manner, the manager can decide the investment required in the pre-disaster situation.

6. Conclusion

Transportation plays a pivotal role in an advanced society by enabling the movement of humans and goods, supporting economic activities, and connecting communities. However, transportation systems are vulnerable to various disruptions including natural disasters, technological failures, and security hazards. Therefore, it is imperative to develop robust strategies and tools to measure and improve the resilience of these systems. Resilience has been studied in the field of transportation engineering. However, most of the research has focused on developing a conceptual framework of resilience using descriptive means rather than using widely acknowledged quantitative measuring

techniques. In this study, the resilience of an actual network was measured by evaluating the total loss on a network based on the variations in the values of widely accepted performance measures. Thus, we integrated structural and traffic engineering. This integration in the context of transportation network resilience holds significant potential for improving the decision-making on transportation-bridge-maintenance strategies. This research study evaluated the advantages and implications of integrating these two disciplines, highlighting the manners in which these can effectively address both physical and operational aspects of network resilience.

The first key observation of this study is that the integration of structural and traffic engineering enables a comprehensive understanding of the vulnerabilities and risks present within transportation networks. By considering the physical aspects of bridges in conjunction with their operational aspects including traffic patterns and congestion points, the network vulnerabilities can be assessed more accurately. This holistic understanding enables engineers and planners to identify and prioritize critical areas for improvement, such as retrofitting or reinforcing infrastructure elements to withstand potential hazards.

Furthermore, the integration of these disciplines enables the development of innovative retrofitting strategies to enhance the resilience of transportation networks. Incorporating structural resilience principles into transportation planning and design processes ensures that infrastructure elements are constructed to withstand and recover from disruptive events.

Furthermore, data-driven decision-making processes were introduced in this study. As AGOOP data can be collected in real-time, post-disaster trips can be computed. In addition, the application of information technology (IT) can enable the collection of traffic network data that would assist a traffic engineer in performing dynamic rerouting. Thus, by leveraging real-time data collection, our proposed traffic simulation can predict traffic congestion and the impact of disruptions. This data-driven approach enables proactive decision-making, enabling resources to be allocated more effectively and facilitating timely maintenance and repairs.

The observations of this study emphasize the significance of collaboration and knowledge sharing between structural and traffic engineering professionals. This interdisciplinary approach induces a holistic and comprehensive understanding of the challenges encountered by transportation networks. This, in turn, promotes the

development of innovative and effective solutions. The approach also emphasizes the importance of incorporating resilience considerations into the early stages of infrastructure planning and design.

This research study developed a comprehensive transportation resilience index that serves as a systematic and objective tool for evaluating the resilience of transportation systems and identifying areas that require attention and improvement. It incorporates multiple dimensions of resilience, including infrastructure, operations, and response capabilities. By considering these aspects, the index provides a holistic assessment of transportation resilience.

The observations of this study underscore the complex characteristic of transportation resilience. The emphasis is on the construction of strong and durable infrastructure and the establishment of efficient operations, fostering of coordination and collaboration among stakeholders, and implementation of effective emergency response measures. The transportation resilience index captures this multifaceted characteristic, thereby enabling policymakers, transportation planners, and stakeholders to gain a comprehensive understanding of the resilience of their systems.

In conclusion, the integration of structural and traffic engineering represents a potential avenue for improving the resilience of transportation networks. Collaboration between these disciplines enables a comprehensive understanding of vulnerabilities, the development of innovative design strategies, and the implementation of data-driven decision-making processes. By adopting this interdisciplinary approach, transportation networks can become more robust, adaptive, and capable of withstanding and recovering from disruptive events. As societies continue to encounter an increasingly complex and uncertain future, the integration of structural and traffic engineering would play a pivotal role in developing resilient transportation systems that better serve the needs of communities.

It is crucial to acknowledge that transportation resilience is an ongoing process that requires continuous monitoring, evaluation, and adaptation. As new challenges and risks emerge, the transportation resilience index should be regularly updated and refined to reflect the evolving landscape. By emphasizing the importance of resilience in transportation planning and policymaking, the project highlighted the need for proactive measures to address robustness and enhance the adaptive capacity of transportation systems. The transportation resilience index is an effective tool for policymakers and

practitioners to assess and improve the resilience of their systems. This would minimize disruptions, mitigate the impact of disasters, and ensure the continuity of essential services.

Further research and application of the transportation resilience index can continue to enhance our understanding of transportation resilience and provide effective insights for decision-making. By prioritizing resilience in transportation planning and investing in measures to enhance the adaptive capacity of transportation systems, we can develop more robust, reliable, and sustainable transportation networks that can effectively withstand and recover from disruptions. Ultimately, the objective is to ensure the continued functioning of transportation systems and the well-being of the communities they serve in a scenario characterized by continuously evolving challenges and uncertainties.

Finally, we wish to provide certain guidelines for our research funding agency, the CDRI, on the utilization of the outcomes of this research. It is well acknowledged that resilience involves costs. Therefore, it is necessary to invest in resources to increase the infrastructure resilience. Investment decisions should be made based on a scenario analysis. Our proposed model can be effective in understanding the trade-off between pre- and post-disaster transportation costs. Thus, the CDRI can inform their client regarding the advantage of pre-disaster investment.

In addition, CDRI can identify bridges where pre-disaster investment may not yield a significant advantage to the society. Therefore, the selection of bridges for pre-disaster investments can be recommended based on the results of our study.

References

1. Adams, T. M., Bekkem, K. R., & Toledo-Durán, E. J. (2012). Freight Resilience Measures. *Journal of Transportation Engineering, 138*(11), 1403-1409.

2. Amdal, J. R., & Swigart, S. L. (2010). *Resilient Transportation Systems in a Post-Disaster Environment : A Case Study of Opportunities Realized and Missed in New Orleans and the Louisiana Coastal Region*. Retrieved from National Transportation library: https://rosap.ntl.bts.gov/view/dot/34311

3. Battelle. (2007). *Evaluation of the Systems' Available Redundancy to Compensate for Loss of Transportation Assets Resulting from Natural Disasters or Terrorist Attacks.* Retrieved from National Transportation library: https://ntl.bts.gov/ntl

4. Cimellaro, G. P., Reinhorn, A. M., & Bruneau, M. (2010). Framework for analytical quantification of disaster resilience. *Engineering Structures*, 3639-3649.

5. Cox, A., Prager, F., & Rose, A. (2011). Transportation security and the role of resilience: afoundation for operational metrics. *Transport Policy, 18*(2), 307-317.

6. Croope, S. V., & McNeil, S. (2011). Improving Resilience of Critical Infrastructure Systems Postdisaster: Recovery and Mitigation. *Transportation Research Record: Journal of the Transportation Research Board, 2234*(1), 3-13.

7. Das, R. (2020). Approach for measuring transportation network resiliency: A case study on Dhaka, Bangladesh. *Case Studies on Transport Policy, 8*(2), 586-592.

8. Gordon, P., Richardson, H., & Davis, B. (1998). Transport-related effects of the Northridge earthquake. *Journal of Transportation and Statistics, 1*(2), 21-36. Retrieved from https://rosap.ntl.bts.gov/view/dot/4496

9. Gunderson, L. H., & Pritchard, L. (2002). *Resilience and the behavior of large-scale Systems.* Washington DC: Island Press.

10. Heaslip, K. L. (2010). A sketch level method for assessing transportation network resiliency to natural disasters and man-made events. ". *89th Annual Meeting of the Transportation Research Board,.* Washington, DC.

11. Holling, C. S. (1973). Resilience and Stability of Ecological Systems. *Annual Review of Ecology and Systematics, 4*, 1-23.

12. Kobayashi, H., & Unjoh, S. (2005). A method for estimating the degree of damage to highway bridges during a large earthquake (in Japanese). *Civil engineering journal, 47*(12), 48-53.

13. Miller-Hooks, E., Zhang, X., & Faturechi, R. (2012). Measuring and maximizing resilience of freight transportation networks. *Computers & Operations Research, 39*(7), 1633-1643.

14. Murray-tuite, P. M. (2006). A Comparison of Transportation Network Resilience under Simulated System Optimum and User Equilibrium Conditions. *the 2006 Winter Simulation Conference*.

15. Nagurney, A., & Qiang, Q. (2009). A relative total cost index for the evaluation of transportation network robustness in the presence of degradable links and alternative travel behavior. *International Transactions in Operational Research, 16*(1), 49-67.

16. Nan, C., & Sansavini, G. (2017). A quantitative method for assessing resilience of interdependent infrastructures. *Reliability Engineering & System Safety, 157*, 35-53.

17. Scott, D. M., Novak, D. C., Aultman-Hall, L., & Guo, F. (2006). Network Robustness Index: A new method for identifying critical links and evaluating the performance of transportation networks. *Journal of Transport Geography, 14*(3), 215-227.

18. Sudakov, B., & Vu, V. (2008). Local resilience of graphs. *Random Structures and Algorithms, 33*, 409-433.

19. USDOT. (2009). *Recovering from Disasters: The National Transportation Recovery Strategy*. Retrieved from U.S. Department of Transportation: https://www7.transportation.gov/policy-initiatives/disaster-recovery/recovering-disasters-national-transportation-recovery-strategy

20. VTPI. (2010). *Evaluating Transportation Resilience*. Retrieved from Evaluating Transportation Resilience: Evaluating The Transportation System's Ability To Accommodate Diverse, Variable and Unexpected Demands With Minimal Risk: https://www.vtpi.org/tdm/tdm88.htm

Robust Approach to Assessing Post-Fire Structural Behaviour of High-Rise Mass Timber Buildings

Satheeskumar Navaratnam

Civil and Infrastructure Engineering

RMIT University, Australia

Under CDRI Fellowship Programme 2022-23

Disclaimer: The views expressed in this paper reflect the opinions of the author and not necessarily the official views of CDRI.

Abstract

Mass timber buildings offer a competitive and innovative sustainable construction alternative to steel framed and concrete buildings. This robust approach to midrise construction offers a number of environmental benefits such as reducing embodied carbon impacts and construction waste. However, there has been a significant barrier preventing the implementation of MTB concerns over the structural fire performance and tighter legislation on the fire design of buildings induced by the Lacrosse fire in Melbourne. This project aims to understand the fire reaction, post-fire performance and collapse mechanisms of floor panel (cross-laminated timber) and mass timber building. The fire performance of cross-laminated timber depends significantly on the strength and behaviour of the adhesive. At elevated temperatures, the adhesives could fail and create severe delamination due to changes in the moisture contents and thermal degradation. Therefore, this study conducted several experimental and numerical model analyses to evaluate the fire performance of adhesive bond strength and compressive strength of cross-laminated timber at elevated temperatures and proposed advanced modified adhesive to improve the fire performance. Then this study developed a numerical model on a 10-story mass timber building subjected to localized fire. Results showed that the fire performance of cross-laminated timber and mass timber building could be improved when the floor panel is made with the proposed modified fireproof adhesive. Further, the proposed finite element and analytical models can be used to predict engineered timber's post-fire residual strength. However, further experimental tests are needed to ensure the capability of modified fireproof adhesive to improve the robustness of mass timber buildings.

Acknowledgments

This research work is funded under the Coalition for Disaster Resilient Infrastructure (CDRI) Fellowship under the mentorship of Late Professor Adrian Mouritz and Dr Srikanth Venkatesan, Civil and Infrastructure Engineering, RMIT University, Australia. The financial support is gratefully acknowledged.

Funding

This research was supported by the 2022–2023 Fellowship of the Coalition for Disaster Resilient Infrastructure (CDRI), Application ID: 210927702.

1. Introduction

The construction industry is leaning towards sustainable and green building construction [1]. Engineered timber products such as cross-laminated timber (CLT), laminated veneer lumber (LVL) and glued laminated timber (GLT) or Glulam (GL) are currently used as sustainable construction materials in mid-to-high-rise building construction. Engineered timber products show high potential in terms of addressing many of the demands of the construction industry, showing structural capacities similar to the commonly used construction materials while also being cost-effective [1-3]. CLT has a high degree of prefabrication, as well as high in-plane and out-plane strength and stiffness, and good acoustic and thermal performance [4-6]. Due to these capabilities, many mid-to-high-rise mass timber buildings in Australia (i.e. International House in Sydney, 25 King Street in Brisbane and Forte Living in Melbourne) and other countries have used CLT as an engineered timber product for floors and walls. Further, the Australian National Construction Code [7] changed the maximum height restriction of timber buildings (up to 25m) without requiring extra approvals. This restriction change will lead to an increase in the number of mid-to-high-rise mass timber buildings in Australia. The probability of progressive collapse will increase along with the possibility of increasing the building height.

Furthermore, timber and Engineered timber products are susceptible to fire damage which can lead to the failure of mass timber building. Hence, the design of mid-to-high-rise mass timber buildings should place significant emphasis on achieving building resilience in order to prevent disproportionate damage to the structure in cases of fire and localized fire. Moreover, the performance of these engineered timber products used in mass timber buildings depends on the strength and behaviour of the adhesive. At elevated temperatures, the adhesives could fail and create delamination due to the changes in the moisture contents. The combustibility nature of engineered timber products limits their application in mid-to-high-rise MTB constructions. Although, research studies have proven that CLT provides the standards (NCC, ASTM E119 or UL 263) required for fire resistance. The fire failure of mass timber buildings is still inherently occurring. Proper fire design measures are implemented for high-rise buildings delaying the rapid spread of fire, and damage often remains localized within proximity of the source. Localized fires induce delamination failures in the adhesive bond of CLT, which causes rapid strength reduction and progressive collapse of the whole building. Thus, the performance of CLT under elevated temperatures remains unknown, and warrants research to ensure fire performance.

Several research studies evaluate the thermal and mechanical response of CLT under fire, including wall and floor structures, the number and thickness of timber layers, the adhesive type, and the fire intensity and structural load levels. Several small to medium-scale fire tests have been conducted to assess the fire performance of CLT. However, some large-scale fire tests have also been conducted to evaluate the structural fire performance of mass timber buildings and their structural elements [8]. In addition to the extensive experimental research into the structural response of CLT exposed to fire, models have been developed to predict the softening and failure of CLT during a fire. Analytical and finite element models have been developed to predict the reduction in load-carrying capacity of CLT structures under combined fire exposure and compression or flexural loading.

The post-fire structural behaviour of CLT has received comparatively less attention. Fire's influence was found to further reduce CLT's load-carrying capacity, and a lack of data on the residual strength after heat exposure was identified[9]. Bai et al.[10] investigating the CLT's post-fire residual compression load capacity highlighted the importance of mechanical properties for accurately modelling the residual load-carrying capacity after the fire. The post-fire integrity of CLT joints has been studied by Xing et al. [11]. Despite the growing body of research concerning the structural performance of CLT after the fire, there needs to be research that systematically investigates the post-fire mechanical properties of CLT.

The residual load-bearing capacity of CLT structures is adversely affected during and after fire exposure. The structure's load-bearing capacity reduction stems from a reduction in the CLT mechanical properties due to the thermal degradation of the CLT constituent materials (e.g., timber and polymer adhesive). It is, therefore, essential to develop a deeper understanding of the influence of fire exposure on the post-fire residual mechanical properties of CLT. Studies have yet to be investigating the residual post-fire mechanical properties of CLT and developing fireproof adhesives to improve fire performance.

Therefore, this research developed a natural fibre-based fireproof epoxy resin adhesive that aims to improve the fire resistance duration, which is allocated for safe evacuation, structural stability and fire performance of mass timber buildings. This proof-of-concept study will advance the knowledge of mechanical properties of CLT and mass timber buildings after the fire, enabling fire safety engineers to appropriately account for residual load-bearing capacity in their designs and fire assessment models.

2. Aim, Objectives, and Scope of the Research Study

This project aims to improve the fire resistance duration, which is allocated for safe evacuation, structural stability and fire performance of mass timber buildings. To achieve this:

- Objective 1: To develop a natural fibre-based fireproof epoxy resin adhesive to improve fire performance and ensure mass timber buildings' structural safety and design.
- Objective 2: Identify the residual strength of CLT after it has been exposed to fire.
- Objective 3: Develop an advanced numerical model using finite element software to identify the post-fire behaviour of mass timber buildings. This will provide residual strength for the building and their element. This also provides information for safe evacuation and rectification of the structure.

3. Methodology

Currently, Purbond polyurethane adhesive is used to produce the CLT. This study developing a natural fibre-based fireproof epoxy resin to improve the fire performance of CLT under elevated temperatures. The high-density fireproof epoxy resin was produced by directly mixing the Purbond polyurethane adhesive, biochar, aqueous solution of glass and branched ceramic. Experimental tests were conducted to assess the thermal response (Section 3.1), compression and bond shear strength (Section 3.2) and structural fire performance (Section 3.3). Moreover, numerical models were developed to evaluate the robustness of mass timber building subjected to localized fire (Section 3.4).

3.1 Thermal response of the CLT exposed to fire

The thermal response of the non-load-carrying CLT panel was assessed by exposing an unloaded test specimen to a constant radiant heat flux for two hours. The temperature-time history of the specimen was recorded at the front and back surfaces as well as internally at the four inter-ply boundaries using K-type thermocouples.

3.2 Evaluation of the compression properties of CLT panels before and after fire exposure

Short-block compression tests were performed after heat exposure for durations between 0

minutes and 120 minutes, corresponding roughly to the time at which the pyrolysis front penetrates each ply. The five test specimens (300 mm x 300 mm) were evaluated after heat exposure durations. The temperature-time history of the test specimen was recorded at the front and back surfaces using K-type thermocouples. The fire-exposed test specimens were cooled to room temperature prior to the evaluation of their residual compression strength. The post-fire specimens were compression-loaded along the warp direction at a loading rate of 2.5 mm/min until failure using a 5 MN MTS machine.

3.3 Structural fire test

Fire tests were carried out for load-bearing CLT panels, which were manufactured with normal Purbond polyurethane adhesive and radiata pine timber. The panel's width, length and thickness are 280 mm, 5400 mm and 560 mm, respectively. The density and moisture content were measured prior to the test. The average density and moisture content of the CLT panel are 474 kg/m^3 and 9.3%, respectively. The test was carried out in the horizontal furnace of the testing laboratory (Figure 1). Specimens were hung from the ceiling of the furnace and exposed to fire on the bottom sides and vertical edges. Three test specimens were tested to increase the accuracy of the results. Tests were carried out for 120 minutes, and the ambient temperature was 17^{o}C. Testing was carried out following the procedures outlined in EN 1365-3:2002 and EN 1363-1:2020. ISO 834 standard fire curve (Figure 2) was used in supplying the heat to the specimen.

Figure 1. Test setup and arrangement

The specimen was supported from the short edges making a clear span of 5200 mm, and the long edges of the specimen were free to deflect. The specimen was exposed to fire on the bottom and both long vertical sides. Two-point loads of 50 kN each were applied with the aid of steel weights, steel beam and a hydraulic jack (Figure 1). The load was applied at

least 15 minutes before the beginning of the test. The ambient temperature for this test was 16^{0}C. Thermocouples were used to obtain the temperature data of the panel, and 11 thermocouples were used in the test. Locations of the thermocouples are given in Figure 3.

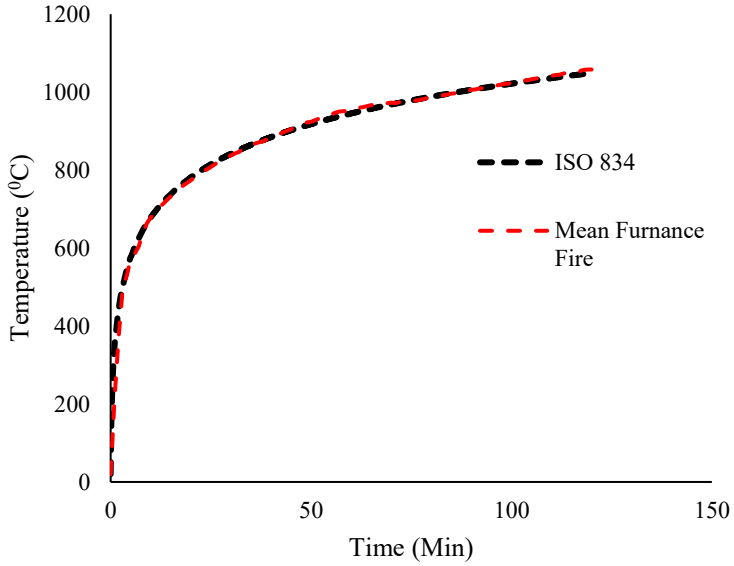

Figure 2. Furnace temperature curve

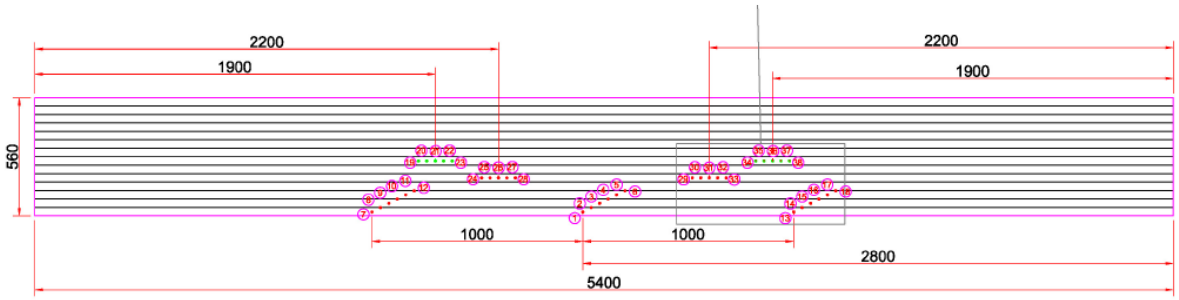

Figure 3. Locations of the thermocouples

3.4 Robustness of mass timber building under localized fire

Figure 4 presents a schematic depiction of the process involved in the progressive collapse of a multi-story timber structure under fire. The process is initiated by a local fire event breaking out in a confined space of the building. Assuming proper fire design measures are implemented that prevent the rapid spread of the fire throughout the building, the fire event will remain localized and only cause damage to nearby structural components. As these components fail, an alternative load path is generated, which needs to be supported by the remaining structural components in order to prevent further collapse. If the surrounding structure is unable to support additional loads, progressive collapse of the building will occur.

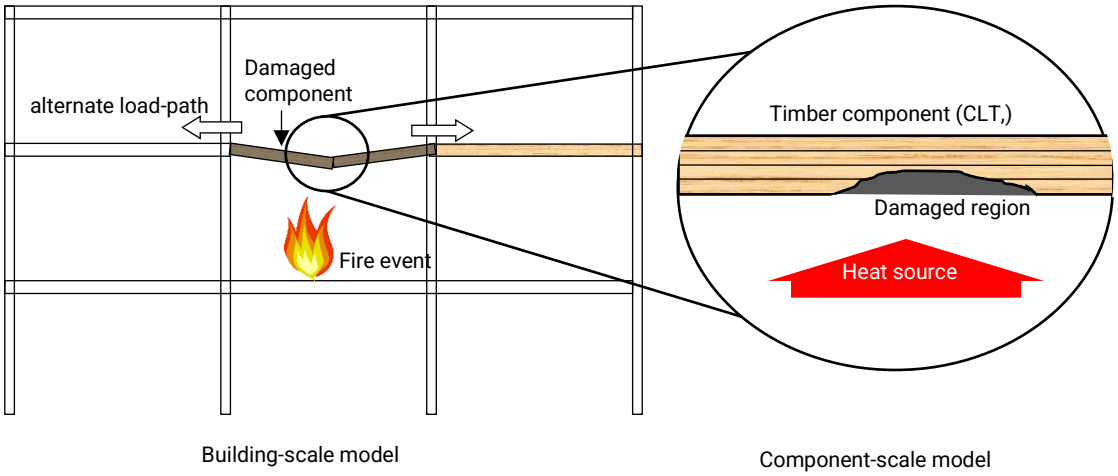

Figure 4. Schematic view of a multi-scale model of multi-story timber structures

To model the resilience of timber structures under fire, this study used the multi-scale modelling approach, which consists of a component-based model of CLT (Section 4.3). A numerical analysis of this study was performed for the 10-storey mid-rise mass timber building depicted in Figure 5. All structural components of the ground floor are made of concrete. The rest of the structure is composed of timber elements, including CLT floor panels, glulam beams and glulam columns. A single CLT panel is used for each floor between the area bounded by four columns. Glulam bracings are provided in both longitudinal and transverse directions of the building to provide lateral stability of the building. The core of the building is constructed of concrete (at Level 1) and CLT (from Level 2 up to the top). The height of each individual panel in the CLT core is 4 m, which is also the typical storey height of the building. The dimensions of the typical glulam sections used in the model at each level are stated in Table 1.

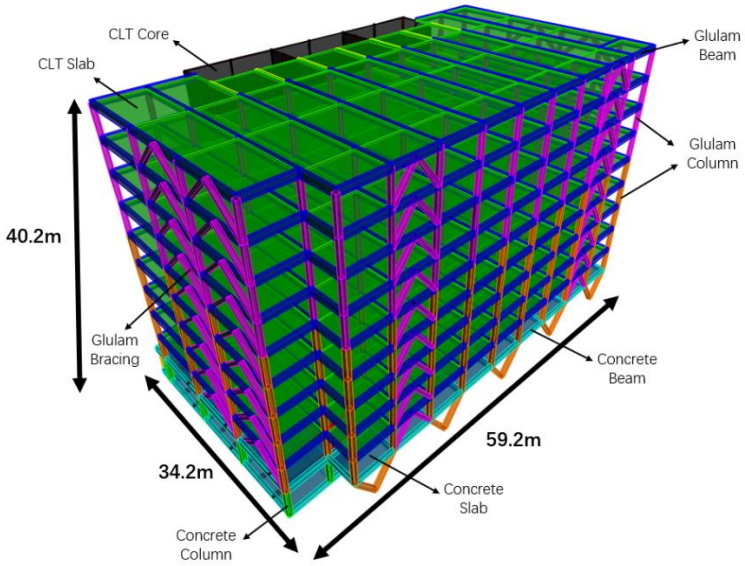

Figure 5. Isometric view showing the main structural components of the building.

Table 1. Typical glulam beam and column dimensions in the building

Level	Beams	Columns
L2-L3	400mm × 800mm	600mm × 600mm
L4-L6	400mm × 800mm	560mm × 560mm
L7-L11	400mm × 800mm	480mm × 480mm

3.4.1 Material Properties

The beams, columns, slab and core within Level 1 are composed of 40 MPa concrete. The rest of the structure is fully timber based. A 5-ply (CL5/205) CLT panel is used for the floor and core. All CLT panels are made of Australian-grown plantation radiata pine. The CLT panels are composed of an alternating arrangement of 45 mm and 35 mm thick layers (known as XLG1 and XLG2, respectively), for which the material properties are specified in Table 2. The timber beams and columns are made of Glulam. Elastic modulus (E), shear modulus (G), bending strength (f_b), compressive strength (f_c) and tensile strength (f_t) in the longitudinal (0°) and transverse (90°) directions were obtained from the standard specifications for CLT [12] and Glulam [13] and are listed in Table 2. Based on the individual layer properties, the characteristic properties of the CLT panel were computed using composite theory as suggested in the CLT handbook [14].

Table 2. Material properties of the timber elements

Component	E_0 (MPa)	E_{90} (MPa)	G_0 (MPa)	f_b (MPa)	$f_{c,0}$ (MPa)	$f_{c,90}$ (MPa)	$f_{t,0}$ (MPa)	Poisson 's ratio
XLG1	8000	267	533	14	18	8.9	6	0.46
XLG2	6000	200	400	10	15	8.9	4	0.38
GL	Average E = 16700		1110	40	33	13	20	0.2

3.4.2 Intercomponent connections parameters

This model considers the concrete wall-to-foundation, column-to-foundation and bracing-to-beam connections as Pin joints. The wall-to-wall connections, column-to-column, panel-to-panel and wall-to-beam connections were designed as semi-rigid connections, which enabled moment and force transfer between the elements. Column-to-beam, column-to-column and shear wall-to-beam connections were designed as nonlinear elastic link elements. The corresponding non-linear properties of the connection for both the rotational and axial directions of the link elements were obtained from the experimental results by Navaratnam et al. [15]. Figures 6a and 6c show the moment-rotation and axial-force

displacement relationship for the column-to-beam GIR connections, respectively. The moment-rotation relationship of the column-to-column connection is presented in Figure 6b.

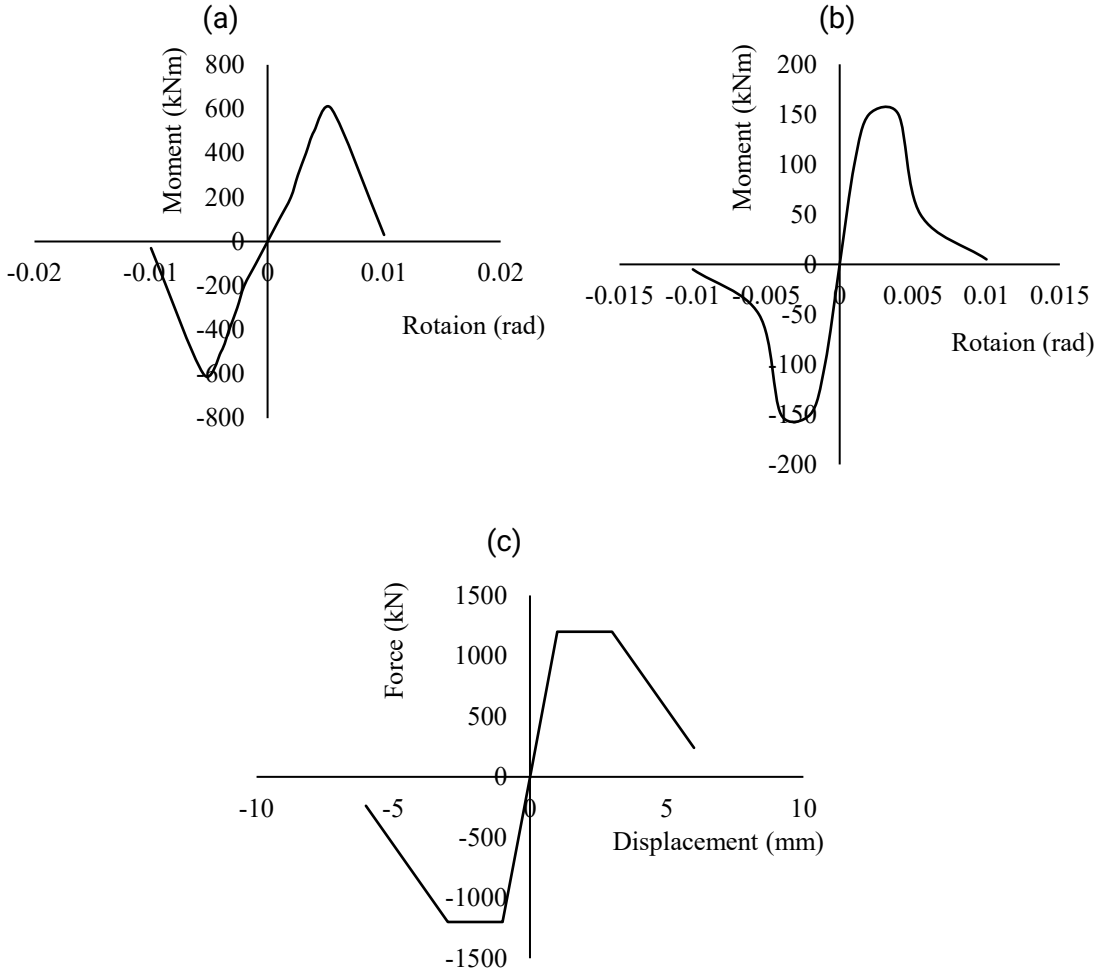

Figure 6. Inter-component connection properties: a) moment-rotation column-to-beam connection; b) moment-rotation column-to-column connection; and c) force-displacement curve of column-to-beam connection

3.4.3 CLT floor panel subjected to a fire

This study also focuses on the effects of a fire spreading on a CLT floor element. The importance of such an analysis has been demonstrated by the collapse of the Seven World Trade Centre (WTC7) building. The September 11 terrorist attack directly initiated the collapse of the Twin Towers (WTC 1 and WTC2- The South and the North Towers) of the New York World Trade Centre Building. The resulting fires were identified as the cause of the collapse of WTC7. The collapse of WTC7 is completely different to that of WTC1 and WTC2 as the building did not encounter sudden impact with the aircraft. The collapse was initiated

due to the spreading of fires from the adjacent buildings. This failure can be considered a progressive collapse induced by fire and is considered to be the first tall building to undergo such failure [16].

Even though the behaviour of CLT under fire has been thoroughly explored [17-21], further full-scale tests are needed to investigate the overall effects of fire on timer-based buildings [5] and also to investigate the possibility of the development of progressive collapse due to a fire. Numerical modelling can provide an insight into what can be expected in case of a mass timber building subjected to a fire. The extent of progressive collapse development and the possible development of load re-distribution mechanisms within the structural elements also should be investigated.

In order to mimic a similar situation, a simplified approach was considered. The CLT floor on Level 2 (between grid C-D and grid 3-4) was considered as the structural element subjected to fire (Figure 7). The spread of the fire was simulated by removing certain sections of the CLT floor at particular time periods. The area subjected to fire was computed based on a char rate of CLT determined in Section 4.1.1. The building floor was exposed to a localized fire for a period of 120 minutes and was assumed to spread outwards to the sides from the starting point of the fire within the panel.

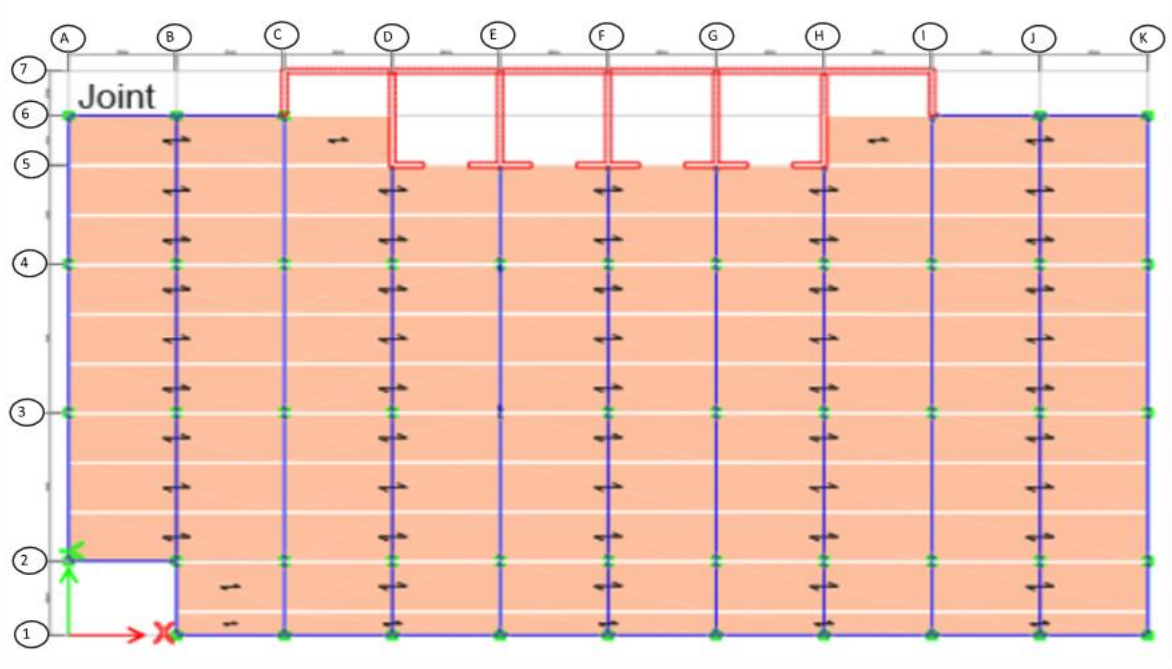

Figure 7: Plan view of case study building.

4. Results and Discussion

4.1 Developed a natural fibre-based fireproof epoxy resin adhesive.

This research developed a natural fibre-based fireproof epoxy resin adhesive to improve the fire performance of CLT. To assess the fire performance, this study manufactured the CLT with three layers (35/20/35). A total of five CLT specimens (300 mm x 300 mm) were made with modified fireproof epoxy resin, and another five samples were made with normal Purbond polyurethane adhesive to compare the results. The modified fireproof epoxy resin was produced with Purbond polyurethane, glass powder and grounded natural fibre. Each specimen was manufactured from Australian Radiata pine timber. The structural grade Radiata pine timber used in the three longitudinal layers was XLG1 (comparable to F7), while the two perpendicular layers are made with XLG2 (comparable to F5) structural grade Radiata pine timber. Table 3 shows the details of test specimens and their material properties (modulus of elasticity (MOE) and shear modulus).

Table 3. Specimens' details

Specimen details				
Type	Lamination grade	Lamination thickness (mm)	Width (mm)	Average density (kg/m3) /COV (%)
CLT	XLG1/XLG2 /XLG1	35/20/35	300	485/11
Mechanical properties				
Lamination grade		XLG2	XLG1	
MOE (MPa)	Parallel to the grain	6000	8000	
	Perpendicular to the grain	200	267	
Shear modulus (MPa)	Longitudinal (G_0)	400	533	
	Rolling shear (G_{RS})	40	53	

4.1.1 Thermal response of the CLT exposed to fire

The thermal response of the CLT panel was assessed by exposing an unloaded test specimen to a constant radiant heat flux for two hours (Figure 8). The temperature-time history of the specimen was recorded at the front and back surfaces as well as internally at the four inter-ply boundaries using K-type thermocouples.

Figure 8: Fire test of CLT

The charring rate was only measured after discrete heat exposure durations. However, the overall behaviour is assumed to be bimodal. In the first region, the charring rate rapidly increased with temperature as the first layer is unprotected and initiates decomposition into carbonous char. After the charring rate reaches a peak, the char growth rate decreases due to establishing a protective layer induced by char. Further, in the sample with a modified adhesive, the fire-proof epoxy generated an additional protective layer (Figure 9) to protect the timber from temperature increases rapidly. Given the relatively short duration of the first region (< 15 minutes), a linear charring rate may be more suitable than a constant charring rate for use in design standards (Figure 10). Figure 10 shows that the charring rate of CLT made with modified adhesive is less than that of the CLT made with traditional adhesive. Figures 9 and 10 indicate that the modified adhesive produces fire resistance by creating productive layers.

(a) (b)

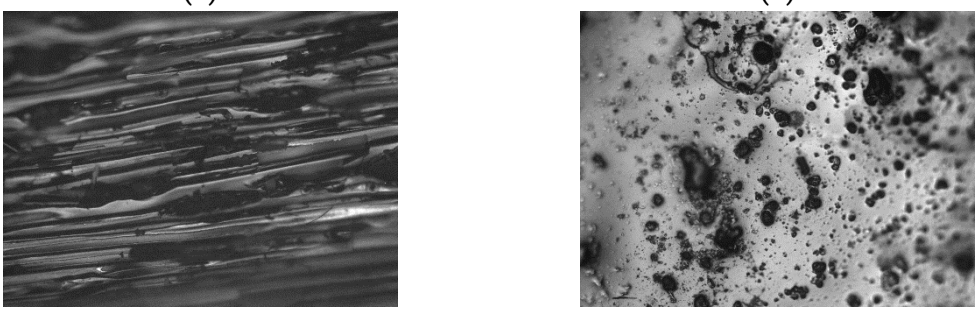

Figure 9. X-ray CT image of the bond layer of CLT: a) CLT with Purbond polyurethane adhesive and b) CLT with modified adhesive

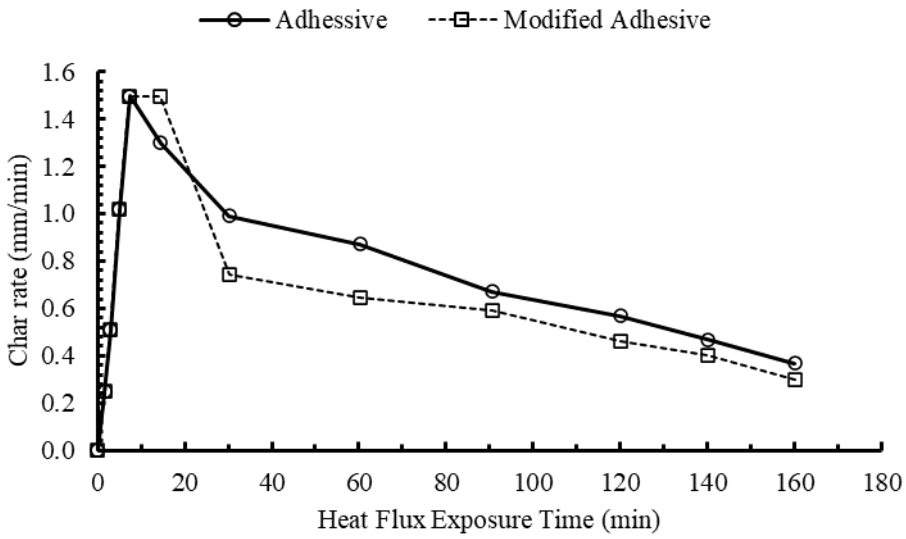

Figure 10. Experimental charring rates of CLT panel after various durations of fire exposure.

4.1.2 Residual strength

An experimental test has been conducted to evaluate the effect of increasing heat exposure duration on post-fire compression and bond strength. The post-fire compression strength decreased with increasing heat exposure duration for the CLT made with general adhesive and modified adhesive (Figure 11). Similar behaviour was observed in the bond strength of the adhesive (Figure 12). Further, the compressive strength reduction after two-hour fire exposure was about 30% less in the CLT made with modified adhesive (Figure 11). Figure 12 shows that the bond strength retained after two hours of fire in the general adhesive is 45% less than that of from modified adhesive.

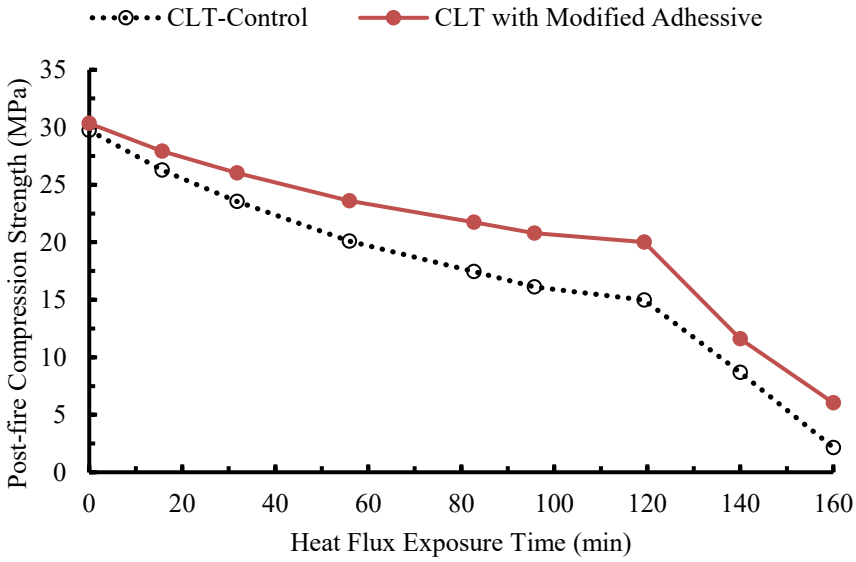

Figure 11. Residual compressive strength of CLT

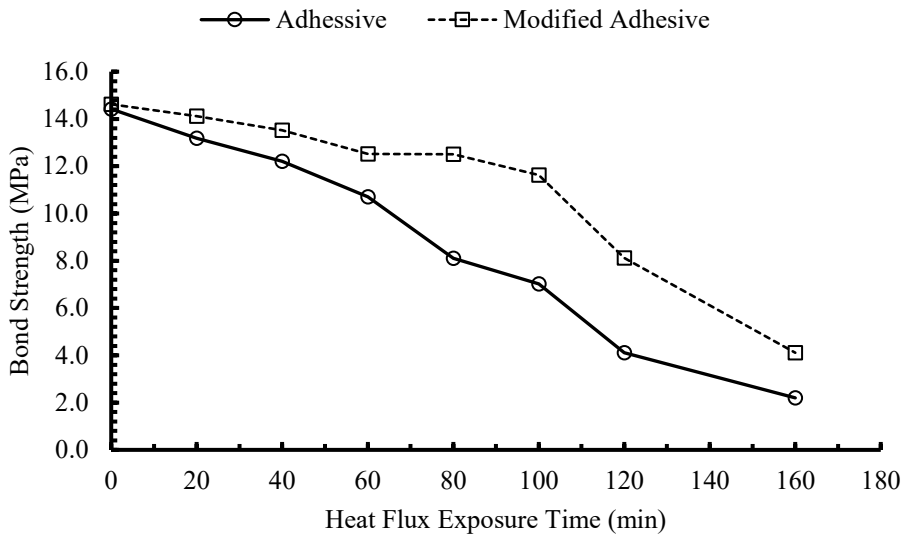

Figure 12. Residual bond strength

4.2 Developing an analytical model to predict the residual compressive strength

Based on the experimental results of this study and literature review data, this study proposed an analytical model to predict the residual compressive strength of CLT post-fire. This model has the capability to predict the residual compressive strength of CLT, which is made with any timber. The model considers the number of layers, density, fire exposure duration and surface temperature as variables to predict the residual CLT compression strength. Variation in density has been reported to significantly influence the material and strength properties of timber. A linear correlation between timber density and the compressive strength parallel to the grain has been reported. Based on these reported findings, this study proposes to derive a linear correlation between the density and residual CLT compressive strength post-fire. The experimental data of this research and the data reported in the literature are used as the basis to derive the linear correlation.

Figure 13 shows the average density vs compressive strength of soft timber. Using a similar approach reported by Tian et al. [22], the following linear regression equation was derived to correlate timber density to compressive strength parallel to the grain:

$$f_{c//} = 0.1508\,\bar{\rho} - 44.712 \qquad (1)$$

where, $f_{c//}$ is the compressive strength of timber parallel to the grain direction and $\bar{\rho}$ is the average timber density.

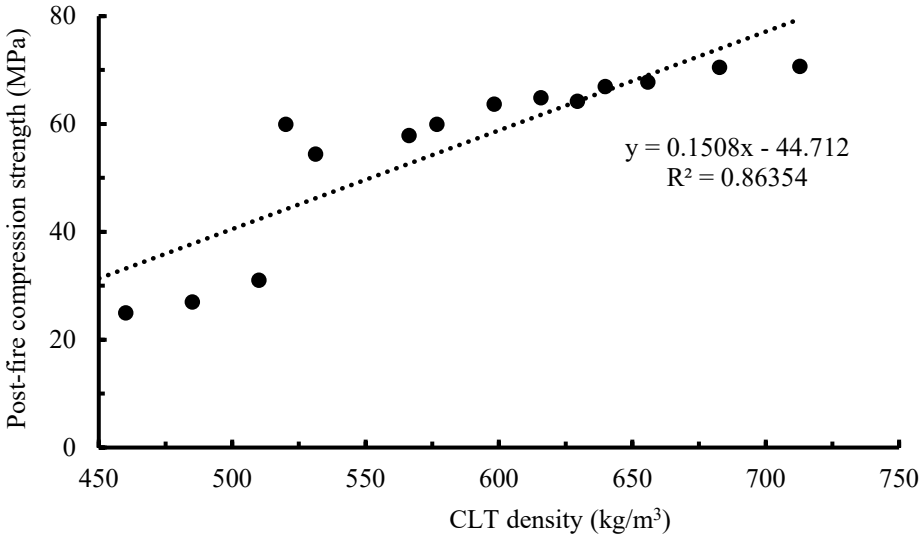

Figure 13. Relationship between average density and compressive strength parallel to the grain direction

The temperature-time dependent CLT density variation with increasing fire exposure duration can be expressed by Eq. 2. Here, the fire exposure duration and CLT surface temperature were used with the response surface method to derive the regression equation (Eq. 2). The regression coefficients were estimated via fitting the regression equation to the response surface values observed at a set of data points. A similar approach has been as used for structural engineering applications.

$$\bar{\rho} = \rho_R - 0.01192T - t \quad (2)$$

where, ρ_R is the CLT density (kg/m^3) at room temperature, and *T* is the surface temperature (^oC) of the CLT after *t* minutes of fire exposure. A comparison of the calculated and experimentally measured CLT density during a fire is presented in Figure 14, and the agreement was excellent. While the model agreement is excellent, validation has only been demonstrated for CLT made using Australian Radiata Pine timber and more experimental tests are needed for validation of CLT made using different timber species.

Tian et al. [22] reported the compressive strength of CLT can be calculated from the timber compressive strength parallel to the grain using Eq. 2. In this equation, *i* and j are, respectively the number of lamina layers parallel and perpendicular to the loading direction, *κ* is the contribution of compressive resistance from the lamina layers located in perpendicular to the loading and $f_{c//}$ is the timber compression strength parallel to the grain.

$$\overline{f_{CLT}} = \frac{i+jK}{i+j} f_{c//} \quad (3)$$

In this study *i* and *j* are respectively 2 and 1, and the compressive strength of the XLG1 grade Radiata Pine timber parallel to the grain is assumed to be approximately 28 MPa. The CLT compression strength at ambient temperature was measured to be 29.5 MPa. By

rearranging Eq. 3 the value of κ was determined to be 1.134 for this CLT type. In reality, the mechanical properties of timber are temperature dependent and during fire time dependent. Eq. 3 can therefore be rewritten for the residual compression strength post-fire exposure as:

$$\overline{f_{CLT}(T,t)} = \frac{2+1\times1.134}{3} f_{c//}\,(T,t) \qquad (4)$$

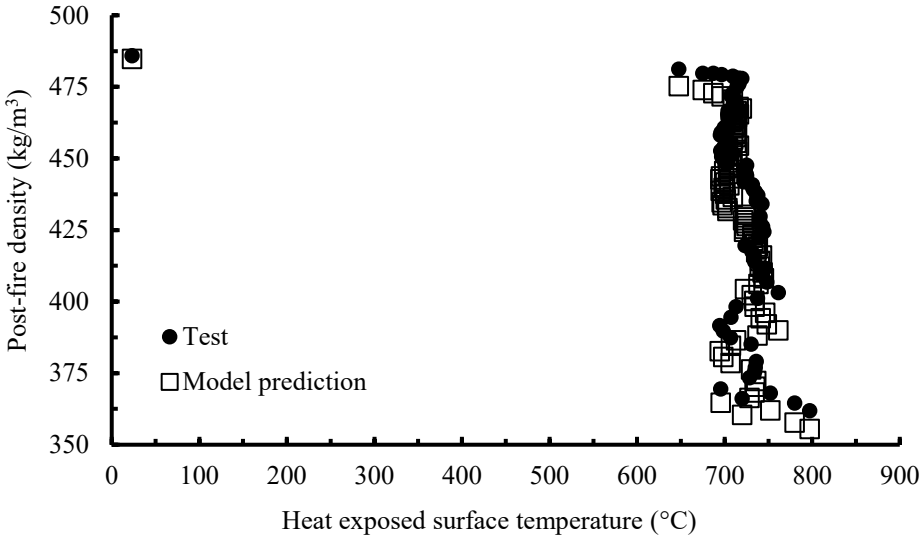

Figure 14. Comparison of the analytically determined (open squares) and experimentally measured (dots) CLT density for different surface temperatures.

Combining Eqns. 1, 2, and 4, the residual CLT compression strength can be expressed as:

$$\overline{f_{CLT}}(T,t) = 1.054\,[0.1508(\rho_R - 0.01192T - t) - 44.712] \qquad (5)$$

Figure 15 shows the comparison of the experimentally measured and numerically calculated residual CLT compressive strength. Results show that the proposed model can predict the residual compressive strength post-fire with reasonable accuracy. The variation between model prediction and experimental tests was a maximum of about 15% when the CLT was exposed to fire for 90 min. This variation was about 30% when the CLT was exposed to fire for 120 min. Thus, the proposed model is more accurate in predicting the compressive strength when the fire exposure duration of 90 min. However, the proposed model can be improved by incorporating more experimental data to predict the compressive strength of CLT exposed fire beyond 90 min.

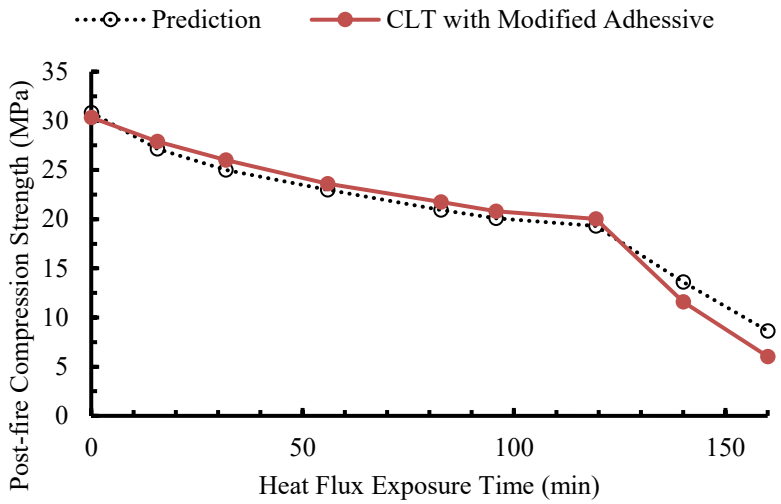

Figure 15. Comparison of the analytically modelled and experimentally determined residual compressive strength of the CLT post-fire exposure

4.3 Structural fire assessment of CLT panel

4.3.1 Experimental test

Flaming of the CLT panel was observed at 2 mins 25s. Thermocouples were used to obtain the temperature data of the panel, and 11 thermocouples were used in the test. The experimental temperature data on the beam thermocouple points are given in Figure 16. The results show that up to point 3 (60 mm), the panel shows uniform temperature decrease where temperatures are 1025^{0}C, 886^{0}C, and 741^{0}C, respectively. The temperature at 80 mm and 100 mm depth shows a higher decline which is 308^{0}C and 70^{0}C. The temperatures beyond 100 mm are not significantly affected by the fire, where the maximum temperature is only reached up to 20^{0}C. Figure 17 shows the failure of the CLT panel during the fire test.

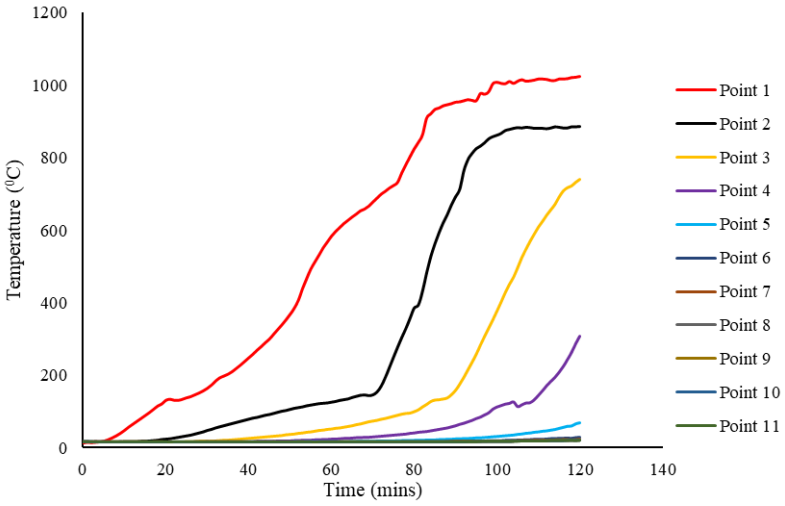

Figure 16. Temperature variation observed at the different depths in the experimental test

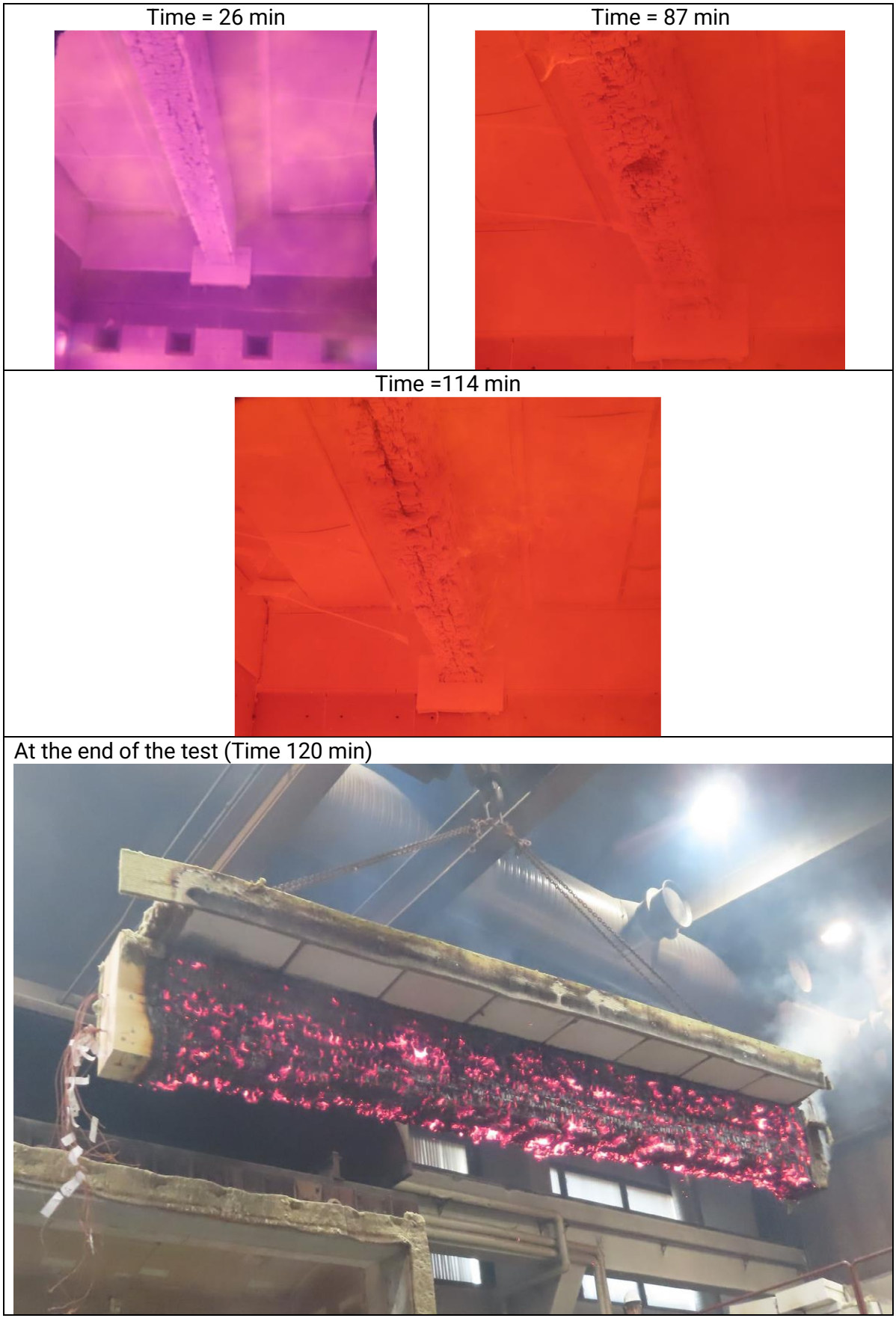

Figure 17. Failure of CLT panel during a fire

4.3.2 Numerical model of CLT panel under fire

Timber is anisotropic and heterogeneous material; assessing the behaviour of timber through numerical modelling requires additional expertise. Modelling the behaviour of timber under fire adds extra complexities due to the non-uniformities in chemical compounds in timber and reactions like pyrolysis. In this study, ABAQUS software with a VUMAT subroutine was used to model the CLT panel. To reduce the computational duration, this study developed a quarter of the tested CLT panel (Figure 18). Three models were developed and combined to develop the numerical structural fire model. First, the fire model was determined considering the room geometry, fuel loads and fire characteristics. In this analysis, ISO 834 standard fire curve was used, which is represented by Equation 06 (temperature(*T*), time(*t*)). Secondly, the heat transfer model was developed. Heat transfer coefficients and thermal properties of timber with element geometry were used for this model. The convective heat transfer coefficient was taken as 25 $Wm^{-2}K^{-1}$, while the surface emissivity of timber and fire emissivity was taken as 1.0 and 0.8. Specific heat values and density ratios presented in Eurocode 5 part 1.2 was adopted in the model. Figure 19(a) shows the variation specific heat capacity of timber with temperature, while Figure 19(b) shows the density ratio of timber, taking the initial moisture content of timber beam as 10.3%. Since the numerical model was modelled using ABAQUS finite element modelling software, coupled temperature displacement elements (C3D8T) and 8-node thermally coupled brick elements were used in the modelling. The adhesive bond between longitudinal and transvers lamellae timbers was replaced by surface-to-surface cohesive contact, and the cohesive properties were obtained from experimental tests (Section 4.1.2). Both normal (Knn) and shear stiffness (Kss and Ktt) of adhesive were taken as same, and fracture energy (Gf) was taken as 0.92 N/mm. Finally, the constitutive model, which is based on the stress-strain relationship, was used for the modelling of the structural model. The structural model was developed in the code of the user subroutine, while the other models were directly input user interface of ABAQUS.

A number of theories and equations were used in the modelling of the constitutive model considering the differences in the longitudinal (L), radial (R) and tangential (T) directions. Elastic constructive equations for orthotropic materials were used in the modelling which is given in Equation 02. Here σ, ε and v represent the stress, strain and the Poisson's ratio in considered directions, while E and G represents the young's modulus and shear modulus.

$$\begin{bmatrix}\sigma_{11}\\ \sigma_{22}\\ \sigma_{33}\\ \sigma_{12}\\ \sigma_{23}\\ \sigma_{31}\end{bmatrix} = \begin{bmatrix} D_{1111} & D_{1122} & D_{1133} & 0 & 0 & 0 \\ D_{1122} & D_{2222} & D_{2233} & 0 & 0 & 0 \\ D_{1133} & D_{2233} & D_{3333} & 0 & 0 & 0 \\ 0 & 0 & 0 & D_{1212} & 0 & 0 \\ 0 & 0 & 0 & 0 & D_{2323} & 0 \\ 0 & 0 & 0 & 0 & 0 & D_{3131} \end{bmatrix} \begin{bmatrix}\varepsilon_{11}\\ \varepsilon_{22}\\ \varepsilon_{33}\\ \varepsilon_{12}\\ \varepsilon_{23}\\ \varepsilon_{31}\end{bmatrix} \quad -Equation\ (7)$$

$$D_{1111} = E_L(1 - \nu_{RT}\nu_{TR})\, g$$

$$D_{2222} = E_R(1 - \nu_{LT}\nu_{TL})\, g$$

$$D_{3333} = E_T(1 - \nu_{LR}\nu_{RL})\, g$$

$$D_{1122} = E_L(\nu_{RL} + \nu_{TL}\nu_{RT})\, g = E_R(\nu_{LR} + \nu_{TR}\nu_{LT})\, g$$

$$D_{1133} = E_L(\nu_{TL} + \nu_{RL}\nu_{TR})\, g = E_T(\nu_{LT} + \nu_{LR}\nu_{RT})\, g$$

$$D_{2233} = E_R(\nu_{TR} + \nu_{LR}\nu_{TL})\, g = E_T(\nu_{RT} + \nu_{RL}\nu_{TL})\, g$$

$$D_{1212} = 2G_{LR}$$

$$D_{2323} = 2G_{RT}$$

$$D_{3131} = 2G_{LT}$$

$$g = {}^{1}/_{1 - \nu_{LR}\nu_{RL} - \nu_{RT}\nu_{TR} - \nu_{TL}\nu_{LT} - 2\nu_{RL}\nu_{TR}\nu_{LT}}$$

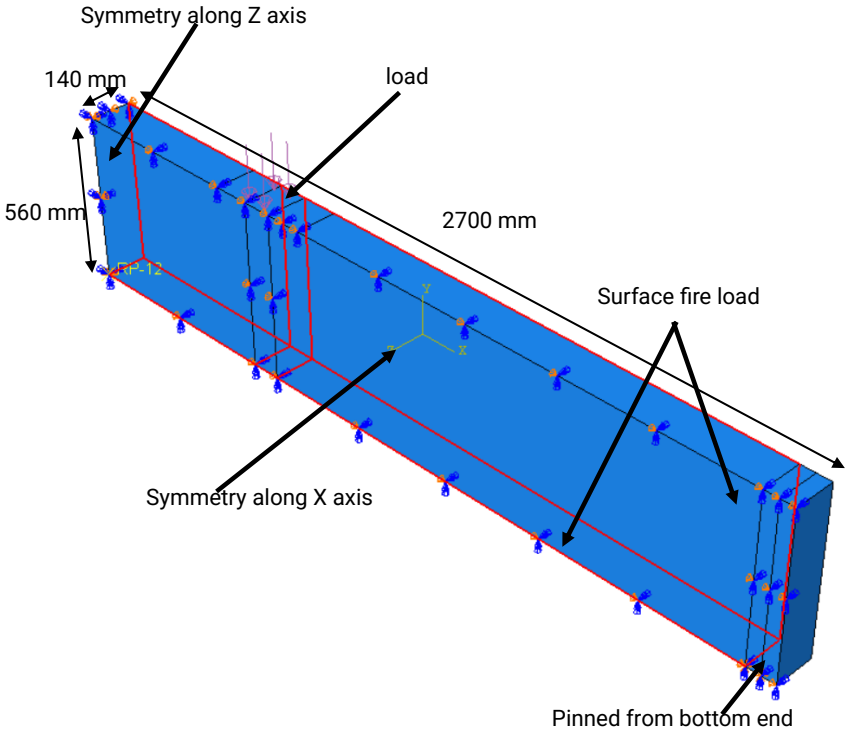

Figure 18. FEM of tested CLT panel

$$T = 20 + 345 \times \log(8t + 1) \qquad -Equation\ (6)$$

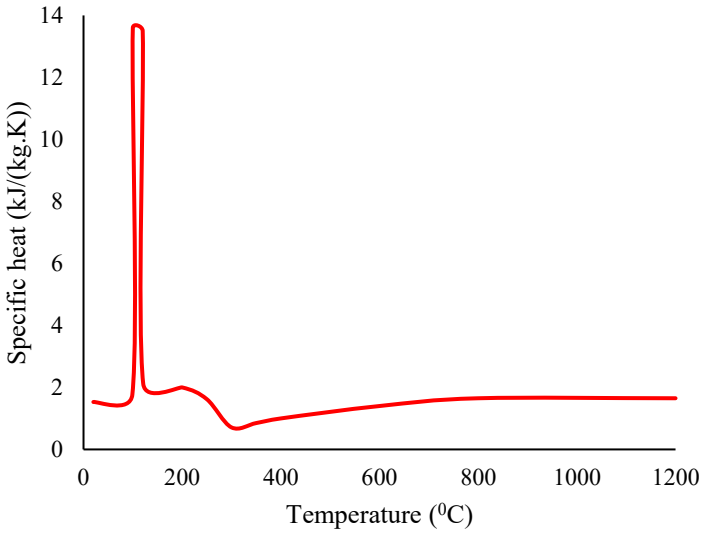

(a)

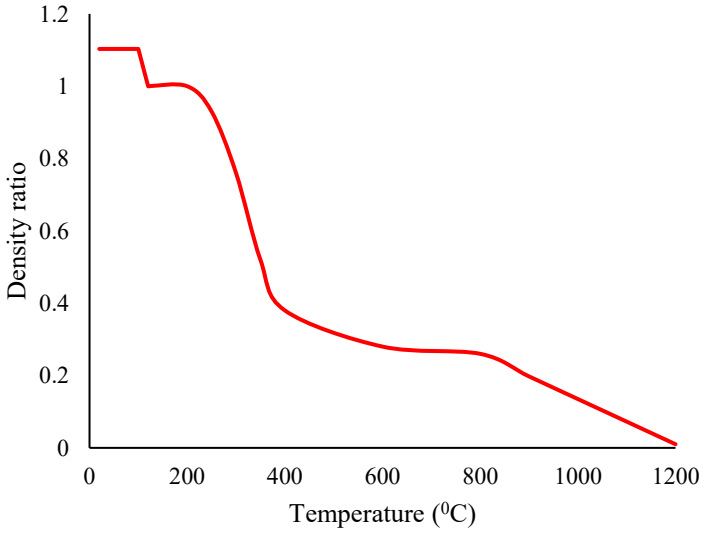

(b)

Figure 19. Thermal properties: (a) Variation of specific heat with temperature; and (b) Variation of density ratio with temperature

Considering the significant strength variation in each direction, the equations 03, 04 and 05 which are derived from extended Yamada-sun strength criterion was used in the model in predicting the failure in the considered directions. In the equations, σ_O represent the strengths in considered directions, where σ_{LO} represent the axial strength in I direction while σ_{LRO} represents the shear in LR plane. The *t* and *c* afterwards represent the tensile or compressive aspects of the strength. Post-peak softening, plastic flow and hardening were also in cooperated in the model.

$$\frac{{\sigma_{11}}^2}{{\sigma_{LO}}^2}+\frac{{\sigma_{12}}^2}{{\sigma_{LRO}}^2}+\frac{{\sigma_{31}}^2}{{\sigma_{TLO}}^2}\leq 1 \quad \sigma_{LO}=\begin{cases}\sigma_{LO,t} & if\ \sigma_{11}\geq 0\\ \sigma_{LO,c} & if\ \sigma_{11}<0\end{cases} \quad -Equation\ (8)$$

$$\frac{{\sigma_{22}}^2}{{\sigma_{RO}}^2}+\frac{{\sigma_{12}}^2}{{\sigma_{LRO}}^2}+\frac{{\sigma_{23}}^2}{{\sigma_{RTO}}^2}\leq 1 \quad \sigma_{LO}=\begin{cases}\sigma_{RO,t} & if\ \sigma_{22}\geq 0\\ \sigma_{RO,c} & if\ \sigma_{22}<0\end{cases} \qquad -Equation\ (9)$$

$$\frac{{\sigma_{33}}^2}{{\sigma_{TO}}^2}+\frac{{\sigma_{31}}^2}{{\sigma_{TLO}}^2}+\frac{{\sigma_{23}}^2}{{\sigma_{RTO}}^2}\leq 1 \quad \sigma_{LO}=\begin{cases}\sigma_{TO,t} & if\ \sigma_{33}\geq 0\\ \sigma_{TO,c} & if\ \sigma_{33}<0\end{cases} \qquad -Equation\ (10)$$

Temperature influence on the structural model was also taken into consideration. The effect of temperature on modulus of elasticity and strength in the longitudinal direction is given in Figure 20.

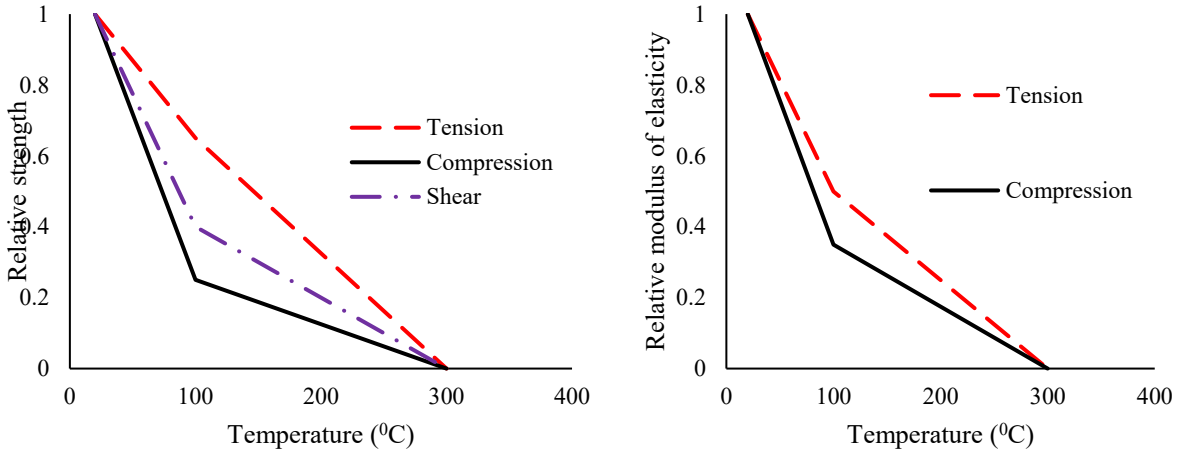

(a) (b)

Figure 20. Effect of temperature on: (a) Strength; and (b) Modulus of elasticity

Among all the locations of the thermocouple, temperatures that were taken at points 01 and 02 along the panel centreline in the experimental tests were compared with the temperature data of the numerical model. The comparison of the resultant temperature is presented in Figure 21. The temperature at 20 mm at the end of 120 minutes is 1025 ^{0}C, while the numerical analysis gives a temperature of 1009 ^{0}C. The maximum furnace temperature and the minimum furnace temperature recorded in the 120th minute are 1093^{0}C and 1049^{0}C, while the temperature at the end of 120 minutes, according to the standard fire curve ISO 83,4 is 1050^{0}C. Numerical analysis data shows a similar trend in the increasing temperature for both points 01 and 02, while in the experimental results sudden increase in temperature was observed at 70 mins time. The variation in these temperature values at different places of the beam and the variation of properties along the beam due to its heterogeneousness explain the changes in the temperature curve.

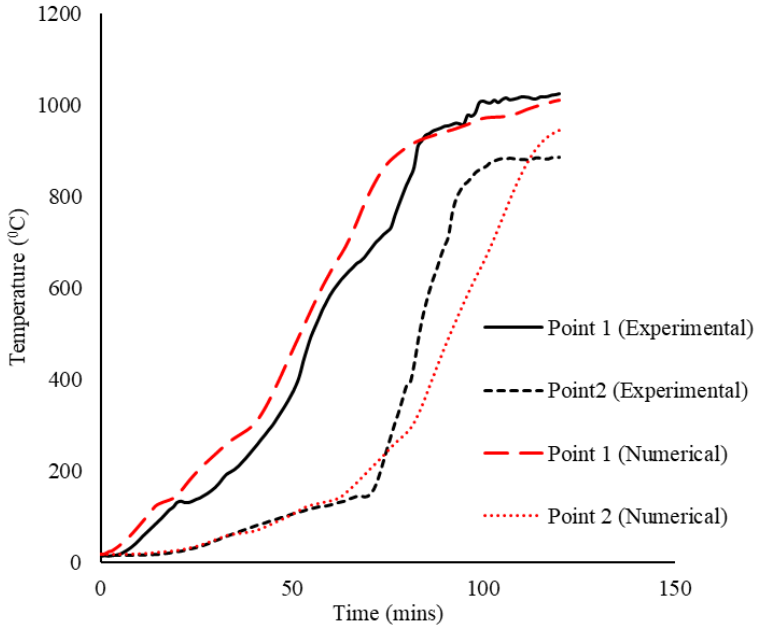

Figure 21. Comparison of the temperature variation of two points in the experimental and numerical test

Figure 22 gives the comparison of CLT panel displacement data at the beam midspan. The displacement at the end of loading (15 mins) without fire is 6 mm. The numerical test shows a near uniform increment where the displacement at 120 mins from the time where the fire started is 25 mm. The experimental test also shows a similar increase in displacement at the end of 20 minutes, but the rate of increasing the displacements shows a different pattern than in the numerical test. From about the 76th minute, the displacement shows a rapid increment in the values.

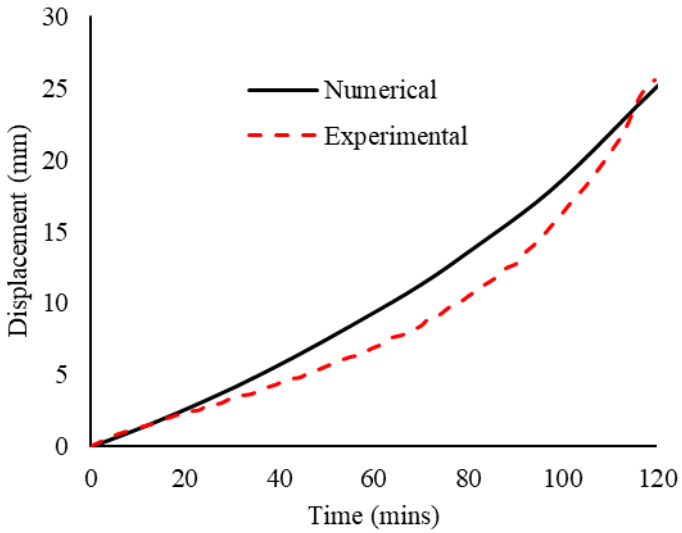

Figure 22. Comparison of midspan deflection between the numerical model and experimental tests

Figure 23 presents the charred layer of the CLT panel at the end of the analysis, while Table

2 compares the charring rate between experimental data and numerical analysis. The experimental setup shows an uneven fire-damaged surface where the width of the remaining section changes from about 110 mm to 138 mm in the specimen. While in the numerical model analysis, it varied between 140 mm to 144 mm. The remaining length of 480 mm was observed in the experimental test, while a length of 483 mm was observed in the numerical test.

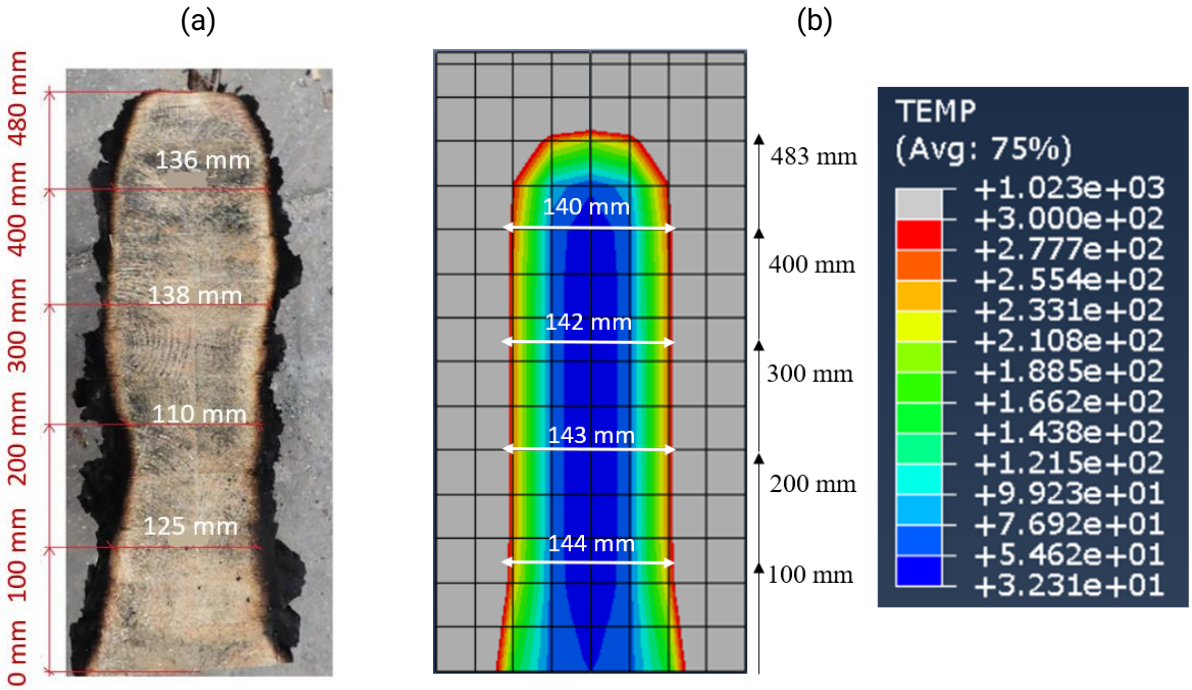

Figure 23. Charred beam cross-sections of: (a) Experimental test (b) Numerical model analysis

Table 4 presents the charring rates of the CLT panel observed in three experimental tests and the numerical model analysis. The charring was considered to happen at 300^0C, and the time taken to reach that temperature at each considered depth was used to calculate the charring rate. The minimum charring rate observed for experimental beams at 20 mm depth is 0.48 mm, while the maximum is 0.52 mm. The charring rate increases with the CLT panel depth where 26%, 5% and 16% increases were observed in the rates at 40 mm depth in the three specimens. At the 60 mm depth, rates increased up to 56%, 40% and 38% from the rates at 20 mm. Compared with the experimental test data, charring rates of the numerical tests are showing similar numbers for all the depths, where no increase is shown at 40 mm and a 4% increase at 60 mm compared to the rate at 20 mm. Overall, the numerical model analysis results show that the proposed model approach can simulate similar experimental behaviour. Thus, the model can predict the fire performance of the CLT panel.

Table 4. Charring rate of the three experimental specimens and the numerical model

	Experimental test			Numerical test
	Specimen 1	Specimen 1	Specimen 1	
Depth	Charring rate (mm/min)	Charring rate (mm/min)	Charring rate (mm/min)	Charring rate (mm/min)
20	0.45	0.52	0.48	0.49
40	0.61	0.55	0.57	0.49
60	1.06	1.28	0.78	0.51

The validated FEM was then used to predict the fire performance of the CLT panel made with modified fireproof epoxy. Figure 24 compares the midspan deflection of the CLT panel between panels made with modified fireproof epoxy and standard adhesive. This figure indicates that the modified fireproof adhesive can help to improve the fire performance of CLT. Thus, it can reduce the midspan deflection by 30% compared to that of the panel made with traditional adhesive.

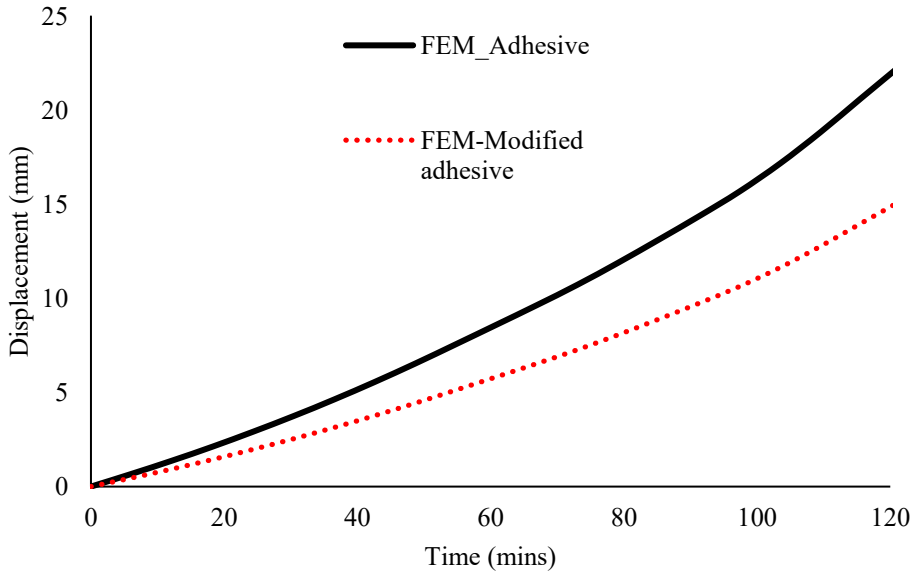

Figure 24. Comparison of midspan deflection between panels made with traditional and modified fireproof adhesive.

4.4 Robustness of mass timber building under localized fire

The CLT floor on Level 3 (between Grid C-D and Grid 6-7) was considered being subjected to a fire. The spread of the fire was represented through the removal of certain sections of the CLT floor at certain time periods. The displacement profile of the building at 30-minute time intervals during the propagation of the fire is shown in Figure 25. It can be observed that the failure due to the fire propagation across the floor had localized effects on the overall building. The damage due to the fire mainly affected the floor panel at which the fire was

initiated, and the adjacent floors were not much affected.

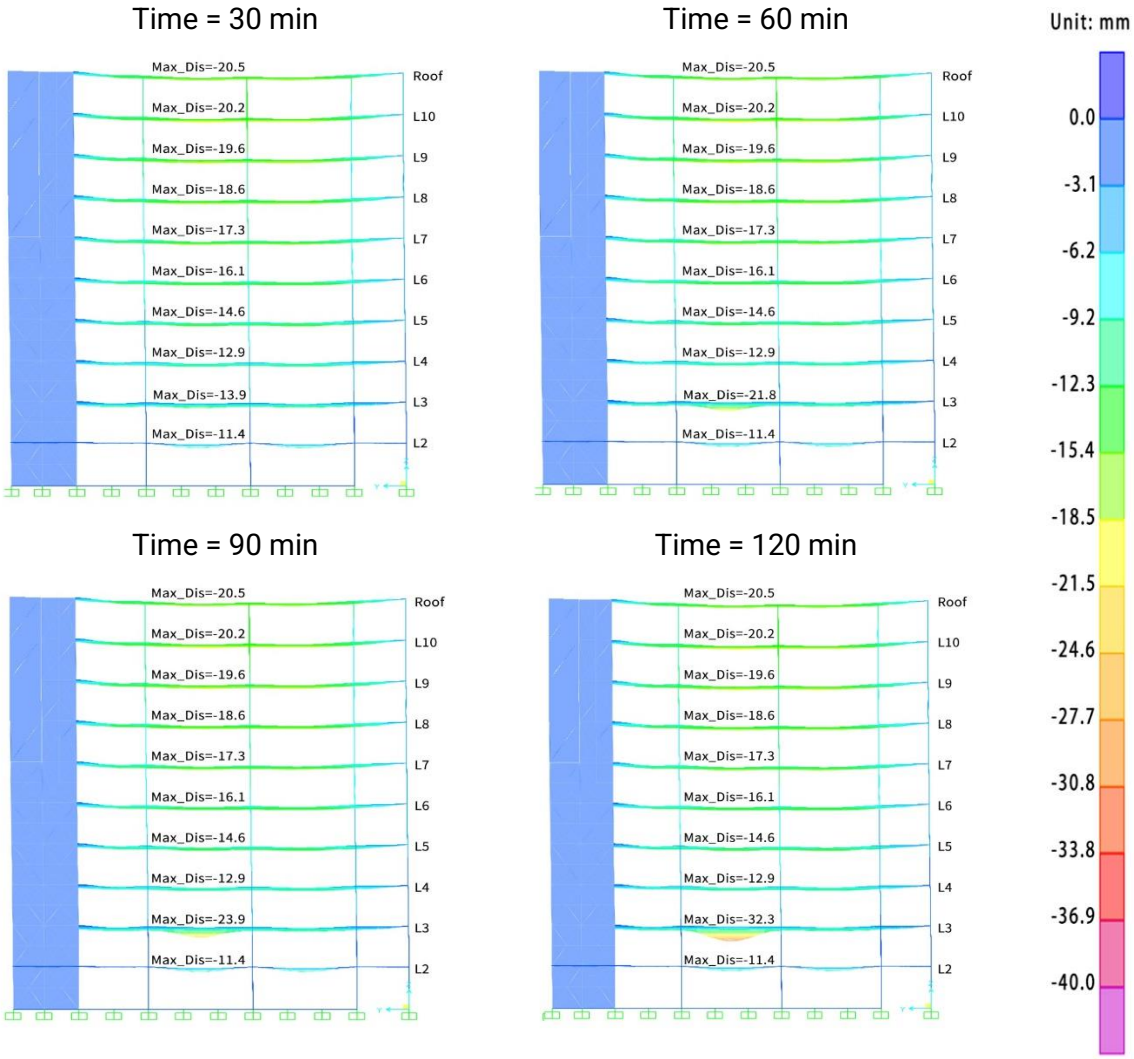

Figure 25. Displacement profile of the building at 30 min intervals during fire propagation

Figures 26 and 27 show the deformation of the floor panel (on the 3rd floor where the fire was initiated). The CLT floor panel was made with standard adhesive, as presented in Figure 26, while Figure 27 shows the CLT floor panel was made with modified adhesive. It was observed that the fire propagation resulted in an increase in the maximum deformation of the floor panel. As the spreading of the fire results in a reduction of the floor thickness, the location at which the maximum deformation is occurring is subject to change with respect to time. These figures illustrate that the CLT floor panel made with a normal adhesive experiences high deformation and thickness reduction (Figure 26) compared with that of from CLT floor panel made with a modified adhesive. The maximum deflection observed after 120 min of fire exposure was 92.5 mm when the CLT floor was made with Purbond polyurethane adhesive (i.e. common adhesive). In contrast, the maximum deflection of 39.3

mm occurred after 120 min of fire when the CLT floor was made with modified fireproof adhesive. This was less than the serviceability deflection (i.e. 40 mm). This indicates that the floor does not fail and is structurally capable of evacuating the people when the CLT panel is made with modified fireproof adhesive.

This indicates that the modified adhesive can be used to improve structural safety and evacuation time. As the thickness reduction and deformation are less than the CLT made with traditional adhesive. In this model, the structural element subjected to the fire was a CLT floor panel. The effects of such an element undergoing fire have effects on the overall building, and the damage does not result in progressive collapse. In reality, a fire initiated in a building will not be localized within a single panel, and a high probability exists of the fire being spread into load-bearing elements such as beams, columns, walls etc. The effect of such an expanded fire could result in progressive collapse. Therefore, further studies are necessary to conclude the structural effect of these implications.

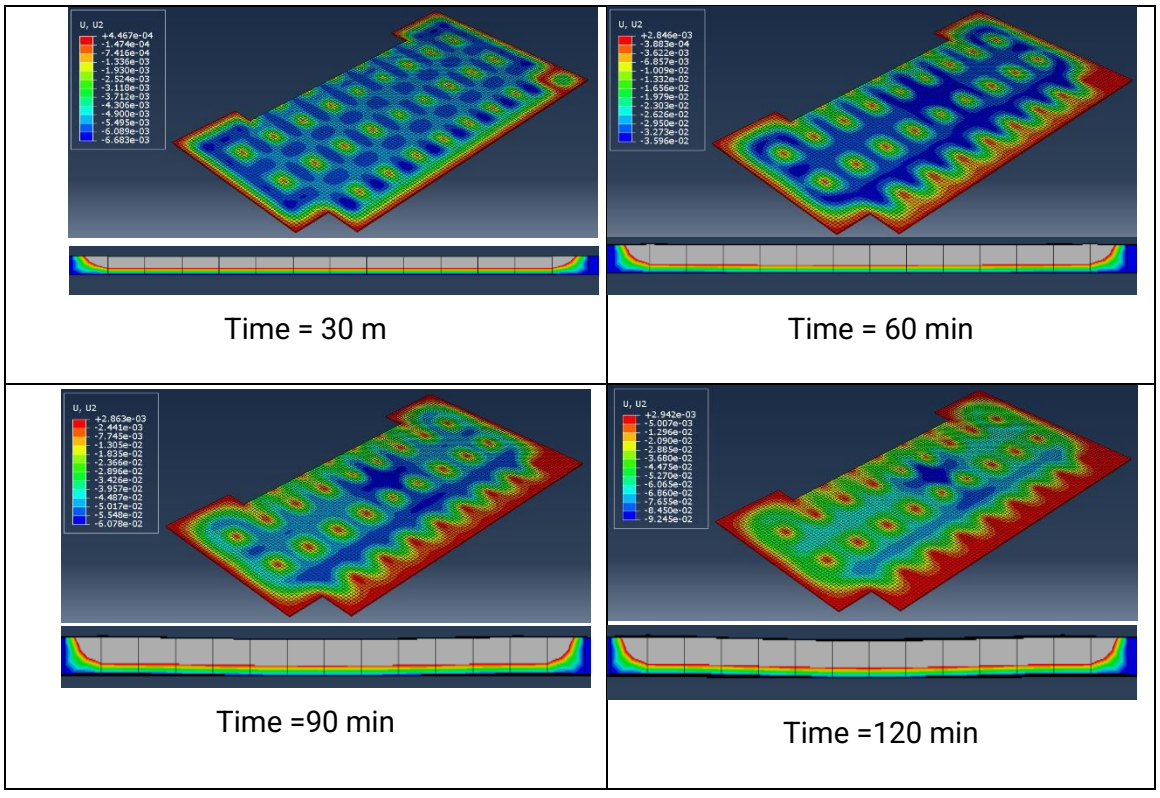

Figure 26. Deformation of floor panel on the 3rd floor, the panel was made with common adhesive

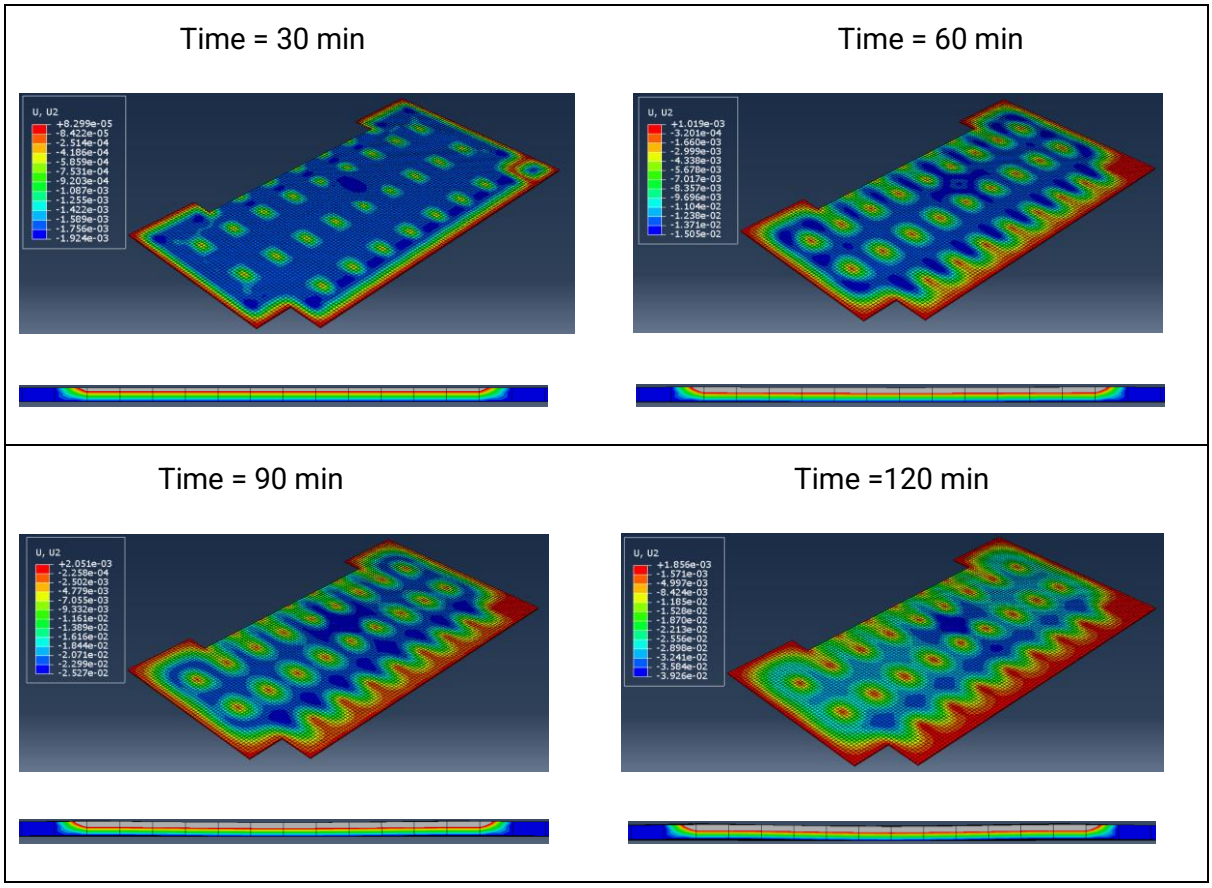

Figure 27. Deformation of floor panel at the 3rd floor, the panel was made with modified adhesive

5. Enablers and Barriers

In this research project, develop a fireproof modified adhesive to improve the robustness of mass timber buildings under fire. To ensure the capability of modified fireproof adhesive, the experimental tests and numerical model analysis were conducted on the timber species from Australia. Thus, the results from these experimental results are limited to Australian-made cross-laminated timber. However, the validated numerical model and analytical model enable to predict the fire performance and post-fire residual strength of cross-laminated timber, which is made from different countries' timber species. Further, in this research project, a limited number of experimental tests were conducted due to the limited funds.

6. Key Takeaways from CDRI Fellowship Programme

The major takeaways from this CDRI Fellowship project:

1) The fireproof modified adhesive to improve the fire performance of cross-laminated timber.
2) The developed numerical model approach to predict the fire performance of cross-laminated timber.
3) Charring rate of cross-laminated timber, which can be used for the fire design of mass timber buildings.
4) The developed analytical model can be used to predict the residual compressive strength of cross-laminated timber.

7.Conclusion

The cross-laminated timber (CLT) is a major construction material used in mid-to-high-rise mass timber buildings. The combustibility nature of CLT limits its application in mass timber building constructions. Localized fires induce delamination failures in the adhesive bond of CLT, soften and decompose, which causes rapid strength reduction and progressive collapse of the whole building. Thus, this study developed a modified fireproof adhesive to improve fire performance. A combined experimental and modelling analysis is presented to predict the post-fire residual compressive and bond strength. Multiple experimental fire exposure tests are performed to characterise the thermal response of the CLT. The numerical model of the 10-storey mass timber building was developed and subjected to localized fire. Based on this analysis following conclusions are highlighted:

1) The charring rate of CLT made with traditional adhesive can be reduced by about 20% when CLT is made with newly developed fireproof adhesive. This will improve the fire performance of CLT.
2) The residual compressive strength of CLT, after two-hour fire exposure, can be increased by about 20% when CLT is made with the fireproof adhesive.
3) Based on the serviceability limit stats design, the robustness of mass timber buildings under localized fire can be improved. When the floor panel is made with modified fireproof adhesive.

Overall, mass timber buildings' robust structural fire performance will benefit consumers and engineered timber manufacturers. The developed methodology and modified fireproof epoxy resin adhesive improve the strength and fire performance of CLT. Thus, increasing the population of mas timber building and revenue for the mas timber construction industry and engineered timber manufacturers. In the long term, the performance-based solution for mass timber buildings is a potential solution to extend the height of mass timber buildings

and loosen the height restriction of timber buildings while reducing the high carbon-intensive construction materials.

Further, the outcome of this research will help to improve the fire safety regulation and building certification legations. As this research proposes a numerical model to assess the post-fire status of mass timber buildings. This will help the certifier and designer assess their design and ensure the safety of occupants. This will train future generations to use engineered timber products and transfer the acquired knowledge to the construction industry.

8. Way Forward

The proposed modified fireproof epoxy resin adhesive is novel and innovative as it seeks to bring about a step-change in the performance of engineered timber composite structural products through harnessing composite action and improving fire performance. This project addresses the current need to improve the fire performance of mass timber buildings. This study proposes the advanced finite element model to predict the post-fire status of mass timber buildings. In addition, the developed model will help to improve the performance-based design of mass timber buildings, structural stability, and ensure the safety of occupants. However, the finding from this research is based on limited experimental (i.e. material and large-scale) tests. Further, results are limited for Australian radiata pine timber. Thus, the application of the experimental results is limited to the Australian timber and construction industries. However, the outcomes from this study proved the capability proposed by modified fireproof epoxy.

Following further research is needed to ensure the finding of this research further:

1) Large-scale structural fire testing of CLT panel made with modified fireproof epoxy.
2) Material scale and large-scale fire tests need to be conducted on the CLT made with different timber species and modified fireproof epoxy.
3) The fire performance of connections that are used in mass-timber buildings needs to be evaluated to improve the finite element models further.

This will enable research and training for future generations as a higher degree by research (PhD). This will help to train future generations to use engineered timber products and transfer the acquired knowledge to the construction industry.

References

1. Li, J. Li, B. Rismanchi, T. Ngo, Feasibility study to estimate the environmental benefits of utilising timber to construct high-rise buildings in Australia, Building and environment 147 (2019) 108-120.
2. S. Navaratnam, D. Widdowfield Small, P. Gatheeshgar, K. Poologanathan, J. Thamboo, C. Higgins, P. Mendis, Development of cross laminated timber-cold-formed steel composite beam for floor system to sustainable modular building construction, Structures 32 (2021) 681-690.
3. X. Li, M. Ashraf, M. Subhani, P. Kremer, H. Li, M. Anwar-Us-Saadat, Rolling shear properties of cross-laminated timber (CLT) made from Australian Radiata Pine – An experimental study, Structures 33 (2021) 423-432.
4. M. Jeleč, D. Varevac, V. Rajčić, Cross-laminated timber (CLT)-a state of the art report, Gradevinar 2 (2018).
5. S. Navaratnam, T. Ngo, T. Gunawardena, D. Henderson, Performance Review of Prefabricated Building Systems and Future Research in Australia, Buildings 9(2) (2019) 38.
6. S. Navaratnam, P.B. Christopher, T. Ngo, T.V. Le, Bending and shear performance of Australian Radiata pine cross-laminated timber, Construction and Building Materials 232 (2020) 117215.
7. NCC, National Construction Code (NCC) series Australian Building Codes Board, Australia, 2019.
8. J. Liu, E.C. Fischer, Review of large-scale CLT compartment fire tests, Construction and Building Materials 318 (2022) 126099.
9. F. Wiesner, L.A. Bisby, A.I. Bartlett, J.P. Hidalgo, S. Santamaria, S. Deeny, R.M. Hadden, Structural capacity in fire of laminated timber elements in compartments with exposed timber surfaces, Engineering Structures 179 (2019) 284-295.
10. Y. Bai, J. Zhang, H. Shen, Residual compressive load-carrying capacity of cross-laminated timber walls after exposed to one-side fire, Journal of Building Engineering 34 (2021) 101931.
11. Z. Xing, J. Zhang, C. Zheng, C. Lu, Experimental study and finite element analysis on residual carrying capacity of CLT wall-floor angle bracket connections after fire, Construction and Building Materials 328 (2022) 127113.
12. XLam, XLam: Australian Cross Laminated Timber Panel Structural Guide, 2017.
13. SmartLam, SmartLam GL17S Design Guide, 2018.

14. E. Karacabeyli, B. Douglas, CLT Handbook, FPInnovations, 2013.
15. S. Navaratnam, J. Thamboo, T. Ponnampalam, S. Venkatesan, K.B. Chong, Mechanical performance of glued-in rod glulam beam to column moment connection: An experimental study, Journal of Building Engineering 50 (2022) 104131.
16. NIST, Questions and Answers about the NIST WTC 7 Investigation 2010.
17. L. Franzoni, D. Dhima, A. Lebée, G. Foret, A Stiffness-based Approach to Analyze the Fire Behaviour of Cross- Laminated Timber Floors, Structural Engineering International 27(2) (2017).
18. S.T. Craft, R. Desjardins, J.R. Mehaffey, Investigation of the behaviour of clt panels exposed to fire, 12th International Conference and Exhibition on Fire and Materials 2011, January 31, 2011 - February 2, 2011, International Association for Fire Safety Science, San Francisco, CA, United states, 2011, pp. 441-454.
19. M. Klippel, J. Schmid, R. Fahrni, A. Frangi, Assessing the adhesive performance in CLT exposed to fire, 2018 World Conference on Timber Engineering, WCTE 2018, August 20, 2018 - August 23, 2018, World Conference on Timber Engineering (WCTE), Seoul, Korea, Republic of, 2018.
20. J. Schmid, M. Klippel, A. Just, A. Frangi, M. Tiso, Simulation of the Fire Resistance of Cross-laminated Timber (CLT), Fire Technology 54(5) (2018) 1113-1148.
21. T.T. Tran, M. Khelifa, A. Nadjai, M. Oudjene, Y. Rogaume, Modelling of fire performance of Cross Laminated Timber (CLT) panels, 3rd European Symposium on Fire Safety Science, ESFSS 2018, September 12, 2018 - September 14, 2018, Institute of Physics Publishing, Nancy, France, 2018.
22. Z. Tian, Y. Gong, J. Xu, M. Li, Z. Wang, H. Ren, Predicting the Average Compression Strength of CLT by Using the Average Density or Compressive Strength of Lamina, Forests, 2022.

Financial Decision Framework for Infrastructures Based on Disaster Damage Rating Models Using Machine Learning Approaches

Saurabh Gupta
PhD Scholar
Indian Institute of Technology Kanpur, India

IIT KANPUR
Indian Institute of Technology, Kanpur

Under CDRI Fellowship Programme 2022-23

CDRI
Coalition for Disaster Resilient Infrastructure

Disclaimer: The views expressed in this paper reflect the opinions of the author and not necessarily the official views of CDRI.

Abstract

Disaster damage assessment plays a vital role not only in understanding the extent of destruction caused by a catastrophe but also in making informed financial decisions. Traditionally, this assessment has been a manual and time-consuming process. However, this study focuses on automating the process using remote sensing technologies and advanced computational methods to facilitate efficient and timely damage assessment. Additionally, this study highlights the significance of this work in supporting finance framework decisions. By automating the damage assessment process, it eliminates the need for manual data collection and analysis, saving valuable time and resources. Real-time damage assessment becomes possible, providing up-to-date information on the scale and severity of the disaster. This timeliness is crucial for making finance framework decisions, as it allows policymakers and financial institutions to quickly assess the financial implications of the disaster and allocate resources accordingly.

The approach in this study for disaster damage assessment uses a segmentation model capable of classifying and localizing different levels of damage, namely "destroyed," "major damage," "minor damage," and "no damage." The first task of our study involved building a localization model to accurately identify the regions within an image that were affected by the disaster. By leveraging advanced computer vision techniques, a model capable of precisely delineating the boundaries of damaged areas is developed. This localization step provides essential information for subsequent damage assessment and aids in targeted relief efforts. The second task focused on the actual assessment of the damage levels. A multi-class segmentation model that could classify the affected regions into one of the four predefined categories: "destroyed," "major damage," "minor damage," or "no damage" Is employed. This classification enables decision-makers and disaster response teams to prioritize their efforts, allocate resources effectively, and plan appropriate recovery strategies.

Different segmentation models and backbones were trained and experimented with as combinations on a large dataset of annotated disaster imagery. The dataset included various types of disasters and encompassed a diverse range of damage scenarios. State-of-the-art deep learning techniques and architectures were leveraged to ensure the model's ability to generalize and handle real-world disaster scenarios effectively. The experimental results demonstrate the effectiveness of the approach in accurately localizing and assessing disaster damage. Promising performance metrics, such as precision, recall, and F1 scores, indicate the model's ability to differentiate between different damage levels. It

was observed that the first task of building localization achieved an IoU score above 0.8 in most experiments, while the second task of disaster damage assessment achieved an F1 score of 0.72 and an IoU score of 0.68 using the best possible combination of the model architecture and backbone. These results emphasize the potential utility of the segmentation model in assisting disaster response and recovery efforts.

Overall, our research contributes to the field of disaster management by providing an automated and efficient method for damage assessment. By combining localization and multi-class segmentation techniques, that enable rapid and accurate identification of affected regions and detailed evaluation of damage severity. This information can aid decision-making processes, facilitate targeted resource allocation, and ultimately expedite the recovery process in the aftermath of disasters.

Acknowledgments

The authors would like to thank the CDRI Fellowship Programme and the CDRI Fellowship Team for providing financial and technical support for this research. We also acknowledge the suggestions of the TEG member Dr Dilip A Patel and Dr Diocel Harold M. Aquino at various stages of this research. The author is also grateful for the support and guidance provided by academic mentor Dr Syam Nair at IIT Kanpur.

The author also thanks Mrs. Vaishali Jain (Research Scholar, IIT Kanpur), for her help in developing machine learning models and writing reports. Also, Harsh Chaudhary, Muskan, Bedant Sharma and Rahul Jha (Under Graduates at IIT Kanpur) for implementing the machine learning model during the execution of the project.

Funding

This research was supported by the 2022–2023 Fellowship of the Coalition for Disaster Resilient Infrastructure (CDRI), Application ID: 210930771

1. Introduction

Immediately after a natural disaster strikes, one of the first critical tasks is to evaluate the extent of the damages incurred promptly. This crucial information is a vital resource for numerous organizations, enabling them to respond swiftly and potentially minimize the number of casualties. Effective planning and assessment based on this system are pivotal in facilitating short-term and long-term recovery efforts. However, it is important to acknowledge that damage detection and estimation accuracy may sometimes be compromised, displaying variations from the ground reality. Such uncertainties can be attributed to employing different data collection and interpretation techniques. Consequently, it becomes imperative to thoroughly investigate and study a wide range of data collection and interpretation methods to ensure the reliability and precision of the assessment process. By enhancing our understanding of these techniques, the assessment system, thereby strengthening disaster response and recovery operations can be refined.

In mapping damage caused by natural hazards, satellite and aerial imagery have emerged as valuable tools recently (Duda & Jones, 2011). With many satellites orbiting the Earth, equipped with high-resolution (less than 1 meter) sensors and increasingly frequent image captures, these advanced imaging technologies offer unprecedented capabilities. Their advantage over traditional satellite imagery is their ability to observe finer details and distinguish smaller objects. While some commercial satellite imagery companies provide post-disaster imagery with only three spectral channels, satellites typically capture images with more spectral bands. Moreover, commercially available satellites can revisit the same location on Earth multiple times a day, week, or month, depending on the specific satellite system. Companies like Planet Earth and Maxar, formerly Digital Globe, have been instrumental in swiftly providing processed RGB imagery, including archives like Maxar's Open Data Portal, to support rapid-onset events and disaster response. Maxar has also contributed processed imagery to the U.S. Defense Innovation Unit Experimental (DIUx) and National Geospatial Intelligence Agency (NGA) *xView* dataset (Dell'Acqua & Polli, 2011), which consists of thousands of labelled satellite imagery scenes. A concept notes of the approach used in this study is shown in Figure 1.

While satellite imaging has shown to be important, aerial imagery acquired by drones or aeroplanes can provide even greater spatial resolution (less than 10 cm) than satellite imageries. Obtaining aerial images, on the other hand, usually necessitates approval from local authorities. Using satellite imaging, researchers have investigated statistical approaches for identifying damage to the built environment, frequently depending on pixel value changes between pre- and post-event photos ((Byun et al., 2015; Dell'Acqua & Polli,

2011; W. Liu et al., 2017; Wu et al., 2021). However, because these approaches are event-specific, they require substantial human supervision and pre-processing if pre-event footage from the same sensor is not available.

To address these limitations and develop a transferable damage detection algorithm applicable to new events, Convolutional Neural Networks (CNNs) have garnered attention. CNNs, widely used in computer vision tasks, simulate the human visual system to extract features and classify objects hierarchically (Lecun et al., 2010). Compared to traditional machine learning methods, CNNs exhibit better generalization and precision as they learn feature extraction patterns directly from images. Fully Convolutional Networks (FCNs) have gained popularity due to their computational efficiency and reduced memory requirements (Lecun et al., 2010). FCNs perform pixel-to-pixel translations using sequential convolutional, subsampling, and upsampling operations, eliminating the need for patches and fully connected layers. This improves processing efficiency by reducing memory costs and the number of parameters (Kaya et al., 2010). FCNs have been widely employed in detecting damage to the built environment (Adriano et al., 2019; Endo et al., 2018; Karimzadeh et al., 2018; Moya et al., 2018).

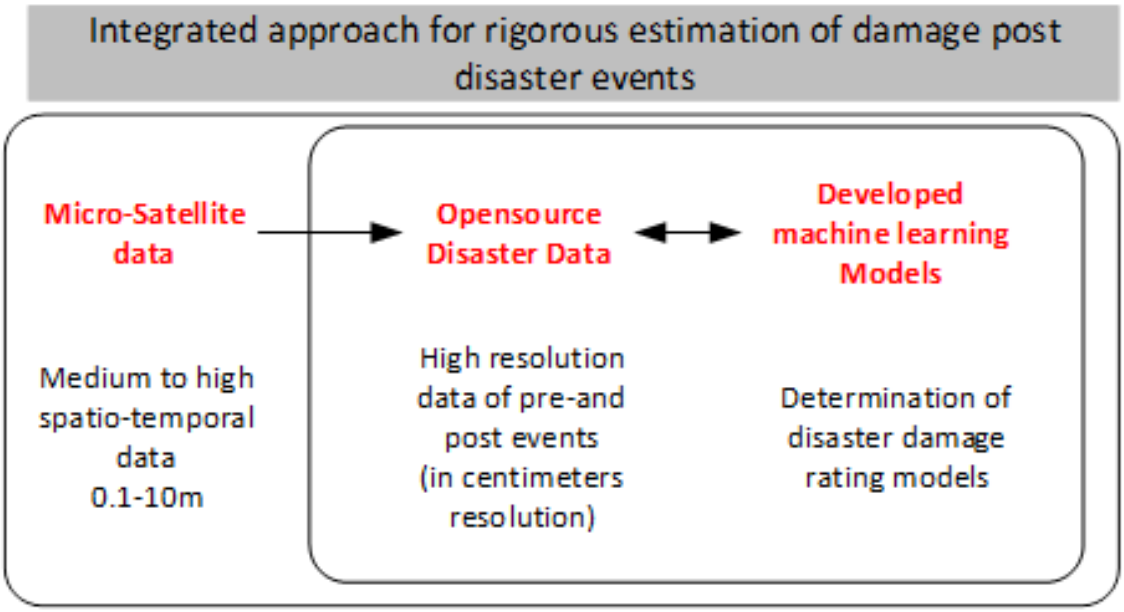

Figure 86. *A concept diagram for the use of satellite data in this study.*

However, in order to guarantee high accuracy and good generalisation of Convolutional Networks, it is essential to generate a vast and diverse training dataset. Overfitting and erroneous forecasts for unseen data might result from relying on data from a single occurrence. When evaluated on novel data, a network with insufficient training samples may also perform poorly. The xView dataset was created by the DIUx and NGA to help with this problem. It contains hundreds of photos taken by the Worldview 3 sensor developed by

Maxar Company and is one of the largest freely available databases of labelled satellite photography (Lam et al., 2018). The dataset is a great resource for creating automatic frameworks to recognise demolished buildings following a natural catastrophe, as it contains both intact and demolished structures that have been labelled.

With the combination of the labelled *xView* dataset and recent advancements in the computer vision community, a significant opportunity exists to create a reliable deep-learning framework for detecting demolished buildings in the aftermath of natural hazards. These advanced techniques, alongside the availability of diverse imagery data, hold immense potential for improving post-disaster assessment and response efforts. A solution for these problem in proposed in Figure 2.

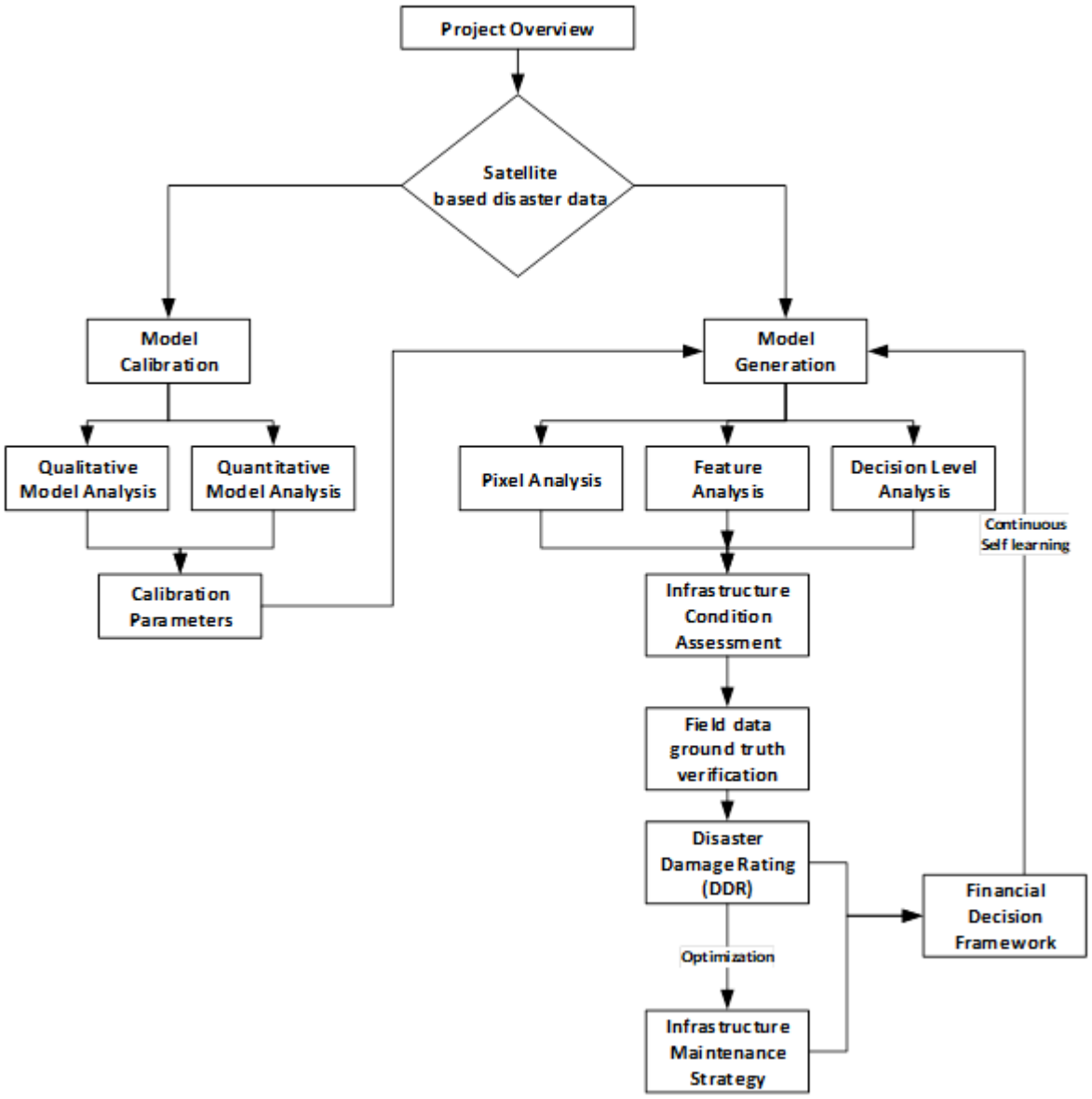

Figure 87 *Proposed Solution for the research problem.*

2. Aim, Objectives, and Scope of the Research Study

2.1 Objectives

- To use of micro satellite data in the field of infrastructure management.
- To implement machine learning algorithms in damage detection applications, which will automate the process and eliminate human errors.
- To provide a framework for formulating financial strategies.
- To develop a rating model, which may be used as a critical parameter for analyzing the financial decision framework.

2.2 Scope

- The proposed research provides an alternative to the obsolete conventional, time taking, and inaccurate method of infrastructural survey.
- The presented study aims to develop a model which involves continuous self-learning using machine learning algorithms which will significantly reduce the monitoring and decision time.
- The obtained model can be reproduced for different scenarios and different regions around the globe.
- The study provides a decision support system in addition to the conventional approach in optimizing long-term and short-term strategies for financial decisions.
- The training database obtained from this research will apply to similar infrastructure. For example, the building construction dataset can be used to test building structures only.

2.3 Practical application and implications

- The research can be compared with the already occurred catastrophic event for accuracy analysis.
- The research helps understand past- financial strategies while reconstructing structural damage and non-functional structures.
- The study provides a framework for the decision-makers to optimize long-term and short-term strategies with trade-offs with available resources.

- The DDR rating can be tagged to each structure for accurate compensation.
- The database created in this work may help academia and researchers to use it as a training dataset for testing their dataset.

3. Methodology

3.1 Literature Survey

The utilization of remote sensing technologies for building damage detection is not a recent development. Over the past two decades, numerous researchers have employed a wide array of remote sensing techniques to estimate the extent of building damage. Satellites, in particular, offer a range of visual and non-visual wavelength bands, including Synthetic Aperture Radar (SAR), high-resolution imagery, multi-spectral and hyper-spectral data. These different bands showcase the remarkable ability of satellite systems to observe and collect valuable information about the Earth.

The literature from the past two decades has extensively documented and explored the use of various remote sensing techniques for building damage detection. A comprehensive overview of these studies is provided in Table 1, consolidating the advancements and findings in the field over the years. The collective efforts of researchers have contributed to an enhanced understanding of remote sensing capabilities and their application in accurately assessing building damage, thereby aiding disaster response and recovery efforts.

Table 32. Summary of remote sensing methodologies used in building damage detection.

Sno	Author	Disaster	Year	Methodology
1.	Turker & Sumer, 2008	Izmit, earthquake, Turkey	1999	Post-earthquake aerial images were collected and further processed using image enhancement and edge detection. Polygons are created over different buildings, and using a watershed segmentation method, then the damage is assessed.
2.	Sui et al., 2014	Beichuan earthquake, China	2006	Aerial images are captured using camera mounted UAV. DSM (Digital Surface Model) is created for pre-disaster and post-disaster data and compared to check building damage. The data is segmented, and shape and texture-based are extracted and compared for pre and post-disaster events to estimate building damage.
3.	Pham et al., 2014	Haiti earthquake	2010	Both LiDAR data and images were captured using an aerial survey. DEM (Digital Elevation Model) and DSM were obtained from LiDAR

				data. The image data is then georeferenced and orthorectified with LiDAR data. Image segmentation and classification using eCognition software. The result was then evaluated with the help of ArcGIS software, having an accuracy between 70-79%.
4.	Janalipour & Mohammadzadeh, 2016	BAM earthquake, Iran	2004	Pre and post-event image data were collected and merged with the old vector map. Then the image is georeferenced to create a building polygon map. The image is then classified and labelled, and geometric features are extracted, to determine damage in the building, the sensitivity analysis is performed using ANFIS. The overall accuracy of 76.36% and a kappa coefficient of 0.63.
5.	Anghel et al., 2016	Chastel landslide	2012	The methodology is based on combining SAR data with LiDAR point cloud data. The point cloud data is comprised of GPS (Global Positioning System) and topographic data.
6.	Ye et al., 2017	Yushu earthquake	2010	Satellite high-resolution images are used along with the building polygon. The building is analysed for the roof edge and interior, improving accuracy. Colour-coded buildings based on the damage. Overall accuracy 84.10%.
7.	Nex et al., 2019	Indonesia, 2016; Nepal, 2015; Italy, 2009; Haiti, 2010; Nepal, 2015; Taiwan, 2016.	2010 - 2016	Satellite, Airborne, UAV, and sets were collected and analysed. Trained and tested using CNN (Convolution Neural Network).
8.	Li et al., 2019	Hurricane Sandy, US	2012	The UAV-mounted camera is used along with machine learning.
9.	Xu et al., 2019	Haiti earthquake	2010	Comparison between pre- and post-earthquake satellite data using CNN.
10.	Erdogan & Yilmaz, 2019	Van City earthquake,	2011	Aerial cameras capture images and compare pre- and post-earthquake DSM models based on geometric properties such as the area and the perimeter extracted.
11.	Merlin & Jiji, 2019	Nagapattinam, Tsunami, India,	2004	Comparison of pre and post Tsunami high-resolution imagery satellite data, using image analysis.
12.	Naito et al., 2020	Kumamoto earthquake	2016	Fixed-wing UAV is used to capture images, and two machine learning methods bag-of-visual-words model and a CNN model, were used for determining damages in 4 different levels based on the damage.

Table 2 discusses several data interpretation techniques that have been explored. Image processing, the oldest method, is the backbone for all subsequent processes. Machine learning and Deep learning approaches are built upon learning algorithms, with researchers utilizing supervised learning to train classifiers and then testing them on actual data.

Table 33 Remote sensing techniques and interpretation techniques for building damage assessment.

Adopted remote sensing techniques	Adopted data interpretation methods
• Satellite Imagery • LiDAR • High-resolution camera with MAV • Camera with UAV	• Image processing • Machine learning (ML) • Deep Learning (DL) • Computer vision • Surface models (DEM, DSM) • Bundled software.

The study of building localization techniques in remote sensing has contributed to developing various approaches that effectively identify and delineate buildings. These methods leverage the distinct characteristics of buildings, such as their shape, texture, and spectral properties, to accurately map their locations. Once the building localization step is completed, the focus shifts to damage classification, where the degree of damage inflicted on each identified building is assessed. This classification process involves analyzing the changes between pre-disaster and post-disaster images, employing various algorithms and techniques to categorize buildings into different damage levels.

Integrating building localization and damage classification within the remote sensing-based building damage assessment framework presents a robust methodology to evaluate the impact of disasters swiftly and comprehensively on infrastructure. By leveraging the potential of remote sensing technologies and utilizing advanced image analysis techniques, responders and relief organizations can efficiently prioritize their efforts, allocate resources effectively, and provide timely assistance to affected communities.

3.2 Research Methodology

It is observed from the literature survey that there are very few studies which have demonstrated disaster damage assessment using remote sensing data and machine learning. The assessment of building damage based on co-registered bitemporal HSR remote sensing images involves two fundamental sub-tasks: building localization and damage classification. Building localization, or building extraction, aims to assign a unique semantic label to each pixel in the pre-disaster image to indicate the building area. This task has been extensively studied in remote sensing (Liu et al., 2021). Subsequently, damage

classification assigns a unique damage level label to each building instance in the post-disaster image, reflecting the degree of damage. Researchers have recently explored using moderate-resolution remote sensing images for building damage assessment through pixel-based and object-based land cover classification (Moya et al., 2018). However, due to spatial resolution limitations, these methods can only assess coarse building-damaged areas.

Advancements in sensor technology have led to the availability of HSR remote sensing images, which capture fine spatial details of each building instance and enable instance-level building damage assessment. Consequently, building damage assessment based on HSR remote sensing images has gained prominence. For instance, Brunner et al., (2010) utilized HSR optical and synthetic aperture radar (SAR) images to extract building instances and assess instance-wise building damage by estimating geometric parameters after an earthquake disaster. (Tong et al., 2012) employed IKONOS images to detect collapsed buildings based on 3D geometric changes during an earthquake disaster. These methods primarily address single disaster scenarios and rely on specific hand-crafted features for SAR and optical images in building damage assessment (Dong & Shan, 2013). The problem of building damage assessment is often formulated as a pre- and post-event change detection problem (Plank, 2014). However, sudden-onset disasters can be unpredictable in terms of occurrence and type, and designing hand-crafted features is time-consuming, impeding the ability to rapidly assess building damage on a large scale for swift disaster response.

Deep learning techniques, particularly deep convolutional neural networks (CNNs), have significantly advanced computer vision and have found successful applications in various remote sensing tasks. These include object detection ((Cheng et al., 2016; Zheng et al., 2020; Zhong et al., 2018), object segmentation (Zheng & Shi, 2020), land-use classification (Huang et al., 2018; Zhang et al., 2018, 2019, 2020), hyperspectral image classification (Zheng et al., 2020), and multi-modality all-weather mapping (Zheng, Ma, et al., 2021). CNNs excel in hierarchical feature representation learning, enabling the extraction of high-level features from raw image data using a data-driven approach. These learned features can be effectively applied to downstream tasks end-to-end, significantly accelerating the entire pipeline of building damage assessment following a sudden- onset disaster.

The experience from the preliminary analysis and thorough investigation from previous literature, the use of the segmentation model (CNN) in two stages, namely building localisation and damage assessment, was finalised.

The sequence of steps to develop a machine-learning approach is in Figure 3. Each step is described later in sub-sections. In brief, the first step is data collection of the high-resolution satellite imageries of pre- and post-disaster, along with ground-based observations. Then after data pre-processing, the data was ready to be fed into the model. Our own developed and compared the model with the existing models and studies. Our developed model is performing well and fast compared to the existing models. The results of our model are then used for the financial decision framework development, which is discussed in subsequent sections.

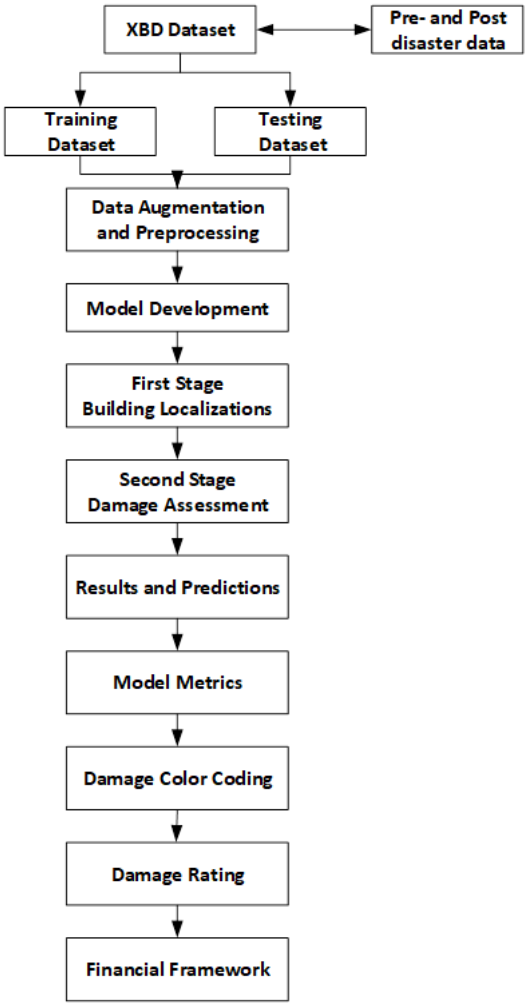

Figure 88. Research approach followed in this study.

3.3 Step 1: Data collection

The training data set was collected using the *xBD* collection, which provides a wide range of high spatial resolution (HSR) bitemporal optical satellite images. These images were obtained through the Maxar/DigitalGlobe Open Data Program, which offers open access to geospatial data for research and development purposes (https://www.digitalglobe.com/ecosystem/open-data). The *xBD* collection, also known as the *Xview 2* dataset (Gupta et al., 2019), consists of 22,068 HSR bitemporal optical satellite images covering an extensive geographical area of 45,361.79 square kilometres worldwide. These images were captured using different satellite platforms, including WorldView-2 and WorldView-3. Within the *xBD* dataset, there are 850,736 instances of buildings, each represented by bounding boxes or polygons that outline their boundaries. This rich dataset includes various building types, sizes, and architectural characteristics, making it suitable for training and analysis purposes. Gupta et al. (2019) described the dataset as containing 19

different disaster events, such as wildfires, earthquakes, cyclones, hurricanes, volcanic eruptions, tsunamis, tornadoes, and floods.

The xBD dataset is divided into two parts: the "train" set, which makes up 80% of the dataset and consists of 18,336 photos and 632,228 building polygons, and the "holdout" set, which comprises the remaining 20% and includes 108,784 building polygons. These distinct portions facilitate effective training and evaluation of machine learning models. In addition to the *xBD* collection, there are other valuable datasets available for building damage assessment. For instance, the NOAA-NASA P-3 Hurricane Imagery provides aerial images captured during hurricane reconnaissance flights, offering high-resolution imagery of hurricane-affected areas for studying building damage caused by hurricanes. Another dataset, the ImageNet Pre-trained Models with Disaster Response Images, consists of pre-trained deep learning models specifically trained on disaster response images. This dataset encompasses a wide range of disaster-related images, including those depicting building damage, and can be utilized for building damage classification and assessment tasks.

Among the available datasets and research studies, the *xView2* dataset was deemed the most suitable for the study due to its numerous advantages. These include a vast and diverse collection of high-resolution satellite images, ground truth annotations, a specific focus on building damage assessment in the context of disaster response, and practical applications for aiding decision-making processes and improving outcomes in disaster response. Figure 4 showcases a sample of image combinations for hurricane Harvey, displaying pre- and post-disaster satellite images.

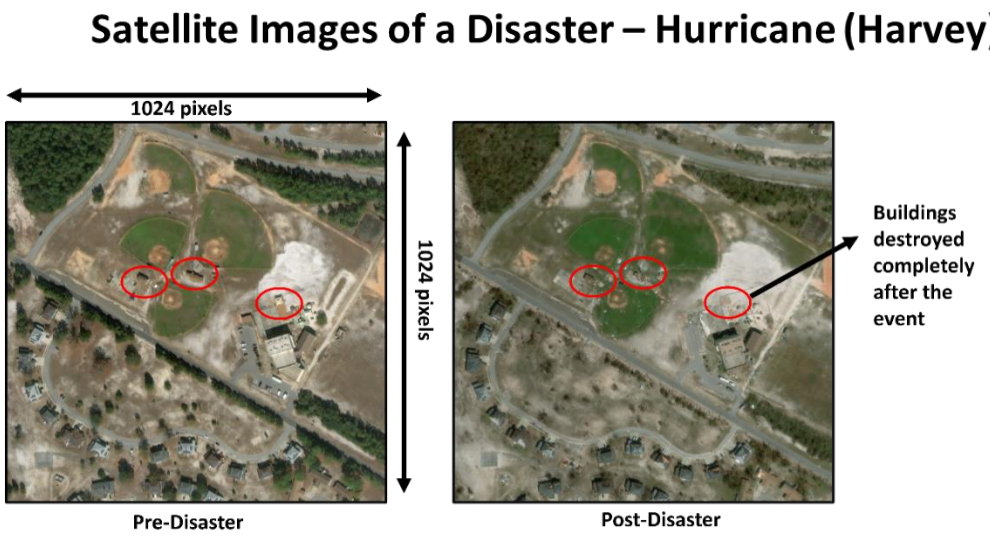

Figure 89. Representation of the sample paired images of pre- and post-disaster images used in the study.

3.4 Step 2: Data pre-processing and augmentation

Various augmentation techniques were employed scientifically to enhance the test dataset size and introduce variability. Augmentation is a common practice in machine learning and computer vision tasks to generate additional training examples without additional data collection artificially. Different augmentation techniques were applied in the context of the *xView2* dataset, as illustrated in Figure 5, such as (1) Horizontal flip, (2) Vertical flip, (3) Rotation augmentation involves rotating the images by a certain angle, such as 90 degrees or 180 degrees, (4) Scaling augmentation involves resizing the images by increasing or decreasing their dimensions. This technique enables the generation of images with different scales, simulating varying distances of the satellite from the disaster-affected areas. Scaling augmentation helps models capture the diversity of building sizes and better generalize to different spatial resolutions encountered in real-world scenarios.

The original raw high-spatial-resolution images were of 1024 by 1024 pixels image sizes. These images were cut down into equal parts (224 by 224-pixel sizes) for better training in the model. Every image file had 4 channels which were converted to 3-channel RGB channels. These changes were made in both training as well as test datasets.

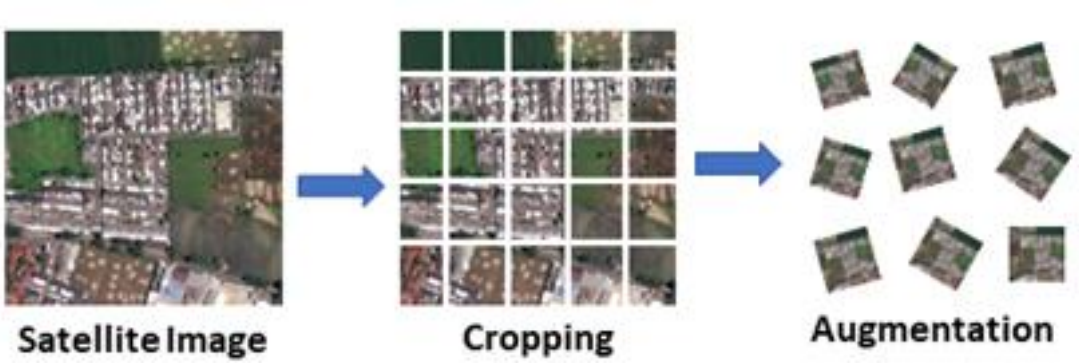

Figure 90. Illustration of data augmentation process for satellite imageries

3.5 Step 3: Model Development

The study aimed to develop a disaster damage assessment model using a two-stage segmentation approach. The first stage involved building localization using either the U-Net or LinkNet model architectures. Both models are convolutional neural networks designed for image segmentation, consisting of encoder and decoder paths to capture features and recover spatial information. While the U-Net model follows a basic architecture, the LinkNet model incorporates shortcuts or "links" between encoder and decoder blocks for improved gradient and information flow. LinkNet is known for its efficiency and is often used in real-time applications or scenarios with limited computational resources. The study compared the performance of these models, considering their size, inference speed, and application

focus, ultimately selecting the LinkNet model for its suitability in real-time disaster damage rating scenarios.

Figure 91. Shows various image Augmentation techniques on orignal image (a), such as (b) Flipped X axis, (c) Rotated Clockwise, (d) Flipped Y-axis, (e)Rotated anticlockwise and, (f) Flipped and rotation.

For the feature extraction component, various backbone networks were utilized with the UNET and LinkNet architectures. The backbones included ResNet34, ResNet50, VGG19, VGG16, and Inception V3. ResNet variants are known for their ability to train deep neural networks effectively, capturing complex features. VGG architectures excel at capturing fine-grained features, while Inception V3 focuses on local and global feature representation. Integrating these backbones into the models enables the extraction of relevant features from input images, enhancing segmentation performance. The choice of backbone depends on factors such as the segmentation task, image complexity, and available computational resources. Previous studies and a comparison of different CNN architectures used as backbones in segmentation models were considered to inform the choice of backbones.

Experimentation is often necessary to find the optimal combination for the specific segmentation task.

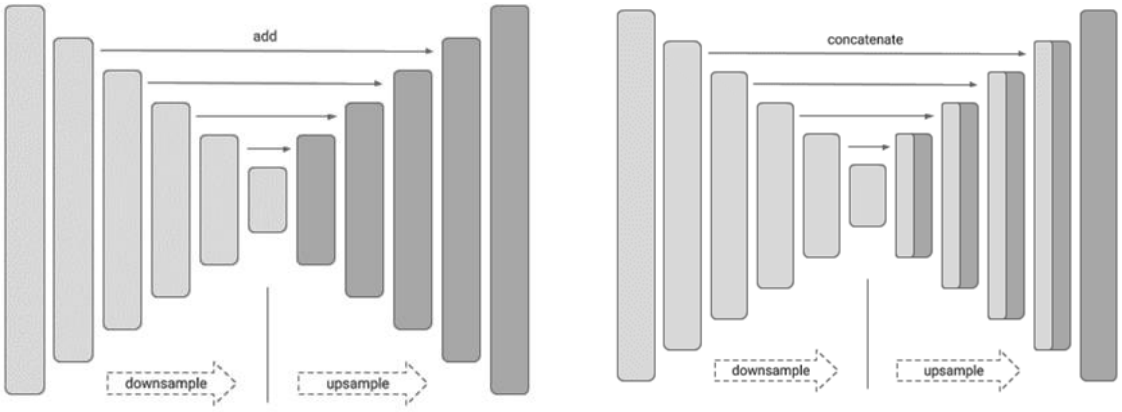

(a) U-Net Model Architecture **(b) LinkNet Model architecture**

Figure 92. Diagrams showing the different segmentation model architectures (a) Unet Model (b) LinkNet model.

3.6 Step 4: Model assessment

3.6.1. Model Training

With the model architecture defined, the next step is to train the UNET and LinkNet models using the annotated training dataset. During training, the input images are fed to the model, and the model's parameters are optimized to minimize the difference between the predicted segmentation masks and the ground truth masks. This optimization is typically achieved through backpropagation and gradient descent algorithms. The choice of loss function is crucial for segmentation tasks, dice loss was selected.

3.6.2. Hyperparameter Tuning

Hyperparameters are configuration settings that affect the training process but are not learned directly from the data. Examples of hyperparameters include the learning rate, batch size, seed and epochs. The hyperparameters were set as the learning rate of 0.001, batch size 16, seed as 24, and epochs 25. Hyperparameter tuning involves experimenting with different combinations of these settings to find the optimal configuration for your model. All the experiments were performed with similar settings for consistency, for example, optimizer set as ‘Adam’, activation = ‘softmax’, loss = ‘Jaccard losses’. The validation set plays a crucial role in this process, as it evaluates and compares the performance of different hyperparameter settings. Techniques like grid search, random search, or more advanced approaches like Bayesian optimization can be employed for efficient hyperparameter tuning.

The algorithm for this project work followed is to first create the mask for the satellite imagery data and then training on large datasets for both damage localization and

classification is performed. To get the optimum result out of our experiment, three hyperparameters are finetuned. The hyperparameters were set to predetermined values based on experimentation and the Learning Rates, batch size, and Seed are fine-tuned. Also, Early Stop is used to find that 25 epochs train the model and do not overfit. Additionally, learned weights from the IMAGENET dataset for pre-training are used. The hyperparameters with different architectures and backbones are applied to all combinations to find the best output. As per the experiment conducted, the combination of UNet + Inception v3 gives the best results.

3.6.3. Model Evaluation

Once the training is complete, it is important to assess the performance of the trained model on the test set. This evaluation provides an unbiased estimate of the model's performance on unseen data. Common evaluation metrics for image segmentation tasks include precision, recall, F1 score, and Intersection over Union (IoU). These metrics measure the model's accuracy in identifying damaged areas compared to the ground truth. Analysing the evaluation metrics helps determine if the model meets the desired level of performance or if further optimization is required. All these evaluation metrics depend on the confusion matrix, as shown in Figure 8. The confusion matrix enables a comprehensive assessment of the model's performance by examining the different types of classification outcomes. It provides valuable insights into the model's strengths, weaknesses, and potential areas of improvement in disaster damage assessment. The confusion matrix consists of four elements; True Positives (TP), True Negatives (TN), False Positives (FP), False Negatives (FN).

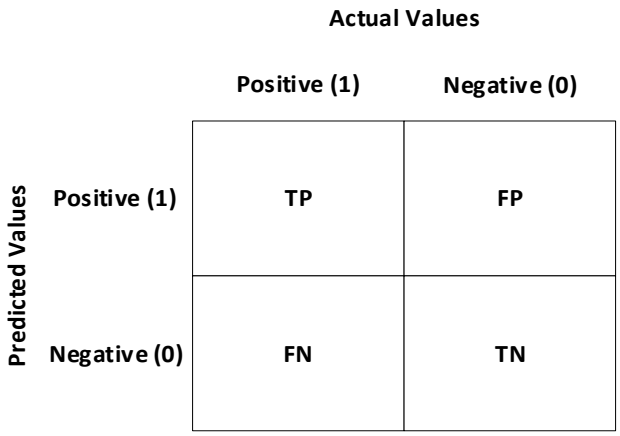

Figure 93 Confusion matrix for ML model assessment

$$\text{Precision} = \frac{TP}{TP + FP} \quad [1]$$

$$\text{Recall} = \frac{TP}{TP + FN} \quad [2]$$

$$\text{F1 Score} = \frac{2}{\frac{1}{\text{Precision}} + \frac{1}{\text{Recall}}} = \frac{2 * \text{Precision} * \text{Recall}}{\text{Precision} + \text{Recall}} \quad [3]$$

$$\text{F1 Score} = \frac{TP}{TP + \frac{1}{2}(FP + FN)} \quad [4]$$

$$\text{IoU Score} = \frac{TP}{(TP + FP + FN)} \quad [5]$$

The evaluation metrics are calculated using the equations and formulas shown in Equation (1)- (5).

3.6.3.1 F1 Score

The F1 score (equation (4)) is a composite metric that balances the precision and recall of a model. It measures the harmonic mean of precision and recall, offering a balanced assessment of the model's performance. Precision refers to the proportion of correctly identified damage instances out of the total predicted damage instances. Conversely, recall quantifies the proportion of correctly identified damage instances out of all actual damage instances.

3.6.3.2 IoU Score

The Intersection over Union (IOU) score (Equation 5), also known as the Jaccard index, is commonly employed in evaluating the overlap between predicted and ground truth damage areas. It calculates the ratio of the intersection of these areas to their union. The IOU score is particularly useful when assessing the spatial agreement between predicted and actual damage regions. A higher IOU score indicates a better alignment of the predicted damage with the ground truth, reflecting the model's ability to accurately delineate damaged areas.

By utilizing the F1 score, analysts can effectively evaluate the overall accuracy of a damage assessment model, balancing both precision and recall. The IOU score aids in quantifying the spatial agreement between predicted and actual damage regions, enabling a more granular assessment of model performance. Therefore, IoU and F1 scores must be evaluated for the damage assessment task.

3.6.4 Model Optimization

To optimize the model's performance, several techniques can be applied. Data augmentation, including rotation, scaling, flipping, and adding random noise, increases the size and diversity of the training dataset, improving generalization. Transfer learning is another approach where a pre-trained model, like the one trained on ImageNet, is fine-tuned using the disaster damage dataset, leveraging learned features to potentially enhance performance. Modifying the model architecture by adjusting layers, increasing capacity, or introducing regularization techniques like dropout or batch normalization, was explored. Multiple experiments were conducted, comparing inference speed, evaluation metrics, and training and validation scores. Achieving the desired performance requires high-quality and diverse datasets, careful model architecture design, and fine-tuning of hyperparameters. The iterative nature of model development may involve multiple iterations for optimization.

3.6.5 First Stage of the Model: Building Localisation

Building localization refers to accurately identifying and delineating buildings or structures within satellite imagery. It is crucial in various applications, including disaster damage assessment, urban planning, and infrastructure development. Traditional methods for building localization often rely on manual inspection or handcrafted features, which are time-consuming and subjective. However, recent advancements in deep learning and computer vision have enabled the development of more robust and automated techniques. In this subsection, A novel approach for building localization utilizing a segmentation model as explained in previous subsections is proposed. Our method leverages the power of supervised learning to accurately identify and classify individual pixels or regions within satellite images, thereby enabling the precise localization of buildings. In the context of building localization using a segmentation model, binary segmentation involves labelling pixels or regions in satellite imagery as either belonging to buildings or not belonging to buildings. This binary classification allows for identifying and differentiating building structures from the surrounding background.

A large dataset of satellite images containing labelled building regions to train the first part of our developed model is utilized. These labelled masks are generated using ground-based information as label files in .geojson formats. Domain experts typically examine the satellite images and manually trace or outline the boundaries of the buildings present in the scene. Various annotation tools and techniques were employed, ranging from simple drawing tools to more sophisticated interactive segmentation methods. The Xview2 dataset comes with images along with the annotated labels. These labels were converted

into ground-truth masks using a Python-based script.

Once the boundaries of the buildings are delineated, the corresponding regions in the satellite images are assigned the label 1, indicating the building class. The remaining regions, which do not overlap with any buildings, are labelled as 0, representing the non-building class. Each pixel in the ground truth mask files is assigned a label, such as 1 for buildings, as shown as a white region and 0 for non-building areas, as represented by a black region. The satellite image with its corresponding masks used in the segmentation model is shown in Figure 9.

The dataset is augmented to enhance the model's generalization capabilities and to handle variations in lighting conditions, perspectives, and occlusions. An end-to-end training strategy, optimizing the model parameters using a suitable loss function, the dice coefficient, to encourage accurate pixel-level predictions are employed. During the inference phase, the trained segmentation model takes as input a satellite image and generates a probability map indicating the likelihood of each pixel belonging to a building class. A post-processing step is then applied to the probability map to refine the segmentation results and eliminate potential false positives or negatives.

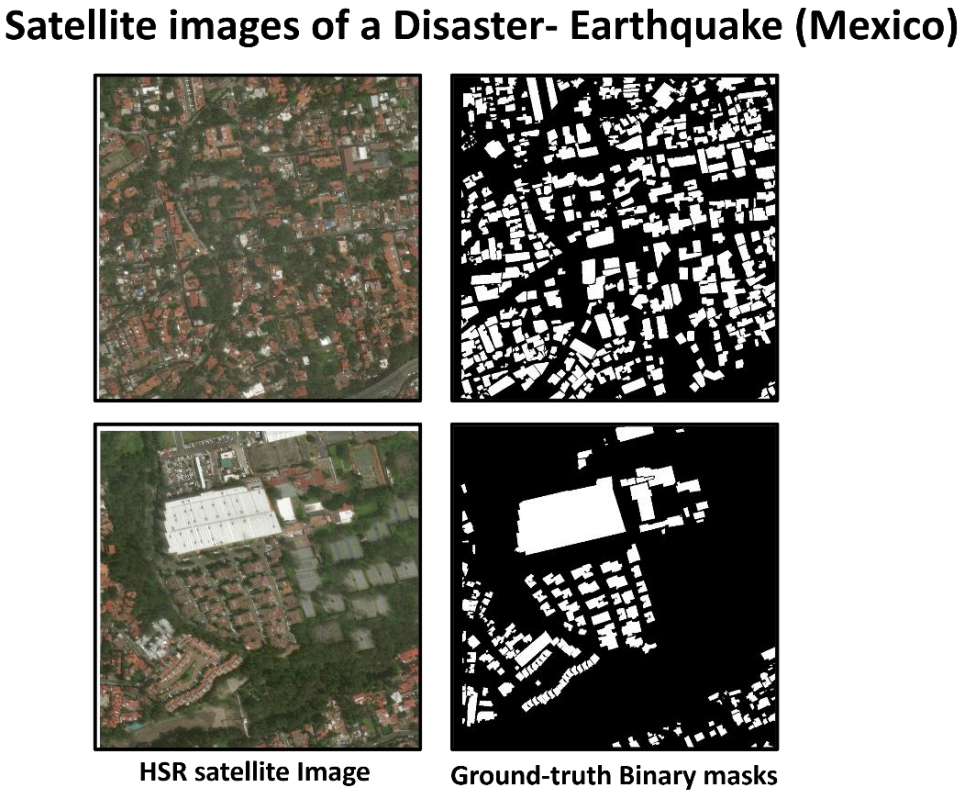

Figure 94. Representation of a sample HSR satellite image with its corresponding binary masks with white and black regions corresponding to the building and no-building area, respectively

To evaluate the performance of our approach, a extensive experiments on a diverse set of satellite images acquired from different regions and time periods is conducted. The obtained result is then compared against state-of-the-art building localization techniques, including the manual annotation and rule-based methods. The evaluation metrics include Intersection over Union (IoU), accuracy, precision, recall, and F1-score. The experimental results demonstrate the effectiveness and superiority of our proposed segmentation-based approach in accurately localizing buildings within satellite imagery. In conclusion, our research presents a novel building localization technique based on a segmentation model, offering a more automated and accurate solution than traditional methods. The proposed approach leverages deep learning and the U-Net/LInkNet architecture to enable precise identification and delineation of buildings within satellite images. The experimental results validate the effectiveness of our approach and its potential for applications in disaster damage assessment, urban planning, and other related fields. Then the weights were used from the first stage of the model for the pre-training of the second stage of the model, i.e., damage assessment.

3.6.6 Second stage of the model: Damage assessment

The task in the second stage of the model, disaster damage assessment, involves classifying and quantifying the extent of damage in satellite imageries. A multi-class segmentation approach is adopted to achieve this, where each pixel or region in the satellite images is assigned, a label corresponding to a specific damage category. For our purpose in this study, A scenario where four labels are used to represent the following damage categories is used, as shown in the Figure 10.

1. **No Damage:** This label represents regions or pixels unaffected by the disaster event. It indicates areas without observable damage and serves as the baseline or reference category.
2. **Minor Damage**: This label represents areas or pixels that have experienced minor damage. Minor damage typically includes superficial or partial destruction, such as small cracks, dents, roof elements missing or partial structural instability.
3. **Major Damage:** This label represents areas or pixels that have experienced severe damage. Severe damage indicates extensive destruction, such as complete collapse, significant loss of structural integrity, wall or roof collapse, and/or complete loss of functionality.
4. **Destroyed:** This label represents areas or pixels that have been destroyed or rendered non-functional due to the disaster event. It indicates the most severe level of damage, where no traces of the original structure or functionality remain.

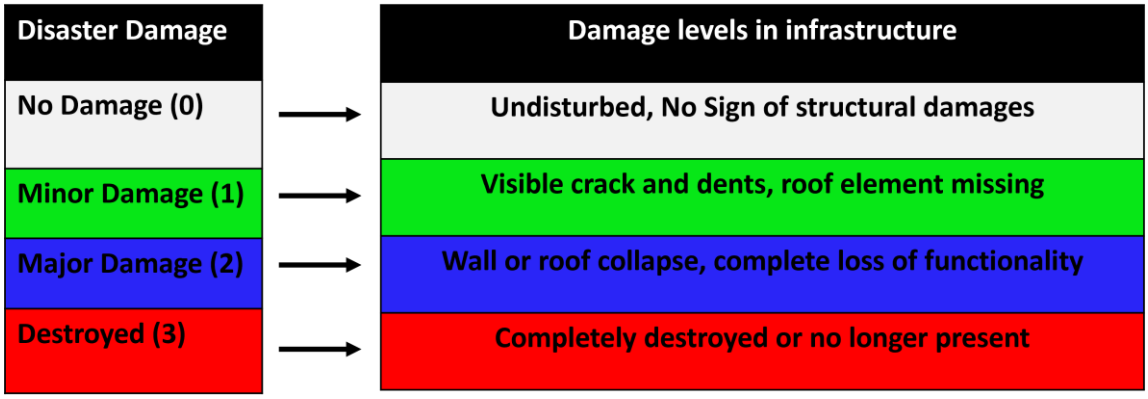

Figure 10. Damage classification scale followed in this research

During annotation, domain experts manually examine the satellite images and assign these labels to the corresponding regions or pixels. The annotation process typically involves visual inspection and analysis of the damage extent and severity based on visible cues such as structural damage, debris, or changes in appearance. The labelled satellite images serve as the ground truth for training the segmentation model. The model learns to map the input satellite images to their corresponding damage labels, enabling it to accurately classify each pixel or region in the images according to its specific damage category.

Similar to the first stage of the model, the annotations for the second stage were also created using label geojson files. These images were labelled as White colour for "no damage" (255, 255, 255), Green colour for "minor damage" (0, 255, 0), Blue colour for "major damage" (0, 0, 255), Red colour for "destroyed" (255, 0, 0). These mask images are shown in the Figure 11.

During inference, the trained segmentation model takes a new satellite image as input and generates a prediction map or mask where each pixel is assigned a label representing the damage category. These predicted masks could be further processed and analysed to quantify the extent and distribution of damage, providing valuable insights for disaster response and recovery efforts.

4. Results and Discussion

4.1 Building localization: Comparison of model outputs, efficiencies, & performance

A detailed description comparing the results of U-Net and LinkNet models with different backbone architectures (ResNet50, ResNet34, VGG16, VGG19 and Inception V3) based on training loss, validation loss, and IoU scores is explained in this section. The results have

been represented and observed in Table 3.

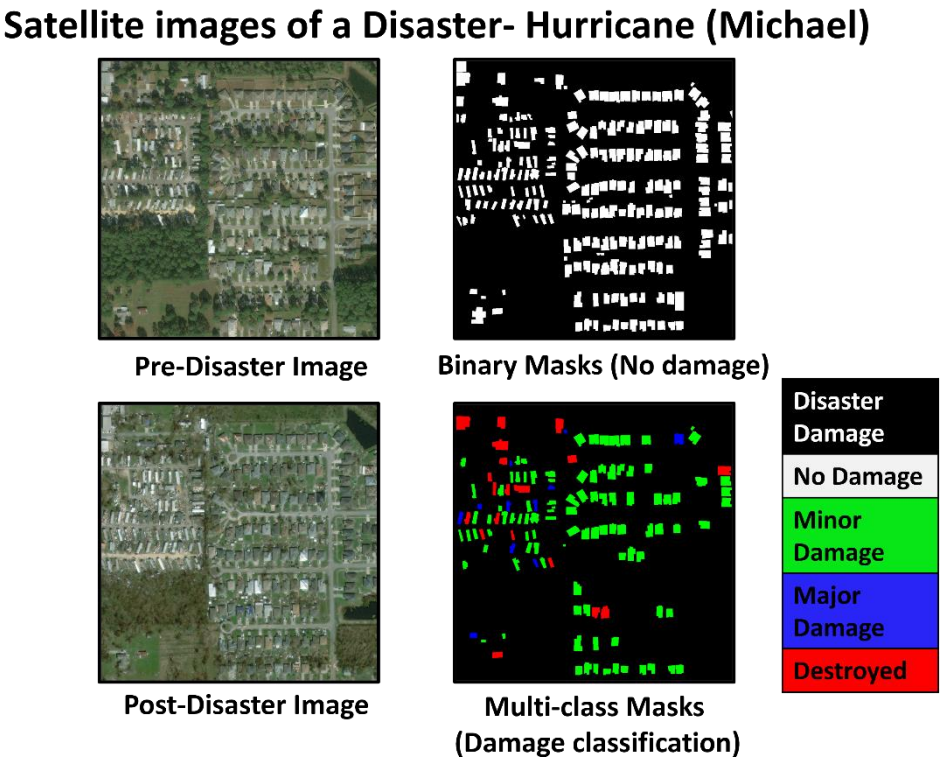

Figure 95. Representation of a sample HSR satellite image with its corresponding multi-class masks for pre- and post-disaster images.

In addition to loss metrics, such as training loss and validation loss, the segmentation performance using IoU scores is evaluated. IoU measures the overlap between predicted segmentation and ground truth masks. Both quantitative metrics (loss and IoU scores) and qualitative aspects (visual inspection of segmentation results) to gain a holistic understanding of the model performance are considered. It is observed that the Inception V3 is working most effectively with both the segmentation model U-Net and LinkNet, with IoU scores of 0.867 and 0.891, respectively. The LinkNet model is performing well for this first stage of the model, building localisation. The VGG16 and VGG19 are performing worst as backbones for U-Net and LinkNet, respectively, with lowest IoU scores of 0.79 and 0.72. The ResNet backbones are performing comparatively well with the previous studies.

For both models, Inception performs the best, followed by ResNet, and then VGG performs the worst. This can be attributed to several factors:

a) Architectural design: Inception models, particularly the newer versions like InceptionV3, incorporate advanced architectural design choices, such as the use of inception modules, residual connections, or efficient dimensionality reduction techniques.

b) Model depth and complexity: Inception models are typically deeper and more

complex than VGG and Resnet models. The increased depth allows Inception models to learn more intricate and abstract features, which can contribute to their better performance.

c) Parameter efficiency: Inception models are designed to be parameter-efficient, meaning they achieve good performance while utilizing fewer parameters compared to VGG models. This parameter efficiency can provide several advantages, such as reducing the risk of overfitting when training data is limited and improving computational efficiency during inference.

d) Generalization ability: Inception models can effectively learn and generalize from diverse patterns and variations in the data. ResNet models, with their skip connections, also help in improving generalisation. VGG models, while they can perform well, may struggle to generalize as effectively due to their limited capacity to capture intricate details and larger receptive fields.

The comparison of the model results is shown in Table 3. Both UNet and LinkNet models exhibited good segmentation performance, with UNet generally outperforming LinkNet across different backbone configurations. Inceptionv3 consistently yielded superior performance among the tested backbones, achieving high IoU scores in both UNet and LinkNet models. However, LinkNet with Inceptionv3 as the backbone achieves the highest IoU score (0.891), outperforming all other models. This suggests that the Inceptionv3 backbone effectively captures intricate patterns and features, enhancing the accuracy of the segmentation process.

Table 34. Comparison of U-Net and LinkNet Models with different backbones regarding IoU score and training loss.

Segmentation Model	Backbone	IoU Score	Training Loss
U-Net	ResNet34	0.8449	0.17
	ResNet50	0.8467	0.1682
	VGG16	0.7977	0.2236
	VGG19	0.8017	0.2187
	Inceptionv3	0.867	0.1449
LinkNet	ResNet34	0.8233	0.1971
	VGG16	0.8430711	0.2074
	VGG19	0.7262	0.3
	Inceptionv3	0.89055103	0.1586
Worst performing		Best performing	

Additionally, the impact of backbone selection was evident, as different backbones produced varying performance levels. In the UNet model, ResNet50 demonstrated improved

segmentation accuracy compared to ResNet34, VGG16, and VGG19. VGG16 also showed competitive performance, while VGG19 had slightly lower scores. In the case of LinkNet, Inceptionv3 as the backbone exhibited the highest IoU score among all configurations, surpassing other backbones. The IoU score served as a vital evaluation metric, reflecting the quality of the predicted segmentation. Higher IoU scores indicate greater accuracy in identifying and labelling objects or regions within images. The obtained scores, ranging from approximately 0.72 to 0.89, suggest favourable segmentation performance across the evaluated models and backbones.

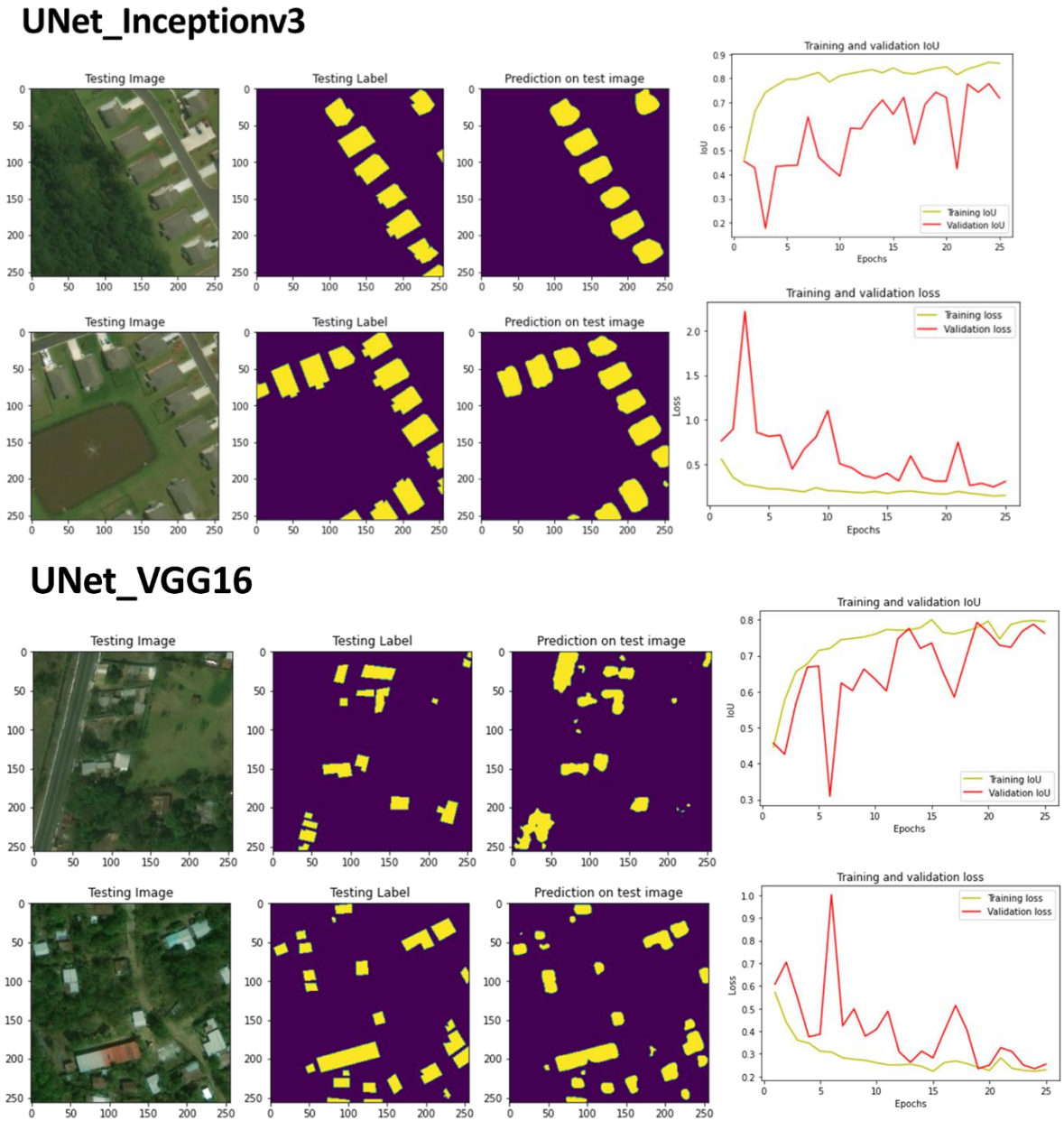

Figure 96 Model results showing the testing image, testing label and the predicted masks on the test image with binary classes for the best-performing backbone (Inception V3) and worst-performing (VGG16) with the segmentation model U-Net. The right-hand-sided graphs show the training and validation IoU scores and training and validation loss for 25 epochs.

Moreover, the loss values obtained during training reflected the convergence and alignment between predicted and ground truth segmentations. Lower loss values indicated better model optimization and minimization of segmentation errors. The observed loss values, ranging from approximately 0.14 to 0.3, indicate successful learning and effective reduction of segmentation discrepancies during training. In conclusion, this comparative analysis emphasized the importance of selecting an appropriate segmentation model and backbone for image analysis tasks. The results demonstrated the superior performance of Inceptionv3 as a backbone architecture while highlighting the competitive capabilities of ResNet50 and VGG16. These findings contribute to the understanding of segmentation model performance and provide insights into selecting suitable architectures for the first stage of our model. The corresponding model results for test images with their corresponding testing labels and predictions are plotted and shown in Figure.12, 13 And Annexures 3.

4.2 Damage assessment: Comparison of model outputs, efficiencies, & performance

The segmentation model utilized in this study has demonstrated promising results in accurately assessing the extent of damage caused by disasters across multiple classes, including destroyed, major damage, minor damage, and no damage. The model was trained on a comprehensive dataset of various disaster scenarios, enabling it to learn and generalize well to unseen data. It was observed that the segmentation model achieved high IoU scores across all damage classes, indicating its effectiveness in accurately identifying and delineating different levels of damage. The model exhibited particularly robust performance in detecting and segmenting destroyed areas, which are often associated with more severe damage. This capability is crucial for effective disaster response and resource allocation, as it allows for prioritization of areas requiring immediate attention. Furthermore, the model demonstrated commendable performance in differentiating major damage from minor damage. This distinction is essential in assessing the severity of the impact and aiding decision-making processes for recovery efforts. By providing detailed and precise segmentation maps, the model facilitates a more comprehensive understanding of the extent and distribution of damage, enabling stakeholders to strategize and allocate resources effectively.

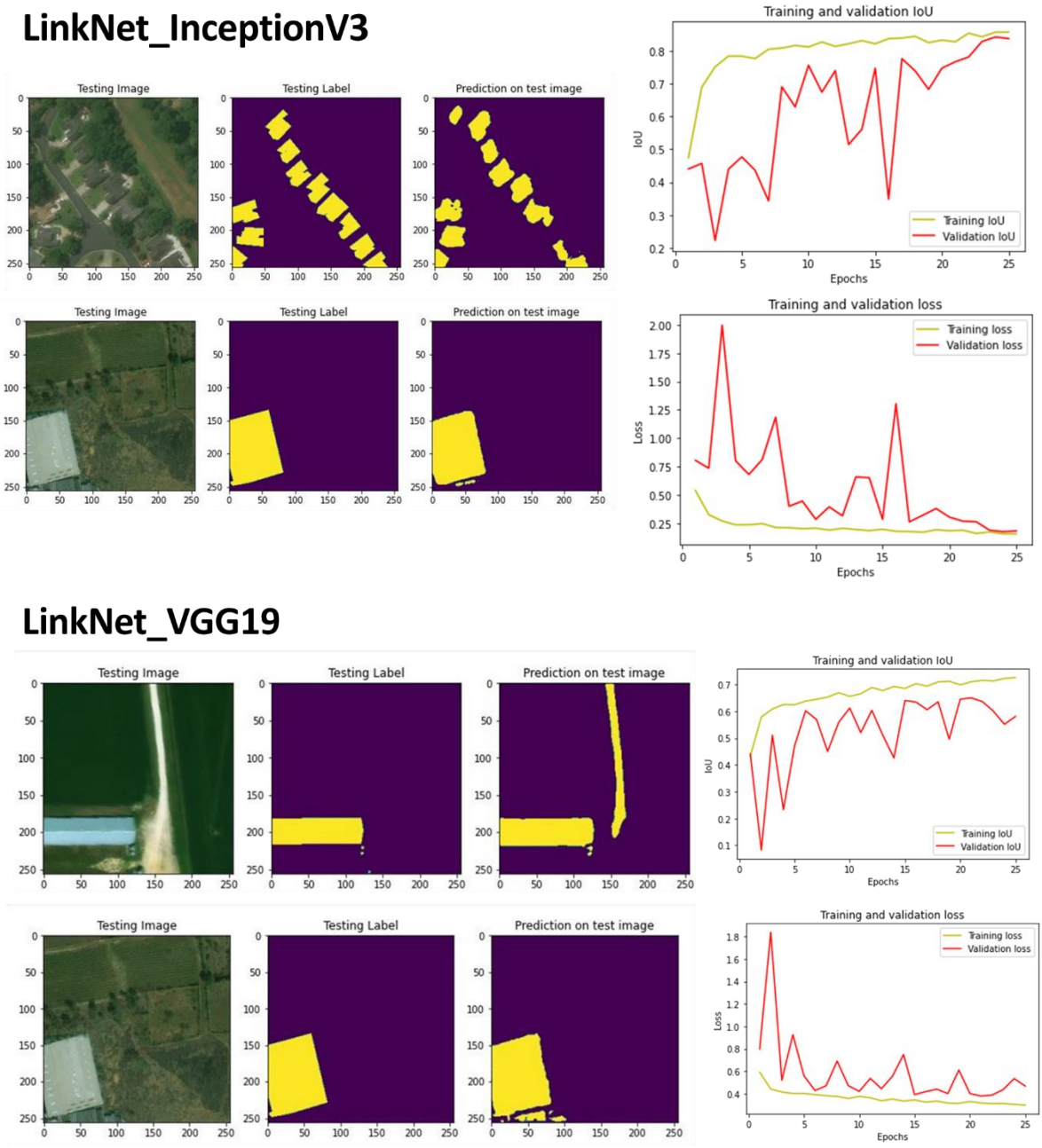

Figure 97. Model results showing the testing image, testing label and the predicted masks on the test image with binary classes for the best-performing backbone (Inception V3) and worst-performing (VGG19) with the segmentation model LinkNet. The right-hand-sided graphs show the training and validation IoU scores and training and validation loss for 25 epochs.

Compared to traditional manual assessment methods, the segmentation model significantly reduces the time and effort required for damage assessment. The automated nature of the model expedites the process, allowing for rapid response and intervention in disaster-stricken areas. While the results of this study highlight the efficacy of the segmentation model, it is important to acknowledge some limitations. The model's performance may vary across disaster types, environmental conditions, and data quality. Further refinement and

expansion of the training dataset can address these limitations and enhance the model's generalizability. Although the *Xview* dataset used in the study has a comprehensive extension and inclusion of many disasters from different geographical regions, more inclusion of the dataset would surely help in the future for the fine-tuning of the model. In conclusion, using the segmentation model in disaster damage assessment has demonstrated promising results. Its accurate and efficient delineation of different damage classes, including destroyed, major, minor, and no damage, provides valuable insights for decision-makers and aids in effective disaster response and recovery efforts.

The Table 4 presents the evaluation results of different models using various backbones for damage classification. The metrics used to assess the performance include Mean IoU Score, Mean F1 score, Class-wise F1 Score, and Class-wise IoU Score. Additionally, the damage classes are categorized as "No damage," "Minor Damage," "Major damage," "Destroyed," and "Unclassified".

The U-Net model with ResNet34 backbone achieved a Mean IoU Score of 0.517 and a Mean F1 score of 0.61. The Class-wise F1 Score varied across the classes, with the highest F1 score of 0.807 observed for "Major damage." However, the model failed to detect any instances of "Destroyed" and "Unclassified" damages. The Class-wise IoU Scores ranged from 0.58 to 0.961. Using Inception V3 as the backbone, the U-Net model performed better, achieving a higher Mean IoU Score of 0.601 and a Mean F1 score of 0.682. The Class-wise F1 Score improved for all classes, with the highest score of 0.844 for "Major damage." A small percentage (0.04) of "No damage" instances were misclassified as "Destroyed." The Class-wise IoU Scores ranged from 0.638 to 0.965.

When ResNet50 was used as the backbone, the U-Net model achieved a Mean IoU Score of 0.573 and a Mean F1 score of 0.656. Similar to the previous model, "Destroyed" and "Unclassified" damages were not detected. The Class-wise F1 Scores ranged from 0.788 to 0.957, and the Class-wise IoU Scores ranged from 0.62 to 0.65. For the Vgg16 and vgg19 backbones, the U-Net model achieved Mean IoU Scores of 0.57 and 0.58, respectively, with Mean F1 scores of 0.665 and 0.683. The Class-wise F1 Scores for "Major damage" were relatively higher, with values of 0.811 and 0.811 for Vgg16 and vgg19, respectively. The Class-wise IoU Scores varied across the models, ranging from 0.56 to 0.594 for Vgg16 and from 0.88 to 0.594 for vgg19.

Table 35. Class wise results obtained from ML models F1 score and IoU score

Model	Backbones	Mean IoU Score	Mean F1 score	Class-wise F1 Score					lass-wise IoU Score				
				No damage	Minor Damage	Major damage	Destroyed	Unclassified	No damage	Minor Damage	Major damage	Destroyed	Unclassified
U-Net	ResNet34	0.517	0.61	0.807	0	0.58	0.731	0.961	0.677	0	0.408	0.576	0.925
	Inception V3	0.601	0.682	0.844	0.04	0.638	0.919	0.965	0.7313	0.02	0.468	0.8511	0.933
	ResNet50	0.573	0.656	0.788	0	0.62	0.917	0.957	0.65	0	0.45	0.84	0.919
	Vgg16	0.57	0.665	0.811	0.09	0.577	0.88	0.958	0.682	0.052	0.405	0.789	0.92
	vgg19	0.58	0.683	0.811	0.19	0.56	0.88	0.95	0.682	0.11	0.39	0.976	0.919
Link Net	ResNet34	0.527	0.622	0.827	0	0.538	0.79	0.953	0.705	0	0.368	0.655	0.91
	Inception V3	0.575	0.656	0.82	0	0.586	0.913	0.961	0.695	0	0.414	0.841	0.924
	ResNet50	0.593	0.723	0.759	0.48	0.6	0.811	0.956	0.612	0.322	0.431	0.682	0.91
	Vgg16	0.561	0.644	0.8	0	0.543	0.913	0.956	0.675	0	0.373	0.841	0.916
	vgg19	0.561	0.647	0.796	0	0.594	0.88	0.958	0.66	0	0.423	0.8	0.92

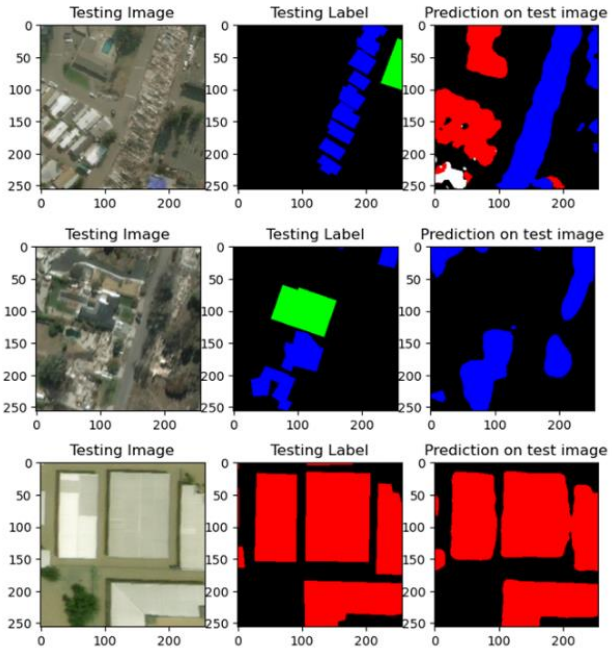

LinkNet_Resnet34

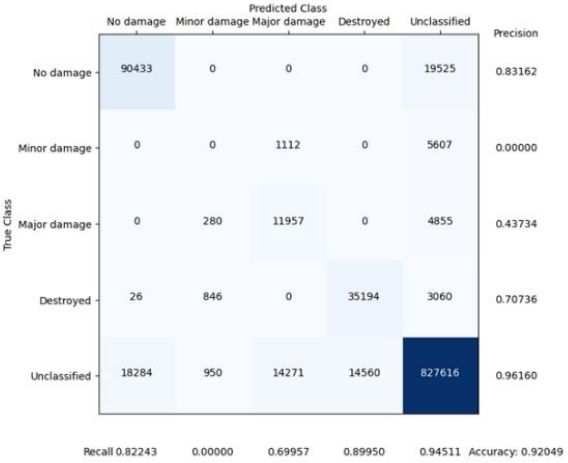

(1)

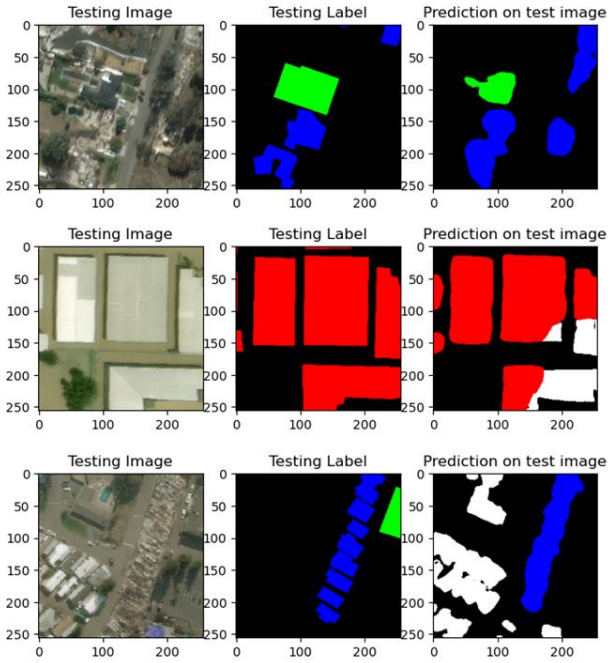

LinkNet_Resnet50

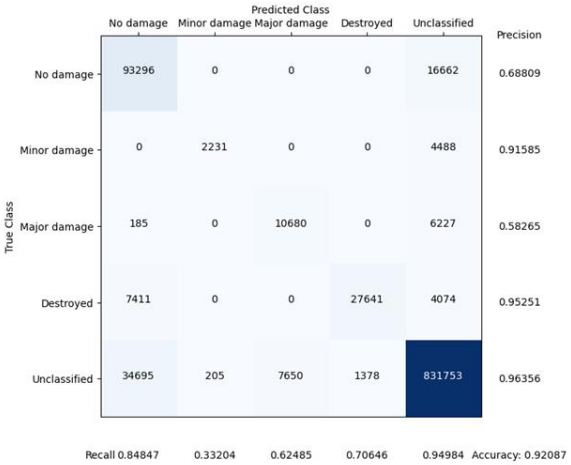

(2)

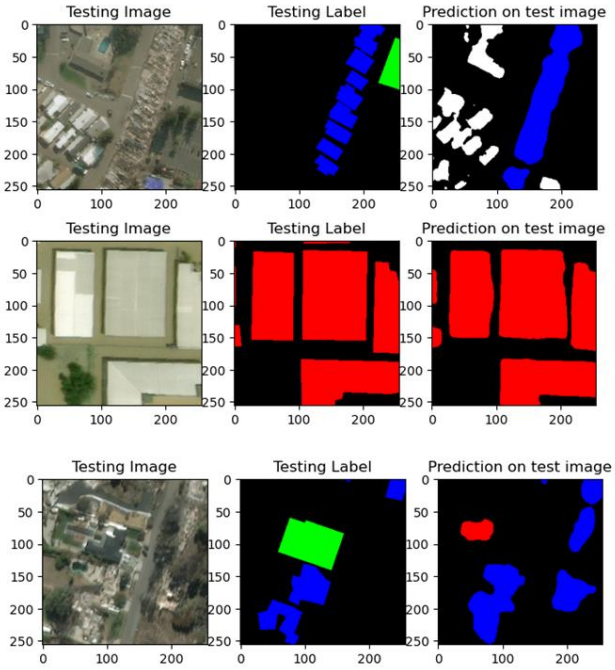

LinkNet_Inception V3

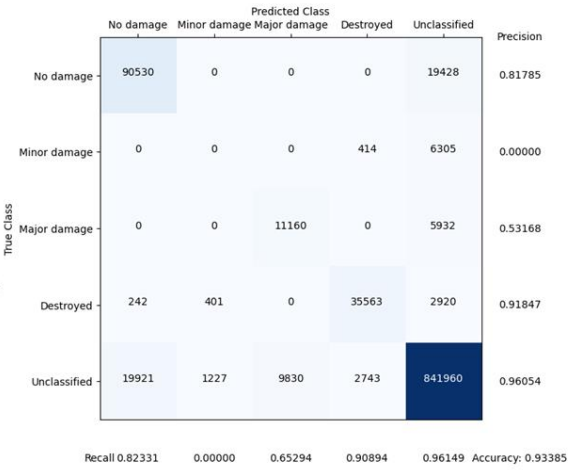

(3)

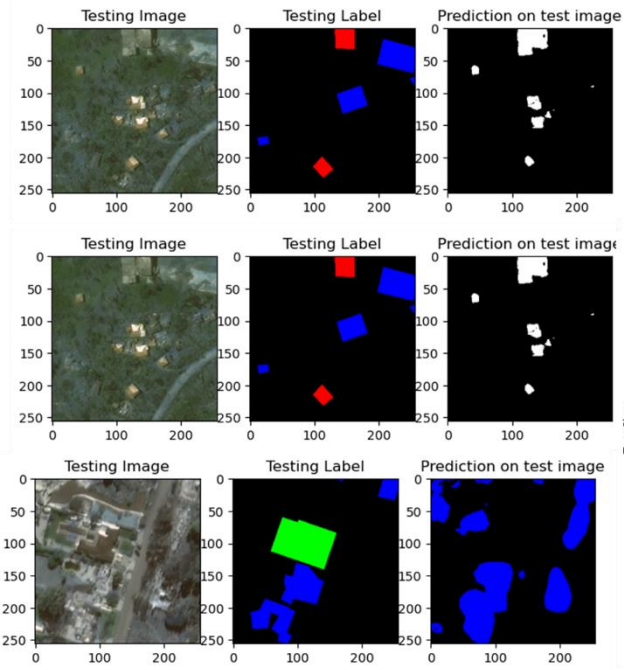

LinkNet_VGG16

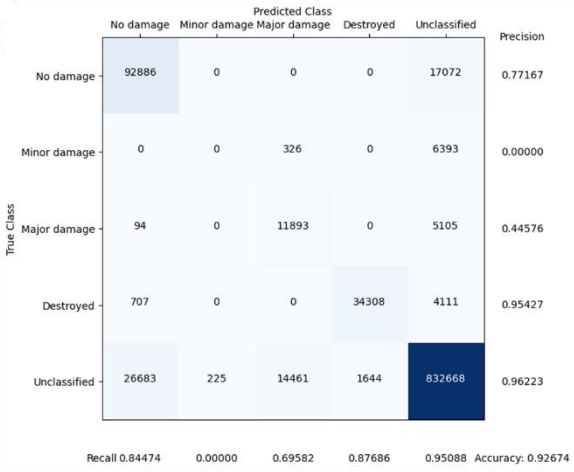

(4)

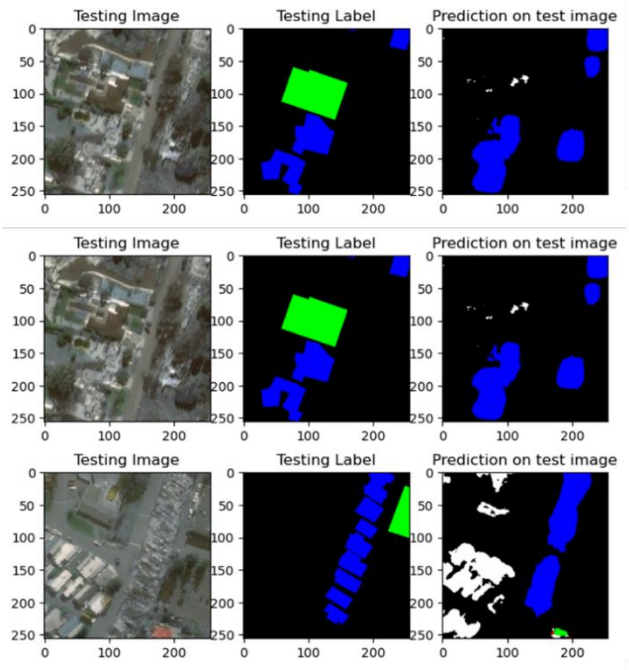

LinkNet_VGG19

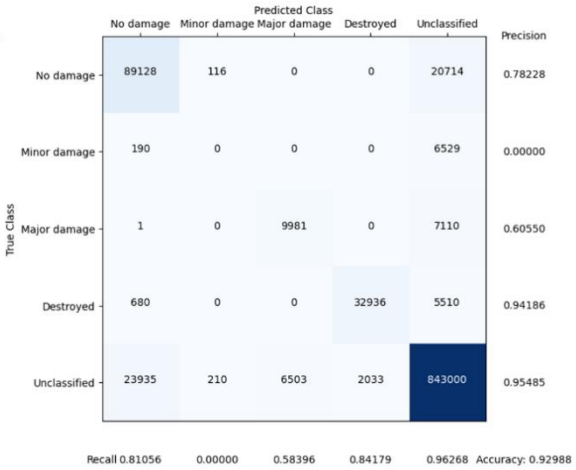

(5)

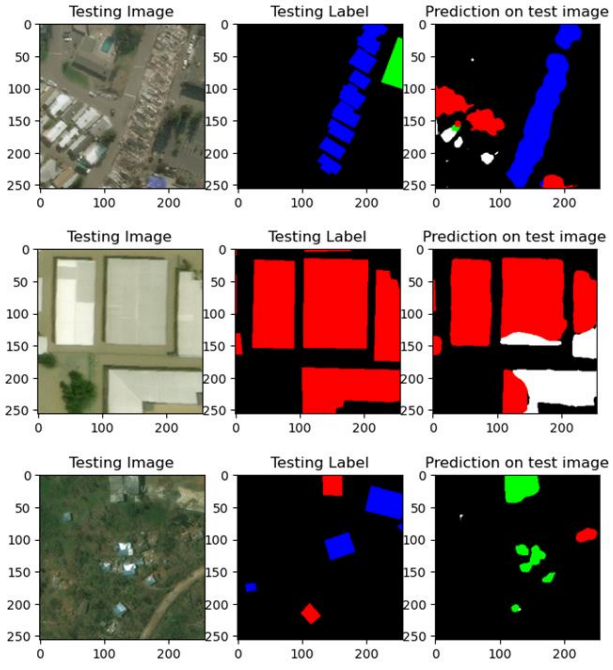

U-Net_Resnet34

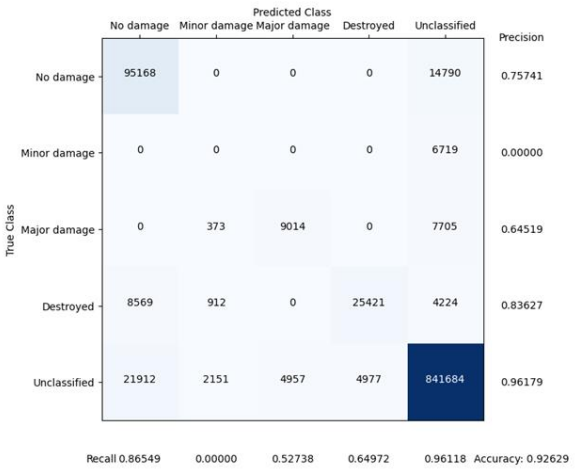

(6)

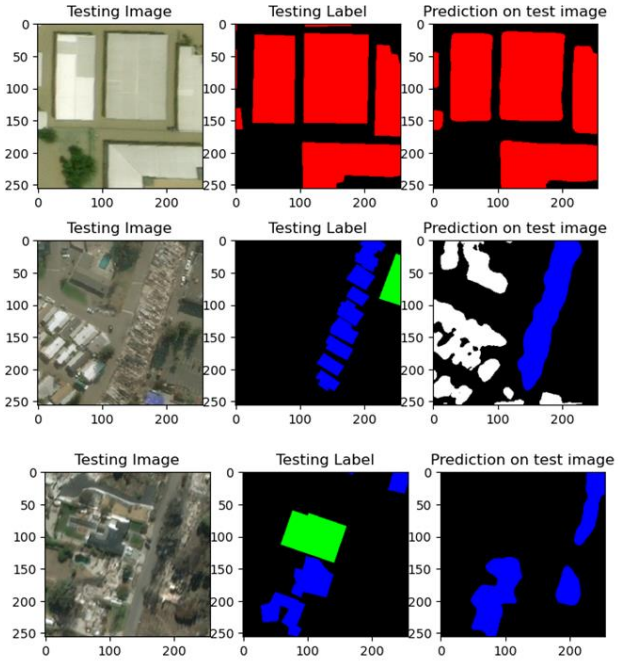

U-Net_Resnet50

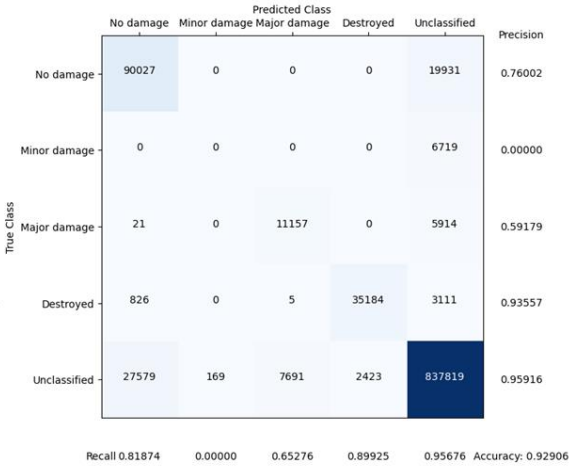

(7)

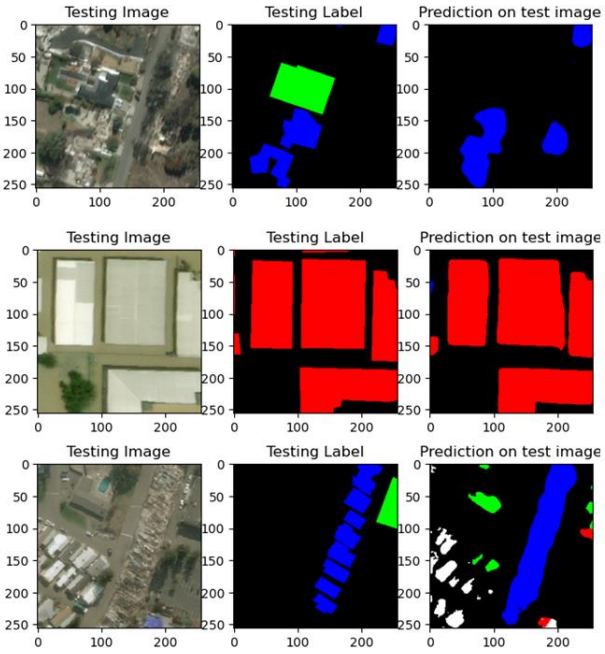

U-Net_Inception V3

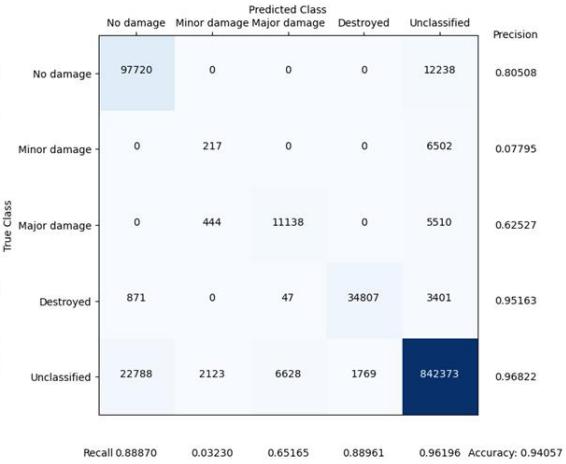

(8)

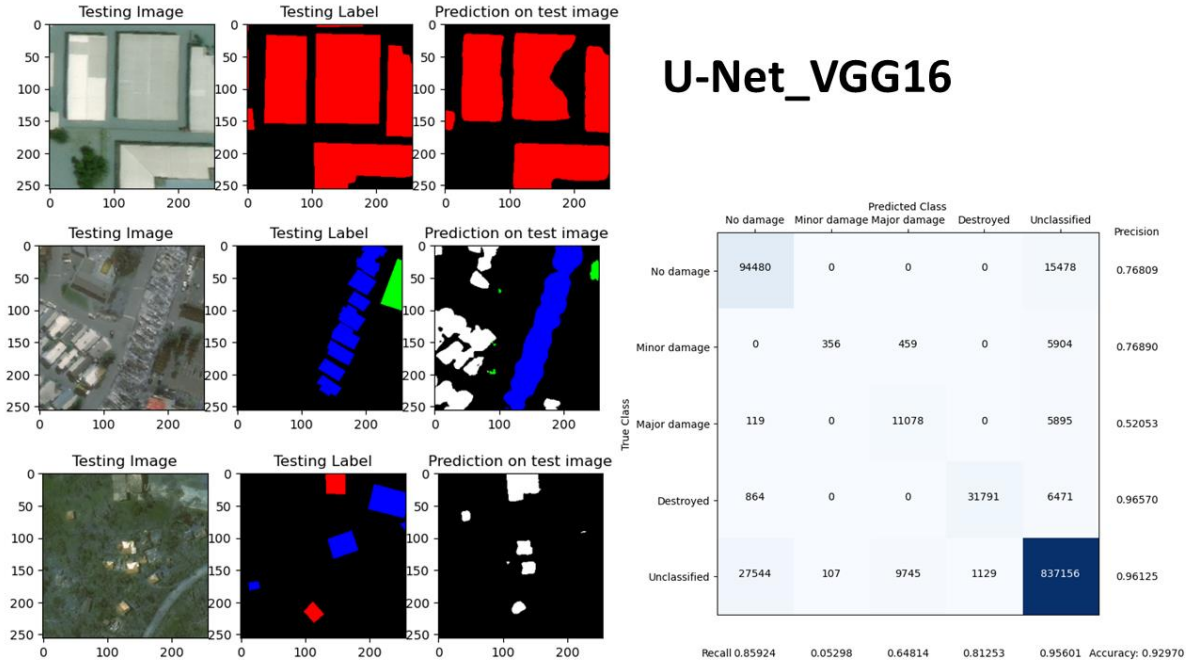

(9)

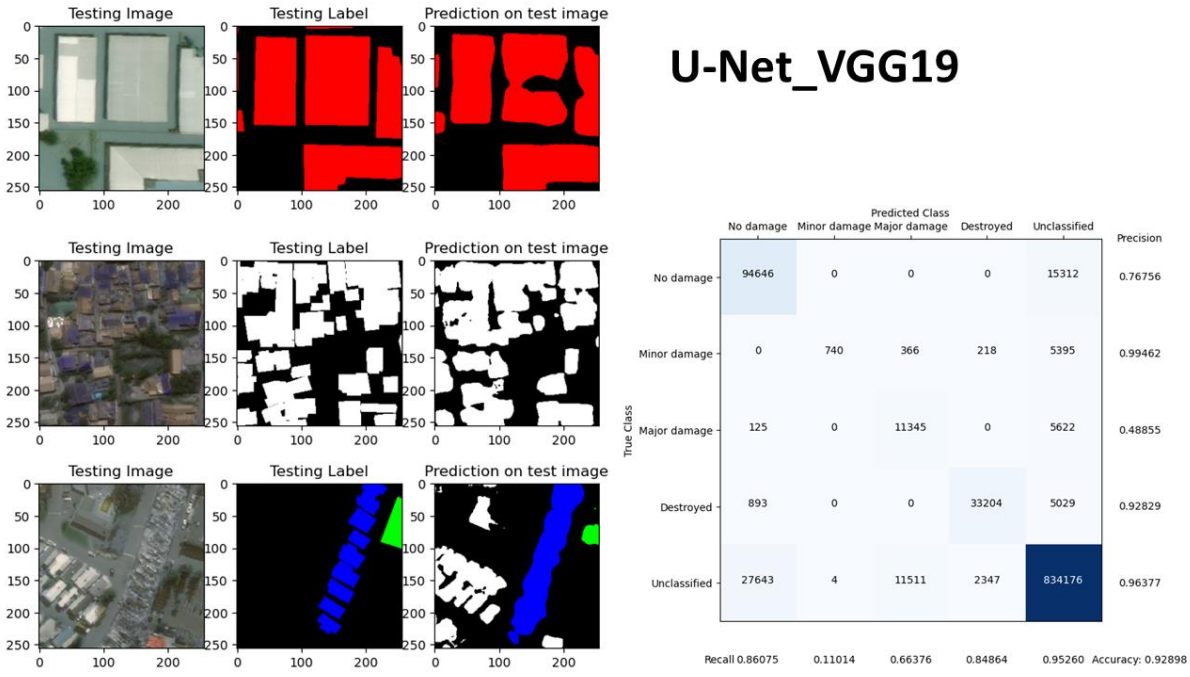

(10)

Figure 98. Comparison of Model results across (1) LinkNet with Resnet34, (2) LinkNet with Resnetr50, LinkNet with Inception v3, (4)LinkNet with VGG 16 (5) LinkNet with VGG19 (6) U-Net with Resnet34, (7) U-Net with ResBer50, (8)U-Net with Inception v3, (9)U-Net with VGG 16 (10) U-Net with VGG19 (a) Representation of the original post disaster HSR test satellite imagery with its companion testing label and model predictions. (b) confusion matrix showing all classes parameters , precison, and recall values.

Switching to the LinkNet model, the results showed similar patterns across the backbones. The Mean IoU Scores ranged from 0.527 to 0.575, while the Mean F1 scores ranged from 0.622 to 0.656. The Class-wise F1 Scores ranged from 0.827 to 0.82, and the Class-wise IoU

Scores ranged from 0.538 to 0.961. Overall, the Inception V3 backbone consistently provided the best results across the models, demonstrating higher Mean IoU Scores and Mean F1 scores. The models generally performed well in detecting "Major damage" but struggled with "Destroyed" and "Unclassified" damages.

Comparing the results of LinkNet and U-Net models with different backbones, there are some differences in their performance observed. When using the ResNet34 backbone, the LinkNet model achieved a slightly higher Mean IoU Score of 0.527 compared to U-Net's score of 0.517. However, U-Net outperformed LinkNet in terms of the Mean F1 score, with a score of 0.61 compared to LinkNet's score of 0.622. The Class-wise F1 Scores were generally higher for U-Net, except for the "No damage" class, where LinkNet achieved a slightly better score of 0.79 compared to U-Net's score of 0.731. In terms of Class-wise IoU Scores, U-Net had higher scores across all classes except for "No damage."

Switching to the Inception V3 backbone, U-Net showed improvement in its performance compared to the ResNet34 backbone. It achieved a higher Mean IoU Score of 0.601 compared to LinkNet's score of 0.575. Similarly, U-Net had a higher Mean F1 score of 0.682 compared to LinkNet's score of 0.656. In terms of Class-wise F1 Scores, U-Net consistently outperformed LinkNet across all classes. The Class-wise IoU Scores also favoured U-Net, except for the "No damage" class, where LinkNet scored slightly higher.

With the ResNet50 backbone, the LinkNet model achieved a higher Mean IoU Score of 0.593 compared to U-Net's score of 0.573. However, U-Net surpassed LinkNet in terms of the Mean F1 score, with a score of 0.656 compared to LinkNet's score of 0.623. U-Net achieved higher Class-wise F1 Scores for "Minor damage," "Destroyed," and "Unclassified" classes, while LinkNet had a slightly higher score for the "No damage" class. In terms of Class-wise IoU Scores, U-Net consistently outperformed LinkNet across all classes.

Overall, the comparison between LinkNet and U-Net models shows that the performance can vary depending on the backbone used. While LinkNet achieved slightly higher Mean IoU Scores in some cases, U-Net generally outperformed LinkNet in terms of Mean F1 score and Class-wise F1 Scores. U-Net also had higher Class-wise IoU Scores in most cases, indicating better localization of damages within each class. It is important to note that the performance of the models can also be influenced by other factors, such as the dataset, training parameters, and specific implementation details.

4.3 Comparison with existing studies and models

In this section, the performance of our proposed model, LinkNet+ResNet50, is compared to three existing studies that also utilized the xBD dataset for disaster damage assessment.

The studies considered for comparison are (R. Gupta et al., 2019; Weber & Kané, 2020; Zheng, Zhong, et al., 2021). Gupta et al, 2019, used the UNet+ResNet50 architecture as their baseline model, achieving an F1 score of 0.265. Although their score was relatively lower compared to the other studies, their methodology may have introduced unique approaches or insights to the field. Weber et al, 2020, employed the FPN+ResNet50 model and obtained an F1 score of 0.73. Their model demonstrated improved performance, likely attributed to the effective feature extraction and representation capabilities of the FPN architecture. (Zheng, Zhong, et al., 2021), proposed the ChangeOS+ResNet50 model, achieving the highest F1 score of 0.78. Their approach incorporated the ChangeOS technique, which likely contributed to enhanced performance by effectively addressing specific challenges in the xBD dataset.

In comparison, our model, LinkNet+ResNet50, attained an F1 score of 0.72. Although, various backbones with U-Net and LinkNet as illustrated in previous sections are also explored. The U-Net with inception V3 has the highest IoU score but lower F1 score than LinkNet with ResNet50. As the baseline model and other studies have reported the results in terms of F1 score, thus considered as appropriate metric for this study. IN this way, it would be easy to compare with the existing models and studies. Our two best models i.e. Unet + Inception v3 and LinkNet+ ResNet50 are considered to be implemented later. While both of them falls between the performance of Gupta et al and Weber et al, it is lower than the score achieved by Zheng et al.

The LinkNet architecture, known for its lightweight design, was combined with the ResNet50 backbone to strike a balance between performance and computational efficiency. The significance of our model lies in its potential to achieve competitive results while utilizing a more lightweight architecture compared to FPN or ChangeOS. This makes our model suitable for scenarios where computational resources are limited or real-time inference is required. Further analysis and experimentation could provide insights into its strengths, weaknesses, and potential areas of improvement.

Table 36. Comparison of the F1 score from our best performing model with the existing models

Study Name	Model Used	F1 Score
Our Model	LinkNet+ ResNet50	0.72
Our Model	U-Net + Inception v3	0.682
Gupta et al, 2019 (Baseline Model)	U-Net	0.265
Weber et al, 2020	FPN+ ResNet50	0.73
Zheng et al, 2021	ChangeOS+ ResNet50	0.78

4.4 Application of the model: Case studies

4.4.1 Case Study 1: Haiti Earthquake 2021

Haiti is a nation in the Caribbean Sea, as shown in Figure 15 (a), (b). On August 14, 2021, a 7.2-magnitude earthquake rocked Haiti, with its epicentre around 7.5 miles northeast of Saint-Louis-du-Sud. As a result of the earthquake, the Haitian Civil Protection General Directorate has warned of a potential massive humanitarian disaster. Landslides occurred in an area covering 2,700 square kilometres (1,000 square miles), causing at least 8,444 damages.

The earthquake destroyed 13,695 dwellings and damaged another 13,785 structures. One notable structure in this study is Hotel Le Manguier, located in Les Cayes, as highlighted in Figure 15 (c). Haiti is chosen as the study area for the following reasons. (1) *xBD* dataset contain images of earthquake only from Mexico City, 2017. No other earthquake-related data is included. Therefore, Haiti Earthquake 2021 is chosen to cover more earthquake events. (2) One of the most severe earthquakes reported globally.

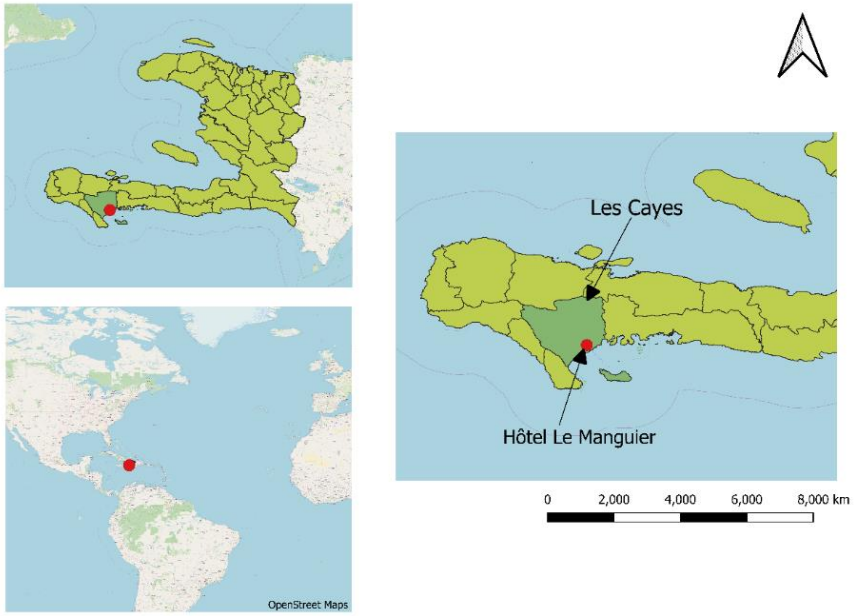

Figure 99: (a) Location of Haiti in WorldMap, (b) Zoomed View of Republic of Haiti (c) Area used in this study (UNOSAT, 2021)

ChangeOS Performance on the Haiti Earthquake Dataset: Upon applying the ChangeOS model to the newly created test dataset for the Haiti earthquake in 2021, promising quantitative results were obtained. The model achieved a weighted F1 score of 96.3% for both building localization and damage classification tasks. Notably, this score surpasses the reported F1 score for man-made disasters like Beirut (64.45% in Zheng et al., 2021) and outperforms the baseline model, which achieved only 23% (as reported in [19]). These comparisons

underscore the effectiveness of the ChangeOS model when applied to the new Haiti earthquake dataset.

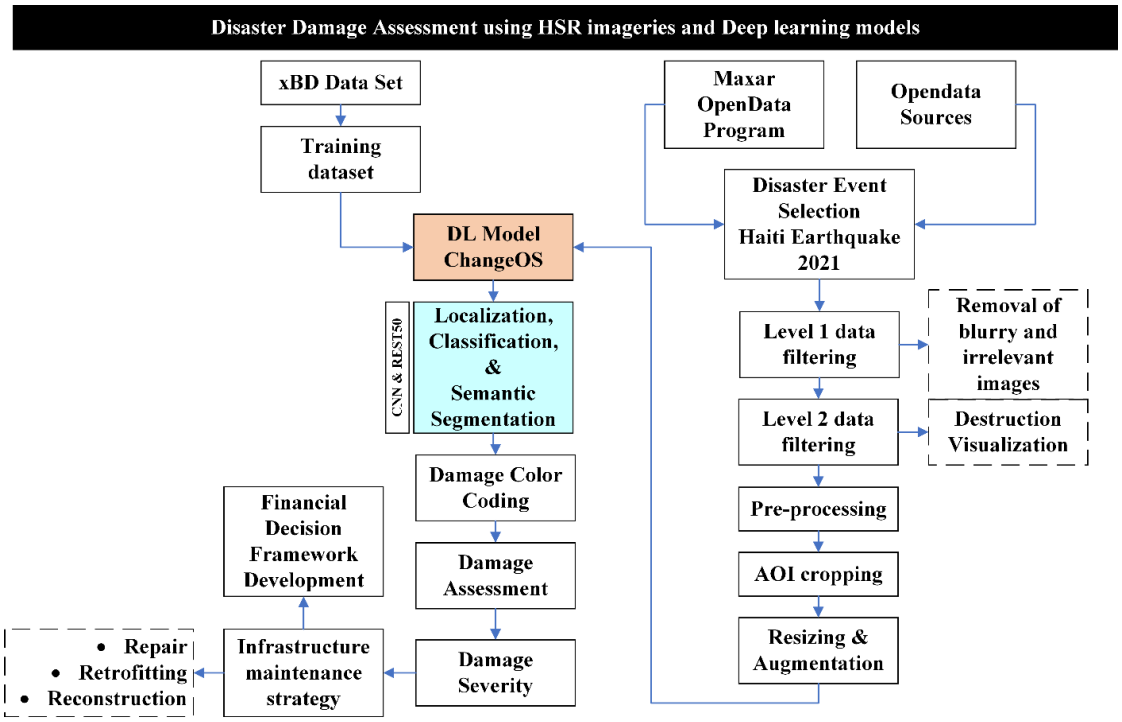

Figure 100. Approach followed in this case study for disaster damage assessment.

Data Pre-processing Techniques and Performance Improvements: Various data pre-processing techniques were employed and evaluated through a series of experiments to further enhance the model's performance. The results, as shown in Table 2, demonstrate the effectiveness of these techniques. Initially, without any cropping or data augmentation, the model achieved a weighted F1 score of 92.759%. However, incorporating cropping improved the score to 94.732%. Finally, by employing cropping, augmentation, and specific criteria outlined in section 3.3, the model attained a remarkable weighted F1 score of 96.306% for the final dataset. Each experiment was repeated five times to ensure the reliability and consistency of the results.

Localization of Hotel Le Manguier and Model-Ground Truth Agreement: One notable achievement of the ChangeOS model for Haiti was accurately identifying the Hotel Le Manguier's location (18.21 N, -73.76 W). The model categorized the hotel under 'Major Damage,' aligning with the ground truth. This successful identification and alignment further validate the model's effectiveness. Figure 19 (a) and (b) depict the location of the hotel in pre- and post-disaster images, respectively, as identified by the model. In Figure 19 (d), the hotel is highlighted in red, indicating 'major damage.' However, it is important to note that the model exhibited limitations in identifying other buildings (Figure 19 (c)), indicating areas for further improvement.

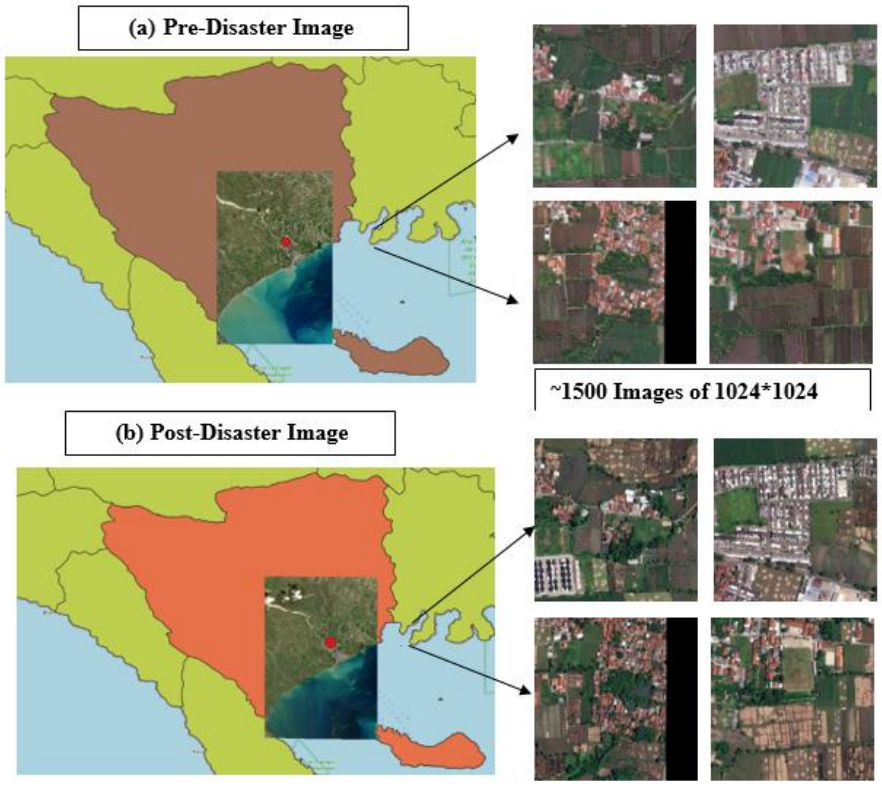

Figure 101. Pre-processing of Dataset and its augmentation for pre and post disaster scenarios.

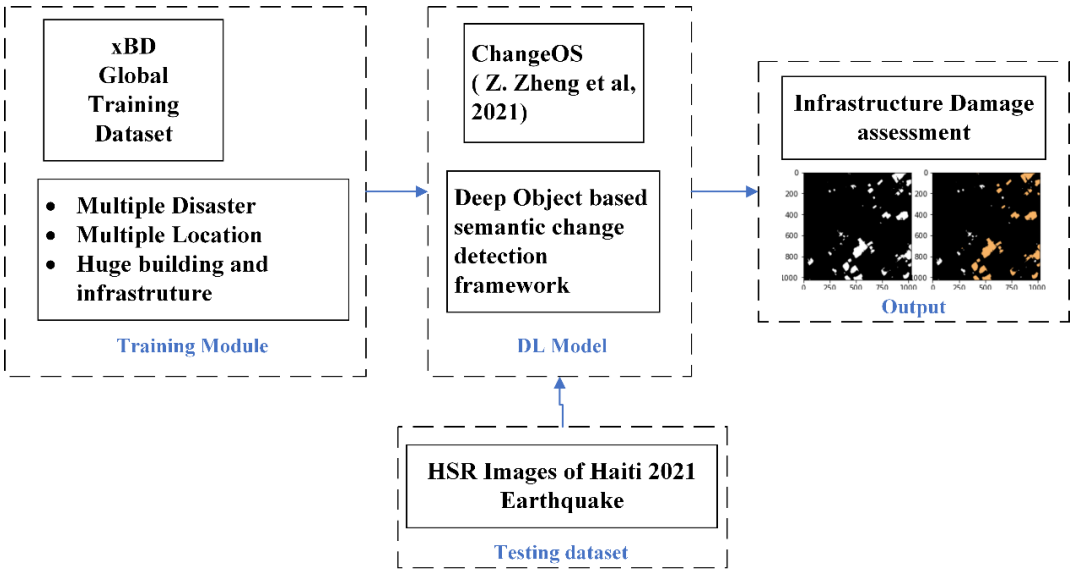

Figure 102. Framework of ChangeOS used in this study adopted from (Z. Zheng et. al, 2021)

Table 37. representing the results from the series of the experiments:

Experiment	Weighted F1 score
Without any cropping and data Augmentation, criteria	92.759%
With cropping but without any augmentation and criteria	94.732%
With cropping, applying Augmentation and criteria as explained in section 3.3 (the final dataset)	96.306%

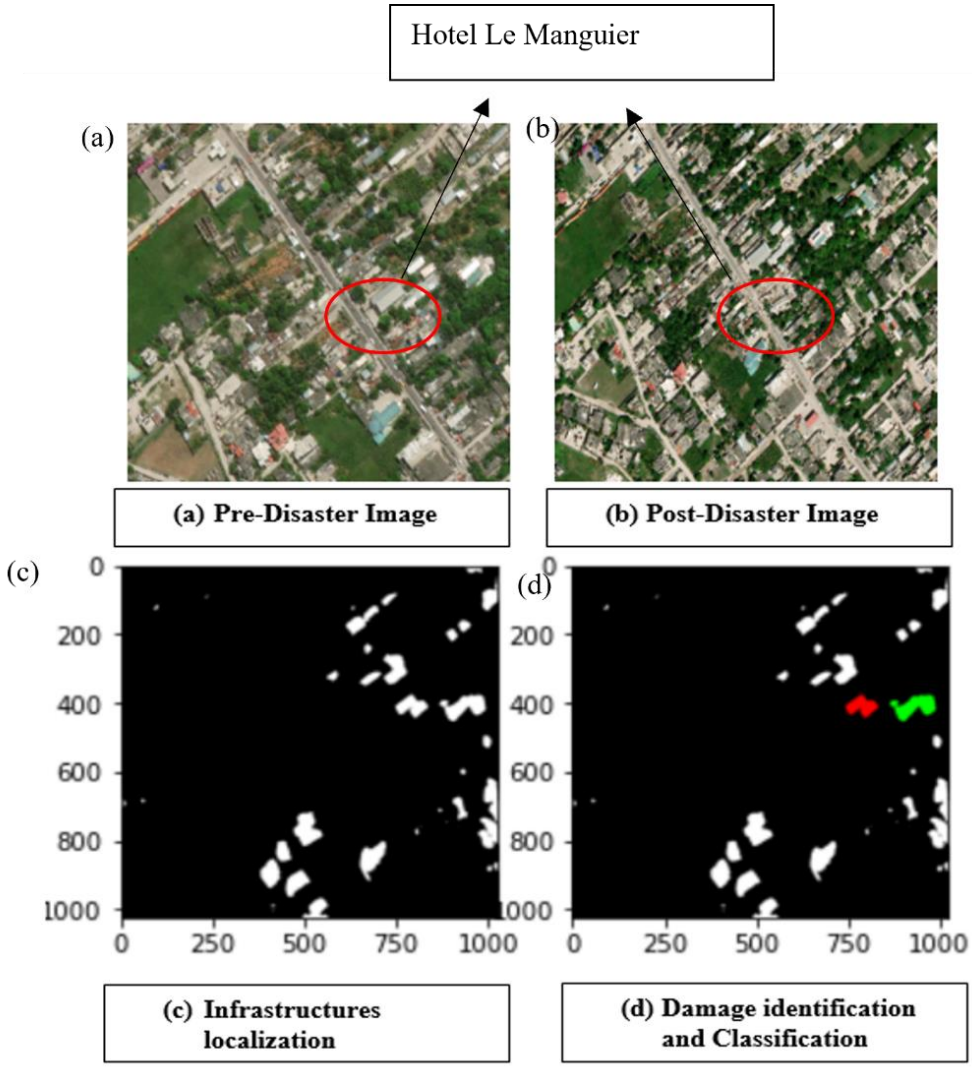

4.4.2 Case Study 2: Indonesia Earthquake 2022

The 5.6-magnitude earthquake that struck Cianjur, West Java, Indonesia, on November 21, 2022, caused significant devastation and loss of life. The seismic event with its epicentre located approximately 10 km southwest of Cianjur Regency. Over 2,000 people were injured, and tens of thousands were displaced. The earthquake's impact was far-reaching, leaving over 2,000 people injured and displacing tens of thousands from their homes. The extensive damage assessments revealed the severity of the destruction, with 22,241 houses classified as seriously damaged, 11,641 as moderately damaged, and 22,090 as slightly damaged (*Indonesia: Earthquake - Nov 2022 | ReliefWeb*, 2022). The Figure 20 underscore the magnitude of the tragedy and the urgent need for comprehensive response and recovery efforts.

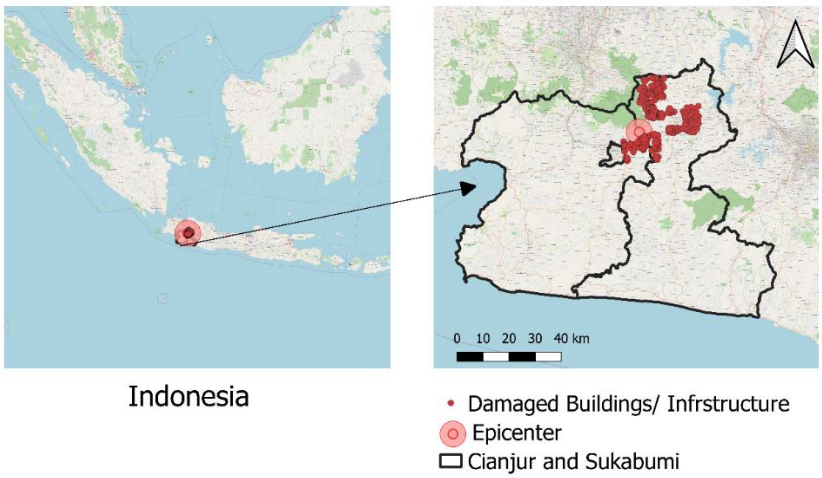

Figure 103. Location of earthquake and its epicentre on geographical map (UNOSAT, 2022)

The Figure 21 shows the representation of our model over the Indonesia 2022 images. These high-resolution satellite imageries were retrieved from the maxar/ open globe dataset. Then these imagers were pre-processed before feeding into the model. These images are not part of *xBD* dataset, instead new dataset is being created for further use. As the Figure 21 shows that without the ground dataset availably, the model is able to predict buildings from the image. Then the disaster damage with the severity is also predicted in pre and post images. This holds a great potential for the application in the future in real-time to be applied just after or on-going disaster. This technique can also improve preparedness and response. By accurately assessing the damage caused by a disaster, authorities and organizations can better understand the extent of the impact and allocate resources accordingly. This information can help in coordinating relief efforts, mobilizing emergency services, and providing timely assistance to affected communities.

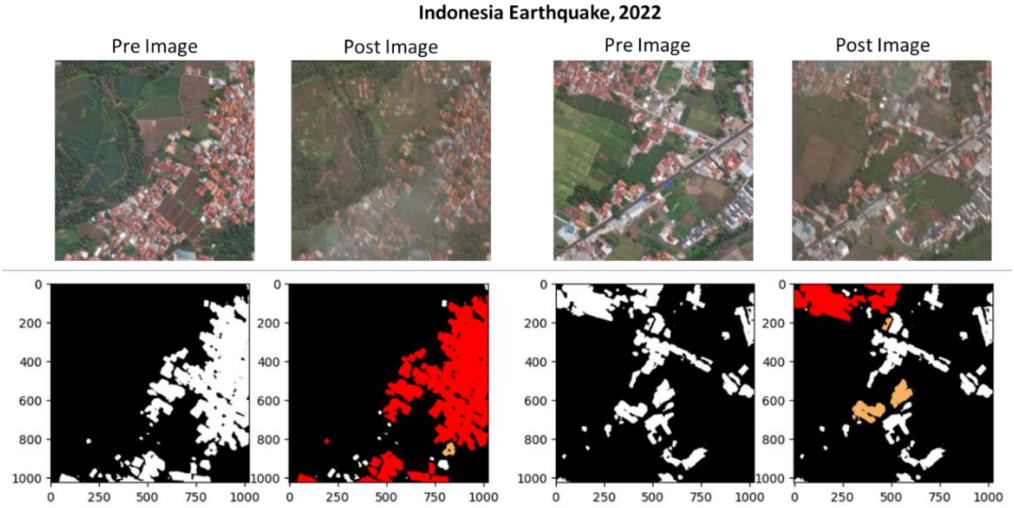

Figure 104. Output obtained using DL model over the Indonesia 2022 HSR images.

Another benefit is the ability to prioritize recovery and reconstruction efforts. By having a comprehensive understanding of the damage incurred, decision-makers can prioritize areas and structures that require immediate attention. This allows for efficient allocation of resources and helps in the timely rebuilding of critical infrastructure, homes, and public facilities, leading to faster recovery and rehabilitation of affected communities.

5.Framework for Financial decisions

MCDM based Financial Decision Framework (FDF)

Multiple Criteria Decision Making (MCDM) also known as Multiple-criteria decision analysis (MCDA) is a branch of operation research that primarily calculate the influence of multiple criteria in the process decision-making. The process involves designing computational and mathematical tools to support the subjective evaluation of a finite number of decision alternatives under a finite number of performance criteria and sub-criteria (Daghouri et al., 2018). TOPSIS is utilised to analyse many objectives simultaneously in our research. There are four phases to the financial decision framework, each with its own set of instructions.as discussed next (S. Gupta & Nair, 2021) :

1. **Stage I Selection of key parameters**

In this step, we'll pick the variables discussed in the literature review. The values from Table 7 are used and reorganized. The parameters are (i) Accommodation, (ii) Agriculture Farming, (iii) Business, (iv) Environmental, (v) Health, (vi) Education, (vii) Other Social. For this project only Key parameters are considered for illustration and sub-parameters are inclusive.

Table 38. Key parameters and their subcategories for financial decisions.

ECONOMIC
Accommodation
Land And Building Compensation
Evacuation Cost / Moving Cost
House Lease Assistance/House Rental Contract
Monthly Living Assistance
Provide Food (3 Times/Day) at Shelter Locations
Provide Amenities and Facilities at Shelter Locations
Agriculture and Farming (The provision of compensation to farmers for mud affected crop failure)
Compensation for Failed Harvests - Rice Fields
Compensation for Failed Harvests - Farms
Compensation for Loss of Future Livelihood
Business

Temporarily Factory Relocations
Permanent Factory Relocations
Evacuation Support
Small Business Compensation
Salary Assistance for workers of Affected Factories
Compensation for Companies that have been Forced to Cease Operating
Environmental
Compensation to Villagers Due to Bad Smells, Dust, Noise, Etc
Provision of Clean Water to Affected Communities (Water Aid)
Reduce Social Impacts Experienced by Residents in the Mudflow Prevention Activities
Social Impacts Arising because of Geological Deformations that Threaten the Safety of Residents
Social Impacts arising because of Geological Deformations that Cause Pollution of Soil and Irrigation Water
Health
Free Medical Services and Facilities
Free Hospitalisation
Burial Assistance
Cost of Life Assurance and Assistance to Affected Communities,
Refugee Management
Education
School Educational and Transport Assistance
Empowerment Programs (Skills Training)
Other Social
Better Deal with the Emotional Stresses
Provide Information, Education and Counselling
Managing Emotional and Spiritual Problems
Source: Public Records and Interviews

2. Stage II Weights for key parameters

In this step, we'll use the existing literature to give parameter weights. Decision-makers may be classified into three broad categories: risk-averse, risk-neutral, and risk-taking (Hatush & Skitmore, 1998). Thus, the weights for all parameters are different for different from the decision-maker (Table 8).

Table 39. Weights for parameters for three cases.

Sno.	Parameters	Abv.	Case 1	Case 2	Case 3
1	Accommodation	P_1	0.8	0.5	0.125
2	Agriculture Farming	P_2	0.1	0.05	0.125
3	Business	P_3	0.1	0.05	0.125
4	Environmental	P_4	0	0.05	0.125
5	Health	P_5	0	0.05	0.125
6	Education	P_6	0	0.2	0.125
7	Other Social	P_7	0	0.05	0.125

3. Stage III Data creation

Four different financial options are created for illustration purposes as shown in Table 9.

Table 40. Radom value for the model

	P_1 (in Mn INR)	P_2	P_3	P_4	P_5	P_6	P_7	P_8
Option 1	10.5	9	10	9	8	8	10	7
Option 2	9.8	10	8	9	7	8	7	6
Option 3	11	10	9	8	9	9	7	7
Option 4	11.2	10	10	9	8	9	7	7

4. Stage IV Evaluation using TOPSIS technique.

The implementation of TOPSIS tool includes the following procedure steps (S. Gupta & Nair, 2021) :

Step 1: The first step is to create a decision matrix, where each row represents a possible course of action, and each column represents a criterion against which those options must be weighed.

$$A_{mn:}\{a_{ij} / i \in (1,2,.....m), j \in (1,2,.....n)\} \quad (6)$$

Step 2: The following equation is used to derive the normalised decision matrix from the decision matrix obtained in Step 1.

$$r_{ij} = x_{ij} / \sqrt{\sum_{j=1}^{j} x_{ij}^2}, j = 1,2,3,....., j \; and \; i = 1,2,3,....n \quad (7)$$

Where x_{ij} = original weight score of decision matric and r_{ij} = normalized weight score of decision matric.

Step 3: The third step involves solving the following equation to generate the weighted normalized decision matrix:

$$v_{ij} = w_i * r_{ij}, j = 1,2,3,....., j \; and \; i = 1,2,3,....n \quad (8)$$

Where w_i = weight of evaluation criteria and r_{ij} = normalized decision matrix.

Step 4: The below equation can be used to decide the optimal course of action, and an understanding of the positive ideal solution (PIS) and the negative ideal solution (NIS) is essential.

$$A^* = \{v_1^*, v_1^*, ..., v_n^*\} \; maximum \; values \quad (9)$$

$$\text{Where } v_i^* = \{\max(v_{ij}) \; if \; j \in J; \; \min(v_{ij}) \; if \; j \in J^-\}$$

$$A^- = \{v_1^-, v_1^-, ..., v_n^-\} \min values \quad (10)$$

$$\text{Where } v_i^- = \{\min(v_{ij}) \; if \; j \in J; \; \max(v_{ij}) \; if \; j \in J^-\}$$

Step 5: Next step is to calculate the separation measures of each alternative from PIS and NIS

$$d_i^* = \sqrt{\sum_{j=1}^{n}(v_{ij} - v_j^*)^2}, j = 1,2,3,.....,J \quad (11)$$

$$d_i^- = \sqrt{\sum_{j=1}^{n}(v_{ij} - v_j^-)^2}, j = 1,2,3,.....,J \quad (12)$$

Step 6: The last step is to use Eq. 13 to get the relative closeness coefficient of each option's optimal solution.

$$CC_i = \frac{d_i^-}{d_i^* + d_i^-} \; i = 1,2,3.....,J \quad (13)$$

Step 7: The best choices are those with the highest proximity coefficient. Therefore, the is utilised to rank the available choices. The greatest worth is found at the top, and the least at the bottom. The procedures detailed in Stage IV are carried out by use of a MATLAB programme..

5. Results

The normalized matric and weighted matrix is shown in Annexure 4. Table 10 displays the outcome of a financial decision analysis. The results may be compared in two ways: (1) to each other, to grasp the significance of adding multi-criteria impacts, and (2) to the state of the art and existing literature. Thus, it will aid strategists in developing more effective plans.

Table 41. Closeness coefficient and Rank obtained for Case 1,2, ands 3

Alternatives	Case 1		Case 2		Case 3	
	CC_i	Rank	CC_i	Rank	CC_i	Rank
Option 1	0.515	2	0.502	2	0.710	1
Option 2	0.831	1	0.660	1	0.353	4
Option 3	0.189	3	0.324	3	0.399	3
Option 4	0.185	4	0.194	4	0.439	2

6. Enablers and Barriers

Enablers

- A prestigious fellowship provided invaluable support, enabling the development of new research connections and the pursuit of challenging projects with confidence.

- Accessible conference travel was made possible through supplemental funding, allowing for networking opportunities and knowledge exchange with experts in the field.
- The ability to hire students and young professionals during research and peak hours brought fresh perspectives and additional support, enriching the overall research process.
- Mentorship from a trusted TEG (Technical Expert Group) member played a pivotal role in guiding the research towards more impactful outcomes, providing valuable insights and expertise.
- The management team at CDRI consistently exhibited exceptional helpfulness and engagement, fostering a collaborative environment conducive to research success.
- Quarterly revisions proved highly beneficial, as they provided opportunities to assess the research's direction and make necessary adjustments. The feedback received on the research topic's clarity, understanding of research problems, and the design's effectiveness further enhanced the quality and progress of the project.

Barriers

- The opensource data for recent events are sometimes not available.
- Pre-processing of data is required as no pre-processed data is available.
- Implementation of machine learning models requires high computing power, thus a time-consuming process.
-

7. Key Takeaways from CDRI Fellowship Programme

With the CDRI Fellowship, we now have a better understanding of practical ways of researching disaster-resilient infrastructure, better contacts to approach for future collaborations and a platform to showcase our research at a global stage. Following are the takeaways experienced during fellowship program.

1. Enhanced Research Connections: The CDRI Fellowship Programme offers a unique opportunity to develop new research connections. Fellows gain access to a network of experts and researchers, fostering collaborations and expanding their professional circle.
2. Support for Challenging Research: Fellows receive support and resources to pursue challenging research projects with confidence. The programme provides

the necessary funding and infrastructure to tackle complex issues and make significant contributions to the field.

3. Conference Travel Opportunities: The fellowship programme makes conference travel accessible through supplemental funding. Fellows have the chance to attend conferences, present their research, and engage with peers and experts from around the world, expanding their knowledge and visibility within the research community. Exceptional
4. Support from CDRI Management: Fellows consistently receive exceptional support and engagement from the management team at CDRI. The programme's administrators and staff go above and beyond to aid, guidance, and resources, creating a conducive environment for successful research outcomes.

8. Conclusion

This report explores the use of remote sensing technologies, particularly satellite and aerial imagery, for damage detection and assessment in the aftermath of natural disasters. The study emphasizes the importance of real-time damage assessment systems in facilitating swift disaster response and recovery efforts. While satellite imagery has been widely employed in this domain, aerial imagery captured using drones or aircraft offers even higher spatial resolution. The report highlights the limitations of existing damage detection methods and proposes the use of Convolutional Neural Networks (CNNs) and segmentation models as a more effective approach. To ensure the accuracy and generalization of CNNs, a large and diverse training dataset is required. The report introduces the *xView* dataset, which contains labelled satellite imagery scenes and is one of the largest publicly available datasets for building damage detection. The combination of this dataset with recent advancements in computer vision offers significant potential for improving post-disaster assessment and response efforts.

The report also discusses the aim, objectives, and scope of the research study, which focuses on developing a deep-learning framework for detecting demolished buildings and providing a rating model for monitoring. The practical applications and implications of the research include accuracy analysis, understanding past financial strategies for reconstruction, and optimizing long-term and short-term strategies for decision-makers. The limitations of the study are acknowledged, including the difficulty of testing the outcome in real-time scenarios and the focus on infrastructure damage rather than vegetation or forests.

Overall, this report highlights the potential of remote sensing technologies, particularly satellite and aerial imagery, in improving post-disaster damage assessment and response efforts. The utilization of machine learning model and the availability of diverse imagery data offer new possibilities for automated frameworks and decision support systems. The research conducted in this study contributes to the existing knowledge in the field and provides insights for future studies and applications.

9.Way Forward

The study's model shows promise in disaster damage assessment, but it's crucial to explore alternative approaches for further improvement. One approach is the utilization of Generative Adversarial Networks (GANs) to generate synthetic images simulating different levels of damage. Training a GAN on pre- and post-disaster images enhances the training data and improves the model's robustness. Spatial-temporal models leveraging temporal data like satellite imagery or aerial photographs capture dynamic changes over time, offering a comprehensive assessment of damage evolution. Deep metric learning enables precise identification of damaged areas and better assessment of change by measuring image similarity. Fusion techniques combining multimodal data enhance model accuracy and robustness. Incorporating explainable AI techniques provides insights into the decision-making process and improves interpretability. Transfer learning from pre-trained models and semi-supervised learning techniques address limited labelled data challenges.

Looking ahead, the disaster damage assessment model has numerous potential applications. Firstly, it can be integrated with remote sensing technologies for real-time damage assessment during and immediately after a disaster, aiding emergency responders. Secondly, deploying the model on UAVs or drones enables rapid and automated damage mapping, supporting timely decision-making for response teams. Thirdly, the model can be integrated into decision support systems, assisting disaster management agencies in prioritizing operations, identifying safe zones, and optimizing resource allocation. Fourthly, the model's ability to assess damage levels contributes to risk assessment and planning for future disasters. Fifthly, it can be utilized for ongoing infrastructure monitoring and maintenance, detecting areas in need of repair. Furthermore, the model streamlines insurance claims processing, improves climate change impact analysis, and informs mitigation strategies. These future applications highlight the model's versatility and potential for enhancing disaster response, decision-making, and community resilience.

References

1. Adriano, B., Xia, J., Baier, G., Yokoya, N., & Koshimura, S. (2019). Multi-source data fusion based on ensemble learning for rapid building damage mapping during the 2018 Sulawesi earthquake and Tsunami in Palu, Indonesia. *Remote Sensing*, *11*(7). https://doi.org/10.3390/RS11070886
2. Anghel, A., Vasile, G., Boudon, R., d'Urso, G., Girard, A., Boldo, D., & Bost, V. (2016). Combining spaceborne SAR images with 3D point clouds for infrastructure monitoring applications. *ISPRS Journal of Photogrammetry and Remote Sensing*, *111*, 45–61. https://doi.org/10.1016/j.isprsjprs.2015.11.008
3. Brunner, D., Lemoine, G., & Bruzzone, L. (2010). Earthquake damage assessment of buildings using VHR optical and SAR imagery. *IEEE Transactions on Geoscience and Remote Sensing*, *48*(5), 2403–2420. https://doi.org/10.1109/TGRS.2009.2038274
4. Cheng, G., Zhou, P., & Han, J. (2016). Learning Rotation-Invariant Convolutional Neural Networks for Object Detection in VHR Optical Remote Sensing Images. *IEEE Transactions on Geoscience and Remote Sensing*, *54*(12), 7405–7415. https://doi.org/10.1109/TGRS.2016.2601622
5. Daghouri, A., Mansouri, K., & Qbadou, M. (2018). Information system performance evaluation and optimization using AHP and TOPSIS: Construction industry case. *Proceedings of the 2018 International Conference on Optimization and Applications, ICOA 2018*, *Mcdm*, 1–8. https://doi.org/10.1109/ICOA.2018.8370589
6. Dell'Acqua, F., & Polli, D. A. (2011). Post-event only VHR radar satellite data for automated damage assessment: A study on COSMO/SkyMed and the 2010 Haiti earthquake. *Photogrammetric Engineering and Remote Sensing*, *77*(10), 1037–1043. https://doi.org/10.14358/PERS.77.10.1037
7. Dong, L., & Shan, J. (2013). A comprehensive review of earthquake-induced building damage detection with remote sensing techniques. *ISPRS Journal of Photogrammetry and Remote Sensing*, *84*, 85–99. https://doi.org/10.1016/j.isprsjprs.2013.06.011
8. Duda, K. A., & Jones, B. K. (2011). USGS remote sensing coordination for the 2010 Haiti earthquake. *Photogrammetric Engineering and Remote Sensing*, *77*(9), 899–908. https://doi.org/10.14358/PERS.77.9.899
9. Endo, Y., Adriano, B., Mas, E., & Koshimura, S. (2018). New insights into multiclass damage classification of Tsunami-induced building damage from SAR images. *Remote Sensing*, *10*(12). https://doi.org/10.3390/RS10122059
10. Erdogan, M., & Yilmaz, A. (2019). Detection of building damage caused by Van Earthquake using image and Digital Surface Model (DSM) difference. *International*

Journal of Remote Sensing, *40*(10), 3772–3786. https://doi.org/10.1080/01431161.2018.1552816

11. Gupta, R., Goodman, B., Patel, N., Hosfelt, R., Sajeev, S., Heim, E., Doshi, J., Lucas, K., Choset, H., & Gaston, M. (2019). Creating XBD: A dataset for assessing building damage from satellite imagery. *IEEE Computer Society Conference on Computer Vision and Pattern Recognition Workshops*, *2019-June*, 10–17.
12. Gupta, S., & Nair, S. (2021). Evaluation of Bid in Construction Industry Based on Multi-criteria Approach Using TOPSIS. *Lecture Notes in Civil Engineering*, *172*, 139–151. https://doi.org/10.1007/978-981-16-4396-5_13/COVER/
13. Hatush, Z., & Skitmore, M. (1998). Contractor Selection Using Multicriteria Utility Theory: An Additive Model. *Building and Environment*, *33*(2–3), 105–115. https://doi.org/10.1016/S0360-1323(97)00016-4
14. Huang, B., Zhao, B., & Song, Y. (2018). Urban land-use mapping using a deep convolutional neural network with high spatial resolution multispectral remote sensing imagery. *Remote Sensing of Environment*, *214*, 73–86. https://doi.org/10.1016/j.rse.2018.04.050
15. *Indonesia: Earthquake - Nov 2022 | ReliefWeb*. (2022). https://reliefweb.int/disaster/eq-2022-000363-idn
16. Janalipour, M., & Mohammadzadeh, A. (2016). Building Damage Detection Using Object-Based Image Analysis and ANFIS from High-Resolution Image (Case Study: BAM Earthquake, Iran). *IEEE Journal of Selected Topics in Applied Earth Observations and Remote Sensing*, *9*(5), 1937–1945. https://doi.org/10.1109/JSTARS.2015.2458582
17. Karimzadeh, S., Matsuoka, M., Miyajima, M., Adriano, B., Fallahi, A., & Karashi, J. (2018). Sequential SAR coherence method for the monitoring of buildings in Sarpole-Zahab, Iran. *Remote Sensing*, *10*(8). https://doi.org/10.3390/RS10081255
18. Kaya, G. T., Ersoy, O. K., & Kamaşak, M. E. (2010). Hybrid SVM and SVSA method for classification of remote sensing images. *International Geoscience and Remote Sensing Symposium (IGARSS)*, 2828–2831. https://doi.org/10.1109/IGARSS.2010.5649062
19. Lam, D., Kuzma, R., McGee, K., Dooley, S., Laielli, M., Klaric, M., Bulatov, Y., & McCord, B. (2018). *xView: Objects in Context in Overhead Imagery*. http://arxiv.org/abs/1802.07856
20. Lecun, Y., Bengio, Y., & 4g332, R. (2010). *Convolutional Networks for Images, Speech, and Time-Series*.

21. Li, Y., Hu, W., Dong, H., & Zhang, X. (2019). Building damage detection from post-event aerial imagery using single shot multibox detector. *Applied Sciences (Switzerland)*, *9*(6). https://doi.org/10.3390/app9061128
22. Liu, Y., Chen, D., Ma, A., Zhong, Y., Fang, F., & Xu, K. (2021). Multiscale U-Shaped CNN Building Instance Extraction Framework with Edge Constraint for High-Spatial-Resolution Remote Sensing Imagery. *IEEE Transactions on Geoscience and Remote Sensing*, *59*(7), 6106–6120. https://doi.org/10.1109/TGRS.2020.3022410
23. Merlin, G. S., & Jiji, G. W. (2019). Building Damage Detection of the 2004 Nagapattinam, India, Tsunami Using the Texture and Spectral Features from IKONOS Images. *Journal of the Indian Society of Remote Sensing*, *47*(1), 13–24. https://doi.org/10.1007/s12524-018-0858-z
24. Moya, L., Perez, L. R. M., Mas, E., Adriano, B., Koshimura, S., & Yamazaki, F. (2018). Novel unsupervised classification of collapsed buildings using satellite imagery, hazard scenarios and fragility functions. *Remote Sensing*, *10*(2). https://doi.org/10.3390/RS10020296
25. Naito, S., Tomozawa, H., Mori, Y., Fujiwara, H., & Shoji, G. (2020). Building-damage detection method based on machine learning utilizing aerial photographs of the Kumamoto earthquake. *Earthquake Spectra*, 1–22. https://doi.org/10.1177/8755293019901309
26. Nex, F., Duarte, D., Tonolo, F. G., & Kerle, N. (2019). Structural building damage detection with deep learning: Assessment of a state-of-the-art CNN in operational conditions. *Remote Sensing*, *11*(23). https://doi.org/10.3390/rs11232765
27. Pham, T. T. H., Apparicio, P., Gomez, C., Weber, C., & Mathon, D. (2014). Towards a rapid automatic detection of building damage using remote sensing for disaster management: The 2010 Haiti earthquake. *Disaster Prevention and Management: An International Journal*, *23*(1), 53–66. https://doi.org/10.1108/DPM-12-2012-0148
28. Plank, S. (2014). Rapid damage assessment by means of multi-temporal SAR-A comprehensive review and outlook to Sentinel-1. *Remote Sensing*, *6*(6), 4870–4906. https://doi.org/10.3390/RS6064870
29. Sui, H., Tu, J., Song, Z., Chen, G., & Li, Q. (2014). A novel 3D building damage detection method using multiple overlapping UAV images. *International Archives of the Photogrammetry, Remote Sensing and Spatial Information Sciences - ISPRS Archives*, *40*(7), 173–179. https://doi.org/10.5194/isprsarchives-XL-7-173-2014
30. Tong, X., Hong, Z., Liu, S., Zhang, X., Xie, H., Li, Z., Yang, S., Wang, W., & Bao, F. (2012). Building-damage detection using pre- and post-seismic high-resolution satellite

stereo imagery: A case study of the May 2008 Wenchuan earthquake. *ISPRS Journal of Photogrammetry and Remote Sensing*, *68*(1), 13–27. https://doi.org/10.1016/j.isprsjprs.2011.12.004

31. Turker, M., & Sumer, E. (2008). Building-based damage detection due to earthquake using the watershed segmentation of the post-event aerial images. *International Journal of Remote Sensing*, *29*(11), 3073–3089. https://doi.org/10.1080/01431160701442096
32. Weber, E., & Kané, H. (2020). *Building Disaster Damage Assessment in Satellite Imagery with Multi-Temporal Fusion*. 1–7. http://arxiv.org/abs/2004.05525
33. Xu, J. Z., Lu, W., Li, Z., Khaitan, P., & Zaytseva, V. (2019). Building Damage Detection in Satellite Imagery Using Convolutional Neural Networks. *33rd Conference on Neural Information Processing Systems (NeurIPS 2019), Vancouver, Canada*, *NeurIPS*. http://arxiv.org/abs/1910.06444
34. Ye, X., Liu, M., Wang, J., Qin, Q., Ren, H., Wang, J., & Hui, J. (2017). Building-Based Damage Detection from Postquake Image Using Multiple-Feature Analysis. *IEEE Geoscience and Remote Sensing Letters*, *14*(4), 499–503. https://doi.org/10.1109/LGRS.2017.2651050
35. Zhang, C., Harrison, P. A., Pan, X., Li, H., Sargent, I., & Atkinson, P. M. (2020). Scale Sequence Joint Deep Learning (SS-JDL) for land use and land cover classification. *Remote Sensing of Environment*, *237*. https://doi.org/10.1016/j.rse.2019.111593
36. Zhang, C., Sargent, I., Pan, X., Li, H., Gardiner, A., Hare, J., & Atkinson, P. M. (2018). An object-based convolutional neural network (OCNN) for urban land use classification. *Remote Sensing of Environment*, *216*, 57–70. https://doi.org/10.1016/j.rse.2018.06.034
37. Zhang, C., Sargent, I., Pan, X., Li, H., Gardiner, A., Hare, J., & Atkinson, P. M. (2019). Joint Deep Learning for land cover and land use classification. *Remote Sensing of Environment*, *221*, 173–187. https://doi.org/10.1016/j.rse.2018.11.014
38. Zheng, Z., Ma, A., Zhang, L., & Zhong, Y. (2021). Deep multisensor learning for missing-modality all-weather mapping. *ISPRS Journal of Photogrammetry and Remote Sensing*, *174*, 254–264. https://doi.org/10.1016/j.isprsjprs.2020.12.009
39. Zheng, Z., & Shi, P. (2020). Sample and restoring algorithm of physiological signals from wireless body area network. *International Journal of Intelligent Internet of Things Computing*, *1*(1), 1. https://doi.org/10.1504/IJIITC.2020.10031017
40. Zheng, Z., Zhong, Y., Ma, A., Han, X., Zhao, J., Liu, Y., & Zhang, L. (2020). HyNet: Hyper-scale object detection network framework for multiple spatial resolution

remote sensing imagery. *ISPRS Journal of Photogrammetry and Remote Sensing*, *166*, 1–14. https://doi.org/10.1016/j.isprsjprs.2020.04.019

41. Zheng, Z., Zhong, Y., Wang, J., Ma, A., & Zhang, L. (2021). Building damage assessment for rapid disaster response with a deep object-based semantic change detection framework: From natural disasters to man-made disasters. *Remote Sensing of Environment*, *265*, 112636. https://doi.org/10.1016/J.RSE.2021.112636
42. Zhong, Y., Han, X., & Zhang, L. (2018). Multi-class geospatial object detection based on a position-sensitive balancing framework for high spatial resolution remote sensing imagery. *ISPRS Journal of Photogrammetry and Remote Sensing*, *138*, 281–294. https://doi.org/10.1016/j.isprsjprs.2018.02.014

Machine Learning Based Unified Seismic Vulnerability Prediction Model for the Heritage Minarets of India

Dr Madappa VR Sivasubramanian
Dr Vinay Shimpi
Dr Nidhi M
National Institute of Technology Puducherry, India

Dr Shamsher Bahadur Singh
Birla Institute of Technology and Science, Pilani, India

Dr Nikolaos Nikitas
(University of Leeds, United Kingdom)

Under CDRI Fellowship Programme 2022-23

CDRI
Coalition for Disaster Resilient Infrastructure

Disclaimer: The views expressed in this paper reflect the opinions of the author and not necessarily the official views of CDRI.

Acronyms and Abbreviations

- PGA: Peak Ground Acceleration
- UNESCO: United Nations Educational, Scientific and Cultural Organization
- ANN: Artificial Neural Network
- 3D FEM: Three-dimensional finite element models
- RF: Random Forest
- NDT: Non-Destructive Test
- ML: Machine Learning
- UPV: Ultrasonic Pulse Velocity
- AVT: Ambient Vibration Testing
- MAE: Mean Absolute Error
- MSE: Mean Squared Error
- Δmax: Maximum Interstory Drift Ratio
- Vmax: Maximum Base Shear
- Δa: Allowable Interstory Drift Ratio
- Va: Allowable Base Shear

Abstract

This study introduces a novel machine learning-based approach for predicting the seismic vulnerability of heritage minarets in India. The methodology employs vibration-based structural condition assessment to identify dynamic properties such as natural frequencies and curvature mode shapes. A three-dimensional numerical model of the minarets is developed using finite element analysis software, incorporating nonlinear material and geometric behaviour. To ensure the accuracy of the proposed modelling techniques, the dynamic characteristics of real minaret structures are compared with their corresponding numerical models. Material and boundary stiffness parameters are adjusted to match numerical dynamic parameters with experimental response. Nonlinear dynamic analysis is performed using various ground motions with Peak Ground Acceleration (PGA) ranging from 0.10g to 0.30g. A vulnerability assessment method is established to identify the vulnerability of the structure and these results are used as input data for the development of a prediction model using a Random Forest algorithm. The data collected from several nonlinear dynamic analyses is split into two subsets: a training set for building the prediction model and a test set for assessing its performance. The results show that the Random Forest model is effective in evaluating the seismic vulnerability of masonry minarets and can be relied upon for future predictions. The developed methodology and prediction model can be applied in practice to evaluate the seismic safety of existing minarets and inform decisions on retrofitting or preservation measures. This approach has the potential to contribute to the preservation of cultural heritage in India by providing a tool for assessing and mitigating seismic risks to historic structures. This approach provides a reliable and efficient way to assess the seismic vulnerability of heritage minarets in India, with potential applications to other structures.

Acknowledgments

The authors acknowledge the support received from the CDRI Fellowship Programme, which provided financial and technical assistance for this research. The authors are also grateful for the support and collaboration of the Archaeological Survey of India.

Funding

This research was supported by the 2022–2023 Fellowship of the Coalition for Disaster Resilient Infrastructure (CDRI), Application ID: 210922630.

1. Introduction

Preservation of architectural heritage plays a critical role in safeguarding historical structures, particularly in countries like India. Masonry minarets, such as the Qutub Minar, Hiran Minar, and Char Minar, are of immense significance and have been designated as UNESCO World Heritage sites. However, these iconic minarets have experienced significant deterioration due to past earthquakes and other natural calamities. The structural stability of minaret structures depends on various factors, including their construction methods, structural information, and seismicity of the region. The uneven shape and mass distribution of these structures along their heights increase their susceptibility to damage from earthquakes. Despite their historical importance, many monumental structures, including minarets, were constructed without considering horizontal actions such as those induced by earthquakes. While heritage structures are vital for attracting tourists and contributing to the economy, their preservation necessitates strict controls and maintenance efforts to ensure their safety and conservation.

Previous investigations have shed light on the seismic vulnerability and conservation of historical structures in India. For instance, Ramos et al. (2006) conducted investigations on the Qutub Minar, utilizing ambient vibration testing and Ultrasonic Pulse Velocity to assess its dynamic response and masonry condition. Pena et al. (2010) further examined the Qutub Minar using nonlinear seismic analysis, emphasizing the need for careful pushover analysis in seismic assessments of masonry structures. Tripathi and Rai (2016) studied the seismic vulnerability of Bodh Gaya monasteries and proposed repair schemes. Similarly, studies on historical structures abroad have provided valuable insights, such as Bakhary et al.'s (2007) proposed artificial neural network (ANN) model establishing a relationship between modal parameters and elastic modulus before and after damage, Gonzalez and Zapico's (2008) development of an ANN model for damage detection using modal parameters and Nohutçu’s (2020) investigation of the patterns of damage caused by earthquakes in an old brick minaret which was conducted using modern finite element models that were updated with data from ambient vibrations.

Considering the popularity of heritage minaret structures as tourist destinations and their significant contributions to tourism revenue, it is crucial to assess their present condition and seismic vulnerability. Furthermore, there is a lack of assessment records regarding the application of vibration testing on heritage structures in India. Therefore, an integrated approach that combines knowledge of vibration characteristics and numerical

model response can be utilized to develop a machine learning-based model for predicting vulnerability in different seismic scenarios. Such a model would assist in planning effective disaster mitigation strategies for the conservation of heritage structures. By addressing these research gaps and employing innovative methodologies, this study aims to contribute to the preservation and seismic assessment of heritage minaret structures. The findings may provide valuable insights for policymakers, conservation agencies, and stakeholders involved in the protection and sustainable development of these iconic architectural treasures. Policymakers can use the results to develop and implement regulations and guidelines for the preservation and retrofitting of these historic structures. Conservation agencies can use the methodology and predicted model to assess the seismic vulnerability of minarets under their care and prioritize interventions to improve their resilience. Stakeholders, such as local communities and heritage organizations, can use the findings to advocate for the protection of these iconic architectural treasures and raise awareness about their cultural significance.

Protecting our architectural heritage is crucial for the cultural vitality of contemporary societies, and studying old masonry buildings is a demanding task. In India, heritage minarets hold immense cultural significance, forming an integral part of the country's architectural heritage that demands preservation. This research conducts a comprehensive comparative analysis of a selection of heritage minarets in India. These minarets exhibit diverse geometries, architectural styles, and regional influences, contributing to the richness and variety of India's architectural heritage. By utilizing detailed full 3D finite element (FE) models, the study investigates the structural behaviour of the minarets under seismic loads, with particular attention to their unique geometric features and construction materials. The minaret structures selected for the research work are shown in figure 1 and the locations of the minarets are shown in figure 2.

The seismic vulnerability of the selected heritage minarets is investigated through a range of simplified procedures, including eigen-frequency analysis and nonlinear static analyses. These procedures provide insights into the structural weaknesses and potential failure modes of the minarets when subjected to seismic forces. These minarets, with their distinctive architectural styles and historical importance, reflect the rich cultural diversity and artistic achievements of the region. However, they are slender in nature and face the challenges of seismic vulnerability, particularly under the impact of earthquakes.

Overall, the findings of this research may contribute to a deeper understanding of the seismic performance and resilience of heritage minarets in India. By identifying their vulnerabilities and developing a unified machine learning vulnerability prediction model, this

study aims to ensure the safeguarding and continued cultural significance of these iconic architectural treasures for future generations to appreciate and admire.

	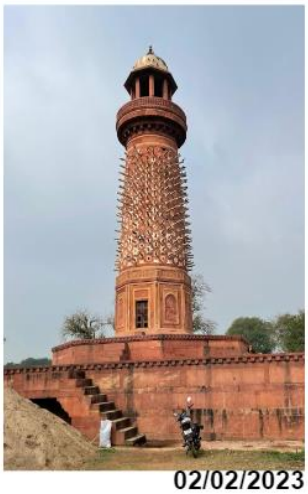	
1. Chand Minar, Aurangabad	2. Hiran Minar, Fatehpur Sikri	3. Jhulta Minar, Ahmedabad

Figure 1. Selected heritage minaret structures in India

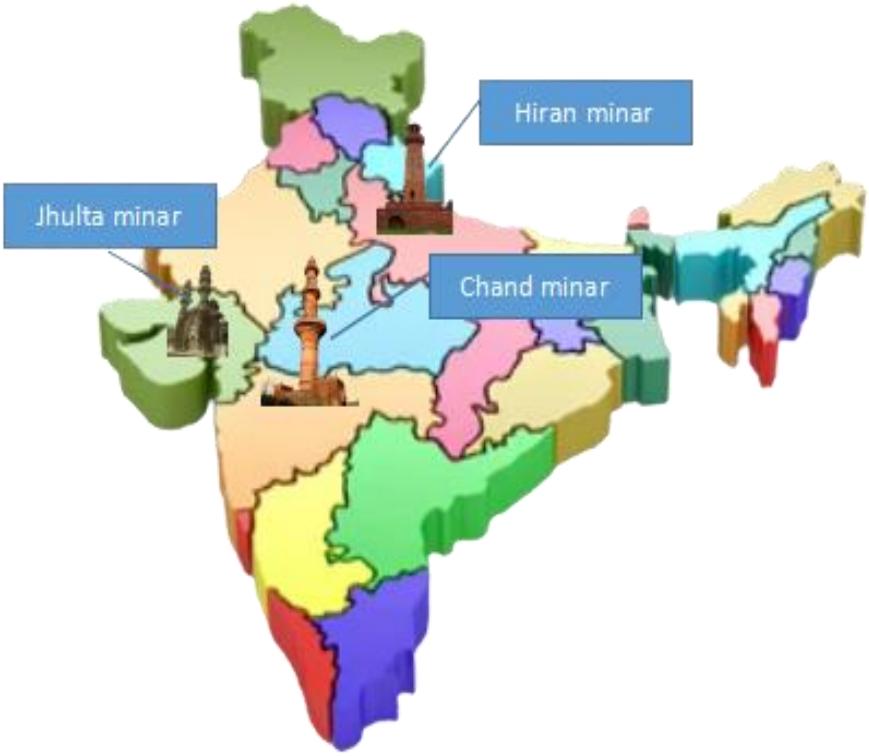

Figure 2. Location of selected heritage minaret structures

2.Research Problem, Aim, Objectives and Scope of the Research Study

2.1 Research problem

Masonry minarets are important historical structures in India, with some designated as World Heritage sites by UNESCO. The resilience of these buildings is influenced by many elements, including their design, building techniques, and the seismic activity in the area. Their tall and slender shape and the way their weight is distributed make them more susceptible to harm during earthquakes. These structures are important tourist attractions and a major source of tourism revenue generation. Therefore, assessing their present condition and seismic vulnerability is an immediate mandate. The seismic vulnerability of masonry minarets in India's architectural heritage is a critical concern. Traditional methods of seismic vulnerability assessment often rely on subjective evaluations and lack precision. Therefore, there is a pressing need for a robust and accurate prediction model that can assess the potential damage levels in masonry minarets under seismic load conditions. The development of such a model would enable proactive measures to mitigate the risk and ensure the preservation of these culturally significant structures.

2.2 Proposed Solution

This study proposes a solution to the research problem of assessing the seismic vulnerability of heritage minarets in India through the development of a unified machine learning-based approach. Dynamic analysis of structures based on vibration is a well-established and effective method for identifying structural characteristics such as natural frequencies and curvature mode shapes, and is employed to accurately identify the dynamic behaviour of the monuments. A 3D simplified numerical model of the minarets is developed using FE analysis software, incorporating nonlinear material and geometric behaviour. The accuracy of the dynamic models is ensured through a comparison between the dynamic characteristics of real measured minaret structures and corresponding numerical models of selected heritage minarets. Material and boundary parameters are adjusted to match the numerical dynamic parameters with the experimental response. Nonlinear dynamic analysis of the reliable numerical model is conducted using a range of ground motions with Peak Ground Acceleration (PGA) values varying from 0.10g to 0.3g. The seismic vulnerability of the minarets is calculated based on data obtained from multiple nonlinear dynamic analyses, providing significant information for further investigation of historical structures.

These results are used as input data for developing a predictive model using a random forest algorithm. The information is partitioned into two distinct subgroups, namely a training set and a test set. The training set is used to construct the prediction model, while the test set evaluates its performance. This machine learning-based approach provides a reliable and efficient way to assess the seismic vulnerability of heritage minarets in India.

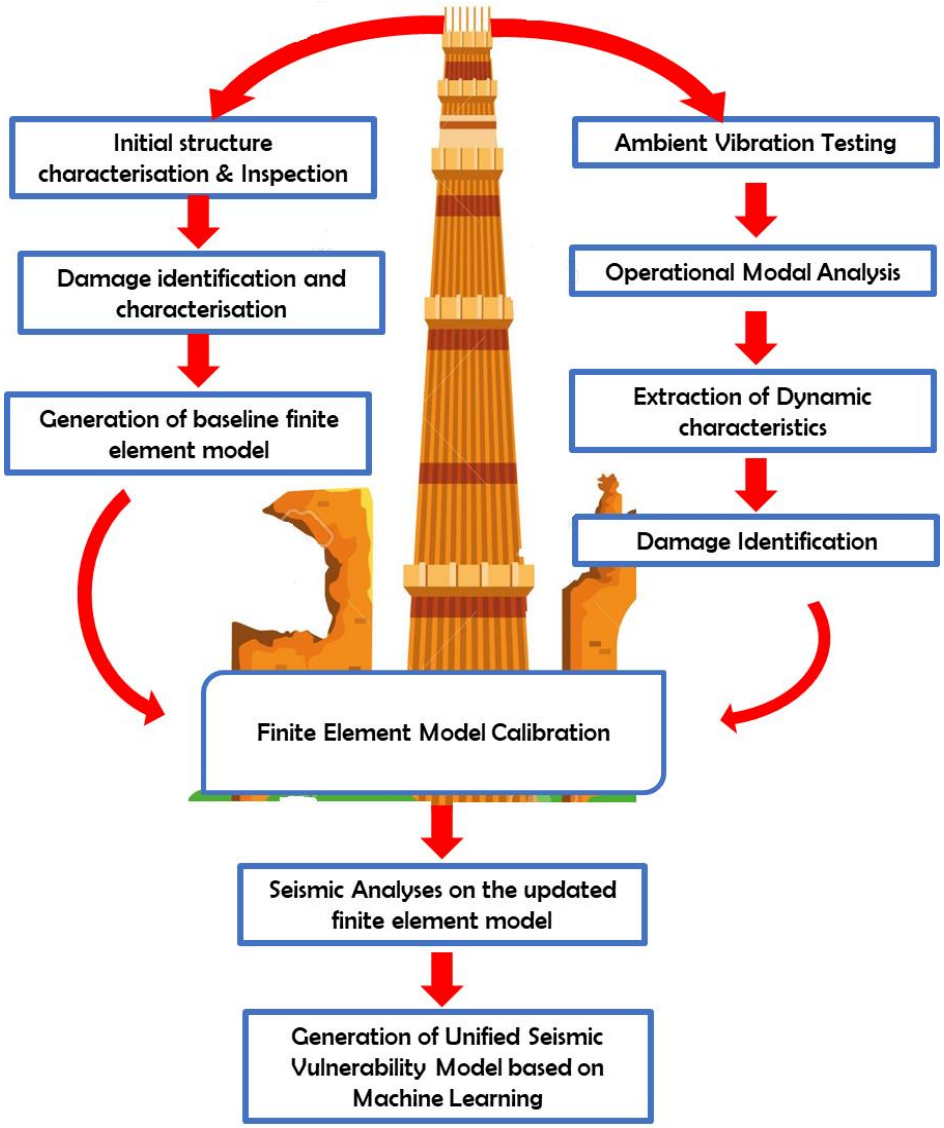

Figure 3. Proposed framework

2.2 Aim

The aim of this project is to develop a machine learning-based unified seismic vulnerability prediction model for the heritage minarets of India.

2.3 Objectives

The primary objective of this research is to develop a machine learning-based prediction model that can accurately assess the seismic vulnerability of masonry minarets in India. The specific objectives include:

- Conducting vibration tests to measure the structural dynamic parameters of masonry minarets
- Configuring a finite element model based on the vibration test results to simulate the structural behaviour under seismic loads. Performing nonlinear dynamic analyses on the finite element model using selected seismic intensities
- Training prediction models utilizing dynamic analysis results with a machine learning-based random forest algorithm

2.4 Scope and limitations

A significant portion of the world's cultural heritage, including masonry monuments, is situated in areas that are prone to earthquakes, with varying degrees of seismic hazard and source characteristics. Examples of such areas include Italy, Turkey and Portugal. These historical masonry monuments were constructed using empirical techniques that primarily focused on the vertical loading resulting from the structure's own weight. However, these methods did not take into account the potential impact of horizontal inertia forces that can be generated during seismic events. As a result, these structures may be more vulnerable to damage during earthquakes. Assessing the seismic vulnerability of a historical building is a more complicated task than assessing that of another existing building. In general, vulnerability refers to the extent of damage inflicted on a minaret structure by an earthquake of a specific intensity.

The scope of research was to develop a unified machine learning-based prediction model to assess the vulnerability of heritage minaret structures in India due to seismic action. A database containing the characteristics of selected minarets was established and a reliable numerical model for the minaret structure was created. A method for seismic vulnerability assessment for slender minaret structures was also developed. The research concluded with the development of a unified seismic vulnerability assessment for heritage minaret structures in India.

The limitations of the research were that the prediction model was developed specifically considering minarets as isolated slender minaret structures due to their simplicity in geometry. Assessing the vulnerability of historical structures was complex, required more computer resources and special equipment, and was time-consuming.

Destructive testing was not allowed on the structures due to their cultural and social value, so approximations had to be attempted. The developed machine learning model assessed the seismic vulnerability of minaret structures in terms of vulnerability index due to seismic action only.

3. Methodology

The research methodology is divided into five parts as shown figure 4, which include Preliminary Inspection, Non-Destructive Testing (NDT) on the Whole Structure, Dynamic Testing of Selected Heritage Structures, Numerical Modelling and Development of a ML-Based Prediction Model.

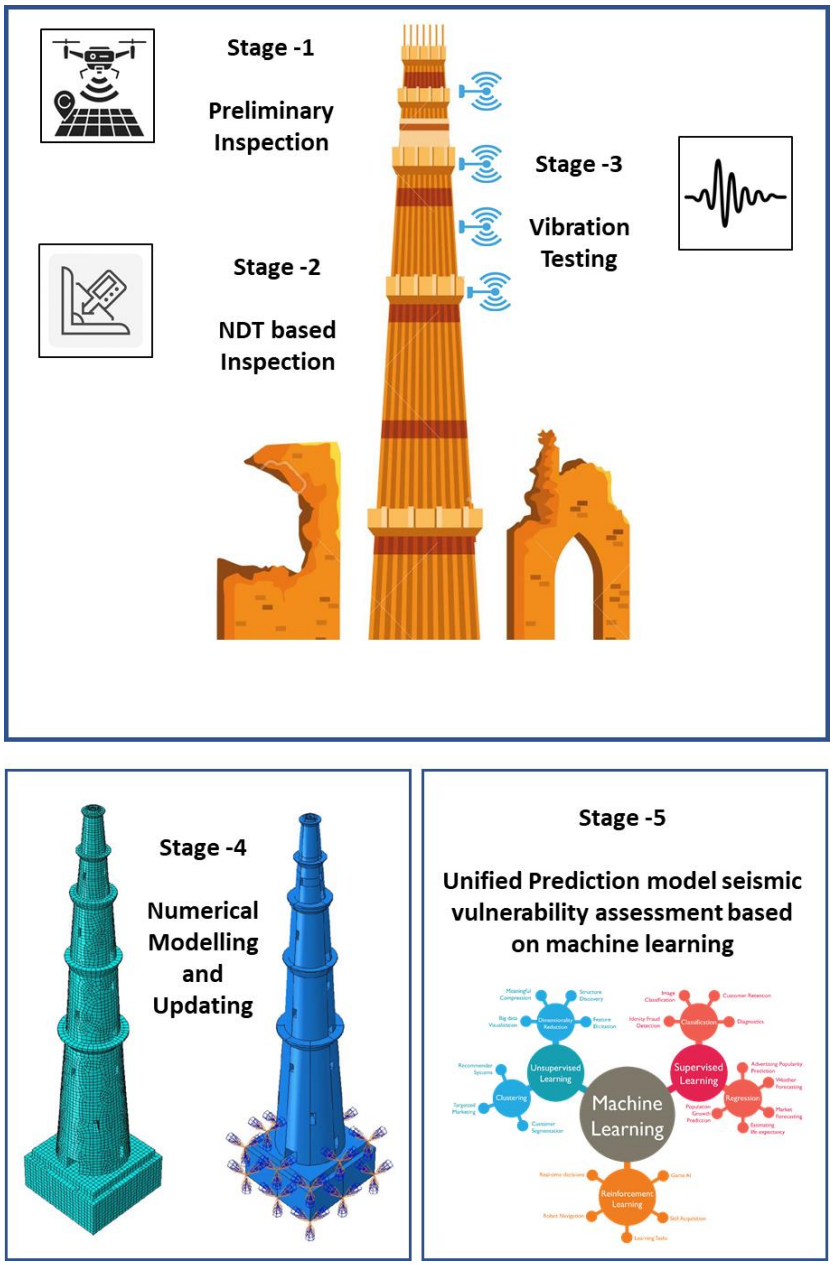

Figure 4. Research methodology

3.1 Step 1: Preliminary inspection

In the first stage, a primary survey was conducted to gather information about the geometry of the structure and nearby places. Documentation about the history of the structure and past seismic activities in the area was collected, along with information about past repair works. A visual inspection was conducted to assess the present condition of the structure and its components. A report was prepared detailing the present condition of the structures and their components.

To accurately assess the architectural features of the selected heritage minarets and obtain reliable data for analysis, a comprehensive geometric survey was conducted. Due to the lack of detailed architectural information, innovative methods were employed, including the use of drone (as shown within the red circle in Figure 5[b]), measuring tape, and laser distance meter (Figure 5[a]).

Figure 5. Geometric survey

3.2 Step 2: NDT on the whole structure

In the second stage, NDT was conducted on the whole structure. This included a crack pattern survey, masonry morphology survey, material degradation assessment and detection of flaws and crack propagation using a sonic test. A report was prepared detailing the mechanical properties and status of damage and degradation of structural materials based on the results of the NDTs.

To assess the material properties of the historic structures without causing damage, a non-destructive testing approach was employed. This involved conducting tests on the stone types used in the minarets without extracting samples from the structures. Five distinct regions or locations within the minarets were chosen for testing each type of stone. Ultrasonic Pulse Velocity (UPV) testing was conducted using a Pundit PL 200 device, with 20

readings taken in each region. The UPV method involves sending ultrasonic waves through the stone and measuring the time it takes for the waves to travel between two points. This provides valuable information about the velocity of the waves, which is directly related to the elastic properties of the stone. Both the direct and indirect methods of UPV testing were utilized. In the direct method, the P (primary) and S (shear) transducers were placed directly on the surface of the stone to measure the velocity of the waves. The results of the UPV tests were analyzed to determine the velocity and modulus of elasticity of the stone. The velocity value indicates the speed at which waves travel through the stone, while the modulus of elasticity reflects the stone's rigidity and its capacity to resist deformation under stress.

3.3 Step 3: Dynamic testing of the selected heritage structures

In the third stage, dynamic testing was conducted on selected heritage structures using ambient vibration testing (AVT). A vibration test setup consisting of accelerometers was used. Sensor locations and monitoring techniques were established to obtain global structure response data for the selected structures. Operational modal analysis (OMA) techniques were used to obtain mode shapes and natural frequencies of the structures. The response of the structures was inspected on a full-scale level.

(a) (b)

Figure 6. (a) 8 Sensors used for the study (b) Sensor placement in minaret

AVT was conducted on Chand Minar, Hiran Minar and Jhulta Minar to capture the dynamic response and assess the structural properties of these historical minarets. The AVT utilized

eight Bean Air 3D wireless accelerometers, strategically placed along the axisymmetric direction of the minarets' walls at balcony level (figure 6[a] and 6[b]). Each minaret was equipped with four triaxial accelerometers, carefully positioned on the balcony level to ensure accurate measurement of environmental vibrations (figure 7).In case of Hiran Minar, additional positions were considered, since only one balcony is available.

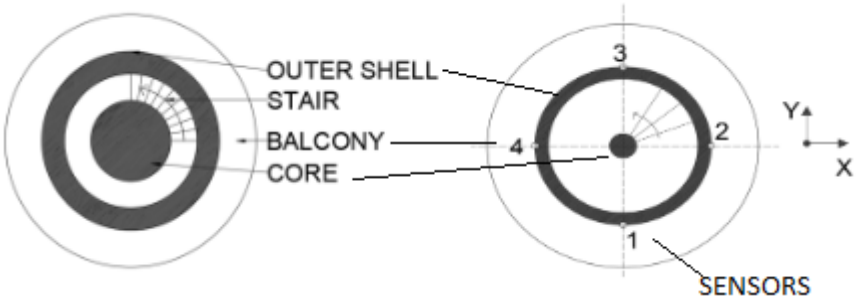

Figure 7. Position of sensors at balcony level

During the AVT, eight triaxial MEMS accelerometers were attached to the minarets' shells, capturing the response of the structures. A reference point at the top of each minaret was selected to measure vibrations in the x, y and z directions. To gather comprehensive data, the sensors were strategically positioned on each balcony level, resulting in a total of 12 data sets recorded for each minaret at balcony level. Each data set had a duration of 20 minutes. The AVT details, including the number of accelerometers, reference points and sampling frequencies, are provided in Table 1.

Table 1. Details of AVT

Minaret	Chand Minar	Jhulta Minar	Hiran Minar
No of position of sensors	14	31	14
Total number of data set	42	92	42
Test setup	5	5	2
Sampling frequency	100Hz	250Hz	100Hz

3.4 Step 4: Numerical modelling

In the fourth stage, a baseline Finite Element (FE) model was created using properties determined by field investigation and NDTs at selected structures. Field results were used for model updating to obtain an accurate FE model for analysis. Nonlinear analyses were performed to calculate seismic vulnerability of minarets. Macro modelling technique was used to model masonry.

3.5 Step 5: Development of the machine learning based prediction model for seismic vulnerability assessment

In the final stage, data obtained from multiple nonlinear dynamic analyses were divided into two subsets: a training set and a test set. The training set was used to construct a machine learning-based prediction model for seismic vulnerability assessment. The prediction model's performance was assessed using the test data set. MATLAB is used for the development of prediction model. The detailed steps involved in vulnerability prediction using Random Forest (RF) is given below.

3.5.1 Step 1: Data collection and preprocessing

Data on three minarets, including their height, base dimension and seismic vulnerability calculated from 30 sets of nonlinear time history analysis, were collected. Additionally, earthquake time history records (e.g., PGA values) were obtained. The dataset contains a total of 150 observations, Necessary preprocessing steps were performed, including the calculation of derived features such as the aspect ratio, and the data was combined into a single dataset.

3.5.2 Step 2: Splitting data and feature selection

The dataset was split into training and validation sets using an appropriate ratio, such as 80 percent for training and 20 percent for validation. To predict seismic vulnerability, the most relevant variables were determined through the application of feature selection methods.

3.5.3 Step 3: Random Forest model training

The training data was used to train a Random Forest model, employing the regression method for predicting vulnerability. The hyperparameters of the Random Forest model were optimized to enhance its performance. The predictions from each individual tree within the Random Forest model were combined to generate an overall prediction. Figure 8 provides an illustration of an RF predictor with n decision trees. The Random Forest model was trained using the training data and the regression method was employed for vulnerability prediction. Hyperparameter optimization techniques were used and the aggregated predictions from individual trees formed the overall prediction.

3.5.4 Step 4: Model evaluation

The vulnerability for the validation data was predicted using the trained Random Forest model. The efficacy of the model was assessed by employing suitable measures, including mean squared error (MSE) and mean absolute error (MAE). The performance of the model

was compared against baselines, such as using the mean vulnerability as a simple baseline.

3.5.5 Step 5: Cross-validation

K-fold cross-validation, typically with k=4, was performed to assess the generalizability of the model and mitigate overfitting. The average MSE and MAE were calculated from the cross-validation results to provide a more robust evaluation of the model's performance.

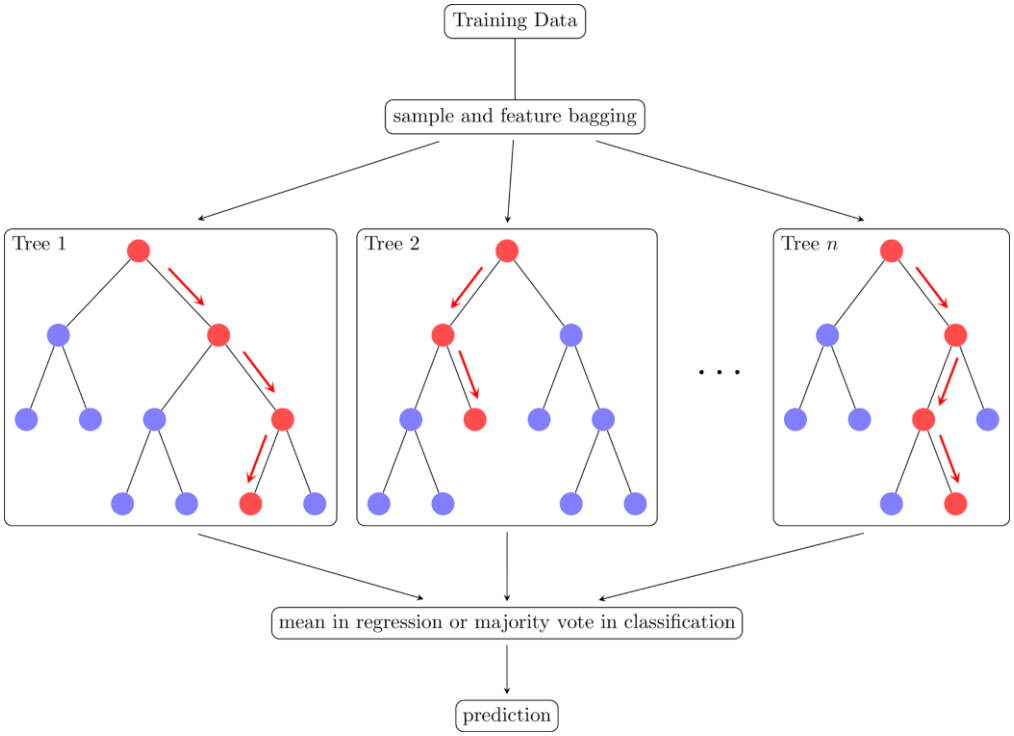

Figure 8. RF prediction

3.5.6 Step 6: External validation

The trained model was validated using unseen data, which included new minaret with its corresponding attributes. The model was used to predict the vulnerability for the new minaret, and its applicability to real-world scenarios was assessed.

4. Results and Discussion

4.1 Architectural description of minarets

4.1.1 Chand Minar

The Chand Minar, constructed in 1445 A.D., is an architectural marvel that stands tall with its unique geometric design. Built with local basalt, this minaret showcases an arched plinth and a towering structure. Its exterior is adorned with a red sandstone-coloured plaster, lending it a captivating aesthetic appeal. As you venture inside, the internal spaces reveal a delightful contrast. The areas within the arches are coated with a pristine white plaster,

creating a visually striking juxtaposition. The minaret has 24 chambers and a small mosque at its base. The plinth of the Chand Minar rises to a height of 4.57 meters, commanding attention with its grandeur. Its catacomb-like ground plan features arched openings of varying widths and depths on each side, showcasing a truly intricate design. The exterior measurements of the minaret span 21.55 meters in length and 10.15 meters in width, emphasizing its substantial presence. With its remarkable architectural features and historical significance, the Chand Minar stands as a testament to the rich heritage and artistic achievements of the region.

4.1.2 Hiran Minar

The Hiran Minar, located on the north-west side of the Fatehpur Sikri ridge, holds a significant position facing the Hathiya-Paur (Elephant-Gate), which served as the formal entrance gate to the Royal township. The minar is connected to the gate by a steep stone-paved ramp, creating a magnificent introduction. Standing on a square platform crafted from red sandstone, the minar measures 21.95 m on each side and reaches a height of 3.00 m. It rests upon an octagonal plinth, 12 m in diameter and 1.18 m in height. The minar itself stands 21.34 m tall, featuring an octagonal structure up to a height of 3.90 m, and the remaining portion is a round and tapering shaft. A circular platform, supported by stone corbels designed as stalactites, rests on this shaft, adorned with an octagonal chhatri (domed canopy) and a projecting balcony. The chhatri is characterized by plain pillars, chhajjah (overhanging eaves), and a cupola roof crowned with mahapadma and kalasa, typical features of Indo-Muslim architecture. Originally, seven of its openings were filled with jaalis (stone screens), while the rough pillars were likely plastered over. The soffit of the minar was adorned with stylized painted designs. An inner spiralling stairway, dimly illuminated by several ventilators, leads from the rectangular doorway facing the Hathiya-Paur to the top of the minar. Constructed entirely from local red sandstone, with grey stone used for inlay to accentuate the outlines of arch forms and plain designs, the minar showcases a captivating combination of colours that adds visual interest to the predominance of red stone. The Hiran-Minar possesses a unique and remarkable feature that sets it apart in Indo-Muslim architecture. The circular tapering shaft of the minar is adorned with many vertically protruding elephant tusks. Originally, these tusks were made of ivory, giving the minar an awe-inspiring and novel appearance. However, the current tusks are made of stone, carefully plastered over to resemble the original ivory tusks. It is believed that Akbar, in the 16th century, used real ivory tusks as a display of the might and grandeur of the Empire, impressing foreign caravans who stayed in the nearby sarai. Unfortunately, these valuable relics were likely plundered between the death of Aurangzeb in 1707 A.D. and

the appointment of Alexander Cunningham as Director of Archaeology in 1862 A.D., becoming prized war trophies for various groups such as the Jats and the Marathas. The Hiran Minar stands not only as a testament to Akbar's reign but also as a remarkable architectural gem with its intricate design, skilled craftsmanship and the awe-inspiring display of elephant tusks, symbolizing the grandeur of the empire.

4.1.3 Jhulta Minar, Sidi Bashir Mosque

The Jhulta Minar, also known as the Shaking Minarets, is a remarkable monument consisting of two cylindrical minarets that vibrate or shake when one of them is disturbed. These minarets stand at a height of 21.1 meters and are separated by 7.5 meters. They are connected by an arched central gateway, which itself measures 8 meters in height. Originally, there were more shaking minarets in the region, such as the ones in the Jama Masjid and Bibi-ki-Masjid, but they have not survived. The Jhulta Minar is the best-preserved example of this unique architectural feature. Another pair of shaking minarets exists in the Monar Jonban, a historical building located in Isfahan, Iran. The Jhulta Minar sustained damage during the conflict between the Marathas and the Mughal governor of Gujarat in 1753. Despite this, two of the minarets and the central arched gateway remained intact. To enhance their stability, horizontal steel belts were installed at the top and bottom levels of the minarets. These belts likely contribute to the overall structural integrity of the shaking minarets. The intriguing shaking or vibrating effect of the minarets is thought to be influenced by their layered construction, characterized by horizontal grooves. This layered design is believed to be a contributing factor to the vibration phenomenon experienced in the minarets. The Jhulta Minar stands as a testament to the unique architectural heritage of India, captivating visitors with its distinctive vibrating minarets and serving as a reminder of the marvels of engineering and craftsmanship from the past.

4.2 Damage survey

During the damage survey of the three minarets, namely Chand Minar, Hiran Minar, and Jhulta Minar, several common issues were observed, including cracks, material decay and discoloration. The cracks were predominantly located in the lower parts of the minarets, particularly in the inner side of the external shell and in the central column (figure 9) . Vertical cracks, horizontal cracks and spalling were evident, indicating a wide damage pattern. Over time, the natural effects and environmental conditions have caused discoloration and colour change in the stone used for the minarets. This is a common phenomenon observed in historical structures. In certain areas, such as the Hiran Minar, the influence of excessive precipitation was evident, resulting in the presence of efflorescence.

Occasional rupture and damage to the stones were also observed in some cases.

Figure 8 displays images depicting the damages and deformations observed in the minarets, providing visual documentation of their current condition. It includes various types of damages observed in minarets. These include horizontal cracks in the inner part of the Chand Minar shell, cracks and spalling in the Jhulta Minar core, vertical cracks at the opening of the Jhulta Minar and cracks in the core of the Hiran Minar at the top portion. Additionally, chemical deposition and discoloration were observed, as well as cracks in the bottom portion core of the Chand Minar.

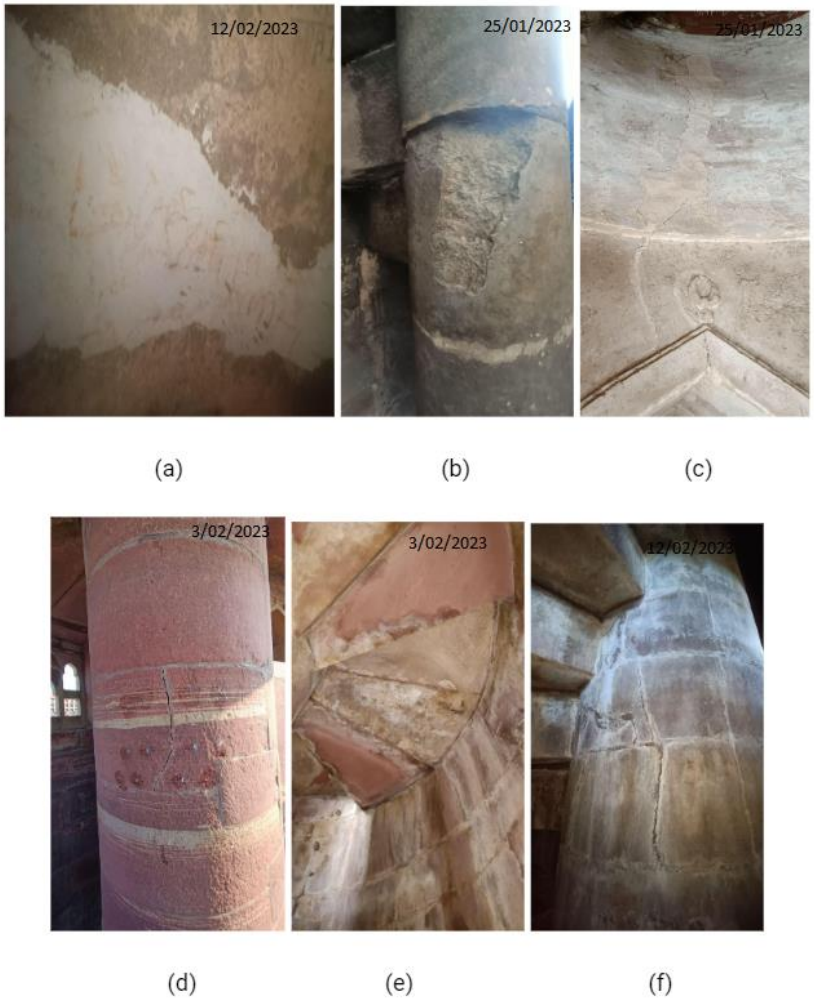

Figure 9. Damages observed in minarets: (a) Horizontal crack in inner part of Chand Minar shell (b) Crack and spalling in Jhulta Minar core (c) Vertical crack at opening of Jhulta Minar (d) Crack in core of the Hiran Minar at top portion (e) Chemical deposition and discoloration (f) Crack in the bottom portion core of Chand Minar

Fortunately, maintenance and restoration activities have been carried out periodically on all three minarets. These measures play a vital role in prolonging the life of the buildings and preserving their originality. Regular maintenance and restoration efforts ensure that necessary repairs are undertaken to address the identified issues, such as cracks and

material decay, preventing further damage and preserving the structural integrity of the minarets. The results of the damage survey highlight the importance of proactive maintenance and restoration in the preservation of architectural heritage. By conducting regular assessments and implementing appropriate repair and conservation measures, the historical significance and structural integrity of the minarets can be maintained, allowing future generations to appreciate and cherish these iconic architectural treasures.

4.3 Material properties and the characteristics of the minarets

The process of homogenization in masonry was carried out based on existing models found in the literature [7-9]. However, it should be noted that these models primarily focus on typical masonry structures in India and do not specifically address historical masonry. The elastic properties of stone masonry were tentatively assigned, as shown in Table 2, due to the scarce mechanical test data for material specimens.

Table 2. Characteristics of minarets

Minaret	Chand Minar, Daulatabad	Jhulta Minar, Ahmedabad	Hiran Minar, Fatehpur Sikri
Construction	1445 AD	1452 AD	1571 to 1585 AD
State	Maharashtra	Gujarat	Uttar Pradesh
Location	19°56'39.9"N 75°13'02.7"E	23°01'25.1"N 72°35'59.3"E	27°05'55.2"N 77°39'45.6"E
Material	Basalt stone	Sandstone	Red sandstone
Seismic zone	II	III	III
No. of balcony	3	3	1
Total height (m)	61.5	21.1	25.5
Height of minar(m)	52	13.1	21.3
Base dimension (m)	6	1.6	4.83
Elasticity modulus of stone (GPa)	57.12	45.62	20.81
Elasticity modulus of	3.18	2.8	2.1

masonry (GPa)			
Poisson's ratio	0.18	0.18	0.18
Density (kg/m^3)	2400	2200	2100

Table 3. Results of UPV test

Minaret	UPV(m/s) (Direct)	UPV(m/s) (Indirect)	E(Gpa)
Chand	1239 ± 45	1455 ± 69	57.12 ± 2.5
Hiran	1440 ± 25	1521 ± 32	20.81 ± 1.5
Jhulta	1294 ± 22	1359 ± 45	45.62 ± 2.4

Figure 10. NDT conducted on minarets

The non-destructive testing approach allowed for the evaluation of the material properties of the minarets' stone types without causing any harm to the historic structures. It provided valuable data on the velocity and modulus of elasticity, which are essential for understanding the structural behaviour and integrity of the minarets. The results of NDT are shown in Table 3.

4.4 Dynamic properties of the minarets

The AVT data served as the foundation for subsequent analyses, OMA was conducted using the recorded ambient vibration response, allowing for the extraction of dynamic behaviour and modal parameters of the minarets. The acquired acceleration data from the AVT was processed using Enhanced Frequency Domain Decomposition (EFDD) technique and the experimental dynamic parameters of the minarets were extracted. The modal behaviour of the minarets were determined, providing valuable insights into the structural response [10,11]. The EFDD technique was utilized to analyze the data sets and the results included the first three frequencies along with their corresponding singular value decomposition (SVD) plots. These plots were obtained by averaging the normalized singular values of the spectral density matrices. Figure 11(a,b,c) displays the SVD plots of Chand Minar, Hiran Minar and Jhulta Minar respectively, while Table 4 summarizes the corresponding findings.

Table 4. Experimental natural frequency of minarets

	Chand Minar			Jhulta Minar			Hiran Minar		
Mod	1	2	3	1	2	3	1	2	3
Frequencies (Hz)	1.23	1.45	3.85	3.98	5.15	10.4	3.67	6.23	13.7

4.5 Baseline model of minarets

In this study, 3D finite element model of the minaret was modelled using ANSYS Inc. (2022) FE software. To create an accurate model, the actual dimensions of all three minarets, including the staircase, were used. For the 3D modelling of the minaret, SOLID 186 element was used. It can handle a variety of material behaviours, including linear and nonlinear elastic, plastic and creep. Ensuring accurate damping parameters is crucial for reliable nonlinear analysis. While inelastic material behaviour handles damping, other sources of damping typically require a viscous damping approach. In this study, the Rayleigh damping approach was implemented. A constant damping value of 2 percent was chosen for the present analysis and the William Warnke material model was utilized to incorporate material nonlinearity. The mechanical properties of the materials used in the finite element modelling is provided in Table 2 [12, 14]. To determine the appropriate mesh size, a convergence analysis was conducted. Initially, a mesh size of 0.50 m was selected for all the minarets and modal analyses were performed for various mesh sizes and the most suitable mesh size range for the minarets were determined to be 0.20 m for Jhulta Minar, 0.25m for Chand

Minar and 0.3m for Hiran Minar (figure 11). It should be noted that this study is limited to the minaret section of the heritage building, and the interaction between the soil and the structure is not considered. The structure is assumed to be fixed at the base. In the case of Jhulta Minar, only the left minaret of the structure was included in the study.

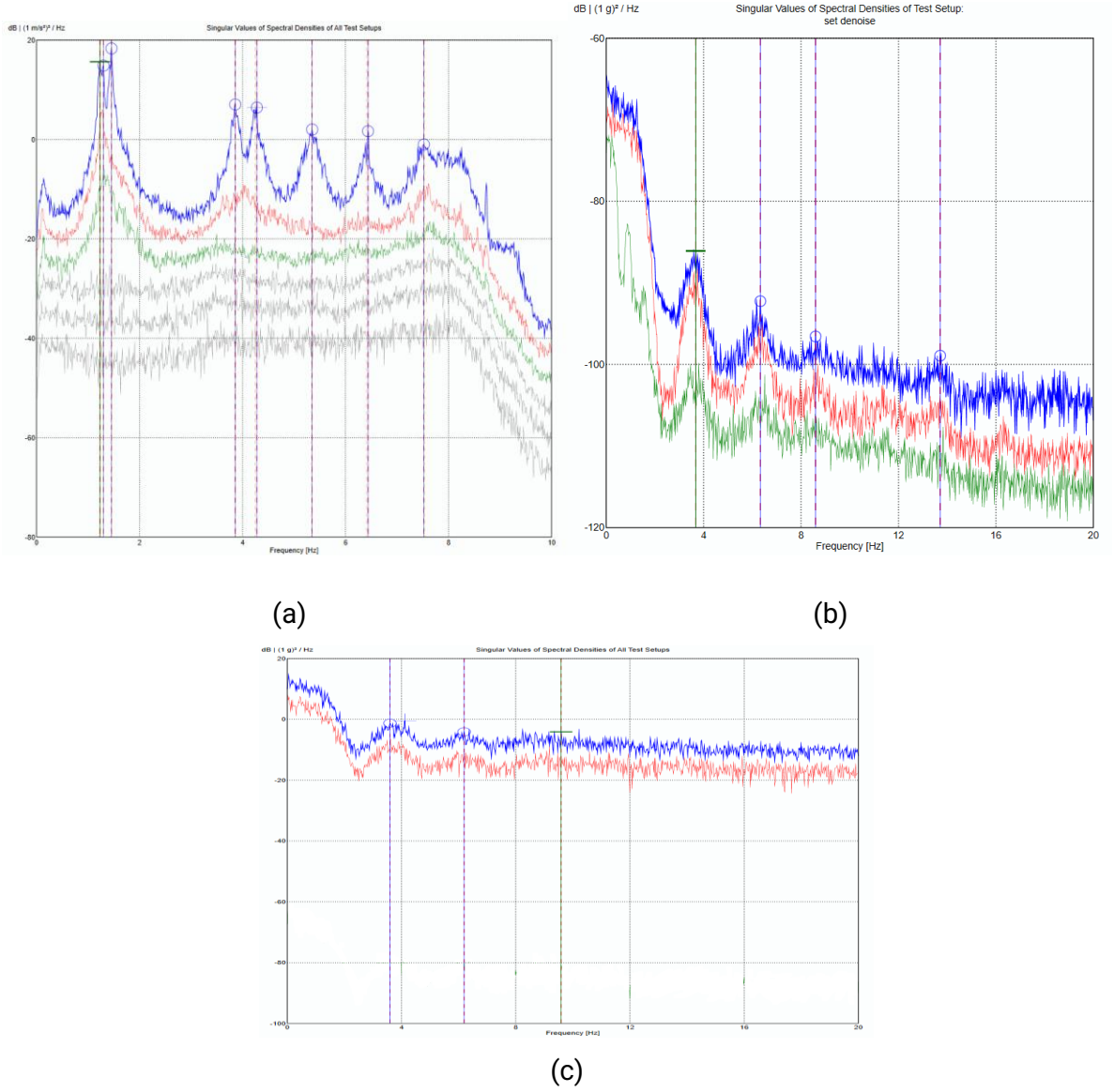

Figure 11. SVD plots

To update the FE Model of the minarets, the modulus of elasticity of the masonry walls was modified. The FEM was adjusted iteratively until the numerical modal analysis results matched the experimentally obtained modes. By modifying the modulus of elasticity, the FEM analysis was able to replicate the observed modal behaviour. The results of the OMA and FEM updating process were summarized in Table 5, showcasing the experimental frequencies, and the calibrated frequencies. Differences were observed between the numerical and experimental frequencies, as indicated in Table 5. To enhance the accuracy

of the FEM, adjustments were made to the Young's modulus of the masonry. The updated FEM was then subjected to modal analysis, resulting in the identification of the first three natural frequency values and mode shapes. Upon comparing the values in Table 5 and the mode shapes in Figure 12-15, it becomes evident that the calibrated frequencies and mode shapes closely match the experimental results. By updating the FEM with the OMA outcomes and adjusting material properties like the Young's modulus, the precision of the model is considerably enhanced. This ensures that the FEM provides a more realistic representation of the dynamic characteristics of the minaret, aligning it closely with the experimental findings.

Table 5. Modal update (C - Chand Minar, H - Hiran Minar, J - Jhulta Minar)

	Experimental frequencies (Hz)			**Numerical frequencies FEM (Hz)**			**Numerical frequencies FEM (Hz) After calibration**			**Maximum difference between frequencies (%)**		
	C	H	J	C	H	J	C	H	J	C	H	J
Mode 1	1.23	3.67	3.98	0.58	1.54	1.68	1.27	3.63	3.9	3.25	1.10	2.01
Mode 2	1.45	6.23	5.15	1.02	4.56	6.21	1.6	6.84	5.7	9.38	9.47	10.29
Mode 3	3.85	10.47	13.7	3.45	8.73	12.5	3.45	11.89	15.67	11.4	13.6	14.31

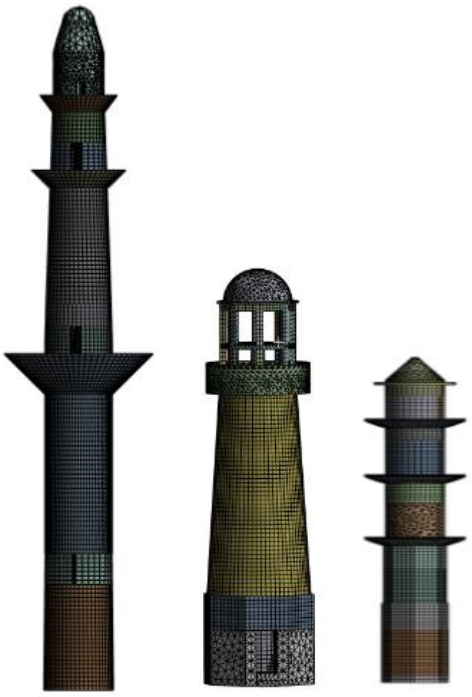

(a) (b) (c)

Figure 12. Finite element model of minarets (a) Chand Minar (b) Hiran Minar (c) Left minar of Jhulta Minar

Table 6. Natural frequencies of Chand Minar baseline modal

Mode shape	Comment	Frequency (Hz) -Numerical analysis
1	1st Bending in X	1.27
2	1st Bending in Y	1.45
3	2nd Bending in X	3.85
4	2nd Bending in Y	4.57
5	1st Torsion	5.35
6	3rd Bending	6.43
7	1st Vertical	7.02

The natural frequency of minarets and mode shapes of updated model is given in table 6 to table 8 and figure 12 to 14 respectively.

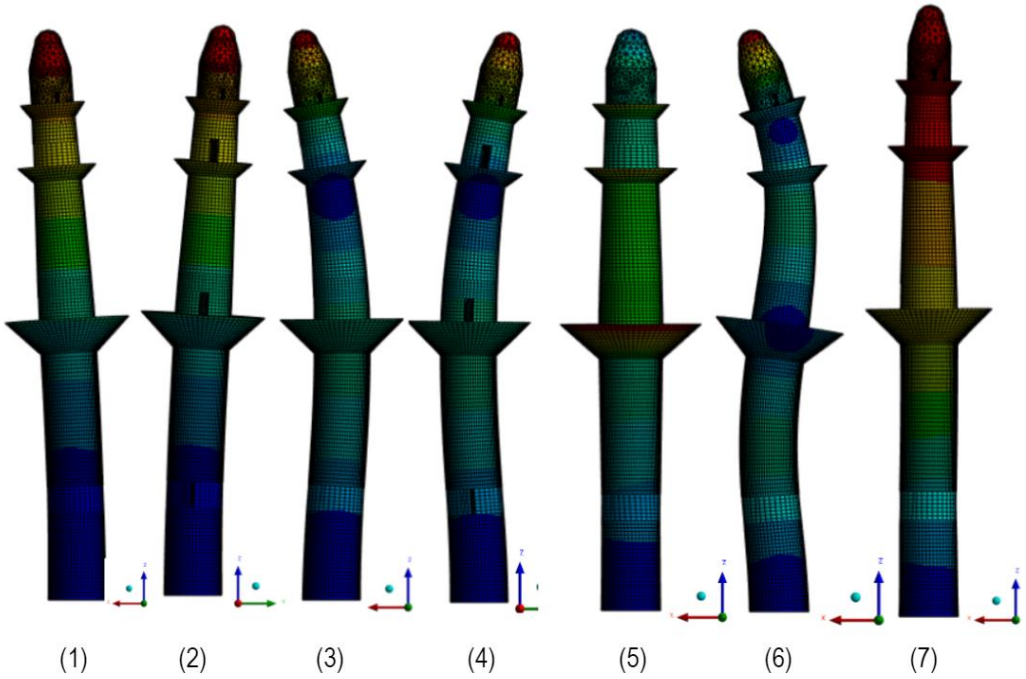

Figure 13. Modal analysis results of Chand Minar

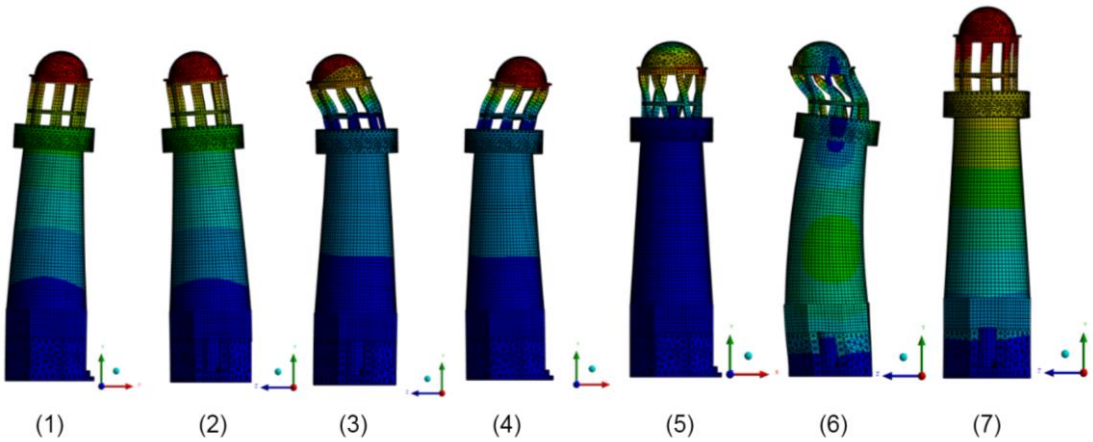

Figure 14. Modal analysis results of Hiran Minar

Table 7. Natural frequencies of Hiran Minar baseline modal

Mode shape	Comment	Frequency (Hz) -Numerical analysis
1	1st Bending in X	3.9
2	1st Bending in Y	3.63
3	2nd Bending in Y	6.23
4	2nd Bending in X	5.7
5	1st Torsion	10.47
6	3rd Bending	14.54
7	1st Vertical	18.02

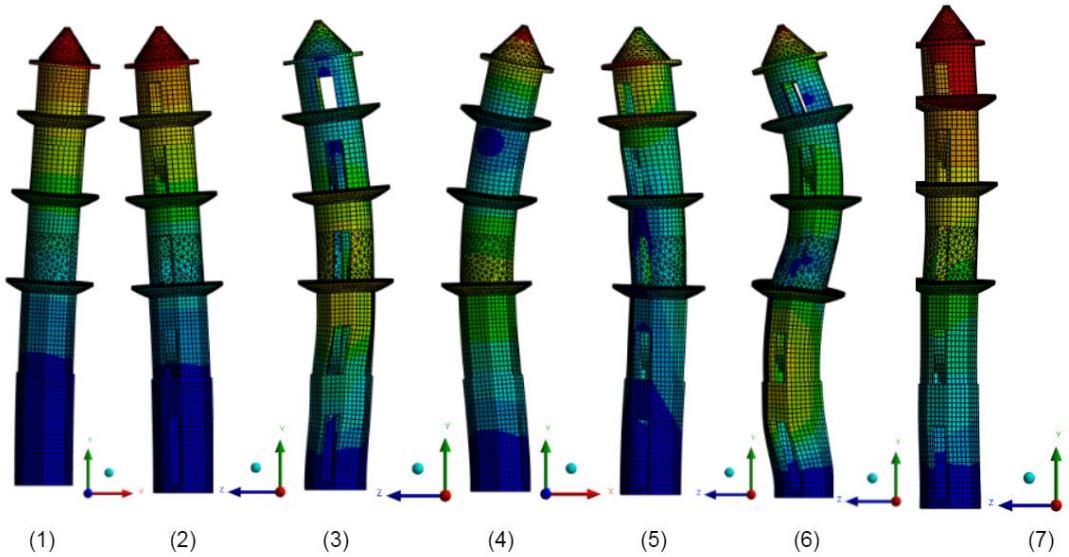

Figure 15. Modal analysis results of Hiran Minar

Table 8. Natural frequencies of Jhulta Minar baseline modal

Mode shape	Comment	Frequency (Hz) -Numerical analysis
1	1st Bending in X	3.19
2	1st Bending in Y	3.98
3	2nd Bending in Y	6.2
4	2nd Bending in X	5.71
5	1st Torsion	11.89
6	3rd Bending	15.6
7	1st Vertical	17.4

4.6 Nonlinear time history analysis

Time-history analyses were performed to assess the minarets' seismic behaviour, using ten chosen earthquake acceleration records. The dynamic analyses considered all three earthquake components in the North-South (X), East-West (Y), and Up-Down (Z) directions,

applied concurrently to the structure. Table 9 presents the properties of the selected ground motion records. Through nonlinear time history analysis, the drift of each storey of the minaret and the base shear value due to each earthquake were obtained as outputs.

A vulnerability index is a measure of a structure's susceptibility to damage from seismic events. The index can be used to categorize structures into different levels of vulnerability, such as low, medium, moderate, and high. The specific thresholds used to categorize structures into these different levels of vulnerability will depend on the methodology used to develop the index and the specific characteristics of the structures being assessed. In general, a lower index value indicates a higher level of vulnerability. The vulnerability index is determined using the maximum inter-story drift ratio and the maximum base shear as indicators. The results highlight the building's vulnerability to earthquakes based on a comparison of the calculated index with the allowable limits defined by the relevant design codes and standards. The maximum inter-story drift ratio measures the relative displacement between consecutive floors during an earthquake. It is expressed as in percentage. Through numerical analysis, the maximum inter-story drift ratio for the building was determined. The maximum base shear represents the total lateral force acting at the base of the building during an earthquake.

The vulnerability index is calculated using the following formula:

Vulnerability Index = $(\Delta_{max} \times V_{max}) / (\Delta_{a} \times V_{a})$

where, Δ_{max} = Maximum Interstory Drift Ratio

V_{max} = Maximum Base Shear

Δ_{a} = Allowable Interstory Drift Ratio

V_{a} = Allowable Base Shear

The allowable interstory drift ratio and allowable base shear in the minarets were calculated based on IS 16700 : 2017 and IS 1893 (Part I). A lower index value indicates a higher level of vulnerability. In seismic performance assessment, the vulnerability index serves as an important metric to categorize buildings based on their level of vulnerability. The suggested vulnerability index thresholds for minarets are as follows:

1. High Level of Vulnerability: Minarets with an index value below 0.2 are considered to have a high level of vulnerability. This indicates that the seismic performance of these minarets is significantly below the acceptable limits, making them more susceptible to damage during earthquakes.
2. Moderate Level of Vulnerability: Minarets with an index value between 0.2 and 0.4

are classified as having a moderate level of vulnerability. These minarets exhibit relatively better seismic performance compared to those with high vulnerability. However, they still require attention and potential structural improvements to enhance their resistance to seismic forces.

3. Medium Level of Vulnerability: Minarets with an index value between 0.4 and 0.6 are considered to have a medium level of vulnerability. While their seismic performance is relatively better, there is still room for improvement to enhance their resilience against earthquakes.
4. Low Level of Vulnerability: Minarets with an index value above 0.6 are classified as having a low level of vulnerability. These minarets demonstrate a satisfactory seismic performance, indicating that they are less prone to damage during earthquakes. However, regular inspections and maintenance should still be carried out to ensure their continued resilience.

The relationship between vulnerability, height and PGA is shown in Figure 16. From the scatter plot, it is clear that the minarets under consideration fall into the moderate to medium vulnerability class.

4.7 Prediction model for seismic vulnerability assessment

4.7.1 Random Forest model training

Random Forest (RF) is a machine learning algorithm known for its robustness and advantageous features, making it suitable for various applications. It offers benefits such as fast training, scalability and relatively high accuracy, even when working with small datasets. One key advantage of RF is its ability to mitigate overfitting, making it particularly valuable for this study. During the training phase of the Random Forest model, a model is constructed using the training dataset. 100 decision trees are utilized to form the Random Forest. The algorithm learns from the training data to understand the relationships between the input features (minaret parameters and earthquake data) and the target variable (seismic vulnerability). By combining the predictions from each individual decision tree, the Random Forest algorithm produces an aggregated prediction. This aggregation process results in a more robust and accurate estimation of the target variable, improving the overall predictive performance of the model [14].]

4.7.2 Model evaluation

The results show the performance of Random Forest model in predicting the seismic vulnerability of minarets. The model is evaluated using two metrics: mean squared error

(MSE) and mean absolute error (MAE). The MSE measures the average squared difference between the predicted and actual vulnerability values, while the MAE measures the average absolute difference between the predicted and actual vulnerability values. Lower values for both metrics indicate better model performance. In this study, the model trained on the training data achieved an MSE of 0.0036 and an MAE of 0.05 on the validation data. These values indicate that, on average, the model's predictions are relatively close to the actual vulnerability values.

Table 9. Selected earthquake details

No	Name of the earthquake	Date	Magnitude	Maximum ground motion acceleration (g)		
				X	Y	Z
1	Bhuj/Kachchh	2001-01-26 03:16:40 UTC	7.0	0.08	0.10	0.07
2	India-Burma border	1997-05-08 02:53:15 UTC	5.6	0.11	0.13	0.03
3	India-Burma border	1995-05-06 01:59:07 UTC	6.4	0.10	0.08	0.04
4	Uttarkashi	1991-10-19 21:23:15 UTC	7.0	0.24	0.25	0.29
5	India-Bangladesh border	1988-02-06 14:50:45 UTC	5.8	0.11	0.10	0.10
6	NE India	1986-09-10 07:50:26 UTC	4.5	0.13	0.11	0.06
7	Chamba	1995-03-24 11:52:33 UTC	4.9	0.12	0.14	0.08
8	Chamoli aftershock	1999-03-30 21:02:10 UTC	5.3	0.03	0.04	0.02
9	Tibet-India border	1996-03-26 08:30:25 UTC	4.8	0.07	0.03	0.03
10	Chamoli aftershock	1999-05-07 17:12:02 UTC	4.5	0.02	0.03	0.02

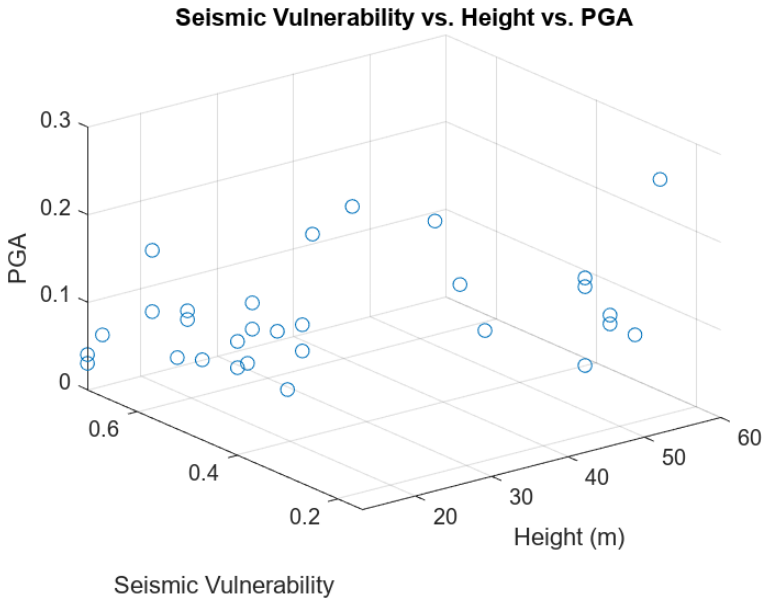

Figure 16. Seismic vulnerability plot

The model was also used to predict the seismic vulnerability of a new minaret with a height of 40 meters, a base width of 1.5 meters and for a PGA of 0.15g. The predicted vulnerability for this minaret using the model trained on the training data is 0.33618. These metrics provide insights into how well the Random Forest model performs in estimating the seismic vulnerability of the minarets in the validation set.

4.7.3 Cross-validation

To further evaluate the generalizability of the Random Forest model, cross-validation is performed. The dataset is divided into k (in this study, k=5) folds, and the model is trained and evaluated k times, each time using a different combination of training and validation data. The average MSE and MAE values are then calculated from the results of the cross-validation. The model's performance was also evaluated using k-fold cross-validation with k=5 folds. The average cross-validation MSE and MAE were 0.0039 and 0.055, respectively. These values are slightly higher than the MSE and MAE obtained on the validation data, indicating that the model's performance may vary depending on the data used for training and validation. The average predicted vulnerability for the new minaret using the models trained on each of the cross-validation folds is 0.34373. This value is similar to the predicted vulnerability obtained using the model trained on the training data.

Overall, the Random Forest model shows promising performance in predicting the seismic vulnerability of the minarets. The input features for the model are minaret parameters and earthquake data, while the target variable is seismic vulnerability. The low MSE and MAE values indicate that the model can accurately estimate the vulnerability levels, while the cross-validation results suggest that the model's performance is consistent across

different subsets of the data. These findings demonstrate the effectiveness of the Random Forest model in assessing the seismic vulnerability of masonry minarets and provide confidence in its reliability for future predictions. The findings indicate that the Random Forest model can reasonably accurately forecast seismic vulnerability, but there may be room for improvement.

5. Enablers and Barriers

The following are the enablers deduced from this study:

- Development of new research connections: A fellowship in hand provided crucial support to pursue challenging research with confidence
- Technological tools and equipment: The utilization of advanced technological tools and equipment, such as accelerometers, drones and Finite Element (FE) modelling software, enhanced the precision and efficiency of the assessment process
- Interdisciplinary collaboration: Collaboration between experts from various disciplines, including civil engineering, architecture and heritage conservation (Archaeological Survey of India), was crucial for a comprehensive assessment of seismic vulnerability

The following are the barriers deduced from this study:

- Fragmented or incomplete historical records made it difficult to gather accurate information about the heritage structure
- Limited accessibility and permissions: Some areas of heritage structures had limited accessibility due to their cultural significance, restricted public access or safety concerns

6.Key Takeaways from CDRI Fellowship Programme

The CDRI Fellowship Programme, with its focus on research excellence, collaboration, practical application, professional development and exposure to industry challenges, significantly impacted our research project. We are grateful for the support and opportunities provided by CDRI, as they played a pivotal role in the success and relevance of our collaborative research efforts.

The Community of Practice was instrumental in enhancing our understanding of each other's research. We believe that in-person meetings with the Fellows could have further strengthened our collaborations and taken effective communication to a higher level.

The virtual platform provided valuable interactions, but the benefits of face-to-face engagement should be considered for future iterations of the CDRI Fellowship Programme.

7.Conclusion

In conclusion, vibration-based structural condition assessment had proven to be a conventional and effective approach for detecting key characteristics of structural mechanisms. However, accurately identifying the dynamic properties of historical monuments was essential to ensure the reliability of the assessment process. Overall, this research combined vibration-based structural condition assessment, numerical modelling, nonlinear dynamic analysis, and machine learning to provide a comprehensive framework for evaluating and predicting the seismic behaviour of heritage minarets. The outcomes of this study could contribute to the preservation and maintenance of historical structures by offering valuable insights into their structural response and potential vulnerability to seismic events. Moving forward, the proposed methodology could serve as a foundation for future research and practical applications in the field of structural engineering and cultural heritage preservation. By continuing to develop and refine these techniques, it may be possible to improve the accuracy and reliability of structural assessments for heritage structures, helping to ensure their preservation for future generations.

8.Way Forward

This research combines vibration-based structural condition assessment, numerical modelling, nonlinear dynamic analysis, and machine learning to provide a comprehensive framework for evaluating and predicting the seismic behaviour of heritage minarets. The outcomes of this study have significant implications for the preservation and maintenance of historical structures, as they offer valuable insights into their structural response and potential vulnerability to seismic events. The following recommendations outline the way forward based on the findings of this research:

1. Preservation and maintenance: The findings of this study can be utilized to prioritize preservation and maintenance efforts for heritage minarets. By identifying the structural response and vulnerability of these structures to seismic events, appropriate retrofitting and strengthening measures can be implemented to ensure their long-term preservation
2. Risk assessment and planning: The comprehensive framework developed in this research can be utilized to conduct risk assessments for heritage minarets in

seismic-prone regions. This will enable stakeholders to prioritize resources and plan for potential seismic events, thereby minimizing the risk to these historical structures

3. Structural rehabilitation and retrofitting: The insights gained from the numerical modelling and nonlinear dynamic analysis can guide structural rehabilitation and retrofitting strategies for heritage minarets. By incorporating the identified vulnerabilities into retrofitting plans, the seismic resilience of these structures can be enhanced while preserving their historical integrity
4. Guidelines and standards: The proposed methodology can contribute to the development of guidelines and standards for the evaluation and seismic design of heritage minarets. These guidelines can provide recommendations for assessing the structural condition, monitoring techniques and retrofitting strategies specific to these unique structures, ensuring their preservation for future generations
5. Future research: This research serves as a foundation for future studies in the field of structural engineering and cultural heritage preservation of minarets in India. Further investigations can focus on expanding the dataset, refining the machine learning algorithms and exploring advanced techniques to improve the accuracy and efficiency of assessing the seismic behaviour of heritage minarets.
6. Applicability in different countries: The machine learning-based approach developed in this study for predicting the seismic vulnerability of heritage minarets in India can potentially be applied to similar structures located in other countries. The methodology, which combines vibration-based structural condition assessment, numerical modelling, nonlinear dynamic analysis and machine learning, provides a comprehensive framework for evaluating and predicting the seismic behaviour of historical masonry constructions.
7. By implementing the recommendations mentioned above, the knowledge gained from this research can be effectively translated into practical applications for the preservation and maintenance of heritage minarets. The collaborative efforts of researchers, structural engineers and conservationists are crucial to ensure the long-term resilience and sustainability of these cultural treasures.

References

1. Ramos, L. F., Casarin, F., Algeri, C., Lourenço, P. B., & Modena, C. (2006). Investigations techniques carried out on the Qutb Minar, New Delhi, India.
2. Peña, F., Lourenço, P. B., Mendes, N., & Oliveira, D. V. (2010). Numerical models for the seismic assessment of an old masonry tower. Engineering Structures, 32(5), 1466-1478.
3. Rai, D. C., Singhal, V., Pradhan, T., & Tripathi, A. (2016). Seismic vulnerability of monastery temples of stone masonry in Sikkim Himalaya. Curr. Sci, 110(10), 1947-1957.
4. Bakhary, N., Hao, H., & Deeks, A. J. (2007). Damage detection using artificial neural network with consideration of uncertainties. *Engineering Structures*, *29*(11), 2806-2815.
5. González, M. P., & Zapico, J. L. (2008). Seismic damage identification in buildings using neural networks and modal data. *Computers & structures*, *86*(3-5), 416-426.
6. Hökelekli, E., Demir, A., Ercan, E., Nohutçu, H., & Karabulut, A. (2020). Seismic assessment in a historical masonry minaret by linear and non-linear seismic analyses. *Periodica Polytechnica Civil Engineering*, *64*(2), 438-448.
7. Kaushik, H. B., Rai, D. C., & Jain, S. K. (2007). Stress-strain characteristics of clay brick masonry under uniaxial compression. Journal of Materials in Civil Engineering, 19(9), 728–739.
8. Gumaste, K. S., Rao, K. S. N., Reddy, B. V. V., & Jagadish, K. S. (2007). Strength and elasticity of brick masonry prisms and wallettes under compression. Materials and Structures, 40, 241–253.
9. Sarangapani, G., Reddy, B. V. V., & Jagadish, K. S. (2002). Structural characteristics of bricks, mortar and masonry. Journal of Structural Engineering (India), 29(2), 101–107.
10. Bayraktar, A., Sevim, B., Altunışık, A. C., & Türker, T. (2009a). Analytical and operational modal analyses of Turkish style reinforced concrete minarets for structural identification. Society for Experimental Mechanics, Dynamic Testing of Civil Engineering Structures Series, March–April, 65-75.
11. Shakya, M., Varum, H., Vicente, R., & Costa, A. (2016). Empirical formulation for estimating the fundamental frequency of slender masonry structures. International Journal of Architectural Heritage, 10(1), 55–66.

12. Kocaman, İ., Kazaz, İ., & Kazaz, E. (2020). Seismic load capacity of historical masonry mosques by rigid body kinetics. International Journal of Architectural Heritage, 14(6), 849-869. https://doi.org/10.1080/15583058.2019.1570389.
13. Kazaz, İ., Gülkan, P., & Kazaz, E. (2021). Numerical assessment of cracks on a freestanding masonry minaret. International Journal of Architectural Heritage, 15(4), 526-547. https://doi.org/10.1080/15583058.2019.1629046.
14. Cutler, D. R., Edwards, T. C., Beard, K. H., Cutler, A., Hess, K. T., Gibson, J., & Lawler, J. J. (2007). Random forest for classification in ecology. Ecology, 88(11), 2783–2792.